Universität Ulm | 89069 Ulm | Germany

Fakultät für
Naturwissenschaften
Institut für
Elektrochemie

Transport Theory for Highly Correlated Electrolytes with Non-Local Species Interactions

Dissertation zur Erlangung des Doktorgrades Dr. rer. nat. der Fakultät für Naturwissenschaften / Mathematik und Wirtschaftswissenschaften der Universität Ulm

Vorgelegt von
Max Josef Schammer
aus München, Deutschland
Erscheinungsjahr 2022

Dekan der Fakultät für Naturwissenschaften
Prof. Dr. Bernhardt

Erstgutachter
Prof. Dr. Arnulf Latz

Zweitgutachter
Prof. Dr. Timo Jacob

Drittgutachter
Prof. Dr. Arik Yochelis

Tag der Promotion
05.07.2023

Declaration of Authorship

Ich versichere hiermit, dass ich die Arbeit selbstandig angefertigt habe und keine anderen als die angegebenen Quellen und Hilfsmittel benutzt sowie die wörtlich oder inhaltlich übernommenen Stellen als solche kenntlich gemacht habe und die Satzung der Universität Ulm zur Sicherung guter wissenschaftlicher Praxis in der jeweils gültigen Fassung beachtet habe.

I hereby declare that I wrote the dissertation independently and used no other aids than those cited. In each individual case, I have clearly identified the source of the passages that are taken word for word or paraphrased from other works.

. . . .

Bobingen, September 06 2022 Max Josef Schammer

Redacted for privacy.

Acknowledgements

Redacted for privacy.

Abstract

The principal research focus of this thesis lies on highly correlated battery electrolytes in the bulk, and near electrified interfaces.

The bulk regime can be characterized as a mesoscopic continuum, which spans over the length scale of a few hundred micrometers. In contrast, the electrochemical double layer (EDL) is a microscopic effect. It is constituted by a charged electrolyte region adjacent to an electrode, and decays towards the electroneutral bulk region with increasing distance from the electrode, typically over some nanometers. As consequence, our research focus spans over various length scales.

In this work, we derive a holistic continuum transport theory for highly correlated electrolytes which captures mesoscopic transport effects of bulk electrolyte, *i.e.* migration, diffusion and convection, and the formation of the EDL in ionic liquids (ILs) near electrified interfaces.

To address this goal, we use the framework of rational thermodynamics (RT), which combines elements from non-equilibrium thermodynamics, mechanics and electromagnetic theory to describe a wide class of materials. RT has a rigorous physics-based foundation which is constituted by mutually coupled universal balancing laws, and the second axiom of thermodynamics. This description takes account for the strong correlations between arbitrary many charged or uncharged electrolyte species, and ensures that the description for the evolution of the system is thermodynamically consistent. The method of Coleman and Noll allows a concise description of the system in the form of constitutive equations via thermodynamic derivatives of the Helmholtz free energy, which is the focal quantity of our constitutive modeling. We obtain a consistent description for the thermodynamic fluxes via using an Onsager approach. This coupling between the fluxes and forces closes our flux-explicit transport theory.

Our manuscript is split into two main parts. In the first part, we present a detailed derivation of our continuum transport theory for the bulk electrolyte. Here, we treat the electrolyte as a continuum at liquid state, and neglect the particle nature of the constituents. This implies that we do not account for microscopic interactions explicitly, but use an averaged description based on macroscopic energy contributions. As consequence, for the bulk, it suffices to focus on modeling the Helmholtz free energy density of the system.

In addition to the balancing laws for mass, momentum, energy and charge, and to the second axiom of thermodynamics, we make use of volume being an extensive

property and account for the volume-filling property of liquid electrolytes.

We use the resulting constraints and identify the independent set of species, fluxes and transport parameters. This simplifies our description and rationalizes the transport theory. Altogether, for an electrolyte mixture composed of N species, we obtain a system of equations which consists of one transport equation for the charges, and N-2 transport equations for the species concentrations. These transport equations are supplemented by the Poisson equation and a heat equation. Because convection plays an important role in electrolyte solutions with high amount of salt, we derive an equation for the convection velocity as function of volume fluxes and local volume productions due to chemical reactions. The set of independent transport parameters follows from the Onsager matrix, and is determined by symmetry arguments, flux constraints and thermodynamic consistency. We clarify the ongoing debate regarding the sign and magnitude of transport parameters via a rational discussion of the frame dependence, and derive transformation rules between different reference frames.

Our consistent coupling of thermodynamics, mechanics and electromagnetic theory yields a constitutive equation for the forces, which accounts for electrostatic forces, Lorentz forces in charged electrolyte regions, forces stemming from volume penalties due to non-equal molar volumes of the species, dissipative friction forces due to the viscosity of the electrolyte, and entropic forces due to concentration gradients. These forces can be supplemented by non-ideal interactions via modification of the thermodynamic factor.

We validate our bulk description for highly correlated electrolytes using numerical methods, and apply it to a zinc ion battery which is based on an electrolyte composed of an IL-mixture with water and salt. A comparison of the simulation results for charging and discharging the battery with experimental results shows that both are quantitatively in very good agreement.

In the second part of this manuscript, we focus on the description of the electrochemical double layer (EDL) of binary ILs and IL / salt mixtures. Typically, the EDL spans over some nanometers, and thus constitutes a system at length scales comparable to the size of the molecules, and the effective range of particle interactions. As consequence, our continuum assumption of a structureless bulk liquid must be relaxed, and we must account for non-local correlations between hardcore particles in our EDL description. For this purpose, we generalize our constitutive approach to modeling the free energy of the system as a functional, with contributions stemming from non-local interactions. Although this does not affect the main structure of our transport theory, it yields constitutive equations in the form of functional derivatives and there appear additional contributions in the transport equations in the form of integrals. In principle, the resulting framework can be used to incorporate a variety of different interactions. Here, we focus on the effect of hardcore particles via modeling a short-ranged repulsive interaction potential.

In a first step, we apply this framework to binary ILs next to electrified interfaces. In this case, the system is completely described by the Poisson equation and one transport equation for the charge.

We show that short-ranged interactions can be approximated systematically by expanding the interaction integral in higher order gradients of the species concentrations. This gradient description has the advantage that it is susceptible to an analytic investigation of the EDL in stationary state, which parametrizes the EDL description and rationalizes the appearance of higher order derivative operators in modified Poisson equations, as recently proposed in this context in the literature. Our analytic analysis of the stationary EDL shows that the charge distribution in the EDL, *i.e.* the shape and width of the long-ranging screening profile, is completely determined by three competing energy scales. These energy scales describe the electrostatic forces between ions, the molecular repulsion between all molecules, and the thermal motion. Depending upon the relative magnitude of the three energy scales, the EDL profile of the charge density can have three different shapes. For negligible molecular repulsion, the screening profile is determined by the competition between charge ordering (due to electrostatics) and thermal disordering, and decays exponentially. However, in the case where the repulsion between molecules is comparable with the thermal energy and the Coulomb interactions, the EDL spans over some ion diameters and is characterized by a nanostructured electrolyte region with charge oscillations ("overscreening"). Finally, once the molecular repulsion becomes dominant, the bulk electrolyte undergoes a phase transition into ionic layers, and the EDL spans over the complete electrolyte region. Eventually, upon further increase of molecular repulsion, the layered structure phase separates into pure ionic layers. We confirm the instability onset of the stationary electrolyte via a linear stability analysis of our dynamical description with respect to the electroneutral bulk state.

Depending upon the magnitude of the electrode polarization, the charge profile saturates near the interface ("crowding"). However, in contrast to the effect of overscreening, this is a "bulk effect" which happens independently from molecular repulsion, and results from the assumption of finite molar volumes. The two characteristic parameters of this crowding effect, *i.e.* the width of the saturation layer and the maximal charge density, are both predicted by our framework.

Our description allows the complete analytical reconstruction of the charge distribution in the EDL. In particular, it predicts the saturation width, the damping parameter, the oscillation frequency and the exact phase boundaries between the three screening phases as function of the energy scales. We validate our description by comparing the EDL forces as obtained from our theory with experimental results obtained from AFM measurements.

We also we apply our EDL formalism to a ternary electrolyte mixture composed of a neat IL with a minor salt. Via an analytic discussion of the stationary state, we predict the critical amount of salt additive, which is necessary to perturb the interface screening by the IL ions, and validate our theoretical prediction using experimental results.

Altogether, our theoretical description yields a rigorous multiscale methodology from atomistic quantum chemistry calculations to phenomenological continuum models. We identify the interaction contribution appearing in the chemical potential with the pair correlation function used in atomistic frameworks and liquid state theory. Also, we rationalize phenomenological continuum EDL models proposed in the literature, *e.g.* the BSK approach, which are comprised in our framework as limiting cases. Furthermore, macroscopic thermodynamic descriptions for ion correlations in non-ideal electrolytes, *e.g.* the Flory Huggins approach, can be obtained from our functional approach via the method of coarse graining.

Teile dieser Dissertation wurden bereits in folgenden Fachartikeln veröffentlicht.

- V. Hoffmann, G. Pulletikurthi, T. Carstens, A. Lahiri, A. Borodin, M. Schammer, B. Horstmann, A. Latz and F. Endres, Phys. Chem. Chem. Phys., 2018, 20, 4760; DOI: 10.1039/C7CP08243F; Publiziert unter der Lizenz CC BY-NC 3.0, https://creativecommons.org/licenses/by-nc/3.0/
- Schammer, Max, Birger Horstmann, and Arnulf Latz. "Theory of transport in highly concentrated electrolytes." Journal of The Electrochemical Society 168.2 (2021): 026511. DOI: 10.1149/1945-7111/abdddf; Publiziert unter der Lizenz CC BY 4.0, https://creativecommons.org/licenses/by/4.0/
- Schammer, Max, Arnulf Latz, and Birger Horstmann. "The role of energy scales for the structure of ionic liquids at electrified interfaces: A theory-based approach." The Journal of Physical Chemistry B 126.14 (2022): 2761-2776. DOI: 10.1021/acs.jpcb.2c00215; Publiziert unter der Lizenz CC BY-NC-ND 4.0, https://creativecommons.org/licenses/by-nc-nd/4.0/

Contents

I Introduction 1

1 Introduction 2

2 Methods: Continuum Modeling, Rational Thermodynamics a nd Computer Simulations 7
- 2.1 Continuum Modeling of Liquid Electrolytes 7
- 2.2 Rational Thermodynamics 9
- 2.3 Computer Simulations From The Perspective of The Philosophy of Science 10

3 Literature Review 13
- 3.1 Modeling of Battery Systems 13
- 3.2 Modeling the Electrochemical Double Layer for Ionic Liquids 15

4 Outline 19

II Transport Theory For Highly Correlated Liquid Electrolytes 20

5 Transport Theory 22
- 5.1 Thermo-Mechanical Balance Laws 23
  - 5.1.1 Balance of Total Mass, Partial Masses and Charges 23
  - 5.1.2 Mechanics: Momentum Balance 26
  - 5.1.3 First and Second Axiom of Thermodynamics: Energy and Entropy 30
- 5.2 Coupling to Electromagnetism 32
  - 5.2.1 Maxwell's Equations in Matter 33
  - 5.2.2 Unification of Mechanics, Thermodynamics and Electromagnetism: Electromagnetic Entropy Inequality 34
  - 5.2.3 The Method of Coleman and Noll 36

5.2.4 Electrostatic Limit 44
5.3 Flux Densities 45
5.3.1 Linear Flux-Force-Couplings 46
5.3.2 Viscosity Tensor 51
5.4 Model For Correlated Liquid Electrolytes 53
5.4.1 Free Energy Density 53
5.4.2 Excluded Volume Effects: Partial Molar Volumes and Euler Equation for the Volume 58
5.4.3 Incompressible Electrolytes And Mechanical Equilibrium . . . 65
5.4.4 Convection Equation 66
5.4.5 Isothermal Equations of Motion 67
5.4.6 "Standard Electrolyte": Ternary System with Neutral Solvent 71
5.4.7 Characterization of Highly Concentrated Electrolytes 74
5.5 Frame Independent Formulation 77
5.5.1 Introduction 77
5.5.2 Universal Convection Velocity 77
5.5.3 Transformation of Reference Frame 83
5.5.4 Internal And External Frames of Reference 87
5.5.5 Comment on Transference Numbers in Binary Electrolytes . 90
5.5.6 Relation to Experiments 90

6 Validation: Quaternary IL-mixture as Electrolyte in a Zinc-Ion Battery 93
6.1 Electrolyte Transport Equations and Electrolyte Composition 93
6.1.1 Reactions and Electrolyte Species 93
6.1.2 Model Equations 95
6.2 Simulation Results 96
6.2.1 Electrolyte Dynamics: Diffusion, Migration and Convection . 96
6.2.2 Increased Electrolyte Dynamics 103
6.2.3 Consistency Check: Varying Reference Species 105
6.3 Electrolyte-Classification 110

III Rational Continuum Modeling of Non-Local Interactions in Liquid Electrolytes 111

7 Introduction 112

8 Modeling Non-Local Interactions in Liquid Electrolyte Transport Theories 115
8.1 Generalized Transport Theory: Functional Formalism 115
8.2 Model for Interacting Liquid Electrolytes 118
8.3 Potentials of Molecular Interactions 120
8.4 Gradient Expansion of Molecular Interactions 122

9 Molecular Interactions in Binary IL Electrolyte 124
9.1 Transport Theory of Binary IL Electrolytes with Molecular Interactions 124
9.2 Energy Scales and Dimensions 127
  9.2.1 Special Case: Symmetric Ion Species ($\chi = 0$) 131
  9.2.2 Non-Convective Case ($\mathbf{v} = 0$) 132
9.3 Stationary State 132

10 Static Asymptotic Analysis 134
10.1 Small and Large Potentials 134
10.2 Mean Steric Effect: Charge Saturation 135
  10.2.1 Static Asymptotic Analysis: Small Potentials $|\tilde{\Phi}| \ll 1$ 135
  10.2.2 Static Asymptotic Analysis: Large Potentials $|\tilde{\Phi}| \gg 1$ 136
  10.2.3 Mean Volume Effect: Symmetric Ions 139
10.3 Non-Local Interactions: Charge Oscillations 140
  10.3.1 Static Asymptotic Analysis: Large Potentials $|\tilde{\Phi}| \gg 1$ 140
  10.3.2 Static Asymptotic Analysis: Small Potentials $|\tilde{\Phi}| \ll 1$ 140
  10.3.3 Double Layer Forces 145
  10.3.4 Analytical Construction of the Screening Profile 146
  10.3.5 Special Case: Zero Order Expansion 146
  10.3.6 Special Case: First Order Expansion 147
10.4 Dynamic Asymptotic Analysis: Linear Bulk-Stability Analysis 148

11 Interaction Model for Hardcore Particles 151

12 Numerical Simulations of the EDL-Structure of Binary ILs 156
12.1 Binary IL-Electrolyte: PYR[1,4]TFSI 156
12.2 Mean Volume Effect 157
  12.2.1 Numerical Simulations: Mean Steric Effect 157
  12.2.2 Analytical Discussion of EDL Screening: Mean Steric Effect . 161
12.3 Non-Local Interactions 162
  12.3.1 Numerical Simulations: Molecular Interactions 163

13 EDL Structures of Ternary Electrolytes: Mean Steric Effect 176
13.1 Transport Theory of Ternary Electrolytes . . . 176
13.2 Numerical Simulations . . . 177
13.3 Stationary State . . . 179
13.4 Static Asymptotic Analysis: Minor Salt Species . . . 180

14 Validation of Our EDL Description With Experiment 182

IV Discussion of Our Multi-Scale Methodology 185

15 Comparison with Literature and Theory 187
15.1 Thermo-Electro-Mechanical Balance Laws . . . 187
15.2 Comparison with the Extended Stefan-Maxwell Approach ("Newman-Model") . . . 189
15.3 From Molecular Dynamics to Non-Equilibrium Thermodynamics . . 193
15.4 From Non-Equilibrium Thermodynamics to BSK Theory . . . 195

16 Coarse Graining: From Non-Local Microscopic Correlations to Macroscopic Phenomenological Thermodynamic Properties 197
16.1 Coarse Graining of Microscopic Interactions . . . 198
16.2 Flory Huggins Solution Theory . . . 199
16.3 Mean Steric Effect . . . 199

V Conclusion and Outlook 204

VI Appendix 208

A Numerical Methods 209
A.1 Numerical Implementation . . . 209
A.2 Numerical Differentiation . . . 210
A.3 Boundary Conditions . . . 212
A.4 Numerical Aspects of Cell Simulations . . . 214
A.5 Numerical Aspects of EDL Simulations . . . 215

B Covariance, Invariance and Symmetry 216
B.1 Introduction . . . 216

B.2 Tensor Formalism . . . 217
B.3 Covariant Formulation of Electrodynamics . . . 218
B.4 Electromagnetic Energy-Momentum Tensor . . . 223
B.5 Euclidean Transformation: Material Frame Indifference . . . 225
B.6 The Role of Symmetry in Rational Thermodynamics . . . 227
B.7 Covariant Unification . . . 232

C Balance Equations for Volumes **233**
C.1 Mathematical Introduction . . . 233
C.2 Global Structure of Balance Laws for Volumes . . . 235
C.3 Transport Theorems for Volumes and Surfaces . . . 235

D Appendix to Part II **237**
D.1 Dimensional Analysis of Maxwell's Equation . . . 237
D.2 Unimodular Deformation Energy . . . 238
D.3 Evaluation of the Poynting Flux . . . 241
D.4 Derivation of Stress Imbalances . . . 242
D.5 Modeling Energy of Deformation . . . 243
D.6 Interpretation of The Strain Rate Tensor . . . 243
D.7 Matrix Formulation of Transport Equations . . . 244
D.8 Transformation of Reference Species . . . 248
D.9 Validation: Supporting Information . . . 254
D.10 Thermal Aspects . . . 258
  D.10.1 Heat Equation . . . 259
  D.10.2 Hydrodynamical Expansion . . . 260

E Appendix to Part III **266**
E.1 Gradient Expansion . . . 266
E.2 Functional Derivative . . . 268
E.3 Symmetry of Conservative Interaction Potentials . . . 269
E.4 Phase Space Analysis . . . 269
E.5 Validation: Supporting Information . . . 272

Bibliography **274**

Part I

Introduction

1 Introduction

The political and social demand for a transition of the energy landscape and of the transportation systems has increased in the last few decades. The main driving forces result from arguments based on climate change, and, recently, from geopolitical developments.

In Germany this trend has been picked up by legislation, and has become federal law in the course of the so-called “Energiewende”. This national endeavour is embedded in the “Energy Union Strategy” of the European Commission, with the goal to reduce the emission of green house gases, and to transition the domestic energy market towards so-called “renewable” and “alternative” energies, *e.g.* nuclear, solar or wind power. This includes transportation, heat and electricity. [1]

Electromobility is one important pillar in this national strategy. It describes the usage of vehicles which are powered fully or partially by batteries, in contrast to vehicles based on combustion engines. An increase in electromobility can have a positive effect on the release of green house gases.

The second pillar of the "Energiewende" is focused on increasing the fraction of green energy sources. This includes conventional energy sources, *e.g.* sources based on nuclear and gas, but also renewable energy sources, *e.g.* solar and wind. However, the renewable energy sources have the disadvantage of a fluctuating production rate. One strategy to address this problem is to develop an efficient infrastructure for the flexible intermediate storage of electrical energy, which can help to balance energy consumption and production. This requirement can be fulfilled by large scale battery systems.

Thus, the legislative act of the "Energiewende" constitutes a huge stimulus for the development of safe, ecologically friendly and high-performance batteries on multiple scales.

Beneath the (geo-)political landscape, this demand becomes also visible in our daily life. Many devices which are in practical use, such as laptops and cell phones, are powered by batteries. Thus, their performance is limited by the electric energy provided by the batteries.

Basic battery set up Batteries are electrochemical devices which are constructed with the purpose of being used only once (primary battery), or with the purpose of being used many times (secondary batteries). In the context discussed above, secondary batteries, *i.e.* rechargeable batteries, are the main focus. The basic functionality of a battery is the conversion of potential energy, in the form of chemical energy, into electrical energy.

Basically, the configuration of a battery cell consists of six components: two current collectors, a positive and negative electrode separated by an electrically isolating, porous separator and an electrolyte solution.[2]

During discharge, the negative electrode is called anode, whereas the positive electrode is called cathode. In standard lithium ion batteries (LIBs), both consist of porous materials, which increase the effective surface area and capacity of the electrodes.[3] The anode of LIBs is typically made of graphite, which is a soft form of carbon, but also different materials have been commercialized, *e.g.* lithium titanate oxide (LTO). Different commercialized cathode materials exist in LIBs, mainly based on material compositions such as lithium manganese oxide (LMO), lithium cobalt oxide (LCO), lithium iron phosphate (LFP) or lithium nickel manganese cobald oxide (NMC).[4,5]

The electrolyte is immersed in the region between both electrodes and the separator. The most widely used types of electrolytes in LIBs are based on Lithiumhexafluorophosphat (LiPF6), dissolved in a mixture of different aprotic solvents.[6] To improve specific electrolyte properties, various additives are added to this solution.[7]

The main objective of the separator is to prevent electrical contact between the electrodes ensuring ionic transport. Usually, these consist of porous membrane materials.[8]

Each of these components influences the performance of the complete cell individually, but also in conjunction with the other components. However, this manuscript focuses on liquid electrolytes.

Electrolytes: Highly Concentrated Electrolytes And Ionic Liquids The electrolyte plays a fundamental role for the performance of the battery.[9–18] There are two main purposes of the electrolyte. First, it serves as a medium acting as an ion conductor, but electron insulator, which should facilitate the transport of ions between pairs of electrodes. Simultaneously, the electrolyte has to withstand the strong oxidizing and reducing forces of the electrodes. These two properties constitute the major metrics of electrolyte design.[13] However, this also involves a trade-off in the electrolyte choice. For example, aqueous electrolytes are often highly conductive, whereas non-aqueous electrolytes usually exhibit enhanced electrochemical stability.[19] For this reason, non-aqueous electrolytes are mainly used in LIBs, with some compromise on ionic transport properties.[20]

However, despite the property that electrolytes in LIBs do not participate in Faradaic reactions at the electrodes, they contribute actively to the interfacial region and make a significant contribution to the performance of LIBs. Due to the thermodynamic instability at the solid / electrolyte interface, a passivating layer is formed ("SEI"), which stabilizes the interface kinetically.[21] The SEI formation is crucial for the operation of LIBs, and depends strongly on the electrolyte composition.[22]

The novel class of superconcentrated aqueous electrolytes, so-called "water-in-salt" electrolytes (WiSE) based on extremely high lithium salt contents (>21 mol LiTFSI in 1 kg H_2O),[23] constitutes a promising type of hybrid aqueous / non-aqueous electrolyte, combining high safety and ionic conductivity of water with a large electrochemical stability window. These electrolytes form an aqueous SEI on various anode surfaces consisting of inorganic metal species.

Ionic liquids (ILs) (also, room temperature ionic liquids) are another class of promising electrolytes.[24–34] From a continuum modeling perspective, ILs constitute the extreme limit of highly concentrated electrolyte, where the amount of neutral solvent vanishes. Although there is no clear definition of ILs,[35] they usually are referred to as salts with melting points below 100 °C.[36] ILs share many properties with molten salts, although molten salts are usually viewed as the high-temperature analogons of ILs. They are typically composed of organic cations and inorganic anions.[37,38] Strong correlations between the complex ions imply various beneficial properties. Among them are a low volatility / negligible vapor pressure, low fammability, high thermal and electrochemical stability (large electrochemical window), high ionic conductivity, and the ability to solvate compounds of widely varying polarity.[39] Furthermore, there a exists a countless number of different configurations of ILs, which allows to tailor-cut them into task specific electrolytes.[40]

ILs posses characteristic properties in the bulk and near electrified interfaces. This makes them highly attractive from a fundamentals point of view. Due to their high amount of salt concentration, convection plays an important role for transport processes. As consequence, the dynamical description based on internal reference frames can deviate significantly from the dynamics as described by an external frame. This has led to some confusion regarding sign and magnitude of transport parameters in ILs,[41–44] although the basic tenet was already well understood in the molten salt chemistry some decades ago.[45–47] Near electrified interfaces, ILs form lang-ranging charged structures, which can span up to several nanometers into the bulk electrolyte.[48] This increased screening length of the electrochemical double layer (EDL) depends upon the structure of the IL molecules, the system parameters, as well as on the boundary conditions.[48,49] In principle, these influences can be used to tune the EDL such that the resulting kinetic hindrance stabilizes the bulk electrolyte, eventually allowing for a control of the Faradaic processes occurring at the interface, *i.e.* chemical reactions.[50–54]

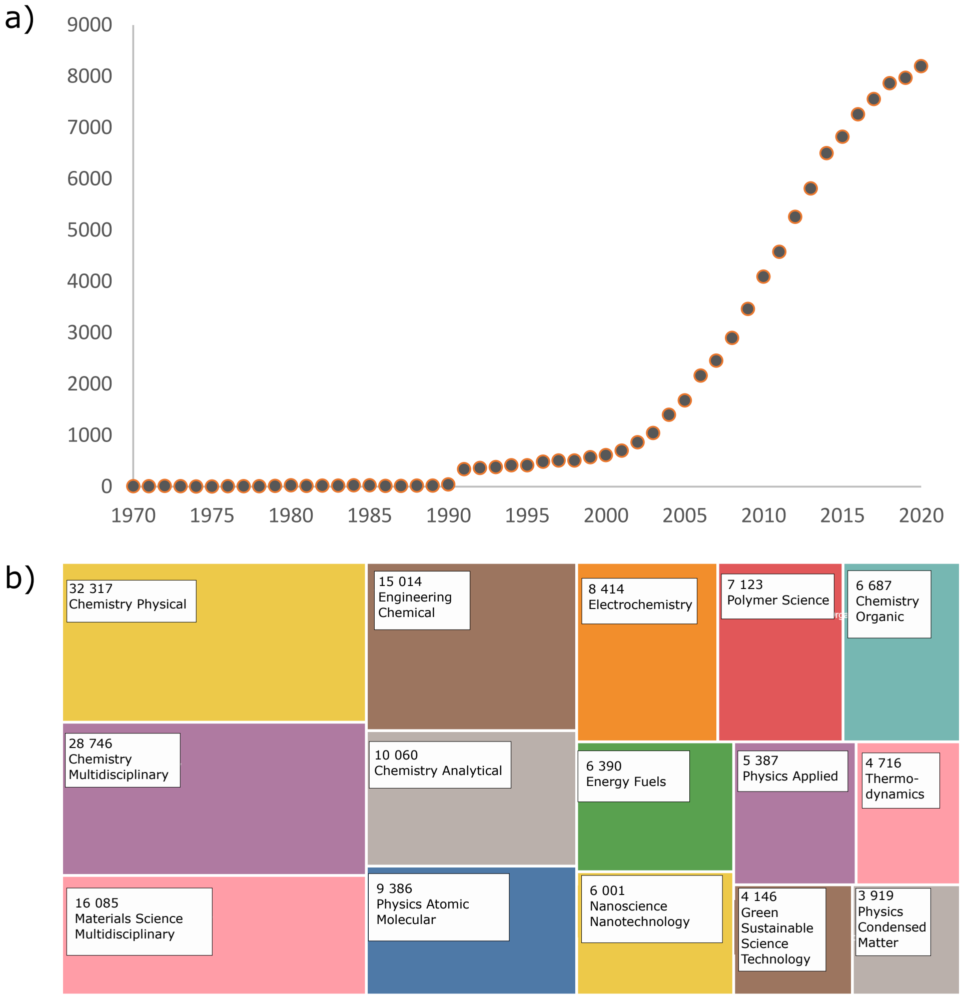

Figure 1.1: List of IL related publications per year and per discipline.

These features make ILs and molten salts highly interesting for a large variety of applications, *e.g.* in energy science, catalysis, pharmaceutics, nuclear fuel reprocessing, waste recycling to name just a few.[55–59] The increased interest in ILs over the past few decades is shown in fig. 1.1, which illustrates the number of publications related to ILs per year (upper figure) and per discipline (lower figure). Apparently, the number of publications has increased almost exponentially over the period between 1995 and 2015, where the range of disciplines covered by these publications spans from fundamental science to industry applications.

Modeling of Battery systems In industry and science there is a clear trend towards more model-based and computer-aided analyses. Modeling can serve as a predictive tool to improve the battery performance, *e.g.* via material recommendations, or optimized geometries for the cell set-up.

However, electrochemical devices are complex systems, which involve effects spanning across multiple phases, and multiple-length scales. The relevant scales span from the microscopic scale involving several atoms, *e.g.* nucleation or intercalation processes, across the mesoscopic scale, *e.g.* transport through porous media, up to the macroscopic scale, *e.g.* thermal management of battery packs. Accordingly, depending upon the focus, different modeling approaches exist.

Because of limited computational resources the discretization of the battery geometry cannot be chosen such that all length scales are properly resolved. Thus, there exists a plethora of different models which constitutes a multi-level and multi-physical landscape of applications. Microscopic processes can be resolved by means of quantum mechanical modelling, *e.g.* Density Functional Theory (DFT) or Ab Initio Molecular Dynamics (AIMD). Meoscopic processes are mostly analyzed using continuum models based on thermodynamics, electrodynamics and mechanics. Finally, macroscopic systems can be described by continuum theories or phenomenological theories, *i.e.* mean field theories and equivalent circuit models.

These different modeling methodologies vary in accuracy and effort. The predictability but also the computational costs of microscopic methods are very high. In contrast, mesoscopic and macroscopic methods exhibit usually a limited predictability combined with the advantage of low computational cost. In addition, they depend crucially on an accurate knowledge of system parameters, which serve as input for evaluating the model. Thus, their applicability can be limited because the experimental determination of such parameters is a challenging task.

2 Methods: Continuum Modeling, Rational Thermodynamics and Computer Simulations

In this chapter we discuss the main theoretical methods used in this work. First, in section 2.1, we discuss the principles of continuum modeling of physical systems at liquid state. Next, in section 2.2, we give a brief summary of the framework of rational thermodynamics which constitutes the theoretical basis for the derivation of our transport theory. Finally, in section 2.3, we give a brief characterization of computer simulations.

In addition, we discuss the numerical methods used in this work in great detail in the appendix, see appendix A.

2.1 Continuum Modeling of Liquid Electrolytes

In this section, we describe the basic assumptions underlying the methodology of continuum modeling for fluids and liquids.

The goal of this work is to derive a continuum transport theory for highly concentrated multi-component electrolytes, and ionic liquids, which applies to bulk effects, and to the electrochemical double layer (EDL). The fundamental assumption underlying our continuum modeling is the continuum hypothesis for liquids.[60,61] This assumption applies to the description of physical systems on a mesoscopic or macroscopic scale, where all physical variables emerge from microscopic quantities via averaging in a representative volume element $\mathrm{d}V$ of the system.[62] By assumption, the continuum hypothesis neglects the particle nature of the system and erases microscopic discontinuities. The advantage of the continuum hypothesis lies in the property that averaged quantities, *e.g.* free energy, temperature, density, pressure, velocity, can be assumed to vary continuously in space. However, this requires that the representative volume element $\mathrm{d}V$ must be large enough such that statistical fluctuations do not lead to significant fluctuations of the averaged quantities. Yet, at the same time, $\mathrm{d}V$ must be small enough to capture macroscopic variations, *e.g.* velocity or concentration gradients.[63] Typically, such representative volume elements are assumed on the order of cubic microns.[61] This is in accordance with the continuum description of bulk transport in electrolytes, where the typical length scales are on the order of microns ($1\,\mu\text{m}=10^{-6}\,\text{m}$).[64,65] As consequence, it suffices for the modeling of bulk effects to focus on the subsystem of the electrolyte given by the representative volume element $\mathrm{d}V$.

The continuum hypothesis is widely used in fluid mechanics and was already applied in the 18th century. According to L. Euler,[66] "*Physical (fluid) properties are assumed to vary continuously in space and each property is essentially a point function. Discontinuities may only occur across interfaces separating two phases and across shock waves. Differential calculus is applicable.*"

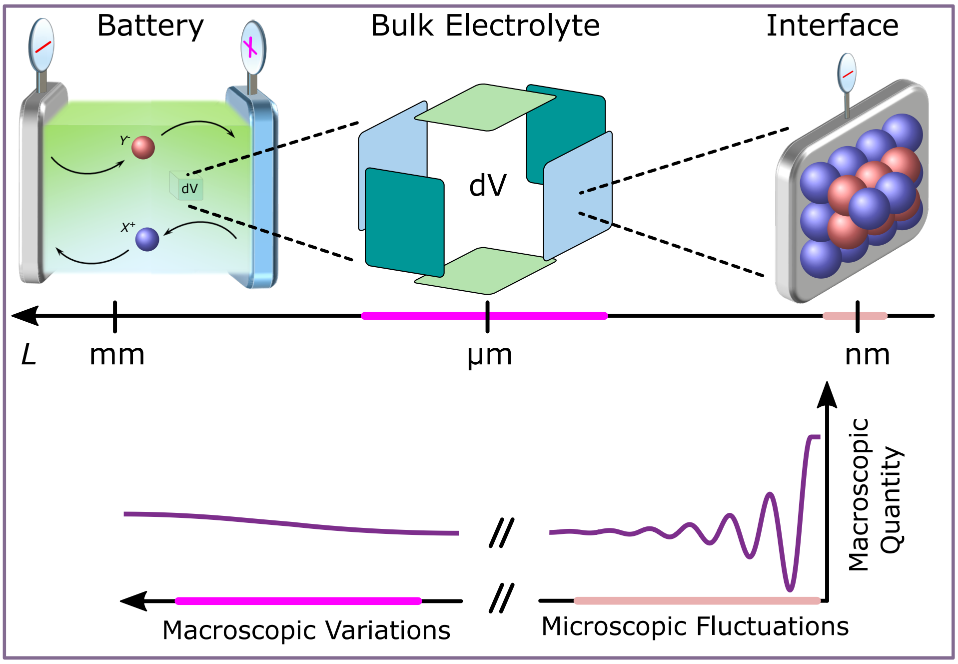

Scheme 2.1: Scheme of the Multi-Scale Methodology. Parts of figure first published in a modified version in Ref. 67 under the license CC BY 4.0, https://creativecommons.org/licenses/by/4.0/.

We use the continuum approach in part II, where we derive our transport theory for highly correlated electrolytes. Thus, our modeling approach for the bulk electrolyte is based on the free energy density, and on differential calculus.

However, the continuum hypothesis becomes deficient for the description of physical systems at microscopic scales, where non-local interactions are dominant.[68] The typical length scale of the electrochemical double layer (EDL) is on the order of nanometers,[48,49] *i.e.* comparable to the diameter of the ions. Furthermore, strong particle interactions play an important role for the formation of equilibrium structures.[69] As consequence, we relax our bulk description based on modeling the free energy density for our description of the EDL, see part III. Instead, we focus on the free energy as a functional, and apply variational calculus for our constitutive modeling.

In Scheme 2.1, we sketch our multi-scale approach and illustrate the different scales of resolution which can be applied when modeling a macroscopic system (here, a battery electrolyte). The resolution by which the system is examined depends upon the effects on which the description is focused. A length bar is shown in the upper subfigure which comprises different scales for the modeling of the real physical system, which can extend over some millimeters. The continuum modeling of the bulk electrolyte focuses on the micrometer scale, see the the intermediate region of the length bar. This description applies to a representative volume, and is based on differential calculus. However, an enhanced resolution is mandatory for the description of microscopic effects, see the right region on the length bar. For this purpose, the continuum assumption must be relaxed, and the system is better described modeling the free energy as a functional (hence, using the calculus of variations for the derivation of the constitutive equations, which take the form of variational derivatives). The lower subfigure in Scheme 2.1 illustrates a representative profile of a macroscopic quantity (here, the ion concentration normalized to the bulk value) on different length scales, *i.e.* different scales of resolution. Typically, profiles for the ion concentrations vary smoothly on the macroscopic scale, *i.e.* on the µm-scale, but exhibit fluctuations at the microscopic scale, *i.e.* the nanometer scale. Note the colored segments of the two length bars on the upper and lower subfigure.

2.2 Rational Thermodynamics

In this section we give a brief overview over the framework of rational thermodynamics, which constitutes the main theoretical description applied in our work.

Rational thermodynamics (RT) is a description of non-equilibrium thermodynamics based on the concepts of continuum mechanics.[70] Pioneered by Trusdell,[71] Coleman and Noll,[72,73] the framework of RT puts emphasis on mathematical rigour, and exhibits an axiomatic basis from which the main results are oftenly derived via Theorems and Lemmata.[74]

Universal balance equations, which follow from rigorous physical assumptions constitute the basis for this framework,[75–78] and are strictly kept distinct from characterizations of the material at hand.[79] However, these universal balance equations are underdetermined and must be supplemented by constitutive equations, in order to obtain a closed set of differential equations.[80] One characteristic property of RT is that the constitutive equations are not arbitrary, but are restricted by material-independent axioms.[81] Most importantly, they are restricted by the laws of thermodynamics ("thermodynamical consistency"), which are supposed to hold at any time, and the universal principle of material symmetry.[74] Thermodynamic consistency of the framework is implemented via the so-called entropy principle.[82]

Beneath these universal constraints, the constitutive equations are subject to material-dependent axioms, which take the form of material laws and cast the yet general framework to the description of classes of material. According to this description, each class of material is represented by constitutive equations which are functions of a characteristic set of ("material") variables, which form the material law.[80] Therefore, to any material is assigned a set of constitutive equations (which replace the state equations appearing in canonical thermodynamics). Via the method of Coleman and Noll,[73,83] the constitutive equations are determined by one focal quantity, commonly the Helmholtz free energy density φ_{H}. As consequence, the material function for φ_{H}, *i.e.* the precise model for φ_{H}, determines the specific material representation of the constitutive quantities (which describe the system). Usually, this constitutive approach is supplemented by a flux-explicit Onsager-description, which closes the set of transport equations. This allows for a consistent description of large classes of materials.

The framework of RT constitutes the methodological basis for the derivation of our transport theory. In part II we highlight each logical step of RT in great detail, *i.e.* the universal part where we derive the balance equations, the constitutive modeling part where we derive the constitutive equations, and the part where we state our material model for liquid electrolytes.

2.3 Computer Simulations From The Perspective of The Philosophy of Science

Computer simulations based on our transport theory are a tool which we use in our manuscript to supplement the theoretical framework. In this section, we discuss the method of computer simulations and it's relation to experiment and theoretical models.

The application of computer simulations ("simulations") in the natural sciences has gained tremendous significance. As consequence, there exists a plethora of different numerical methods and methodologies. It has even been argued that the rise of computer simulations implies that the traditional dichotomy of experiment and theory has become obsolete in the natural sciences.[84] However, performing simulations is usually differentiated from experimental work, or purely analytical work.

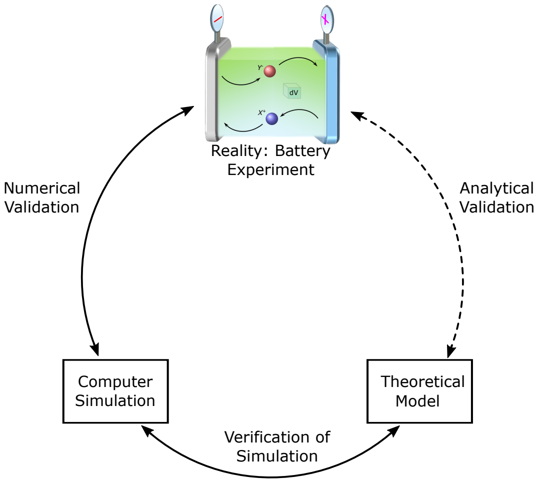

Scheme 2.2: Scheme of a so-called Sargent-cycle, which illustrates the relation between a scientific theory, computer simulations and experiment (real physical system). Parts of figure first published in a modified version in Ref. 67 under the license CC BY 4.0, https://creativecommons.org/licenses/by/4.0/.

This raises some fundamental questions, *e.g.* what is a simulation, what is the relation to modeling and experiments, and how can the scientific value of a computer simulation be assessed.

These questions are relatively new in comparison with the canonical problems studied in the literature on the philosophy of sciences, *e.g.* the problem of induction,[85] or the problem of demarcation.[86] As consequence, they are not directly discussed within seminal treatises of the scientific method, due to, *e.g.*, Karl Popper,[87] Thomas Kuhn,[88] or the Bayesian school of epistemology.[89] The situation is complicated by the fact that simulations are used for a plethora of different purposes, and in a plethora of different fields. Among others, simulations are used for prediction (*e.g.*, in the climate sciences), as explanation (*e.g.*, in the material sciences), for model validation (*e.g.*, cosmology), and data analysis in experiments (*e.g.*, high energy physics)

Here, we take a somewhat minimalistic approach and state that a simulation is the implementation of dynamical equations into a computer program with the aim to solve them using numerical methods. As consequence, by construction, any simulations represents merely a model, which is implemented into the computer program. In this sense, the model is the more fundamental quantity. Traditionaly, the significance of any given model is evaluated with respect to it's ability to yield analytical predictions, and in the validation of these predictions by comparison with experiment. However, it is often not possible to derive predictions from the model analytically. In this case, the simulation is a vital tool for evaluating the significance of a scientific model. Thus, a simulation can potentially restore the falsifiability of a model, *i.e.* the criterion for a scientific theory to be predictive and testable.[87]

However, simulations themselves are not to be interpreted as being identical to experiments, although both procedures generate data, which is often visualized and analyzed in similar ways. In fact, there are conceptual differences between the two. In contrast to experiments, simulations do not interact with the system which they shall investigate. Furthermore, a simulation does not observe an external system, as does an experiment, but relates to an artificial system which is completely determined by the pre-defined, and completely known, initial configuration and boundary conditions. Thus, up to numerical issues discussed below, the outcome of a simulation is pre-determined by the underlying assumptions. Finally, simulations cannot be used to investigate systems which contain unknown dynamical laws.

The attempt to asses the credibility of a simulation is called validation. This assessment usually involves the comparison of simulations results with experimental data. By construction, the validation of a simulation also relates to the credibility of the underlying model and the parametrization of the model. Furthermore, there exists another layer which influences the validation. Numerical issues can lead to corrupt results for an otherwise "accurate" model. Also, undetected errors in the implementation of the model equations into the computer program can lead to corrupted results. Thus, it is in many cases difficult to separate "wrong" elements from "correct" elements of the model and simulation ("opacity problem"[90]). For this purpose, it can be beneficial to split the validation process into multiple steps. The first step is to "verify" the numerical implementation. This can be done by focusing on a specific, not necessarily realistic, effect which is well predicted by the theory. If the simulation results are in accordance with these analytical predictions, then this enhances the probability of a "correct" implementation. In a second step, the computer program can then be used to simulate a scenario which relates to the experiment. A comparison between the numerical results obtained from the verified implementation, and the experimental result then allows to asses the theoretical framework, *i.e.* to validate it. In Scheme 2.2 we illustrate this relation between the experiment, theoretical model and simulations in a simplified "Sargent-cycle".[91]

In this publication, we supplement our theoretical findings by numerical simulations. First, in chapter 6, we validate our bulk transport theory discussed in part II, and apply it to the case of a secondary battery which was described in the literature. Second, in chapter 14, we validate our description for the electrochemical double layer, derived in part III. For this purpose, we focus on experimental results obtained from AFM measurements.

3 Literature Review

In this chapter we review the literature with respect to the research topic of this manuscript.

First, in section 3.1, we present an overview of the literature on the modeling of electrolyte transport in batteries. Second, in section 3.2, we focus on the literature with respect to the modeling of the electrochemical double layer (EDL). In part IV we provide a detailed comparison of our theory with prominent alternative descriptions from the literature.

3.1 Modeling of Battery Systems

Here, we review the literature on modeling electrolyte transport in batteries.

The most basic constitutive model for diffusive fluxes is Fick's law.[92] According to this description, the flux of a species is proportional to it's concentration gradient (directed "against" it's gradient).[93] The Nernst-Planck (NP) model provides a description for electrolyte transport, where Fick's diffusion is supplemented by migration, *i.e.* species-fluxes due to gradients in electrical potential, and by motion of bulk-material (convection).[94,95] The NP model is often solved along with the Poisson-equation, yielding the so-called "PNP"-model.[96] Furthermore, since the coupling of momentum to diffusion plays a fundamental role in concentrated solution theory,[97,98] the PNP-description is often supplemented by the Navier-Stokes equation for viscous fluids. This results in the "PNP/NS"-model, which constitutes what is sometimes called the "standard-model" for the mechanically coupled PNP-based description.[99]

(P)NP-models are often used due to their similarity to Fick's law, and due to the property that transport is separated into migrational and diffusive terms.[100–103] However, besides being inconsistent with basic requirements of irreversible thermodynamics,[70,104] they do not account for diffusional drags due to inter-species correlations. Thus, these models are valid only in the limit of extreme dilution. Cross-effects due to inter-species correlations are well known to appear in reality. For example, in multicomponent mixtures, strong inter-species couplings can cause "uphill-diffusion", where a species diffuses up it's own concentration gradient,[105] and not "down", as stated by Fick's law (such phenomena are well-described in experimental works, see, *e.g.*, the classical experiment by Duncan and Torr[106]). Therefore, concentrated solution theories must take account for such effects. For a detailed analysis of the underlying assumptions, and short-comings of the (P)NP-models (and related models), we refer to Ref. 97

Onsager provided a more complete transport description for concentrated multi-component mixtures.[107–109] According to this linear framework, the driving force of each species is coupled to all species-fluxes via phenomenological coefficients. As consequence, the Onsager-coefficients comprise the complete set of self-/ and inter-species-correlations. The Onsager approach resolves a number of fundamental problems of the NP-based models. Because the linear flux-force-relations take account for all couplings, the Onsager framework establishes entropic completeness. Most importantly, thermodynamic consistency can be implemeneted into the Onsager description via imposing restrictions on the Onsager-coefficients. Furthermore, the Onsager description does not rely on the designation of a solvent-species, and thus all species are based on the same conceptual footing.

However, it is sometimes argued that the Onsager flux-explicit approach does not conclude on how to obtain realistic concentration-dependent diffusion matrices.[105] An alternative approach is the Maxwell-Stefan approach.[110–112] The Maxwell-Stefan equations for multi-component diffusion rely on the assumptions that the thermodynamic driving forces are in local equilibrium with the friction forces between the species, and that these mutual friction forces are proportional to the relative species-velocities (differences of the species-velocities), and to the species concentrations.[100,113–115] In addition to entropic completeness, the Maxwell-Stefan approach complies with the physical criterion that the driving-forces for inter-diffusion shall be invariant with respect to the choice of the reference-velocity.[116]

A drawback of this force-explicit framework is that the Maxwell-Stefan equations obfuscate the role of convective transport.[117] Also, the analysis of transport processes by comparison with intuitive transport-concepts (Ohm's law, Fick's law, Fourier's law) is much easier in the flux-explicit Onsager-description, than in force-explicit descriptions.[116] Thus, it is favorable to transform any given force-explicit apporoach in order to to obtain flux-related transport equations. Although the principle of driving-force-invariance (with respect to the reference-velocities) may yield singular transport matrices, it is possible to invert the Stefan-Maxwell approach to a flux-explicite description.[100,118] This procedure constitutes the basis for the extended Stefan-Maxwell transport theory.[119,120] The so-called "Newman-model" applies this theory to electrolytes, and has become a standard-framework for concentrated solutions.[113–115,121–125] A detailed discussion of the Newman-model is given in Ref. 100. The Newman model is widely used in academia and was extended by various effects, *e.g.* solvent aspects,[126–128] convection[117,129], thermal aspects,[130–132], and was applied to the description of solid electrolytes.[133] Furthermore, the Newman model is also used in industrial applications.[134–137]

Recently, the framework of rational thermodynamics (RT)[71,73] has been used for the modeling of electrochemical systems. This development was mainly driven by two working groups, Latz et al.,[64,138,139] and Dreyer et al.[79,98,140,141] Our transport modeling presented in this document is also based on the framework of RT, and we present a detailed introduction to this framework in section 2.2.

Bazant et al. developed a theory for concentrated solutions based on non-equilibrium thermodynamics and transition state theory.[99,142] Their rigorous approach states modified electrokinetic equations, and provides a general framework for concentrated solutions which takes account for finite-sized ions.

3.2 Modeling the Electrochemical Double Layer for Ionic Liquids

In this section, we give a brief overview over the existing literaure regarding modeling approaches of the electrochemical double layer (EDL).

Due to their complex molecular structure, ILs exhibit a plethora of characteristic bulk-properties on the microscale (see Ref. 143 for an excellent overview). These bulk-properties are supplemented by unique IL-structures, which form when subjected to external agents, *e.g.* near electrified interfaces.[49] Thus, in addition to the significant importance of electrode-electrolyte-interfaces for the operation of batteries,[144] ILs are highly attractive both from fundamental and application points of view. Depending upon the length-scale of interest, different theoretical frameworks are available for the examination of ILs.

Prominent techniques among the microscopic models are density functional theory (DFT), and molecular dynamics (MD). The nanometer-resolution of these methods comprises atomistic scales, usually described by DFT simulations, up to molecular scales (MD). The atomistic resolution (classical, time-dependent DFT) deals with microscopic particle-properties, and delivers detailed insights into the arrangement of single molecules in the EDL,[145–150] but also describes bulk properties (like ion-pair formation),[151] and even dynamic processes (like ion-diffusion) in small-scale electrochemical systems.[149] MD simulations resolve the complete molecular arrangement of anions and cations (*e.g.* length of alkyl chains, molecular segregation into polar and non-polar parts, conformational properties, formation of neutral/charged aggregates), and reveal the evolution of the nano-/ and meso-structured bulk-landscape of ILs (formed by polar-/ and charge-ordering),[152–155] as well as the influence of temperature, electric fields and pressure thereon.[156–158] Furthermore, dynamical bulk-processes like ion-pair-formation,[159,160] ionicity[151], and transport properties[161–164] are also described in great detail. Also, MD applies to mixtures of ILs,[165–168] and of ILs with water / water in salt mixtures,[169,170] which both are of great interest for applications in electrochemistry. Besides bulk-properties of ILs, the investigation of the EDL gained much attention in the MD community, and contributed significantly to the understanding of fundamental processes.[171–180]

However, DFT/MD simulations at length-scales above the nanometer scale are limited due to their computational costs. Thus, continuum-/ and mean-field-theories for applying to the EDL provide a complimentary, valid methodology for the simulation of transport processes, and dynamic simulations of larger systems where the microscopic details can be neglected.

The simplest of such models describing concentration-profiles is based on the assumption that the ions are in quasi-thermal equilibrium.[181] Hence, the concentration profile around a bulk-ion is described by a Boltzmann distribution, *i.e.* the concentration decays exponentially with the ratio $e\Phi/k_\mathrm{B}T$ between the electric potential and the thermal voltage gauge. Via insertion into the Poisson equation, this Ansatz can be used for a naïve description of the EDL, and constitutes the Poisson-Boltzmann equation (PB).[144] The Debye-Hückel theory (DH) is based on this description, and assumes that the electric potential is much smaller than the thermal voltage (at room temperature, $\Phi \ll k_\mathrm{B}T/e \approx 25\,\mathrm{mV}$). This DH-approximation provides the possibility to discuss the linearized Boltzmann distribution via an asymptotic analysis.[182,183] However, for symmetric binary electrolytes, the PB equations can be solved analytically, as was done by by Gouy and Chapman (GC).[184,185] According to this description, the diffuse charge is confined in a compact region near the solid surface (“double layer”), where the width of the charged region is given by the Debye-screening length.[186] In principle, this description still represents our nowadays understanding of electrolytes subjected to electrified interfaces. However, the description of the double-layer-width by the Debye-screening-length, as well as the exponential concentration profile must be relaxed, taking more structural, chemical, and dynamical aspects into account.[49,144]

The short-comings of dilute solution theories, comprised in Debye-Hückel theory (DH), Gouy-Chapman theory (GC), the Poisson-Boltzmann (PB) equations and the Poisson-Nernst-Planck equations (PNP) for dynamics of diluted solutions subject to time- dependent applied voltages, were recognized already by Bikermann,[187] Eigen et al.[188,189] and Freise[190] in the first half of the previous century. For example, the supposition of a Boltzmann distribution for the counterionic species leads to excessively high ion densities in the EDL.[102] Thus, the exponential profile must be replaced by models which take steric-effects, like finite molar volumes, hydration processes, dissociation-/ and solvent-effects into account. These effects become prevalent with increasing salt-concentration. In particular, the early literature on molten salts (solvent-free, purely ionic solutions) already used such constraints to describe transport properties of solvent-free solutions,[45,191–193] correlations leading to charge-oscillations ("overscreening"),[194] and metal-molten-salt interfaces.[195,196] Unfortunately, these concepts did not gain much interest in the electrochemical community, and some confusion arose recently regarding effects, which are well-described in these early works (*e.g.*, the set of independent IL-transport-parameters).[41,44,197].

However, EDL effects in concentrated solution theory regained much attention with the advent of electrochemical energy applications.[100,198] Mean field theories (MFT) accounting for finitemolar volumes of the species were proposed as an approach to overcome the short-comings of the classical PNP theory for the description of the EDL.[181,199–201]

In a series of papers, Kornyshev et al. systematically developed a phenomenological MFT for ILs. Their approach is based on a Poisson-Boltzmann lattice-gas model, with modifications to account for finite ion size.[202] These steric effects lead to ion-saturation in the EDL ("crowding"), and explains the recent experimental observations of the anomalous differential-capacitance-shape of ILs (which shows a bell-shape rather than the U-shape as predicted by dilute solution theory). This approach was validated by MD-/ and and Monte-Carlo-simulations (MC) of the MFT,[203,204] which also considered asymmetric ions. Subsequent MC simulations[205] of the influence of cation shape asymmetry (differing lengths of alkyl chains) on differential capacitance, and MD/DFT simulations on the influence of water,[206,207] and molecular structure[208] on the EDL of pure ILs refined the results. The MFT was also used for the study of "underscreening".[209,210]

In a widely recognized publication,[69] Bazant, Storey and Kornyshev (BSK) proposed a phenomenological continuum framework based on a generalized Ginzburg-Landau functional, to predict the structure of the EDL. BSK predict that, at large voltages, steric constraints due to finite ion sizes prevail over short-ranged Coulomb correlations, which results in charge saturation. In contrast, at small voltages, Coulombic correlations are the dominant effect, which leads to charge oscillations ("overscreening"). BSK is tailor-cut to describe binary ILs near electrified interfaces, and assumes a structure-less bulk. Thus, it cannot explain transport properties, or the emergence of bulk nanostructure.

The BSK-approach was rationalized and extended in a series of publications authored by Yochelis et al. First,[211] they applied asymptotic methods of spatial dynamics to a semi-phenomenological, modified PNP-framework.[212–214] Thereby, Yochelis et al. identify the formation of temporally unstable patterns in the bulk, which are stabilized by external agents, *e.g.* voltage. This explains a variety of effects, including similarities of ILs to dilute electrolytes,[215–218] and the observation of charge-oscillations in confined ILs with no voltage applied[219]. Their work highlights that the bulk morphology of ILs influence the EDL. Thus, bulk properties must be taken into account to obtain a complete EDL description. By modification of the BSK-approach,[220] they identified how applied voltage, domain size, molecular packing, and short-range electrostatic correlations influence distinct diffuse layer characteristics. Their model also describes ion-association/dissociation, and the formation of ion-aggregates, similar to structures in block copolymers (like micelles and co-networks).[221] Furthermore, Yochelis et al. rationalized the BSK-model,[222] by coupling an Onsager Ansatz in the MFT of phase-separation (Cahn-Hilliard[223–225] /Elliott[226]) to the Poisson-equation, in combination with a gradient-flow approach (Flory-Huggins[227,228]). The corresponding extended, mechanistic model describes the bulk-nanostructure of ILs composed of symmetric ions, and combines long-ranged Coulomb interactions with short-range interactions of the ions. This approach is also applied to ILs composed of asymmetric ions.[229] This reveals the spatial ordering of the bulk morphology and shows transition from isotropic to anisotropic ordering, from bulk to EDL. Interestingly, this description bears similarity to deblock copolymer theory in the Ohta-Kawasaki formalism.[230,231] The formalism is consistent, as it reduces to BSK in the solvent-free limit. The nanoscale bulk-morphology is due to (non-)linear bifurcations in a Ginzburg-Landau-type amplitude equation. In addition, they extended this formalism to ternary systems, and identified non-monotonic variations of the EDL-structure with salt-concentration ("underscreening").[232] Methods of spatial linearization are used to investigate the parameter space, which reveals three regions of different EDL/bulk morphologies. Altogether, the Yochelis framework constitutes an effective, scaled formalism which (i) bears tremendous potential for qualitative comparison with experiments,[233] (ii) extends continuum IL-modeling from the EDL to the bulk, and, (iii) rationalizes "phenomenological" arguments (BSK). Interestingly, this approach highlights that ILs show dilute behavior under certain conditions, and hence relates modelling of ILs to dilute solutions.

However, the transition from monotonic to non-monotonic (oscillating) charge profiles was already described by Kirkwood in the 1930ies, using statistical methods ("Kirkwood line").[234] Recently, Frydel et al. rationalized, and extended this approach to EDLs, using "smeared out ions".[235,236]

Another framework for the rigorous modelling of electrostatic interactions in highly concentrated electrolytes was derived by Kjellander et al.[237–239] The frameworks of "dressed-ions-theory", and its extension, "dressed-molecule-theory",[240–242] are based on methods from statistical mechanics, and describe oscillatory (non-monotonic), and monotonic charge-profiles via electrostatic interactions.[243]

For an excellent overview of ionic liquids at electrified interfaces, see Ref. 49. A concise summary of theroretical investigations of ILs can also be found in Ref. 244.

4 Outline

This manuscript is structured into four main parts.

First, in part II, we present a detailed derivation of our bulk transport theory, see chapter 5, and validate our description by applying it to a zinc ion battery in chapter 6 using numerical simulations. (Note that the derivation of our transport theory is based on theoretical tools which are covered in two supplementary chapters comprised in the appendix. Appendix B discusses symmetry arguments which are necessary for the unification of thermodynamics, mechanics and electromagnetic theory, where appendix C covers the universal form of balance equations for volumes, as stated by the Leibnitz Reynolds Transport Theorems).

Second, in part III, we generalize this framework to account for non-local species interactions. For this purpose, in chapter 8, we reformulate the bulk continuum transport theory discussed in part II using a functional formalism. Next, in chapter 9, we apply this description to binary IL electrolytes, and simplify the mathematical structure by introducing a non-dimensional formulation. In chapter 10 we make an asymptotic analysis and discuss the EDL description using a systematic perturbation expsansion of the short ranged interactions. Next, we specify our description and incorporate hardcore particles in our model for the IL electrolyte in chapter 11. Finally, we focus on the stationary description to study the formation of structures formed in the electrochemical double layer (EDL) of binary ILs near electrified interfaces in chapter 12. Next, in chapter 13 we use our EDL description and consider the case of ternary electrolytes composed of a binary IL mixed with minor amount of silver. We validate the cases of binary and ternary IL electrolytes in chapter 14, where we compare our numerical results with experimental results.

In part IV we discuss our multiscale framework. First, in chapter 15 we compare our theory with alternative methodologies proposed in the literature. Second, in chapter 16, we show that our description of non-local species interactions can be used to rationalize effective thermodynamic descriptions via the method of coarse graining.

Finally, in part V, we conclude our manuscript with an outlook on further applications and modifications of our framework.

Part II

Transport Theory For Highly Correlated Liquid Electrolytes

> Thermodynamics is the much
> abused slave of many masters.
>
> Ingo Müller

In this part we derive our transport theory for highly correlated liquid electrolytes. The main scope is to describe variations of macroscopic quantities on the µm-scale. In particular, because we do not resolve microscopic effects explicitly (only via averaged contributions to the free energy), we can safely assume the continuum hypothesis of liquids for our bulk description (see section 2.1). Furthermore, we apply the methodology of rational thermodynamics (RT) using differential calculus (see section 2.2).

To address this goal, we structure this part as follows. In chapter 5, we derive our transport theory. This chapter is based on mathematical tools comprised in two supplementary chapters in the appendix. First, the symmetry arguments underlying the framework of RT and which are necessary for the unification of mechanics with electromagnetic theory are covered in appendix B. Second, in appendix C we discuss the general form of the universal balance equations which constitute the material independent basis for the framework of RT. Finally, in chapter 6, we validate our theoretical description and compare numerical results obtained from computer simulations with experimental results.

5 Transport Theory

> Whether we like it or not, it is an inescapable fact, that, from a theoretical point of view, a macroscopic body is *not* an assembly of particles.
>
> Attay Kovetz

In this chapter, we derive our transport theory for highly correlated electrolytes. Because of the complex nature of highly correlated electrolytes, this involves the consistent coupling of mechanics and electromagnetics within a thermodynamical framework. This bears some conceptual difficulties.[74,79,81] In general, the motion of a continuous medium is governed by the laws of mechanics. However, macroscopic bodies exhibit some kind of irreversible behaviour, subject to thermodynamic laws, which cannot be derived from mechanics. Thus, mechanics and thermodynamics constitute two independent disciplines. Furthermore, due to effects of polarization / magnetization, electrodynamics must be taken account for as third independent discipline. Thus, the correct continuum-description of macroscopic media requires the unification of these three disciplines (see appendix B). Various approaches exist for doing so, which differ in rigour (and phenomenology). However, in any framework, the crucial point where the three disciplines meet first are the balance-laws. Therefore, the universal balance laws for mass, energy, momentum, and the entropy inequality, are of paramount importance for the fusion of the three different branches. Although the balance laws arise from a rigorous basis, using only basic physical assumptions, they exhibit a certain amount of ambiguity stemming from non-unique modeling approaches. Due to mutual couplings between the balance laws, these models cannot be chosen independently. Second, the precise formulation of the balance-laws and the choice of electromagnetic variables impacts the materials law and determines which variable will be defined by a constitutive equation.[245] Third, symmetry arguments can be exerted, demanding that the conserved quantities be objective.

We structure this chapter as follows. First, in section 5.1, we discuss the universal balance laws for mass, momentum and energy in a purely mechanical context, and couple them with thermodynamics. This thermomechanical discussion provides a rigorous framework, which serves as limiting case when electromagnetic effects are incorporated. In section 5.2, we extend this toy model by electromagnetic contributions, and derive the constitutive equations of our fully coupled transport theory. Our procedure is based on the method of Coleman and Noll, which ensures consistency with the axioms of thermodynamics. Next, in section 5.3, we close our consistent description and determine the thermodynamic fluxes using an Onsager approach. Yet, this constitutes the universal part of our framework, which describes a large class of materials. In section 5.4, we specify this general description to liquid electrolytes. In order to highlight the canonical structure of this model, we (first) neglect thermal effects in this discussion. In section 5.5 we make a detour and discuss the role of the reference frame for our transport theory. For this purpose, we present a frame-independent formulation, and derive transformation laws between different reference frames. Finally, in appendix D.10 we incorporate thermal aspects of our constitutive model into our theory.

5.1 Thermo-Mechanical Balance Laws

In this section we state the thermomechanical balance laws for mass, momentum, and energy, and the entropy inequality for a highly correlated electrolyte composed of N species, where we do not yet consider electromagnetic contributions. This thermomechanical description serves as basis for section 5.2, where we supplement it by electromagnetic effects and represents a limiting case of vanishing electromagnetic fields for the complete balance laws.

To address this goal, we make use of the results presented in appendix C, where we derived the universal form for local balance equations. For completeness, we restate the local form of the local balance equations in the material and spatial formulation (see eqs. (C.14) and (C.15)),

$$\partial_t \psi_A = -\boldsymbol{\nabla}\left(\psi_A \otimes \mathbf{v} + \boldsymbol{\Xi}_A\right) + \mathcal{P}_A, \tag{5.1}$$

$$\dot{\psi}_A = -\psi_A\left(\boldsymbol{\nabla}\mathbf{v}\right) - \boldsymbol{\nabla}\boldsymbol{\Xi}_A + \mathcal{P}_A. \tag{5.2}$$

5.1.1 Balance of Total Mass, Partial Masses and Charges

We assume an electrolyte mixture composed of N species. We denote the specific mass densities by ρ_α ($[\rho] = \mathrm{kg\,m^{-3}}$), where the total mass density is defined by

$$\rho = \sum_{\alpha=1}^{\mathrm{N}} \rho_\alpha. \tag{5.3}$$

The molar masses M_α for each species have dimension $\mathrm{kg\,mol^{-1}}$, and relate to the species concentrations c_α via $\rho_\alpha = M_\alpha c_\alpha$. For each species we introduce an (averaged) species velocity $\mathbf{v}_\alpha$, and define the center-of-mass velocity (bulk momentum per unit mass) by

$$\rho\mathbf{v} = \sum_{\alpha=1}^{N} \rho_\alpha \mathbf{v}_\alpha. \tag{5.4}$$

This quantity plays a fundamental role for our transport theory, since we use it to define the convection velocity. This choice determines the fluxes appearing in the transport equations, and fixes the reference frame in the corresponding dynamical description. We emphasize that the convection velocity can be defined differently, *e.g.* via the volume flux (see section 5.5 for a detailed discussion regarding the role of the reference frame, and how to transform between different reference frames).

Mass Conservation

A fundamental principle underlying our continuum modelling is the axiom of mass-conservation, where ρ changes only due to convective mass-fluxes (*i.e.* $\mathcal{P} = 0$ and $\boldsymbol{\Xi} = 0$ in eqs. (5.1) and (5.2)),

$$\partial_t \rho = -\boldsymbol{\nabla}\left(\rho\mathbf{v}\right), \quad \text{or} \quad \dot{\rho} = \partial_t\rho + (\mathbf{v}\cdot\boldsymbol{\nabla})\rho = -\rho\cdot\boldsymbol{\nabla}\mathbf{v}. \tag{5.5}$$

Because our description of material bodies is represented by material points (see appendix C), there exists an intricate connection between the dynamical continuum-description of the medium in the form of coordinates, and the matter-field of the body,[246] *i.e.* between the deformation tensor $\boldsymbol{F}$ and the total mass density ρ,

Lemma 1. The Lagrangian representation of mass conservation implies a coupling between the deformation tensor and the total mass density,

$$\rho(\boldsymbol{X},t)\cdot\det\boldsymbol{F}(\boldsymbol{X},t) = \rho_0(\boldsymbol{X}). \tag{5.6}$$

Proof. Since there is no mass-production, the change of ρ in the Lagrangian description, as measured by an observer comoving with the fluid, is due to expansion / dilation alone. For this purpose, let V_0 ba a volume element at t_0, with homogeneous mass density ρ_0 such that qthe mass comprised by the volume element $\rho_0 V_0$ is a material invariant. At later times, the density of the deformed body is ρ, and the deformed volume is $V = V_0 \cdot \det\boldsymbol{F}$. Because both are equal by assumption, $\rho\det\boldsymbol{F} = \rho_0$. □

For the local balance equations of field densities defined with respect to volume averages, $\Psi = \int \mathrm{d}V\, \rho\tilde{\psi}$, the LRTT eq. (C.10) yields

$$\dot{\Psi} = \frac{\mathrm{d}}{\mathrm{d}t} \int \mathrm{d}V\, \rho\tilde{\psi} = \int_{V(t)} \mathrm{d}V\, \rho\dot{\tilde{\psi}}, \tag{5.7}$$

where we used eq. (5.5). Thus, the time-derivative of $\tilde{\psi}$ suffices for the time-evolution of $\rho\tilde{\psi}$. A similar result follows also from balance-eqs. (5.1) and (5.2) with respect to $\psi = \rho\tilde{\psi}$, since then $\tilde{\psi}$ does not change due to convective-fluxes $\rho\dot{\tilde{\psi}} = -\boldsymbol{\nabla}\boldsymbol{\Xi} + \mathcal{P}$.

Balance of Partial Masses

The evolution of each quantity ρ_α is described by one balance equation (see eq. (5.3)). However, in contrast to the total mass density, the specific mass densities are not conserved. Hence, they evolve due to convective fluxes $\rho_\alpha \mathbf{v}$, non-convective mass fluxes $M_\alpha \boldsymbol{\mathcal{N}}_\alpha$, and chemical reactions $M_\alpha r_\alpha$,

$$\partial_t \rho_\alpha = -\boldsymbol{\nabla}\left(\rho_\alpha \mathbf{v} + M_\alpha \boldsymbol{\mathcal{N}}_\alpha\right) + M_\alpha r_\alpha, \quad \text{or} \quad \dot{\rho}_\alpha = -\rho \cdot \boldsymbol{\nabla}\mathbf{v} - M_\alpha \boldsymbol{\nabla}\boldsymbol{\mathcal{N}}_\alpha + M_\alpha r_\alpha. \tag{5.8}$$

Here, $\boldsymbol{\mathcal{N}}_\alpha$ are non-convective mass fluxes which measure the amount of substance of species α transported through a unit surface area perpendicular to the direction of the flux, and per unit time, relative to the center-of-mass motion,

$$\boldsymbol{\mathcal{N}}_\alpha = \boldsymbol{n}_\alpha - c_\alpha \mathbf{v} = c_\alpha \cdot \left(\mathbf{v}_\alpha - \mathbf{v}\right). \tag{5.9}$$

The corresponding mass-flux in the rest-frame is denoted by $\boldsymbol{n}_\alpha = c_\alpha \mathbf{v}_\alpha$. From mass conservation (eq. (5.5)) follows a trivial flux-constraint,

$$\sum_{\alpha=1}^{\mathrm{N}} M_\alpha \cdot \boldsymbol{\mathcal{N}}_\alpha = 0. \tag{5.10}$$

and a trivial constraint on the bulk reactions, $\sum_{\alpha=1}^{\mathrm{N}} M_\alpha \cdot r_\alpha = 0$.

Alternatively, balance of partial masses can be expressed via the N species concentrations $c_1, \ldots, c_{\mathrm{N}}$,

$$\partial_t c_\alpha = -\boldsymbol{\nabla}\left(c_\alpha \mathbf{v} + \boldsymbol{\mathcal{N}}_\alpha\right) + r_\alpha, \quad \text{or} \quad \dot{c}_\alpha = -c_\alpha \cdot \boldsymbol{\nabla}\mathbf{v} - \boldsymbol{\nabla}\boldsymbol{\mathcal{N}}_\alpha + r_\alpha. \tag{5.11}$$

Charge Balance

We assume that the total charge density of the electrolyte ϱ_{F} is completely determined by the charge-carrying species,

$$\varrho_{\mathrm{F}} = F \sum_{\alpha=1}^{\mathrm{N}} z_\alpha \cdot c_\alpha. \tag{5.12}$$

Here F is Faraday's constant, and z_α denotes the valence of species α, which can be any integer number (positive or negative). In accordance with the definition of the mass fluxes relative to the center-of-mass motion, eq. (5.9), we define the conduction current density,

$$\boldsymbol{\mathcal{J}}_{\mathrm{F}} = F \sum_{\alpha=1}^{\mathrm{N}} z_\alpha \mathbf{N}_\alpha = \mathbf{j}_{\mathrm{F}} - \varrho_{\mathrm{F}} \mathbf{v}, \tag{5.13}$$

which measures charge flux relative to the center-of-mass motion. Here, $\mathbf{j}_{\mathrm{F}} = F \sum_{\alpha=1}^{\mathrm{N}} z_\alpha c_\alpha \mathbf{v}_\alpha$ is the rest-frame electric current. Equation (5.12) implies that balance of partial masses, eq. (5.5) relates to balance of charge,

$$\partial_t \varrho_{\mathrm{F}} = F \sum_{\alpha=1}^{\mathrm{N}} z_\alpha r_\alpha - \boldsymbol{\nabla} \left(\varrho_{\mathrm{F}} \mathbf{v} + \boldsymbol{\mathcal{J}}_{\mathrm{F}} \right), \text{ or } \dot{\varrho}_{\mathrm{F}} = F \sum_{\alpha=1}^{\mathrm{N}} z_\alpha r_\alpha - \varrho_{\mathrm{F}} \boldsymbol{\nabla} \mathbf{v} - \boldsymbol{\nabla} \boldsymbol{\mathcal{J}}_{\mathrm{F}}. \tag{5.14}$$

5.1.2 Mechanics: Momentum Balance

In this section, we discuss balance of momentum and angular momentum. Both concepts are fundamental to describe the mechanics of material bodies.

Any arbitrary volume element $\mathrm{d}V$ within the electrolyte is subject to forces which tend to deform and dislocate it. To describe these effects, we thus need precise definitions for the concepts of momentum, force, angular momentum and torque.

The mechanical concept of momentum relies only on the fundamental quantities mass and center-of-mass velocity,

$$\mathcal{G} = \int \mathrm{d}M \, \mathbf{v} = \int \mathrm{d}V \, \rho \mathbf{v}. \tag{5.15}$$

Usually, the total force acting upon a volume element $\mathrm{d}V$ of bulk matter in a material body is split into short-ranged forces and long-ranged forces. Both are characterized by their typical effective range. Long ranged forces are characterized by the property that the extension of a typical volume element $\mathrm{d}V$ is negligible, when compared to variations in these force. Thus, they penetrate into all of the fluid, and act equally on all matter comprised in each fluid elements $\mathrm{d}V$. As consequence,

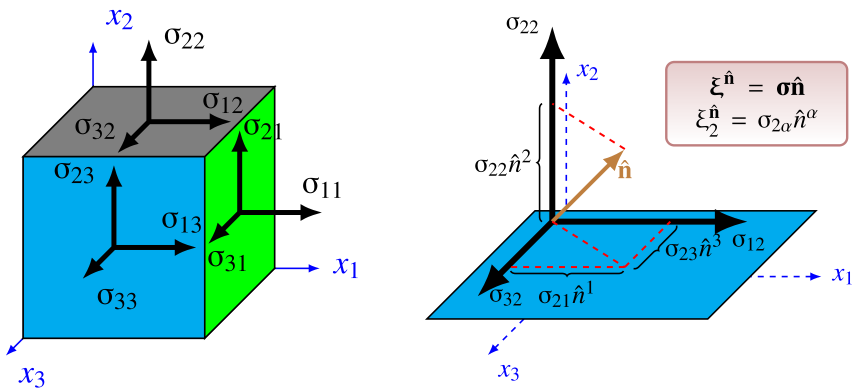

Scheme 5.1: The left figure illustrates the components of the Cauchy stress tensor, comprising surface-forces acting on the volume-element $\mathrm{d}V$. The stresses appearing at any surface element are decomposed along the three principal directions x_1, x_2, x_3. Here, $\boldsymbol{\sigma} \cdot \hat{\boldsymbol{n}}_{\mathcal{A}}$ is the stress exerted by one mass element on another element with surface area $\hat{\boldsymbol{n}}_{\mathcal{A}} \cdot \mathrm{d}A$, where $\hat{\boldsymbol{n}}_{\mathcal{A}}$ is pointing outwards the latter mass element (thus anti-parallel to the stress exerted). The right part of the figure illustrates the principal stress-components along the x_1-x_3 plane. Note the Einstein summation convention, *i.e.* $\sigma_{2i}\hat{n}^i_{\mathcal{A}} = \sum_{i=1}^{\mathrm{N}} \sigma_{2i}\hat{n}^i_{\mathcal{A}}$.

these "body forces" are constant and can be assumed as being proportional to the mass. We express the total body force acting upon the volume via

$$\int_V \mathrm{d}V\, \rho\mathbf{b}. \tag{5.16}$$

Gravitational forces constitute the most prominent example for such long ranging body forces. Because they decay with the inverse of the squared distance, they are long ranging when compared to intermolecular forces (*e.g.*, van der Waals forces which decay typically via power laws to the sixth order or higher), and can safely be assumed as constant throughout the volume element. The second type of forces is constituted by short-ranged forces (usually, of molecular origin), which decay rapidly over the extensions of volume elements $\mathrm{d}V$. Such surface forces are due to momentum diffusion, *i.e.,* transport of momentum between neighbouring fluid layers. For example, non-uniform convection generates momentum diffusion between neighbouring fluid elements (note that Brownian motion implies that there is momentum diffusion between neighbouring particles even when the two fluid elements are at rest relative to each other). Effectively, surface-forces have compact supports over scales determined by molecular distances, and thus become important when the boundaries of interacting fluid elements have mechanical contact to each other.

The penetration depth of surface forces into volume elements is negligible compared to the lateral dimensions of the boundary of the volume element. The surface forces

$$\oint_{\mathcal{A}} \mathrm{d}A\, \boldsymbol{\xi}^{\hat{\boldsymbol{n}}_{\mathcal{A}}}, \tag{5.17}$$

are determined by the surface-area of the boundary, and not by the volume of the fluid element. Here, $\boldsymbol{\xi}^{\hat{\boldsymbol{n}}_{\mathcal{A}}}$ are stresses acting on surface elements $\mathrm{d}A$ along the direction $\hat{\boldsymbol{n}}_{\mathcal{A}}$. Due to the directional dependence of the relative motion between neighbouring fluid layers, the total of these stresses are comprised in the Cauchy-stress tensor $\boldsymbol{\sigma}$,

$$\boldsymbol{\xi}^{\hat{\boldsymbol{n}}_{\mathcal{A}}} = \boldsymbol{\sigma} \cdot \hat{\boldsymbol{n}}_{\mathcal{A}}. \tag{5.18}$$

Thus, $\boldsymbol{\sigma}$ comprises in its components the stresses along all directions. We illustrate the components of the stress tensor and the of the stress vector in Scheme 5.1. Using Stokes' Theorem, we transfer the surface integral eq. (5.17) to a volume integral, $\oint_{\mathcal{A}} \mathrm{d}A\, \boldsymbol{\xi}^{\hat{\boldsymbol{n}}_{\mathcal{A}}} = \oint_{\mathcal{A}} \mathrm{d}A\, \boldsymbol{\sigma}\hat{\boldsymbol{n}}_{\mathcal{A}} = \int_V \mathrm{d}V\ \boldsymbol{\nabla}\boldsymbol{\sigma}$, where we use the convention

$$(\boldsymbol{\nabla}\boldsymbol{\sigma})_i = \partial \sigma_{ij} / \partial x_j. \tag{5.19}$$

The phenomenological distinction into body-/ and surface-forces is not always well-defined and may lead to some confusion.[247] The categorization into long-ranging forces and short-ranging forces should be defined relative to the extension of a local volume element $\mathrm{d}V$. It is mathematically possible to reformulate stresses as sources, and vice versa.[247] Thus, the same quantity can be incorporated into the universal balance laws either as source-terms or fluxes.[248] Arguably, the proper description of surface forces is via the stress-tensor which has (in general) nine independent coefficients, whereas the force-vector has only three independent components. Hence, physical degrees of freedom may be lost when substituting surface stresses by body forces. As consequence, the interpretation of some quantities being either a flux-term or source-term differs in the literature.[249] For example,[247] the Lorentz force is characterized as a body-force in Ref. 141, whereas it is classified as a surface-force in Ref. 250 (Ref. 81 disputes the relevance of the Lorentz-force at all). Altogether, the total force reads

$$\mathsf{F} = \int_V \mathrm{d}V\, \boldsymbol{\nabla}\boldsymbol{\sigma} + \int_V \mathrm{d}V\, \rho \mathbf{b}. \tag{5.20}$$

According to Euler's first law of mechanics there exist designated "inertial" frames, in which momentum-change, *i.e.* acceleration, equals imbalance of forces,[251]

$$\dot{\mathcal{G}} = \mathsf{F}. \tag{5.21}$$

We assume that all quantities appearing in $\mathcal{G}$ and F are smooth and use Stoke's Theorem to derive the local form of momentum balance. By substitution of eqs. (5.15) and (5.20), this yields Cauchy's first equation ("force-law")

$$\rho\dot{\mathbf{v}} = \boldsymbol{\nabla}\boldsymbol{\sigma} + \rho\mathbf{b}. \tag{5.22}$$

In this work, we do not consider surfaces across which the quantities are discontinuous and for which suitable jump conditions must be formulated.[140]

We define the mechanical concepts of angular momentum L, and torque M pointwise via local wedge-products between momentum and force,

$$L_p = \int \mathrm{d}V\,(\mathbf{x}-\mathbf{x}_p)\wedge\rho\mathbf{v}, \tag{5.23}$$

$$M_p = \oint \mathrm{d}A\,(\mathbf{x}-\mathbf{x}_p)\wedge(\boldsymbol{\sigma}\cdot\hat{\boldsymbol{n}}_{\mathcal{A}}) + \int \mathrm{d}V\,(\mathbf{x}-\mathbf{x}_p)\wedge\rho\mathbf{b}. \tag{5.24}$$

Euler's second law of mechanics states that, in an inertial frame located at $\mathbf{x}_p$, the change of angular momentum equals torque-imbalance,

$$\dot{L}_p = M_p. \tag{5.25}$$

However, the concepts of angular momentum and torque are usually of minor importance for electrolytes. Nevertheless, Euler's second law of mechanics bears a surprising consequence for the stress tensor.

Lemma 2. Euler's second law of mechanics, eq. (5.25), implies that the non-electromagnetic stress-tensor is symmetric, $\boldsymbol{\sigma} = \boldsymbol{\sigma}^T$.

Proof. We define the vector of the rotation axis by $\boldsymbol{x} = \mathbf{x} - \mathbf{x}_p$, where $\dot{\boldsymbol{x}} = \mathbf{v}$ and $\partial_i x^j = \delta^i_j$. Furthermore, we define the tensor-valued wedge-product between a vector $\mathcal{X}$ and a matrix $\mathcal{M}$ by

$$(\mathcal{X}\wedge\mathcal{M})_{ij} = \epsilon_{ikl}\mathcal{X}^k\mathcal{M}^l{}_j. \tag{5.26}$$

Via this notation, it is easy to show that $\boldsymbol{x}\wedge(\boldsymbol{\sigma}\cdot\hat{\boldsymbol{n}}_{\mathcal{A}}) = (\boldsymbol{x}\wedge\boldsymbol{\sigma})\cdot\hat{\boldsymbol{n}}_{\mathcal{A}}$. Hence, using Stokes Theorem, the torque reads $M_p = \int \mathrm{d}V\,\boldsymbol{\nabla}(\boldsymbol{x}\wedge\boldsymbol{\sigma}) + \boldsymbol{x}\wedge\rho\mathbf{b}$. We evaluate the left side of Euler's second law using the LRTT for volumes (appendix C.3), the relation $\dot{\boldsymbol{x}} = \mathbf{v}$, and Euler's first law (eq. (5.22)), such that $\dot{L}_p = \int \mathrm{d}V\,[\boldsymbol{x}\wedge(\boldsymbol{\nabla}\boldsymbol{\sigma}) + \boldsymbol{x}\wedge\rho\mathbf{b}]$. Thus, locally, Euler's second law reads $\boldsymbol{x}\wedge(\boldsymbol{\nabla}\boldsymbol{\sigma}) = \boldsymbol{\nabla}(\boldsymbol{x}\wedge\boldsymbol{\sigma})$. However, since

$$\boldsymbol{\nabla}(\boldsymbol{x}\wedge\boldsymbol{\sigma}) = \boldsymbol{x}\wedge(\boldsymbol{\nabla}\boldsymbol{\sigma}) - (\boldsymbol{\sigma}\boldsymbol{\nabla})\wedge\boldsymbol{x}, \tag{5.27}$$

Euler's second law implies $(\boldsymbol{\sigma}\boldsymbol{\nabla})\wedge\boldsymbol{x}=0$. Component-wise, this condition is equivalent to $\epsilon^{ikl}\sigma_{ij}\partial^j x_k{=}0$ for all components i, l. Because $\partial_j x_k{=}\delta_j^k$, this becomes $\epsilon^{ikl}\sigma_{ik}{=}0$ for all components l, which is equivalent to $\boldsymbol{\sigma}{=}\boldsymbol{\sigma}^T$. □

When internal rotational degrees of freedom (*e.g.*, spin) are considered,[82] then the definition of L_p based on the velocity $\mathbf{v}$ must be relaxed, and Euler's second law does not imply symmetry of $\boldsymbol{\sigma}$ (see Lemma 3).

5.1.3 First and Second Axiom of Thermodynamics: Energy and Entropy

We supplement the mechanical aspects discussed above by thermodynamics and introduce the additional concepts energy of the system $\mathcal{E}$, temperature T, heating of a material body $\mathcal{Q}$, powers of the forces acting on a system $\mathit{\Pi}$, and entropy $\mathcal{S}$.

We assume that these quantities are for a given material body continuous functions of the corresponding mass of the material body body, and can thus be associated to the material points of the body.

The total energy $\mathcal{E} = \int \mathrm{d}V\, \rho\varepsilon$ changes due to heating and due to forces acting upon the system, which both contribute to the rate of change of $\mathcal{E}$, although not being time-derivative themselves. We split the heating of a body $\mathcal{Q}$ into a surface-flux ("heat flux") $\mathbf{q}$, which describes heat conduction through the boundary, and a source-term h, which measures local production of heat,

$$\mathcal{Q} = \int \mathrm{d}V\, \rho h - \oint \mathrm{d}A\, \mathbf{q} \cdot \hat{\boldsymbol{n}}_{\mathcal{A}}. \tag{5.28}$$

Heat production arises either from internal processes, *e.g.* radioactive decay, or from heat-absorption of external long-ranging sources, *e.g.* radiation. The quantity $\mathcal{Q}$ can be positive or negative ("cooling"). If $\mathcal{Q} = 0$ over a period of time, then the body undergoes an adiabatic process. Thermal insulators are defined by the property that there arises no heat flux, $\mathbf{q} = 0$, and heating is due only to production. In contrast, $\mathcal{Q} = 0$ corresponds to the case where a body is thermally insulated.

We comprise the mechanical forces acting upon a body in the so-called powers of the forces. Because this quantity is of mechanical origin, it scales locally with the bulk momentum $\mathbf{v}$ and the forces eq. (5.20),

$$\mathit{\Pi}(F, \mathbf{v}) = \oint \mathrm{d}A\, \mathbf{v} \cdot (\boldsymbol{\sigma}\hat{\boldsymbol{n}}_{\mathcal{A}}) + \int \mathrm{d}V\, \mathbf{v} \cdot (\rho \mathbf{b})\,. \tag{5.29}$$

Note that $\mathbf{v} \cdot (\boldsymbol{\sigma}\hat{\boldsymbol{n}}_{\mathcal{A}}) = \hat{\boldsymbol{n}}_{\mathcal{A}} \cdot (\boldsymbol{\sigma}^T \mathbf{v})$ (which can easily be shown component-wise). We use Stoke's Theorem and transform the first integral on the right side into a volume integral,

$$\mathit{\Pi} = \int_V \mathrm{d}V\, \boldsymbol{\nabla} \left(\boldsymbol{\sigma}^T \cdot \mathbf{v}\right) + \int_V \mathrm{d}V\, \rho \mathbf{v} \mathbf{b}. \tag{5.30}$$

This is the general form of $\mathit{\Pi}$, which is correct also for the electromagnetic extension.

Next, we transform the surface forces (using $\boldsymbol{\sigma}^T\!=\!\boldsymbol{\sigma}$ see Lemma 2) , $\boldsymbol{\nabla}(\boldsymbol{\sigma}\cdot\mathbf{v})=\boldsymbol{\nabla}(\boldsymbol{\sigma}^T\cdot\mathbf{v})=\sum_{i,j}\partial_i(\sigma_{ji}v_j)=\sum_{i,j}[(\partial_i\sigma_{ji})v_j+\sigma_{ji}(\partial_i v_j)]=\mathbf{v}\cdot\boldsymbol{\nabla}\boldsymbol{\sigma}+\boldsymbol{\sigma}\colon\mathrm{grad}\,\mathbf{v}=\mathbf{v}\cdot\boldsymbol{\nabla}\boldsymbol{\sigma}+\boldsymbol{\sigma}\colon\boldsymbol{\kappa}$, and substitute $\rho\mathbf{b}=\rho\dot{\mathbf{v}}-\boldsymbol{\nabla}\boldsymbol{\sigma}$,

$$\mathit{\Pi}(\boldsymbol{\sigma},\mathbf{b},\mathbf{v})=\int_V \mathrm{d}V\ [\mathbf{v}\cdot\boldsymbol{\nabla}\boldsymbol{\sigma}+\boldsymbol{\sigma}:\boldsymbol{\kappa}+\rho\mathbf{v}\mathbf{b}]=\int \mathrm{d}V\ (\boldsymbol{\sigma}:\boldsymbol{\kappa}+\rho\mathbf{v}\dot{\mathbf{v}})\,. \tag{5.31}$$

The first axiom of thermodynamics states that the balance-law for the energy of a body is determined by the imbalance of mechanical power and heating,

$$\dot{\mathcal{E}}=\mathit{\Pi}+\mathcal{Q}. \tag{5.32}$$

By assumption, all quantities appearing on the right side of eqs. (5.28) and (5.31) are smooth. Thus, we obtain the local expression of energy balance,

$$\rho\dot{\varepsilon}=\boldsymbol{\sigma}:\boldsymbol{\kappa}+\rho\mathbf{v}\dot{\mathbf{v}}+\rho h-\boldsymbol{\nabla}\mathbf{q}. \tag{5.33}$$

Next, we shift our focus from the evolution of ε to the energy itself. We define the total energy density as the sum of the specific internal energy density, and the kinetic energy density

$$\varepsilon=u+\mathbf{v}^2/2 \tag{5.34}$$

The characteristic property of the non-kinematic quantity u is that it cannot be eliminated by a suitable observer-transformation. It's thermomechanical Legendre-transformed is the specific Helmholtz free energy density

$$\varphi_{\mathrm{H}}=u-Ts. \tag{5.35}$$

According to the principles of thermodynamics the quantity φ_{H} measures the maximum amount of energy, which can theoretically be extracted from u.

Next, we introduce the (abstract) concept of temperature $T(\mathbf{x},t)$, and assume that T is related to the material points of a body, and that there exists a lower bound for T. In the literature, temperature is measured either in degrees of Celsius or Kelvin, or in units of energy (high-energy-physics). Note that there exist various "schools of thermodynamics", which use different definitions of temperature. 74

Another important quantity in thermodynamics is the entropy $\mathcal{S}$ of the system,

$$\mathcal{S}=\int_V \mathrm{d}V\,\rho s. \tag{5.36}$$

Unlike for energy, mass and momentum no "true" balance-law for entropy exists. However, the second law of thermodynamics, expressed in the Clausius-Duhem formulation,[252] states that the entropy of a body increases at least at the rate

$$\dot{\mathcal{S}} = \int_V \mathrm{d}V\, \rho \dot{s} \geq -\oint_{\mathcal{A}} \mathrm{d}A\, \boldsymbol{\xi}_s + \int_V \mathrm{d}V\, \rho h/T\,. \tag{5.37}$$

The non-convective entropic surface-flux $\boldsymbol{\xi}_s(\mathbf{q}, \mu_\alpha, \boldsymbol{\mathcal{N}}_\alpha)$ comprises $\mathbf{q}$, and a chemical surface-term $\sum_{\alpha=1}^{\mathrm{N}} \mu_\alpha \boldsymbol{\mathcal{N}}_\alpha$ which is important for multi-component mixtures,

$$\boldsymbol{\xi}_s = \mathbf{q}/T - \sum_{\alpha=1}^{\mathrm{N}} \mu_\alpha \boldsymbol{\mathcal{N}}_\alpha/T\,. \tag{5.38}$$

In higher-order theories (like the kinetic theory of gases),[253] $\boldsymbol{\xi}_s$ comprises viscous contributions appear.[74]

During time-intervals where $\dot{\mathcal{S}} = 0$, the body is undergoing so-called reversible processes (as opposed to irreversible processes where $\dot{\mathcal{S}} \neq 0$).

The axiom eq. (5.37) fixes the dimension of $\mathcal{S}$ because the product $(\mathcal{S} \cdot T)$ has dimension of energy (Joule). Thus, if temperature is measured in units of energy, then $\mathcal{S}$ is dimensionless, whereas if T is measured in degrees of Kelvin, then $[\mathcal{S}] = \mathrm{J\,K^{-1}}$. The local expression of the Clausius-Duhem inequality becomes

$$\rho \dot{s} \geq \rho h/T - \boldsymbol{\nabla} \boldsymbol{\xi}_s. \tag{5.39}$$

In thermodynamic equilibrium, eq. (5.39) becomes an equation. Since $\boldsymbol{\xi}_s$ is not yet determined by a constitutive equations, we assume that the residual expression

$$\mathcal{R} = \rho \dot{s} T - \rho h + T \boldsymbol{\nabla} \boldsymbol{\xi}_s, \tag{5.40}$$

called entropy production rate, acts as source-term for entropy. Apparently, this quantity measures the deviation from thermodynamic equilibrium, and $\mathcal{R}/T$ constitutes the irreversible part of the entropy production. Furthermore, the second axiom of thermodynamics implies that $\mathcal{R}$ is strictly non-negative. As we lay out in the next sections, this quantity is of principal importance in our methodology, since it serves as agent-provocateur for our constitutive modelling and the closure-relations, and guarantees thermodynamic consistency.

5.2 Coupling to Electromagnetism

Here, we supplement the thermomechanical description derived in section 5.1 by electromagnetic theory and incorporate electromagnetic effects into the balance-laws.

First, in section 5.2.1, we discuss electromagnetic theory in media, introduce the concepts of polarization and magnetization, and motivate the Galilei-invariant formulation of the Maxwell-equations in matter. In sections 5.2.2 and 5.2.3, we incorporate electromagnetic contributions step by step into the balance-laws, and derive the constitutive equations using the method of Coleman and Noll. Finally, in section 5.2.4 we discuss electrostatic limit.

5.2.1 Maxwell's Equations in Matter

Here, we state Maxwell's equations in matter. See Ref. 254 for a detailed discussion.

We already discussed the threedimensional Maxwell's equations for the complete collection of charges in appendix B.3 (see eqs. (B.4) and (B.5)). However, experiments show that most material bodies respond when subjected to electromagnetic fields via the emergence of induced charge -/ and current-distributions $\varrho_\mathrm{R}, \mathbf{j}_\mathrm{R}$. We restrict to the least specific description,[81] and assign to the material-response the derived potentials $\mathbf{P}$ (polarization), and $\mathbf{M}$ (Lorentz magnetization), which follow from the material responses via $\boldsymbol{\nabla}\mathbf{P} = -\boldsymbol{\nabla}\varrho_\mathrm{R}$ and $\partial_t\mathbf{P} + \boldsymbol{\nabla}\wedge\mathbf{M} = \mathbf{j}_\mathrm{R}$. In addition, so called "free" charge-current distributions $\varrho_\mathrm{F}, \mathbf{j}_\mathrm{F}$ exist in material bodies, where we define potentials $\mathbf{D}_\mathrm{F} = \mathbf{D}_\mathrm{T} + \mathbf{P}$, called "electric displacement", and $\mathbf{H}_\mathrm{F} = \mathbf{H}_\mathrm{T} - \mathbf{M}$ which are associated to the quantities $\varrho_{\mathrm{F},\mathrm{R}}$ and $\mathbf{j}_{\mathrm{F},\mathrm{R}}$ via Maxwell's equation in matter,

$$0 = \boldsymbol{\nabla}\mathbf{B}, \qquad 0 = \partial_t\mathbf{B} + \boldsymbol{\nabla}\wedge\mathbf{E}, \tag{5.41}$$
$$\varrho_\mathrm{F} = \boldsymbol{\nabla}\mathbf{D}_\mathrm{F}, \qquad \mathbf{j}_\mathrm{F} = -\partial_t\mathbf{D}_\mathrm{F} + \boldsymbol{\nabla}\wedge\mathbf{H}_\mathrm{F}. \tag{5.42}$$

In appendix B.3 we show that the quantities $\mathbf{D}_{\mathrm{F},\mathrm{T}}, \mathbf{B}, \mathbf{P}$ are covariant with respect to Galilei transformations, whereas $\mathbf{E}, \mathbf{M}, \mathbf{j}_{\mathrm{F},\mathrm{T},\mathrm{R}}$ and $\mathbf{H}_{\mathrm{F},\mathrm{T}}$ are not. Thus we introduce the objective quantities

$$\boldsymbol{\mathcal{E}} = \mathbf{E} + \mathbf{v}\wedge\mathbf{B}, \qquad \boldsymbol{\mathcal{M}} = \mathbf{M} + \mathbf{v}\wedge\mathbf{P}, \tag{5.43}$$
$$\boldsymbol{\mathcal{J}}_{\mathrm{F},\mathrm{T},\mathrm{R}} = \mathbf{j}_{\mathrm{F},\mathrm{T},\mathrm{R}} - \varrho_{\mathrm{F},\mathrm{T},\mathrm{R}}\mathbf{v}, \qquad \boldsymbol{\mathcal{H}}_{\mathrm{F},\mathrm{T}} = \mathbf{H}_{\mathrm{F},\mathrm{T}} - \mathbf{v}\wedge\mathbf{D}_{\mathrm{F},\mathrm{T}}, \tag{5.44}$$

where $\boldsymbol{\mathcal{E}}$ is the electromotive intensity, $\boldsymbol{\mathcal{J}}_\mathrm{F}$ is the conduction current density, $\boldsymbol{\mathcal{M}}$ is the magnetization, and $\boldsymbol{\mathcal{H}}_\mathrm{F}$ is the magnetomotive intensity. In an aether-frame $\mathsf{F}^{\mathsf{aether}}$ (see appendix B.3), where $\mathbf{D}_\mathrm{T} = \varepsilon_0\mathbf{E}$ and $\mathbf{B} = \mu_0\mathbf{H}_\mathrm{T}$, the quantities are mutually coupled to each other,

$$\mathbf{D}_\mathrm{F} = \varepsilon_0\mathbf{E} + \mathbf{P}, \qquad \mathbf{H}_\mathrm{F} = \mathbf{B}/\mu_0 - \mathbf{M}, \qquad \boldsymbol{\mathcal{H}}_\mathrm{F} = \mathbf{B}/\mu_0 - \mathbf{v}\wedge\varepsilon_0\mathbf{E} - \boldsymbol{\mathcal{M}}. \tag{5.45}$$

We make our our first constitutive modeling assumption, and assume linear dielectric and magnetic materials, *i.e.* $\mathbf{P} = \varepsilon_0\chi\mathbf{E}$ and $\mathbf{M} = \mathbf{B}\cdot\chi_\mathrm{B}/\mu_0$, such that

$$\mathbf{D}_\mathrm{F}{=}\varepsilon_0\varepsilon_\mathrm{R}\mathbf{E}, \qquad \text{where} \quad \varepsilon_\mathrm{R}{=}1+\chi, \tag{5.46}$$

$$\mathbf{H}_\mathrm{F}{=}\mathbf{B}/\mu_0\mu_\mathrm{R} \quad \text{and} \quad \mathcal{H}_\mathrm{F}{=}\mathbf{B}/\mu_0\mu_\mathrm{R} - \varepsilon_0\varepsilon_\mathrm{R}\mathbf{E}, \quad \text{where} \quad \mu_\mathrm{R}{=}(1-\chi_\mathrm{B})^{-1}. \tag{5.47}$$

In appendix B.3, we showed that the transformation behaviour of the the Maxwell equations follows naturally from the four-dimensional description in Minkowski space-time. However, there exists a threedimensional formulation of Maxwell's equations, based on flux derivatives (see definition 7),[81] which is covariant with respect to Galilei-transformations,

$$\nabla\mathbf{B} = 0, \qquad \nabla\wedge\mathcal{E} = -\overset{*}{\mathbf{B}}, \tag{5.48}$$

$$\nabla\mathbf{D}_\mathrm{F} = \varrho_\mathrm{F}, \qquad \nabla\wedge\mathcal{H}_\mathrm{F} = \overset{*}{\mathbf{D}}_\mathrm{F} + \mathcal{J}_\mathrm{F}. \tag{5.49}$$

5.2.2 Unification of Mechanics, Thermodynamics and Electromagnetism: Electromagnetic Entropy Inequality

In this section we extend the universal balance-laws derived in section 5.1 by electromagnetic effects. Most of the results remain valid when supplemented by electromagnetic theory. However, the Euler-law and the law of energy balance must be modified.[81] As consistency check, we assume that generalized description reduces to the thermomechanical description in the limit of vanishing electromagnetic fields.

In mechanics, the material velocity $\mathbf{v}$ describes momentum per unit mass. However, in order to account for the fact that electromagnetic fields carry momentum too,[254] we introduce an abstract momentum $\mathbf{g}(\mathbf{v},\mathbf{E},\mathbf{B})$. This quantity replaces the mechanical momentum $\mathbf{v}$, to which it shall reproduce in the limit of vanishing electromagnetic fields. We generalize Euler's first law of mechanics (see eq. (5.22)) using the total momentum $\mathcal{G} = \int_V \mathrm{d}V\, \rho\mathbf{g}$, *viz.*

$$\dot{\mathcal{G}} = F, \qquad \text{i.e.} \qquad \rho\dot{\mathbf{g}} = \nabla\boldsymbol{\sigma} + \rho\mathbf{b}, \tag{5.50}$$

where $\boldsymbol{\sigma}$ is the complete stress tensor, comprising mechanical and electromagnetic contributions (the same holds for $\mathbf{b}$). Still, change of momentum equals imbalance of applied forces. Yet, in contrast to thermomechanics, it does not equal acceleration.

Next, we define angular momentum, $L_p = \int \mathrm{d}V\, (\mathbf{x}-\mathbf{x}_p)\wedge\mathbf{g}$, where the definition of the torque, see eq. (5.24), remains valid. Thus, Euler's second law of mechanics reads $\dot{L}_p = M$. Still, imbalance of torque equals change of angular momentum. However, in contrast to thermomechanics, changes in angular momentum are not directly related to material acceleration. The electromagnetic fields break the symmetry of thermomechanics (see Lemma 2).

Lemma 3. Locally, Euler's second law of mechanics reads $\rho[\mathbf{v}\otimes\mathbf{g}+\mathbf{g}\otimes\mathbf{v}]+[\boldsymbol{\sigma}-\boldsymbol{\sigma}^T]=0$. Thus, the quantity $\rho\mathbf{v}\otimes\mathbf{g}+\boldsymbol{\sigma}$ is symmetric.

Proof. For this proof, we use the same rationale as in the proof of Lemma 2, which yields the result that $\mathbf{v}\wedge\rho\mathbf{g}+(\boldsymbol{\sigma}\boldsymbol{\nabla})\wedge\boldsymbol{x}=0$. This is equivalent to the requirement that $\rho\epsilon^{ijk}(v_j g_k+\sigma_{jk})=0$ for all components i, which is true exactly if $\rho\mathbf{v}\otimes\mathbf{g}+\boldsymbol{\sigma}$ is symmetric. □

Although it becomes a function of the electromagnetic fields via $\boldsymbol{\sigma}$ and $\mathbf{b}$, the definition of $\mathit{\Pi}$ remains unchanged (see eq. (5.30)). However, when we substitute eq. (5.50) for the body force, $\rho\mathbf{v}\mathbf{b}(\mathbf{g})=\rho\mathbf{v}\dot{\mathbf{g}}-\mathbf{v}(\boldsymbol{\nabla}\boldsymbol{\sigma})$, we find $\mathit{\Pi}=\int_V \mathrm{d}V\,\rho\mathbf{v}\dot{\mathbf{g}}-\mathbf{v}\cdot(\boldsymbol{\nabla}\boldsymbol{\sigma})+\boldsymbol{\nabla}(\boldsymbol{\sigma}^T\mathbf{v})$. We simplify this expression using $\boldsymbol{\nabla}(\boldsymbol{\sigma}^T\mathbf{v})=\mathbf{v}\cdot(\boldsymbol{\nabla}\boldsymbol{\sigma})+\boldsymbol{\sigma}:\operatorname{grad}\mathbf{v}$ (see above), such that

$$\mathit{\Pi}=\int_V \mathrm{d}V\,\boldsymbol{\sigma}:\operatorname{grad}\mathbf{v}+\rho\mathbf{v}\dot{\mathbf{g}}. \tag{5.51}$$

This expression differs from the mechanical analogue because the stress tensor is not automatically symmetric (*i.e.*, $\boldsymbol{\sigma}:\operatorname{grad}\mathbf{v}\neq\boldsymbol{\sigma}:\boldsymbol{\kappa}$).

Since the heating of a body $\mathcal{Q}$ must also be supplemented by electromagnetic fields, we add an electromagnetic heat flux $\oint\mathrm{d}\boldsymbol{A}\,\mathcal{H}_\mathrm{F}\wedge\mathcal{E}$ (see appendix B.4), such that

$$\mathcal{Q}=\int \mathrm{d}V\,\rho h-\boldsymbol{\nabla}(\mathbf{q}+\mathcal{E}\wedge\mathcal{H}_\mathrm{F}) \tag{5.52}$$

The definition for the total energy remains unchanged (see eq. (5.32)), and the local balance-law for energy follows from the modified quantities $\mathit{\Pi}$ and $\mathcal{Q}$ (see eqs. (5.51) and (5.52)).

$$\rho\dot{\varepsilon}=\boldsymbol{\sigma}:\operatorname{grad}\mathbf{v}+\rho\mathbf{v}\dot{\mathbf{g}}+\rho h-\boldsymbol{\nabla}\mathbf{q}+\boldsymbol{\nabla}\left(\mathcal{H}_\mathrm{F}\wedge\mathcal{E}\right). \tag{5.53}$$

Thus, even when thermally insulated (no heating) and at rest (no mechanical powers acting), the energy changes when subjected to electromagnetic fields. Mass conservation and the entropy inequality remain the same, such that

$$\mathcal{R}=T\rho\dot{s}-\rho h+T\boldsymbol{\nabla}\boldsymbol{\xi}_s\geq 0. \tag{5.54}$$

We derive the electromagnetic entropy inequality by solving eq. (5.53) for ρh, and substitute the result into eq. (5.54),

$$\mathcal{R}=\rho T\dot{s}-\rho\dot{\varepsilon}+\boldsymbol{\sigma}:\operatorname{grad}\mathbf{v}+\rho\mathbf{v}\dot{\mathbf{g}}-\boldsymbol{\nabla}\mathbf{q}-\boldsymbol{\nabla}\left(\mathcal{E}\wedge\mathcal{H}_\mathrm{F}\right)+T\boldsymbol{\nabla}\boldsymbol{\xi}_s. \tag{5.55}$$

5.2.3 The Method of Coleman and Noll

Next, we derive the constitutive equations via the method of Coleman and Noll.

To address this goal, we bring eq. (5.55) in a form which allows to identify conjugate pairs of variables.

First, we reexpress the Poynting-flux $\boldsymbol{\nabla}(\mathcal{H}_\mathrm{F}\wedge\boldsymbol{\mathcal{E}}) = \boldsymbol{\mathcal{E}}(\boldsymbol{\nabla}\wedge\mathcal{H}_\mathrm{F}) - \mathcal{H}_\mathrm{F}(\boldsymbol{\nabla}\wedge\boldsymbol{\mathcal{E}})$ appearing in eq. (5.55). Due to our linear constitutive model eq. (5.45) this can be done in various ways, where each form for $\boldsymbol{\nabla}(\mathcal{H}_\mathrm{F}\wedge\boldsymbol{\mathcal{E}})$ leads to a different set of conjugate pair of electromagnetic variables. One choice is to focus on conjugate pairs of covariant electromagnetic variables (see also appendix B.3) by using the covariant Maxwell's equations (see eqs. (5.48) and (5.49)). In appendix D.3 we show that this yields, $\boldsymbol{\nabla}(\mathcal{H}_\mathrm{F}\wedge\boldsymbol{\mathcal{E}}) = \boldsymbol{\mathcal{E}}\boldsymbol{\mathcal{J}}_\mathrm{F} + \boldsymbol{\mathcal{E}}\dot{\mathbf{D}}_\mathrm{F} + \mathcal{H}_\mathrm{F}\dot{\mathbf{B}} + [(\boldsymbol{\mathcal{E}}\mathbf{D}_\mathrm{F} + \mathcal{H}_\mathrm{F}\mathbf{B})\,\mathbf{Id} - \boldsymbol{\mathcal{E}}\otimes\mathbf{D}_\mathrm{F} - \mathcal{H}_\mathrm{F}\otimes\mathbf{B}] : \operatorname{grad}\mathbf{v}$, such that

$$\begin{aligned}\mathcal{R} = -\rho\,[\dot{\varepsilon} - T\dot{s} - \mathbf{v}\dot{\mathbf{g}}] + [\boldsymbol{\sigma} + (\boldsymbol{\mathcal{E}}\mathbf{D}_\mathrm{F} + \mathcal{H}_\mathrm{F}\mathbf{B})\,\mathbf{Id} - \boldsymbol{\mathcal{E}}\otimes\mathbf{D}_\mathrm{F} - \mathcal{H}_\mathrm{F}\otimes\mathbf{B}] : \operatorname{grad}\mathbf{v} \\ + \boldsymbol{\mathcal{E}}\dot{\mathbf{D}}_\mathrm{F} + \mathcal{H}_\mathrm{F}\dot{\mathbf{B}} - \boldsymbol{\nabla}\mathbf{q} + T\boldsymbol{\nabla}\boldsymbol{\xi}_s + \boldsymbol{\mathcal{E}}\boldsymbol{\mathcal{J}}_\mathrm{F}\end{aligned} \qquad (5.56)$$

The products $\varPsi_A\cdot\dot{\varUpsilon}_B$ appearing in eq. (5.56) are similar to the total differentials of thermodynamic potentials P ("characteristic functions"), which take the form

$$\mathrm{d}\mathsf{P}(\boldsymbol{\varUpsilon}) = \sum_A \partial\mathsf{P}/\partial\varUpsilon_A\cdot\mathrm{d}\varUpsilon_A. \qquad (5.57)$$

where $\varPsi_A = \partial\mathsf{P}/\partial\varUpsilon_B$. The set of variables $\boldsymbol{\varUpsilon} = \{\varUpsilon_A, \varUpsilon_B, \ldots\}$ forms the "materials' law", which determines the specific system described by $\mathsf{P}(\boldsymbol{\varUpsilon})$, where pairs $(\varPsi_B = \partial\mathsf{P}/\partial\varUpsilon_A, \varUpsilon_A)$ determine the "conjugate variables".

Thus, the choice of the electromagnetic variables for the material's law $\boldsymbol{\varUpsilon}$ determines the electromagnetic conjugate pairs. This observation outlines the method of Coleman and Noll, where the conjugate pairs appearing in the entropy inequality determine the constitutive equations. However, symmetry arguments imply that not all such pairs appearing in $\mathcal{R}$ can be resolved by this method (see the discussion in chapter 15). Because we aim at $\mathbf{P}$ and $\boldsymbol{\mathcal{M}}$ for the electromagnetic variables in the materials law, we use (see appendix D.3)

$$\begin{aligned}\boldsymbol{\nabla}(\mathcal{H}_\mathrm{F}\wedge\boldsymbol{\mathcal{E}}) = \frac{\mathrm{d}}{\mathrm{d}t}\Big[\varepsilon_0\mathbf{E}^2/2 + \boldsymbol{\mathcal{E}}\mathbf{P} + \mathbf{B}^2/2\mu_0 - \varepsilon_0(\mathbf{E}\wedge\mathbf{B})\mathbf{v}\Big] + \boldsymbol{\mathcal{E}}\boldsymbol{\mathcal{J}}_\mathrm{F} - \boldsymbol{\mathcal{M}}\dot{\mathbf{B}} - \\ + \varepsilon_0(\mathbf{E}\wedge\mathbf{B})\dot{\mathbf{v}} - \mathbf{P}\dot{\boldsymbol{\mathcal{E}}} + \Big[\Big(\varepsilon_0\mathbf{E}^2 + \boldsymbol{\mathcal{E}}\mathbf{P} + (\mathbf{B}/\mu_0 - \boldsymbol{\mathcal{M}})\,\mathbf{B} - \varepsilon_0(\mathbf{E}\wedge\mathbf{B})\mathbf{v}\Big)\,\mathbf{Id} - \\ - \varepsilon_0\mathbf{E}\otimes\mathbf{E} - \boldsymbol{\mathcal{E}}\otimes\mathbf{P} - \mathbf{B}\otimes\mathbf{B}/\mu_0 + \boldsymbol{\mathcal{M}}\otimes\mathbf{B} - \varepsilon_0(\mathbf{E}\wedge\mathbf{B})\otimes\mathbf{v}\Big] : \operatorname{grad}\mathbf{v}.\end{aligned} \qquad (5.58)$$

Thus, in an aether-frame and due to our linear constitutive model (eq. (5.47)),

$$\frac{1}{2}\frac{\mathrm{d}(\varepsilon_0\varepsilon_\mathrm{R}\mathbf{E}^2+\mathbf{B}^2/\mu_0\mu_\mathrm{R}\,)}{\mathrm{d}t}=\Big(\Big[\varepsilon_0\varepsilon_\mathrm{R}\mathbf{E}\otimes\mathbf{E}+\mathbf{B}\otimes\mathbf{B}/\mu_0\mu_\mathrm{R}\,-\varepsilon_0\varepsilon_\mathrm{R}\mathbf{E}^2+\mathbf{B}^2/\mu_0\mu_\mathrm{R}\,\Big]\,\mathbf{Id}$$
$$-\left[\left(\varepsilon_0\varepsilon_\mathrm{R}\mathbf{E}\wedge\mathbf{v}\right)\mathbf{B}\right]\mathbf{Id}\,-\varepsilon_0\varepsilon_\mathrm{R}\left(\mathbf{B}\wedge\mathbf{E}\right)\otimes\mathbf{v}\Big):\mathrm{grad}\,\mathbf{v}+\mathbf{v}\frac{\mathrm{d}}{\mathrm{d}t}\left(\varepsilon_0\varepsilon_\mathrm{R}\mathbf{E}\wedge\mathbf{B}\right)$$
$$+\boldsymbol{\nabla}\left(\boldsymbol{\mathcal{H}}_\mathrm{F}\wedge\boldsymbol{\mathcal{E}}\right)-\boldsymbol{\mathcal{E}}\boldsymbol{\mathcal{J}}_\mathrm{F}. \quad (5.59)$$

Thus, in the limit $\mathbf{v}=0$, the term $\boldsymbol{\nabla}(\boldsymbol{\mathcal{H}}_\mathrm{F}\wedge\boldsymbol{\mathcal{E}})$ describes the energy-flux of the electromagnetic fields, in accordance with the conservation of the electromagnetic energy-momentum tensor $\partial_A T^{AB}=0$ (see appendix B.4). We insert eq. (5.58) into eq. (5.55),

$$\mathcal{R}=\rho T\dot{s}-\rho\dot{\varepsilon}+\boldsymbol{\sigma}:\mathrm{grad}\,\mathbf{v}+\rho\mathbf{v}\dot{\mathbf{g}}-\boldsymbol{\nabla}\mathbf{q}+\frac{\mathrm{d}}{\mathrm{d}t}\left[\frac{\varepsilon_0\mathbf{E}^2}{2}+\boldsymbol{\mathcal{E}}\mathbf{P}+\mathbf{B}^2/2\mu_0\,-\varepsilon_0(\mathbf{E}\wedge\mathbf{B})\mathbf{v}\right]-\boldsymbol{\mathcal{M}}\dot{\mathbf{B}}$$
$$+\varepsilon_0(\mathbf{E}\wedge\mathbf{B})\dot{\mathbf{v}}-\mathbf{P}\dot{\boldsymbol{\mathcal{E}}}+\Big[\Big(\varepsilon_0\mathbf{E}^2+\boldsymbol{\mathcal{E}}\mathbf{P}+\left(\mathbf{B}/\mu_0\,-\boldsymbol{\mathcal{M}}\right)\mathbf{B}-\varepsilon_0(\mathbf{E}\wedge\mathbf{B})\mathbf{v}\Big)\,\mathbf{Id}\,-\varepsilon_0\mathbf{E}\otimes\mathbf{E}$$
$$-\boldsymbol{\mathcal{E}}\otimes\mathbf{P}-\mathbf{B}\otimes\mathbf{B}/\mu_0\,+\boldsymbol{\mathcal{M}}\otimes\mathbf{B}-\varepsilon_0(\mathbf{E}\wedge\mathbf{B})\otimes\mathbf{v}\Big]:\mathrm{grad}\,\mathbf{v}+\boldsymbol{\mathcal{E}}\boldsymbol{\mathcal{J}}_\mathrm{F}+T\boldsymbol{\nabla}\boldsymbol{\xi}_s. \quad (5.60)$$

The quantity ε appearing in eq. (5.60) is a function of the internal energy or it's Legendre transformed, the Helmholtz free energy density, see eqs. (5.34) and (5.35). Our next step is to model the electromagnetic generalization for φ_H. To address this goal, we identify two constraints on φ_H. In eq. (5.60) the desired conjugated pairs $\mathbf{P}\dot{\boldsymbol{\mathcal{E}}}$ and $\boldsymbol{\mathcal{M}}\dot{\mathbf{B}}$ are supplemented by electromagnetic terms comprised in the time-derivative of the first bracked term. To ensure that $\mathbf{P}\dot{\boldsymbol{\mathcal{E}}}$ and $\boldsymbol{\mathcal{M}}\dot{\mathbf{B}}$ are the only electromagnetic conjugate variables, we define φ_H such that the first bracked term vanishes when we insert φ_H into eq. (5.55). Next, in section 5.1, we defined $u=\varepsilon-\mathbf{v}^2/2$ such that $\varphi_\mathrm{H}=u-Ts$, which now serves as limiting case for vanishing electromagnetic fields. In accordance with both constraints, we define

$$\varphi_\mathrm{H}=\varepsilon-\mathbf{v}\mathbf{g}+\mathbf{v}^2/2\;-Ts-\left[\varepsilon_0\mathbf{E}^2/2\;+\boldsymbol{\mathcal{E}}\mathbf{P}+\mathbf{B}^2/2\mu_0\;-\left(\varepsilon_0\mathbf{E}\wedge\mathbf{B}\right)\cdot\mathbf{v}\right]/\rho\,. \quad (5.61)$$

We evaluate the time-derivative of eq. (5.61), and substitute for $\rho\dot{\varepsilon}$ in eq. (5.60),

$$\mathcal{R}=\boldsymbol{\tau}:\mathrm{grad}\,\mathbf{v}-\rho\dot{\varphi}_\mathrm{H}-\rho\mathbf{v}\left[\mathbf{g}-\mathbf{v}-\left(\varepsilon_0\mathbf{E}\wedge\mathbf{B}\right)/\rho\,\right]-\rho s\dot{T}+\boldsymbol{\mathcal{E}}\boldsymbol{\mathcal{J}}_\mathrm{F}-\boldsymbol{\mathcal{M}}\dot{\mathbf{B}}-\mathbf{P}\dot{\boldsymbol{\mathcal{E}}}-$$
$$-\boldsymbol{\nabla}\sum_{\alpha=1}^{\mathrm{N}}\mu_\alpha\mathcal{N}_\alpha-\boldsymbol{\xi}_s\boldsymbol{\nabla}T, \quad (5.62)$$

where we collected all tensorial terms which are contracted with the velocity gradient in the viscosity tensor,

$$\boldsymbol{\tau} = \boldsymbol{\sigma} + \Big(\varepsilon_0\mathbf{E}^2/2 + \mathbf{B}^2/2\mu_0 - \boldsymbol{\mathcal{M}}\mathbf{B}\Big)\,\mathbf{Id} - \varepsilon_0\mathbf{E}\otimes\mathbf{E} - \boldsymbol{\mathcal{E}}\otimes\mathbf{P} - \mathbf{B}\otimes\mathbf{B}/\mu_0 + \\ + \boldsymbol{\mathcal{M}}\otimes\mathbf{B} - (\varepsilon_0\mathbf{E}\wedge\mathbf{B})\otimes\mathbf{v}. \quad (5.63)$$

Equation (5.62) is the basis for a wide class of materials, and serves as restriction on the constitutive equations. It depends on $\dot{\varphi}_{\mathrm{H}}$ via the material model $\varphi_{\mathrm{H}}(\boldsymbol{\Upsilon})$ via the chain rule,

$$\rho\dot{\varphi}_{\mathrm{H}} = \rho\sum_{\Upsilon_A}\frac{\partial\varphi_{\mathrm{H}}}{\partial\Upsilon_A}\cdot\dot{\Upsilon}_A, \quad (5.64)$$

Note that definitions for φ_{H} different than eq. (5.61) are possible, which are all equivalent in the non-relativistic case (see 245 for a detailed discussion). In particular, moving electromagnetic terms from to eq. (5.61) (and vice versa) modifies the pair of conjugated electromagnetic variables and, hence, the constitutive equations and the materials law. For example, moving $\boldsymbol{\mathcal{M}}\mathbf{B}$ from eq. (5.62) to φ_{H} yields a constitutive equation for the magnetic field (instead of for $\boldsymbol{\mathcal{M}}$) $\mathbf{B}{=}\partial(\rho\varphi_{\mathrm{H}})/\partial\boldsymbol{\mathcal{M}}$ (such that $\boldsymbol{\mathcal{M}}{\in}\boldsymbol{\Upsilon}$), and moving $\boldsymbol{\mathcal{E}}\mathbf{P}$ from φ_{H} to eq. (5.62) yields a constitutive equation for the electric field (instead of for $\mathbf{P}$) $\boldsymbol{\mathcal{E}}{=}\partial(\rho\varphi_{\mathrm{H}})/\partial\mathbf{P}$ (such that $\mathbf{P}{\in}\boldsymbol{\Upsilon}$). However, it shall be noted though that the energy is a gauge field, *i.e.* only variations $\mathrm{d}(\rho\varphi_{\mathrm{H}})$ can be measured (see eq. (8.11), and our discussion in section 15.1).

Next, we restrict the yet universal formalism by modeling the materials law $\boldsymbol{\Upsilon}$ for electrolytes (note that we showed in appendix B that symmetry arguments restrict the material law $\boldsymbol{\Upsilon}$), as viscoelastic ($\boldsymbol{\kappa}$ and $\boldsymbol{F}^{\mathrm{uni}}$), multicomponent ($c_\alpha$), polarizable ($\boldsymbol{\mathcal{E}}$), magnetizable ($\mathbf{B}$) and heat-conducting ($T$ and $\boldsymbol{\nabla}T$) media at liquid state,

$$\boldsymbol{\Upsilon} = \Big\{c_1, \ldots, c_{\mathrm{N}}, T, \boldsymbol{\nabla}T, \boldsymbol{\mathcal{E}}, \mathbf{B}, \boldsymbol{\kappa}, \boldsymbol{F}^{\mathrm{uni}}\Big\}. \quad (5.65)$$

Viscous liquids are described via $\boldsymbol{\kappa}$, and extend to viscoelastic liquids via $\boldsymbol{F}^{\mathrm{uni}}$. We use the isochoric unimodular deformation $\boldsymbol{F}^{\mathrm{uni}}{=}(\det\boldsymbol{F})^{-1/3}\,\boldsymbol{F}$ instead of the deformation because $\boldsymbol{F}$ is not an independent variable ($\boldsymbol{F}$ couples to the concentrations via $\dot{\rho}{+}\rho\,\mathrm{tr}(\dot{\boldsymbol{F}}\cdot\boldsymbol{F}^{-1}){=}0$, see Lemma 1). For $\rho\dot{\varphi}_{\mathrm{H}}$ we use $\dot{c}_\alpha = -c_\alpha\,\mathbf{Id}:\mathrm{grad}\,\mathbf{v}{-}\boldsymbol{\nabla}\boldsymbol{\mathcal{N}}_\alpha$, see section 5.1.1, and $\partial\varphi_{\mathrm{H}}/\partial\,\mathrm{grad}\,\mathbf{v}{:}\overset{\cdot}{\mathrm{grad}}\,\mathbf{v}{=}\partial\varphi_{\mathrm{H}}/\partial\boldsymbol{\kappa}{:}\dot{\boldsymbol{\kappa}}$. For matrix-quantities $\boldsymbol{\mathcal{M}}$ (like $\boldsymbol{F}^{\mathrm{uni}}$ and $\boldsymbol{\kappa}$), we use the notation $\partial\varphi_{\mathrm{H}}/\partial\boldsymbol{\mathcal{M}}{:}\boldsymbol{\mathcal{M}} = \sum_{ij}\partial\varphi_{\mathrm{H}}/\partial\mathcal{M}_{ij}{:}\mathcal{M}_{ij}$. In appendix D.2 we show that

$$\frac{\partial(\rho\varphi_{\mathrm{H}})}{\partial\,\boldsymbol{F}^{\mathrm{uni}}} : \dot{\boldsymbol{F}}^{\mathrm{uni}} = \Big(\boldsymbol{\mathfrak{D}} - \frac{1}{3}\,\mathrm{tr}\,\boldsymbol{\mathfrak{D}}\cdot\mathbf{Id}\Big) : \boldsymbol{\kappa} = \boldsymbol{\mathfrak{D}}_{\mathrm{tf}}{:}\boldsymbol{\kappa}, \quad (5.66)$$

where $\boldsymbol{\mathfrak{D}} = \partial(\rho\varphi_{\mathrm{H}})/\partial\,\boldsymbol{F}^{\mathrm{uni}}\cdot(\boldsymbol{F}^{\mathrm{uni}})^T$ is a symmetric matrix. Thus $\boldsymbol{F}^{\mathrm{uni}}\in\boldsymbol{\Upsilon}$ accounts for non-isotropic deformations, as only the trace-free part of it's irreducible decomposition contributes to $\dot{\varphi}_{\mathrm{H}}$, whereas the derivatives $\dot{c}_\alpha$ account for isotropic expansions. The remaining terms in $\dot{\varphi}_{\mathrm{H}}$ are trivial. Altogether, we find

$$\begin{aligned}\mathcal{R}=&\Big(\boldsymbol{\tau}+\rho\sum_{\alpha=1}^{\mathrm{N}}c_\alpha\partial\varphi_{\mathrm{H}}/\partial c_\alpha\cdot\mathbf{Id}-\mathfrak{D}_{\mathrm{tf}}\Big):\mathrm{grad}\,\mathbf{v}-\sum_{\alpha=1}^{\mathrm{N}}\boldsymbol{\mathcal{N}}_\alpha\boldsymbol{\nabla}\mu_\alpha+\sum_{\alpha=1}^{\mathrm{N}}(\rho\partial_{c_\alpha}\varphi_{\mathrm{H}}-\mu_\alpha)\,\boldsymbol{\nabla}\boldsymbol{\mathcal{N}}_\alpha\\ &+\boldsymbol{\mathcal{E}}\boldsymbol{\mathcal{J}}_{\mathrm{F}}-\boldsymbol{\xi}_s\boldsymbol{\nabla}T-\partial_{\mathrm{grad}\,T}(\rho\varphi_{\mathrm{H}}):\overset{\cdot}{\mathrm{grad}\,T}-\partial_{\boldsymbol{\kappa}}(\rho\varphi_{\mathrm{H}}):\dot{\boldsymbol{\kappa}}-\rho\,(s+\partial_T\varphi_{\mathrm{H}})\,\dot{T}\\ &-[\mathbf{P}+\partial_{\boldsymbol{\mathcal{E}}}(\rho\varphi_{\mathrm{H}})]\,\dot{\boldsymbol{\mathcal{E}}}-[\boldsymbol{\mathcal{M}}+\partial_{\mathbf{B}}(\rho\varphi_{\mathrm{H}})]\,\dot{\mathbf{B}}-\rho\dot{\mathbf{v}}\,(\mathbf{g}-\mathbf{v}-\varepsilon_0\mathbf{E}\wedge\mathbf{B}/\rho\,)\,. \qquad (5.67)\end{aligned}$$

We determine the constitutive equations, by identification of the conjugate pairs,

$$s=-\frac{\partial\varphi_{\mathrm{H}}}{\partial T}, \qquad (5.68)$$

$$\boldsymbol{\mathcal{M}}=-\frac{\partial(\rho\varphi_{\mathrm{H}})}{\partial\mathbf{B}}, \qquad (5.69)$$

$$\mathbf{P}=-\frac{\partial(\rho\varphi_{\mathrm{H}})}{\partial\boldsymbol{\mathcal{E}}}, \qquad (5.70)$$

$$0=\frac{\partial(\rho\varphi_{\mathrm{H}})}{\partial\,\mathrm{grad}\,T}, \qquad (5.71)$$

$$0=\frac{\partial(\rho\varphi_{\mathrm{H}})}{\partial\boldsymbol{\kappa}}, \qquad (5.72)$$

$$\mathbf{g}=\mathbf{v}+\varepsilon_0\mathbf{E}\wedge\mathbf{B}/\rho\,. \qquad (5.73)$$

From eq. (5.68)), and via the Legendre-transformation $\varphi_{\mathrm{H}}=u-Ts$, we find a constitutive equation for the internal energy density,

$$\rho u=-T^2\cdot\partial(\rho\varphi_{\mathrm{H}}/T\,)/\partial T. \qquad (5.74)$$

Next, we determine the constitutive equation for the chemical potentials from the fifth term in eq. (5.67). Using the trivial flux constraint $\sum_{\alpha=1}^{\mathrm{N}}M_\alpha\boldsymbol{\mathcal{N}}_\alpha=0$ (see eq. (5.10)), it follows that

$$\begin{aligned}\sum_{\alpha=1}^{\mathrm{N}}(\rho\frac{\partial\varphi_{\mathrm{H}}}{\partial c_\alpha}-\mu_\alpha)\boldsymbol{\nabla}\boldsymbol{\mathcal{N}}_\alpha&=\sum_{\alpha=1}^{\mathrm{N}}(\frac{\partial(\rho\varphi_{\mathrm{H}})}{\partial c_\alpha}-\varphi_{\mathrm{H}}M_\alpha-\mu_\alpha)\boldsymbol{\nabla}\boldsymbol{\mathcal{N}}_\alpha \qquad (5.75)\\ &=\sum_{\alpha=1}^{\mathrm{N}}(\frac{\partial(\rho\varphi_{\mathrm{H}})}{\partial c_\alpha}-\mu_\alpha)\boldsymbol{\nabla}\boldsymbol{\mathcal{N}}_\alpha-\varphi_{\mathrm{H}}\boldsymbol{\nabla}(\sum_{\alpha=1}^{\mathrm{N}}M_\alpha\boldsymbol{\mathcal{N}}_\alpha) \qquad (5.76)\\ &=\sum_{\alpha=1}^{\mathrm{N}}\left(\frac{\partial(\rho\varphi_{\mathrm{H}})}{\partial c_\alpha}-\mu_\alpha\right)\boldsymbol{\nabla}\boldsymbol{\mathcal{N}}_\alpha. \qquad (5.77)\end{aligned}$$

This suggests the canonic constitutive equation for the chemical potential,

$$\mu_\alpha = \partial(\rho\varphi_\mathrm{H})/\partial c_\alpha. \tag{5.78}$$

However, the derivation of the constitutive equation eq. (5.78) from the entropy inequality eq. (5.67) is not unique. We can add terms $\xi \cdot M_\alpha$, where $\dim \xi = \mathrm{J\,kg^{-1}}$, to the brackets without changing the left side of eq. (5.75). Hence, the constitutive equation for the chemical potential is ambiguous up to,

$$\mu_\alpha^\xi = \partial(\rho\varphi_\mathrm{H})/\partial c_\alpha - \xi \cdot M_\alpha. \tag{5.79}$$

This ambiguity is an artefact from the fact that we have not yet identified the correct set of independent material variables. As we will see, only N-1 species concentrations are independent ($\boldsymbol{\Upsilon}$ comprises all N quantities c_α). Below, we resolve this ambiguity and introduce a set of N-1 chemical potentials (see eq. (5.106)),

$$\tilde{\mu}_\alpha^\xi = \mu_\alpha^\xi - M_\alpha/M_1 \cdot \mu_1^\xi = \mu_\alpha - M_\alpha/M_1 \cdot \mu_1 = \tilde{\mu}_\alpha. \tag{5.80}$$

From the constitutive equations for the electromagnetic variables follows the important symmetry property that the material velocity cannot be a material variable.

Lemma 4. Because the electromagnetic variables in the materials law are covariant under Galilei transformations, the material velocity cannot be a material variable.

Proof. Let us assume that $\mathbf{v} \in \boldsymbol{\Upsilon}$. Then, the formal evaluation of $\varphi_\mathrm{H}(\boldsymbol{\Upsilon})$ via eq. (5.64) would yield a contribution $\partial\rho\varphi_\mathrm{H}/\partial\mathbf{v}$ to eq. (5.67), and modify the constitutive equation for $\mathbf{g}$ according to (see eq. (5.73))

$$\mathbf{g} = \mathbf{v} + \varepsilon_0 \mathbf{E} \wedge \mathbf{B}/\rho \; - \partial\varphi_\mathrm{H}/\partial\mathbf{v}. \tag{5.81}$$

However, this is in conflict with universal symmetry arguments. The constraint that $\mathbf{g}$ shall reproduce the material velocity $\mathbf{v}$ in the absence of electromagnetic fields, applied to the eq. (5.81), requires that

$$\partial\varphi_\mathrm{H}(\boldsymbol{\Upsilon})/\partial\mathbf{v}|_{\mathbf{B},\mathcal{E}=0} = 0. \tag{5.82}$$

Both electromagnetic variables, $\mathbf{P}$ and $\boldsymbol{\mathcal{M}}$, are objective quantities, whereas the material velocity is not (see Lemma 8). This implies for, *e.g.*, the polarization,

$$0 = \frac{\partial\mathbf{P}}{\partial\mathbf{v}} = -\frac{\partial}{\partial\mathbf{v}}\frac{\partial\rho\varphi_\mathrm{H}}{\partial\mathcal{E}} = -\frac{\partial}{\partial\mathcal{E}}\frac{\partial\rho\varphi_\mathrm{H}}{\partial\mathbf{v}} = \frac{\partial}{\partial\mathcal{E}}\frac{\partial\varphi_\mathrm{H}}{\partial\mathbf{v}}, \tag{5.83}$$

since we may commute the partial derivatives. A similar argument holds for $\mathbf{B}$.

Thus, $\partial\varphi_{\mathrm{H}}/\partial\mathbf{v}$ is independent of $\boldsymbol{\mathcal{E}}$ and $\mathbf{B}$. Hence, the condition eq. (5.82) is independent of the electromagnetic variables, such that $\partial\varphi_{\mathrm{H}}/\partial\mathbf{v} = 0$ always. ◻

The first term appearing on the right side of eq. (5.67) yields the constitutive equation for the stress tensor. However, we first note that

$$\rho \sum_{\alpha=1}^{\mathrm{N}} c_\alpha \frac{\partial\varphi_{\mathrm{H}}}{\partial c_\alpha} = \sum_{\alpha=1}^{\mathrm{N}} c_\alpha \mu_\alpha - \rho\varphi_{\mathrm{H}}, \tag{5.84}$$

which follows form the constitutive equation for the chemical potential eq. (5.78). Thus, expanding the viscosity tensor as in eq. (5.63) yields for the stress tensor

$$\begin{aligned} \boldsymbol{\sigma} = \boldsymbol{\tau} - \Big(\varepsilon_0\mathbf{E}^2/2 + \mathbf{B}^2/2\mu_0 - \boldsymbol{\mathcal{M}}\mathbf{B} + \sum_{\alpha=1}^{\mathrm{N}} c_\alpha\mu_\alpha - \rho\varphi_{\mathrm{H}}\Big)\,\mathbf{Id} + \boldsymbol{\mathfrak{D}}_{\mathrm{tf}} + \varepsilon_0\mathbf{E}\otimes\mathbf{E} + \boldsymbol{\mathcal{E}}\otimes\mathbf{P} + {} \\ + \mathbf{B}\otimes\mathbf{B}/\mu_0 - \boldsymbol{\mathcal{M}}\otimes\mathbf{B} + (\varepsilon_0\mathbf{E}\wedge\mathbf{B})\otimes\mathbf{v}. \end{aligned} \tag{5.85}$$

Here, we assume that the viscosity tensor $\boldsymbol{\tau}(\boldsymbol{\kappa})$ is a symmetric function of the strainrate-tensor.[70] As outlined above, the contribution stemming from the unimodular deformation $\boldsymbol{\mathfrak{D}}_{\mathrm{tf}}$ account for isochoric deformations. Since this quantity is trace-free, it comprises only anisotropic stresses. In contrast, isotropic stresses due to elastic expansion are comprised in the quantity $\sum_{\alpha=1}^{\mathrm{N}} c_\alpha\mu_\alpha - \rho\varphi_{\mathrm{H}}$ which induce elastic pressure-forces, see eq. (5.90) below.

All but the quantities $\mathbf{P}\otimes\boldsymbol{\mathcal{E}}$, $\boldsymbol{\mathcal{M}}\otimes\mathbf{B}$ and the Minkowski-momentum $(\varepsilon_0\mathbf{E}\wedge\mathbf{B})\otimes\mathbf{v}$ appearing in eq. (5.85) are symmetric. Thus, due to these terms, the electromagnetic stress tensor is not a-priori symmetric. However, we still must evaluate Euler's second law of mechanics (Lemma 3), which implies that the quantities $\mathbf{g}$ and $\boldsymbol{\sigma}$ satisfy the constraint

$$\rho\mathbf{v}\otimes\mathbf{g} - \rho\mathbf{g}\otimes\mathbf{v} + \boldsymbol{\sigma} - \boldsymbol{\sigma}^T = 0. \tag{5.86}$$

Since $\mathbf{g}$ and $\boldsymbol{\sigma}$ both follow from the free energy density φ_{H} via constitutive equations, this constitutes a symmetry constraint on φ_{H}.

Lemma 5. Euler's second law of mechanics implies that φ_{H} must be objective with respect to the electromagnetic variables $\boldsymbol{\mathcal{E}}$ and $\mathbf{B}$.

Proof. Using the constitutive equation for $\mathbf{g}$, eq. (5.73) and the stress tensor eq. (5.85) we find for eq. (5.86)

$$0 = \rho\mathbf{v}\otimes\mathbf{g} - \rho\mathbf{g}\otimes\mathbf{v} + \boldsymbol{\sigma} - \boldsymbol{\sigma}^T = \boldsymbol{\mathcal{E}}\otimes\mathbf{P} - \mathbf{P}\otimes\boldsymbol{\mathcal{E}} + \boldsymbol{\mathcal{M}}\otimes\mathbf{B} - \mathbf{B}\otimes\boldsymbol{\mathcal{M}}. \tag{5.87}$$

The Minkowski-term appearing in the constitutive equation for $\mathbf{g}$ and $\boldsymbol{\sigma}$ cancel each other. Thus, the two quantities $\boldsymbol{\mathcal{E}} \otimes \mathbf{P}$ and $\boldsymbol{\mathcal{M}} \otimes \mathbf{B}$ are symmetric. However, since $\boldsymbol{\mathcal{E}} \otimes \mathbf{P} = \boldsymbol{\mathcal{E}} \otimes \partial \rho \varphi_{\mathrm{H}} / \partial \boldsymbol{\mathcal{E}}$, and $\boldsymbol{\mathcal{M}} \otimes \mathbf{B} = \mathbf{B} \otimes \partial \rho \varphi_{\mathrm{H}} / \partial \mathbf{B}$ consist of conjugate pairs (see eqs. (5.69) and (5.70)), Theorem 2 implies that φ_{H} is objective with respect to the electromagnetic variables $\boldsymbol{\mathcal{E}}$ and $\mathbf{B}$. □

Thus, in the electromagnetic case, Euler's second law of mechanics is equivalent to the axiom of material frame indifference, discussed in appendix B.5. There, we proved that such objective functions $\varphi_{\mathrm{H}}(\boldsymbol{\mathcal{E}}, \mathbf{B})$ can only be functions of the invariant quantities $\boldsymbol{\mathcal{E}}^2$, $\mathbf{B}^2$, $\boldsymbol{\mathcal{E}} \cdot \mathbf{B}$, or $\boldsymbol{\mathcal{E}} \wedge \mathbf{B} = \boldsymbol{\mathcal{E}} \cdot \mathbf{B} - \boldsymbol{\mathcal{E}}^2 \mathbf{B}^2$, see eq. (B.45).

Furthermore $\boldsymbol{\sigma}$ is antisymmetric only due to the Minkowski-momentum $(\varepsilon_0 \mathbf{E} \wedge \mathbf{B}) \otimes \mathbf{v}$. However, when magnetic fields can be neglected, this term vanishes, and the stress tensor becomes symmetric. This constitutes the electrostatic limit which we discuss below (see section 5.2.4).

The total energy density follows from substituting $\mathbf{g}$ (eq. (5.73)) and φ_{H} (eq. (5.61)),

$$\epsilon = \varphi_{\mathrm{H}} + \mathbf{v}^2/2 + Ts + [\varepsilon_0 \mathbf{E}^2/2 + \boldsymbol{\mathcal{E}} \mathbf{P} + \mathbf{B}^2/2\mu_0]/\rho\,. \tag{5.88}$$

Thus, due to the terms $\mathbf{v}^2$ and $\mathbf{E}^2$, the energy density ϵ is not objective with respect to Galilei transformations. Likewise, the momentum density eq. (5.73), and the stress tensor eq. (5.85) are also not Galilei-invariant.

The stress tensor determines the pressure via the isotropic stress forces,[255]

$$p = -\mathrm{tr}\,(\boldsymbol{\sigma})\,/3\,. \tag{5.89}$$

The non-electromagnetic contributions are the viscous stresses, which lead to momentum dissipation (see section 5.3.2). Stresses due to the isotropic deformation $\sum_{\alpha=1}^{\mathrm{N}} \mu_\alpha c_\alpha - \rho \varphi_{\mathrm{H}}$ define the elastic pressure,[141]

$$\mathcal{P}^{\mathrm{el}}(\boldsymbol{\Upsilon}) = \sum_{\alpha=1}^{\mathrm{N}} \mu_\alpha c_\alpha - \rho \varphi_{\mathrm{H}}. \tag{5.90}$$

Both, p and $\mathcal{P}^{\mathrm{el}}$, depend on electromagnetic fields. In contrast to p, the quantity $\mathcal{P}^{\mathrm{el}}$ corresponds to the instantaneous pressure of the system.[255]

Note that gradients in the elastic pressure can be formally evaluated

$$\boldsymbol{\nabla} \mathcal{P}^{\mathrm{el}} = \boldsymbol{\nabla} \left(\sum_{\alpha=1}^{\mathrm{N}} \mu_\alpha c_\alpha - \rho \varphi_{\mathrm{H}} \right) = \sum_{\alpha=1}^{\mathrm{N}} c_\alpha \boldsymbol{\nabla} \mu_\alpha - \sum_{\Upsilon_A \neq c_\alpha} \left(\frac{\partial (\rho \varphi_{\mathrm{H}})}{\partial \Upsilon_A} \boldsymbol{\nabla} \right) \Upsilon_A. \tag{5.91}$$

Finally, we use the constitutive equations for $\boldsymbol{\sigma}$ and $\mathbf{g}$ and derive an equation of motion for the material velocity. For this pupose, we show in appendix D.4, that

$$\boldsymbol{\nabla\sigma} = \boldsymbol{\nabla\tau} - \boldsymbol{\nabla}\left(\sum_{\alpha=1}^{\mathrm{N}} \mu_\alpha c_\alpha - \rho\varphi_{\mathrm{H}}\right) + \boldsymbol{\nabla}\mathfrak{D}_{\mathrm{tf}} + (\boldsymbol{\mathcal{M}}\boldsymbol{\nabla})\,\mathbf{B} + \boldsymbol{\mathcal{M}}\wedge(\boldsymbol{\nabla}\wedge\mathbf{B}) + (\mathbf{P}\boldsymbol{\nabla})\,\boldsymbol{\mathcal{E}} + \\ + \varrho_{\mathrm{F}}\boldsymbol{\mathcal{E}} + \boldsymbol{\mathcal{J}}_{\mathrm{F}}\wedge\mathbf{B} + \overset{*}{\mathbf{P}}\wedge\mathbf{B} + \rho\frac{\mathrm{d}}{\mathrm{d}t}\left(\varepsilon_0\mathbf{E}\wedge\mathbf{B}/\rho\right), \quad (5.92)$$

and substitute this result into eq. (5.50). Apparently, the last term in eq. (5.92) also appears in the constitutive equation for $\mathbf{g}$. Thus, we can solve for the Euler equation with respect to the material acceleration,

$$\rho\dot{\mathbf{v}} = \boldsymbol{\nabla\tau} - \boldsymbol{\nabla}\left(\sum_{\alpha=1}^{\mathrm{N}} \mu_\alpha c_\alpha - \rho\varphi_{\mathrm{H}}\right) + \boldsymbol{\nabla}\mathfrak{D}_{\mathrm{tf}} + (\boldsymbol{\mathcal{M}}\boldsymbol{\nabla})\,\mathbf{B} + \boldsymbol{\mathcal{M}}\wedge(\boldsymbol{\nabla}\wedge\mathbf{B}) + (\mathbf{P}\boldsymbol{\nabla})\,\boldsymbol{\mathcal{E}} + \\ + \varrho_{\mathrm{F}}\boldsymbol{\mathcal{E}} + \boldsymbol{\mathcal{J}}_{\mathrm{F}}\wedge\mathbf{B} + \overset{*}{\mathbf{P}}\wedge\mathbf{B} + \rho\mathbf{b}. \quad (5.93)$$

This equation of motion is covariant with respect to Galilei-transformations, and can be viewed as the matter-related expression of Euler's first law of mechanics. It is totally equivalent to the expression eq. (5.50), except when discontinuities across surfaces are considered. In such cases, the force-law eq. (5.50) must be complemented by suitable jump-conditions. The contributions $\varrho_{\mathrm{F}}\boldsymbol{\mathcal{E}} + \boldsymbol{\mathcal{J}}_{\mathrm{F}}\wedge\mathbf{B}$ in eq. (5.93) represent forces which are independent of material properties. Thus, the Lorentz-force density $\varrho_{\mathrm{F}}\boldsymbol{\mathcal{E}}$ emerges in our framework from the surface-forces (comprised in $\boldsymbol{\sigma}$), and from the constitutive modelling. This is different from alternative continuum approaches, where the Lorentz force is incorporated as body-force in the balancing laws (for a detailed discussion, see chapter 15 or, *e.g.* Ref. 247). This is also different from theories of charged particles, where the Lorentz force is usually stated as axiom which couples mechanics with electromagnetic aspects of the particle, and is mandatory to define the electromagnetic SI-units.[81,254]. Due to $\varrho_{\mathrm{F}} = \boldsymbol{\nabla}\mathbf{D}_{\mathrm{F}}$ and the aether-relations, $\varrho_{\mathrm{F}}\boldsymbol{\mathcal{E}}$ acts on any space-charge present, including the electromagnetic self-fields. Note that the contribution of Minowski-momentum, $\varepsilon_0\mathbf{E}\wedge\mathbf{B}$ has completely dropped out of this version of the force-law.

After evaluating the constitutive equations, the electromagnetic entropy inequality, eq. (5.67), reduces to a constraint on $\boldsymbol{\tau}$ and the fluxes $\boldsymbol{\mathcal{J}}_{\mathrm{F}}$, $\boldsymbol{\xi}_s$, $\boldsymbol{\mathfrak{N}}_\alpha$,

$$\mathcal{R} = \boldsymbol{\tau} : \boldsymbol{\kappa} + \boldsymbol{\mathcal{J}}_{\mathrm{F}}\cdot\boldsymbol{\mathcal{E}} - \boldsymbol{\xi}_s\cdot\boldsymbol{\nabla}T - \sum_{\alpha=1}^{\mathrm{N}} \boldsymbol{\mathfrak{N}}_\alpha\boldsymbol{\nabla}\mu_\alpha \geq 0. \quad (5.94)$$

Although $\boldsymbol{\mathcal{J}}_{\mathrm{F}}\cdot\boldsymbol{\mathcal{E}}$ is an artefact of the electromagnetic energy flux $\boldsymbol{\mathcal{E}}\wedge\boldsymbol{\mathfrak{H}}_{\mathrm{F}}$, and thus no true heating-source, is is often called "Joule heating".

In section 5.3 we determine the fluxes $\boldsymbol{\mathcal{J}}_{\mathrm{F}}$, $\boldsymbol{\xi}_s$ and $\mathbf{N}_\alpha$ using an Onsager-approach instead of the constitutive modeling of Coleman and Noll.

5.2.4 Electrostatic Limit

As special case, we consider our viscous electrolyte model in the electrostatic limit (see appendix D.1), where we neglect contributions stemming from magnetic fields, temperature variations, and the unimodular deformation and where $\mathbf{E} = -\boldsymbol{\nabla}\Phi$. Thus, the material law reduces to $\bar{\boldsymbol{\Upsilon}} = \{c_1, \dots, c_{\mathrm{N}}, \mathbf{E}, \boldsymbol{\kappa}\}$ (see eq. (5.65)), and the electromagnetic entropy-inequality becomes

$$\mathcal{R} = \boldsymbol{\tau} : \operatorname{grad} \mathbf{v} + \boldsymbol{\mathcal{J}}_{\mathrm{F}} \cdot \mathbf{E} - \boldsymbol{\xi}_s \cdot \boldsymbol{\nabla} T - \sum_{\alpha=1}^{\mathrm{N}} \mathbf{N}_\alpha \boldsymbol{\nabla} \mu_\alpha \geq 0. \tag{5.95}$$

In this limit, and using sing $\mathcal{P}^{\mathrm{el}} = \sum_{\alpha=1}^{\mathrm{N}} \mu_\alpha c_\alpha - \rho\varphi_{\mathrm{H}}$ (see eq. (5.90)), the stress tensor and the total pressure (see eqs. (5.85) and (5.89), simplify to

$$\boldsymbol{\sigma}|_{\bar{\boldsymbol{\Upsilon}}} = \boldsymbol{\tau} + \mathbf{E} \otimes (\varepsilon_0 \mathbf{E} + \mathbf{P}) - \varepsilon_0 \mathbf{E}^2/2 \cdot \mathbf{Id} - \mathcal{P}^{\mathrm{el}} \cdot \mathbf{Id} \tag{5.96}$$

$$p|_{\bar{\boldsymbol{\Upsilon}}} = -\operatorname{tr}(\boldsymbol{\tau})/3 + \varepsilon_0 \mathbf{E}^2/6 - \mathbf{E}\mathbf{P}/3 + \mathcal{P}^{\mathrm{el}}. \tag{5.97}$$

Lemma 6. The stress tensor in the electrostatic limit, eq. (5.96), is symmetric.

Proof. In section 5.2.3, we showed that $\mathbf{E} \otimes \mathbf{P}$ is symmetric (since $\mathbf{E} \otimes \mathbf{P} = \mathbf{E} \otimes \partial\rho\varphi_{\mathrm{H}}/\partial\mathbf{E}$). Hence, since $\boldsymbol{\tau}$ is symmetric, this completes the proof. □

In the electrostatic limit, the electromagnetic force-law (eq. (5.50)) reduces to the material force-law (eq. (5.93)),

$$\rho\dot{\mathbf{v}}|_{\bar{\boldsymbol{\Upsilon}}} = \boldsymbol{\nabla}\boldsymbol{\sigma}|_{\bar{\boldsymbol{\Upsilon}}} = \boldsymbol{\nabla}\boldsymbol{\tau} - \boldsymbol{\nabla}\mathcal{P}^{\mathrm{el}} + \varrho_{\mathrm{F}}\mathbf{E} + (\mathbf{P}\boldsymbol{\nabla})\,\mathbf{E} + \rho\mathbf{b}. \tag{5.98}$$

Here, the expression $\boldsymbol{\nabla}\mathcal{P}^{\mathrm{el}}$ can be evaluated according to eq. (5.91), and the remainder-term becomes $\sum_{\Upsilon_A \neq c_\gamma} [\partial(\rho\varphi_{\mathrm{H}})/\partial\Upsilon_A \cdot \boldsymbol{\nabla}]\Upsilon_A = -(\mathbf{P}\boldsymbol{\nabla})\mathbf{E}$. Hence,

$$\boldsymbol{\nabla}\mathcal{P}^{\mathrm{el}}\Big|_{\bar{\boldsymbol{\Upsilon}}} = \sum_{\alpha=1}^{\mathrm{N}} c_\alpha \boldsymbol{\nabla}\mu_\alpha + (\mathbf{P}\boldsymbol{\nabla})\,\mathbf{E}, \tag{5.99}$$

such that

$$\rho\dot{\mathbf{v}}|_{\bar{\boldsymbol{\Upsilon}}} = \boldsymbol{\nabla}\boldsymbol{\tau} - \sum_{\alpha=1}^{\mathrm{N}} c_\alpha \boldsymbol{\nabla}\mu_\alpha + \varrho_{\mathrm{F}}\mathbf{E} + \rho\mathbf{b}. \tag{5.100}$$

Neglecting body forces, *e.g.* gravitation, and inertial terms *i.e.* assuming mechanical equilibrium ($\dot{\mathbf{v}} \approx 0$), reproduces the Gibbs-Duhem relations (see section 5.4.5).

$$\sum_{\alpha=1}^{\mathrm{N}} c_\alpha \boldsymbol{\nabla} \mu_\alpha = \varrho_{\mathrm{F}} \mathbf{E} + \boldsymbol{\nabla} \boldsymbol{\tau}, \quad \text{or,} \quad \sum_{\alpha=1}^{\mathrm{N}} c_\alpha \left(\boldsymbol{\nabla} \mu_\alpha + F z_\alpha \boldsymbol{\nabla} \Phi \right) = \boldsymbol{\nabla} \boldsymbol{\tau}. \tag{5.101}$$

5.3 Flux Densities

In this section, we determine the flux-densities $\boldsymbol{\mathcal{J}}_{\mathrm{F}}$, $\boldsymbol{\xi}_s$ and $\boldsymbol{\mathcal{N}}_\alpha$. Note that these are all defined relative to the center-of-mass velocity. From now on, we neglect magnetic fields and assume the electrostatic limit described in section 5.2.4.

To obtain the thermodynamically consistent fluxes, we follow the same rationale as for the derivation of the constitutive equations. The fluxes cannot take any arbitrary form but must ensure positivity of $\mathcal{R}$. Hence, we model the fluxes by taking account for the thermodynamic flux constraints comprised in the electromagnetic entropy inequality (see eq. (5.94)),

$$\mathcal{R} = \boldsymbol{\tau} : \boldsymbol{\kappa} + \boldsymbol{\mathcal{J}}_{\mathrm{F}} \cdot \mathbf{E} - \boldsymbol{\xi}_s \cdot \boldsymbol{\nabla} T - \sum_{\alpha=1}^{\mathrm{N}} \boldsymbol{\mathcal{N}}_\alpha \cdot \boldsymbol{\nabla} \mu_\alpha \geq 0. \tag{5.102}$$

Apparently, all three flux-terms appearing on the right side are composed of the product of fluxes ($\boldsymbol{\mathcal{J}}_{\mathrm{F}}, \boldsymbol{\mathcal{N}}, \boldsymbol{\xi}_s$) and driving forces ($\mathbf{E} = \boldsymbol{\nabla}\Phi, \boldsymbol{\nabla} T, \boldsymbol{\nabla} \mu_\alpha$), where the fluxes are yet to be determined by constitutive functions.

Here, we use the Onsager-formalism to determine the fluxes and assume that the closure relations couple the fluxes with the driving forces (see also section 3.1). Because these couplings are subject to the constraint eq. (5.102), they constitute the thermodynamic consistent material functions. Since we describe all fluxes relative to the center-of-mass velocity, we obtain transport-parameters specific to this reference-frame. In section 5.5, we discuss different reference-frames, and derive conversion-relations between the transport parameters defined relative to the different frames. Here, we restrict to linear flux-force couplings (including cross-couplings), which are observed in experiments, and are suggested by results from statistical mechanics.[70,74] Since we describe all fluxes relative to the center-of-mass velocity, we obtain transport-parameters specific to this reference-frame. In section 5.5, we discuss different reference-frames, and derive conversion-relations between the transport parameters defined relative to the different frames. Note that the linear model is insufficient for processes far from equilibrium (*e.g.*, adsorption processes or chemical reactions), which exhibit non-linear coupling-relations.[256,257]

5.3.1 Linear Flux-Force-Couplings

Before we apply the Onsager method, we reduce the flux-force couplings appearing in eq. (5.102) to the set of independent fluxes.

Beneath the thermodynamic constraint on the flux-force couplings (no-negativity of $\mathcal{R}$) we account for the trivial flux-constraint imposed by section 5.1.1

$$\sum_{\alpha=1}^{\mathrm{N}} M_\alpha \cdot \boldsymbol{\mathcal{N}}_\alpha = 0. \tag{5.103}$$

As consequence, only N-1 independent fluxes $\boldsymbol{\mathcal{N}}_\alpha$ exist in a N-component mixture. We use this property and designate, by convention, the flux of the first species,

$$\boldsymbol{\mathcal{N}}_1(\boldsymbol{\mathcal{N}}_2, \ldots, \boldsymbol{\mathcal{N}}_{\mathrm{N}}) = -\sum_{\alpha=2}^{\mathrm{N}} \boldsymbol{\mathcal{N}}_\alpha \cdot M_\alpha / M_1 \,. \tag{5.104}$$

We reduce the flux-terms in the entropy inequality and introduce reduced sets of N-1 valencies, N-1 chemical potentials and N-1 electrochemical potentials,

$$\tilde{z}_\alpha = z_\alpha - z_1 \cdot M_\alpha / M_1 \,, \tag{5.105}$$

$$\tilde{\mu}_\alpha = \mu_\alpha - \mu_1 \cdot M_\alpha / M_1 \,, \tag{5.106}$$

$$\tilde{\mu}_\alpha^{\mathrm{el}} = F \tilde{z}_\alpha \Phi + \mu_\alpha^{\mathrm{el}} \tag{5.107}$$

We use these reduced parameters and expand the conduction current density and the couplings of the mass-fluxes with the driving forces via

$$\boldsymbol{\mathcal{J}}_{\mathrm{F}} = F \sum_{\alpha=1}^{\mathrm{N}} z_\alpha \cdot \boldsymbol{\mathcal{N}}_\alpha = F \sum_{\alpha=2}^{\mathrm{N}} \tilde{z}_\alpha \cdot \boldsymbol{\mathcal{N}}_\alpha, \tag{5.108}$$

$$\sum_{\alpha=1}^{\mathrm{N}} \boldsymbol{\mathcal{N}}_\alpha \cdot \boldsymbol{\nabla} \mu_\alpha = \sum_{\alpha=2}^{\mathrm{N}} \boldsymbol{\mathcal{N}}_\alpha \cdot \boldsymbol{\nabla} \tilde{\mu}_\alpha. \tag{5.109}$$

The parameters eqs. (5.105) and (5.106) can lead to counter-intuitive properties. For example, $\tilde{z}_1 = 0$ even if $z_1 = 0$, or $\tilde{z}_{\alpha \neq 1} \neq 0$ even if $z_\alpha = 0$. Altogether, we find

$$\mathcal{R} = \boldsymbol{\tau} : \boldsymbol{\kappa} - \boldsymbol{\xi}_s \cdot \boldsymbol{\nabla} T - \sum_{\alpha=2}^{\mathrm{N}} \boldsymbol{\mathcal{N}}_\alpha \cdot (\boldsymbol{\nabla} \tilde{\mu}_\alpha + F \tilde{z}_\alpha \cdot \boldsymbol{\nabla} \Phi) \tag{5.110}$$

$$= \boldsymbol{\tau} : \boldsymbol{\kappa} - \boldsymbol{\xi}_s \cdot \boldsymbol{\nabla} T - \sum_{\alpha=2}^{\mathrm{N}} \boldsymbol{\mathcal{N}}_\alpha \cdot \boldsymbol{\nabla} \tilde{\mu}_\alpha^{\mathrm{el}} \geq 0. \tag{5.111}$$

We highlight the structure of the flux-force pairs, and define the “vector” of thermodynamic forces $\mathcal{X}_{(\alpha)}$ (with components $\mathcal{X}^{A}_{(\alpha)}$), and the “vector” of thermodynamic fluxes $\varPsi_{(\alpha)}$ (with components $\varPsi^{A}_{(\alpha)}$),

$$\mathcal{X}_{(\alpha)} = (\boldsymbol{\nabla}\tilde{\mu}^{\mathrm{el}}_{2}, \ldots, \boldsymbol{\nabla}\tilde{\mu}^{\mathrm{el}}_{\mathrm{N}}, \boldsymbol{\nabla}T)^{T}, \tag{5.112}$$

$$\varPsi_{(\alpha)} = (\boldsymbol{\mathcal{N}}_{2}, \ldots, \boldsymbol{\mathcal{N}}_{\mathrm{N}}, \boldsymbol{\xi}_{s})^{T}. \tag{5.113}$$

The subscripts in brackets indicate that only the ionic contributions are species-related. This description highlights the binary structure of the entropy inequality,

$$\mathcal{R} = \boldsymbol{\tau} : \boldsymbol{\kappa} - \sum_{(\alpha)} \varPsi_{(\alpha)} \cdot \mathcal{X}_{(\alpha)} \geq 0. \tag{5.114}$$

We evaluate the flux-force constraint imposed by eq. (5.114), and transfer the products to quadratic-terms via a bilinear Onsager-matrix $\boldsymbol{\mathcal{L}}$,

$$\varPsi_{(\alpha)} = -\sum_{\beta=2}^{\mathrm{N}} \mathcal{L}_{(\alpha)(\beta)} \cdot \mathcal{X}_{(\beta)}, \tag{5.115}$$

or, using a matrix-notation,

$$\begin{pmatrix} \boldsymbol{\mathcal{N}}_{2} \\ \vdots \\ \boldsymbol{\mathcal{N}}_{\mathrm{N}} \\ \boldsymbol{\xi}_{s} \end{pmatrix} = -\begin{pmatrix} \mathcal{L}_{22} & \ldots & \mathcal{L}_{2\mathrm{N}} & \mathcal{L}_{2T} \\ \vdots & \ddots & \vdots & \vdots \\ \mathcal{L}_{2\mathrm{N}} & \ldots & \mathcal{L}_{\mathrm{NN}} & \mathcal{L}_{\mathrm{N}T} \\ \mathcal{L}_{2T} & \ldots & \mathcal{L}_{\mathrm{N}T} & \mathcal{L}_{TT} \end{pmatrix} \cdot \begin{pmatrix} \boldsymbol{\nabla}\tilde{\mu}^{\mathrm{el}}_{2} \\ \vdots \\ \boldsymbol{\nabla}\tilde{\mu}^{\mathrm{el}}_{\mathrm{N}} \\ \boldsymbol{\nabla}T \end{pmatrix}. \tag{5.116}$$

Thus, in this description, thermodynamic consistency ($\mathcal{R} \geq 0$) transfers to the requirement that the Onsager matrix be semi-positive definite,

$$\mathcal{R} = \boldsymbol{\tau} : \boldsymbol{\kappa} + \boldsymbol{\mathcal{L}}(\mathcal{X}, \mathcal{X}) \geq 0. \tag{5.117}$$

The quadratic form above is non-negative if all diagonal elements are positive, $\mathcal{L}_{\alpha\alpha} \geq 0$, and all cross-coefficients fulfill $(\mathcal{L}_{\alpha\beta} + \mathcal{L}_{\beta\alpha})^{2} \leq 4\mathcal{L}_{\alpha\alpha}\mathcal{L}_{\beta\beta}$.[74] Furthermore, we assume that the thermodynamic forces can be evaluated independently, such that $\mathcal{L}_{TT} \geq 0$. Since all diagonal $\mathcal{L}_{\alpha\alpha} \geq 0$, the corresponding fluxes and forces have opposite direction. This is characteristic of dissipative processes, which aim to equilibrate the system (see section 3.1).

The symmetry of $\boldsymbol{\mathcal{L}}$ depends on the parity of the forces $\mathcal{X}_{(\alpha)}$,[74] which is determined by their dimension $[\mathcal{X}_{(\alpha)}]$,[79] and on the presence of magnetic fields. In our case, and because we neglect magnetic fields,[74] the Onsager matrix is symmetric and has N(N+1)/2 independent components. The N(N+1)/2 independent Onsager coefficients define N(N+1)/2 independent transport parameters.[258]

To some extent, the Onsager coefficients can be interpreted using linear response theory.[259] In dilute solutions, the Onsager matrix is effectively diagonal, and the diagonal elements measure self-species correlations (*e.g.*, cation-cation-/ and anion-anion-correlations). The off-dagonal elements account for inter-species correlations, *e.g.*, cation-anion correlations, or electro-osmotic drag through a membrane,[260] or asymmetric transference numbers.[261] Inter-species correlation become more dominant with increasing salt-concentration, and experimental results suggest that these can dominate self-species correlations in highly concentrated electrolytes.[262]

The Onsager approach implies that the fluxes are linear functions of gradients of the electric potential, species-concentration, and temperature (via the forces), which leads to migration, diffusion, and thermo-electricity. These physico-chemical effects can be related to the Onsager coefficients via defining transport parameters. As first step, we determine $\mathcal{J}_\mathrm{F}$ by substituting eq. (5.115) into eq. (5.108). This suggests defining the electric conductivity κ, the Seebeck coefficient β the thermal conductivity γ, and N-1 transference numbers t_α,

$$\kappa = F^2 \sum_{\alpha,\beta=2}^{\mathrm{N}} \mathcal{L}_{\alpha\beta}\tilde{z}_\alpha\tilde{z}_\beta, \tag{5.118}$$

$$\beta = \frac{F}{\kappa}\sum_{\alpha=2}^{\mathrm{N}} \mathcal{L}_{\alpha T}\tilde{z}_\alpha, \tag{5.119}$$

$$t_\alpha = \frac{F^2\tilde{z}_\alpha}{\kappa}\sum_{\beta=2}^{\mathrm{N}} \mathcal{L}_{\alpha\beta}\tilde{z}_\beta \tag{5.120}$$

$$\gamma = T\mathcal{L}_{TT} \tag{5.121}$$

such that

$$\mathcal{J}_\mathrm{F} = -\kappa\boldsymbol{\nabla}\Phi - \kappa\sum_{\beta=2}^{\mathrm{N}} \frac{t_\beta}{F\tilde{z}_\beta}\boldsymbol{\nabla}\tilde{\mu}_\beta - \kappa\beta\boldsymbol{\nabla}T. \tag{5.122}$$

Because the Onsager matrix is positive semi-definite, κ and γ are positive, and all t_α are positive if the Onsager matrix is diagonal (*e.g.*, for dilute solutions). By construction, only N-2 of the N-1 transference numbers t_α are independent

$$\sum_{\alpha=2}^{\mathrm{N}} t_\alpha = 1. \tag{5.123}$$

In section 5.5.5, we discuss binary electrolytes where the only independent transference number is $t_2^{\mathrm{N}=2} = 1$.

The Onsager coefficients and the transport parameters depend upon the choice for the drift velocity and on the choice of the designated species.[263–265] We discuss both topics in section 5.5 and appendix D.8.

We obtain a simple interpretation for the parameters t_α when we formulate the flux densities $\boldsymbol{\mathcal{N}}_\alpha$, and the entropy flux density $\boldsymbol{\xi}_s$, in terms of $\boldsymbol{\mathcal{J}}_\text{F}$ instead of Φ. For this purpose, we substitute $\boldsymbol{\nabla}\Phi$ for $\boldsymbol{\mathcal{J}}_\text{F}$ using eq. (5.122), and transform the expansion eq. (5.115),

$$\boldsymbol{\mathcal{N}}_\alpha = \frac{t_\alpha \boldsymbol{\mathcal{J}}_\text{F}}{F\tilde{z}_\alpha} - \left(\mathcal{L}_{\alpha T} - \frac{\beta\kappa t_\alpha}{F\tilde{z}_\alpha}\right)\boldsymbol{\nabla}T - \sum_{\beta=2}^{\text{N}}\left(\mathcal{L}_{\alpha\beta} - \frac{\kappa t_\alpha t_\beta}{F^2\tilde{z}_\alpha\tilde{z}_\beta}\right)\boldsymbol{\nabla}\tilde{\mu}_\beta, \tag{5.124}$$

$$\boldsymbol{\xi}_s = \beta\boldsymbol{\mathcal{J}}_\text{F} - \left(\frac{\gamma}{T} - \beta^2\kappa\right)\boldsymbol{\nabla}T - \sum_{\beta=2}^{\text{N}}\left(\mathcal{L}_{\beta T} - \beta\frac{\kappa t_\beta}{F\tilde{z}_\beta}\right)\boldsymbol{\nabla}\tilde{\mu}_\beta. \tag{5.125}$$

Thus, the parameters t_α relate the fluxes $\boldsymbol{\mathcal{N}}_\alpha$ with $\boldsymbol{\mathcal{J}}_\text{F}$, and the fluxes $\boldsymbol{\xi}_s$ with $\boldsymbol{\mathcal{J}}_\text{F}$, and the ratios $t_\alpha/\tilde{z}_\alpha$ measure the sign and magnitude of the migration part $\boldsymbol{\mathcal{N}}_\alpha^\text{migr} = t_\alpha/\tilde{z}_\alpha \cdot \boldsymbol{\mathcal{J}}_\text{F}$ relative to the flux $\boldsymbol{\mathcal{J}}_\text{F}$. Thus, if $\text{sign}(t_\alpha/\tilde{z}_\alpha) = -1$, then $\boldsymbol{\mathcal{N}}_\alpha^\text{migr}$ has opposite direction than $\boldsymbol{\mathcal{J}}_\text{F}$, although $\boldsymbol{\mathcal{N}}_\alpha$ may still be directed along $\boldsymbol{\mathcal{J}}_\text{F}$ if the thermal part / diffusion part (second and third term on the right side of eq. (5.124)) overcompensate migration. Thus, only the complete knowledge of t_α and $\tilde{z}_\alpha$ bears physical insight. We discuss this topic in more detail in section 6.2.3.

Equations (5.118) to (5.121) constitute N+1 out of N(N+1)/2 independent transport parameters. We determine the remaining parameters and define N(N+1)/2 coefficients of the symmetric diffusion matrix $\boldsymbol{\mathcal{D}}$,

$$\mathcal{D}_{\alpha\beta} = \mathcal{L}_{\alpha\beta} - \frac{\kappa t_\alpha t_\beta}{F^2\tilde{z}_\alpha\tilde{z}_\beta}, \quad \mathcal{D}_{\alpha T} = \mathcal{L}_{\alpha T} - \frac{\beta\kappa t_\alpha}{F\tilde{z}_\alpha}, \quad \mathcal{D}_{TT} = \frac{\gamma}{T} - \beta^2\kappa. \tag{5.126}$$

The coefficient $\mathcal{D}_{TT}$ is determined by γ, β and κ, and thus eqs. (5.118), (5.119), (5.121) and (5.126) yield N(N+3)/2 transport coefficients. This exceeds the number of N(N+1)/2 independent Onsager coefficients. However, the coupling eq. (5.108) between $\boldsymbol{\mathcal{J}}_\text{F}$ and $\boldsymbol{\mathcal{N}}_\alpha$ implies further N constraints,

$$\sum_{\beta=2}^{\text{N}} \mathcal{D}_{\alpha\beta}\tilde{z}_\beta = 0, \quad \text{and} \quad \sum_{\beta=2}^{\text{N}} \mathcal{D}_{T\beta}\tilde{z}_\beta = 0. \tag{5.127}$$

This suggests that we designate one further species. By convention we choose the species related to $\alpha = 2$,

$$\mathcal{D}_{2\alpha} = -\sum_{\beta=3}^{\text{N}} \mathcal{D}_{\alpha\beta} \cdot \tilde{z}_\beta/\tilde{z}_2\,, \quad \text{and} \quad \mathcal{D}_{2T} = -\sum_{\beta=3}^{\text{N}} \mathcal{D}_{T\beta} \cdot \tilde{z}_\beta/\tilde{z}_2\,, \tag{5.128}$$

where,

$$\mathcal{D}_{22} = \sum_{\beta,\gamma=3}^{\mathrm{N}} \mathcal{D}_{\beta\gamma}\tilde{z}_\beta\tilde{z}_\gamma/(\tilde{z}_2)^2\,. \tag{5.129}$$

Thus, only N(N-1)/2 diffusion coefficients are independent. Altogether, in total, we have introduced N(N+1)/2 transport parameters composed of N(N-1)/2 independent diffusion coefficients, N-2 independent transference numbers, the electric conductivity, and the Seebeck coefficient. Altogether, this constitute the complete set of physically motivated free parameters.

In eq. (5.126), $\boldsymbol{\mathcal{D}} - \boldsymbol{\mathcal{L}}$ measures the diffusion contribution stemming from electrostatic correlations. Depending on the sign of $\kappa t_\alpha t_\beta/F^2\tilde{z}_\alpha\tilde{z}_\beta$, these de-/ or increase diffusion. However, for inter-species diffusion, where $t_\alpha/\tilde{z}_\alpha = t_\beta/\tilde{z}_\beta$, diffusion is mitigated by the Coulomb contribution, and the entropic and Coulombic effects are in competition. For counterionic species which have both positive transference-numbers, the Coulombic diffusion contribution enhances $\mathcal{D}_{\alpha\beta}$, as the ions are attracted and may even form ionic complexes (ion pairs or ion clusters).[44]

Note that in binary systems (N=2), $\mathcal{D}_{22}^{\mathrm{N}=2} = 0$ and $\mathcal{D}_{2T}^{\mathrm{N}=2} = 0$, *i.e.* there is no diffusion flux in $\boldsymbol{\mathcal{N}}_\alpha$ (except from the diffusion contributions comprised in $\boldsymbol{\mathcal{J}}_\mathrm{F}$), and no diffusion coefficients are needed.

However, substituting the diffusion coefficients into eqs. (5.124) and (5.125) suggests introducing the set of N-2 reduced chemical potentials defined relative to the designated species $\alpha = 2$,

$$\tilde{\tilde{\mu}}_\beta = \tilde{\mu}_\beta - \tilde{\mu}_2 \cdot \tilde{z}_\beta/\tilde{z}_2\,. \tag{5.130}$$

Thus N-1 independent thermodynamic fluxes $(\boldsymbol{\mathcal{N}}_3, \ldots, \boldsymbol{\mathcal{N}}_\mathrm{N}, \boldsymbol{\xi}_s)$ exist,

$$\boldsymbol{\mathcal{N}}_\alpha = \frac{t_\alpha}{F\tilde{z}_\alpha}\boldsymbol{\mathcal{J}}_\mathrm{F} - \mathcal{D}_{\alpha T}\boldsymbol{\nabla}T - \sum_{\beta=3}^{\mathrm{N}} \mathcal{D}_{\alpha\beta}\boldsymbol{\nabla}\tilde{\tilde{\mu}}_\beta, \quad \alpha \geq 3 \tag{5.131}$$

$$\boldsymbol{\xi}_s = \beta\boldsymbol{\mathcal{J}}_\mathrm{F} - \mathcal{D}_{TT}\boldsymbol{\nabla}T - \sum_{\beta=3}^{\mathrm{N}} \mathcal{D}_{\beta T}\boldsymbol{\nabla}\tilde{\tilde{\mu}}_\beta, \tag{5.132}$$

where $\boldsymbol{\mathcal{N}}_1$ is determined by mass conservation (eq. (5.104)), and $\boldsymbol{\mathcal{N}}_2$ is determined by the electric flux (eq. (5.108))

$$\boldsymbol{\mathcal{N}}_2 = \frac{t_2}{F\tilde{z}_2}\boldsymbol{\mathcal{J}}_\mathrm{F} + \sum_{\beta=3}^{\mathrm{N}} \mathcal{D}_{\beta T}\frac{\tilde{z}_\beta}{\tilde{z}_2}\boldsymbol{\nabla}T + \sum_{\beta,\gamma=3}^{\mathrm{N}} \mathcal{D}_{\beta\gamma}\frac{\tilde{z}_\beta}{\tilde{z}_2}\boldsymbol{\nabla}\tilde{\tilde{\mu}}_\gamma. \tag{5.133}$$

The electrolyte potential Φ is the electrostatic Maxwell potential which appears in the Poisson equation, and relates to the electric field via $\mathbf{E} = -\boldsymbol{\nabla}\Phi$. However, it can be beneficial to use the an alternative potential,[64,100]

$$\varphi(\Phi, \mu_{1,2}, M_{1,2}, z_{1,2}) = \Phi + \tilde{\mu}_2/F\tilde{z}_2 \;= \tilde{\mu}_2^{\mathrm{el}}/F\tilde{z}_2\,, \tag{5.134}$$

such that $\boldsymbol{\mathcal{J}}_{\mathrm{F}}$ can be expressed analogous to the flux-densities $\boldsymbol{\mathcal{N}}_\alpha$ and $\boldsymbol{\xi}_s$ (see eqs. (5.131) and (5.132))

$$\boldsymbol{\mathcal{J}}_{\mathrm{F}} = -\kappa\boldsymbol{\nabla}\varphi - \beta\kappa\boldsymbol{\nabla}T - \frac{\kappa}{F}\sum_{\beta=3}^{\mathrm{N}}\frac{t_\beta}{\tilde{z}_\beta}\boldsymbol{\nabla}\tilde{\tilde{\mu}}_\beta. \tag{5.135}$$

If the designated species ($\alpha = 1$) is neutral, then $\varphi = \Phi + \mu_2/Fz_2$ corresponds to the electro-chemical potential of the second designated species.

Next, we define the reduced diffusion-matrix $\boldsymbol{\mathcal{D}}_{\mathrm{red}} = (\mathcal{D}_{(\alpha)(\beta)})|_{\alpha,\beta\geq 3}$ and reduced sets of fluxes Ψ_{red} and of forces $\mathcal{X}_{\mathrm{red}}$,

$$\Psi_{\mathrm{red}} = (\boldsymbol{\mathcal{N}}_3 - t_3\boldsymbol{\mathcal{J}}_{\mathrm{F}}/F\tilde{z}_3\,, \ldots, \boldsymbol{\mathcal{N}}_{\mathrm{N}} - t_{\mathrm{N}}\boldsymbol{\mathcal{J}}_{\mathrm{F}}/F\tilde{z}_{\mathrm{N}}\,, \boldsymbol{\xi}_s - \beta\boldsymbol{\mathcal{J}}_{\mathrm{F}})^T, \tag{5.136}$$

$$\mathcal{X}_{\mathrm{red}} = (\boldsymbol{\nabla}\tilde{\tilde{\mu}}_3, \ldots, \boldsymbol{\nabla}\tilde{\tilde{\mu}}_{\mathrm{N}}, \boldsymbol{\nabla}T)^T, \tag{5.137}$$

such that the transport eqs. (5.131) and (5.132) become,

$$\Psi_{\mathrm{red}} = -\boldsymbol{\mathcal{D}}_{\mathrm{red}} \cdot \mathcal{X}_{\mathrm{red}}. \tag{5.138}$$

In particular, the dissipation mechanisms which produce entropy become

$$\mathcal{R} = \boldsymbol{\tau} : \boldsymbol{\kappa} + \boldsymbol{\mathcal{J}}_{\mathrm{F}}^2/\kappa + (\boldsymbol{\nabla}\tilde{\tilde{\mu}}_3, \ldots \boldsymbol{\nabla}\tilde{\tilde{\mu}}_{\mathrm{N}}, \boldsymbol{\nabla}T) \cdot \mathcal{D}_{\mathrm{red}} \cdot (\boldsymbol{\nabla}\tilde{\tilde{\mu}}_3, \ldots \boldsymbol{\nabla}\tilde{\tilde{\mu}}_{\mathrm{N}}, \boldsymbol{\nabla}T)^T \tag{5.139}$$

$$= \boldsymbol{\tau} : \boldsymbol{\kappa} + \boldsymbol{\mathcal{J}}_{\mathrm{F}}^2/\kappa + \mathcal{X}_{\mathrm{red}}^T \cdot \boldsymbol{\mathcal{D}}_{\mathrm{red}} \cdot \mathcal{X}_{\mathrm{red}} \geq 0. \tag{5.140}$$

Thus, entropy production comprises three contributions. The first term describes mechanical dissipation due to internal friction. In section 5.3.2, we determine $\boldsymbol{\tau}(\boldsymbol{\kappa})$ by a linear constitutive Ansatz such that $\boldsymbol{\tau}{:}\boldsymbol{\kappa}{\geq}0$ always. The second term describes Joule-heating due to migration. Since the electric conductivity is non-negative, this contribution increases entropy, $\boldsymbol{\mathcal{J}}_{\mathrm{F}}^2/\kappa\,{\geq}0$. The last term describes entropy production due to diffusion, heat conduction, and mixing of the electrolyte-composition. Since thermodynamic consistency requires that $\boldsymbol{\mathcal{D}}_{\mathrm{red}}$ is semi-positive definite, it is invertible, and $(\boldsymbol{\mathcal{D}}_{\mathrm{red}})^{-1}$ is positive definite,[266] which allows to invert eq. (5.138), and to solve for the forces $\mathcal{X}_{\mathrm{red}}{=}{-}\boldsymbol{\mathcal{D}}_{\mathrm{red}}^{-1}{\cdot}\Psi_{\mathrm{red}}$. This yields a flux-explicit form for $\mathcal{R}$,

$$\mathcal{R} = \boldsymbol{\tau} : \boldsymbol{\kappa} + \boldsymbol{\mathcal{J}}_{\mathrm{F}}^2/\kappa + \Psi_{\mathrm{red}}^T \cdot \boldsymbol{\mathcal{D}}_{\mathrm{red}}^{-1} \cdot \Psi_{\mathrm{red}} \geq 0. \tag{5.141}$$

5.3.2 Viscosity Tensor

Equation (5.141) shows that all fluids exhibit internal dissipative processes, leading to irreversible loss of momentum due to microscopic viscous friction stemming from the exertion of stress between fluid layers. Normal stress is imparted by random thermal (Brownianian) motion, and is superposed on the mean drift of the bulk-fluid (convection) as the individual molecules bounce against each other and generate an average momentum transfer across surfaces of fluid layers. Shear stress emerges due to velocity gradients in directions transverse to the convective bulk-flow.

In contrast to solids, fluids cannot resist shear stress,[267] and a relation between stress and strain fails for fluids, However, in accordance with experiments,[268] we assume a linear relation between rate of strain and rate of stress $\boldsymbol{\tau}(\operatorname{grad}\mathbf{v})$. The Representation-Theorems of Isotropic Tensors,[269,270] uniquely determine the most general linear form $\boldsymbol{\tau}(\rho, T, \boldsymbol{\kappa}) = \alpha(\rho, T)\,\mathbf{Id} + \lambda(\rho, T)\operatorname{tr}(\boldsymbol{\kappa})\,\mathbf{Id} + 2\eta(\rho, T)\boldsymbol{\kappa}$, up to three material parameters (see eq. (B.47)). Since we assume that $\boldsymbol{\tau}$ vanishes in equilibrium ($\alpha = 0$), the symmetric, irreducible decomposition reads

$$\boldsymbol{\tau} = \gamma(\rho, T)\boldsymbol{\nabla}\mathbf{v} \cdot \mathbf{Id} + 2\eta(\rho, T) \cdot \boldsymbol{\kappa}_{\mathrm{tf}}, \tag{5.142}$$

where $\gamma = \lambda + 2\eta/3$ is the “bulk viscosity” and η is the “shear viscosity”.[73,74] Both are constrained by the second axiom of thermodynamics via (see eq. (5.141))

$$\boldsymbol{\tau} : \boldsymbol{\kappa} = \gamma \cdot (\boldsymbol{\nabla}\mathbf{v})^2 + 2\eta \cdot \boldsymbol{\kappa}_{\mathrm{tf}} : \boldsymbol{\kappa}_{\mathrm{tf}} \geq 0 \tag{5.143}$$

and thermodynamic consistency requires that

$$\gamma \geq 0, \text{ and } \eta \geq 0 \text{ or}, \lambda \geq -2\eta/3 \text{ and } \eta \geq 0. \tag{5.144}$$

The viscosity tensor comprises viscous surface-forces in the stress tensor. Thus, the isotropic components thereof contribute to pressure-forces via

$$p^{\mathrm{visc}} = -\operatorname{tr}\boldsymbol{\tau}/3 = -\gamma \cdot \boldsymbol{\nabla}\mathbf{v}. \tag{5.145}$$

Since $\boldsymbol{\nabla}\mathbf{v}$ measures the expansion of a local volume element $\mathrm{d}V$ (see appendix D.6), $\operatorname{tr}\boldsymbol{\tau} = 3\gamma\boldsymbol{\nabla}\mathbf{v}$ measures the amount of momentum-density consumed by isotropic deformation. Thus, larger bulk-viscosities γ imply a lesser amount of isotropic momentum transferred into mechanical deformations, and larger amount of momentum is irreversibly transferred into heat. A similar statement can be made for the shearing.

Equation (5.142) determines the viscous forces appearing in the force-law eq. (5.100)

$$\boldsymbol{\nabla}\boldsymbol{\tau} = \boldsymbol{\nabla}\left[(\gamma + \eta)\,\boldsymbol{\nabla}\mathbf{v}\right] + \boldsymbol{\nabla}^2\left(\eta\mathbf{v}\right). \tag{5.146}$$

The linear assumption for $\boldsymbol{\tau}(\boldsymbol{\kappa})$ is not realistic for rheological fluids, *e.g.* polymer solutions, which exhibit large relaxation times due to their macromolecular structure. In the corresponding non-linear viscoelastic models, γ, η depend on $\operatorname{grad}\mathbf{v}$.[74]

5.4 Model For Correlated Liquid Electrolytes

> The secret to modeling is not being perfect.
>
> Karl Lagerfeld

The transport equations of our electrolyte-model constitute a yet universal framework, subject to specific forms of the free energy density φ_{H}. Once the model for φ_{H} is specified, all transport equations follow from pure mathematics. Thus, the free energy density epitomises the focal point of our modeling.

We structure this chapter as follows. First, in section 5.4.1, we define our electrolyte-model φ_{H}. Second, in section 5.4.2, we introduce the Euler equation for the volume, discuss incompressible electrolytes, and derive the partial molar volumes from the stress tensor. In section 5.4.4, we derive the convection equation. Next, in section 5.4.5, we evaluate our model, and derive the dynamic transport equations in mechanical equilibrium. In section 5.4.6, we discuss the most basic battery electrolyte composed of a ternary system in electroneutral state.[100] Finally, in section 5.4.7, we characterize electrolytes as "highly concentrated" based on the concentration and molar volume of the salts.

5.4.1 Free Energy Density

In this section, we state our model free energy density φ_{H}. In the isothermal limit, this closes our framework by evaluation of the constitutive equations.

Here, we assume the electrostatic limit discussed in section 5.2.4 for linear dielectric electrolytes, where the materials law reduces to

$$\boldsymbol{\Upsilon} = \{c_1, \ldots, c_{\mathrm{N}}, T, \mathbf{E}, \boldsymbol{\kappa}\}\,. \tag{5.147}$$

Furthermore, we neglect elastic contributions described by $\boldsymbol{F}^{\mathrm{uni}}$, and temperature gradients $\boldsymbol{\nabla} T$ in the materials law.[64,141] In a local aether-frames, our linear model $\mathbf{P} = \varepsilon_0\chi\mathbf{E}$ implies $\mathbf{D}_{\mathrm{F}} = \varepsilon_0\varepsilon_{\mathrm{R}}\mathbf{E} = \varepsilon_{\mathrm{R}}\mathbf{D}_{\mathrm{T}}$, where $\varepsilon_{\mathrm{R}} = 1+\chi$ (see section 5.2.1). Hence, the set of constitutive equations eqs. (5.68) to (5.73), (5.78) and (5.96) reduces to

$$s = -\partial\varphi_{\mathrm{H}}/\partial T\,, \tag{5.148}$$

$$\mathbf{P} = -\partial(\rho\varphi_{\mathrm{H}})/\partial\mathbf{E}\,, \tag{5.149}$$

$$0 = \partial(\rho\varphi_{\mathrm{H}})/\partial\boldsymbol{\kappa}\,, \tag{5.150}$$

$$\mu_\alpha = \partial(\rho\varphi_{\mathrm{H}})/\partial c_\alpha, \tag{5.151}$$

$$\boldsymbol{\sigma} = \boldsymbol{\tau} + \mathbf{E} \otimes \mathbf{D}_{\mathrm{F}} - \varepsilon_0 \mathbf{E}^2/2 \cdot \mathbf{Id} - \mathcal{P}^{\mathrm{el}}(\boldsymbol{\Upsilon}) \cdot \mathbf{Id}, \tag{5.152}$$

where the elastic pressure is defined by $\mathcal{P}^{\mathrm{el}}(\boldsymbol{\Upsilon}) = \sum_{\alpha=1}^{\mathrm{N}} c_\alpha \mu_\alpha - \rho\varphi_{\mathrm{H}} = \sum_{\alpha=1}^{\mathrm{N}} c_\alpha \cdot \partial(\rho\varphi_{\mathrm{H}})/\partial c_\alpha - \rho\varphi_{\mathrm{H}}$ (see eq. (5.90)).

Our model for φ_{H} is restricted by symmetry arguments (see appendix B), and must comply with Euler's second law of mechanics (see Lemma 3). As consequence, φ_{H} must be objective with respect to the electromagnetic material variables (see Lemma 5). Altogether, because of material symmetry, and due to eq. (5.149), the free energy is a function $\varphi_{\mathrm{H}}(\mathbf{E}^2)$ (see eq. (B.45)). Partly, the model free energy can be reconstructed from the constitutive equations by "integrating" them up.[140]However, we choose a different approach and state our physically motivated model free energy density,

$$\rho\varphi_{\mathrm{H}} = -\frac{\varepsilon_0 \chi}{2}\mathbf{E}^2 + \frac{\mathcal{K}}{2}\left(1 - \sum_{\alpha=1}^{\mathrm{N}} \nu_\alpha^0 c_\alpha\right)^2 + RT \sum_{\alpha=1}^{\mathrm{N}} c_\alpha \cdot \ln\left(\frac{c_\alpha}{c}\right) + \rho\varphi_{\mathrm{H}}^{\mathrm{int}}(c_\alpha) + \rho\varphi_{\mathrm{H}}^{\mathrm{therm}}. \tag{5.153}$$

The first term comprises the electrostatic energy-density of polarizable media,[254] and satisfies material symmetry (see Lemma 5). Because we neglect a dependence of the susceptibility on ion-concentrations, the chemical potentials do not depend on polarization effects (see appendix D.10.2).

The second term comprises volumetric energy-contributions due to eladue to elastic volume deformations, expressed relative to a stable reference state with partial molar volumes ν_α^0. $\mathcal{K}$ is the bulk-modulus which acts as a Lagrange-mutliplier in the case of incompressible electrolytes (see section 5.4.2). This energy contribution allows to easily transfer to incompresssible media, see section 5.4.2.We motivate this term in appendix D.5.

The third term accounts for the entropy of mixture of non-interacting systems and extremizes the energy via favouring an equal number of molecules for each species. This contribution widely used for bulk electrolytes.[64,141] It neglects contributions from inter-molecular interactions and can be derived in analogy to ideal gases using statistical thermodynamics.[140,271] Densely packed systems are often described using alternative statistics, *e.g.*, the Flory-Huggins theory describes (see part III).[272]

The fourth term allows to phenomenologically account for non-ideal interactions in $\rho\varphi_{\mathrm{H}}^{\mathrm{int}}(c_\alpha)$, and serves as a portal for extending and customizing our model. Oftenly, such contributions are captured in the activity coefficients f_α. These account for excess chemical potentials, which measure the deviation from ideal electrolytes (where $f_\alpha c = 1$)

$$RT \ln(f_\alpha c) = \frac{\partial(\rho\varphi_{\mathrm{H}}^{\mathrm{int}})}{\partial c_\alpha} \tag{5.154}$$

Here, $\varphi_{\mathrm{H}}^{\mathrm{int}}(c_\alpha)$ contributes via the constitutive equations only to the chemical potentials. If we would consider more general contributions $\varphi_{\mathrm{H}}^{\mathrm{int}}(\boldsymbol{\Upsilon})$, then this would lead to modified constitutive equations $\partial[\rho(\varphi_{\mathrm{H}}^{\mathrm{bulk}} + \varphi_{\mathrm{H}}^{\mathrm{int}})]/\partial \Upsilon_A$.

The last term comprises thermal energy contributions. We discuss these contributions in appendix D.10, where we derive our thermal model relative,

$$\rho\varphi_{\mathrm{H}}^{\mathrm{therm}} = (T - T_{\mathrm{R}} - T\ln T/T_{\mathrm{R}}) \sum_{\alpha=1}^{\mathrm{N}} C_\alpha \rho_\alpha. \tag{5.155}$$

Here, C_α are the specific heat capacities of the system in the reference configuration, which follow from the free energy via

$$C = \sum_\alpha C_\alpha = -T \cdot \frac{\partial^2(\rho\varphi_{\mathrm{H}}^{\mathrm{int}})}{\partial T^2} = \rho T \cdot \frac{\partial s}{\partial T} = \rho \cdot \frac{\partial u}{\partial T}. \tag{5.156}$$

Next, we evaluate our model free energy and calculate the chemical potentials, and the stress tensor. Using eq. (5.151), we find

$$\mu_\alpha = RT\left[\ln\left(\frac{c_\alpha}{c}\right) + \ln(f_\alpha c)\right] + \frac{2\mathcal{P}^{\mathrm{vol}}\nu_\alpha^0}{1+\sum_{\beta=1}^{\mathrm{N}}\nu_\beta^0 c_\beta} + \frac{(1-\sum_{\beta=1}^{\mathrm{N}}\nu_\beta^0 c_\beta)^2}{2}\frac{\partial\mathcal{K}}{\partial c_\alpha} - \frac{\varepsilon_0 \mathbf{E}^2}{2}\frac{\partial\chi}{\partial c_\alpha}. \tag{5.157}$$

The first two terms in eq. (5.157) comprise entropic contributions due to mixing and inter-molecular interactions. The third term stems from the elastic deformations, and constitutes a pressure contribution to the chemical potential which follows from the assumption of non-zero specific molar volumes,[271] where

$$\mathcal{P}^{\mathrm{vol}} = \mathcal{K} \cdot \frac{\left(\sum_{\beta=1}^{\mathrm{N}}\nu_\beta^0 c_\beta\right)^2 - 1}{2}. \tag{5.158}$$

Thus, the third term in eq. (5.157) reads $\mathcal{K}(\sum_{\beta=1}^{\mathrm{N}}\nu_\beta^0 c_\beta - 1)\nu_\alpha^0 = \mathcal{K}\nu_\alpha^0(\sqrt{1+2\mathcal{P}^{\mathrm{vol}}/\mathcal{K}} - 1)$. The fourth and fifth term in eq. (5.157) measure the composition dependence of the bulk modulus and of the susceptibility.

If thermal aspects are included (see appendix D.10), then eq. (5.157) is extended via ,

$$\mu_\alpha^{\mathrm{therm}} = M_\alpha C_\alpha (T - T_{\mathrm{R}} - T \cdot \ln[T/T_{\mathrm{R}}]). \tag{5.159}$$

Next, we derive the stress tensor via eq. (5.152). The only component of $\boldsymbol{\sigma}$ which depends upon the model free energy is the elastic pressure (see eq. (5.90)),

$$\mathcal{P}^{\mathrm{el}} = \sum_{\alpha=1}^{\mathrm{N}} \mu_\alpha c_\alpha - \rho\varphi_{\mathrm{H}} = \frac{\varepsilon_0 \mathbf{E}^2}{2}\tilde{\chi} + \mathcal{P}^{\mathrm{int}} + \mathcal{P}^{\mathrm{vol}} + \frac{(1-\sum_{\beta=1}^{\mathrm{N}} \nu_\beta^0 c_\beta)^2}{2} \sum_{\alpha=1}^{\mathrm{N}} c_\alpha \frac{\partial \mathcal{K}}{\partial c_\alpha}. \tag{5.160}$$

where $\tilde{\chi}=\chi-\sum_{\alpha}^{\mathrm{N}} c_\alpha \partial\chi/\partial c_\alpha$, and

$$\mathcal{P}^{\mathrm{int}} = \sum_{\alpha=1}^{\mathrm{N}} c_\alpha \cdot \frac{\partial(\rho\varphi_{\mathrm{H}}^{\mathrm{int}})}{\partial c_\alpha} - \rho\varphi_{\mathrm{H}}^{\mathrm{int}} = \rho \sum_{\alpha=1}^{\mathrm{N}} c_\alpha \cdot \frac{\partial \varphi_{\mathrm{H}}^{\mathrm{int}}}{\partial c_\alpha}. \tag{5.161}$$

Note that the set of material variables for the free energy $\varphi_{\mathrm{H}}(c_1, \ldots, c_{\mathrm{N}})$ can be changed to $\varphi_{\mathrm{H}}(\rho, \mathrm{y}_1, \ldots, \mathrm{y}_{\mathrm{N}})$, where $\mathrm{y}_\alpha = \rho_\alpha/\rho$ (such that $\sum_{\alpha=1}^{\mathrm{N}} \mathrm{y}_\alpha = 1$). Then, using $\partial/\partial c_\alpha = M_\alpha/\mathrm{y}_\alpha \cdot \partial/\partial\rho$, the elastic pressure $\mathcal{P}^{\mathrm{el}} = \sum_{\alpha=1}^{\mathrm{N}} c_\alpha \mu_\alpha - \rho\varphi_{\mathrm{H}}$ is determined by a constitutive relation,[273]

$$\mathcal{P}^{\mathrm{el}} = \rho^2 \cdot \frac{\partial \varphi_{\mathrm{H}}}{\partial \rho}. \tag{5.162}$$

Altogether, we find for the symmetric stress tensor,

$$\begin{aligned} \boldsymbol{\sigma} &= -\left(\mathcal{P}^{\mathrm{el}} + \varepsilon_0 \mathbf{E}^2/2\right) \cdot \mathbf{Id} + \mathbf{E} \otimes \mathbf{D}_{\mathrm{F}} + \boldsymbol{\tau} && (5.163) \\ &= \boldsymbol{\Sigma} + \boldsymbol{\tau} - \left(\mathcal{P}^{\mathrm{vol}} + \mathcal{P}^{\mathrm{int}} - \frac{\varepsilon_0 \mathbf{E}^2}{2} \sum_{\alpha=1}^{\mathrm{N}} c_\alpha \frac{\partial \chi}{\partial c_\alpha} + \frac{(1-\sum_{\beta=1}^{\mathrm{N}} \nu_\beta^0 c_\beta)^2}{2} \sum_{\alpha=1}^{\mathrm{N}} c_\alpha \frac{\partial \mathcal{K}}{\partial c_\alpha}\right) \mathbf{Id}, && (5.164) \end{aligned}$$

where the viscosity tensor is $\boldsymbol{\tau} = \gamma \boldsymbol{\nabla} \mathbf{v} \cdot \mathbf{Id} + 2\eta \cdot \boldsymbol{\kappa}_{\mathrm{tf}}$ (see section 5.3.2), and where the Maxwell stress tensor is $\boldsymbol{\Sigma} = \mathbf{E} \otimes \mathbf{D}_{\mathrm{F}} - (\mathbf{E}\mathbf{D}_{\mathrm{F}}/2)\,\mathbf{Id}$ (see appendix B.4).

Next, we derive the complete pressure $p = -\operatorname{tr}(\boldsymbol{\sigma})/3$ (see eq. (5.89)), which comprises $\mathcal{P}^{\mathrm{vol}}, \mathcal{P}^{\mathrm{el}}$ and $\mathcal{P}^{\mathrm{int}}$. Entropy, volume-deformation and the electrostatics yield isotropic stress terms (in the aether-frames, $\mathbf{E} \otimes \mathbf{D}_{\mathrm{F}}$ is a symmetric matrix). Thus, the non-isotropic parts in $\boldsymbol{\sigma}$ arise from viscous stresses comprised in $\boldsymbol{\kappa}_{\mathrm{tf}}$. Altogether,

$$p = \frac{\mathbf{E}\mathbf{D}_{\mathrm{F}}}{6} - \gamma \boldsymbol{\nabla} \mathbf{v} + \mathcal{P}^{\mathrm{vol}} + \mathcal{P}^{\mathrm{int}} - \frac{\varepsilon_0 \mathbf{E}^2}{2} \sum_{\alpha=1}^{\mathrm{N}} c_\alpha \frac{\partial \chi}{\partial c_\alpha} + \frac{(1-\sum_{\beta=1}^{\mathrm{N}} \nu_\beta^0 c_\beta)^2}{2} \sum_{\alpha=1}^{\mathrm{N}} c_\alpha \frac{\partial \mathcal{K}}{\partial c_\alpha}, \tag{5.165}$$

where $\operatorname{tr}(\boldsymbol{\tau})/3 = \gamma \boldsymbol{\nabla} \mathbf{v}$ measures isotropic, viscous surface forces (see eq. (5.145)). Because p depends upon the viscous contribution $\gamma \cdot \boldsymbol{\nabla} \mathbf{v}$, it is not time-reversible. The corresponding reversible, "thermodynamic pressure" is

$$p^{\mathrm{td}} = p + \gamma \cdot \boldsymbol{\nabla} \mathbf{v}. \tag{5.166}$$

In contrast to p, the thermodynamic quantity p^{td} usually relates to equilibrium states of the system where the equation of state expresses the density as function of pressure (here, p^{td}) and temperature. Thus, p^{td} mimics the hypothetical quantity which would exist if the system were, at given temperature and local density, in equilibrium. Moreover, the discrepancy $\gamma\boldsymbol{\nabla}\mathbf{v}$ between p and p^{td} measures the competition between dissipation of momentum-density and mechanical deformation (see section 5.3.2). This is in accordance with results derived from statistical mechanics, which show that the difference between p and p^{td} depends on the rate at which the fluid density is changing with time (beneath the molecular composition of the fluid, comprised in γ).[255] However, in appendix D.6 we show that $\boldsymbol{\nabla}\mathbf{v} = \mathrm{tr}\,\boldsymbol{\kappa}$ measures the expansion of local volume-elements, see eq. (D.42) (note also balance of total mass, $\dot{\rho} = -\rho \cdot \boldsymbol{\nabla}\mathbf{v}$). Thus, $\boldsymbol{\nabla}\mathbf{v}$ is the simplest invariant quantity which measures the rate of density change with time. From the second axiom of thermodynamics, follows that $\gamma \geq 0$, see section 5.3.2. Therefore, the relation $p^{\mathrm{td}} = p + \gamma(\boldsymbol{\nabla}\mathbf{v})$ states that $p^{\mathrm{td}} > p$ when the volume increases ($\boldsymbol{\nabla}\mathbf{v} > 0$), *i.e.* when the mechanical pressure decreases. Similar, when the mechanical pressure increases ($\boldsymbol{\nabla}\mathbf{v} < 0$), the thermodynamic pressure is lower than p. Thus, p^{td} always "lags behind" p under density-changes.

We substitute eq. (5.165) into eq. (5.157) and reexpress the chemical potentials via the pressure

$$\mu_\alpha = RT\ln(f_\alpha c_\alpha) + \frac{2\nu_\alpha^0}{1+\sum_{\beta=1}^{\mathrm{N}}\nu_\beta^0 c_\beta}\left(p + \gamma\boldsymbol{\nabla}\mathbf{v} - \mathcal{P}^{\mathrm{int}} - \frac{\mathbf{E}\mathbf{D}_{\mathrm{F}}}{6}\right) -$$
$$- \left(\sum_{\gamma=1}^{\mathrm{N}}\delta_\alpha^\gamma - \frac{2\nu_\alpha^0 c_\gamma}{1+\sum_{\beta=1}^{\mathrm{N}}\nu_\beta^0 c_\beta}\right)\cdot\left(\frac{\varepsilon_0\mathbf{E}^2}{2}\frac{\partial\chi}{\partial c_\gamma} - \frac{(1-\sum_{\beta=1}^{\mathrm{N}}\nu_\beta^0 c_\beta)^2}{2}\cdot\frac{\partial\mathcal{K}}{\partial c_\gamma}\right) \tag{5.167}$$

Apparently,

$$\frac{\partial\mu_\alpha}{\partial p} = \frac{2\nu_\alpha^0}{1+\sum_{\beta=1}^{\mathrm{N}}\nu_\beta^0 c_\beta}\left[1 - \frac{p/\mathcal{K}}{(1+\sum_{\beta=1}^{\mathrm{N}}\nu_\beta^0 c_\beta)\sum_{\beta=1}^{\mathrm{N}}\nu_\beta^0 c_\beta}\right] \tag{5.168}$$

$$= \frac{2\nu_\alpha^0}{1+\sqrt{1+2\mathcal{P}^{\mathrm{vol}}/\mathcal{K}}}\left[1 - \frac{1}{(\mathcal{K}/p + 2\mathcal{P}^{\mathrm{vol}}/p)\sqrt{1+2\mathcal{P}^{\mathrm{vol}}/\mathcal{K}}}\right]. \tag{5.169}$$

As consequence, the pressure-dependence of the chemical potentials vanishes exactly for vanishing ν_α^0.

For hardly compressible electrolytes, *i.e.* $\mathcal{K} \gg \mathcal{P}^{\mathrm{vol}}$ or $\mathcal{K} \gg p$, this reproduces the well-known fact that the chemical potentials depend linearly on the pressure.[274] To see this, we use the expansion $\sum_{\beta=1}^{\mathrm{N}}\nu_\beta^0 c_\beta = \sqrt{1+2\mathcal{P}^{\mathrm{vol}}/\mathcal{K}}$ (see eq. (5.158)), such that

$$\sum_{\alpha=1}^{\mathrm{N}} c_\alpha \cdot \nu_\alpha^0 = \sqrt{1+\frac{2\mathcal{P}^{\mathrm{vol}}}{\mathcal{K}}} \approx 1+\frac{\mathcal{P}^{\mathrm{vol}}}{\mathcal{K}}, \quad \text{and} \quad \frac{1}{1++\sum_{\beta=1}^{\mathrm{N}} \nu_\beta^0 c_\beta} \approx \frac{1}{2}-\frac{1}{8}\frac{\mathcal{P}^{\mathrm{vol}}}{\mathcal{K}}. \tag{5.170}$$

In this limit, the contribution involving $\partial\mathcal{K}/\partial c_\alpha$ in eq. (5.167) vanishes. Furthermore, up to the first order in $\mathcal{P}^{\mathrm{vol}}/\mathcal{K}$, and if we assume $\partial\chi/\partial c_\alpha{=}0$ eq. (5.167) becomes

$$\mu_\alpha \approx RT\ln(f_\alpha c_\alpha)+\nu_\alpha^0\left(1-\mathcal{P}^{\mathrm{vol}}/4\mathcal{K}\right)\left(p+\gamma\boldsymbol{\nabla}\mathbf{v}-\mathcal{P}^{\mathrm{int}}-\mathbf{E}\mathbf{D}_{\mathrm{F}}/6\right). \tag{5.171}$$

Thus, for hardly compressible electrolytes, eq. (5.169) becomes

$$\partial\mu_\alpha/\partial p \approx \nu_\alpha^0\left(1-3\mathcal{P}^{\mathrm{vol}}/4\mathcal{K}\right). \tag{5.172}$$

In the limit $\mathcal{K}\to\infty$, this is reminiscent of a thermodynamic relation (see eq. (5.176)).

5.4.2 Excluded Volume Effects: Partial Molar Volumes and Euler Equation for the Volume

Volume is among the most fundamental quantities describing the kinematic state of a material system.[275,276] However, the volume of a multicomponent electrolyte is realized by contributions from all electrolyte species. Thus, the volume depends on the composition of the system. We assume that the volume is a function of

$$\boldsymbol{\Upsilon}^V = \{\mathcal{N}_1,\ldots,\mathcal{N}_{\mathrm{N}},p,T,\boldsymbol{\mathcal{E}},\mathbf{B}\}, \quad \text{i.e.} \quad V(\mathcal{N}_1,\ldots,\mathcal{N}_{\mathrm{N}},p,T,\boldsymbol{\mathcal{E}},\mathbf{B}). \tag{5.173}$$

Hence, the variation of the volume takes the canonical form[133]

$$\mathrm{d}V = V\cdot\alpha_V\cdot\mathrm{d}T-\frac{V}{\mathcal{K}^V}\cdot\mathrm{d}p+\sum_{\alpha=1}^{\mathrm{N}}\nu_\alpha\cdot\mathrm{d}\mathcal{N}_\alpha+\frac{\partial V}{\partial\boldsymbol{\mathcal{E}}}\cdot\mathrm{d}\boldsymbol{\mathcal{E}}+\frac{\partial V}{\partial\mathbf{B}}\cdot\mathrm{d}\mathbf{B}, \tag{5.174}$$

where $1/\mathcal{K}^V{=}{-}1/V\cdot\partial V/\partial p|_{T,\mathcal{N}_\alpha,\boldsymbol{\mathcal{E}}}$ is the inverse isothermal compressibility, and $\alpha_V{=}1/V\cdot\partial V/\partial T|_{p,\boldsymbol{\mathcal{E}},\mathcal{N}_\alpha}$ is the thermal expansion. Here, the partial molar volumes are defined by

$$\nu_\alpha(\boldsymbol{\Upsilon}^V) = \left.\frac{\partial V}{\partial\mathcal{N}_\alpha}\right|_{\boldsymbol{\Upsilon}^V\setminus\mathcal{N}_\alpha}, \tag{5.175}$$

and measure the change of volume of the solution under the variation of amount of one of the solute species,[277] *i.e.* the contributions of the individual species volumes to the overall material volume.

Beneath this thermodynamic perspective, ν_α depends on microscopic inter-species correlations between the solute species α and all other species, including solvation effects (this helps explain the observation of negative partial molar volumes).[278–280]

An alternative definition for the partial molar volumes is (see eq. (5.172)),[281]

$$\nu_\alpha = \partial\mu_\alpha/\partial p|_{\boldsymbol{\Upsilon}^V\backslash p}\,. \tag{5.176}$$

Volume is an extensive property, which is a homogeneous function of first degree with respect to the (molar) particle numbers $\mathcal{N}_\alpha$. This basic observation implies a fundamental relation constraining the volume fractions $c_\alpha\nu_\alpha$ of the electrolyte species. From Euler's homogeneous function theorem,[282] follows the volume-filling property of the electrolyte mixture, *i.e.* the Euler equation for the volume,[98,190]

$$V = \sum_{\alpha=1}^{\mathrm{N}} \frac{\partial V}{\partial \mathcal{N}_\alpha} \cdot \mathcal{N}_\alpha = \sum_{\alpha=1}^{\mathrm{N}} \nu_\alpha \cdot \mathcal{N}_\alpha, \tag{5.177}$$

or

$$1 = \sum_{\alpha=1}^{\mathrm{N}} \nu_\alpha \cdot c_\alpha, \tag{5.178}$$

Hence, the species volumes V_α relate to the corresponding partial molar volumes via $V_\alpha{=}\nu_\alpha\mathcal{N}_\alpha$, and constitute the overall volume, $V{=}\sum_{\alpha=1}^{\mathrm{N}} V_\alpha$. Note that the Euler equation for the volume is always true, *i.e.* for compressible and incompressible electrolytes.

By construction, the partial molar volumes exhibit various symmetry properties. To see this, we observe that the definition eq. (5.175) implies

$$\frac{\partial \nu_\alpha}{\partial \mathcal{N}_\beta} = \frac{\partial^2 V}{\partial \mathcal{N}_\beta \partial \mathcal{N}_\alpha} = \frac{\partial^2 V}{\partial \mathcal{N}_\alpha \partial \mathcal{N}_\beta} = \frac{\partial \nu_\beta}{\partial \mathcal{N}_\alpha}. \tag{5.179}$$

This relation is supplemented by another symmetry property, which follows from the extensitivity of the volume. Using eq. (5.177), we find

$$\nu_\alpha{=}\frac{\partial V}{\partial \mathcal{N}_\alpha}{=}\frac{\partial}{\partial \mathcal{N}_\alpha}\sum_{\beta=1}^{\mathrm{N}} \mathcal{N}_\beta\nu_\beta{=}\sum_{\beta=1}^{\mathrm{N}}\left(\delta_\alpha^\beta{\cdot}\nu_\beta{+}\mathcal{N}_\beta{\cdot}\frac{\partial \nu_\beta}{\partial \mathcal{N}_\alpha}\right) = \nu_\alpha + \sum_{\beta=1}^{\mathrm{N}} \mathcal{N}_\beta \cdot \frac{\partial \nu_\beta}{\partial \mathcal{N}_\alpha}. \tag{5.180}$$

Comparing both sides, and using the symmetry property eq. (5.179), we find

$$\sum_{\beta=1}^{\mathrm{N}} \mathcal{N}_\beta \cdot \frac{\partial \nu_\beta}{\partial \mathcal{N}_\alpha} = \sum_{\beta=1}^{\mathrm{N}} \mathcal{N}_\beta \cdot \frac{\partial \nu_\alpha}{\partial \mathcal{N}_\beta} = 0. \tag{5.181}$$

Next, we show that the variation of the volume, and the Euler equation for the volume, imply a Gibbs-Duhem equation for the partial molar volumes. For this purpose, we use eq. (5.177) such that $\mathrm{d}V = \sum_{\alpha=1}^{\mathrm{N}}(\mathcal{N}_\alpha{\cdot}\,\mathrm{d}\nu_\alpha{+}\nu_\alpha{\cdot}\,\mathrm{d}\mathcal{N}_\alpha)$, and substitute this result into the fundamental expansion of the volume, eq. (5.174). This yields the Gibbs-Duhem equation for the partial molar volumes

$$\sum_{\alpha=1}^{\mathrm{N}} c_\alpha \cdot \mathrm{d}\nu_\alpha = \alpha_V \cdot \mathrm{d}T - \frac{1}{\mathcal{K}^V} \cdot \mathrm{d}p + \frac{1}{V} \cdot \frac{\partial V}{\partial \boldsymbol{\mathcal{E}}} \cdot \mathrm{d}\boldsymbol{\mathcal{E}} + \frac{1}{V} \cdot \frac{\partial V}{\partial \mathbf{B}} \cdot \mathrm{d}\mathbf{B}. \tag{5.182}$$

However, because the partial molar volumes depend on the same set of variables $\boldsymbol{\Upsilon}^V$ as the volume (see eq. (5.173)), *i.e.* $\nu_\alpha(\mathcal{N}_1,\ldots,\mathcal{N}_\mathrm{N},p,T,\boldsymbol{\mathcal{E}},\mathbf{B})$, it follows that

$$\mathrm{d}\nu_\alpha = \left.\frac{\partial \nu_\alpha}{\partial T}\right|_{\boldsymbol{\Upsilon}^V\backslash T} \mathrm{d}T + \left.\frac{\partial \nu_\alpha}{\partial p}\right|_{\boldsymbol{\Upsilon}^V\backslash p} \mathrm{d}p + \left.\frac{\partial \nu_\alpha}{\partial \boldsymbol{\mathcal{E}}}\right|_{\boldsymbol{\Upsilon}^V\backslash \boldsymbol{\mathcal{E}}} \mathrm{d}\boldsymbol{\mathcal{E}} + \left.\frac{\partial \nu_\alpha}{\partial \mathbf{B}}\right|_{\boldsymbol{\Upsilon}^V\backslash \mathbf{B}} \mathrm{d}\mathbf{B} + \\ + \sum_{\beta=1}^{\mathrm{N}} \left.\frac{\partial \nu_\alpha}{\partial \mathcal{N}_\beta}\right|_{\boldsymbol{\Upsilon}^V\backslash \mathcal{N}_\beta} \mathrm{d}\mathcal{N}_\beta. \tag{5.183}$$

From the comparison of eqs. (5.182) and (5.183) follow various relations.

$$\sum_{\alpha=1}^{\mathrm{N}} c_\alpha \cdot \partial\nu_\alpha/\partial p|_{\boldsymbol{\Upsilon}^V\backslash p} = 1/V \cdot \partial V/\partial p|_{\boldsymbol{\Upsilon}^V\backslash p} = -1/\mathcal{K}^V \,, \tag{5.184}$$

$$\sum_{\alpha=1}^{\mathrm{N}} c_\alpha \cdot \partial\nu_\alpha/\partial T|_{\boldsymbol{\Upsilon}^V\backslash T} = 1/V \cdot \partial V/\partial T|_{\boldsymbol{\Upsilon}^V\backslash T} = \alpha_V, \tag{5.185}$$

$$\sum_{\alpha=1}^{\mathrm{N}} c_\alpha \cdot \partial\nu_\alpha/\partial \boldsymbol{\mathcal{E}}|_{\boldsymbol{\Upsilon}^V\backslash \boldsymbol{\mathcal{E}}} = 1/V \cdot \partial V/\partial \boldsymbol{\mathcal{E}}|_{\boldsymbol{\Upsilon}^V\backslash \boldsymbol{\mathcal{E}}} \,, \tag{5.186}$$

$$\sum_{\alpha=1}^{\mathrm{N}} c_\alpha \cdot \partial\nu_\alpha/\partial \mathbf{B}|_{\boldsymbol{\Upsilon}^V\backslash \mathbf{B}} = 1/V \cdot \partial V/\partial \mathbf{B}|_{\boldsymbol{\Upsilon}^V\backslash \mathbf{B}} \,, \tag{5.187}$$

$$\sum_{\alpha=1}^{\mathrm{N}} c_\alpha \cdot \partial\nu_\alpha/\partial \mathcal{N}_\beta|_{\boldsymbol{\Upsilon}^V\backslash \mathcal{N}_\beta} = 0. \tag{5.188}$$

Equation (5.174) implies that if the volume does not depend on pressure, *i.e.* $\partial V/\partial p|_{\boldsymbol{\Upsilon}^V\backslash p} = 0$, then $1/\mathcal{K}^V \rightarrow 0$, or, equivalently, $\mathcal{K}^V \rightarrow \infty$. However, this also implies that $\sum_{\alpha=1}^{\mathrm{N}} c_\alpha \cdot \partial\nu_\alpha/\partial p = 0$, see eq. (5.184). Thus, $\partial\nu_\alpha/\partial p = 0$ for all partial molar volumes is a sufficient condition for that the volume does not vary under pressure variations. This argument suggests defining incompressible electrolytes via the condition that $\partial_p \nu_\alpha = 0$ for all species α (since then $\partial_p V = 0$, and the volumetric bulk modulus diverges, *i.e.* $\mathcal{K}^V \rightarrow \infty$). The coefficient α_V appearing in eq. (5.185) is the thermal expansion. However, it is often argued that thermodynamic axioms imply that $\partial_T \nu_\alpha = 0$ for incompressible liquids, *i.e.* when $\partial_p \nu_\alpha = 0$.[283] This is the core of the so-called Müller Paradox,[284–286] because it contradicts the experimentally well-established Boussinesq-Approximation,[287] in which incompressible fluids exhibit thermal expansion.[288] Equations (5.186) and (5.187) measure the electric and magnetic contributions to the expansion of the volume. Note that the Maxwell equations in the aether frame imply that when $\mathrm{d}\boldsymbol{\mathcal{E}}$ is evaluated with respect to spatial variations ($\boldsymbol{\nabla}\boldsymbol{\mathcal{E}}$), then there appears a contribution involving the the charge density in eq. (5.182), and if $\mathrm{d}\boldsymbol{\mathcal{E}}$ and $\mathrm{d}\mathbf{B}$ are evaluated for time variations ($\partial_t\boldsymbol{\mathcal{E}}$ and $\partial_t\mathbf{B}$), there appears a contribution from the electric current and from the rotation of the electric field. The thermodynamic result eq. (5.188) reproduces our finding from eq. (5.181). In addition, the variation of the trivial form of the Euler equation for the volume (eq. (5.178)) also implies some useful relations. Using the Gibbs-Duhem equation for the partial molar volumes, eq. (5.182), we find

$$0{=}\mathrm{d}\left(\sum_{\alpha=1}^{\mathrm{N}}\nu_\alpha c_\alpha\right)=\sum_{\alpha=1}^{\mathrm{N}}\nu_\alpha{\cdot}\mathrm{d}c_\alpha{+}\sum_{\alpha=1}^{\mathrm{N}}c_\alpha\left[\frac{\partial\nu_\alpha}{\partial T}{\cdot}\mathrm{d}T{+}\frac{\partial\nu_\alpha}{\partial p}{\cdot}\mathrm{d}p{+}\frac{\partial\nu_\alpha}{\partial\boldsymbol{\mathcal{E}}}{\cdot}\mathrm{d}\boldsymbol{\mathcal{E}}\right]. \tag{5.189}$$

Evaluating the formal variation for spatial inhomogeneities yields

$$\sum_{\alpha=1}^{\mathrm{N}}\nu_\alpha\boldsymbol{\nabla}c_\alpha{=}\frac{1}{\mathcal{K}^V}\boldsymbol{\nabla}p{-}\sum_{\alpha=1}^{\mathrm{N}}c_\alpha\left[\frac{\partial\nu_\alpha}{\partial T}\boldsymbol{\nabla}T{+}\frac{\partial\nu_\alpha}{\partial\boldsymbol{\mathcal{E}}}\left(\frac{\varrho_{\mathrm{F}}}{\varepsilon_0\varepsilon_{\mathrm{R}}}{-}\frac{\boldsymbol{\mathcal{E}}}{\varepsilon_{\mathrm{R}}}\boldsymbol{\nabla}\chi\right)\right], \tag{5.190}$$

whereas the temporal variation yields an equation for the evolution of the pressure

$$\frac{1}{\mathcal{K}^V}\frac{\partial p}{\partial t}=\sum_{\alpha=1}^{\mathrm{N}}\nu_\alpha\frac{\partial c_\alpha}{\partial t}+\sum_{\alpha=1}^{\mathrm{N}}c_\alpha\left[\frac{\partial\nu_\alpha}{\partial T}\frac{\partial T}{\partial t}-\frac{\partial\nu_\alpha}{\partial\boldsymbol{\mathcal{E}}}\left(\frac{\mathbf{j}_{\mathrm{F}}}{\varepsilon_0\varepsilon_{\mathrm{R}}}+\frac{\boldsymbol{\mathcal{E}}}{\varepsilon_{\mathrm{R}}}\frac{\partial\chi}{\partial t}\right)-\frac{\partial\nu_\alpha}{\partial\mathbf{B}}\left(\boldsymbol{\nabla}\wedge\mathbf{E}\right)\right]. \tag{5.191}$$

In accordance with the property that the pressure is a macroscopic quantity, which does not depend on the state of an observer, the transport contribution $\sum_{\alpha=1}^{\mathrm{N}}\nu_\alpha\partial_t c_\alpha$ appearing in eq. (5.191) is objective, since it consists of objective scalars and time derivatives of objective scalars (see Lemma 13). In particular,

$$\sum_{\alpha=1}^{\mathrm{N}}\nu_\alpha\partial_t c_\alpha{=}-\sum_{\alpha=1}^{\mathrm{N}}\nu_\alpha\cdot\boldsymbol{\nabla}\left(c_\alpha\mathbf{v}_\alpha\right)+r_\alpha, \tag{5.192}$$

does not depend on convection (here we used that $\partial_t c_\alpha{=}r_\alpha{-}\boldsymbol{\nabla}(c_\alpha\mathbf{v}_\alpha)$, see eq. (5.11)). However, eq. (5.192) can be reformulated via $\sum_{\alpha=1}^{\mathrm{N}}\nu_\alpha\boldsymbol{\nabla}(c_\alpha\mathbf{v}_\alpha)=\sum_{\alpha=1}^{\mathrm{N}}[\boldsymbol{\nabla}(\nu_\alpha c_\alpha\mathbf{v}_\alpha){-}c_\alpha\mathbf{v}_\alpha\boldsymbol{\nabla}\nu_\alpha]$, such that it does designate one particular frame of reference. Apparently, the first term in brackets constitutes a reference frame which is defined by $\psi_\alpha{=}\nu_\alpha c_\alpha$. Indeed, this is exactly the volume averaged frame, where the corresponding convection velocity is defined by $\mathbf{v}^{\mathsf{Volume}}{=}\sum_{\alpha=1}^{\mathrm{N}}c_\alpha\nu_\alpha\mathbf{v}_\alpha$. Hence,

$$\sum_{\alpha=1}^{\mathrm{N}}\nu_\alpha\partial_t c_\alpha=-\boldsymbol{\nabla}\mathbf{v}^{\mathsf{Volume}}+\sum_{\alpha=1}^{\mathrm{N}}c_\alpha\mathbf{v}_\alpha\cdot\boldsymbol{\nabla}\nu_\alpha+\sum_{\alpha=1}^{\mathrm{N}}\nu_\alpha\cdot r_\alpha. \tag{5.193}$$

Frames based on different drift velocities $\mathbf{v}^{\psi}$ (where $\mathbf{v}^{\psi}=\sum_{\alpha=1}^{\mathrm{N}}\psi_\alpha \mathbf{v}_\alpha$) relate to this description via $\mathbf{v}^{\mathsf{Volume}}=\mathbf{v}^{\psi}+\sum_{\alpha=1}^{\mathrm{N}}\nu_\alpha \boldsymbol{\mathcal{N}}_\alpha^{\psi}$, where $\boldsymbol{\mathcal{N}}_\alpha^{\psi}=c_\alpha(\mathbf{v}_\alpha-\mathbf{v}^{\psi})$ (see section 5.5). Hence, using any other frame of reference, eq. (5.193) becomes

$$\sum_{\alpha=1}^{\mathrm{N}}\nu_\alpha\partial_t c_\alpha = -\boldsymbol{\nabla}\mathbf{v}^{\psi} - \sum_{\alpha=1}^{\mathrm{N}}\nu_\alpha\cdot\boldsymbol{\nabla}\boldsymbol{\mathcal{N}}_\alpha^{\psi} + \mathbf{v}^{\psi}\cdot\sum_{\alpha=1}^{\mathrm{N}}c_\alpha\boldsymbol{\nabla}\nu_\alpha + \sum_{\alpha=1}^{\mathrm{N}}\nu_\alpha\cdot r_\alpha. \tag{5.194}$$

The two expansions constituted by eqs. (5.193) and (5.194) can both be used in the equation for the pressure (eq. (5.191)). However, the expansion based on the volume frame offers a convenient description of incompressible electrolytes. Altogether, the evolution of the pressure reads (eq. (5.191))

$$\frac{1}{\mathcal{K}^V}\frac{\partial p}{\partial t} = -\boldsymbol{\nabla}\mathbf{v}^{\mathsf{Volume}} + \sum_{\alpha=1}^{\mathrm{N}}c_\alpha\mathbf{v}_\alpha\boldsymbol{\nabla}\nu_\alpha + \alpha_V\frac{\partial T}{\partial t} - \sum_{\alpha=1}^{\mathrm{N}}c_\alpha\frac{\partial\nu_\alpha}{\partial\boldsymbol{\mathcal{E}}}\left(\frac{\mathbf{j}_{\mathrm{F}}}{\varepsilon_0\varepsilon_{\mathrm{R}}}+\frac{\boldsymbol{\mathcal{E}}}{\varepsilon_{\mathrm{R}}}\frac{\partial\chi}{\partial t}\right)+ \\ + \sum_{\alpha=1}^{\mathrm{N}}c_\alpha\frac{\partial\nu_\alpha}{\partial\mathbf{B}}\cdot\boldsymbol{\nabla}\wedge\mathbf{E} + \sum_{\alpha=1}^{\mathrm{N}}\nu_\alpha r_\alpha. \tag{5.195}$$

Note that in incompressible and isothermal electrolytes, the equation for the pressure transfers to an algebraic equation for the convection velocity, which does not involve time derivatives (see eq. (5.221)).

Finally, we derive a more canonical Gibbs-Duhem relation. The material law for the free energy, $\boldsymbol{\Upsilon}=\{c_1,\ldots,c_{\mathrm{N}},\boldsymbol{\mathcal{E}},\mathbf{B},T\}$, and the constitutive equations imply

$$\mathrm{d}(\rho\varphi_{\mathrm{H}}) = -\mathbf{P}\cdot\mathrm{d}\boldsymbol{\mathcal{E}} - \boldsymbol{\mathcal{M}}\cdot\mathrm{d}\mathbf{B} - \rho s\cdot\mathrm{d}T + \sum_{\alpha=1}^{\mathrm{N}}\mu_\alpha\cdot\mathrm{d}c_\alpha. \tag{5.196}$$

We substitute the variation of the elastic pressure $\mathcal{P}^{\mathrm{el}}=\sum_{\alpha=1}^{\mathrm{N}}\mu_\alpha c_\alpha-\rho\varphi_{\mathrm{H}}$ into eq. (5.196), which yields the canonical Gibbs-Duhem equation,[133,289]

$$\sum_{\alpha=1}^{\mathrm{N}}c_\alpha\cdot\mathrm{d}\mu_\alpha = \mathrm{d}\mathcal{P}^{\mathrm{el}} - \mathbf{P}\cdot\mathrm{d}\boldsymbol{\mathcal{E}} - \boldsymbol{\mathcal{M}}\cdot\mathrm{d}\mathbf{B} - \rho s\cdot\mathrm{d}T. \tag{5.197}$$

Hence, using eq. (5.160) it follows that for constant susceptibilities, and if magnetic and thermal veriations are neglected, the Gibbs-Duhem equation becomes

$$\sum_{\alpha=1}^{\mathrm{N}}c_\alpha\cdot\mathrm{d}\mu_\alpha = \mathrm{d}\mathcal{P}^{\mathrm{vol}} + \mathrm{d}\mathcal{P}^{\mathrm{int}}. \tag{5.198}$$

Next, we show that that in our theory the partial molar volumes follow from the surface forces acting upon the material volume, *i.e.* the stress tensor. To derive this result, we assume a homogeneous system, where viscosity can be neglected.Thus, the complete pressure reduces to the thermodynamic pressure $p=p^{\mathrm{td}}$, see eq. (5.166), and is a function of concentrations c_α, temperature T, and electric field $\mathbf{E}$ via the stress tensor (see eq. (5.164)),

$$p = p^{\mathrm{td}} = f(c_\alpha, T, \mathbf{E}). \tag{5.199}$$

Above, we used molar particle numbers $\mathcal{N}_\alpha$ and V instead of concentrations c_α in the materials law, such that eq. (5.199) implicitly determines the volume as function of $\mathcal{N}_\alpha$, p, T, and $\mathbf{E}$ via $V(\mathcal{N}_\alpha, p, T, \mathbf{E})$. We use implicit differentiation to obtain an expression for the molar volumes,

$$\begin{aligned} 0= \left.\frac{\partial f}{\partial \mathcal{N}_\alpha}\right|_{p,T,\mathbf{E}} &= \sum_{\beta=1}^{\mathrm{N}} \frac{\partial f}{\partial c_\beta}\left.\left(\frac{\partial c_\beta}{\partial \mathcal{N}_\alpha} + \frac{\partial c_\beta}{\partial V}\frac{\partial V}{\partial \mathcal{N}_\alpha}\right)\right|_{p,T,\mathbf{E}} = \sum_{\beta=1}^{\mathrm{N}} \frac{\partial f}{\partial c_\beta}\left.\left(\frac{\delta_\beta^\alpha}{V} - \frac{\mathcal{N}_\beta}{V^2}\frac{\partial V}{\partial \mathcal{N}_\alpha}\right)\right|_{p,T,\mathbf{E}} \\ &= \frac{1}{V}\cdot\left[\left.\frac{\partial f}{\partial c_\alpha}\right|_{p,T,\mathbf{E}} - \nu_\alpha \cdot \sum_{\beta=1}^{\mathrm{N}} c_\beta \cdot \left.\frac{\partial f}{\partial c_\beta}\right|_{p,T,\mathbf{E}}\right]. \end{aligned} \tag{5.200}$$

This implies that the partial molar volumes are determined by the stress tensor,

$$\nu_\alpha = \left.\frac{\partial V}{\partial \mathcal{N}_\alpha}\right|_{p,T,\mathbf{E}} = \left.\frac{\partial f/\partial c_\alpha}{\sum_{\beta=1}^{\mathrm{N}} c_\beta \cdot \partial f/\partial c_\beta}\right|_{p,T,\mathbf{E}}. \tag{5.201}$$

Note that this result is independent from the free energy model.

Next, we evaluate this result and calculate the partial molar volumes following from our model for the free energy density. We restrict to the case where the material parameters χ and $\mathcal{K}$ do not depend on composition, and neglect interaction contributions. Thus, we find

$$\nu_\alpha = \frac{\nu_\alpha^0}{\sum_{\beta=1}^{\mathrm{N}} \nu_\beta^0 c_\beta} = \frac{\nu_\alpha^0}{\sqrt{1 + 2\mathcal{P}^{\mathrm{vol}}/\mathcal{K}}} \tag{5.202}$$

such that

$$\partial\nu_\alpha/\partial p = -\nu_\alpha/(\mathcal{K} + 2\mathcal{P}^{\mathrm{vol}}). \tag{5.203}$$

Hence, the partial molar volumes decrease with increasing pressure. We substitute this result into eq. (5.184) and relate $\mathcal{K}$ to $\mathcal{K}^V$,

$$\mathcal{K}^V - \mathcal{K} = 2\mathcal{P}^{\mathrm{vol}}. \tag{5.204}$$

Thus, $\mathcal{K}$ is indeed a bulk-modulus. From eq. (5.202), we obtain

$$\frac{\partial\nu_\alpha}{\partial\mathbf{E}} = \frac{\nu_\alpha}{3\mathcal{K}} \cdot \frac{\mathbf{E}\varepsilon_0\varepsilon_{\mathrm{R}}}{1 + 2\mathcal{P}^{\mathrm{vol}}/\mathcal{K}}, \tag{5.205}$$

such that the pressure equation becomes (see eq. (5.195))

$$\frac{1}{\mathcal{K}}\frac{\partial p}{\partial t} = \left(1 + \frac{2\mathcal{P}^{\mathrm{vol}}}{\mathcal{K}}\right) \cdot \left(-\boldsymbol{\nabla}\mathbf{v}^{\mathsf{Volume}} + \sum_{\alpha=1}^{\mathrm{N}} c_\alpha \mathbf{v}_\alpha \boldsymbol{\nabla}\nu_\alpha\right) - \frac{\mathbf{j}_{\mathrm{F}}\mathbf{E}}{3\mathcal{K}} + \sum_{\alpha=1}^{\mathrm{N}} \nu_\alpha r_\alpha. \tag{5.206}$$

Furthermore, the spatial variation of the pressure force reads (see eq. (5.190))

$$\frac{1}{\mathcal{K}}\boldsymbol{\nabla}p = \frac{\varrho_{\mathrm{F}}\mathbf{E}}{3\mathcal{K}} + \left(1 + \frac{2\mathcal{P}^{\mathrm{vol}}}{\mathcal{K}}\right) \sum_{\alpha=1}^{\mathrm{N}} \nu_\alpha \boldsymbol{\nabla} c_\alpha, \tag{5.207}$$

whereas the gradient of the partial molar volumes follows from eqs. (5.183) and (5.205)

$$\boldsymbol{\nabla}\nu_\alpha = \frac{\nu_\alpha}{\mathcal{K} + 2\mathcal{P}^{\mathrm{vol}}} \cdot \left(\frac{\varrho_{\mathrm{F}}\mathbf{E}}{3} - \boldsymbol{\nabla}p\right) = -\frac{\nu_\alpha}{\mathcal{K} + 2\mathcal{P}^{\mathrm{vol}}} \cdot \boldsymbol{\nabla}\left(\mathcal{P}^{\mathrm{el}} + \mathcal{P}^{\mathrm{int}} - \frac{\mathrm{tr}\boldsymbol{\tau}}{3}\right). \tag{5.208}$$

Substituting eq. (5.208) into eq. (5.206) yields

$$\frac{1}{\mathcal{K}}\frac{\partial p}{\partial t} = -\left(1 + \frac{2\mathcal{P}^{\mathrm{vol}}}{\mathcal{K}}\right)\left(\boldsymbol{\nabla}\mathbf{v}^{\mathsf{Volume}} + \frac{\mathbf{v}^{\mathsf{Volume}}}{\mathcal{K}+2\mathcal{P}^{\mathrm{vol}}}\boldsymbol{\nabla}\left[\mathcal{P}^{\mathrm{vol}} + \mathcal{P}^{\mathrm{int}} + p^{\mathrm{visc}}\right]\right) - \frac{\mathbf{j}_{\mathrm{F}}\mathbf{E}}{3\mathcal{K}} + \sum_{\alpha=1}^{\mathrm{N}} \nu_\alpha r_\alpha. \tag{5.209}$$

The contribution $\mathbf{j}_{\mathrm{F}}\mathbf{E}$ appearing in eq. (5.206) is the Joule heating. It is an artefact from the momentum of the electromagnetic fields (comprised in the Poynting vector) which is transferred to the polarizable medium (and appears also in the electromagnetic entropy inequality). Furthermore, the quantity $\varrho_{\mathrm{F}}\mathbf{E}$ appearing in eq. (5.207) is the Lorentz force density, which plays an important role in highly confined regions of the electrolyte (note that eq. (5.207) follows from eq. (5.208)). However, we emphasize that eqs. (5.202) to (5.208) are true only in the case where the susceptibility and the bulk modulus do not depend on composition, and must be extended by additional contributions in the more general case.

In section 5.2.4 we showed that the force law can be expressed via pressure forces when body forces are neglected

$$\rho\dot{\mathbf{v}} = \boldsymbol{\nabla}\boldsymbol{\sigma} = \boldsymbol{\nabla}\boldsymbol{\Sigma} + \boldsymbol{\nabla}\boldsymbol{\tau} - \boldsymbol{\nabla}\mathcal{P}^{\mathrm{el}}, \tag{5.210}$$

where (recall that $\mathcal{P}^{\mathrm{vol}} = \sum_{\alpha=1}^{\mathrm{N}} c_\alpha \mu_\alpha - \rho\varphi_{\mathrm{H}}$)

$$\boldsymbol{\nabla}\mathcal{P}^{\mathrm{el}} = \sum_{\alpha=1}^{\mathrm{N}} c_\alpha \boldsymbol{\nabla}\mu_\alpha - \sum_{\Upsilon_B \neq c_\alpha} \frac{\partial(\rho\varphi_{\mathrm{H}})}{\partial \Upsilon_B}\boldsymbol{\nabla}\Upsilon_B = \sum_{\alpha=1}^{\mathrm{N}} c_\alpha \boldsymbol{\nabla}\mu_\alpha + (\mathbf{P}\boldsymbol{\nabla})\mathbf{E}. \tag{5.211}$$

Note that eq. (5.211) reproduces our thermodynamical finding for the Gibbs-Duhem equation from above, see eq. (5.197). Furthermore, $\boldsymbol{\nabla}\boldsymbol{\Sigma} = \varrho_{\mathrm{F}}\mathbf{E} + (\mathbf{P}\boldsymbol{\nabla})\mathbf{E}$

$$\rho\dot{\mathbf{v}} = \boldsymbol{\nabla}\boldsymbol{\tau} - \sum_{\alpha=1}^{\mathrm{N}} c_\alpha \cdot \boldsymbol{\nabla}\mu_\alpha - \varrho_{\mathrm{F}} \cdot \boldsymbol{\nabla}\Phi. \tag{5.212}$$

The chemical forces are

$$\boldsymbol{\nabla}\mu_\alpha=\Big(\frac{1-\sum_{\beta=1}^{\mathrm{N}}\nu_\beta^0 c_\beta}{\mathcal{K}}\frac{\partial\mathcal{K}}{\partial c_\alpha}+\frac{2\nu_\alpha^0}{1+\sum_{\beta=1}^{\mathrm{N}}\nu_\beta^0 c_\beta}\Big)\frac{\boldsymbol{\nabla}\mathcal{P}^{\mathrm{vol}}}{\sum_{\beta=1}^{\mathrm{N}}\nu_\beta^0 c_\beta}+RT\boldsymbol{\nabla}\ln(f_\alpha c_\alpha)+ \\ +\frac{(1-\sum_{\beta=1}^{\mathrm{N}}\nu_\beta^0 c_\beta)^2}{2}\boldsymbol{\nabla}\frac{\partial\mathcal{K}}{\partial c_\alpha}-\varepsilon_0\mathbf{E}\left(\boldsymbol{\nabla}\mathbf{E}\cdot\frac{\partial\chi}{\partial c_\alpha}+\frac{\mathbf{E}}{2}\cdot\boldsymbol{\nabla}\frac{\partial\chi}{\partial c_\alpha}\right) \tag{5.213}$$

However, in many cases the dependence of the dielectric susceptibility and the bulk modulus on the composition is neglected. Hence, when we assume $\partial\chi/\partial c_\alpha = 0$ and $\partial\mathcal{K}/\partial c_\alpha = 0$, then eq. (5.167) reduces to

$$\mu_\alpha = RT\ln(f_\alpha c_\alpha)+\frac{2\nu_\alpha^0}{1+\sum_{\beta=1}^{\mathrm{N}}\nu_\beta^0 c_\beta}\left(p+\gamma\boldsymbol{\nabla}\mathbf{v}-\mathcal{P}^{\mathrm{int}}-\mathbf{E}\mathbf{D}_{\mathrm{F}}/6\right). \tag{5.214}$$

Furthermore, the elastic pressure becomes $\mathcal{P}^{\mathrm{el}}{=}\varepsilon_0\chi\mathbf{E}^2/2+\mathcal{P}^{\mathrm{int}}{+}\mathcal{P}^{\mathrm{vol}}$ (see eq. (5.160)), such that $\boldsymbol{\sigma}{=}\boldsymbol{\Sigma}{+}\boldsymbol{\tau}{-}(\mathcal{P}^{\mathrm{vol}}{+}\mathcal{P}^{\mathrm{int}}{-}\varepsilon_0\chi\mathbf{E}^2/2\,)\,\mathbf{Id}$ and $p{=}\mathbf{E}\mathbf{D}_{\mathrm{F}}/6-\gamma\boldsymbol{\nabla}\mathbf{v}{+}\mathcal{P}^{\mathrm{vol}}{+}\mathcal{P}^{\mathrm{int}}$. However, the chemical forces reduce to (see eq. (5.213))

$$\boldsymbol{\nabla}\mu_\alpha = RT\boldsymbol{\nabla}\ln(f_\alpha c_\alpha)+2\nu_\alpha^0\Big(\sum_{\beta=1}^{\mathrm{N}}\nu_\beta^0 c_\beta[1+\sum_{\beta=1}^{\mathrm{N}}\nu_\beta^0 c_\beta]\Big)^{-1}\cdot\boldsymbol{\nabla}\mathcal{P}^{\mathrm{vol}}, \tag{5.215}$$

such that

$$\sum_{\alpha=1}^{\mathrm{N}} c_\alpha\boldsymbol{\nabla}\mu_\alpha = RT\sum_{\alpha=1}^{\mathrm{N}} c_\alpha\cdot\boldsymbol{\nabla}\ln(f_\alpha c)+2\cdot\Big(1+\sum_{\beta=1}^{\mathrm{N}}\nu_\beta^0 c_\beta\Big)^{-1}\cdot\boldsymbol{\nabla}\mathcal{P}^{\mathrm{vol}}, \tag{5.216}$$

where we used that $\sum_{\alpha=1}^{\mathrm{N}} c_\alpha\boldsymbol{\nabla}\ln(c_\alpha/c\,){=}0$. The pressure forces $\boldsymbol{\nabla}\mathcal{P}^{\mathrm{vol}}$ appearing in the chemical forces depend on the bulk modulus via $\mathcal{P}^{\mathrm{vol}}{=}\mathcal{K}[(\sum_{\beta=1}^{\mathrm{N}}\nu_\beta^0 c_\beta)^2{-}1]/2$.

5.4.3 Incompressible Electrolytes And Mechanical Equilibrium

From now on, we consider incompressible electrolytes where $\partial\nu_\alpha/\partial p = 0$ for all species α. Because of eqs. (5.203) and (5.204), our definition of incompressibility implies that the bulk moduli diverge, $\mathcal{K}\to\infty$ and $\mathcal{K}^V\to\infty$. The latter property implies that the volume V becomes independent of pressure. In addition, it follows from eq. (5.208), that the actual partial molar volumes equal the partial molar volumes of the reference configuration, and are constant,

$$\nu_\alpha = \nu_\alpha^0, \quad \text{such that} \quad \sum_{\alpha=1}^{\mathrm{N}} c_\alpha\nu_\alpha^0 = 1, \quad \text{and} \quad \boldsymbol{\nabla}\nu_\alpha = 0. \tag{5.217}$$

Furthermore, incompressibility implies that (see eq. (5.172))

$$\sum_{\alpha=1}^{N} \nu_\alpha \cdot \nabla c_\alpha = 0, \tag{5.218}$$

and that for isothermal electrolytes in electroneutral state, eq. (5.207) becomes

$$\partial\mu_\alpha/\partial p = \nu_\alpha. \tag{5.219}$$

Thus, in the incompressible limit, the Euler equation for the volume, constitutes an incompressibility constraint on the system. As consequence, the quantity $\mathcal{P}^{\text{vol}}$ cannot be defined via eq. (5.158) anymore, and the thermodynamic definition of pressure as in eq. (5.166) is not valid anymore. Incompressibility thus implies that the role of pressure transitions from a thermodynamic quantity into a purely mechanical quantity, ensuring continuity (mass conservation).[255] Below, we resolve this ambiguity and determine the elastic volumetric contributions in the chemical potentials by assuming mechanical equilibrium (see eq. (5.237)).

5.4.4 Convection Equation

The Euler equation for the volume imposes a constraint on electrolyte transport. Because eq. (5.178) must always be fulfilled, local volume variations are balanced by volume transport of bulk electrolyte. Thus, volume redistribution leads to bulk convection. However, local imbalance of volume (as described by $\nabla \mathbf{v}$ (see appendix D.6) may also result from Faradaic volume-effects, *i.e.* species reactions.

In the incompressible limit, this follows directly from the equation for the pressure, eq. (5.206), which constitutes an equation for the determination of the volume averaged convection velocity without involving time-derivatives (note that $\nabla\nu_\alpha{=}0$ and that terms weighted by $1/\mathcal{K}$ vanish),

$$\nabla \mathbf{v}^{\text{Volume}} = \sum_{\alpha=1}^{N} \nu_\alpha r_\alpha, \tag{5.220}$$

or, in the center of mass frame,

$$\nabla \mathbf{v} = -\sum_{\alpha=1}^{N} \nu_\alpha \cdot \nabla \mathcal{N}_\alpha + \sum_{\alpha=1}^{N} \nu_\alpha \cdot r_\alpha. \tag{5.221}$$

In section 5.5 we show that such an equation can be stated for any choice of the convection velocity, *i.e.* $\nabla \mathbf{v}^\psi = -\sum_{\alpha=1}^{N} \nu_\alpha \cdot \nabla \mathcal{N}_\alpha^\psi + \sum_{\alpha=1}^{N} \nu_\alpha r_\alpha$. The left side of eq. (5.221) measures the local, isotropic volume expansion (since $\nabla \mathbf{v} = \operatorname{tr}(\boldsymbol{\kappa})$, see appendix D.6), whereas the right side comprises transport of bulk volume, and volume expansion due to chemical reactions of species with different molar volumes.

We use the Euler equation for the volume and the expansion $\varrho_{\mathrm{F}}{=}F\sum_{\alpha=1}^{\mathrm{N}} c_\alpha z_\alpha$ and reduce the number of independent species concnetrations,

$$c_1(c_3,\dots,c_{\mathrm{N}},\varrho_{\mathrm{F}}) = (1-\nu_2 c_2 - \sum_{\alpha=3}^{\mathrm{N}} \nu_\alpha c_\alpha)/\nu_1\,, \tag{5.222}$$

$$c_2(c_3,\dots,c_{\mathrm{N}},\varrho_{\mathrm{F}}) = \Big(z_1 - \nu_1\varrho_{\mathrm{F}}/F - \sum_{\alpha=3}^{\mathrm{N}} c_\alpha[\nu_\alpha z_1 - \nu_1 z_\alpha]\Big)/\left(\nu_2 z_1 - \nu_1 z_2\right)\,. \tag{5.223}$$

We use this reduced description and derive the independent formulation of the convection equation (using eqs. (5.103) and (5.108)).

$$\boldsymbol{\nabla}\mathbf{v} = -\frac{\tilde{\nu}_2}{F\tilde{z}_2}\cdot\boldsymbol{\nabla}\boldsymbol{\mathcal{J}}_{\mathrm{F}} - \sum_{\alpha=3}^{\mathrm{N}} \tilde{\tilde{\nu}}_\alpha\cdot\boldsymbol{\nabla}\boldsymbol{\mathcal{N}}_\alpha + \sum_{\alpha=1}^{\mathrm{N}} \nu_\alpha\cdot r_\alpha, \tag{5.224}$$

where

$$\tilde{\nu}_\alpha = \nu_\alpha - M_\alpha/M_1\cdot\nu_1, \quad \text{and} \quad \tilde{\tilde{\nu}}_\alpha = \tilde{\nu}_\alpha - \tilde{z}_\alpha/\tilde{z}_2\cdot\tilde{\nu}_2. \tag{5.225}$$

In section 5.5, we show that the quantities $\tilde{\nu}_\alpha$ transform the center-of-mass drift to the volume averaged drift velocity. For an electrolyte in electroneutral state ($\boldsymbol{\nabla}\boldsymbol{\mathcal{J}}_{\mathrm{F}}=0$), we find $\boldsymbol{\nabla}\mathbf{v} = -\sum_{\alpha=3}^{\mathrm{N}}\tilde{\tilde{\nu}}_\alpha\cdot\boldsymbol{\nabla}\boldsymbol{\mathcal{N}}_\alpha + \sum_{\alpha=1}^{\mathrm{N}}\nu_\alpha\cdot r_\alpha$.

In the absence of reactions, eq. (5.221) implies that the volume averaged drift velocity $\mathbf{v}^{\mathsf{Volume}} = \sum_{\alpha=1}^{\mathrm{N}} c_\alpha\nu_\alpha\mathbf{v}_\alpha$ (see section 5.5) is conserved,

$$\boldsymbol{\nabla}\sum_{\alpha=1}^{\mathrm{N}}\nu_\alpha c_\alpha\mathbf{v}_\alpha|_{r_\alpha=0} = 0. \tag{5.226}$$

Hence, the LRTTs for volumes (see eq. (C.10)) imply that $\dot{V}(\Omega(t)) = \mathrm{d}/\mathrm{d}t\int_{\Omega(t)}\mathrm{d}V = \int_{\Omega(t)}\mathrm{d}V\,\boldsymbol{\nabla}\mathbf{v} = \oint_{\mathcal{A}=\partial\Omega}\mathrm{d}A\,\mathbf{v}\cdot\hat{\boldsymbol{n}}_{\mathcal{A}}$. where $\hat{\boldsymbol{n}}_{\mathcal{A}}$ is the unit surface-normal pointing “outwards”. Thus, the isotropic volume-evolution is described by the surface of the moving boundary: if the surface is moving “outwards” ($\mathbf{v}\cdot\hat{\boldsymbol{n}}_{\mathcal{A}} > 0$), then the volume increases, and vice-versa. Locally this corresponds to $\boldsymbol{\nabla}\mathbf{v} > 0$ ($\boldsymbol{\nabla}\mathbf{v} < 0$), see appendix D.6. The case of a homogeneous liquid composed of only one species constitutes a special case. Here, the trivial flux constraint $\sum_{\alpha=1}^{\mathrm{N}}\boldsymbol{\mathcal{N}}_\alpha M_\alpha = 0$ (see eq. (5.103)) implies that $\boldsymbol{\mathcal{N}}_1 = 0$. Thus, the drift velocities of the center of mass and the species are equal, $\mathbf{v} = \mathbf{v}_1$, and, due to eq. (5.221), $\boldsymbol{\nabla}\mathbf{v} = 0$.

5.4.5 Isothermal Equations of Motion

In this section we close our system of equations, and state the complete system of equations.

In principle, the force law can be used to determine the convection velocity, and the equation for the pressure (eq. (5.206)) can be used to determine the bulk modulus. However, the force law takes the form of a Navier Stokes equation involving inertial effects, which can be challenging to solve.[290]

We do not consider gravitational body forces in our description for highly viscous media, and assume that the system quickly relaxes towards a stationary state. Hence, to a good approximation, we can neglect inertial terms, $\rho\dot{\mathbf{v}}{=}\boldsymbol{\nabla}\boldsymbol{\sigma}{\approx}0$, *viz.*

$$\sum_{\alpha=1}^{\mathrm{N}} c_\alpha \boldsymbol{\nabla}\mu_\alpha = \boldsymbol{\nabla}\mathcal{P}^{\mathrm{vol}} + \boldsymbol{\nabla}\mathcal{P}^{\mathrm{int}} = -\varrho_{\mathrm{F}}\boldsymbol{\nabla}\Phi + \boldsymbol{\nabla}\boldsymbol{\tau}, \tag{5.227}$$

defines mechanical equilibrium (see eq. (5.212)). Here, $\boldsymbol{\nabla}\mathcal{P}^{\mathrm{vol}} = \mathcal{K}\sum_{\beta=1}^{\mathrm{N}} \nu_\beta \boldsymbol{\nabla} c_\beta$ and $\boldsymbol{\nabla}\mathcal{P}^{\mathrm{int}} = \sum_{\alpha=1}^{\mathrm{N}} c_\alpha \boldsymbol{\nabla}\partial(\rho\varphi_{\mathrm{H}}^{\mathrm{int}})/\partial c_\alpha$. Because the stress tensor is continuous at electrochemical surfaces only when the equilibrated surface stress vanishes, this trivial equilibrium condition does not transfer to electrochemical surfaces (used for stress-measurements in polarizable liquids.[291]) As consequence, it is indeed the total stress $\boldsymbol{\sigma}$, which is susceptible to experiments and shall therefore be used in the force law (and not, *e.g.* the "elastic stress tensor", or the Maxwell stress tensor).[141]

Still, our description is not yet completely closed, due to the unsusceptible bulk-modulus in the chemical potentials (see eq. (5.214))

$$\mu_\alpha{=}RT\ln(f_\alpha c_\alpha){+}\mathcal{K}\nu_\alpha\Big(\sum_{\alpha=1}^{\mathrm{N}}\nu_\alpha c_\alpha{-}1\Big)/2\,, \tag{5.228}$$

and in the forces eq. (5.215)

$$\boldsymbol{\nabla}\mu_\alpha = RT\boldsymbol{\nabla}(\ln c_\alpha/c\,) + \boldsymbol{\nabla}\partial(\rho\varphi_{\mathrm{H}}^{\mathrm{int}})/\partial c_\alpha + \mathcal{K}\nu_\alpha\sum_{\beta=1}^{\mathrm{N}}\nu_\beta\boldsymbol{\nabla} c_\beta. \tag{5.229}$$

Therefore, instead of solving the dynamical force law, we solve the trivial force force law for the unsusceptible quantity appearing in eqs. (5.228) and (5.229),

$$\boldsymbol{\nabla}\mathcal{P}^{\mathrm{vol}} = \mathcal{K}\sum_{\beta=1}^{\mathrm{N}}\nu_\beta\boldsymbol{\nabla} c_\beta = \varrho_{\mathrm{F}}\mathbf{E} + \boldsymbol{\nabla}\boldsymbol{\tau} - \boldsymbol{\nabla}\mathcal{P}^{\mathrm{int}}. \tag{5.230}$$

Hence, when viscous forces and interaction contributions $\varphi_{\mathrm{H}}^{\mathrm{int}}$ are neglected, mechanical equilibrium implies the balance between steric-/ and electrostatic forces,[271]

$$\boldsymbol{\nabla}\boldsymbol{\sigma} = 0 \quad \Rightarrow \quad \boldsymbol{\nabla}\mathcal{P}^{\mathrm{vol}} = -\varrho_{\mathrm{F}}\boldsymbol{\nabla}\Phi. \tag{5.231}$$

Thus, strong pressure gradients are to be expected in charged regions of the electrolyte, *e.g.* in the electrochemical double layers where the Lorentz force density $\varrho_{\mathrm{F}}\boldsymbol{\nabla}\Phi$ is balanced by strong pressure gradients $\boldsymbol{\nabla}\mathcal{P}^{\mathrm{vol}}$ (see eq. (10.46) and section 9.2 and chapter 14). Note that in the incompressible limit, eq. (5.158) is not a valid definition for the steric pressure $\mathcal{P}^{\mathrm{vol}}$, and p is also not well-defined. However, this is fixed in mechanical equilibrium via the local force-balance expressed by pressure-force $\boldsymbol{\nabla}\mathcal{P}^{\mathrm{vol}}$. We substitute eq. (5.230) into eq. (5.229), such that

$$\boldsymbol{\nabla}\mu_\alpha = \sum_{\beta=1}^{\mathrm{N}} \left(\delta_\alpha^\beta - \nu_\alpha c_\beta\right) \cdot \boldsymbol{\nabla}\frac{\partial(\rho\varphi_{\mathrm{H}}^{\mathrm{int}})}{\partial c_\beta} + RT\boldsymbol{\nabla}\ln\left(\frac{c_\alpha}{c}\right) + \nu_\alpha\left(\varrho_{\mathrm{F}}\mathbf{E} + \boldsymbol{\nabla}\boldsymbol{\tau}\right), \quad (5.232)$$

where $\boldsymbol{\nabla}\boldsymbol{\tau} = \boldsymbol{\nabla}([\gamma+\eta]\boldsymbol{\nabla}\mathbf{v}) + \boldsymbol{\nabla}^2(\eta\mathbf{v})$ (see eq. (5.146)). However, the forces appearing in the fluxes are the electrochemical forces $\boldsymbol{\nabla}\mu_\alpha^{\mathrm{el}} = \boldsymbol{\nabla}\mu_\alpha + Fz_\alpha\boldsymbol{\nabla}\Phi$, which satisfy the Gibbs-Duhem relation

$$\sum_{\alpha=1}^{\mathrm{N}} c_\alpha \cdot \boldsymbol{\nabla}\mu_\alpha^{\mathrm{el}} = \boldsymbol{\nabla}\boldsymbol{\tau}. \quad (5.233)$$

The electrolyte is in chemical equilibrium if $\boldsymbol{\nabla}\mu_\alpha = 0$ for all species α, and is in mechanical equilibrium if $\boldsymbol{\nabla}\boldsymbol{\sigma} = 0$. However, equilibrium of the system corresponds to a stationary state where all fluxes vanish. Hence, due to our Onsager Ansatz (see eq. (5.115)) and eq. (5.221), equilibrium equals vanishing electrochemical forces, *i.e.*

$$0 = \boldsymbol{\nabla}\mu_\alpha^{\mathrm{el}} = \sum_{\beta=1}^{\mathrm{N}} \left[\delta_\alpha^\beta - \nu_\alpha c_\beta\right] \boldsymbol{\nabla}[Fz_\beta\Phi + \partial(\rho\varphi_{\mathrm{H}}^{\mathrm{int}})/\partial c_\beta] + RT\boldsymbol{\nabla}\ln c_\alpha/c\,, \quad (5.234)$$

where we used $\varrho_{\mathrm{F}}{=}\sum_{\alpha=1}^{\mathrm{N}} Fz_\alpha c_\alpha$. In equilibrium, the Gibbs-Duhem relation becomes trivial, and only N-1 equations $\boldsymbol{\nabla}\mu_\alpha^{\mathrm{el}}{=}0$ are necessary to describe equilibrium. For non-interacting electrolytes ($\varphi_{\mathrm{H}}^{\mathrm{int}}{=}0$), the equilibrium-condition becomes

$$\boldsymbol{\nabla}\ln\left[c_\alpha/c\right] = (\nu_\alpha\varrho_{\mathrm{F}} - Fz_\alpha)/RT \cdot \boldsymbol{\nabla}\Phi. \quad (5.235)$$

Usually, the first two mixing terms in eq. (5.232) are comprised in the so-called thermodynamic factor. We relate to this description, and use the activity coefficients f_α and the relation $\partial\ln(\mathsf{f}_\beta c_0)/\partial(c_\gamma/c_0){=}\partial\ln(\mathsf{f}_\beta c_0)/\partial\ln(c_\gamma/c_0)\cdot 1/c_\gamma$ to define

$$\mathsf{TDF}_{\alpha\gamma} = \sum_{\beta=1}^{\mathrm{N}} \left(\delta_\alpha^\beta - \nu_\alpha c_\beta\right) \cdot \left(\delta_\beta^\gamma + \frac{\partial\ln(\mathsf{f}_\beta c_0)}{\partial\ln(c_\gamma/c_0)}\right). \quad (5.236)$$

Here, c_0 is some constant concentration which non-dimensionalizes the logarithmic terms (usually set to $c_0 = 1\,\mathrm{mol\,L^{-1}}$). Thus, the chemical forces become

$$\boldsymbol{\nabla}\mu_\alpha = RT\sum_{\gamma=1}^{\mathrm{N}} \mathit{TDF}_{\alpha\gamma}(\boldsymbol{\nabla}c_\gamma)/c_\gamma + \nu_\alpha\varrho_\mathrm{F}\mathbf{E} + \nu_\alpha[\boldsymbol{\nabla}([\gamma+\eta]\boldsymbol{\nabla}\mathbf{v}) + \boldsymbol{\nabla}^2(\eta\mathbf{v})]. \tag{5.237}$$

Our definition for the thermodynamic factor differs from the canonical expression in the literature,[292] $\mathit{TDF}^{\mathrm{lit}}_{\alpha\gamma} = \delta_{\alpha\gamma} + \partial\ln(f_\alpha c_0)/\partial\ln(c_\gamma/c_0\,)\,)$, and extends the non-ideal contributions by steric penalties due to excluded volume effects. Thus, even for "ideal" electrolytes ($f_\alpha c = 1$), our expression for the thermodynamic factor

$$\mathit{TDF}_{\alpha\beta}\big|_{\mathrm{ideal}} = \delta^\beta_\alpha - \nu_\alpha c_\beta, \tag{5.238}$$

leads to inter-species couplings in the mixing terms, when the species have different molar volume,

$$\boldsymbol{\nabla}\mu^{\mathrm{mixing}}_\alpha\Big|_{\mathrm{ideal}} = RT\left((\boldsymbol{\nabla}c_\alpha)/c_\alpha + \sum_{\beta\neq\alpha}^{\mathrm{N}}[\nu_\beta - \nu_\alpha]\,\boldsymbol{\nabla}c_\beta\right). \tag{5.239}$$

To obtain a better understanding of the volumetric contributions comprised in the thermodynamic factor, we consider two limiting cases. First, weassume that one first species is much larger than all others, *i.e.* $\nu_1 \ll \nu_\alpha$. Then, if the species composition of the mixture is not pathological, this implies that $1 \approx c_1\nu_1$ (see eq. (5.178)). Thus, the components of TDF with respect to the large species consist entirely of cross-couplings with the smaller species,

$$\mathit{TDF}_{11} = -\,\nu_1\sum_{\gamma\neq1}^{\mathrm{N}} c_\gamma\cdot\frac{\partial\ln f_\gamma}{\partial\ln c_1}, \text{ and } \mathit{TDF}_{1\beta}\big|_{\beta\neq1} = -\,\nu_1 c_\beta - \sum_{\gamma\neq1}^{\mathrm{N}} c_\gamma\cdot\frac{\partial\ln f_\gamma}{\partial\ln c_\beta}. \tag{5.240}$$

Thus, the chemical forces related to the designated species are due only to correlations with species of minor volume, and there is no self-correlation

$$\boldsymbol{\nabla}\mu_1 = -\nu_1 RT\sum_{\beta\neq1}^{\mathrm{N}}\boldsymbol{\nabla}c_\beta - \nu_1 RT\sum_{\beta,\gamma\neq1}^{\mathrm{N}}\frac{c_\gamma}{c_\beta}\cdot\frac{\partial\ln f_\gamma}{\partial\ln c_\beta}\cdot\boldsymbol{\nabla}c_\beta. \tag{5.241}$$

This pertains even to the ideal case ($\ln f_\gamma = 0$). In contrast, the components of the thermodynamic factor related to the species of minor volume become canonical,

$$\mathit{TDF}_{\alpha\beta}\big|_{\alpha,\beta\neq1} = \mathit{TDF}^{lit}_{\alpha\beta} = \delta_{\alpha\gamma} + \partial\ln(f_\alpha c_0)/\partial\ln(c_\gamma/c_0\,)\,), \tag{5.242}$$

and the forces acting on the smaller species decouple in the ideal case.

Second, we assume the ideal case eq. (5.239) for a mixture composed of equally sized species, $\nu_\alpha \equiv \nu$ for all species $\alpha = 1,\ldots,\mathrm{N}$. Then, $1 = c\nu$, such that $\boldsymbol{\nabla}(c\nu) =$

0. This implies that all species decouple from each other, and exhibit ideal behaviour, $\boldsymbol{\nabla}\mu_\alpha^{\text{mixing}} = RT \cdot \boldsymbol{\nabla} c_\alpha / c_\alpha$.

We close the set of equations by coupling Φ with ϱ_F via Poisson's equation,

$$\varrho_\text{F} = -\varepsilon_\text{R}\varepsilon_0 \Delta\Phi, \tag{5.243}$$

$$\frac{\partial \varrho_\text{F}}{\partial t} = -\boldsymbol{\nabla}\boldsymbol{\mathcal{J}}_\text{F} - \boldsymbol{\nabla}\left(\varrho_\text{F}\mathbf{v}\right) + \sum_{\alpha=1}^{\text{N}} F z_\alpha r_\alpha, \tag{5.244}$$

$$\frac{\partial c_\alpha}{\partial t} = -\boldsymbol{\nabla}\boldsymbol{\mathcal{N}}_\alpha - \boldsymbol{\nabla}\left(c_\alpha \mathbf{v}\right) + r_\alpha, \qquad \alpha \geq 3, \tag{5.245}$$

$$\boldsymbol{\nabla}\mathbf{v} = -\frac{\tilde{\nu}_2}{F\tilde{z}_2} \cdot \boldsymbol{\nabla}\boldsymbol{\mathcal{J}}_\text{F} - \sum_{\alpha=3}^{\text{N}} \tilde{\tilde{\nu}}_\alpha \cdot \boldsymbol{\nabla}\boldsymbol{\mathcal{N}}_\alpha + \sum_{\alpha=1}^{\text{N}} \nu_\alpha r_\alpha. \tag{5.246}$$

Apparently, eq. (5.245) comprises N-2 equations for the set of N-2 independent concentrations $c_3, \ldots, c_\text{N}$. Alternatively, eqs. (5.243) to (5.248) can be expressed using a matrix-formulation (see appendix D.7). We restate the fluxes (where $\varphi = \Phi + \tilde{\mu}_2 / F\tilde{z}_2$, see eq. (5.134)),

$$\boldsymbol{\mathcal{N}}_\alpha = \frac{t_\alpha}{F\tilde{z}_\alpha}\boldsymbol{\mathcal{J}}_\text{F} - \mathcal{D}_{\alpha T}\boldsymbol{\nabla} T - \sum_{\beta=3}^{\text{N}} \mathcal{D}_{\alpha\beta}\boldsymbol{\nabla}\tilde{\tilde{\mu}}_\beta, \tag{5.247}$$

$$\boldsymbol{\mathcal{J}}_\text{F} = -\kappa\boldsymbol{\nabla}\varphi - \beta\kappa\boldsymbol{\nabla} T - \frac{\kappa}{F}\sum_{\beta=3}^{\text{N}} \frac{t_\beta}{\tilde{z}_\beta}\boldsymbol{\nabla}\tilde{\tilde{\mu}}_\beta. \tag{5.248}$$

We supplement the set of isothermal equations (eqs. (5.243) to (5.246)) by an equation for temperature ("heat equation") in appendix D.10.

5.4.6 "Standard Electrolyte": Ternary System with Neutral Solvent

Electrolytes consisting of a neutral solvent species and two ionic species, are among the most commonly used electrolyte systems in commercial applications and constitute the standard-electrolyte for lithium ion batteries.[6,293] In this section, we discuss this standard electrolyte in isothermal, electroneutral state.

Electroneutrality implies that $\alpha = 3 = \mathsf{Li}$ is the only independent species. We denote the common concentration of the two ion-species c_Li such that

$$z_2 = -z_3, \quad \text{and} \quad c_\mathsf{Li} = c_2 = c_3. \tag{5.249}$$

Using eqs. (5.222) and (5.223), we find

$$c_1(c_\mathsf{Li}) = \left[1 - c_\mathsf{Li}\left(\nu_2 + \nu_\mathsf{Li}\right)\right] / \nu_1\,. \tag{5.250}$$

such that

$$c_{\mathsf{Li}}\tilde{\tilde{\nu}}_{\mathsf{Li}} = 1 - \nu_1 \rho / M_1 = 1 - \nu_1 c_1 \rho / \rho_1. \tag{5.251}$$

Three independent transport parameters exist in a ternary electrolyte, κ, t_{Li} and $\mathcal{D}_{\mathsf{Li}}$. The independent variables $\Phi, \mathbf{v}, c_{\mathsf{Li}}$ are determined by (see section 5.4.5)

$$0 = -\boldsymbol{\nabla} \boldsymbol{\mathcal{J}}_{\mathrm{F}} + \sum_{\alpha=1}^{3} F z_\alpha r_\alpha, \tag{5.252}$$

$$\boldsymbol{\nabla} \mathbf{v} = -\tilde{\nu}_2 / F\tilde{z}_2 \cdot \boldsymbol{\nabla} \boldsymbol{\mathcal{J}}_{\mathrm{F}} - \tilde{\tilde{\nu}}_{\mathsf{Li}} \boldsymbol{\nabla} \boldsymbol{\mathcal{N}}_{\mathsf{Li}} + \sum_{\alpha=1}^{3} \nu_\alpha r_\alpha, \tag{5.253}$$

$$\partial_t c_{\mathsf{Li}} = -\boldsymbol{\nabla} \boldsymbol{\mathcal{N}}_{\mathsf{Li}} - \boldsymbol{\nabla} \left(c_{\mathsf{Li}} \mathbf{v} \right) + r_{\mathsf{Li}}. \tag{5.254}$$

We set z_1=0 for the neutral solvent,[64]) *i.e.* $\tilde{z}_\alpha = z_\alpha$ and assume that only Li reacts,

$$r_1 = 0, \quad \text{and} \quad r_2 = 0. \tag{5.255}$$

As consequence, eq. (5.252) becomes $\boldsymbol{\nabla} \boldsymbol{\mathcal{J}}_{\mathrm{F}} = F z_{\mathsf{Li}} r_{\mathsf{Li}}$. We substitute this expression for $\boldsymbol{\nabla} \boldsymbol{\mathcal{J}}_{\mathrm{F}}$ into eq. (5.253) and use the relation eq. (5.251),

$$\boldsymbol{\nabla} \mathbf{v} = \left(\nu_{\mathsf{Li}} + \nu_2 - \nu_1 \cdot M_2 / M_1 \right) \cdot r_{\mathsf{Li}} - \tilde{\tilde{\nu}}_{\mathsf{Li}} \cdot \boldsymbol{\nabla} \boldsymbol{\mathcal{N}}_{\mathsf{Li}} \tag{5.256}$$

$$= \left(\tilde{\tilde{\nu}}_{\mathsf{Li}} + \nu_1 \cdot M_{\mathsf{Li}} / M_1 \right) \cdot r_{\mathsf{Li}} - \tilde{\tilde{\nu}}_{\mathsf{Li}} \cdot \boldsymbol{\nabla} \boldsymbol{\mathcal{N}}_{\mathsf{Li}}. \tag{5.257}$$

With this result we reexpress eq. (5.254), and solve eq. (5.256) for

$$\boldsymbol{\nabla} \boldsymbol{\mathcal{N}}_{\mathsf{Li}} = -1 / \tilde{\tilde{\nu}}_{\mathsf{Li}} \cdot \boldsymbol{\nabla} \mathbf{v} + \left[M_1 (\nu_{\mathsf{Li}} + \nu_2) - \nu_1 M_2 \right] / \tilde{\tilde{\nu}}_{\mathsf{Li}} M_1 \cdot r_{\mathsf{Li}}, \tag{5.258}$$

and substitute for $\boldsymbol{\nabla} \boldsymbol{\mathcal{N}}_{\mathsf{Li}}$ in eq. (5.254), *viz.*

$$\partial_t c_{\mathsf{Li}} = \frac{1}{\tilde{\tilde{\nu}}_{\mathsf{Li}}} \left(\boldsymbol{\nabla} \left[\left(1 - c_{\mathsf{Li}} \tilde{\tilde{\nu}}_{\mathsf{Li}} \right) \mathbf{v} \right] - \frac{M_{\mathsf{Li}}}{M_1} \nu_1 r_{\mathsf{Li}} \right) = \frac{\nu_1}{M_1 \tilde{\tilde{\nu}}_{\mathsf{Li}}} \left(\boldsymbol{\nabla} \left[\rho \mathbf{v} \right] - M_{\mathsf{Li}} r_{\mathsf{Li}} \right). \tag{5.259}$$

Because the right side of eq. (5.258) equals total mass-balance ($\partial_t \rho = -\boldsymbol{\nabla}(\rho \mathbf{v})$, see eq. (5.5)), the evolution of all concentrations is determined by the variation of the center-of-mass motion

$$\partial_t c_{\mathsf{Li}} = -\nu_1 / M_1 \tilde{\tilde{\nu}}_{\mathsf{Li}} \cdot \partial_t \rho. \tag{5.260}$$

Thus, the evolution of the ion-species equals (up to a constant prefactor) the evolution of the total mass-density of the electrolyte. This is a direct consequence of the assumption of electroneutrality, which prevents the formation of charge-profiles. Hence, migration and diffusion of the two species are mutually coupled, and the cations cannot move freely from the anions (and vice versa). This result can also be motivated from the fact that $c_2 = c_3 \equiv c_{\mathsf{Li}}$ and $c_1 = 1/\nu_1 - (\nu_2 + \nu_{\mathsf{Li}})c_{\mathsf{Li}}/\nu_1$. Hence,

$$\partial_t \rho = \sum_{\alpha=1}^{\mathrm{N}} M_\alpha \partial_t c_\alpha = \left[M_2 + M_{\mathsf{Li}} - \frac{M_1(\nu_2 + \nu_{\mathsf{Li}})}{\nu_1} \right] \partial_t c_{\mathsf{Li}} = -\frac{\tilde{\tilde{\nu}}_{\mathsf{Li}} M_1}{\nu_1} \cdot \partial_t c_{\mathsf{Li}}. \tag{5.261}$$

This argument relies heavily on the condition of electroneutrality, and that there are only two ionic species. In particular, this result does not hold in the case of more than two ionic species, and / or a non-neutral solvent species.

Next, we determine the fluxes $\boldsymbol{\mathcal{J}}_{\mathrm{F}}$ and $\boldsymbol{\mathcal{N}}_{\mathsf{Li}}$, see eqs. (5.247) and (5.248). However, we first use the non-trivial Gibbs-Duhem equation (see eq. (5.101)), $\sum_{\alpha=1}^{3} c_\alpha (F z_\alpha \boldsymbol{\nabla} \Phi + \boldsymbol{\nabla} \mu_\alpha) = \varrho_{\mathrm{F}} \boldsymbol{\nabla} \Phi_\alpha + \sum_{\alpha=1}^{3} c_\alpha \boldsymbol{\nabla} \mu_\alpha = \sum_{\alpha=1}^{3} c_\alpha \boldsymbol{\nabla} \mu_\alpha = \boldsymbol{\nabla} \boldsymbol{\tau}$, where $\boldsymbol{\nabla}\boldsymbol{\tau} = \boldsymbol{\nabla}[(\gamma + \eta) \boldsymbol{\nabla} \mathbf{v}] + \boldsymbol{\nabla}^2 (\eta \mathbf{v})$ are the viscous stress-forces (see eq. (5.146) in section 5.3.2). This allows to eliminate the chemical force of the designated species,

$$\boldsymbol{\nabla} \mu_1 = (\boldsymbol{\nabla}\boldsymbol{\tau} - c_{\mathsf{Li}} \boldsymbol{\nabla} \mu_{\mathsf{ternary}}) / c_1 \,, \text{ such that } \boldsymbol{\nabla} \tilde{\tilde{\mu}}_{\mathsf{Li}} = \rho/\rho_1 \cdot \boldsymbol{\nabla} \mu_{\mathsf{ternary}} - (M_2 + M_{\mathsf{Li}})/\rho_1 \cdot \boldsymbol{\nabla}\boldsymbol{\tau}, \tag{5.262}$$

where the independent binary chemical potential is defined by

$$\boldsymbol{\nabla} \mu_{\mathsf{ternary}} = \boldsymbol{\nabla} \mu_2 + \boldsymbol{\nabla} \mu_{\mathsf{Li}}. \tag{5.263}$$

Furthermore, we introduce the canonical reference-electrochemical potential φ^{N} defined relative to the second species (usually Li$^+$, see, *e.g.* Eq.(A9), Ref. 294),

$$\boldsymbol{\nabla} \varphi^{\mathsf{N}} = \boldsymbol{\nabla} \Phi + \boldsymbol{\nabla} \mu_2 / F z_2 \,. \tag{5.264}$$

This expression differs from the corresponding quantity $\boldsymbol{\nabla} \varphi = \boldsymbol{\nabla} \Phi + \boldsymbol{\nabla} \tilde{\mu}_2 / F \tilde{z}_2$, appearing in our formalism (see eq. (5.134)). However, both are related via

$$\boldsymbol{\nabla} \varphi = \boldsymbol{\nabla} \varphi^{\mathsf{N}} + \rho_2 / F z_2 \rho_1 \cdot \boldsymbol{\nabla} \mu_{\mathsf{ternary}} - M_2 / \rho_1 F z_2 \cdot \boldsymbol{\nabla}\boldsymbol{\tau} \tag{5.265}$$

Thus, we find for the fluxes (see eqs. (5.247) and (5.248)),

$$\boldsymbol{\mathcal{J}}_{\mathrm{F}} = -\kappa \varphi^{\mathsf{N}} + \frac{\kappa}{F z_2} \frac{\rho t_{\mathsf{Li}} - \rho_2}{\rho_1} \boldsymbol{\nabla} \mu_{\mathsf{ternary}} + \frac{\kappa}{F z_2} \frac{M_2 - t_{\mathsf{Li}}(M_2 + M_{\mathsf{Li}})}{\rho_1} \boldsymbol{\nabla}\boldsymbol{\tau}, \tag{5.266}$$

$$\boldsymbol{\nabla} \boldsymbol{\mathcal{N}}_{\mathsf{Li}} = -\left[t_{\mathsf{Li}} r_{\mathsf{Li}} + \boldsymbol{\nabla} \mathcal{D}_{\mathsf{Li}} \left(\rho/\rho_1 \cdot \boldsymbol{\nabla} \mu_{\mathsf{ternary}} - (M_2 + M_{\mathsf{Li}})/\rho_1 \cdot \boldsymbol{\nabla}\boldsymbol{\tau} \right) \right]. \tag{5.267}$$

Altogether, we find for the complete set of transport equations for this ternary electrolyte in electroneutral state,

$$0 = -\boldsymbol{\nabla} \boldsymbol{\mathcal{J}}_{\mathrm{F}} + F z_{\mathsf{Li}} r_{\mathsf{Li}}, \tag{5.268}$$

$$\boldsymbol{\nabla} \mathbf{v} = (\nu_{\mathsf{Li}} + \nu_2 - \nu_1 \cdot M_2/M_1 \,) \, r_{\mathsf{Li}} - \tilde{\tilde{\nu}}_{\mathsf{Li}} \cdot \boldsymbol{\nabla} \boldsymbol{\mathcal{N}}_{\mathsf{Li}}, \tag{5.269}$$

$$\partial_t c_{\mathsf{Li}} = \nu_1 / M_1 \tilde{\tilde{\nu}}_{\mathsf{Li}} \cdot \boldsymbol{\nabla} \left(\rho \mathbf{v} \right), \tag{5.270}$$

where the flux $\mathcal{J}_\mathrm{F}$ and the quantity $\boldsymbol{\nabla}\mathcal{N}_\mathsf{Li}$ are given by eqs. (5.266) and (5.267). Equation (5.269) allows to examine how relevant convective effects are in the presence of a dominant neutral solvent species. For this purpose, we use

$$\tilde{\tilde{\nu}}_\mathsf{Li} = (1 - c_1\nu_1)/c_\mathsf{Li} - \nu_1(\rho - \rho_1)/c_\mathsf{Li}M_1\,. \tag{5.271}$$

Therefore, in the limit where the solvent dominates electrolyte mass and volume,

$$\rho_1 \approx \rho, \quad \text{and} \quad c_1\nu_1 \approx 1, \quad \text{we find} \quad \tilde{\tilde{\nu}}_\mathsf{Li} \approx 0. \tag{5.272}$$

Hence, eq. (5.269) reduces to $\boldsymbol{\nabla}\mathbf{v} \approx \nu_1 M_\mathsf{Li}/M_1 \cdot r_\mathsf{Li}$. Thus, the limit eq. (5.272) implies that the convection velocity is completely determined by the boundary conditions. However, in the limit eq. (5.272) the identity eq. (5.258) becomes ill-defined, and the transport equation for mass must be expressed in the canonical form (eq. (5.254)).

Many theoretical descriptions of this standard electrolyte do not consider convection.[64,142] In this case, our description reduces to

$$0 = -\boldsymbol{\nabla}\mathcal{J}_\mathrm{F}|_{\mathsf{v}=0} + Fz_\mathsf{Li}r_\mathsf{Li}, \tag{5.273}$$

$$\partial_t c_\mathsf{Li}|_{\mathsf{v}=0} = -\boldsymbol{\nabla}\mathcal{N}_\mathsf{Li} + r_\mathsf{Li}, \tag{5.274}$$

Above, we derived that, in the limit eq. (5.272), the convection profiles becomes constant. The corresponding set of transport equations for this case, eqs. (5.273) and (5.274), must be supplemented by the corresponding set of flux-expressions,

$$\mathcal{J}_\mathrm{F}|_{\substack{c_1\nu_1\approx 1\\ \rho/\rho_1\approx 1}} = \kappa t_\mathsf{Li}/Fz_2\,\boldsymbol{\nabla}\mu_\mathsf{ternary} + \kappa[M_2 - t_\mathsf{Li}(M_2 + M_\mathsf{Li})]/Fz_2\rho_1\,\boldsymbol{\nabla}\boldsymbol{\tau} - \kappa\varphi^\mathsf{N}, \tag{5.275}$$

$$\boldsymbol{\nabla}\mathcal{N}_\mathsf{Li}|_{\substack{c_1\nu_1\approx 1\\ \rho/\rho_1\approx 1}} = -\left[t_\mathsf{Li}r_\mathsf{Li} + \boldsymbol{\nabla}\left(\mathcal{D}_\mathsf{Li}\boldsymbol{\nabla}\mu_\mathsf{ternary}\right) - \boldsymbol{\nabla}((M_2 + M_\mathsf{Li})/\rho_1) \cdot \boldsymbol{\nabla}\boldsymbol{\tau}\right] \tag{5.276}$$

In section 15.2 we compare our description with the literature .

5.4.7 Characterization of Highly Concentrated Electrolytes

Our hypothesis is that an electrolyte is “highly concentrated” if effects due to interspecies correlations become dominant, and if convection becomes comparable to diffusion and migration. In this section, we show that the initial electrolyte configuration specified by ν_α, ρ_α and M_α suffices to probe both propperties and to classify a given electrolytes as being “highly concentrated”.

The “ideal” chemical potential of dilute solutions,[100] $\mu_\alpha = RT\ln c_\alpha$, does not couple to other species,[181] and must be supplemented by inter-species couplings when increasing concentrations are assumed. Usually, the corresponding “excess” contributions are comprised in the activity coefficient f_α, or in the thermodynamic factor,[292] $\mathit{TDF}^{lit}_{\alpha\beta} = \delta_{\alpha\beta} + \partial \ln f_\alpha / \partial \ln c_\beta$, which leads to inter-species couplings in the chemical forces (the "ideal case" quantity reads $\mathit{TDF}^{lit}_{\alpha\beta} = \delta_{\alpha\beta}$).

The thermodynamic factor derived in section 5.4.5 extends the canonical expression by inter-species-correlations due to excluded volume effects, (see eq. (5.236)),

$$\mathit{TDF}_{\alpha\gamma} = \sum_{\beta=1}^{\mathrm{N}} (\delta_{\alpha\beta} - \nu_\alpha c_\beta) \cdot (\delta_{\beta\gamma} + \partial \ln f_\beta / \partial \ln c_\gamma) \,. \tag{5.277}$$

Even in the "ideal" case (f_α=0), $\mathit{TDF}_{\alpha\beta}|_{\text{ideal}}{=}\delta^\beta_\alpha{-}\nu_\alpha c_\beta$, *i.e.* inter-species correlations appear, and the ideal forces depend on species asymmetry (see eq. (5.239)),

$$\boldsymbol{\nabla} \mu^{\text{mixing}}_\alpha \Big|_{\text{ideal}} = RT(\boldsymbol{\nabla} c_\alpha / c_\alpha + \sum_{\beta\neq\alpha}^{\mathrm{N}} [\nu_\beta - \nu_\alpha] \boldsymbol{\nabla} c_\beta). \tag{5.278}$$

This suggests that the relative magnitudes of the specific molar-volumes ν_α serve as measure for "non-ideality", hence for the classification of "concentrated electrolytes".

Next, we examine the relevance of convection transport in multi-component electrolytes. The condition $\boldsymbol{\nabla}\mathbf{v}$=0 is often used for complex electrolyte-mixtures.[65,141,295] We argue that this can be a bad approximation. In section 5.4.6 we derive a limiting-criterion for the relevance of convective effects in the ternary standard electrolyte (see eq. (5.272)), where

$$\boldsymbol{\nabla}\mathbf{v} = [(1 - c_1\nu_1)/c_{\mathsf{Li}} - (\rho - \rho_1)/c_{\mathsf{Li}} M_1/\nu_1\,] \cdot \boldsymbol{\nabla}\boldsymbol{\mathcal{N}}_{\mathsf{Li}} \tag{5.279}$$

Here, c_1 denotes the concentration of the neutral solvent species, and $c_{\mathsf{Li}} = c_3$ is the only independent species. The right side vanishes if the solvent species dominates mass and volume of the electrolyte, $\rho \approx \rho$ and $c_1\nu_1 \approx 1$.

We supplement this argument by estimating the significance of convective transport versus non-convective transport and compare the variation of the convective flux density with the variation of the non-convective flux density. We neglect reactions, $\boldsymbol{\nabla}\mathbf{v} = \tilde{\tilde{\nu}}_{\mathsf{Li}} \cdot \boldsymbol{\nabla}\boldsymbol{\mathcal{N}}_{\mathsf{Li}}$ (see eq. (5.253)), and multiply with c_{Li},

$$|c_3 \boldsymbol{\nabla}\mathbf{v} / \boldsymbol{\nabla}\boldsymbol{\mathcal{N}}_3\,| = |c_{\mathsf{Li}} \cdot \tilde{\tilde{\nu}}_{\mathsf{Li}}| = |1 - c_1\nu_1\rho/\rho_1\,|\,. \tag{5.280}$$

Thus, the ratio of the two variations on the left side is determined by the relative mass density of the neutral solvent species (ρ/ρ_1), and the volume fraction of this species ($c_1\nu_1$). Convection is constant for dominant solvent species, if $\rho_1{\approx}\rho$ and $c_1\nu_1{\approx}1$. In contrast, the right side is large if the solvent mass is negligible ($\rho_1{\ll}\rho$), which implies that the center-of-mass flux dominates over the relative variation of the salt-flux. Thus, the quantities ρ_1/ρ and $c_1\nu_1$ suffice for the electrolyte classification.

In the case of an electroneutral ternary electrolyte composed of two salts with one common species, we find for the crucial factor

$$c_3\tilde{\tilde{\nu}}_3 = c_3 \cdot [\nu_3 - (\tilde{M}_3 - z_3\chi) \cdot \nu] = c_3\nu \cdot [\gamma_3 - (\tilde{M}_3 - \chi z_3)] \tag{5.281}$$

appearing in the evaluation of $|c_3\boldsymbol{\nabla}\mathbf{v}/\boldsymbol{\nabla}\mathcal{N}_3| = |c_3\tilde{\tilde{\nu}}_3|$, where we introduced $\nu = \nu_1 + \nu$2- $\gamma_\alpha = \nu_\alpha/\nu$, $\tilde{M}_\alpha = M_\alpha/(M_1 + M_2)$ and $\chi = \tilde{M}_1\gamma_2 - \tilde{M}_2\gamma_1$. The convection in this system is constant if $c_3\nu_3 \ll 1$ and $2c_3 \ll (c_1 + c_2)$ (*i.e.* $c_3\nu \ll 1$).

In addition to bulk-convection due to volume fluxes, we discuss the convection induced by Faradaic reactions involving species of unequal molar volumes occurring at the electrode-electrolyte interfaces, where the non-convective species fluxes $\mathcal{N}_\alpha + c_\alpha\mathbf{v} = c_\alpha\mathbf{v}_\alpha$ are subject to flux boundary-conditions (FBCs). By modelling reaction source-terms via interfacial currents, the FBCs follow from the fixed-frame description at the interface Γ via the condition $0 = \partial_t c_\alpha = -\boldsymbol{\nabla}(c_\alpha\mathbf{v} + \mathcal{N}_\alpha) + r_\alpha^\Gamma\nu_\alpha^\Gamma$. Here ν_α^Γ denote the stoichiometries of the particular interface reaction. Upon integration, we find for the interfacial flux boundary conditions

$$c_\alpha\mathbf{v}_\alpha|_\Gamma = \mathcal{R}_\alpha^\Gamma\nu_\alpha^\Gamma, \tag{5.282}$$

where $\mathcal{R}_\alpha^\Gamma = \int \mathrm{d}\mathbf{x} r_\alpha^\Gamma/\nu_\alpha^\Gamma$. The FBCs eq. (5.282) relate the interfacial current with the center-of-mass convection. To see this, we multiply both sides with the specific molar masses and sum over all species, $\mathcal{R}_\alpha^\Gamma = \rho\mathbf{v}/\sum_{\alpha=1}^{\mathrm{N}} M_\alpha\nu_\alpha^\Gamma$, and substitute this for the reaction rate in eq. (5.282). Thus, for each species which participates in interface-reactions, we can state the ratio of mass-/ and convective fluxes,

$$|\mathcal{N}_\alpha/c_\alpha\mathbf{v}| = |1 - \rho/\rho_\alpha \cdot M_\alpha\nu_\alpha^\Gamma / \sum_{\beta=1}^{\mathrm{N}} M_\beta\nu_\beta^\Gamma|. \tag{5.283}$$

Equation (5.283) constitutes the relevance of convective fluxes due to interface-reactions. Like for bulk-convection, the crucial parameter is the mass-ratio ρ_α/ρ.

Altogether, we conclude that the mass densities, the volume fractions, and the relative magnitudes of the molar volumes can be used to probe the relevance of inter-species correlations and of convection. Therefore, we suggest that these material parameters can be used for the classification of electrolytes into “highly concentrated”. In section 6.3, we validate this classification-scheme for a specific electrolyte.

5.5 Frame Independent Formulation

5.5.1 Introduction

In this section we discuss the fundamental role which the the convection velocity plays for our transport theory.

Because the fluxes appearing in our transport theory are functions of the species velocities, they satisfy a universal flux constraint when they are defined relative to some convection velocity. It is beneficial to use these fluxes in the formulation of the transport theory, since the resulting constraint reduces the number of independent fluxes. However, the specific choice for the convection velocity constitutes an "internal" reference for the fluxes, and for the definition of the transport parameters in our Onsaager approach. This property becomes most apparent in solutions where no neutral solvent is present, and has been a well-established fact in the early literature for molten salts.[45–47,191,192,296–298] Besides this technical aspect, convection plays an important role as transport process in highly concentrated electrolytes,[126,299,300] see also the discussion in section 5.4.7.

We structure this section as follows. First, in section 5.5.2, we discuss the general definition for the convection velocity, and formulate the transport theory with respect to this arbitrary choice. Next, in section 5.5.3, we derive the exact transformation rules between different reference frames. In section 5.5.4, we apply these findings and discuss three different frames. We discuss the binary electrolyte in section 5.5.5. Finally, in section 5.5.6, we discuss the relation to experimental methods for measuring the transference numbers.

5.5.2 Universal Convection Velocity

The reference frame in Eulerian description is defined using the "external" coordinates of a fixed laboratory set-up. In contrast, in the Lagrangian description, the reference frame is defined with respect to "internal" coordinates comoving with some dynamical bulk-quantity.[301,302] Note that the macroscopic behaviour of the system is invariant with respect to the choice of reference frame.

There exists a plethora of dynamical electrolyte quantities which can be used to define a convection velocity. However, it can be beneficial to choose the reference frame in accordance with the set-up of the physical system, and with the boundary conditions. As consequence, there exist many different choice for the bulk convection velocity in the literature,[133] including the mass average velocity,[303,304] the volume average velocity,[275,276,301,302] and some more exotic candidates as the mole-averaged velocity and the enthalpy velocity.[305,306] Another prominent candidate is to choose the species velocity of some abundant bulk species, *e.g.* a solvent species, as reference.[100]

Since convection is fundamentally related to the species fluxes, *i.e.* to the species velocities $\mathbf{v}_\alpha$, it must be a linear combination of the species velocities,[307]

$$\mathbf{v}^\psi = \sum_{\alpha=1}^{\mathrm{N}} \psi_\alpha \mathbf{v}_\alpha. \tag{5.284}$$

This defines the "ψ"-frame of reference, and $\mathbf{v}^\psi$ is the "ψ"-averaged convection velocity. Because the non-dimensional coefficients are normalized

$$\sum_{\alpha=1}^{\mathrm{N}} \psi_\alpha = 1, \tag{5.285}$$

only N-1 independent quantities ψ_α exist. Usually, the choice for the electrolyte quantity ψ_α is motivated by the experimental set-up, or boundary conditions, and it defines a derivative operator which describes the evolution of some electrolyte quantity relative to $\mathbf{v}^\psi$,

$$\frac{\mathrm{D}^\psi}{\mathrm{d}t} = \frac{\partial}{\partial t} + \mathbf{v}^\psi \cdot \boldsymbol{\nabla}. \tag{5.286}$$

Note that the Eulerian time-derivative $\partial/\partial t$, which measures the evolution of a quantity with respect to fixed external coordinates, does not depend upon the reference frame and is invariant under changing the reference frames. In the reference frame defined by $\mathbf{v}^\psi$, species transport is measured by frame-dependent fluxes

$$\mathcal{N}_\alpha^\psi = c_\alpha \left(\mathbf{v}_\alpha - \mathbf{v}^\psi\right). \tag{5.287}$$

By construction, in all reference frames, there exists a universal flux constraint

$$\sum_{\alpha=1}^{\mathrm{N}} \frac{\psi_\alpha}{c_\alpha} \cdot \mathcal{N}_\alpha^\psi = 0. \tag{5.288}$$

which is related to local balance of the quantities ψ_α. Thus, only N-1 independent fluxes $\mathcal{N}_\alpha^\psi$ are independent. Species transport $\partial_t c_\alpha = \boldsymbol{\nabla}(c_\alpha \mathbf{v}_\alpha)$ becomes,

$$\frac{\mathrm{D}^\psi}{\mathrm{d}t} c_\alpha = -c_\alpha \boldsymbol{\nabla} \mathbf{v}^\psi - \boldsymbol{\nabla} \mathcal{N}_\alpha^\psi + r_\alpha. \tag{5.289}$$

The electric flux associated with fluxes $\boldsymbol{\mathcal{N}}^{\psi}_{\alpha}$ of charged species is given by

$$\boldsymbol{\mathcal{J}}^{\psi}_{\mathrm{F}} = \sum_{\alpha=1}^{\mathrm{N}} F z_\alpha c_\alpha \mathbf{v}_\alpha - \varrho_{\mathrm{F}} \mathbf{v}^{\psi} = \sum_{\alpha=2}^{\mathrm{N}} F \tilde{z}^{\psi}_{\alpha} \boldsymbol{\mathcal{N}}^{\psi}_{\alpha} . \boldsymbol{\mathcal{J}}^{\psi}_{\mathrm{F}} = \sum_{\alpha=2}^{\mathrm{N}} F \tilde{z}^{\psi}_{\alpha} \boldsymbol{\mathcal{N}}^{\psi}_{\alpha}, \tag{5.290}$$

where we introduced N-1 valencies

$$\tilde{z}^{\psi}_{\alpha} = z_\alpha - \frac{c_1 \psi_\alpha}{c_\alpha \psi_1} \cdot z_1 . \tag{5.291}$$

Thus, in electroneutral systems ($\varrho_{\mathrm{F}} = 0$), the electric current is the same in all reference frames, *i.e.* invariant with respect to transformations between reference-frames.

In section 5.4.4, we made use of the Euler equation for the volume, $\sum_{\alpha=1}^{\mathrm{N}} \nu_\alpha c_\alpha = 1$, to derive an equation for the center-of-mass convection velocity $\mathbf{v}^{\mathsf{CMF}}$. Next, we show that such an equation for $\mathbf{v}^{\psi}$ can be derived in any frame. To address this goal, we use that for incompressible electrolytes, the variation of the Euler equation for the volume becomes (since $\delta\nu_\alpha$=0, see eq. (5.189)) $0 = \sum_{\alpha=1}^{\mathrm{N}} \nu_\alpha \cdot \mathrm{d}c_\alpha$. Thus, we can evaluate $\mathrm{d}c_\alpha$ for the time evolution, using any frame derivative, $\delta c_\alpha \rightarrow \mathrm{D}^{\psi} c_\alpha / \mathrm{d}t$ via eq. (5.289),

$$\boldsymbol{\nabla} \mathbf{v}^{\psi} = - \sum_{\alpha=1}^{\mathrm{N}} \nu_\alpha \cdot \boldsymbol{\nabla} \boldsymbol{\mathcal{N}}^{\psi}_{\alpha} + \sum_{\alpha=1}^{\mathrm{N}} \nu_\alpha \cdot r_\alpha . \tag{5.292}$$

Because the right side does not vanish in general, the assumption that $\boldsymbol{\nabla}\mathbf{v}^{\psi} = 0$ for incompressible electrolytes maybe a bad approximation, see also section 5.4.7. However, the appearance of the (generalized) molar volumes on the right side of eq. (5.292) highlights the special role of the volume averaged reference frame defined by $\psi_\alpha = c_\alpha \nu_\alpha$. In this frame, the universal flux constraint eq. (5.288) becomes $\sum_{\alpha=1}^{\mathrm{N}} \nu_\alpha \boldsymbol{\mathcal{N}}^{\mathsf{Volume}}_{\alpha} = 0$, which implies that $\sum_{\alpha=1}^{\mathrm{N}} \nu_\alpha \boldsymbol{\nabla} \boldsymbol{\mathcal{N}}^{\mathsf{Volume}}_{\alpha} = - \sum_{\alpha=1}^{\mathrm{N}} \boldsymbol{\mathcal{N}}^{\mathsf{Volume}}_{\alpha} \boldsymbol{\nabla} \nu_\alpha$. Thus, if there are no reactions occurring (r_α=0) the volume averaged velocity is spatially constant,

$$\boldsymbol{\nabla} \mathbf{v}^{\mathsf{Volume}} = \sum_{\alpha=1}^{\mathrm{N}} \boldsymbol{\mathcal{N}}^{\mathsf{Volume}}_{\alpha} \cdot \boldsymbol{\nabla} \nu_\alpha = 0 . \tag{5.293}$$

Hence, $\mathbf{v}^{\mathsf{Volume}}$ is a constant, and is completely determined by the boundary conditions. Thus, if $\mathbf{v}^{\mathsf{Volume}}$ vanishes at some point, it vanishes everywhere. In particular, in the case where $\mathbf{v}^{\mathsf{Volume}} = 0$, the volume averaged description becomes equal to the lab-frame description based on an external, fixed reference frame. We emphasize that the equivalence of $\boldsymbol{\nabla}\mathbf{v}^{\mathsf{Volume}} = 0$ and incompressibility is a unique feature of the volume based description, which is not true automatically in all other frames.

Finally, we observe that the expansion eq. (5.292) involves redundant fluxes. To obtain the independent form, we use the constraint eq. (5.288)

$$\nabla \mathbf{v}^{\psi} = -\sum_{\alpha=2}^{\mathrm{N}} \tilde{\nu}_{\alpha}^{\psi} \cdot \nabla \boldsymbol{\mathcal{N}}_{\alpha}^{\psi} + \nu_1 \sum_{\alpha=2}^{\mathrm{N}} \boldsymbol{\mathcal{N}}_{\alpha}^{\psi} \cdot \nabla(\psi_\alpha c_1/\psi_1 c_\alpha), \tag{5.294}$$

by introducing reduced generalized molar volumes

$$\tilde{\nu}_{\alpha}^{\psi} = \nu_\alpha - \psi_\alpha c_1/\psi_1 c_\alpha \cdot \nu_1. \tag{5.295}$$

Alternatively, the expansion eq. (5.294) can be expressed by the current $\boldsymbol{\mathcal{J}}_{\mathrm{F}}^{\psi}$ and N-2 fluxes $\boldsymbol{\mathcal{N}}_{\alpha}^{\psi}$ using the relation eq. (5.290). This form may be beneficial for the description of electroneutral systems.[67]

We encountered the designated role played by the volume frame when we derived the pressure equation (see eq. (5.195)). By construction, it follows straightforwardly that the quantity $\sum_{\alpha=1}^{\mathrm{N}} \nu_\alpha \cdot \partial_t c_\alpha$ appearing in the pressure equation is equal in any frame, and is given exactly by the variation of the volume averaged convection velocity up to variations of the partial molar volumes,

$$\sum_{\alpha=1}^{\mathrm{N}} \nu_\alpha \cdot \partial_t c_\alpha = -\nabla \mathbf{v}^{\mathsf{Volume}} + \sum_{\alpha=1}^{\mathrm{N}} c_\alpha \mathbf{v}_\alpha \nabla \nu_\alpha + \sum_{\alpha=1}^{\mathrm{N}} \nu_\alpha \cdot r_\alpha. \tag{5.296}$$

Next, we express the entropy production rate via the universal fluxes

$$\mathcal{R} = -\sum_{\alpha=1}^{\mathrm{N}} \boldsymbol{\mathcal{N}}_{\alpha}^{\mathsf{CMF}} \cdot \nabla \mu_{\alpha}^{\mathrm{el}} = -\sum_{\alpha=1}^{\mathrm{N}} \boldsymbol{\mathcal{N}}_{\alpha}^{\psi} \cdot \nabla \mu_{\alpha}^{\mathrm{el}} - \left(\mathbf{v}^{\psi} - \mathbf{v}^{\mathsf{CMF}}\right) \cdot \nabla \boldsymbol{\tau} \tag{5.297}$$

$$= -\sum_{\alpha=2}^{\mathrm{N}} \boldsymbol{\mathcal{N}}_{\alpha}^{\psi} \cdot \nabla \tilde{\mu}_{\alpha}^{\mathrm{el};\,\psi} - \left(\mathbf{v}^{\psi} - \mathbf{v}^{\mathsf{CMF}}\right) \cdot \nabla \boldsymbol{\tau}, \tag{5.298}$$

(see section 5.3.1), where we introduced a reduced set of N-1 chemical potentials

$$\nabla \tilde{\mu}_{\alpha}^{\mathrm{el};\,\psi} = F \tilde{z}_{\alpha}^{\psi} \nabla \Phi + \nabla \tilde{\mu}_{\alpha}^{\psi}, \qquad \text{and} \qquad \nabla \tilde{\mu}_{\alpha}^{\psi} = \nabla \mu_\alpha - c_1 \psi_\alpha / c_\alpha \psi_1 \, \nabla \mu_1, \tag{5.299}$$

where the chemical forces are $\nabla \mu_\alpha = -\nu_\alpha \varrho_{\mathrm{F}} \nabla \Phi + RT \sum_{\beta=1}^{\mathrm{N}} \mathit{TDF}_{\alpha\beta} \cdot (\nabla c_\beta)/c_\beta + \nu_\alpha \nabla \boldsymbol{\tau}$. However, the viscous forces can be expressed alternatively using the Gibbs-Duhem relation $\sum_{\alpha=1}^{\mathrm{N}} c_\alpha \nabla \mu_{\alpha}^{\mathrm{el}} = \nabla \boldsymbol{\tau}$ see eqs. (5.297) and (5.298), such that

$$\mathcal{R} = -\sum_{\alpha=1}^{\mathrm{N}} \boldsymbol{\mathcal{N}}_{\alpha}^{\psi} \cdot \nabla \mu_{\alpha}^{\mathrm{el}} \Big|_{\nabla \boldsymbol{\tau}=0} - \left(\mathbf{v}^{\mathsf{Volume}} - \mathbf{v}^{\mathsf{CMF}}\right) \cdot \nabla \boldsymbol{\tau} \tag{5.300}$$

$$= -\sum_{\alpha=2}^{\mathrm{N}} \boldsymbol{\mathcal{N}}_{\alpha}^{\psi} \cdot \nabla \tilde{\mu}_{\alpha}^{\mathrm{el};\,\psi} \Big|_{\nabla \boldsymbol{\tau}=0} - \left(\mathbf{v}^{\mathsf{Volume}} - \mathbf{v}^{\mathsf{CMF}}\right) \cdot \nabla \boldsymbol{\tau}. \tag{5.301}$$

Surprisingly, the volume averaged convection velocity defined by $\psi_\alpha = c_\alpha \nu_\alpha$ appears as designated reference-frame in the explicit viscous-expansion eqs. (5.300) and (5.301). This is reminiscent of the intimate relation between the rate-of-strain tensor, which measures volume-evolution, and the volume-flux. Note that the crucial mathematical property here is the universal relation

$$\sum_{\alpha=2}^{\mathrm{N}} \boldsymbol{\mathcal{N}}_\alpha^\psi \cdot \tilde{\mathrm{v}}_\alpha^\psi = \mathbf{v}^{\mathsf{Volume}} - \mathbf{v}^\psi. \tag{5.302}$$

This rationalizes the introduction of quantities $\tilde{\mathrm{v}}_\alpha^\psi$, which emerge naturally in the derivation of the independent form of the convection velocity in the CMF-frame. Apparently, these quantities are exactly the transformation from the mas fixed description to the volume fixed description.

From now on, we set the forces $\boldsymbol{\nabla\tau}$ to zero and examine the Onsager Ansatz for the fluxes $\boldsymbol{\mathcal{J}}_{\mathrm{F}}^\psi$ and $\boldsymbol{\mathcal{N}}_\alpha^\psi$,

$$\boldsymbol{\mathcal{N}}_\alpha^\psi = \sum_{\beta=2}^{\mathrm{N}} \boldsymbol{\mathcal{L}}_{\alpha\beta}^\psi \cdot \boldsymbol{\nabla} \tilde{\mu}_\beta^{\mathrm{el};\psi} \quad \text{for} \quad \alpha \geq 2. \tag{5.303}$$

The frame-dependent quantities $\boldsymbol{\mathcal{L}}_{\alpha\beta}^\psi$ constitute the N(N-1)/2 independent coefficients of the symmteric Onsager matrix in the ψ-frame. We define N-1 transference numbers

$$\boldsymbol{\mathcal{N}}_\alpha^\psi|_{\alpha\geq 2} = \tilde{t}_\alpha^\psi / F \tilde{z}_\alpha^\psi \cdot \boldsymbol{\mathcal{J}}_{\mathrm{F}}^\psi, \tag{5.304}$$

which satisfy the normalization constraint

$$\sum_{\alpha=2}^{\mathrm{N}} \tilde{t}_\alpha^\psi = 1, \tag{5.305}$$

i.e. only N-2 quantities $\tilde{t}_\alpha^\psi$ are independent. Note that we have shifted the notation, when compared with section 5.3. Throughout this chapter, we use the notation that the transference numbers which are weighted by the tilded quantities $\tilde{z}_\alpha^\psi$ are also tilded. As consequence, the transference numbers appearing in the main derivation of our transport theory are $t_\alpha \to \tilde{t}_\alpha^{\mathsf{CMF}}$.

In addition to the quantities $\tilde{t}_\alpha^\psi$, we introduce N transference numbers t^ψ for each species $\alpha = 1, \ldots, \mathrm{N}$,

$$\boldsymbol{\mathcal{N}}_\alpha^\psi = t^\psi / F z_\alpha \cdot \boldsymbol{\mathcal{J}}_{\mathrm{F}}^\psi. \tag{5.306}$$

By construction, for all species $\alpha \geq 2$ the quantities t_α^ψ and $\tilde{t}_\alpha^\psi$ are related to each other via "flux-ratios",

$$\tau_\alpha^\psi = t_\alpha^\psi / z_\alpha = \tilde{t}_\alpha^\psi / \tilde{z}_\alpha^\psi\,. \tag{5.307}$$

Hence, for $\alpha \geq 2$, the parameters t_α^ψ and τ_α^ψ are derived quantities which follow directly from $\tilde{t}_\alpha^\psi$, *i.e.* from the Onsager coefficients. However, in contrast to the coefficients $\tilde{t}_\alpha^\psi$, there exist parameters t_1^ψ and τ_1^ψ for the designated first species. These follow from the Ansatz $\mathcal{N}_1^\psi = t_1^\psi / F z_1 \cdot \mathcal{J}_{\mathrm{F}}^\psi$, and evaluating eqs. (5.290) and (5.304),

$$t_1^\psi = \sum_{\alpha=2}^{\mathrm{N}} \frac{\psi_\alpha c_1 z_1 \tilde{t}_\alpha^\psi}{\psi_\alpha c_1 z_1 - \psi_1 c_\alpha z_\alpha} = \sum_{\alpha=2}^{\mathrm{N}} \tilde{t}_\alpha^\psi \cdot \left(1 - \frac{\psi_1 c_\alpha z_\alpha}{\psi_\alpha c_1 z_1}\right)^{-1}. \tag{5.308}$$

Charge conservation and the universal flux constraint eq. (5.288) reduce the numebr of independent quantities $\tilde{t}^\psi$ to N-2. These constraints transfer to the quantities t_α^ψ and N quantities τ_α^ψ,

$$\text{Charge continuity:} \qquad \sum_{\alpha=1}^{\mathrm{N}} z_\alpha \tau_\alpha^\psi = \sum_{\alpha=1}^{\mathrm{N}} t_\alpha^\psi = \sum_{\alpha=2}^{\mathrm{N}} \tilde{z}_\alpha \tau_\alpha^\psi = 1, \tag{5.309}$$

$$\text{Flux constraint:} \qquad \sum_{\alpha=1}^{\mathrm{N}} \frac{\psi_\alpha}{F c_\alpha} \cdot \tau_\alpha^\psi = \sum_{\alpha=1}^{\mathrm{N}} \frac{\psi_\alpha}{F z_\alpha c_\alpha} \cdot t_\alpha^\psi = 0. \tag{5.310}$$

Thus, only N-2 independent flux-ratios τ_α^ψ, and N-2 independent quantities t_α^ψ exist in a N-component electrolyte.

As consequence, the binary electrolyte constitutes a somewhat exceptional system, because there does not exist an independent transference number and the only transference number is fixed, $\tilde{t}_2^\psi = 1$. However, we still can assign parameters t_1^ψ and t_2^ψ to the binary system (see eq. (5.308)). If $\psi_2 \neq 0$ (note that $z_1 = -z_2$),

$$t_1^\psi = \left(1 + \psi_1 c_2 / \psi_2 c_1\right)^{-1}, \quad \text{and} \quad t_2^\psi = 1 - t_2^\psi = \left(1 + \psi_2 c_1 / \psi_1 c_2\right)^{-1}. \tag{5.311}$$

In section 5.5.5 we discuss the binary case in more detail.

Altogether, we have introduced three different sets of quantities which measure some type of fractional current carried by each species. It remains to discuss how these different quantities relate to the intuitive understanding of a transference number.

In principle, the transference number of an ion species is defined as the fraction of current carried by the molar flux $\mathcal{N}_\alpha^{\mathsf{LF}}$ of the respective species, with respect to the overall current I_{total},

$$t_\alpha^{\mathsf{LF}} = \mathcal{N}_\alpha^{\mathsf{LF}} / I_{\text{total}} \tag{5.312}$$

According to this description, the fluxes and currents are measured relative to an external rest-frame, usually the fixed laboratory. As consequence, the corresponding transference numbers are also defined relative to the external coordinates. In our description, the ratio of current carried by the molar flux of an ion-species with respect to the overall current $\boldsymbol{\mathcal{J}}_{\mathrm{F}}^{\psi}$ is (assuming chemical equilibrium),

$$F\boldsymbol{\mathcal{N}}_{\alpha}^{\psi}/\boldsymbol{\mathcal{J}}_{\mathrm{F}}^{\psi} = \tilde{t}_{\alpha}^{\psi}/\tilde{z}_{\alpha}^{\psi} \; = t_{\alpha}^{\psi}/z_{\alpha} \; = \tau_{\alpha}^{\psi}. \tag{5.313}$$

Thus, the intuitive understanding of transference numbers from above, see eq. (5.312), relates best to the quantities τ_{α}^{ψ}, because the two other quantities are weighted by the valencies z_{α} and $\tilde{z}_{\alpha}^{\psi}$. It has to be noted though, that the fluxes $\boldsymbol{\mathcal{N}}_{\alpha}^{\psi} = \boldsymbol{\mathcal{N}}_{\alpha}^{\mathsf{LF}} - c_{\alpha}\mathbf{v}^{\psi}$ and the current $\boldsymbol{\mathcal{J}}_{\mathrm{F}}^{\psi} = I_{\text{total}} - \varrho_{\mathrm{F}}\mathbf{v}^{\psi}$ differ from the rest frame fluxes $\boldsymbol{\mathcal{N}}_{\alpha}^{\mathsf{LF}} = c_{\alpha}\mathbf{v}_{\alpha}$ and $I_{\text{total}} = \sum_{\alpha=1}^{\mathrm{N}} F z_{\alpha} c_{\alpha}\mathbf{v}_{\alpha}$ via convective corrections. Thus, in the case where the quantities $\boldsymbol{\mathcal{N}}_{\alpha}^{\psi}/c_{\alpha}\mathbf{v}^{\psi}$ and $\boldsymbol{\mathcal{J}}_{\mathrm{F}}^{\psi}/\varrho_{\mathrm{F}}\mathbf{v}^{\psi}$ are not negligible, the internal flux ratios τ_{α}^{ψ} deviate from the ratios $F\boldsymbol{\mathcal{N}}^{\mathsf{LF}}/I_{\text{total}}$. In section 5.5.6 we supplement these three types of transference numbers by the species mobilities, which can be determined from eNMR experiments.

5.5.3 Transformation of Reference Frame

Here, we derive simple transformation rules between different frames of reference from eq. (5.285), and the universal flux-constraint, eq. (5.288).

The transformation rule for the convection velocity follows from the normalization condition via $\mathbf{v}^{\tilde{\psi}} - \mathbf{v}^{\psi} = \sum_{\alpha=1}^{\mathrm{N}} \tilde{\psi}_{\alpha}\mathbf{v}_{\alpha} - \mathbf{v}^{\psi} = \sum_{\alpha=1}^{\mathrm{N}} \tilde{\psi}_{\alpha}(\mathbf{v}_{\alpha} - \mathbf{v}^{\psi})$. We express the bracked term via fluxes $\boldsymbol{\mathcal{N}}_{\alpha}^{\psi}$, and repeat the same calculation with respect to the ψ-frame. Altogether,

$$\mathbf{v}^{\tilde{\psi}} - \mathbf{v}^{\psi} = \sum_{\alpha=1}^{\mathrm{N}} \tilde{\psi}_{\alpha}/c_{\alpha} \cdot \boldsymbol{\mathcal{N}}_{\alpha}^{\psi} = -\sum_{\alpha=1}^{\mathrm{N}} \psi_{\alpha}/c_{\alpha} \cdot \boldsymbol{\mathcal{N}}_{\alpha}^{\tilde{\psi}}. \tag{5.314}$$

This expansion can be reduced by substitution of $\boldsymbol{\mathcal{N}}_{1}^{\psi}$,

$$\mathbf{v}^{\tilde{\psi}} - \mathbf{v}^{\psi} = \sum_{\alpha=2}^{\mathrm{N}} \left(\frac{\tilde{\psi}_{\alpha}}{\psi_{\alpha}} - \frac{\tilde{\psi}_{1}}{\psi_{1}}\right) \frac{\psi_{\alpha}\boldsymbol{\mathcal{N}}_{\alpha}^{\psi}}{c_{\alpha}} = \sum_{\alpha=2}^{\mathrm{N}} \left(\frac{\psi_{1}}{\tilde{\psi}_{1}} - \frac{\psi_{\alpha}}{\tilde{\psi}_{\alpha}}\right) \frac{\tilde{\psi}_{\alpha}\boldsymbol{\mathcal{N}}_{\alpha}^{\tilde{\psi}}}{c_{\alpha}}. \tag{5.315}$$

We define frame transformation matrices between the reference frame $\tilde{\psi}$ and the reference frame ψ,

$$\mathcal{U}_{\alpha}^{\tilde{\psi}\psi} = \tilde{\psi}_{\alpha}/c_{\alpha} \cdot (\psi_{1}/\tilde{\psi}_{1} - \psi_{\alpha}/\tilde{\psi}_{\alpha}), \quad \mathcal{U}_{\alpha\beta}^{\tilde{\psi}\psi} = \delta_{\alpha}^{\beta} + c_{\alpha}\mathcal{U}_{\beta}^{\tilde{\psi}\psi}. \tag{5.316}$$

By construction, the inverse transformation, *i.e.* from ψ to $\tilde{\psi}$, is

$$\mathcal{U}_{\alpha}^{\psi\tilde{\psi}} = \left(\mathcal{U}_{\alpha}^{\tilde{\psi}\psi}\right)^{-1} = -\tilde{\psi}_{1}/\psi_{1} \cdot \mathcal{U}_{\alpha}^{\tilde{\psi}\psi}, \quad \text{and} \quad \mathcal{U}_{\alpha\beta}^{\psi\tilde{\psi}} = \left(\mathcal{U}_{\alpha\beta}^{\tilde{\psi}\psi}\right)^{-1} = \delta_{\alpha}^{\beta} + c_{\alpha}\mathcal{U}_{\beta}^{\psi\tilde{\psi}}. \tag{5.317}$$

The latter relation can easily be checked by verifying that $\sum_{\beta=2}^{\mathrm{N}}(\delta_\alpha^\beta + c_\alpha \mathcal{U}_\beta^{\tilde\psi\psi})(\delta_\beta^\gamma + c_\beta \mathcal{U}_\gamma^{\psi\tilde\psi}) = \delta_\alpha^\gamma$. Thus, we find that

$$\mathbf{v}^{\psi} - \mathbf{v}^{\tilde\psi} = -\sum_{\beta=2}^{\mathrm{N}} \mathcal{U}_\beta^{\tilde\psi\psi} \cdot \boldsymbol{\mathcal{N}}_\beta^{\tilde\psi}. \tag{5.318}$$

This allows to derive the transformation rule for the fluxes between two reference frames,

$$\boldsymbol{\mathcal{N}}_\alpha^{\psi} = \boldsymbol{\mathcal{N}}_\alpha^{\tilde\psi} + c_\alpha \cdot \left(\mathbf{v}^{\tilde\psi} - \mathbf{v}^{\psi}\right) = \sum_{\beta=2}^{\mathrm{N}} \mathcal{U}_{\alpha\beta}^{\tilde\psi\psi} \cdot \boldsymbol{\mathcal{N}}_\beta^{\tilde\psi}. \tag{5.319}$$

Note that this relation holds for all species-fluxes $\boldsymbol{\mathcal{N}}_\alpha^{\psi}$ (*i.e.*, $\alpha = 1, \ldots, \mathrm{N}$). From this we derive the transformation behaviour of the electric currents (see eq. (5.290)),

$$\boldsymbol{\mathcal{J}}_{\mathrm{F}}^{\psi} = \boldsymbol{\mathcal{J}}_{\mathrm{F}}^{\tilde\psi} + \varrho_{\mathrm{F}} \sum_{\beta=2}^{\mathrm{N}} \mathcal{U}_\beta^{\tilde\psi\psi} \boldsymbol{\mathcal{N}}_\beta^{\tilde\psi} \tag{5.320}$$

This reproduces our finding from above, that the currents are the same in all frmaes in the electroneutral case.

Each reference frame leads to a specific set of transport parameters defined by the Onsager-coefficients appearing in the corresponding Onsager-expansion $\boldsymbol{\mathcal{N}}_\alpha^{\psi} = -\sum_{\beta=1}^{\mathrm{N}} \boldsymbol{\mathcal{L}}_{\alpha\beta}^{\psi} \cdot \boldsymbol{\nabla} \mu_\beta^{\mathrm{el}}$.

Above, we showed that charge conservation (eq. (5.290)), and the universal flux-constraint (eq. (5.288)) reduce the set of independent fluxes, where the independent flux expansion was based on quantities $\tilde{z}_\alpha^{\psi}$ and $\tilde{\nu}^{\psi}$ (see eqs. (5.291) and (5.295)). In order to derive the transformation rules for these quantities, we use that

$$z_1 = \frac{\psi_1}{c_1} \cdot \left(\varrho_{\mathrm{F}} - \sum_{\alpha=2}^{\mathrm{N}} c_\alpha \tilde{z}_\alpha^{\psi}\right) \quad \text{and} \quad \nu_1 = \frac{\psi_1}{c_1} \cdot \left(1 - \sum_{\alpha=2}^{\mathrm{N}} c_\alpha \tilde{\nu}_\alpha^{\psi}\right). \tag{5.321}$$

Furthermore, we use that $z_1 = \tilde{z}_\alpha^{\psi} + \psi_\alpha c_1 z_1 / c_\alpha \psi_1$. Finally, we obtain

$$\begin{pmatrix} \tilde{z}_2^{\tilde\psi} \\ \vdots \\ \tilde{z}_{\mathrm{N}}^{\tilde\psi} \end{pmatrix} = \left(\boldsymbol{\mathcal{U}}^{\tilde\psi\psi}\right)^T \begin{pmatrix} \tilde{z}_2^{\psi} \\ \vdots \\ \tilde{z}_{\mathrm{N}}^{\psi} \end{pmatrix} - \varrho_{\mathrm{F}} \begin{pmatrix} \mathcal{U}_2^{\tilde\psi\psi} \\ \vdots \\ \mathcal{U}_{\mathrm{N}}^{\tilde\psi\psi} \end{pmatrix} \quad \text{and} \quad \begin{pmatrix} \tilde{\nu}_2^{\tilde\psi} \\ \vdots \\ \tilde{\nu}_{\mathrm{N}}^{\tilde\psi} \end{pmatrix} = \left(\boldsymbol{\mathcal{U}}^{\tilde\psi\psi}\right)^T \begin{pmatrix} \tilde{\nu}_2^{\psi} \\ \vdots \\ \tilde{\nu}_{\mathrm{N}}^{\psi} \end{pmatrix} - \begin{pmatrix} \mathcal{U}_2^{\tilde\psi\psi} \\ \vdots \\ \mathcal{U}_{\mathrm{N}}^{\tilde\psi\psi} \end{pmatrix},$$

or, in components,

$$\tilde{z}_\alpha^{\tilde\psi} = \left(\sum_{\beta=2}^{\mathrm{N}} \delta_\alpha^\beta + c_\beta \mathcal{U}_\alpha^{\tilde\psi\psi}\right) \tilde{z}_\beta^{\psi} - \varrho_{\mathrm{F}} \mathcal{U}_\alpha^{\tilde\psi\psi} \text{ and } \tilde{\nu}_\alpha^{\tilde\psi} = \left(\sum_{\beta=2}^{\mathrm{N}} \delta_\alpha^\beta + c_\beta \mathcal{U}_\alpha^{\tilde\psi\psi}\right) \tilde{\nu}_\beta^{\psi} - \mathcal{U}_\alpha^{\tilde\psi\psi}. \tag{5.322}$$

Next, we calculate the transformation rule for the reduced set of electrochemical forces. A straightforward calculation shows that $\boldsymbol{\nabla}\tilde{\mu}_\alpha^{\mathrm{el};\psi} = \boldsymbol{\nabla}\tilde{\mu}_\alpha^{\mathrm{el};\tilde{\psi}} + \mathcal{U}_\alpha^{\tilde{\psi}\psi} \cdot c_1 \boldsymbol{\nabla}\mu_1^{\mathrm{el}}/\psi_1$. However, the quantity $\boldsymbol{\nabla}\mu_1^{\mathrm{el}}$ is not independent. Using the Gibbs-Duhem equation,

$$c_1 \boldsymbol{\nabla}\mu_1^{\mathrm{el}} = \tilde{\psi}_1 \cdot \boldsymbol{\nabla}\boldsymbol{\tau} - \tilde{\psi}_1 \cdot \sum_{\alpha=2}^{\mathrm{N}} c_\alpha \boldsymbol{\nabla}\tilde{\mu}_\alpha^{\mathrm{el};\tilde{\psi}}. \tag{5.323}$$

Altogether, the transformation rule of the electrochemical forces reads

$$\begin{aligned}
\boldsymbol{\nabla}\tilde{\mu}_\alpha^{\mathrm{el};\psi} &= \sum_{\beta=2}^{\mathrm{N}} \left(\delta_\alpha^\beta + c_\beta \mathcal{U}_\alpha^{\psi\tilde{\psi}}\right) \cdot \boldsymbol{\nabla}\tilde{\mu}_\beta^{\mathrm{el};\tilde{\psi}} - \mathcal{U}_\alpha^{\psi\tilde{\psi}} \cdot \boldsymbol{\nabla}\boldsymbol{\tau} && (5.324)\\
&= \sum_{\beta=2}^{\mathrm{N}} \left(\mathscr{U}_{\alpha\beta}^{\psi\tilde{\psi}}\right)^T \cdot \boldsymbol{\nabla}\tilde{\mu}_\beta^{\mathrm{el};\tilde{\psi}} - \mathcal{U}_\alpha^{\psi\tilde{\psi}} \cdot \boldsymbol{\nabla}\boldsymbol{\tau} && (5.325)\\
&= \sum_{\beta=2}^{\mathrm{N}} [(\mathscr{U}_{\alpha\beta}^{\tilde{\psi}\psi})^{-1}]^T \cdot \boldsymbol{\nabla}\tilde{\mu}_\beta^{\mathrm{el};\tilde{\psi}} - \mathcal{U}_\alpha^{\psi\tilde{\psi}} \cdot \boldsymbol{\nabla}\boldsymbol{\tau}. && (5.326)
\end{aligned}$$

This transformation seems to be in conflict with the transformation rule found for the valencies $\tilde{z}_\alpha^\psi$, see eq. (5.322). We show that the transformation rules eqs. (5.322) and (5.326) are consistent with each other, and expand $\boldsymbol{\nabla}\boldsymbol{\tau} = \sum_{\beta=1}^{\mathrm{N}} c_\beta \cdot \boldsymbol{\nabla}\tilde{\mu}_\beta^{\mathrm{el}}$, and split eq. (5.326) into it's electric and chemical part,

$$\boldsymbol{\nabla}\tilde{\mu}_\alpha^{\mathrm{el};\tilde{\psi}} = \Big(\sum_{\beta=2}^{\mathrm{N}} \mathscr{U}_{\beta\alpha}^{\tilde{\psi}\psi} F \tilde{z}_\beta^\psi - \mathcal{U}_\alpha^{\tilde{\psi}\psi} \varrho_{\mathrm{F}}\Big) \boldsymbol{\nabla}\Phi + \sum_{\beta=2}^{\mathrm{N}} \mathscr{U}_{\beta\alpha}^{\tilde{\psi}\psi} \boldsymbol{\nabla}\tilde{\mu}_\beta^{\mathrm{el};\psi} - \mathcal{U}_\alpha^{\tilde{\psi}\psi} \sum_{\gamma=1}^{\mathrm{N}} c_\gamma \boldsymbol{\nabla}\mu_\gamma. \tag{5.327}$$

The first bracked term reproduces exactly the transformation behaviour of the valencies $\tilde{z}_\alpha^\psi$, which we derived above, see eq. (5.322). The second and third term determine the transformation behaviour of the chemical forces $\boldsymbol{\nabla}\tilde{\mu}_\alpha^\psi$.

The transformation behaviour of the fluxes determines the transformation behaviour of the transport parameters. A simple calculation shows that

$$\tau_\alpha^\psi \cdot \boldsymbol{\mathcal{J}}_{\mathrm{F}}^\psi = \sum_{\beta=2}^{\mathrm{N}} \left[\delta_{\alpha\beta} + c_\alpha \mathcal{U}_\beta^{\tilde{\psi}\psi}\right] \cdot \tau_\beta^{\tilde{\psi}} \cdot \boldsymbol{\mathcal{J}}_{\mathrm{F}}^{\tilde{\psi}}. \tag{5.328}$$

Next, we transform the electric current on the left side using eq. (5.320), such that

$$\tau_\alpha^{\psi} = \frac{\sum_{\beta=2}^{N} \left[\delta_{\alpha\beta} + c_\alpha \mathcal{U}_\beta^{\tilde{\psi}\psi}\right] \cdot \tau_\beta^{\tilde{\psi}}}{\sum_{\alpha=1}^{N} F z_\alpha \sum_{\beta=2}^{N} \left[\delta_{\alpha\beta} + c_\alpha \mathcal{U}_\beta^{\tilde{\psi}\psi}\right] \cdot \tau_\beta^{\tilde{\psi}}} = \frac{\sum_{\beta=2}^{N} \left[\delta_{\alpha\beta} + c_\alpha \mathcal{U}_\beta^{\tilde{\psi}\psi}\right] \cdot \tau_\beta^{\tilde{\psi}}}{1 + \varrho_{\mathrm{F}} \sum_{\beta=2}^{N} \mathcal{U}_\beta^{\tilde{\psi}\psi} \tau_\beta^{\tilde{\psi}}}. \tag{5.329}$$

Thus, in the electroneutral case, the transformation behaviour of the transference numbers between different frames reads

$$\tau_\alpha^{\psi} = \sum_{\beta=2}^{N} \left[\delta_{\alpha\beta} + c_\alpha \mathcal{U}_\beta^{\tilde{\psi}\psi}\right] \tau_\beta^{\tilde{\psi}} = \tau_\alpha^{\tilde{\psi}} + c_\alpha \sum_{\beta=2}^{N} \mathcal{U}_\beta^{\tilde{\psi}\psi} \cdot \tau_\beta^{\tilde{\psi}} = \sum_{\beta=2}^{N} \mathcal{U}_{\alpha\beta}^{\tilde{\psi}\psi} \cdot \tau_\beta \tag{5.330}$$

or, in matrix form

$$\left(\tau_2^{\psi}, \ldots, \tau_{\mathrm{N}}^{\psi}\right)^T = \boldsymbol{\mathcal{U}}^{\tilde{\psi}\psi} \cdot \left(\tau_2^{\tilde{\psi}}, \ldots, \tau_{\mathrm{N}}^{\tilde{\psi}}\right)^T \tag{5.331}$$

Next, we derive the transformation behaviour of the elctrolyte electric conductivities. For this puprose, we assume that $\boldsymbol{\nabla} \tilde{\mu}_\alpha^{\mathrm{el};\,\psi} = F \tilde{z}_\alpha \boldsymbol{\nabla} \Phi$, and use the expansions $\boldsymbol{\mathcal{J}}_{\mathrm{F}}^{\psi} = F \sum_{\alpha=2}^{\mathrm{N}} \tilde{z}_\alpha^{\psi} \boldsymbol{\mathcal{N}}_\alpha^{\psi}$ and $\boldsymbol{\mathcal{N}}_\alpha^{\psi} = -\sum_{\beta=2}^{\mathrm{N}} \boldsymbol{\mathcal{L}}_{\alpha\beta}^{\psi} F \tilde{z}_\beta^{\psi} \boldsymbol{\nabla} \Phi$, such that

$$\kappa^{\psi} = \kappa^{\tilde{\psi}} + \varrho_{\mathrm{F}} \sum_{\alpha,\beta=2}^{N} \mathcal{U}_\alpha^{\tilde{\psi}\psi} F \tilde{z}_\beta \boldsymbol{\mathcal{L}}_{\alpha\beta}^{\tilde{\psi}}. \tag{5.332}$$

Thus, if $\varrho_{\mathrm{F}}=0$, the electrolyte electric currents are the same in all frames.

Finally, we derive the transformation behaviour of the Onsager coefficients. For this purpose, we use the Onsager Ansatz $-\sum_{\beta=2}^{\mathrm{N}} \boldsymbol{\mathcal{L}}_{\alpha\beta}^{\psi} \boldsymbol{\nabla} \tilde{\mu}_\beta^{\mathrm{el};\,\psi} = \boldsymbol{\mathcal{N}}_\alpha^{\psi}$, and transform the fluxes on the right side to the $\tilde{\psi}$ -frame. Next, we express the fluxes $\boldsymbol{\mathcal{N}}_\alpha^{\tilde{\psi}}$ via the corresponding Onsager expansion (setting $\boldsymbol{\nabla\tau} \approx 0$) , such that the transformation of the Onsager matrix becomes

$$\boldsymbol{\mathcal{L}}^{\psi} = \boldsymbol{\mathcal{U}}^{\tilde{\psi}\psi} \cdot \boldsymbol{\mathcal{L}}^{\tilde{\psi}} \left(\boldsymbol{\mathcal{U}}^{\tilde{\psi}\psi}\right)^T. \tag{5.333}$$

The transformation behaviour of the Onsager matrix determines the transformation behaviour of all transport parameters. In particular, eqs. (5.329) and (5.333) constitute implicitely the transformation behaviour of the diffusion coefficients $\mathcal{D}_{\alpha\beta}^{\psi} = \mathcal{L}_{\alpha\beta}^{\psi} - \kappa^{\psi} t_\alpha^{\psi} t_\beta^{\psi} / F^2 z_\alpha z_\beta$. As consistency check, we calculate the transformation of the flux ratios from the transformation rule of the Onsager matrix, eq. (5.333) in electroneutral case,

$$\begin{pmatrix}\tau_2^{\psi}\\ \vdots\\ \tau_N^{\psi}\end{pmatrix} = \frac{F^2}{\kappa}\mathcal{L}^{\psi}\begin{pmatrix}\tilde{z}_2^{\psi}\\ \vdots\\ \tilde{z}_N^{\psi}\end{pmatrix} = \frac{F^2}{\kappa}\mathcal{U}^{\tilde{\psi}\psi}\mathcal{L}^{\tilde{\psi}}(\mathcal{U}^{\tilde{\psi}\psi})^T(\mathcal{U}^{\tilde{\psi}\psi})^{-T}\begin{pmatrix}\tilde{z}_2^{\psi}\\ \vdots\\ \tilde{z}_N^{\tilde{\psi}}\end{pmatrix} = \mathcal{U}^{\tilde{\psi}\psi}\begin{pmatrix}\tau_2^{\tilde{\psi}}\\ \vdots\\ \tau_N^{\tilde{\psi}}\end{pmatrix}. \tag{5.334}$$

This reproduces exactly the transformation rule which we found above, see eq. (5.331).

5.5.4 Internal And External Frames of Reference

The set of reference frames can be split into “internal farmes”, which depend on the dynamics of the electrolyte, and “external frames”, which are independent of the internal electrolyte dynamics.

The internal description makes use of the universal flux constraint (eq. (5.288)), and it is beneficial to choose the internal frame in accordance with the boundary conditions of the physical set up. Hence, there exist many definitions for internal frames in the literature,[133]), which apply to different systems.

Here, we discuss three different reference-frames which are related by simple transformation rules, where we assume thermal equilibrium, and neglect viscous forces and chemical reactions.

Our main transport theory is based on the center of mass velocity, $\psi_\alpha = M_\alpha c_\alpha/\rho$, where $\mathbf{v}^{\mathsf{CMF}} = \sum_{\alpha=1}^{N}\rho_\alpha\mathbf{v}_\alpha/\rho$. The universal flux constraint eq. (5.288) in this frame is $\sum_{\alpha=1}^{N} M_\alpha\boldsymbol{\mathcal{N}}_\alpha^{\mathsf{CMF}} = 0$.

Another example of an internal frame is the volume averaged frame defined by $\psi_\alpha = c_\alpha\nu_\alpha$, where $\mathbf{v}^{\mathsf{Volume}} = \sum_{\alpha=1}^{N} c_\alpha\nu_\alpha\mathbf{v}_\alpha$. The universal flux constraint eq. (5.288) becomes $\sum_{\alpha=1}^{N}\nu_\alpha\boldsymbol{\mathcal{N}}^{\mathsf{Volume}} = 0$, and is reminiscent of the Euler equation for the volume ($\sum_{\alpha=1}^{N}\nu_\alpha c_\alpha = 1$). Because $\psi_\alpha c_1/\psi_1 c_\alpha = \nu_\alpha/\nu_1$,

$$\tilde{z}_\alpha^{\mathsf{Volume}} = z_\alpha - z_1\nu_\alpha/\nu_1\,, \quad \tilde{\nu}_\alpha^{\mathsf{Volume}} = \nu_\alpha - \nu_1\nu_\alpha/\nu_1 = 0, \quad \tilde{\mu}_\alpha^{\mathsf{Volume}} = \mu_\alpha - \mu_1\nu_\alpha/\nu_1\,. \tag{5.335}$$

As shown in section 5.5.2, the volume averaged description has the unique property that the convection equation becomes trivial for incompressible electrolytes, $\boldsymbol{\nabla}\mathbf{v}^{\mathsf{Volume}} = 0$.

Another example is the so-called solvent frame, or internal velocity reference-frame (IVRF), which designates one species velocity as reference. This can be a good approximation for electrolytes with an excess solvent species, *e.g.* aqueous electrolytes or polymer electrolytes. In this case $\psi_\alpha^{\mathsf{IVRF}} = \delta_1^\alpha$ such that $\mathbf{v}^{\mathsf{IVRF}} = \mathbf{v}_1$. The universal flux constraint reads $\boldsymbol{\mathcal{N}}_1^{\mathsf{IVRF}} = 0$, and, by construction, $t_1^{\mathsf{IVRF}} = 0$.

Because $\psi_\alpha c_1/\psi_1 c_\alpha = \delta_1^\alpha$,

$$\tilde{z}_\alpha^{\mathsf{IVRF}}|_{\alpha\geq 2} = z_\alpha, \quad \tilde{\nu}_\alpha^{\mathsf{IVRF}}|_{\alpha\geq 2} = \nu_\alpha, \quad \tilde{\mu}_\alpha^{\mathsf{IVRF}}|_{\alpha\geq 2} = \mu_\alpha. \tag{5.336}$$

Next, we derive the transformation rules between these internal reference frames in the electroneutral case, see eq. (5.329). As shown in section 5.5.3, these depend upon the transformation matrices $\mathcal{U}_\alpha^{\tilde{\psi}\psi}$ defined by eq. (5.316). We find for the transformation between the center of mass description and the volume averaged description,

$$\mathcal{U}_\alpha^{\mathsf{CMF;Volume}} = -\tilde{\nu}^{\mathsf{CMF}}. \tag{5.337}$$

This reproduces our finding from above (eq. (5.302)), that the quantities $\tilde{\nu}^{\mathsf{CMF}}$ transform the mass fixed description to the volume fixed description. Thus,

$$\tau_\alpha^{\mathsf{Volume}} = \tau_\alpha^{\mathsf{CMF}} - c_\alpha \sum_{\beta=2}^{\mathrm{N}} \tilde{\nu}_\beta^{\mathsf{CMF}} \cdot \tau_\beta^{\mathsf{CMF}}. \tag{5.338}$$

Therefore, the transference numbers in both frames are similar if $\sum_{\beta=2}^{\mathrm{N}} \tilde{\nu}_\beta \cdot \tau_\beta^{\mathsf{CMF}} \ll 1$, *e.g.*, if all products satisfy $\nu_\alpha M_1 \approx \nu_1 M_\alpha$.

For the transformation between the center of mass description and the solvent frame, *i.e.* the IVRF description, we find $\mathcal{U}_\alpha^{\mathsf{CMF;IVRF}} = M_\alpha/M_1 c_1$, such that

$$\tau_\alpha^{\mathsf{IVRF}} = \tau_\alpha^{\mathsf{CMF}} - c_\alpha/c_1 \cdot \tau_1^{\mathsf{CMF}}. \tag{5.339}$$

Thus, the transference numbers in the two descriptions coincide in the limit where the solvent is the bulk excessive species, $c_1 \gg c_\alpha|_{\alpha\geq 2}$, or if $\tau_1^{\mathsf{CMF}} = 0$.

In table 5.1 we summarize the different examples for internal reference frames which we discussed above.

We compare these formulations based on internal frames with the external description. For this purpose, we define the fluxes in the laboratory frame (LF) via

$$\mathcal{N}_\alpha^{\mathsf{LF}} = \mathcal{N}_\alpha^\psi + c_\alpha \mathbf{v}^\psi = c_\alpha \mathbf{v}_\alpha, \quad \text{and} \quad \boldsymbol{\mathcal{J}}_{\mathrm{F}}^{\mathsf{LF}} = \boldsymbol{\mathcal{J}}_{\mathrm{F}}^\psi + \varrho_{\mathrm{F}} \mathbf{v}^\psi = F z_\alpha c_\alpha \mathbf{v}^\psi, \tag{5.340}$$

and the LF-frame transference numbers by $\mathcal{N}_\alpha^{\mathsf{LF}} = t^{\mathsf{LF}}/F z_\alpha \cdot \boldsymbol{\mathcal{J}}_{\mathrm{F}}^{\mathsf{LF}}$. The normalization condition $\sum_{\alpha=1}^{\mathrm{N}} t_\alpha^{\mathrm{LF}} = 1$ implies that only N-1 transference numbers t_α^{LF} are independent. A simple calculation shows that, assuming chemical equilibrium,

$$\mathcal{N}_\alpha^\psi = \frac{t_\alpha^\psi \boldsymbol{\mathcal{J}}_{\mathrm{F}}^\psi}{F z_\alpha} = \mathcal{N}_\alpha^{\mathsf{LF}} - c_\alpha \mathbf{v}^\psi = \frac{t_\alpha^{\mathsf{LF}} \boldsymbol{\mathcal{J}}_{\mathrm{F}}^\psi}{F z_\alpha} - c_\alpha \sum_{\beta=1}^{\mathrm{N}} \psi_\beta \mathbf{v}_\beta = \sum_{\beta=1}^{\mathrm{N}} \frac{t_\beta^{\mathsf{LF}} \boldsymbol{\mathcal{J}}_{\mathrm{F}}^\psi}{F z_\beta} \left(\delta_\alpha^\beta - \frac{\psi_\beta c_\alpha}{c_\beta} \right). \tag{5.341}$$

In the last step we substituted $\mathbf{v}_\beta = \boldsymbol{\mathcal{N}}_\beta^{\mathsf{LF}}/c_\beta = t_\beta^{\mathsf{LF}} \boldsymbol{\mathcal{J}}_{\mathrm{F}}^{\mathsf{LF}}/F z_\beta c_\beta$. Because $\boldsymbol{\mathcal{J}}_{\mathrm{F}}^{\psi} = \boldsymbol{\mathcal{J}}_{\mathrm{F}}^{\mathsf{LF}}$ in the electroneutral case, we find that

$$t_\alpha^{\psi} = \sum_{\beta=1}^{\mathrm{N}} \frac{z_\alpha}{z_\beta} \cdot \left(\delta_\alpha^\beta - \psi_\beta c_\alpha / c_\beta \right) \cdot t_\beta^{\mathsf{LF}} \tag{5.342}$$

Thus, the difference between the transference numbers in the ψ-frame and the transference numbers in the LF-frame depends on the ion concentrations. Furthermore, we find that the electric conductivity in the LF description equals the corresponding quantity in the ψ- description in the case of electroneutrality,

$$\kappa^{\psi} = \kappa^{\mathsf{LF}} - \varrho_{\mathrm{F}} \mathbf{v}^{\psi} \cdot \mathbf{E}/\mathbf{E}^2 \,. \tag{5.343}$$

Frame	ψ_α	$\mathbf{v}^\psi$	Flux constraint	Systems
CMF	$\frac{\rho_\alpha}{\rho}$	$\mathbf{v}^{\mathsf{CMF}} = \sum_{\alpha=1}^{\mathrm{N}} \frac{\rho_\alpha \mathbf{v}_\alpha}{\rho}$	$\sum_{\alpha=1}^{\mathrm{N}} M_\alpha \boldsymbol{\mathcal{N}}_\alpha^{\mathsf{CMF}} = 0$	ILs / Concentrated Electrolytes
Volume	$c_\alpha \nu_\alpha$	$\mathbf{v}^{\mathsf{Volume}} = \sum_{\alpha=1}^{\mathrm{N}} c_\alpha \nu_\alpha \mathbf{v}_\alpha$	$\sum_{\alpha=1}^{\mathrm{N}} \nu_\alpha \boldsymbol{\mathcal{N}}^{\mathsf{Volume}} = 0$	ILs / Concentrated Electrolytes
IVRF	δ_1^α	$\mathbf{v}^{\mathsf{IVRF}} = \mathbf{v}_1$	$\boldsymbol{\mathcal{N}}_1^{\mathsf{IVRF}} = 0$	Aqueous / Polymers

Table 5.1: Summary of the different examples for internal reference frames discussed in section 5.5.4.

Interestingly, the discrepancy between the external and internal descriptions depend upon the relative orientation between the center-of-mass motion, and the electric field. For example, in the highly artificial case where the reference-velocity is normal to the electric field ($\mathbf{v}_\gamma \perp \mathbf{E}$ and $\mathbf{v} \perp \mathbf{E}$), all electrolyte conductivities are equal.

In particular, the relation between the solvent frame and the external frame is given by (note that $t_1^{\mathsf{IVRF}} = 0$),

$$t_\alpha^{\mathsf{IVRF}}|_{\alpha \geq 2} = t_\alpha^{\mathsf{LF}} - z_\alpha c_\alpha / z_1 c_1 \cdot t_1^{\mathsf{LF}} . \tag{5.344}$$

Thus, in the case where the solvent species is much larger than the other species, $c_\alpha|_{\alpha \neq 1} \ll c_1$, the transference numbers are approximately the same.

The relation of the transference numbers between the CMF description and the

LF description is

$$t_\alpha^{\mathsf{CMF}} = (1 - M_\alpha c_\alpha/\rho\,)\, t_\alpha^{\mathsf{LF}} - \sum_{\beta\neq\alpha} z_\alpha/z_\beta \cdot M_\beta c_\alpha/\rho \cdot t_\beta^{\mathsf{LF}}. \tag{5.345}$$

Hence, in the case where there exists a dominant solvent species, $M_{\alpha^*}c_{\alpha^*} \approx \rho$, the transference number of the solvent species in the CMF description is completely determined by the external transference numbers of the minor species, $t_{\alpha^*}^{\mathsf{CMF}} \approx -\sum_{\beta\neq\alpha^*} z_{\alpha^*} M_\beta t_\beta^{\mathsf{LF}}/z_\beta M_{\alpha^*}$, whereas the transference numbers of the minor species are $t_{\gamma\neq\alpha^*}^{\mathsf{CMF}} \approx t_{\gamma\neq\alpha^*}^{\mathsf{LF}} - \sum_{\beta\neq\alpha^*} z_\gamma c_\gamma M_\beta t_\beta^{\mathsf{LF}}/z_\beta M_{\alpha^*} c_{\alpha^*}$.

Note that similar results hold for the relation between the Volume description and the LF description, where the masses are to replaced by the molar volumes.

5.5.5 Comment on Transference Numbers in Binary Electrolytes

Because only N-2 independent transference numbers exist in a N-component electrolyte mixture (see section 5.5.2), the concept of transference numbers in a binary electrolyte becomes somewhat arbitrary. In particular, $\tilde{t}_1^\psi$=0 and $\tilde{t}_2^\psi$=1. Nevertheless, there exist completely fixed transference numbers t_1^ψ and t_2^ψ, see eq. (5.311).

In the center of mass description, the transference numbers are completely determined by the mass ratio of the two ionic species(“Sundheim’s Golden rule”),[298]

$$t_1^{\mathsf{CMF}} = (1 + M_1/M_2\,)^{-1}\,, \quad \text{and} \quad t_2^{\mathsf{CMF}} = (1 + M_2/M_1\,)^{-1}\,, \tag{5.346}$$

whereas the transference numbers in the volume averaged description are completely determined by the ratio of the two molar volumes ,

$$t_1^{\mathsf{Volume}} = (1 + \nu_1/\nu_2\,)^{-1}\,, \quad \text{and} \quad t_2^{\mathsf{Volume}} = (1 + \nu_2/\nu_1\,)^{-1}\,, \tag{5.347}$$

and, in the the solvent frame (see eq. (5.308))

$$t_1^{\mathsf{IVRF}} = 0, \quad \text{and} \quad t_2^{\mathsf{IVRF}} = 1. \tag{5.348}$$

5.5.6 Relation to Experiments

There exist many different definitions for transference numbers in the literature. This bears the potential for confusion, and relates also to the experimental determination of transference numbers. Recently, there is an ongoing debate in the literature, regarding the sign and magnitude of transference numbers for highly concentrated electrolytes, and ILs.[41,43,44]

A reporting of transference numbers should be accompanied by a complete characterization of the underlying concepts. In particular, the number of independent parameters, and the reference-frame should be stated clearly. Also, the knowledge of the parameters t_α does not comprise much physical insight, unless the quantities $\tilde{z}_\alpha$ are known (see the discussion in section 6.2.3). In this sense, the ratios $t_\alpha/\tilde{z}_\alpha$ are the more fundamental transport parameters. In section 5.5.4, we discussed different reference-frames. These relate to differing experimental set ups, and must be probed in agreement with experiments. However, experimental methods must take account for all inter-species correlations, including the formation of ionic clusters and ion-aggregates.[308] Thus, the experimental measurement of transference numbers is challenging.

For concentrated electrolytes, the applicability of NMR/PFG-NMR experiments for the determination of transport parameters is limited, due to various problems. First, this method neglects the formation of ionic complexes. Second, transference numbers are derived from diffusion coefficients via Nernst-Einstein relations, which are valid only for ideal electrolytes. Third, this method provides only averaged values.[261,262,308] Another prominent experiment is based on non-blocking electrodes,[261] but is limited to metal ions.[43] A novel experiment for measuring ion mobilities is electrophoretic NMR (eNMR),[41,43,309,310] which applies to a wide variety of concentrated electrolytes, neat ILs and IL-mixtures.

Depending upon the experimental method, internal and external flux-descriptions can be useful. For example, IVRF-descriptions relate naturally to “Hittorf”-type measurements of transference numbers,[117,192] whereas the CMF- and LF description relates to the moving-boundary method.[191,296] In addition, the volume averaged Volume-description relates to the determination of transference numbers based on experiments using electrophoretic-NMR (eNMR).[44,310]

Finally, we discuss the relation to ionic mobilities, as measured in eNMR experiments. For this purpose, we assume the limiting case where eq. (5.304) is valid (*i.e.* all chemical potentials and the temperature gradients vanish). Then, $\mathcal{J}_\mathrm{F}^\psi = \kappa\mathbf{E}$. In eNMR experiments, a uniform electric field $\mathbf{E}^\mathrm{ext}$ is applied externally for a very short period of time upon the electrolyte. This external field polarizes the liquid electrolyte, and induces a constant force upon the ions. However, the resulting acceleration of the ions is quickly dissipated by friction forces, and the ions reach a constant drift velocity $\mathbf{v}_\alpha^\mathrm{drift}$ which is, to a good approximation, proportional to the external electric field (in accordance with linear response theory). We define the corresponding species mobilities m_α via $\mathbf{v}_\alpha^\mathrm{drift} = m_\alpha\mathbf{E}^\mathrm{ext}$. Thus, by construction, the species mobilities are frame-independent, *i.e.* invariant under frame transformations. Next, we identify the drift velocity of the ion species with the species velocities, $\mathbf{v}_\alpha^\mathrm{drift} = \mathbf{v}_\alpha = \tau_\alpha^\psi\mathbf{E}/c_\alpha\kappa^\psi + \mathbf{v}^\psi$, and obtain a relation between the species mobilities and transport coefficients,

$$\tau_\alpha^\psi\mathbf{E}\kappa^\psi/F = \mathbf{E}^\mathrm{ext} m_\alpha c_\alpha + \mathbf{v}^\psi c_\alpha. \tag{5.349}$$

Assuming $\mathbf{v}^{\text{drift}}=\mathbf{v}_\alpha$, and using eq. (5.284), we find

$$\mathbf{E}^{\text{ext}} \cdot \sum_{\alpha=1}^{\text{N}} m_\alpha \psi_\alpha = \mathbf{v}^\psi, \tag{5.350}$$

which corresponds to the universal flux constraint eq. (5.288). Hence, in the case where the convection velocity vanishes, $\mathbf{v}^\psi=0$, this implies $\sum_{\alpha=1}^{\text{N}} m_\alpha \psi_\alpha = 0$. In addition, charge conservation (eq. (5.309))

$$\mathbf{E} \cdot \kappa^\psi = \mathbf{E}^{\text{ext}} \cdot \sum_{\alpha=1}^{\text{N}} F m_\alpha c_\alpha z_\alpha + \varrho_{\text{F}} \mathbf{v}^\psi. \tag{5.351}$$

Thus there exist only N-2 independent species mobilities. However, the precise form for the independent parameters m_α depends crucially upon the boundary conditions, since these determine the relation between the applied external agent $\mathbf{E}^{\text{ext}}$ and the electrolyte electric field $\mathbf{E}$. In addition, in the case of electroneutrality or in the case where the convection velocity vanishes, the constraint eq. (5.351) implies $\mathbf{E} \cdot \kappa^\psi = \mathbf{E}^{\text{ext}} \cdot \sum_{\alpha=1}^{\text{N}} F m_\alpha c_\alpha z_\alpha$. In the approximation $\mathbf{E} = \mathbf{E}^{\text{ext}}$, *i.e.* when the polarization of the electrolyte is ideal, and if the convection velocity vanishes, then eq. (5.349) implies

$$m_\alpha = \tau_\alpha^\psi \kappa^\psi / F c_\alpha \,, \tag{5.352}$$

and

$$\sum_{\alpha=1}^{\text{N}} m_\alpha \psi_\alpha = 0, \quad \text{such that} \quad \kappa^\psi = F \sum_{\alpha=2}^{\text{N}} m_\alpha c_\alpha \tilde{z}_\alpha^\psi. \tag{5.353}$$

Hence, in a binary electrolyte at electroneutral state, where $z_+ = -z_-$, and the bulk concentration $c^{\text{b}} = 1(\nu_+ + \nu_-)$, we find that in the volume description

$$m_+ = \kappa \nu_2 / F z_1 \,, \quad \text{and} \quad m_- = \kappa \nu_1 / F z_2 \,, \tag{5.354}$$

whereas in the mass description,

$$m_+ = \kappa M_2 / F z_1 \rho \,, \quad \text{and} \quad m_- = \kappa M_1 / F z_2 \rho \,. \tag{5.355}$$

6 Validation: Quaternary IL-mixture as Electrolyte in a Zinc-Ion Battery

Here, in this chapter. we validate our transport-theory for a battery-system based on a highly-concentrated electrolyte. In section 6.1, we introduce the cell-set-up and electrolyte-composition, and state the transport equations and the reactions. Next, in section 6.2, we present the simulation results of our numerical investigation. Finally, in section 6.3, we classify the electrolyte as highly concentrated (see section 5.4.7) using the as-discussed electrolyte. We provide additional information in the appendix, see appendix D.9.

6.1 Electrolyte Transport Equations and Electrolyte Composition

In order to validate our transport theory, we model a secondary zinc-ion battery (ZIB) with IL-water mixture as electrolyte which was described experimentally in Refs. 311,312.

The ZIB consists of a porous zinc-anode (zinc powder), and a Prussian-blue-analogue (PBA) cathode, which allows a reversible Zn^{2+} insertion into the host structure $FeFe(CN)_6$.[311] The electrolyte is composed of [Ch]OAc with 30 wt % water, and minor amount of zinc acetate ($Zn(OAc)_2$) (despite the high amount of water, this electrolyte can still be viewed as "highly concentrated",[311] see section 6.3).

6.1.1 Reactions and Electrolyte Species

We assume a complete dissociation of the electrolyte into Ch^+, OAc^-, $[Zn(OAc)_3]^-$, Zn^{2+}, and water according to the bulk-reactions (see table D.2)

$$\begin{aligned} [\mathrm{Ch}]\mathrm{OAc} &\rightleftharpoons \mathrm{Ch}^+ + \mathrm{OAc}^-, & (6.1)\\ 3\,\mathrm{Zn}(\mathrm{OAc})_2 &\rightleftharpoons \mathrm{Zn}^{2+} + 2\,[\mathrm{Zn}(\mathrm{OAc})_3]^-, & (6.2)\\ \mathrm{Zn}(\mathrm{OAc})_2 &\rightleftharpoons \mathrm{Zn}^{2+} + 2\,(\mathrm{OAc})^-. & (6.3)\end{aligned}$$

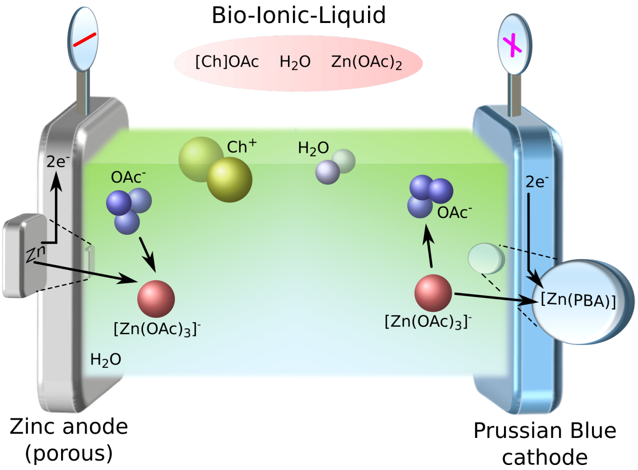

Scheme 6.1: Scheme of the zinc ion battery. Figure first published in Ref. 67.

Beneath 6.2, zinc-complexes also form via the secondary bulk-reaction

$$\mathrm{Zn^{2+}} + 3\,\mathrm{OAc^-} \rightleftharpoons [\mathrm{Zn(OAc)_3}]^-. \tag{6.4}$$

We assume that, zinc ions in the bulk electrolyte occur mainly via the complexified species $[\mathrm{Zn(OAc)_3}]^-$,[313] and that the reactions producing the zinc-complex $\mathrm{Zn(OAc)_2}$ are very fast. Beneath the bulk-reactions, heterogeneous reactions at the electrolyte-electrode interphases occur. Zinc gets deposited at the zinc-anode during charging of the cell, and dissolves from the zinc-anode during discharging the cell, $\mathrm{Zn} \rightleftharpoons \mathrm{Zn^{2+}} + 2\,\mathrm{e^-}$. However, the dissolved $\mathrm{Zn^{2+}}$-ions complexify via eq. (6.4), where we neglect the inverse reaction. Likewise, during charging the cell, zinc-ions are extracted from the cathodic PBA-structure, and inserted into the host-structure of the cathode during discharging the cell, $\mathrm{Zn^{2+}} + 2\,\mathrm{e^-} + [\mathrm{Fe(III)(CN)_6}] \rightleftharpoons [\mathrm{ZnFe(III)(CN)_6}]$. Altogether, the resulting reactions are

$$\mathrm{Zn} + 3\,\mathrm{OAc^-} \rightleftharpoons {}_2\,\mathrm{e^-} + [\mathrm{Zn(OAc)_3}]^-, \tag{6.5}$$

$$[\mathrm{Zn(OAc)_3}]^- + 2\,\mathrm{e^-} + [\mathrm{Fe(III)(CN)_6}] \rightleftharpoons {}_3\,\mathrm{OAc^-} + [\mathrm{ZnFe(III)(CN)_6}]. \tag{6.6}$$

Note that the ionic choline-species only participates in the dissociation reaction eq. (6.1), and is thus modelled non-reactive in our approach. We illustrate the electrolyte composition and the species reactions in Scheme 6.1 (see also appendix D.9 for more details).

6.1.2 Model Equations

Here, we state the complete set of electrolyte-transport-equations using porous electrode theory. For supplemental material, see appendix D.9.

The electrolyte is composed of water, Ch^+, OAc^-, and $[\mathrm{Zn(OAc)_3}]^-$. Here, we choose water as first species, *i.e.* $\tilde{z}_\alpha = z_\alpha$ (section 6.2.3 for different choices). Because of electroneutrality, *i.e.* $\varrho_\mathrm{F} = 0$, the charge density is not a free variable. Hence, we discard the Poisson equation and replace $\partial_t \varrho_\mathrm{F} = 0$ by $\boldsymbol{\nabla} \boldsymbol{\mathcal{J}}_\mathrm{F} = 0$. By assumption, temperature appears only as constant parameter and we neglect non-ideal contributions ($f_\alpha c = 1$) such that $\varphi_\mathrm{H}^\mathrm{int} = 0$, and we assume a constant viscosity ($\lambda = 25.3\,\mathrm{mPa\,s}$ and $\eta = 0$).[314] The two independent concentrations c_3 and c_4 determine c_1 and c_2 via eqs. (5.222) and (5.223) (where $\varrho_\mathrm{F} = 0$).

According to porous electrode theory, we modify the set of transport equations, eqs. (5.244) to (5.246)).[315] ,

$$\partial_t \left(\varepsilon c_\alpha\right)|_{\alpha=3,4} = -\boldsymbol{\nabla}\left(\varepsilon c_\alpha \mathbf{v}\right) - \boldsymbol{\nabla}\left(\varepsilon^\beta \boldsymbol{\mathcal{N}}_\alpha\right) + r_\alpha, \tag{6.7}$$

$$0 = \boldsymbol{\nabla}\left(\varepsilon^\beta \boldsymbol{\mathcal{J}}_\mathrm{F}\right) = -\boldsymbol{\nabla}\left(\varepsilon \varrho_\mathrm{F} \mathbf{v}\right) + \sum_{\alpha=1}^{4} F z_\alpha r_\alpha, \tag{6.8}$$

$$\boldsymbol{\nabla}\left(\varepsilon \mathbf{v}\right) = \sum_{\alpha=1}^{4} \nu_\alpha \cdot r_\alpha - \frac{\tilde{\nu}_2}{F \tilde{z}_2} \cdot \boldsymbol{\nabla}\left(\varepsilon^\beta \boldsymbol{\mathcal{J}}_\mathrm{F}\right) - \sum_{\alpha=3}^{4} \tilde{\tilde{\nu}}_\alpha \cdot \boldsymbol{\nabla}\left(\varepsilon^\beta \boldsymbol{\mathcal{N}}_\alpha\right). \tag{6.9}$$

where $\varepsilon = V^\mathrm{l}/V$ is the volume-fraction of the liquid phase relative to the overall volume (often called "porosity") and the material parameter β is the so-called Bruggemann coefficient, which phenomenologically accounts for the specific microstructure.

We neglect bulk reactions and model the chemical reactions occuring at the electrodes, eqs. (6.5) and (6.6), as source-terms for eqs. (6.7) to (6.9) via

$$r_\alpha = \sum_k a^\Gamma \cdot \nu_{k;\alpha}^\Gamma \cdot i_k^\Gamma. \tag{6.10}$$

Thus, the species reactions r_α include all reactions k of species α at all electrodes Γ. Each species-reaction contributes via a stoichiometric factor $\nu_{k;\alpha}^\Gamma$. The specific electrode-surfaces a^Γ measure the surface to volume ratio of the electrode Γ. The quantity i_k^Γ is the surface-reaction rate, which comprises the interface-conditions between the electrodes and the electrolyte via a Butler-Vollmer Ansatz.[316]

6.2 Simulation Results

In this section, we discuss the results of our numerical simulations. First, in section 6.2.1, we simulate galvanostatic discharge and charge of the ZIB by applying a moderate discharge current, and compare the results for the specific capacities and cell voltage with experimental observations, and study the evolution of the spatial profiles for the species concentrations and the convection velcoity. In section 6.2.2, we probe for increased discharge dynamics . Finally, in section 6.2.3, we show simulation results for discharging the cell using different reference frames.

6.2.1 Electrolyte Dynamics: Diffusion, Migration and Convection

We apply an external current density of $I = 0.1\,\mathrm{mA\,cm^2}$ and study the galvanostatic discharge and charge of the ZIB. Subfigure a) in fig. 6.1 illustrates the specific cell capacities and the cell voltage during discharging and charging the cell, where the results of simulations and experiment are in good agreement. Because our model does not capture atomistic processes in the solid phase, it cannot reproduce the two discharge-phases (with transition at roughly $20\,\mathrm{mA\,h\,g^{-1}}$) in experimental curve, which can be attributed to two different electro-reactivities of the PBA-material, stemming from distinct spin-phases of Fe(III).[311]

Next, we discuss the interplay between the transport mechanisms migration, diffusion and convection with electrode reactions, and the influence on cell performance. For this purpose, we designate characteristic moments of discharge. Subfigure b) in fig. 6.1 shows the cell voltage versus time of discharge, and all designated moments highligting the initial phase ($t = 250\,\mathrm{s}, 420\,\mathrm{s}, 520\,\mathrm{s}$), the intermediate phase ($t = 15\,000\,\mathrm{s}, 25\,000\,\mathrm{s}$), and the moment of complete cell-discharge ($t = 48\,000\,\mathrm{s}$). We show that the dynamical quantities $\mathbf{v}$, $\mathbf{v}_\alpha$, c_α, Φ at these moments reveal all significant discharge-processes during cell-operation.

Figure 6.2 shows the evolution of the convection velocity (subfigure a), and the

Species	$\tilde{z}_\alpha$	c_α^0 / mol m^{-3}	$\rho_\alpha^0/\sum_{\alpha=1}^4 \rho_\alpha^0$	ν_α / m^3 mol^{-1}	$c_\alpha^0 \nu_\alpha/-$
H_2O	0	$19.43{\cdot}10^3$	0.25	$1.8{\cdot}10^{-5}$	0.35
Ch^+	1	$5.00{\cdot}10^3$	0.39	$7.0{\cdot}10^{-5}$	0.35
OAc^-	−1	$4.00{\cdot}10^3$	0.18	$5.5{\cdot}10^{-5}$	0.22
$[Zn(OAc)_3]^-$	−1	$1.00{\cdot}10^3$	0.18	$8.0{\cdot}10^{-5}$	0.08

Table 6.1: Initial electrolyte composition and effective species-valences in the reference-frame where water is the designated species ($\alpha = 1$).

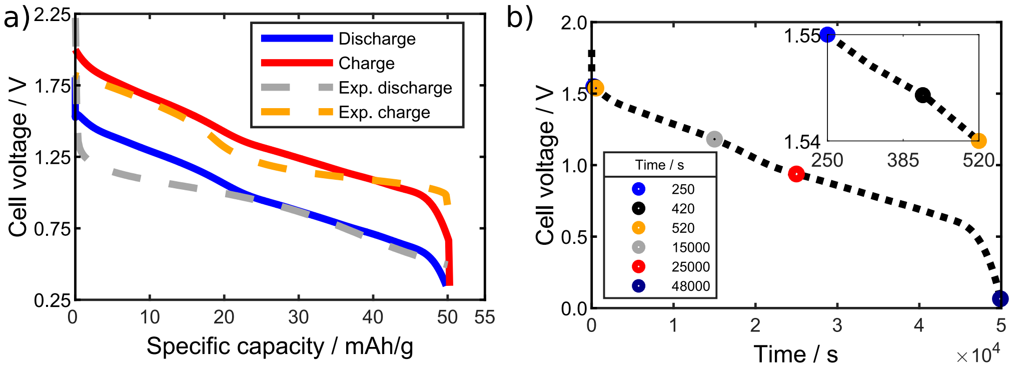

Figure 6.1: a) Cell voltage versus specific capacities during galvanostatic discharging and charging the cell (applied external current density $I = 0.1\,\mathrm{mA\,cm^2}$). b) Cell voltage during discharge versus discharge time. The bullets illustrate designated moments during the discharge-process. The inset highlights the designated moments in the initial discharge-phase. Figures first published in Ref. 67.

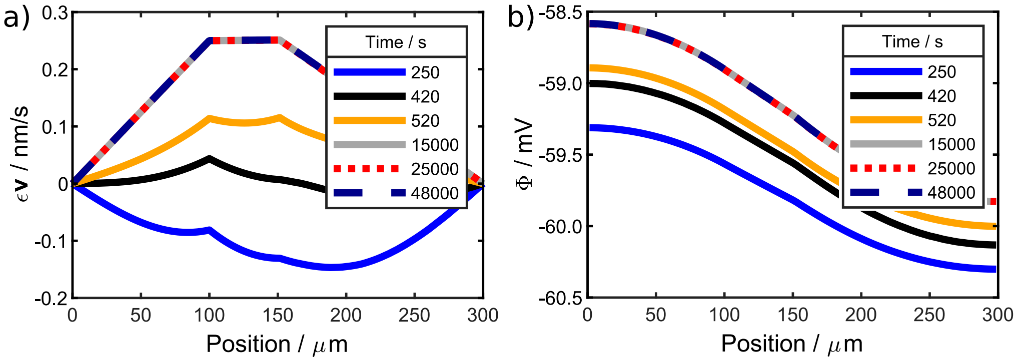

Figure 6.2: Temporal evolution of the convection profile (subfigure a), and the electric potential (subfigure b). Apparently, the convection velocity changes direction during discharge, and the cathode is more electronegative than the anode. Figures first published in Ref. 67.

electric potential (subfigure b). Both exhibit a similar behaviour: the initial phase is characterized by major changes in the profile, which quickly relax towards stationarity, whereas, at later times, the profiles remain effectively constant. This suggests that the initial phase constitutes a transient phase, during which the electrolyte exhibits strong dynamics and relaxes towards a quasi-stationary state.

The convection velocity changes it's direction from towards the anode (negative sign), to towards the cathode (positive sign) during the transient phase (see subfigure a) in fig. 6.2). At all later times, the convection velocity is directed towards the cathode. In contrast, the electrolyte electric potential Φ exhibits roughly a constant gradient from anode to cathode ($\Delta\Phi \approx -0.1\,\mathrm{mV}$) at all times during discharge (see subfigure b in fig. 6.2). Thus, the cathode is more electronegative than the anode, which implies that migration pulls OAc^--ions and $[\mathrm{Zn(OAc)_3}]^-$-ions towards the anode, and Ch^+-cations towards the cathode. Thus migration hinders the cell-operation, which relies on the cathode reactions involving the $[\mathrm{Zn(OAc)_3}]^-$-ions, see eq. (6.6). As consequence, diffusion and convection must overcompensate migration to sustain cell operation.

Figure 6.3 shows the evolution of the volume-fractions $c_\alpha \mathrm{v}_\alpha$, *i.e.* of the species concentrations (since the partial molar volumes are constant). Similar to the behaviour of $\mathbf{v}$ and Φ (fig. 6.2), the concentration-profiles exhibit an initial dynamical phase, where concentration differentials from anode to cathode grow, followed by a quasi-stationary phase.

Dynamics	t/s	Direction $\mathbf{v}_{\mathrm{H_2O}}$	$\mathbf{v}_{\mathrm{Ch}^+}$	$\mathbf{v}_{\mathrm{OAc}^-}$	$\mathbf{v}_{[\mathrm{Zn(OAc)_3}]^-}$
Transient phase	250	chaotic/mixed	cathodic	anodic	cathodic
	420	chaotic/mixed	cathodic	anodic	mixed
	520	chaotic/mixed	cathodic	anodic	cathodic
Quasi-stationary	15000	anodic	anodic	anodic	cathodic
	25000	anodic	anodic	anodic	cathodic
	48000	anodic	anodic	anodic	cathodic

Table 6.2: Species veolicities $\mathbf{v}_\alpha$ at different moments of discharge. "Anodic" direction: negative velocity-profile; "cathodic": positive velocity-profile.

Table 6.2 summarizes the directions of the species-velocities $\mathbf{v}_\alpha$ during discharge. The motion of the OAc^--ions towards the anode, and of the $[\mathrm{Zn(OAc)_3}]^-$-ions towards the cathode both favor the crucial electrode reactions eqs. (6.5) and (6.6) which thus sustains cell operation. In contrast, the velocities of water and the Ch^+-ions exhibit change direction. The direction of water is highly non-uniform during the transient phase, and relaxes towards an averaged anodic direction at later times. Likewise, the direction of the non-reacting Ch^+-velocity switches from towards the cathode to towards the anode after the transient phase.

Because of the mutually coupled transport equations, see eqs. (6.7) to (6.9), similar dynamical behaviour and common transient times of $\mathbf{v}$, Φ, c_α and $\mathbf{v}_\alpha$ is to be

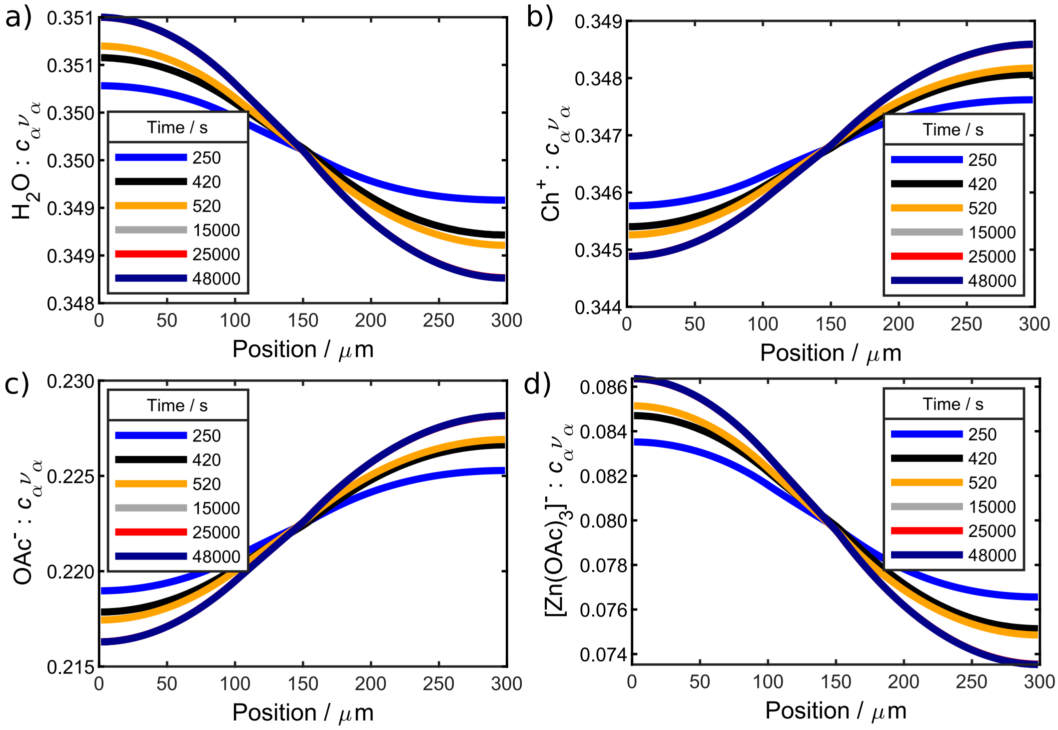

Figure 6.3: Temporal evolution of the volume fractions of all species. Since ν_α are constant, these figures illustrate the time-evolution of the species-concentrations. See table 6.1 for the values of c^0_α, and ν_α. Figures first published in Ref. 67.

expected from an analytical point of view, and suggests that there exists common initiation-mechanism. Initially, the electrolyte is in equilibrium, where all quantities $\mathbf{v}$, Φ, c_α, $\mathbf{v}_\alpha$ are homogenously constant (see table 6.1). The application of external discharge currents pushes the electrolyte out of this equilibrium state, where spontaneous electrode reactions drive the interface-dynamics, and the system variables experience a dynamical phase. The electrolyte evolves towards a quasi-stationary state (for the constant discharge currents), and, after some transient time, the quantities remain almost constant.

In the following, we give a detailed analysis of the evolution of each electrolyte species, and derive a rational interpretation of the electrolyte behaviour.

We first discuss the dynamics of the reacting species, *i.e.* $[Zn(OAc)_3]^-$ and OAc^-, which sustain cell-operation via the electrode reactions eqs. (6.5) and (6.6). The concentration of the nagative zinc-complex increases at the anode and decreases at the cathode at all times during discharging the cell (see fig. 6.3d)). However, the formation of the concentration gradient is in competition with the net flux of

$[Zn(OAc)_3]^-$ towards the cathode at all times (see table 6.2). Thus, the net increase of $[Zn(OAc)_3]^-$-concentration at the anode during the transient-phase implies that the process of $[Zn(OAc)_3]^-$-production via the dissolution of zinc near the anode (see eq. (6.5)) dominates over transport towards the cathode. This favors cell-operation, as it ensures a sufficient supply of $[Zn(OAc)_3]^-$-ions for transport towards the cathode (which is crucial for the operation of the cell, see eq. (6.6)). After this transient phase, transport and species production are balanced and the concentration profile of $[Zn(OAc)_3]^-$ becomes quasi-stationary. Nevertheless, there is a net flux of $[Zn(OAc)_3]^-$-ions towards the cathode at all times (see table 6.2). This suggests that $[Zn(OAc)_3]^-$-diffusion towards the cathode, due to stark concentration gradients (see subfigure d in fig. 6.3), dominates over the migrational pull of the$[Zn(OAc)_3]^-$-anions towards the more electro-positive anode (see fig. 6.2).

We make a similar observation for the dynamics of the OAc^--ions. Initially, during the transient phase, the concentration of OAc^--ions increases near the cathode and decreases near the anode, see fig. 6.3c). Due to the net flux of OAc^--ions towards the anode at all times (see table 6.2), local production of OAc^--ions at the cathode via eq. (6.6) dominates over the anodic flux of OAc^--ions. As for the $[Zn(OAc)_3]^-$-ions, both competing processes are in quasi-equilibrium after the transient-phase. In contrast to the $[Zn(OAc)_3]^-$-ions, the negative OAc^--flux is a combined result of diffusion and migration, which both push the OAc^--ions into the same direction towards the anode.

During the transient phase, concentration gradients of Ch^+-ions are formed. At all times, the concentration of Ch^+-ions at the more electronegative cathode is higher than at the anode (see fig. 6.3b)). During the initial phase, the pulls of migration of the Ch^+-ions towards the cathode is supported by a net flux directed towards the cathode (see table 6.2). Once the system becomes quasi-stationary, the net-flux of Ch^+-ions reverses it's direction towards the anode. Together with diffusion, it is then in equilibrium with the migrational pull of the Ch^+-ions towards the cathode.

In contrast to the charged species, the neutral water exhibits a highly non-homogeneous velocity-profile during the transient phase (see table 6.2). This suggests that water serves as local supply for volume-compensation due to volumetric redistributions, and effectively balances local volume-inhomogeneities. After relaxation of the system, the velocity of water is directed towards the anode. Note that, in our model, water has by far the lowest partial molar volume , and is abundant compared to the ionic species (see table 6.1).

Next, we evaluate the influence of the electrode-reactions on convection (see eqs. (6.5) and (6.6)). A simple balancing shows that, although $[Zn(OAc)_3]^-$-ions have the largest partial molar volume, OAc^--ions are the dominant species with respect to volume-production (see table 6.1). The consumption of one $[Zn(OAc)_3]^-$-ion

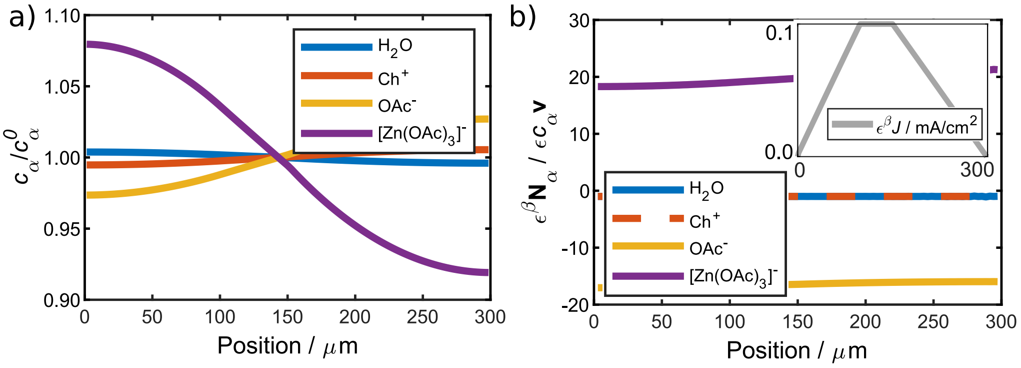

Figure 6.4: a) Normalized concentration profiles at end-of-discharge. b) Convective versus non-convective species-transport at end-of-discharge. The inset illustrates the conduction current density at end-of-discharge. Figures first published in Ref. 67.

per cathode reaction (eq. (6.6)) produces three OAc$^-$-ions at the cathode, and thus consumes a net-molar-volume of $3\nu_{\mathrm{OAc}^-} - \nu_{[\mathrm{Zn(OAc)_3}]^-} > 0$. Thus, near the cathode, "molar volume is produced", which pushes bulk electrolyte towards the anode. The same, "inverse" process (per reaction) occurs at the anode, where a net volume (occupied by three OAc$^-$-ions) is at disposal for replacement of bulk-electrolyte. Thus, in each anode-reaction, a net amount of "available" volume is produced, which is then compensated by bulk electrolyte. Therefore, during the transient phase, where the electrode-reactions are dominant, both processes induce anodic convection. This is in agreement with subfigure a) in fig. 6.2, which shows a "negative" convection during the initial phase. As discussed above, after the initial phase, the reactions are in equilibrium with transport. Then, convection is the delicate trade-off between the transient currents.

Subfigure a) in fig. 6.4 illustrates the normalized concentration profiles of all electrolyte species at end-of-discharge. Water and Ch$^+$-ions exhibit moderate gradients. Because water is electrically neutral, it is not susceptible to migration. Thus, the concentration profile is formed via diffusion and convection. As explained above, positive Ch$^+$-ions acumulate near the more electronegative cathode, whereas the concentration gradient throughout the cell is not very pronounced. Although OAc$^-$-ions and [Zn(OAc)$_3$]$^-$-ions are both negatively charged, their concentration gradients have opposite direction. This property is mandatory for cell-operation. Large concentration gradients of the [Zn(OAc)$_3$]$^-$-ions imply that diffusion towards the anode overcompensate migration towards the more electropositive anode, which sustains cell operation via eq. (6.6). Likewise, a net transport of OAc$^-$-ions towards the anode is mandatory (see eq. (6.5)), which is constituted by the collaboration of migrational, and diffusion (due to the small concentration gradient).

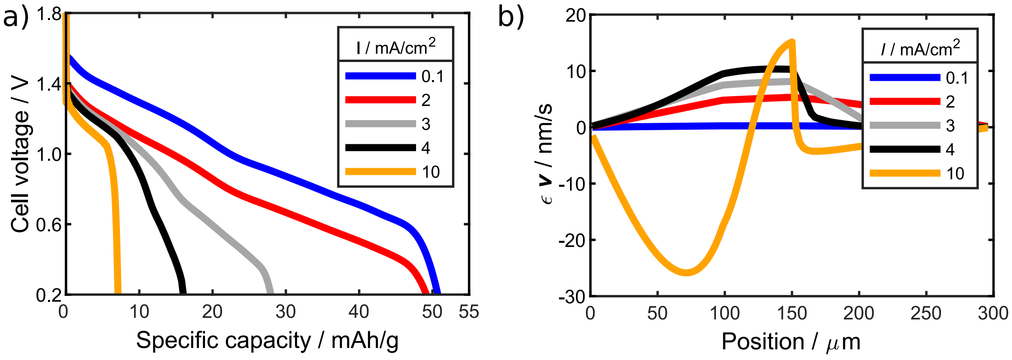

Figure 6.5: a) Cell voltage versus specific capacity under increased discharge currents. b) Convection profiles at end-of-discharge under increased discharge currents. Figures first published in Ref. 67.

Subfigure b) in fig. 6.4 illustrates the relevance of convective versus non-convective transport for all electrolyte species. The inset shows the center-of-mass electric current $\varepsilon^{\beta}\boldsymbol{\mathcal{J}}_{\mathrm{F}}$ at end-of-discharge. The quantity $\varepsilon^{\beta}\boldsymbol{\mathfrak{N}}_{\alpha} = \varepsilon^{\beta}c_{\alpha}(\mathbf{v}_{\alpha} - \mathbf{v})$ measures flux-densities within the center-of-mass system, whereas the quantity $\varepsilon c_{\alpha}\mathbf{v}$ measures the mass flux of species α induced by the center-of-mass velocity. As consequence, the ratio $|\varepsilon^{\beta}\boldsymbol{\mathfrak{N}}_{\alpha}/\varepsilon c_{\alpha}\mathbf{v}|$ is larger than one (roughly one), if convection is negligible (dominant) for the transport in the corresponding species. However, beneath the magnitude of this ratio, it's sign also bears important data. The positivity of $\mathbf{v}$ at end-of-discharge (see fig. 6.2) implies that negative (positive) ratios correspond to species-fluxes $\boldsymbol{\mathfrak{N}}_{\alpha}$ towards the anode (cathode). We shall first evaluate the (absolute) magnitudes of the flux-ratio $|\varepsilon^{\beta}\boldsymbol{\mathfrak{N}}_{\alpha}/\varepsilon c_{\alpha}\mathbf{v}|$. Apparently, convective flux contributions are negligible for the two negative species. In contrast, convection plays a significant role for the dynamics of water, and the Ch^{+}-ions. Thus, convection is important for those species that do not contribute to the half-cell reactions. This endorses our interpretation from above, that water serves as local "volume-supply", which balances volumetric redistributions as consequence of electrode-reactions. Next, we infer from the sign of the flux-ratio $\varepsilon^{\beta}\boldsymbol{\mathfrak{N}}_{\alpha}/\varepsilon c_{\alpha}\mathbf{v}$ that, at end-of-discharge, OAc^{-}-ions move towards the anode, whereas $[\mathrm{Zn(OAc)_3}]^{-}$-ions move towards the cathode. The latter property confirms our previous finding that diffusion of $[\mathrm{Zn(OAc)_3}]^{-}$-ions overcompensates migration.

6.2.2 Increased Electrolyte Dynamics

In this section, we study how increased external discharge currents affect the electrolyte dynamics. This investigation illustrates the power-limiting mechanisms of the IL electrolyte.

Figure 6.5a) illustrates the cell performance under increased discharge currents. Apparently, for moderately increased discharge currents (up to $2\,\mathrm{mA\,cm^{-2}}$), the discharge curves preserve their shape, despite being shifted to decreased discharge capacities. At higher discharge currents ($3\,\mathrm{mA\,cm^{-2}}$ to $10\,\mathrm{mA\,cm^{-2}}$), steep voltage drops lead to strong capacity fades. This suggests that, under increased discharge currents, diffusion becomes too slow, as to supply the cathodic interfacial reaction mechanism with sufficient amount of $[\mathrm{Zn(OAc)_3}]^-$-ions. We confirm this assumption below, which is typical for highly viscous electrolytes.[317]

Figure 6.5b) illustrates the profiles for the convection velocity at end-of-discharge for each discharge current. Apparently, for all but the highest current, the convection velocities are directed towards the cathode (at end-of-discharge). However, for the limiting discharge current $I = 10\,\mathrm{mA\,cm^{-2}}$, we observe a heterogeneous profile for the convection velocity, which changes it's direction across the cell. Notably, a steep decrease can be observed between the separator and the cathode (at $15\,\mathrm{\mu m}$). Apparently, convection velocity pushes bulk electrolyte towards the anode everywhere, except for the separator-region. We discuss this anomalous behaviour below.

Figure 6.6 shows the normalized species concentrations at end-of-discharge for all discharge currents. For all but the highest current, the concentration-gradients increase with increasing currents. Hence, for these currents, increasing the electrolyte dynamics leads to more pronounced. However, subfigures a) and b) illustrate that, even for the limiting discharge currents, the dynamics of the non-reacting species water and $\mathrm{Ch^+}$-ions is not dramatically affected. Although the concentration gradients increase, enhancing the dynamics does not lead to cell regions where these species are effectively depleted. This is in contrast to the reacting species $\mathrm{OAc^-}$-ions and $\mathrm{Zn(OAc)_2}$-ions. Except for the limiting discharge current ($I = 10\,\mathrm{mA\,cm^{-2}}$), increasing the dynamics favors $\mathrm{OAc^-}$-depletion near the anode, and $[\mathrm{Zn(OAc)_3}]^-$-depletion near the cathode. This confirms our explanation from above, that diffusion becomes too slow as to supply the interfacial reaction-mechanisms with sufficient amount of salt-species (increasing the discharge current increases the interfacial reaction-rates).

Finally, we shall investigate the anomalous electrolyte profiles appearing for the limiting discharge current. Figure 6.7 illustrates the electrolyte dynamics for the discharge current $I = 10\,\mathrm{mA\,cm^{-2}}$. We follow the rationale from section 6.2.1 and designate characteristic moments during discharge of the cell, see subfigure a). Compared to the capacities obtained by moderate discharge currents (see fig. 6.5), the capacity of the cell is highly reduced, approximately from $50\,\mathrm{mA\,h\,g^{-1}}$ to roughly $7\,\mathrm{mA\,h\,g^{-1}}$.

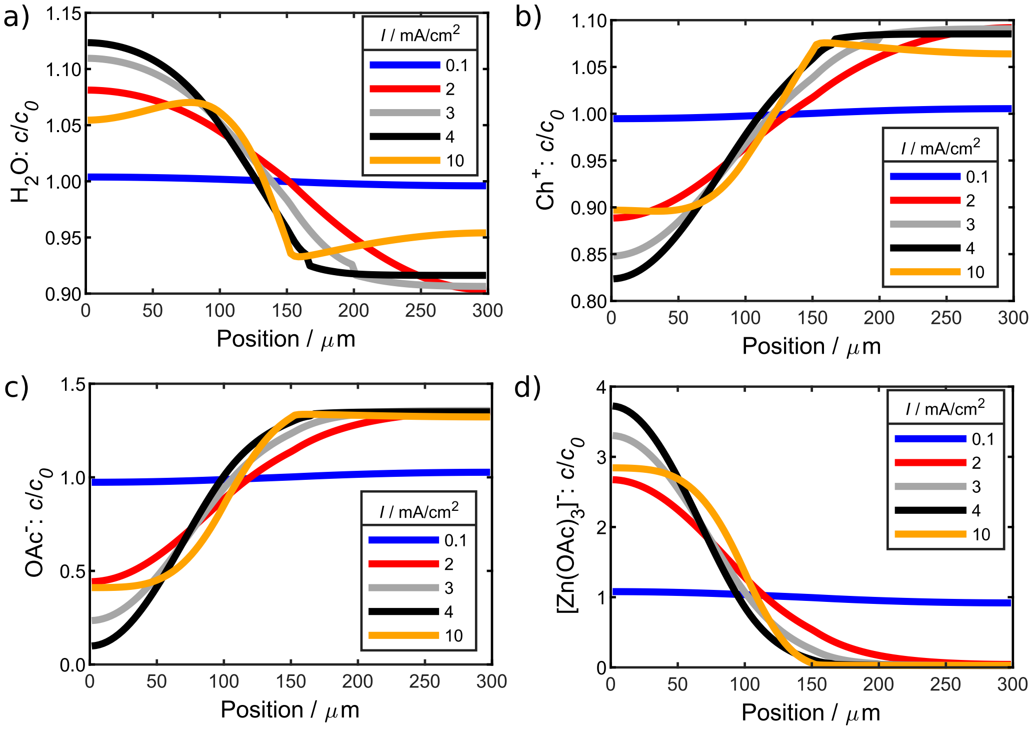

Figure 6.6: Normalized species-concentrations at end-of-discharge under increased discharge currents. See table 6.1 for the initial species-concentrations c_α. Figures first published in Ref. 67.

This sggests that the enhanced electrolyte dynamics leads to a premature breakdown of cell-operation. Subfigure b) shows the normalized concentration profiles at the designated moments. Apparently, at end of discharge, the $[\mathrm{Zn(OAc)_3}]^-$-species gets completely depleted at the cathode and the cell-operation cannot be sustained anymore (see eq. (6.6)). As consequence, the discharging process stops. The inset in subfigure b) in fig. 6.7 illustrates the profile for the convection velocity at the designated moments. At all times, the profiles exhibit a highly non-uniform shape. However, towards the end-of-discharge, convection stops at the cathode. We suggest that this is also due to reactand depletion. Following our argument from above (see section 6.2.1), the Faradaic convection-stimulus stops, when no more OAc^--ions are formed anymore due to the breakdown of the interface reaction eq. (6.6). The premature breakdown of cell-operation also explains the concentration profiles near the interfaces for the highest discharge current (see fig. 6.6). Diffusion limitation stops cell-operation before a quasi-stationary state can be established.

Altogether, increased discharge dynamics lead to enhanced electrolyte-profiles.

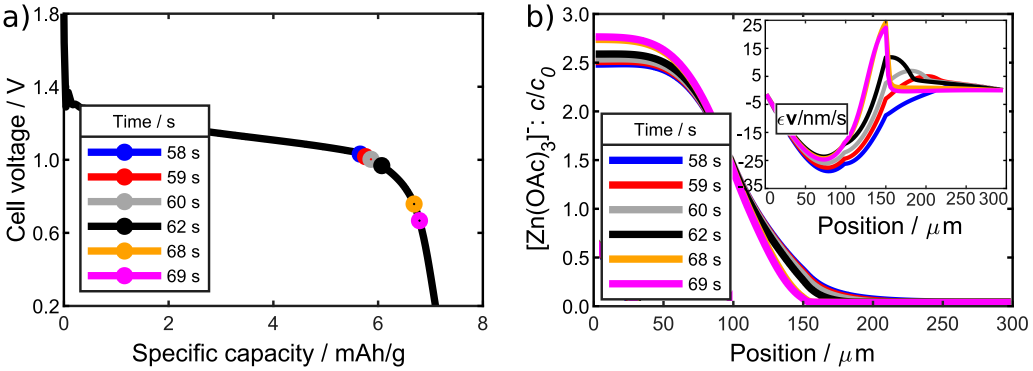

Figure 6.7: a) Cell voltage for limiting discharge current $I = 10\,\mathrm{mA\,cm}^2$, and designated moments. b) Normalized concentration profile for the $[\mathrm{Zn(OAc)_3}]^-$-species. The inset illustrates the convection profile at the designated moments. Figures first published in Ref. 67.

However, this trend is restricted by diffusion limitation. Once the dynamics become too fast, the interplay between the different transport mechanisms (diffusion, migration and convection) becomes unstable and cell operation breaks down.

6.2.3 Consistency Check: Varying Reference Species

In this section we probe the consistency of our framework by varying the designated reference species. For this purpose, we simulate discharging of the battery with $I = 0.1\,\mathrm{mA\,cm}^{-2}$ in two different frames. based on charged ion-species as reference-species, see table 6.3.

Because the representations of the Onsager matrices in the different frames cannot be chosen independently, the differing descriptions are not independent. In a mixture of N species, a total of N(N+1)/2 transport parameters exist (see section 5.3.1). All follow from $\boldsymbol{\mathcal{L}}$, which is defined relative to the designated species. However, $\boldsymbol{\mathcal{L}}$ comprises the complete set of inter-species correlations, including correlations involving the designated species. This follows directly from the closure-relation for the independent mass-fluxes eq. (5.115), which implicitely determine $\boldsymbol{\mathcal{N}}_1$ via eq. (5.103). Thus, the Onsager-matrices with respect to different designated species are mutually coupled, and cannot be stated independently from each other. In appendix D.8, we derive simple conversion relations, which allow to transfer Onsager-coefficients (eq. (D.84)) and transference numbers (eqs. (D.89) and (D.91)) between the different choices of reference species. In appendix D.8, we derive the exact transformations, see eqs. (D.104) to (D.106).

Reference	Species	$\tilde{z}_\alpha$	t_α	$t_\alpha/\tilde{z}_\alpha$	$\mathcal{N}_\alpha^{\mathsf{migr}} \updownarrow\updownarrow \mathcal{J}_\mathrm{F}$
Water	Water	0	*n.d.*	*n.d.*	*n.d.*
	Ch^+	1	0.166	0.166	$\mathcal{N}_\alpha^{\mathsf{migr}} \upuparrows \mathcal{J}_\mathrm{F}$
	OAc^-	-1	0.129	-0.129	$\mathcal{N}_\alpha^{\mathsf{migr}} \uparrow\downarrow \mathcal{J}_\mathrm{F}$
	$[\mathrm{Zn(OAc)_3}]^-$	-1	0.705	-0.705	$\mathcal{N}_\alpha^{\mathsf{migr}} \uparrow\downarrow \mathcal{J}_\mathrm{F}$
Ch^+	Water	-0.170	-1.549	9.112	$\mathcal{N}_\alpha^{\mathsf{migr}} \upuparrows \mathcal{J}_\mathrm{F}$
	Ch^+	0	*n.d.*	*n.d.*	*n.d.*
	OAc^-	-1.570	0.203	-0.129	$\mathcal{N}_\alpha^{\mathsf{migr}} \uparrow\downarrow \mathcal{J}_\mathrm{F}$
	$[\mathrm{Zn(OAc)_3}]^-$	-3.330	2.346	-0.704	$\mathcal{N}_\alpha^{\mathsf{migr}} \uparrow\downarrow \mathcal{J}_\mathrm{F}$
$[\mathrm{Zn(OAc)_3}]^-$	Water	0.074	0.665	8.986	$\mathcal{N}_\alpha^{\mathsf{migr}} \upuparrows \mathcal{J}_\mathrm{F}$
	Ch^+	1.430	0.237	0.166	$\mathcal{N}_\alpha^{\mathsf{migr}} \upuparrows \mathcal{J}_\mathrm{F}$
	OAc^-	-0.757	0.098	-0.129	$\mathcal{N}_\alpha^{\mathsf{migr}} \uparrow\downarrow \mathcal{J}_\mathrm{F}$
	$[\mathrm{Zn(OAc)_3}]^-$	0	*n.d.*	*n.d.*	*n.d.*

Table 6.3: Spatially averaged results for the transference-numbers t_α, with respect to different reference-frames. In each reference frame, $\sum_{\alpha=2}^{\mathrm{N}} t_\alpha = 1$, and no transference-numbers for the designated species ($\alpha = 1$) exist (*n.d.*, not defined).

In order to probe consistency at different length scales, we first discuss simulation results for the cell-voltage and the concentration of the $[\mathrm{Zn(OAc)_3}]^-$-ions, which both must not depend upon the choice of reference species, and, next, discuss simulation results for the frame dependent transference numbers (see also appendix D.8).

Invariant Elelctrolyte Quantities: Cell Voltage and Species Concentrations

Figure 6.8a) shows that the discharge curves in the three different reference-frames agree. Since the cell-voltage is a mesoscopic observable, which is easily accessible to experimental measurements, this proves consistency. Next, we compare simulation results for microscopic quantities. Figure 6.8b) shows that the results for $c_{[\mathrm{Zn(OAc)_3}]^-}$ at end of discharge, and for two different frames of reference, agree. This proves microscopic consistency (note that the $[\mathrm{Zn(OAc)_3}]^-$-ions serve as designated species in the second frame, see table 6.3). The inset shows that the relative error between the results lies within numerical accuracy of the simulations (see appendix D.9).

Altogether, we conclude that our framework produces consistent results, independent of the choice of designated species for different length scales.

Non-invariant Electrolyte Quantities: Transference Numbers

Transport parameters, *e.g*, transference numbers, depend on the choice of refer-

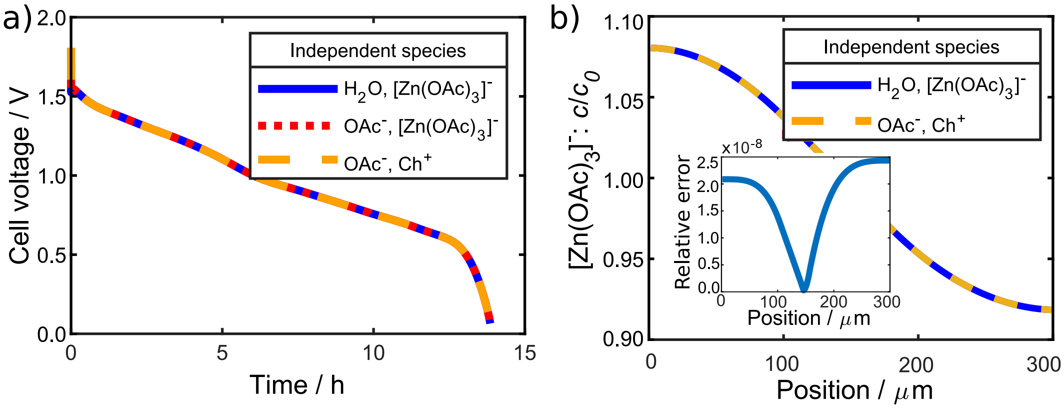

Figure 6.8: Comparison of simulation results using different physical species as reference. Subfigure a) shows the discharge curve for three different reference-species. Subfigure b) shows the concentration profile of the $[Zn(OAc)_3]^-$-ions at end of discharge in two different reference frames. The inset in subfigure b) shows the relative error of the $[Zn(OAc)_3]^-$-concentrations. See table 6.3 for the definitions of the different reference-frames. Figures first published in Ref. 67.

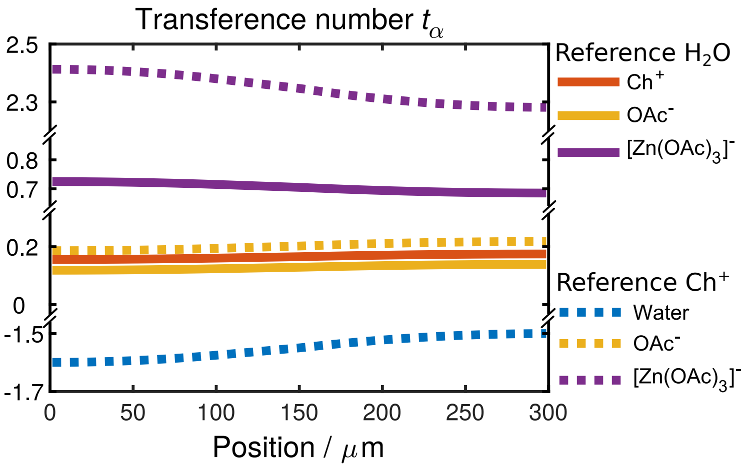

Figure 6.9: Transference numbers with respect to the indicated reference-frames. Figure first published in Ref. 67.

ence species (see appendix D.8). Here, we discuss the simulation results for the transference numbers at end-of-discharge for the three different reference species.

In this quaternary electrolyte, only two out of the three transference numbers are independent. When we use a charged reference-species, then $\tilde{z}_\alpha \neq z_\alpha$, *i.e.* neutral water becomes effectively charged and contributes to the center-of-mass flux $\mathcal{J}_\mathrm{F}$.

In fig. 6.9, we show the transference numbers for two different reference-frames. This figure is supplemented by table 6.3, which summarizes the spatially averaged t_α-values for all three reference-frames at end-of-discharge, and where the valences $\tilde{z}_\alpha$ in the three frames are stated (note that $\tilde{z}_\alpha \neq z_\alpha$ if $z_1 \neq 0$). Furthermore, table 6.3 comprises the quantities $t_\alpha/\tilde{z}_\alpha$ in the different frames. These ratios relate the migration-part $\mathcal{N}_\alpha^\mathsf{migr}$ of the mass-flux $\mathcal{N}_\alpha$ to the current-flux $\mathcal{J}_\mathrm{F}$ via (see eq. (5.131))

$$\mathcal{N}_\alpha^\mathsf{migr} = t/F\tilde{z}_\alpha \cdot \mathcal{J}_\mathrm{F}. \tag{6.11}$$

Thus, if the quantity $t_\alpha/\tilde{z}_\alpha$ is negative (positive), then $\mathcal{N}_\alpha^\mathsf{migr}$ and $\mathcal{J}_\mathrm{F}$ have opposite (like) direction. However, in the case $t_\alpha/\tilde{z}_\alpha < 0$, the "complete" mass-flux can still be directed along the flux $\mathcal{J}_\mathrm{F}$, if the diffusion-part in $\mathcal{N}_\alpha$ overcompensates the migration-part (this is the case for the $[\mathrm{Zn(OAc)_3}]^-$-species). Furthermore, the absolute values $|t_\alpha/\tilde{z}_\alpha|$ serve as measure for the overall current-contribution of the species. In this sense, the quantities $t_\alpha/\tilde{z}_\alpha$ comprise more physical data than the transference-numbers t_α. In other words, sign and magnitude of a transference number is meaningless, if the quantities $\tilde{z}_\alpha$ are not known.

In accordance with our analytic finding in appendix D.8, we observe in fig. 6.9 that sign and magnitude of transference numbers for like species differ between the frames. Thus, the transference numbers depend on the reference species.

Intuitive choice for the reference-species is the setting where water serves as designated species. In this setting, the signs of transference numbers endorse our interpretation of the overall electrolyte dynamics, discussed above. Apparently, at end-of-discharge, the migration-part of the mass-flux, $\mathcal{N}^\mathsf{migr}_{[\mathrm{Zn(OAc)_3}]^-}$, and the current $\mathcal{J}_\mathrm{F}$ have opposite direction, see table 6.3. However, we infer from the inset in fig. 6.4 that $\mathcal{J}_\mathrm{F}$ is directed towards the cathode, and from fig. 6.2b), and fig. 6.4b), that the complete mass-flux $\mathcal{N}_{[\mathrm{Zn(OAc)_3}]^-}$ is directed towards the cathode. Thus, diffusion dominates over migration and is the main driving force for cell operation. In the reference-frames defined by Ch^+, and $[\mathrm{Zn(OAc)_3}]^-$, water acquires an effective charge and contributes to the electric current. The corresponding transference number is negative in the Ch^+-frame, and positive in the $[\mathrm{Zn(OAc)_3}]^-$-frame. Interestingly, t_{OAc^-} is almost similar in the neutral frame, and the frame defined by Ch^+. In contrast, a significant discrepancy is observed for $t_{[\mathrm{Zn(OAc)_3}]^-}$.

Next, we probe these numerical results by comparison with our analytical findings for the conversion relations for transference numbers between different reference-frames derived in appendix D.8.

For this purpose, we use the numerical results for the transference numbers in the frame where water is the designated species, and calculate the corresponding transference numbers in the two other (charged) frames via eqs. (D.89) and (D.91). Then, we compare these analytical results with the numerical results in these frames. However, we first clarify the notation, and state the conversion relations (derived in appendix D.8),

$$t_B^{(A)}|_{B\neq A,C} = \tilde{z}_B^{(A)}/\tilde{z}_B^{(C)} \cdot t_B^{(C)}, \tag{6.12}$$

$$t_C^{(A)}|_{C\neq A} = -\sum_{D\neq C} \frac{M_D}{M_C} \cdot \tilde{z}_C^{(A)}/\tilde{z}_D^{(C)} \cdot t_D^{(C)} = 1 - \sum_{D\neq A,C} t_D^{(A)}. \tag{6.13}$$

Here, the bracked superscripts specify the designated species. Thus, we set the designated species appearing on the right side of eq. (6.12) to $C = \mathrm{H_2O}$, and calculate the corresponding parameters $t_{B\neq A}^{(A)}$ for the cases $A = \mathrm{Ch}^+$, and $A = [\mathrm{Zn(OAc)_3}]^-$ (since these define the two different, charged frames). Since the designated species is neutral ($C = \mathrm{H_2O}$), the effective valences equal the physical valences, $\tilde{z}_B^{(\mathrm{H_2O})} = z_B$ (for the three species $B \neq \mathrm{H_2O}$). Using the data for $\tilde{z}_B^{(\mathrm{Ch}^+)}$, $\tilde{z}_B^{([\mathrm{Zn(OAc)_3}]^-)}$ and $t_{B\neq A}^{(\mathrm{H_2O})}$ comprised in table 6.3, we find for the transference numbers relative to the designated species $A = \mathrm{Ch}^+$

$$t_{\mathrm{OAc}^-}^{(\mathrm{Ch}^+)} = 0.129 \cdot (-1.570) \cdot (-1) = 0.203, \tag{6.14a}$$

$$t_{[\mathrm{Zn(OAc)_3}]^-}^{(\mathrm{Ch}^+)} = 0.705 \cdot 3.330 = 2.350, \tag{6.14b}$$

$$t_{\mathrm{H_2O}}^{(\mathrm{Ch}^+)} = 1 - t_{(\mathrm{OAc}^-)}^{(\mathrm{Ch}^+)} - t_{[\mathrm{Zn(OAc)_3}]^-}^{(\mathrm{Ch}^+)} = -1.560, \tag{6.14c}$$

and for the transference numbers relative to the designated species $[\mathrm{Zn(OAc)_3}]^-$,

$$t_{\mathrm{Ch}^+}^{([\mathrm{Zn(OAc)_3}]^-)} = 0.166 \cdot 1.430 = 0.237, \tag{6.14d}$$

$$t_{\mathrm{OAc}^-}^{([\mathrm{Zn(OAc)_3}]^-)} = -1 \cdot 0.129 \cdot (-0.757) = 0.098, \tag{6.14e}$$

$$t_{\mathrm{H_2O}}^{([\mathrm{Zn(OAc)_3}]^-)} = 1 - t_{(\mathrm{OAc}^-)}^{([\mathrm{Zn(OAc)_3}]^-)} - t_{\mathrm{Ch}^+}^{([\mathrm{Zn(OAc)_3}]^-)} = 0.665 \tag{6.14f}$$

The values obtained in eqs. (6.14a) to (6.14f) coincide almost exactly with the numerical results comprised in table 6.3. The small discrepancies arise from the fact that the numerical results comprised in table 6.3 are stated as cell-averaged values. This validates our numerical results, and proves consistency of the framework.

6.3 Electrolyte-Classification

In this section, we discuss the interpretation of the as-modelled electrolyte being "highly concentrated", using the rationale described in section 5.4.7.

For this purpose, we evaluate the interface-relation eq. (5.283) using the parameters comprised in tables 6.1 and D.4, which yields

$$\left|\varepsilon^{\beta}\mathbf{N}_{\alpha}/\varepsilon c_{\alpha}\mathbf{v}\right|_{\alpha=[\mathrm{Zn(OAc)_3}]^-} \approx 0.05, \text{ and } \left|\varepsilon^{\beta}\mathbf{N}_{\alpha}/\varepsilon c_{\alpha}\mathbf{v}\right|_{\alpha=\mathrm{OAc}^-} \approx 0.06, \tag{6.15}$$

Both values suggest that convection is relevant, but not dominant. Hence, we conclude that electrolyte is right above the threshold to a concentrated electrolyte.

We probe this interpretation and calculate the mass-ratios between the salt species and water, *i.e.* $\rho_{\mathrm{OAc}^-}/\rho_{\mathrm{water}}$ and $\rho_{\mathrm{OAc}^-}/\rho_{\mathrm{water}}$ (see table 6.1). In both cases, the mass fraction of water is comparable to the mass fraction of the salt-species, but not negligible. Thus, the argument given below eq. (5.280) also suggests that our electrolyte is highly concentrated. We compare the analytic finding eq. (6.15) (based on material parameters) with our numerical results, using the data comprised in subfigure b) of fig. 6.4,

$$\varepsilon^{\beta}\mathbf{N}_{\alpha}/\varepsilon c_{\alpha}\mathbf{v}\,|_{[\mathrm{Zn(OAc)_3}]^-}\approx 0.05, \text{ and } \varepsilon^{\beta}\mathbf{N}_{\alpha}/\varepsilon c_{\alpha}\mathbf{v}\,|_{[\mathrm{Zn(OAc)_3}]^-}\approx 0.06. \tag{6.16}$$

This is consistent with the analytic finding eq. (6.15), for which we used the mass ratios and the stoichiomnetries of the electrode reactions.

Part III

Rational Continuum Modeling of Non-Local Interactions in Liquid Electrolytes

7 Introduction

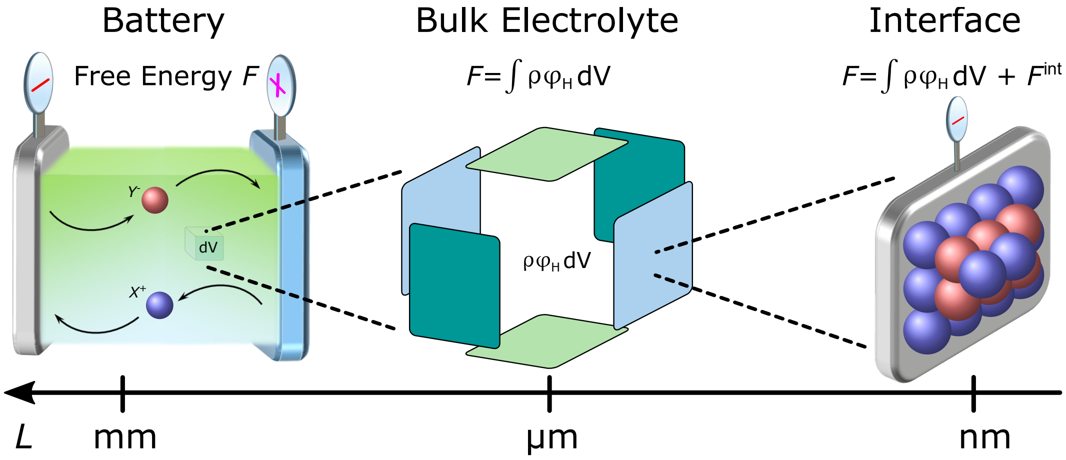

Scheme 7.1: Scheme of the modeling framework.

In part II, we derived our continuum transport theory for strongly correlated electrolytes. This description was based on modelling the free energy density $\rho\varphi_{\mathrm{H}}(\boldsymbol{\Upsilon})$, with the energy $F = \int \mathrm{d}V\, \rho\varphi_{\mathrm{H}}$. The free energy density is a function of the material variables $\boldsymbol{\Upsilon}$, which specifies the model to material specific properties. As discussed in section 2.1 this approach is based on the continuum hypothesis for liquids, which constitutes the canonical continuum description for bulk electrolytes on a macroscopic scale (*e.g.* on the µm- scale). However, the continuum approach becomes deficient for the description of crowded environments in microscopic systems. At length scales comparable to the size of the constituents, *i.e.* the ions, non local particle interactions become important, and must be resolved in the model explicitely. This is in contrast to the macroscopic scale, where these interactions are described via averaged quantities. As consequence, the continuum description for such non-local interactions is based on the free energy functional $F[\boldsymbol{\Upsilon}]$, and the bulk framework which is based on differential calculus must be generalized to the calculus of variations. Scheme 7.1 illustrates the applicability of the different methodologies on different length scales.

The relevance of strong ion correlations on the microscopic scale applies to biology, chemistry and physics,[318–320] and these correlations account for a plethora of phenomena like the compaction of genetic material in viruses via DNA packing,[321,322] cytoskeleton organization,[323] ion channels in the human body,[324] or the thermodynamic stability of plasmas and charged colloidal suspensions.[325–328] Hence, the derivation of a universal description for such non-local correlations promises a broad range of applicability, and offers an interdisciplinary description for these complex phenomena.

However, here we focus on ionic liquids (ILs). Because ILs consist only of positive and negative ions, the EDL structures formed by ILs near electrified interfaces constitute the archetype for such crowded environments, where strong electrostatic correlations play a pivotal role. These correlations lead to characteristic properties near electrified interfaces,[329] but also in the electroneutral bulk region,[330,331] which makes them highly attractive from both fundamental and applied perspectives.[57,332–339]

In our bulk description derived in part II, we account for the non vanishing molar volume of the ion species via imposing the condition of local volume-filling of the electrolyte, *i.e.* the Euler equation for the volume. This implies a constraint on the electrolyte, which stabilizes the bulk structure against Coulomb collapse, due to unbalanced ion-attraction.[63] Furthermore, it restricts the available volume for the ions, which leads to charge-saturation near electrified interfaces. Hence, the ion concentration of the counter species is bounded by the inverse volume of the species. This resolves the deficiencies of the classical Poisson-Boltzmann (PB) theory. Since the PB theory does not account for finite molar volumes, it predicts unrealistically high interface-concentrations.[102] In addition, we saw in part II that the assumption of finite molar volumes leads to a pressure dependence of the chemical potentials.[340] However, our bulk-framework from part II cannot describe the emergence of long-range structures in ILs near electrified interfaces. Hence, we supplement the mean volume effect from part II by an additional volume effect. In particular, we incorporate molecular volume exclusion due to hardcore particles into our model. The hardcore repulsion constitutes a repulsive correlation between the ions which scales with the ion sizes.

For this purpose, we generalize our local bulk description to a functional approach, where we model the free energy of the complete system via modeling the energy functional. This holistic continuum framework thus couples dynamic transport processes occurring in the bulk-electrolyte with interfacial electrochemical processes, and bridges the length-scales from nano-meters (the EDL), to millimeters (battery cells), see Scheme 7.1. Thereby, our framework connects the continuum description with atomistic modeling approaches.

We structure the EDL part of this document as follows. First, in chapter 8, we derive a thermodynamically consistent transport theory based on a functional approach. We find that our dynamical theory yields a description of the non-local correlations via integral equations. However, we show that this description can be approximated by a gradient expansion for short ranged non-local correlations. Next, in chapter 9, we apply our framework to the case of binary ILs near electrified interfaces. In order to better understand the influence of the system parameters on the screening profiles, we supplement this description by an asymptotic analysis based on the gradient expansion of the transport equations in stationary state in chapter 10. In chapter 11, we specify our model for non-local correlations to the case of hardcore particles via a Gauss-shaped interaction functional. Finally, in chapter 12, we perform numerical simulations of binary ILs near electrified interfaces. In addition, in chapter 13, we study the formation of EDL structures of ternary IL based electrolytes. We derive the transport equations for this system, discuss the stationary state and perform numerical simulations. We supplement these results by a discussion of the limiting case of minor salt additives. Finally, in chapter 14, we compare our results with experiments, and validate our EDL model.

8 Modeling Non-Local Interactions in Liquid Electrolyte Transport Theories

In this chapter we derive our model for the electrochemical double layer (EDL) based on a functional approach. We structure this chapter as follows. In section 8.1, we state the universal balance laws from a global perspective, and derive the (local) constitutive equations. Next, in section 8.2, we state our universal energy functional, based on the bulk free energy described in section 5.4. However, we do not yet specify the interaction functional, as to keep the framework general. This determines the forces appearing in our description. However, in section 8.3 we restrict our formalism to certain types of non-local interactions based on convolution integrals. Finally, in section 8.4 we discuss the limiting case of our theory where the interactions can be approximated using a gradient expansion.

8.1 Generalized Transport Theory: Functional Formalism

In this section, we extend our continuum transport theory from chapter 5 to also account for non-local interactions. To address this goal, we generalize our approach from above to a functional description for the universal balancing laws. Our derivation follows the same rationale as used for the derivation of the "bulk" framework. However, we use a global perspective to obtain the universal balance equations, and replace the field densities for momentum, energy, and entropy, appearing in the bulk description, by functional expressions.

As first step, we state the global form of the force law of mechanics (see eq. (5.50)),

$$\dot{\boldsymbol{\mathfrak{G}}} = \dot{\boldsymbol{\mathfrak{G}}}^{\mathrm{int}} + \int \mathrm{d}V \; (\rho \mathbf{b} + \boldsymbol{\nabla} \boldsymbol{\sigma}) = \int \mathrm{d}V \left(\frac{\delta \boldsymbol{\mathfrak{G}}^{\mathrm{int}}}{\delta t} + \rho \mathbf{b} + \boldsymbol{\nabla} \boldsymbol{\sigma} \right) . \tag{8.1}$$

Here, $\boldsymbol{\mathfrak{G}}$ is the complete momentum, which consists of the "bulk" part described section 5.1 supplemented by an interaction contribution $\boldsymbol{\mathfrak{G}}^{\mathrm{int}}$, where $\dot{\boldsymbol{\mathfrak{G}}}^{\mathrm{int}} = \int \mathrm{d}V \, \frac{\delta \boldsymbol{\mathfrak{G}}^{\mathrm{int}}}{\delta t}$.

Next, we formulate the global form for energy balance, see eq. (5.53), as the sum of the powers of the forces acting on the system and heating,

$$\dot{\mathcal{E}} = \mathit{\Pi} + \mathcal{Q}. \tag{8.2}$$

Since $\mathit{\Pi}(\mathcal{G})$ is a function of the total momentum, we extend it's definition from above, see eq. (5.51), by an additional term, *viz.* $\mathit{\Pi} = \mathit{\Pi}^{\text{int}} + \int \mathrm{d}V\, [\rho \mathbf{b}\mathbf{v} + \boldsymbol{\nabla}(\boldsymbol{\sigma}^T\mathbf{v})]$. In contrast, we assume that the heating of the system remains unchanged (eq. (5.52)), $\mathcal{Q} = \int \mathrm{d}V\, \rho h - \boldsymbol{\nabla}(\mathbf{q} + \boldsymbol{\mathcal{E}} \wedge \boldsymbol{\mathcal{H}}_{\mathrm{F}})$.

We use these definitions and evaluate the couplings of momentum-balance and energy-balance, (see eqs. (8.1) and (8.2)) with respect to the non-kinematic energy

$$\dot{\mathcal{U}} = \dot{\mathcal{E}} - \dot{\mathcal{G}}. \tag{8.3}$$

Thus, we substitute the momentum equation for the body force-term $\int \mathrm{d}V\, \rho\mathbf{b}$ and make use of the relation $\boldsymbol{\nabla}(\boldsymbol{\sigma}^T\mathbf{v}) = \mathbf{v}(\boldsymbol{\nabla}\boldsymbol{\sigma}^T) + \boldsymbol{\sigma} : \operatorname{grad}\mathbf{v}$, such that

$$\dot{\mathcal{U}} = \mathit{\Pi}^{\text{int}} + \int \mathrm{d}V\, [-\frac{\delta \mathcal{G}^{\text{int}}}{\delta t} \cdot \mathbf{v} + \boldsymbol{\sigma} : \operatorname{grad}\mathbf{v} - \boldsymbol{\nabla}(\mathbf{q} + \boldsymbol{\mathcal{E}} \wedge \boldsymbol{\mathcal{H}}_{\mathrm{F}}) + \rho h] \tag{8.4}$$

We ensure thermodynamic consistency of our extended framework by proceeding as in section 5.1.3. For this purpose, we generalize our formulation of the second axiom of thermodynamics. Let $\mathcal{S} = \mathcal{S}^{\text{int}} + \int \mathrm{d}V\, \rho s$ denote the entropy of the system, such that eq. (5.39) becomes

$$\dot{\mathcal{S}} = \int \mathrm{d}V \left[\rho\dot{s} + \frac{\delta \mathcal{S}^{\text{int}}}{\delta t}\right] \geq \int \mathrm{d}V \left(-\boldsymbol{\nabla}\boldsymbol{\xi}_s + \frac{\rho h}{T}\right). \tag{8.5}$$

The right side measures the deviation from equilibrium due to the entropy-flux $\boldsymbol{\xi}_s$, and due to the heating-process $\rho h/T$. The corresponding irreversible loss of energy $T \cdot \mathcal{S}$, must be taken account for in the balance law of energy. To measure the rate of irreversible entropy production, we define

$$\int \mathrm{d}V\, \mathcal{R} = T\dot{\mathcal{S}} + \int \mathrm{d}V\, [T\boldsymbol{\nabla}\boldsymbol{\xi}_s - \rho h] \tag{8.6}$$

$$= T\dot{\mathcal{S}} - \dot{\mathcal{U}} + \mathit{\Pi}^{\text{int}} + \int \mathrm{d}V \Big(T\boldsymbol{\nabla}\boldsymbol{\xi}_s - \frac{\delta \mathcal{G}^{\text{int}}}{\delta t} \cdot \mathbf{v} + \boldsymbol{\sigma} : \operatorname{grad}\mathbf{v} - \boldsymbol{\nabla}\mathbf{q} + \\ + \boldsymbol{\nabla}\left(\boldsymbol{\mathcal{H}}_{\mathrm{F}} \wedge \boldsymbol{\mathcal{E}}\right)\Big). \tag{8.7}$$

Here, we assumed that the temperature of the system is constant, such that $T \cdot \mathcal{S} = T \cdot \mathcal{S}^{\text{int}} + \int \mathrm{d}V\, \rho s T$, and substituted $\int \mathrm{d}V\, \rho h$ using eq. (8.4). Note that the right side eq. (8.6) suggests the identification

$$\mathit{\Pi}^{\mathrm{int}} = \int \mathrm{d}V \, (\delta \mathfrak{G}^{\mathrm{int}} / \delta t \, \cdot \mathbf{v}). \tag{8.8}$$

Focal quantity in our framework is the Helmholtz free energy, which is the Legendre transformed quantity with respect to internal energy, *i.e.* $F = \mathcal{U} - T\mathcal{S}$. Hence, we aim to reexpress $\dot{\mathcal{U}}$ by $\dot{F}$ in eq. (8.6),

$$\int \mathrm{d}V \, \mathcal{R} = -\dot{F} - \dot{T}\mathcal{S} + \int \mathrm{d}V \, \left(T \boldsymbol{\nabla} \boldsymbol{\xi}_s + \boldsymbol{\sigma} : \mathrm{grad}\mathbf{v} - \boldsymbol{\nabla}\mathbf{q} + \boldsymbol{\nabla}\left(\boldsymbol{\mathcal{H}}_{\mathrm{F}} \wedge \boldsymbol{\mathcal{E}}\right)\right). \tag{8.9}$$

Here, we used eq. (8.8). This is the global form of the entropy inequality corresponding to eq. (5.55). Therefore, eq. (8.9) determines the constitutive equations of the model subject to the form of $\dot{F}$, *i.e.* subject to the materials law $\boldsymbol{\Upsilon}$, which restrict the formalism to classes of materials described by $F[\boldsymbol{\Upsilon}]$. However, in order to account for molecular interactions, we expand the free energy of the system via

$$F[\mathit{\Upsilon}] = F^{\mathrm{int}}[\boldsymbol{\Upsilon}] + F^{\mathrm{b}}(\boldsymbol{\Upsilon}) = F^{\mathrm{int}}[\boldsymbol{\Upsilon}] + \int \mathrm{d}V \, \rho \varphi_{\mathrm{H}}. \tag{8.10}$$

We supplement the canonical materials law which, is defined by the hydrodynamic description for the energy of polarizable liquids[289]

$$\delta F = \int \mathrm{d}V \, \boldsymbol{\mathcal{E}} \cdot \delta \mathbf{D}_{\mathrm{F}} + \boldsymbol{\mathcal{H}}_{\mathrm{F}} \cdot \delta \mathbf{B} + \rho s \cdot \delta T + \sum_{\alpha=1}^{\mathrm{N}} \mu_\alpha \cdot \delta c_\alpha + \rho \varphi_{\mathrm{H}} \cdot \boldsymbol{\nabla} \mathbf{v}, \tag{8.11}$$

by the strain-rate tensor $\boldsymbol{\kappa}$, which constitutes the liquid state of our system. Thus, we set $\boldsymbol{\Upsilon} = \{\mathbf{D}_{\mathrm{F}}, \mathbf{B}, T, c_\alpha, \boldsymbol{\kappa}\}$.

Next, we derive the constitutive equations comprising contributions from the non-local quantities F^{int}. For this purpose, we evaluate $\dot{F}$ in eq. (8.9) according to the scheme eq. (5.57) with respect to the material law $\boldsymbol{\Upsilon}$. Also, we use mass-balance $\dot{c}_\alpha = -\boldsymbol{\nabla}\boldsymbol{\mathcal{N}}_\alpha - c_\alpha \boldsymbol{\nabla}\mathbf{v}$ (see eq. (5.11)), substitute eq. (5.58) for $\boldsymbol{\nabla}\left(\boldsymbol{\mathcal{H}}_{\mathrm{F}} \wedge \boldsymbol{\mathcal{E}}\right)$, and use $T\boldsymbol{\nabla}\boldsymbol{\xi}_s = -\boldsymbol{\xi}_s \boldsymbol{\nabla} T + \boldsymbol{\nabla}\mathbf{q} - \boldsymbol{\nabla}\sum_{\alpha=1}^{\mathrm{N}} \mu_\alpha \boldsymbol{\mathcal{N}}_\alpha$. This allows to identify the generalized constitutive equations for entropy density s, electric field strength $\boldsymbol{\mathcal{E}}$, magnetic field $\boldsymbol{\mathcal{H}}_{\mathrm{F}}$, and chemical potentials μ_α via functional-derivatives

$$\rho s = -\rho \frac{\partial \varphi_{\mathrm{H}}}{\partial T} - \frac{\delta F^{\mathrm{int}}}{\delta T}, \tag{8.12}$$

$$\boldsymbol{\mathcal{E}} = \rho \frac{\partial \varphi_{\mathrm{H}}}{\partial \mathbf{D}_{\mathrm{F}}} + \frac{\delta F^{\mathrm{int}}}{\delta \mathbf{D}_{\mathrm{F}}}, \tag{8.13}$$

$$\boldsymbol{\mathcal{H}}_{\mathrm{F}} = \rho \frac{\partial \varphi_{\mathrm{H}}}{\partial \mathbf{B}} + \frac{\delta F^{\mathrm{int}}}{\delta \mathbf{B}}, \tag{8.14}$$

$$\mu_\alpha = \frac{\partial(\rho\varphi_\mathrm{H})}{\partial c_\alpha} + \frac{\delta F^\mathrm{int}}{\delta c_\alpha}. \tag{8.15}$$

Equations (8.12) to (8.15) are supplemented by $\partial\varphi_\mathrm{H}/\partial\boldsymbol{\kappa}{=}\delta F^\mathrm{int}/\delta\boldsymbol{\kappa}{=}0$, and by the generalized constitutive equation for the stress tensor,

$$\boldsymbol{\sigma}{=}\boldsymbol{\tau} - \left(\sum_{\alpha=1}^{\mathrm{N}} c_\alpha \left[\frac{\partial(\rho\varphi_\mathrm{H})}{\partial c_\alpha} {+} \frac{\delta F^\mathrm{int}}{\delta c_\alpha}\right] {-}\rho\varphi_\mathrm{H}{+}\boldsymbol{\mathcal{E}}\mathbf{D}_\mathrm{F}{+}\boldsymbol{\mathcal{H}}_\mathrm{F}\mathbf{B}\right)\mathbf{Id}\,{+}\boldsymbol{\mathcal{E}}{\otimes}\mathbf{D}_\mathrm{F}{+}\boldsymbol{\mathcal{H}}_\mathrm{F}{\otimes}\mathbf{B}. \tag{8.16}$$

Here $\boldsymbol{\tau}$ is the viscosity tensor discussed in Section 5.3.2, see eq. (5.143).

Apparently, all constitutive equations are supplemented by functional derivatives with respect to the conjugate material variables.

For the remaining part of this discussion, we assume that temperature is constant, and assume the electrostatic limit (where $\mathbf{B} = 0$ and $\boldsymbol{\mathcal{H}}_\mathrm{F} = 0$, see section 5.2.4). This determines the electric field $\mathbf{E} = \boldsymbol{\mathcal{E}}$ by the electrostatic potential, $\mathbf{E} = -\boldsymbol{\nabla}\Phi$. Finally, the residual expression for the entropy inequality, see eq. (8.9), after the evaluation of the constitutive equations can be expressed locally

$$\int \mathrm{d}V\,\mathcal{R} = \int \mathrm{d}V\,[-\boldsymbol{\mathcal{J}}_\mathrm{F}\boldsymbol{\nabla}\Phi - \sum_{\alpha=1}^{\mathrm{N}} \boldsymbol{\mathcal{N}}_\alpha\boldsymbol{\nabla}\mu_\alpha - \boldsymbol{\xi}_s\boldsymbol{\nabla}T + \boldsymbol{\tau}:\boldsymbol{\kappa}]. \tag{8.17}$$

8.2 Model for Interacting Liquid Electrolytes

Next, we state the Helmholtz free energy $F = F^\mathrm{int}[c_\alpha] + \int \mathrm{d}V\,\rho\varphi_\mathrm{H}$ for liquid electrolytes which accounts for non-local interactions. We split F into a bulk part $\mathrm{d}V\,\rho\varphi_\mathrm{H}$ and an energy functional F^int. We model the bulk part of the free energy as above, see eq. (5.153), with the only difference that we use an alternative mixing entropy,

$$F{=}F^\mathrm{int}[c_\alpha]{+}\int \mathrm{d}V\left(\frac{\mathbf{E}\mathbf{D}_\mathrm{F}}{2}{+}\frac{\mathcal{K}}{2}\left[1{-}\sum_{\alpha=1}^{\mathrm{N}}\nu_\alpha^0 c_\alpha\right]^2{+}RT\sum_{\alpha=1}^{\mathrm{N}} c_\alpha\ln(c_\alpha\nu_\alpha)\right). \tag{8.18}$$

The last term in eq. (8.18) describes mixing entropy according to the "Flory-Huggins"-approach.[341,342] This description expresses entropy of mixture via volume fractions $c_\alpha\cdot\nu_\alpha$, instead of mole fractions c_α/c. This entropy thus favours equal volumes for each species instead of equal numbers of molecules, and accounts for the averaged impact of short ranged repulsion on particle distributions. The Flory-Huggins approach is often used to model liquid systems exhibiting solid-like-, or crystalline behaviour, *e.g.* polymers.[343,344] However, since we incorporate the interaction contributions into the functional F^int, we neglect all Flory-Huggins-parameters χ, see also the remark at end of section 8.3. This mixing-entropy is related to the mixing-entropy of ideal gases used in section 5.4, via bulk activity coefficents $f_\alpha = \nu_\alpha$. The electric field in eq. (8.18) is $\mathbf{E} = \mathbf{D}_\mathrm{F}/\varepsilon_0\varepsilon_\mathrm{R}$, and $\mathcal{K}$ constitutes a bulk-modulus (see section 5.4).

Furthermore, we restrict the materials law to $\boldsymbol{\Upsilon}^\mathrm{int} = \{c_\alpha\}$ such that $F^\mathrm{int}[c_\gamma]$. This implies that only the chemical potentials and the stress tensor experience non-trivial constitutive equations, see eqs. (8.15) and (8.16).

Similar to the description in section 5.4, the chemical potentials corresponding to the modified bulk-model eq. (8.18) still depend on unspecified elastic properties,

$$\mu_\alpha = RT\,(1 + \ln c_\alpha \nu_\alpha) + \delta F^\mathrm{int}[c_\gamma]/\delta c_\alpha \; - \mathcal{K}\nu_\gamma \cdot (1 - \sum_{\beta=1}^{\mathrm{N}} c_\beta \cdot \nu^0_\beta). \tag{8.19}$$

However, this poses no problem, since we assume incompressible electrolytes $\mathcal{K} \to \infty$. Hence, the diverging bulk modulus, enforces the Euler equation for the volume eq. (5.178), *viz.* $\sum_{\alpha=1}^{\mathrm{N}} c_\alpha \nu_\alpha = 1$.

Next, we determine the forces $\boldsymbol{\nabla}\mu^\mathrm{el}_\alpha = \boldsymbol{\nabla}(\mu_\alpha + F z_\alpha \boldsymbol{\nabla}\Phi)$. Because we lack a constitutive equation for the bulk-modulus, the chemical potentials are underdetermined and the force-equations cannot be closed,

$$\boldsymbol{\nabla}\mu^\mathrm{el}_\alpha = F z_\alpha \boldsymbol{\nabla}\Phi + RT\boldsymbol{\nabla}\ln\left[c_\alpha\nu_\alpha\right] + \boldsymbol{\nabla}\frac{\delta F^\mathrm{int}[c_\gamma]}{\delta c_\alpha} + \mathcal{K}\nu_\alpha \sum_{\beta=1}^{\mathrm{N}} \nu_\beta \cdot \boldsymbol{\nabla} c_\beta. \tag{8.20}$$

We encountered the same problem for the bulk-theory in section 5.4. There, we used the assumption of mechanical equilibrium to substitute for the unknown term appearing in the forces eq. (8.20). Here, we follow the same rational. For vanishing body-forces, the assumption of mechanical equilibrium, $\dot{\mathfrak{G}} \approx 0$, allows to solve eq. (8.1) for $\int \mathrm{d}V\, \boldsymbol{\nabla}\boldsymbol{\sigma} = -\int \mathrm{d}V\, \delta\mathfrak{G}^\mathrm{int}[c_\gamma]/\delta t$. The left side of this expression can be substituted using the constitutive equation for $\boldsymbol{\sigma}$, eq. (8.16), subject to our model free energy eq. (8.18). Thus, we find

$$\mathcal{K}\sum_{\beta=1}^{\mathrm{N}} \nu_\beta \cdot \boldsymbol{\nabla} c_\beta = -\varrho_\mathrm{F}\boldsymbol{\nabla}\Phi - RT\cdot\boldsymbol{\nabla}c - \boldsymbol{\nabla}\sum_{\beta=1}^{\mathrm{N}} c_\beta \cdot \frac{\delta F^\mathrm{int}}{\delta c_\beta} + \frac{\delta\mathfrak{G}^\mathrm{int}}{\delta t} + \boldsymbol{\nabla}\boldsymbol{\tau}. \tag{8.21}$$

Finally, we substitute eq. (8.21) into eq. (8.20) and obtain the following expression for the electrochemical forces appearing in our description,

$$\boldsymbol{\nabla}\mu^\mathrm{el}_\alpha = \sum_{\beta=1}^{\mathrm{N}} \left(\delta^\beta_\alpha - \nu_\alpha c_\beta\right) \cdot \boldsymbol{\nabla}\left(F z_\beta \Phi + \frac{\delta F^\mathrm{int}}{\delta c_\beta}\right) - \nu_\alpha\left(\sum_{\beta=1}^{\mathrm{N}} \frac{\delta F^\mathrm{int}}{\delta c_\beta}\boldsymbol{\nabla}c_\beta - \frac{\delta\mathfrak{G}^\mathrm{int}}{\delta t}\right) +$$

$$+ \nu_\alpha \boldsymbol{\nabla} \boldsymbol{\tau} + RT \left(\boldsymbol{\nabla} \ln c_\alpha \nu_\alpha - \nu_\alpha \boldsymbol{\nabla} c \right). \tag{8.22}$$

Apparently, these forces are still underdetermined, as we have not yet specified the exact form for the continuum-contribution $\delta \mathcal{G}^{\text{int}} / \delta t$ which account for the non-local interactions in momentum-balance eq. (8.1). However, the Gibbs-Duhem equation corresponding to eq. (8.22) takes the form

$$\sum_{\alpha=1}^{\mathrm{N}} c_\alpha \boldsymbol{\nabla} \mu_\alpha^{\text{el}} = \boldsymbol{\nabla} \boldsymbol{\tau} - \sum_{\gamma=1}^{\mathrm{N}} \frac{\delta F^{\text{int}}[c_\alpha]}{\delta c_\gamma} \cdot \boldsymbol{\nabla} c_\gamma + \frac{\delta \mathcal{G}^{\text{int}}}{\delta t}[c_\gamma]. \tag{8.23}$$

We assume that both sides vanish for stationary states (when the system is in equilibrium). This constraint is fulfilled always exactly if we identify

$$\dot{\mathcal{G}}^{\text{int}}[c_\gamma] = \int \mathrm{d}V \, \frac{\delta \mathcal{G}^{\text{int}}}{\delta t}[c_\gamma] = \int \mathrm{d}V \, \sum_{\alpha=1}^{\mathrm{N}} \frac{\delta F^{\text{int}}[c_\gamma]}{\delta c_\alpha} \cdot \boldsymbol{\nabla} c_\alpha. \tag{8.24}$$

This is reminiscent of conservative forces, appearing in classical mechanics. Substituting eq. (8.24) into eq. (8.22) yields the final form for the forces, and closes our description up to F^{int},

$$\boldsymbol{\nabla} \mu_\alpha^{\text{el}} = \sum_{\beta=1}^{\mathrm{N}} \left(\delta_\beta^\alpha - \nu_\alpha c_\beta \right) \boldsymbol{\nabla} \left(F z_\beta \Phi + \frac{\delta F^{\text{int}}}{\delta c_\beta} \right) + RT \left(\boldsymbol{\nabla} \ln c_\alpha \nu_\alpha - \nu_\alpha \boldsymbol{\nabla} c \right) + \nu_\alpha \boldsymbol{\nabla} \boldsymbol{\tau}. \tag{8.25}$$

Thus, we obtain inter-species couplings of the electrochemical forces, in agreement with the Gibbs-Duhem relation for the bulk-description (see eq. (5.101)),

$$\sum_{\gamma=1}^{\mathrm{N}} c_\gamma \cdot \boldsymbol{\nabla} \mu_\gamma^{\text{el}} = \boldsymbol{\nabla} \boldsymbol{\tau}. \tag{8.26}$$

Note the striking similarity between eq. (8.25) and the corresponding bulk term eq. (5.234), *i.e.* the similar role of the quantities $\delta F^{\text{int}}[c_\alpha] / \delta c_\beta$ and $\partial (\rho \varphi_{\mathrm{H}}^{\text{int}}) / \partial c_\alpha$.

8.3 Potentials of Molecular Interactions

We model hardcore-interactions via convolution-functionals,

$$F^{\text{int}}[c_\alpha] = \frac{1}{2} \mathcal{V}^0 \left(N_{\mathrm{A}} \right)^2 \sum_{\alpha, \beta}^{\mathrm{N}} \iint \mathrm{d}\mathbf{x}^3 \mathrm{d}\mathbf{y}^3 \; \tilde{\mathcal{F}}_{\alpha\beta}(|\mathbf{x} - \mathbf{y}|) c_\alpha(\mathbf{x}) c_\beta(\mathbf{y}). \tag{8.27}$$

The symmetric interaction potential $\mathcal{F}_{\alpha\beta}$ determines the correlation length ℓ_{int}, and the magnitude of the interaction. Here, we have factorized $\mathcal{F}_{\alpha\beta}$ into a dimensional prefactor $\mathcal{V}^0 \cdot (N_\text{A})^2$, which characterize the magnitude of the interaction, and a dimensionless shape-function $\tilde{\mathcal{F}}$, which characterizes the correlation length of the interaction, *viz.*

$$\mathcal{F}_{\alpha\beta}\left(\mathcal{V}^0, \ell_{\text{int}}\right) = \mathcal{V}^0 \cdot (N_\text{A})^2 \cdot \tilde{\mathcal{F}}_{\alpha\beta}(\ell_{\text{int}}). \tag{8.28}$$

We assume that the shape-function $\tilde{\mathcal{F}}_{\alpha\beta}$ is a conservative potentials, *i.e.* exhibits spherical symmetry. The number of interaction parameters depends upon the model for $\mathcal{F}_{\alpha\beta}$. Experimental results suggest that ion-correlations in electrolytes typically decay after some ionic diameters.[345] Hence ℓ_{int} is large compared to the exponential decay of the electric field (Debye-length),[346,347] yet small compared to the battery cell. Because we parametrize the correlation length of our model for hardcore particles via the ion-sizes of the particles, only $\mathcal{V}^0$ is introduced as a novel independent material parameter.

The most important feature of hardcore particles is that they experience strong repulsive forces at small distances, which origin from the Pauli exclusion principle (prohibiting overlaping electron shells). The resulting short-ranged order is typical for systems at liquid state.[348] However, an additional cohesive energy is required to stabilize the liquid. These attractive dispersion forces vary smoothly over particle-distances, and constitute an attractive background which stabilizes the bulk. The liquid model of hardcore particles moving in a uniform, attractive background potential was established by van-der-Waals and proved very successful.[63] Accordingly, the interaction potential is often split into a repulsive and attractive parts[349] The repulsive part models impenetrable hardcore particles and extends over short distances determined by the particle-size a. In principle, hardcore potentials should be modeled via an infinite square-well, corresponding to incompressible particles. However, largely for reasons of numerical and analytical convenience, they are usually modelled by inverse power laws.[63] The attractive part describes longer-ranged attractive forces. A prominent two-fold approach are “twelve-six-potentials” of Lennard-Jones type,[350–352] $\mathcal{F}(r) = \mathcal{V}^0(N_\text{A})^2[(a/r)^{12} - (a/r)^6]$, where the first term describes short-ranged repulsion and the second term describes attractive contributions from dipole-dipole interactions.[345,353–358]

Here, we restrict to short ranged repulsive potentials, since we focus on the modeling of hardcore particles. Furthermore, since

$$\frac{\delta^2 F^{\text{int}}}{\delta c_\gamma(\mathbf{z})\delta c_\alpha(\mathbf{x})} = \mathcal{F}_{\alpha\gamma}(|\mathbf{x}-\mathbf{z}|) = \mathcal{V}^0 \cdot (N_\text{A})^2 \cdot \tilde{\mathcal{F}}_{\alpha\beta}(|\mathbf{x}-\mathbf{z}|), \tag{8.29}$$

the potentials $\tilde{\mathcal{F}}_{\alpha\gamma}$ determine the direct pair correlation functions used in liquid state theory,[63] see also our discussion in section 15.3 for more details.

The material law determines the interaction contributions via eqs. (8.12) to (8.16)). For $\boldsymbol{\Upsilon}^{\text{int}} = \{c_\alpha\}$ the interaction contributes only to the chemical potentials. The corresponding result for the constitutive equation subject via (see appendix E.2)

$$\frac{\delta F^{\text{int}}}{\delta c_\alpha}(\mathbf{x}) = \mathcal{V}^0 \cdot (N_{\text{A}})^2 \cdot \sum_{\beta}^{\text{N}} \int \mathrm{d}\mathbf{y}^3 \; \tilde{\mathcal{F}}_{\alpha\beta}(|\mathbf{x}-\mathbf{y}|) c_\beta(\mathbf{y}). \tag{8.30}$$

8.4 Gradient Expansion of Molecular Interactions

In this section, we focus on repulsive potentials which describe hardcore-particles, *i.e.* potentials $\mathcal{F}_{\alpha\beta}$ which range over the size of one molecule.

In appendix E.1 we show that interaction functionals which depend on short-ranged potentials $\mathcal{F}$ can be approximated in power series of concentration gradients,

$$F^{\text{int}}[c_\gamma] = \frac{1}{2}\mathcal{V}^0 \cdot (N_{\text{A}})^2 \cdot \sum_{\alpha,\,\beta}^{\text{N}} \sum_{n=0}^{\infty} \Gamma^{2n}_{\alpha\beta} \int \mathrm{d}y^3 \; c_\alpha(\mathbf{y}) \cdot \boldsymbol{\nabla}^{2n} c_\beta(\mathbf{y}). \tag{8.31}$$

where

$$\Gamma^{2n}_{\alpha\beta}\left(\tilde{\mathcal{F}}_{\alpha\beta}\right) = 1/(2n)! \int \mathrm{d}x^3 \, \tilde{\mathcal{F}}_{\alpha\beta}(|\mathbf{x}|) \cdot \mathbf{x}^{2n} \tag{8.32}$$

are symmetric perturbation coefficients of dimension $[\Gamma^{2n}_{\alpha\beta}] = \mathrm{m}^{3+2n}$. The perturbation modes (the spherically symmetric interaction potentials) simplify in spherical coordinates ,

$$\Gamma^{2n}_{\alpha\beta}\left(\tilde{\mathcal{F}}_{\alpha\beta}\right) = 4\pi/(2n)! \int \mathrm{d}r \; \tilde{\mathcal{F}}_{\alpha\beta}(r) \cdot r^{2(n+1)}, \tag{8.33}$$

where the zero-order mode is given by the integral over the interaction potential,

$$\Gamma^{0}_{\alpha\beta}\left(\tilde{\mathcal{F}}_{\alpha\beta}\right) = \int \mathrm{d}x^3 \; \tilde{\mathcal{F}}_{\alpha\beta}(|\mathbf{x}|) = 4\pi \int \mathrm{d}r \; \tilde{\mathcal{F}}_{\alpha\beta}(r) \cdot r^2. \tag{8.34}$$

This integral can be solved analytically for all potentials of the Lennard-Jones type, and Gaussian type for all perturbation modes (see chapter 11). The complete free energy functional for IL electrolytes becomes in the gradient description

$$F = \int \mathrm{d}V \left[\mathbf{E}\mathbf{D}_{\text{F}}/2 + RT \sum_{\alpha=1}^{\text{N}} c_\alpha \ln(c_\alpha \nu_\alpha) + \mathcal{K}/2 \left(1 - \sum_{\alpha=1}^{\text{N}} c_\alpha \nu_\alpha\right)^2 + \right.$$
$$\left. + \mathcal{V}^0/2 \; (N_{\text{A}})^2 \sum_{\alpha,\,\beta}^{\text{N}} \sum_{n=0}^{\infty} \Gamma^{2n}_{\alpha\beta} c_\alpha \boldsymbol{\nabla}^{2n} c_\beta \right]. \tag{8.35}$$

The functional derivative with respect to the gradient expansion reads (eq. (8.35))

$$\delta F^{\mathrm{int}}/\delta c_\gamma(\mathbf{z}) \ = \mathcal{V}^0 \cdot (N_{\mathrm{A}})^2 \cdot \sum_{\beta=1}^{\mathrm{N}} \sum_{n=0}^{\infty} \Gamma_{\gamma\beta}^{2n} \cdot \boldsymbol{\nabla}^{2n} c_\beta(\mathbf{z}). \tag{8.36}$$

Hence, we find for the electrochemical forces (see eq. (8.25))

$$\boldsymbol{\nabla}\mu_\gamma^{\mathrm{el}} = (F z_\gamma - \nu_\gamma \varrho_{\mathrm{F}}) \boldsymbol{\nabla}\Phi + \mathcal{V}^0 (N_{\mathrm{A}})^2 \sum_{n=0}^{\infty} \sum_{\alpha,\beta}^{\mathrm{N}} (\delta_\alpha^\gamma - \nu_\gamma c_\alpha) \Gamma_{\alpha\beta}^{2n} \boldsymbol{\nabla}^{2n+1} c_\beta + RT \left(\frac{\boldsymbol{\nabla} c_\gamma}{c_\gamma} - \nu_\gamma \boldsymbol{\nabla} c \right). \tag{8.37}$$

9 Molecular Interactions in Binary IL Electrolyte

Here, we apply our formalism to binary ILs at electrified interfaces. We structure this chapter as follows. In section 9.1, we specify our transport theory to binary electrolytes. Next, in section 9.2, we simplify the description and remove the physical dimensions form the equations. Finally, in section 9.3, we discuss the stationary state.

9.1 Transport Theory of Binary IL Electrolytes with Molecular Interactions

The minimal variable set for the description of a binary electrolyte consists of Φ, ϱ_F, and $\mathbf{v}$ (where ion-concentrations are functions $c_\pm(\varrho_\mathrm{F}, \nu_\alpha)$. The electroneutral bulk-state, $c_+ = c_- = c^\mathrm{b}$, determines the total molar volume $\nu = 1/c^\mathrm{b}$, and we define relative molar volumes

$$\gamma_\alpha = \nu_\alpha/\nu = \nu_\alpha \cdot c^\mathrm{b}, \quad \text{where} \quad \gamma_+ + \gamma_- = 1, \tag{9.1}$$

i.e. there exists only one independent quantity γ_+.

In section 5.4.2, we used thermodynamic arguments to derive the partial molar volumes from the stress tensor. Here, we use a micrscopic approach and define parametrize the molar volumes by the ion sizes a, using a dimensionless form-function $\tilde{\nu}$,[359]

$$\nu = N_\mathrm{A} \tilde{\nu} a^3. \tag{9.2}$$

The form function $\tilde{\nu}$ determines our model for the molar volumes. One common choice is to model the molecules as spheres of radius $a/2$, *i.e.* $\tilde{\nu} = \pi/6$.[360] Because this model does not take account for non-trivial packing effects leading to excess molar volumes,.[361] it is often corrected via $\tilde{\nu} = \eta\pi/6$.[69,345] The packing ratio η can be estimated from the statistical analysis of random packing of hard spheres, which suggests $\eta = 0.63$.[362] Here, we use simple "block"-geometry for our model, *i.e.* $\tilde{\nu} = 1$.

The ion-concentrations are thus functions (see eqs. (5.222) and (5.223)), *viz.*

$$c_\pm(a, \varrho_\mathrm{F}, \tilde{\nu}, z_+, \gamma_+) = c^\mathrm{b} \pm \varrho_\mathrm{F}\gamma_\mp / F z_+ \tag{9.3}$$

The Euler equation for the volume implies that saturation of charges may occur near electrified interfaces. Thus, there exist maximal values $\varrho_\mathrm{F}^\mathrm{sat}$ and $c_\pm^\mathrm{sat}$,

$$c_\alpha^\mathrm{sat} = 1/\nu_\alpha = c^\mathrm{b}/\gamma_\alpha\,, \qquad \text{and} \qquad \varrho_\mathrm{F}^\mathrm{sat} = F z_{\alpha^*} c^\mathrm{b}/\gamma_{\alpha^*}\,. \tag{9.4}$$

Here, the index α^* denotes the saturating species, usually defined by the sign of the interface-potential $\Delta\phi$ via the condition $\mathrm{sign}(z_{\alpha^*}) = -\mathrm{sign}(\Delta\phi)$.

Furthermore, the electric conductivity κ is the only independent transport parameter in a binary electrolyte (see section 5.3). The complete set of dynamical transport equations reads (see eqs. (5.243) to (5.246))

$$\partial_t \varrho_\mathrm{F} = -\boldsymbol{\nabla}\left(\varrho_\mathrm{F}\mathbf{v}\right) - \boldsymbol{\nabla}\boldsymbol{\mathcal{J}}, \tag{9.5}$$

$$\varrho_\mathrm{F} = -\varepsilon_0 \boldsymbol{\nabla}\varepsilon_\mathrm{R}\boldsymbol{\nabla}\Phi, \tag{9.6}$$

$$\boldsymbol{\nabla}\mathbf{v} = (M_+\nu_- - M_-\nu_+) F z_+ M_\mathrm{IL} \cdot \boldsymbol{\nabla}\boldsymbol{\mathcal{J}}. \tag{9.7}$$

Here, $M_\pm$ are the molar masses of the ionic species which sum to M_IL, and $\boldsymbol{\mathcal{J}}$ is the electric current relative to the center-of-mass motion,

$$\boldsymbol{\mathcal{J}} = \kappa / F z_+ \cdot \Big(M_+/M_\mathrm{IL} \cdot \boldsymbol{\nabla}\mu_-^\mathrm{el} - M_-/M_\mathrm{IL} \cdot \boldsymbol{\nabla}\mu_+^\mathrm{el} \Big)\,. \tag{9.8}$$

We restrict our set-up to one spatial dimension, and assume that the inert electrified interface is located at $x = 0$ to which we apply the half-cell potential $\Delta\phi$. Since the electric potential Φ is continuous across the electrode-electrolyte interface, $\Phi(0)$ in the electrolyte is subject to the boundary condition

$$\Phi(0) - \Phi(x \to \infty) = \Delta\phi. \tag{9.9}$$

Without loss of generality, we set the electrolyte potential in the bulk to zero, $\lim_{x\to\infty}\Phi = 0$. Hence, $\Delta\phi = \Phi(0)$ is the potential applied to the electrode. The electroneutral boundary condition $\varrho_\mathrm{F}(x{\to}\infty) = 0$ implies that the bulk concentration $c^\mathrm{b} = c_\pm(x{\to}\infty)$ is completely determined by the total molar volume $\nu = \nu_+ + \nu_-$ via $c^\mathrm{b} \cdot \nu = 1$. Since binary ILs are electrically neutral, $z_+ = -z_+$, and we choose $z_+ > 0$.

Because we neglect viscous forces, $\boldsymbol{\nabla}\boldsymbol{\tau} = 0$, the Gibbs-Duhem relation (eq. (8.26)) becomes $c_+\boldsymbol{\nabla}\mu_+^\mathrm{el} + c_-\boldsymbol{\nabla}\mu_-^\mathrm{el} = 0$, and couples the chemical forces,

$$\boldsymbol{\nabla}\mu_+^\mathrm{el} = -c_-/c_+ \cdot \boldsymbol{\nabla}\mu_-^\mathrm{el}, \tag{9.10}$$

such that eq. (9.8) simplifies to

$$\mathcal{J} = \kappa\rho/Fz_+c_+M_{\mathrm{IL}} \cdot \nabla\mu_-^{\mathrm{el}}, \tag{9.11}$$

where we used the chemical potential of the anion-species to determine the IL-electrolyte,

$$\nabla\mu_-^{\mathrm{el}}{=}-\nu c_+\nabla\left(Fz_+\Phi{-}\gamma_+\frac{\delta F^{\mathrm{int}}}{\delta c_-}{+}\gamma_-\frac{\delta F^{\mathrm{int}}}{\delta c_+}{-}RT\left[\gamma_+\ln\frac{c_-}{c^{\mathrm{b}}}{-}\gamma_-\ln\frac{c_+}{c^{\mathrm{b}}}\right]\right). \tag{9.12}$$

The prefactor “c_+ on the right side has significant implications, as it cancels the concentration appearing in the formula for the electric current, see eq. (9.11) (this cancelling allows for an analytical discussion of the screening profiles, see below). Insertion of eq. (9.12) into the current flux yields

$$\mathcal{J}_{\mathrm{F}} = -\kappa/Fz_+ \cdot \left(1+\chi\cdot\left[\gamma_+^2+\gamma_-^2\right]\varrho_{\mathrm{F}}\nu/Fz_+\right)\cdot\nabla\mu_{\mathrm{IL}}^{\mathrm{el}}, \tag{9.13}$$

where we define the electrochemical potential of the IL electrolyte

$$\nabla\mu_{\mathrm{IL}}^{\mathrm{el}}{=}\nabla\left(Fz_+\Phi{-}2\gamma_-\cdot\delta F^{\mathrm{int}}/\delta c_+{-}RT[\gamma_+\ln(c_-/c^{\mathrm{b}}){-}\gamma_-\ln(c_+/c^{\mathrm{b}})]\right). \tag{9.14}$$

Similar to the relative molar volumes γ_α defined above, we introduce relative molar masses,

$$\tilde{M}_\pm = M_\pm/M_{\mathrm{IL}}\,, \tag{9.15}$$

which are normalized via $\tilde{M}_+ + \tilde{M}_-{=}1$, and introduce an asymmetry parameter (note that $1=\gamma_+ + \gamma_-$),

$$\chi = (\tilde{M}_+\gamma_- - \tilde{M}_-\gamma_+)/(\gamma_+^2+\gamma_-^2)\ = (\tilde{M}_+-\gamma_+)/[2(\gamma_+)^2+1-2\gamma_+]\,. \tag{9.16}$$

The “asymmetry” parameter χ scales the flux $\mathcal{J}_{\mathrm{F}}$ in eq. (9.13) and depends crucially on the species parameters $\tilde{M}_+$ and γ_+. If the ion-species have equal size, $\gamma^{\mathrm{sym}}=1/2$, the asymmetry parameter becomes $\chi(\gamma_\alpha^{\mathrm{sym}})=\tilde{M}_+-1/2$. Furthermore, in the case of completely symmetric ion species, *i.e.* where $\tilde{M}_+=\gamma_+=1/2$, the asymmetry parameter vanishes identically. Furthermore, if the molar volume of the ion-species are assumed being linear functions of the molar masses, *i.e.* if $\nu_\alpha = b\cdot M_\alpha$ for all species α (where $[b]=\mathrm{m}^3\,\mathrm{kg}^{-1}$), then $\gamma_\alpha=\tilde{M}_\alpha$ and the asymmetry parameter vanishes identically. An example for such a scaling is the model $\nu_\alpha = M_\alpha/\rho$, which implies $\gamma_\alpha=\tilde{M}_\alpha$. Note that such assumptions correlate with the model $\tilde{\nu}=b\cdot M_\alpha/N_{\mathrm{A}}a^3$ (se also fig. 9.1 and section 9.2.1).

In eq. (9.14), we used the coupling between c_+ and c_- imposed by the Euler equation for the volume such that

$$\frac{\delta}{\delta c_-}=\frac{\delta c_+}{\delta c_-}\cdot\frac{\delta}{\delta c_+}=-\frac{\gamma_-}{\gamma_+}\cdot\frac{\delta}{\delta c_+},\text{ such that }\gamma_+\frac{\delta F^{\text{int}}}{\delta c_-}-\gamma_-\frac{\delta F^{\text{int}}}{\delta c_+}=2\gamma_-\frac{\delta F^{\text{int}}}{\delta c_+}. \tag{9.17}$$

The quantity $\mu^{\text{el}}_{\text{IL}}$ is the only electrochemical potential necessary to describe the electrolyte transport of the binary system. This is a consequence from the property that the electric flux is the only independent flux in a binary systems, and from the property that all species-couplings are taken into account. The complete set of transport equations thus reads,

$$\varrho_{\text{F}} = -\varepsilon_0\boldsymbol{\nabla}\left(\varepsilon_{\text{R}}\boldsymbol{\nabla}\Phi\right), \tag{9.18}$$

$$\partial_t\varrho_{\text{F}}=-\boldsymbol{\nabla}\left(\varrho_{\text{F}}\mathbf{v}\right)+\kappa/Fz_+\cdot\boldsymbol{\nabla}\left[\left(1+\chi\cdot\left(\gamma_+^2+\gamma_-^2\right)\cdot\varrho_{\text{F}}\nu/Fz_+\right)\cdot\boldsymbol{\nabla}\mu^{\text{el}}_{\text{IL}}\right], \tag{9.19}$$

$$\boldsymbol{\nabla}\mathbf{v}=-\kappa\chi\nu/(Fz_+)^2\cdot\left(\gamma_+^2+\gamma_-^2\right)\cdot\boldsymbol{\nabla}\left[\left(1+\chi\cdot\left(\gamma_+^2+\gamma_-^2\right)\cdot\varrho_{\text{F}}\nu/Fz_+\right)\cdot\boldsymbol{\nabla}\mu^{\text{el}}_{\text{IL}}\right]. \tag{9.20}$$

The forces $\boldsymbol{\nabla}\mu^{\text{el}}_{\text{IL}}$ described by eq. (9.14) can be evaluated using either the integral description (eq. (8.30)), or the gradient description (eq. (8.36)). The integral description follows from substitution of eq. (8.30),

$$\gamma_-\boldsymbol{\nabla}\frac{\delta F^{\text{int}}}{\delta c_+}=\frac{\gamma_-}{\nu}\boldsymbol{\nabla}_{\mathbf{x}}\int \mathrm{d}y^3\mathcal{F}_{\alpha\beta}(|\mathbf{x}-\mathbf{y}|)-\frac{\gamma_-\gamma_+}{Fz_+}\boldsymbol{\nabla}_{\mathbf{x}}\int \mathrm{d}y^3\mathcal{F}_{\alpha\beta}(|\mathbf{x}-\mathbf{y}|)\varrho_{\text{F}}(\mathbf{x}) \tag{9.21}$$

$$=\mathcal{V}^0N_{\text{A}}\gamma_-\gamma_+/ez_+\cdot\boldsymbol{\nabla}\int \mathrm{d}x^3\tilde{\mathcal{F}}_{\alpha\beta}(|\mathbf{x}-\mathbf{y}|)\cdot\varrho_{\text{F}}(\mathbf{x}). \tag{9.22}$$

Here, we used that $\boldsymbol{\nabla}_{\mathbf{x}}\int \mathrm{d}y^3\mathcal{F}_{\alpha\beta}(|\mathbf{x}-\mathbf{y}|)=0$ for spherically symmetric potentials $\mathcal{F}_{\alpha\beta}$ (see lemma 29), and used the elementary charge for $F{=}N_{\text{A}}e$. Alternatively, the gradient expansion eq. (8.36) yields

$$2\gamma_-\boldsymbol{\nabla}(\delta F^{\text{int}}/\delta c_+) = \mathcal{V}^0N_{\text{A}}2\gamma_+\gamma_-/ez_+\cdot\sum_{n=0}^{\infty}\Gamma^{2n}_{+-}\cdot\boldsymbol{\nabla}^{2n+1}\varrho_{\text{F}}. \tag{9.23}$$

9.2 Energy Scales and Dimensions

Next, we simplify the set of equations and bring them into non-dimensional form.

An inspection of eq. (9.14) suggests that we divide both sides by RT and define

$$\tilde{\Phi} = Fz_+/RT\cdot\Phi,\quad\text{and}\quad\tilde{\mu}^{\text{el}}_{\text{IL}} = 1/RT\cdot\mu^{\text{el}}_{\text{IL}}. \tag{9.24}$$

Substituting the non-dimensional chemical potential for $\mu^{\text{el}}_{\text{IL}}$ in eq. (9.19) suggests

$$\tilde{\varrho}_{\text{F}} = \nu\tilde{c}^{\text{b}}/Fz_+\cdot\varrho_{\text{F}},\quad\text{and}\quad\tilde{c}^{\text{b}} = (\gamma_+)^2+(\gamma_-)^2. \tag{9.25}$$

We use the non-dimensional quantities $\tilde{\varrho}_{\mathrm{F}}$ and $\tilde{\Phi}$ and remove the physical dimensions from the Poisson equation. This defines the Debye-length,

$$L_{\mathrm{D}} = \sqrt{k_{\mathrm{B}}Ta^3\tilde{\nu}\tilde{c}^{\mathrm{b}}\varepsilon_0\varepsilon_{\mathrm{R}}/(ez_+)^2}\,. \tag{9.26}$$

This differs from the canonical definition by the ion-asymmetry, *i.e.* the parameters $\gamma_\pm$ appearing in $\tilde{c}^{\mathrm{b}}$,[144] but reproduces the textbook definition for symmetric ions ($\gamma_\pm = 0.5$). Ion asymmetry increases L_{D}, which becomes minimal for $\gamma_\pm$=0.5 because the mixing entropy of a binary electrolyte is extremal for equal ion-size (we discuss the influence of the system parameters on the Debye-length in more detail in fig. 10.1). We use L_{D} to non-dimensionalize our grid,

$$\tilde{x} = x/L_{\mathrm{D}}\,, \qquad \text{and} \qquad \tilde{\boldsymbol{\nabla}} = L_{\mathrm{D}}\cdot\boldsymbol{\nabla}. \tag{9.27}$$

This non-dimensionalization the ion-size, $\tilde{a}$=a/L_{D} , and Debye-length, $\tilde{L}_{\mathrm{D}}$=1. We substitute all non-dimensional quantities into eq. (9.19) and define

$$\partial/\partial\tilde{t} = \varepsilon_0\varepsilon_{\mathrm{R}}/\kappa\cdot\partial/\partial t\,, \quad \text{and} \quad \tilde{\mathbf{v}} = \varepsilon_0\varepsilon_{\mathrm{R}}/\kappa L_{\mathrm{D}}\cdot\mathbf{v}. \tag{9.28}$$

We substitute $\tilde{\varrho}_{\mathrm{F}}$ for the charge density in the expansion ϱ_{F}=$Fz_+(c_+$−$c_-)$ and define

$$\tilde{c}_\alpha = \tilde{c}^{\mathrm{b}}/c^{\mathrm{b}}\cdot c_\alpha. \tag{9.29}$$

Thus, the relation between $\tilde{\varrho}_{\mathrm{F}}$ and ion-concentrations reads (see eq. (9.3))

$$\tilde{\varrho}_{\mathrm{F}} = \tilde{c}_+ - \tilde{c}_-, \qquad \text{where} \qquad \tilde{c}_\pm = \tilde{c}^{\mathrm{b}} \pm \tilde{\varrho}_{\mathrm{F}}\gamma_\mp, \tag{9.30}$$

and the Euler equation for the volume and eq. (9.4) become

$$\tilde{c}^{\mathrm{b}} = \tilde{c}_+\gamma_+ + \tilde{c}_-^{\mathrm{b}}\gamma_-, \text{ and } \tilde{c}^{\mathrm{sat}} = \tilde{c}^{\mathrm{b}}/\gamma_\alpha^*\,, \text{ and } \tilde{\varrho}_{\mathrm{F}}^{\mathrm{sat}} = \mathrm{sign}(z_{\mathrm{sat}})\cdot\tilde{c}^{\mathrm{b}}/\gamma_{\alpha^*}\,. \tag{9.31}$$

From $\tilde{\mathbf{v}}$ and $\tilde{c}_\alpha$ (see eqs. (9.28) and (9.29)) follows

$$\tilde{\boldsymbol{\mathcal{J}}}_{\mathrm{F}} = ez_+L_{\mathrm{D}}/\kappa k_{\mathrm{B}}T\cdot\boldsymbol{\mathcal{J}}_{\mathrm{F}}. \tag{9.32}$$

Next, we introduce two energy scales which appear in the definition of the Debye-length eq. (9.26). First, we substitute the thermal contribution in L_{D} by

$$E_{\mathrm{th}} = k_{\mathrm{B}}T\cdot\tilde{c}^{\mathrm{b}}/2\gamma_+\gamma_- \tag{9.33}$$

In the case of symmetric ion-species ($\gamma_\pm = 1/2$), $E_{\mathrm{th}} \to k_{\mathrm{B}}T$, eq. (9.33) reproduces the canonical definition for the thermal energy.[63] Note that E_{th} becomes extremal for symmetric ions. This can be seen using the ion-ratio $\nu_-/\nu_+ = \gamma_r$, such that $E_{\mathrm{th}} = k_{\mathrm{B}}T\cdot[\gamma_r + 1/(\gamma_r)^2]$. Apparently, $E_{\mathrm{th}}(\gamma_r)$ has a global minimum at $\gamma_r = 1$, *i.e.* for ion-species having the same molar volume, $\nu_- = \nu_+$.

Next, we substitute the electrostatic energy scale appearing in L_{D}. However, this requires the introduction of a characteristic length scale. Here, we choose the ion-size and parametrize the corresponding energy scale via

$$E_{\mathrm{el}} = (ez_+)^2/16\pi\varepsilon_0\varepsilon_{\mathrm{R}}\gamma_+\gamma_- a\,. \tag{9.34}$$

Like the thermal energy scale, $E_{\mathrm{el}} = E_{\mathrm{el}}(r=a)$ takes the textbook form for Coulomb energy of charges at distance a in the case of symmetric ions $\gamma_\pm = 0.5$. Since the relative volumes are bounded by $0 < \gamma_\pm < 1$, the electrostatic energy is minimal at equal ion-sizes ($\nu_- = \nu_+$). Both energy scales are coupled by the length scale L_{D},

$$E_{\mathrm{th}}/E_{\mathrm{el}} = 8\pi/\tilde{\nu}\cdot(L_{\mathrm{D}}/a)^2 = 8\pi/\tilde{\nu}\tilde{a}^2\,. \tag{9.35}$$

Our theory also contains a generalized Bjerrum-length L_{B}, which measures the distance at which the electrostatic energy and the thermal energy become comparable, *i.e.* $E_{\mathrm{el}}(r = L_{\mathrm{B}}) = E_{\mathrm{th}}$. Thus,

$$\tilde{L}_{\mathrm{B}} = 1/8\pi\cdot 1/L_{\mathrm{D}}\,(ez_+)^2/k_BT\varepsilon_0\varepsilon_{\mathrm{R}}\tilde{c}^{\mathrm{b}} = \tilde{\nu}/8\pi\cdot\tilde{a}^3. \tag{9.36}$$

The dimensionless Poisson-equation reads $\tilde{\varrho}_{\mathrm{F}} = -\tilde{\boldsymbol{\nabla}}^2\tilde{\Phi}$. Thus, the coupling between $\tilde{\varrho}_{\mathrm{F}}$ and $\tilde{\Phi}$, as described by the Poisson equation, depends only on the two energy scales thermal energy and electrostatic energy. Furthermore, the dimensionless Poisson equation suggests to introduce non-dimensional electrostatic fields

$$\tilde{\mathbf{D}}_{\mathrm{F}} = \nu\tilde{c}^{\mathrm{b}}/FL_{\mathrm{D}}z_+\cdot\mathbf{D}_{\mathrm{F}}, \qquad \text{and} \qquad \tilde{\mathbf{E}} = \varepsilon_{\mathrm{R}}\varepsilon_0\nu\tilde{c}^{\mathrm{b}}/L_{\mathrm{D}}Fz_+\cdot\mathbf{E}, \tag{9.37}$$

such that $\tilde{\varrho}_{\mathrm{F}} = \tilde{\boldsymbol{\nabla}}\tilde{\mathbf{D}}_{\mathrm{F}}$, $\tilde{\mathbf{E}} = -\tilde{\boldsymbol{\nabla}}\tilde{\Phi}$, and $\tilde{\mathbf{D}}_{\mathrm{F}} = \tilde{\mathbf{E}}$.

Next, we use these dimensionless quantities to obtain the non-dimensional form for the system of equations, given by eqs. (9.18) to (9.20). Altogether, we find

$$\tilde{\varrho}_{\mathrm{F}} = -\tilde{\boldsymbol{\nabla}}^2\tilde{\Phi}, \tag{9.38}$$

$$\partial_{\tilde{t}}\tilde{\varrho}_{\mathrm{F}} = -\tilde{\boldsymbol{\nabla}}\left(\tilde{\varrho}_{\mathrm{F}}\tilde{\mathbf{v}}\right) - \tilde{\boldsymbol{\nabla}}\tilde{\boldsymbol{\mathcal{J}}}_{\mathrm{F}}, \tag{9.39}$$

$$\tilde{\boldsymbol{\nabla}}\tilde{\mathbf{v}} = \chi\tilde{\boldsymbol{\nabla}}\tilde{\boldsymbol{\mathcal{J}}}_{\mathrm{F}}, \tag{9.40}$$

where

$$\tilde{\boldsymbol{\mathcal{J}}}_{\mathrm{F}} = -\left(1 + \chi\tilde{\varrho}_{\mathrm{F}}\right)\tilde{\boldsymbol{\nabla}}\tilde{\mu}^{\mathrm{el}}_{\mathrm{IL}}. \tag{9.41}$$

This system of equations is subject to the explicit form of the chemical forces $\tilde{\boldsymbol{\nabla}}\tilde{\mu}^{\mathrm{el}}_{\mathrm{IL}}$, which can be expressed either using the integral description (see eq. (9.22)), or using the gradient description (see eq. (9.23)). We find for the integral description in non-dimensional form

$$\tilde{\boldsymbol{\nabla}}\tilde{\upmu}^{\mathrm{el}}_{\mathrm{IL}} = \tilde{\boldsymbol{\nabla}}\left(\tilde{\Phi} - \mathcal{V}^0/8\pi E_{\mathrm{el}} \cdot \sqrt{E_{\mathrm{th}}/8\pi E_{\mathrm{el}}} \cdot 1/\tilde{\nu} \cdot \int \mathrm{d}x^3\, \tilde{\mathfrak{F}}_{+-}(|\tilde{\mathbf{x}} - \tilde{\mathbf{y}}|)\tilde{\varrho}_{\mathrm{F}}(\tilde{\mathbf{x}}) - \right.$$
$$\left. -\gamma_+ \cdot \ln\left[\tilde{c}_-/\tilde{c}^{\mathrm{b}}\right] + \gamma_- \cdot \ln\left[\tilde{c}_+/\tilde{c}^{\mathrm{b}}\right]\right). \quad (9.42)$$

In a similar manner, we find for the chemical forces in the gradient description,

$$\tilde{\boldsymbol{\nabla}}\tilde{\upmu}^{\mathrm{el}}_{\mathrm{IL}} = \tilde{\boldsymbol{\nabla}}\left(\tilde{\Phi} - \gamma_+ \ln\left[\tilde{c}_-/\tilde{c}^{\mathrm{b}}\right] + \gamma_- \ln\left[\tilde{c}_+/\tilde{c}^{\mathrm{b}}\right] - \mathcal{V}^0/E_{\mathrm{th}} \cdot \sum_{n=0}^{\in} \tilde{\Gamma}^{2n}_{+-}\, \tilde{\boldsymbol{\nabla}}^{2n}\tilde{\varrho}_{\mathrm{F}}\right), \quad (9.43)$$

where we introduced the non-dimensional perturbation modes

$$\tilde{\Gamma}^{2n}_{+-} = \Gamma^{2n}_{+-}/a^3\tilde{\nu}(L_{\mathrm{D}})^{2n}\,. \quad (9.44)$$

We summarize our choice for removing the physical dimensions from our electrolyte description in table 9.1.

Quantity	Dimension	Non-dimensional
Electrolyte electric potential	$[\Phi] = \mathrm{kg\,m^2\,A^{-1}\,s^{-3}}$	$\tilde{\Phi} = \Phi \cdot Fz_+/RT$
Electroneutral bulk concentration	$\left[c^{\mathrm{b}}\right] = \mathrm{mol\,m^{-3}}$	$\tilde{c}^{\mathrm{b}} = (\gamma_+)^2 + (\gamma_-)^2$
Concentration	$[c_\alpha] = \mathrm{mol\,m^{-3}}$	$\tilde{c}_\alpha = c_\alpha \cdot \nu\tilde{c}^{\mathrm{b}}$
Charge density	$[\varrho_{\mathrm{F}}] = \mathrm{A\,s\,m^{-3}}$	$\tilde{\varrho}_{\mathrm{F}} = \varrho_{\mathrm{F}} \cdot \nu\tilde{c}^{\mathrm{b}}/Fz_+$
Position from electrode	$[x] = \mathrm{m}$	$\tilde{x} = x/L_{\mathrm{D}}$
Gradient	$[\boldsymbol{\nabla}] = \mathrm{m^{-1}}$	$\tilde{\boldsymbol{\nabla}} = \boldsymbol{\nabla} \cdot L_{\mathrm{D}}$
Time	$[t] = \mathrm{s}$	$\tilde{t} = t \cdot \kappa/\varepsilon_0\varepsilon_{\mathrm{R}}$
Velocity	$[\mathbf{v}] = \mathrm{m\,s^{-1}}$	$\tilde{\mathbf{v}} = \mathbf{v} \cdot \varepsilon_0\varepsilon_{\mathrm{R}}/L_{\mathrm{D}}\kappa\chi$
Electric field	$[\boldsymbol{E}] = \mathrm{kg\,m\,A^{-1}\,s^{-3}}$	$\tilde{\boldsymbol{E}} = \boldsymbol{E} \cdot L_{\mathrm{D}}ez_+/k_{\mathrm{B}}T$
Dielectric displacement	$[\boldsymbol{D}] = \mathrm{A\,s\,m^{-2}}$	$\tilde{\boldsymbol{D}} = \boldsymbol{D} \cdot a\tilde{c}^{\mathrm{b}}/L_{\mathrm{D}}ez_+$
Chemical potential	$[\upmu_\alpha] = \mathrm{kg\,m^2\,mol^{-1}\,s^{-2}}$	$\tilde{\upmu}_\alpha = \upmu_\alpha/RT$

Table 9.1: Sumarry of non-dimensional quantities.

We briefly discuss the influence of the asymmetry parameter χ (see eq. (9.16)) on the system of transport equations. The asymmetry parameter scales the fluxes convection velocity $\mathbf{v}$ and $\tilde{\mathcal{J}}_{\mathrm{F}}$ via $1 + \chi\tilde{\varrho}^{\mathrm{sat}}_{\mathrm{F}}$ (see eq. (9.41)). However, the charge density becomes maximal / minimal in the case of saturation (see eq. (9.31)), $\tilde{\varrho}^{\mathrm{sat}}_{\mathrm{F}} = \mathrm{sign}(z_{\alpha^*})\tilde{c}^{\mathrm{b}}/\gamma_{\alpha^*}$, such that the asymmetry-correction has as maximal magnitude

$$1 + \chi\tilde{\varrho}^{\mathrm{sat}}_{\mathrm{F}} = 1 + \mathrm{sign}(z_{\alpha^*}) \cdot (\tilde{M}_+ - \gamma_+/\gamma_{\alpha^*}) = \tilde{M}_{\alpha^*}/\gamma_{\alpha^*}\,. \quad (9.45)$$

In fig. 9.1, we show a parameter-study for χ, and the maximal flux-correction eq. (9.45) to $\mathcal{J}_{\mathrm{F}}$ (see eq. (9.39)). As can be inferred from fig. 9.1a), χ ranges between

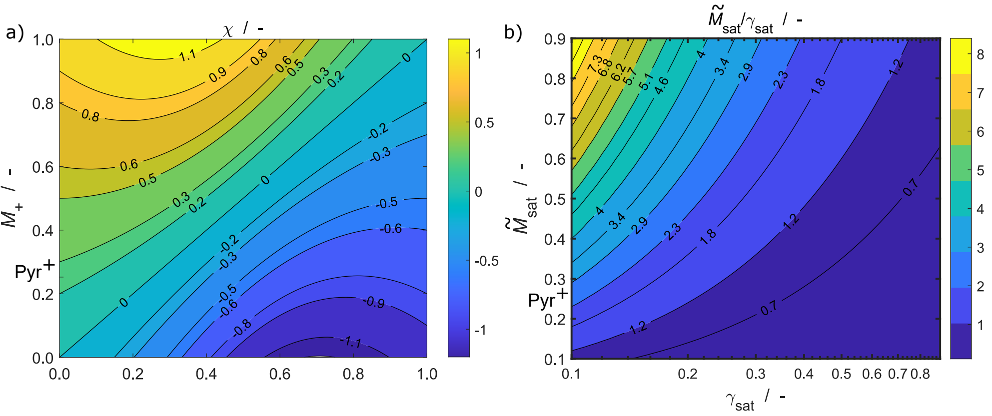

Figure 9.1: a) Parameter study of the asymmetry parameter χ (see eq. (9.16)). b) Parameter study for the flux-correction $\chi\varrho_F^{\mathrm{sat}}$ (see eq. (9.41) and eq. (9.45)).

zero and one. The mass-ratio for the Pyr-cation is roughly $\tilde{M}_{\mathrm{Pyr}}$=0.25. Also, as it is shown in fig. 9.1b), the flux correction $\tilde{M}_{\alpha^*}/\gamma_{\alpha^*}$ does not deviate much from one for reasonable parameters $(\tilde{M}_+, \gamma_+)$.

The non-dimensional form for the dynamical transport equations highlight the role of the system parameters. Here, both the relative masses and the relative molar volumes appear in the asymmetry parameter and the flux-correction. However, the role of these parameters changes in the stationary case as the masses disappear from the stationary equations, and only the volumes remain as system parameters. Thus, the Euler equation for the volume and the existence of finite molar volumes are crucial in the model.

9.2.1 Special Case: Symmetric Ion Species ($\chi = 0$)

Here, we discuss the special case of symmetric ion species, *i.e.* χ=0.

As discussed above, χ=0 holds if the ion species have equal molar volumes and masses, or if the molar volumes are proportional to the molar masses.

When $\chi = 0$, the convection velocity becomes constant, $\tilde{\boldsymbol{\nabla}}\tilde{\mathbf{v}} = 0$ (see eqs. (9.38) to (9.40)), and is completely determined by the boundary conditions (BCs). When we assume no-flux BCs, *i.e.* $\mathbf{v}(x{=}0){=}0$, then $\mathbf{v}$=0 everywhere. Furthermore, the system of equations can be reduced to one single equation

$$\left.\begin{aligned} \tilde{\varrho}_{\mathrm{F}} &= -\tilde{\boldsymbol{\nabla}}^2\tilde{\Phi}, \\ \partial_{\tilde{t}}\tilde{\varrho}_{\mathrm{F}} &= \tilde{\boldsymbol{\nabla}}^2\tilde{\mu}^{\mathrm{el}}_{\mathrm{IL}} \end{aligned}\right\} \quad \underset{\chi=0}{\Longrightarrow} \quad \partial_{\tilde{t}}\tilde{\boldsymbol{\nabla}}^2\tilde{\Phi} = -\tilde{\boldsymbol{\nabla}}^2\tilde{\mu}^{\mathrm{el}}_{\mathrm{IL}}. \tag{9.46}$$

We eliminate the gradients appearing on both sides of eq. (9.46) via integration using electroneutral boundary conditions (EBCs). These EBCs are defined by the condition that the electrolyte is electrically neutral in the bulk $x \to \infty$,

$$\tilde{\mathbf{E}}(x \to \infty) = 0, \quad \tilde{\varrho}_{\mathrm{F}}(x \to \infty) = 0, \quad \tilde{\Phi}(x \to \infty) = 0, \quad \tilde{c}_{\pm}(x \to \infty) = \tilde{c}^{\mathrm{b}}. \tag{9.47}$$

Thus, when we assume that the derivatives $\partial_{\tilde{t}}$ and $\tilde{\boldsymbol{\nabla}}$ "commute" with each other, we can omit the spatial derivatives such that eq. (9.46) reads

$$\partial_{\tilde{t}}\tilde{\Phi} = -\tilde{\mu}^{\mathrm{el}}_{\mathrm{IL}}. \tag{9.48}$$

Next, we assume that χ=0 due to symmetric ion species, *i.e.* $\gamma_{\pm}$=$\tilde{M}_{\pm}$=1/2. Hence, the concentrations become (see eq. (9.30))

$$\tilde{c}_{\pm} = (1 \pm \tilde{\varrho}_{\mathrm{F}})/2, \qquad \text{and} \qquad \gamma_{\pm}/\tilde{c}^{\mathrm{b}} = 1. \tag{9.49}$$

Thus, the logarithmic terms appearing on the right side of eqs. (9.42) and (9.43) can be cast into one single term. THe integral description,

$$\partial_{\tilde{t}}\tilde{\Phi} = \frac{1}{2}\ln\left(\frac{1+\tilde{\Phi}''}{1-\tilde{\Phi}''}\right) - \tilde{\Phi} - \frac{\mathcal{V}^0}{8\pi E_{\mathrm{el}}}\sqrt{\frac{E_{\mathrm{th}}}{8\pi E_{\mathrm{el}}}}\,\frac{1}{\tilde{\nu}}\int \mathrm{d}x^3\, \tilde{\mathcal{F}}_{+-}(|\tilde{\mathbf{x}}-\tilde{\mathbf{y}}|)\tilde{\Phi}''(\tilde{\mathbf{x}}), \tag{9.50}$$

whereas the gradient description reads

$$\partial_{\tilde{t}}\tilde{\Phi} = \frac{1}{2}\ln\left(\frac{1+\tilde{\Phi}''}{1-\tilde{\Phi}''}\right) - \left(1 + \frac{\mathcal{V}^0}{E_{\mathrm{th}}}\sum_{n=0}^{\infty}\tilde{\Gamma}^{2n}_{+-}\cdot\tilde{\boldsymbol{\nabla}}^{2(n+1)}\right)\tilde{\Phi}. \tag{9.51}$$

9.2.2 Non-Convective Case ($\mathrm{v} = 0$)

Here, we consider the case where the equation for convection (eq. (9.40)) is not taken into account in the system of equations, and where the velocity is set to zero in the remaining equations. Thus, we find that this case equals exactly the case of symmetric ions except the dangling correction $\tilde{\boldsymbol{\nabla}}[\chi\tilde{\varrho}_{\mathrm{F}}\tilde{\boldsymbol{\nabla}}\tilde{\mu}^{\mathrm{el}}_{\mathrm{IL}}]$,

$$\tilde{\varrho}_{\mathrm{F}} = -\tilde{\boldsymbol{\nabla}}^2\Phi, \qquad \text{and} \qquad \partial_{\tilde{t}}\tilde{\varrho}_{\mathrm{F}} = \tilde{\boldsymbol{\nabla}}\left[(1+\chi\tilde{\varrho}_{\mathrm{F}})\,\tilde{\boldsymbol{\nabla}}\tilde{\mu}^{\mathrm{el}}_{\mathrm{IL}}\right]. \tag{9.52}$$

9.3 Stationary State

One common focus in the study of ILs near electrified interfaces lies on the formation of equilibrium structures. Here, we address this goal, and discuss the system of equations in the stationary limit.

We define the stationary state by the condition $\partial_{\tilde{t}}\tilde{\varrho}_\mathrm{F} = 0$, and via no-flux boundary conditions (NFBCs) at the interface, $\tilde{\boldsymbol{\mathcal{J}}}_\mathrm{F}(x{=}0){=}\mathbf{v}(x{=}0){=}0$. Thus, eq. (9.39) implies that $\tilde{\varrho}_\mathrm{F}\tilde{\mathbf{v}}{+}\tilde{\boldsymbol{\mathcal{J}}}_\mathrm{F}{=}0$ everywhere. However, because the fluxes vanish at the interface, they vanish everywhere.

$$\tilde{\boldsymbol{\mathcal{J}}}_\mathrm{F} = 0, \qquad \text{and} \qquad \tilde{\mathbf{v}} = 0. \tag{9.53}$$

The system of equations describing a binary IL-electrolyte in stationary state reduces to two equations,

$$\tilde{\varrho}_\mathrm{F} = -\tilde{\boldsymbol{\nabla}}^2\tilde{\Phi}, \tag{9.54}$$

$$0 = \tilde{\boldsymbol{\nabla}}\tilde{\mu}^\mathrm{el}_\mathrm{IL}. \tag{9.55}$$

Apparently, this reproduces exactly the electrochemical equilibrium defined by eq. (5.234): here, the only independent force relates to the fluxes via $\tilde{\boldsymbol{\mathcal{J}}}_\mathrm{F} \propto \tilde{\boldsymbol{\nabla}}\tilde{\mu}^\mathrm{el}_\mathrm{IL}$ and $\tilde{\mathbf{v}} \propto \tilde{\boldsymbol{\nabla}}\tilde{\mu}^\mathrm{el}_\mathrm{IL}$ (see eqs. (9.40) and (9.41)), *i.e.* $\tilde{\boldsymbol{\nabla}}\tilde{\mu}^\mathrm{el}_\mathrm{IL} = 0$ implies that all fluxes vanish identically.

Next, we use electroneutral BCs, eq. (9.47), and integrate both sides of eq. (9.55). Thus, the stationary integral description reads (see eq. (9.42))

$$0 = \tilde{\Phi} - \gamma_+ \ln\frac{\tilde{c}_-}{\tilde{c}^\mathrm{b}} + \gamma_- \ln\frac{\tilde{c}_+}{\tilde{c}^\mathrm{b}} - \frac{\mathcal{V}^0\sqrt{E_\mathrm{th}}}{(8\pi E_\mathrm{el})^{3/2}}\frac{1}{\tilde{\nu}}\int \mathrm{d}x^3\,\tilde{\mathcal{F}}_{+-}(|\tilde{\mathbf{x}}{-}\tilde{\mathbf{y}}|)\tilde{\varrho}_\mathrm{F}(\tilde{\mathbf{x}}), \tag{9.56}$$

whereas using the gradient description (see eq. (9.43)), eq. (9.55) becomes

$$0 = \tilde{\Phi} - \gamma_+ \ln\left[\tilde{c}_-/\tilde{c}^\mathrm{b}\right] + \gamma_- \ln\left[\tilde{c}_+/\tilde{c}^\mathrm{b}\right] - \mathcal{V}^0/E_\mathrm{th}\cdot\sum_{n=0}^{\infty}\tilde{\Gamma}^{2n}_{+-}\tilde{\boldsymbol{\nabla}}^{2n}\tilde{\varrho}_\mathrm{F}. \tag{9.57}$$

Apparently, the molar masses appearing as parameters in the dynamical transport equations via the asymmetry parameter χ (see eqs. (9.7), (9.8), (9.39), (9.40), (9.42) and (9.43) become irrelevant in the stationary limit. This is a consequence of the fact that electrolyte momentum is important only for dynamical processes. In contrast, because the Euler equation for the volume holds in any state, the volume parameters $\gamma_\pm$ remain as exclusive system parameters in the system of stationary equations, see eqs. (9.55) to (9.57).

10 Static Asymptotic Analysis

The gradient description of the stationary state (see eq. (9.57)) renders useful to analytical investigations. These analytical investigations, however, are based on different limiting assumptions, which we discuss in this chapter. First, in section 10.1, we discuss the limiting cases of small and large potentials, derive approximations for our variables and implement these results into our stationary description. In section 10.2, we focus on the limit of vanishing molecular interactions $\mathcal{V}^0 \to 0$. Finally, in section 10.3, we discuss also the case of interacting electrolytes.

10.1 Small and Large Potentials

The set of equations, which are necessary to describe a binary IL in stationary state, eq. (9.54) and either eq. (9.57) or eq. (9.56), can be solved using numerical methods. However, here, we focus on the analytical analysis of the gradient description. Our strategy is to focus on two different electrolyte regions. First, we discuss the region far away from the interface, and assume that this region can be described by small perturbations from the electroneutral bulk state. Second, we focus on the region close to the interface, where we expect strong electric fields and where assume charge saturation. For completeness, we restate the complete set of stationary equations,

$$\tilde{\varrho}_{\mathrm{F}} = -\tilde{\boldsymbol{\nabla}}^2 \tilde{\Phi}, \tag{10.1}$$

$$0 = \tilde{\Phi} - \gamma_+ \ln\left[\tilde{c}_-/\tilde{c}^{\mathrm{b}}\right] + \gamma_- \ln\left[\tilde{c}_+/\tilde{c}^{\mathrm{b}}\right] - \mathcal{V}^0/E_{\mathrm{th}} \cdot \sum_{n=0}^{\in} \tilde{\mathit{\Gamma}}_{+-}^{2n} \dot{\tilde{\boldsymbol{\nabla}}}^{2n} \tilde{\varrho}_{\mathrm{F}}. \tag{10.2}$$

The higher order gradients and the differing volumes appearing on the right side of eq. (10.2) hinder our analysis. To overcome these obstacles, we distinguish different limiting cases in our analysis.

First, we focus on the electrolyte region far away from the electrode where we assume that the electrolyte deviates only slightly from the electroneutral state. This motivates the limiting case of small charge-densities, $\tilde{\varrho}_{\mathrm{F}} \ll 1$, corresponding to small potentials. We reexpress the ion concentrations via the charge density, see eq. (9.30), *i.e.* $\tilde{c}_\pm/\tilde{c}^{\mathrm{b}} = 1 \pm \tilde{\varrho}_{\mathrm{F}} \gamma_\mp / \tilde{c}^{\mathrm{b}}$, and expand the logarithmic terms in eq. (10.2) up to first order around the electroneutral state $\tilde{\varrho}_{\mathrm{F}} = \tilde{\varrho}_{\mathrm{F}}^{\mathrm{bulk}} = 0$,

$$\gamma_{+} \ln\left(\tilde{c}_{-}/\tilde{c}^{\mathrm{b}}\right) - \gamma_{-} \ln\left(\tilde{c}_{+}/\tilde{c}^{\mathrm{b}}\right) \approx -\tilde{\varrho}_{\mathrm{F}}. \tag{10.3}$$

Substituting this result into the trivial force law, eq. (10.2), yields

$$\tilde{\varrho}_{\mathrm{F}} = -\tilde{\boldsymbol{\nabla}}^{2}\tilde{\Phi}, \tag{10.4}$$

$$0 = \tilde{\Phi} + \hat{\varepsilon}_{\mathrm{R}}\tilde{\varrho}_{\mathrm{F}}, \tag{10.5}$$

where we introduced the dielectric operator

$$\hat{\varepsilon}_{\mathrm{R}} = 1 - \frac{\mathcal{V}^{0}}{E_{\mathrm{th}}} \sum_{n=0}^{\infty} \tilde{\Gamma}_{+-}^{2n} \cdot \tilde{\boldsymbol{\nabla}}^{2}. \tag{10.6}$$

In the absence of molecular repulsion, $\mathcal{V}^{0}$=0, the non-dimensional dielectric operator reduces to the canonical scalar-valued non-dimensional dielectric parameter $\hat{\varepsilon}_{\mathrm{R}} \rightarrow 1$. Quantities like $\hat{\varepsilon}_{\mathrm{R}}$ usually arise in the liquid state theory of classical statistical mechanics. We emphasize that the introduction of a dielectric operator like eq. (10.6) can be implemented in various types. For example, $\hat{\varepsilon}_{\mathrm{R}}^{\Gamma} = \mathcal{V}^{0}/E_{\mathrm{th}} \cdot \sum_{n=0}^{\infty} \tilde{\Gamma}_{+-}^{2n} \cdot \tilde{\boldsymbol{\nabla}}^{2}$, is not subject to the assumption of small potentials. Based on this definition, the gradient description of the chemical forces (see eq. (9.43)) becomes $\tilde{\boldsymbol{\nabla}}\tilde{\mu}_{\mathrm{IL}}^{\mathrm{el}} = \tilde{\boldsymbol{\nabla}}(\tilde{\Phi} - \gamma_{+}\ln[\tilde{c}_{-}/\tilde{c}^{\mathrm{b}}] + \gamma_{-}\ln[\tilde{c}_{+}/\tilde{c}^{\mathrm{b}}] - \hat{\varepsilon}_{\mathrm{R}}^{\Gamma}\tilde{\varrho}_{\mathrm{F}})$. Another approach is to implement the Poisson equation directly into the forces which implies that $\tilde{\Phi}$ is the only variable, and yields $\hat{\varepsilon}_{\mathrm{R}}^{\tilde{\Phi}} = -\hat{\varepsilon}_{\mathrm{R}} \cdot \tilde{\boldsymbol{\nabla}}^{2}$ occurring in the trivial force equation.

10.2 Mean Steric Effect: Charge Saturation

In this section, we neglect non-local interactions, $\mathcal{V}^{0}$=0, and discuss the EDL structure based on the bulk free energy $F^{\mathrm{int}} = \int \mathrm{d}V\, \rho\varphi_{\mathrm{H}}$ (see eq. (8.10)). The corresponding system of equations reads (see eqs. (10.1) and (10.2))

$$0 = \tilde{\Phi} - \gamma_{+}\ln(\tilde{c}_{-}/\tilde{c}^{\mathrm{b}}) + \gamma_{-}\ln(\tilde{c}_{+}/\tilde{c}^{\mathrm{b}}). \tag{10.7}$$

10.2.1 Static Asymptotic Analysis: Small Potentials $|\tilde{\Phi}| \ll 1$

In this section, we study the EDL far away from the electrode, *i.e.* close to the electroneutral bulk (large $\tilde{x}$) and assume small potentials $|\tilde{\Phi}| \ll 1$. Since we non-dimensionalized Φ using the energy scale E_{th} (see eq. (9.24)), this coincides with the regime of high temperatures. According to eq. (10.7), small potentials correspond to small dimensionless charge densities $\tilde{\varrho}_{\mathrm{F}} \ll 1$. We approach the EDL from the electroneutral bulk region along the direction of decreasing values $\tilde{x}$. Inserting eq. (10.4) into eq. (10.5) (where $\hat{\varepsilon}_{\mathrm{R}} = 1$) reduces our description to one equation,

$$\tilde{\boldsymbol{\nabla}}^2 \tilde{\Phi} = \tilde{\Phi}. \tag{10.8}$$

We solve this equation using the electroneutral BCs from above (see eq. (9.47)),

$$\tilde{\Phi}(\tilde{x}) = \Delta\tilde{\phi} \cdot \exp(-\tilde{x}), \quad \text{and} \quad \tilde{\varrho}_{\mathrm{F}}(\tilde{x}) = -\Delta\tilde{\phi} \cdot \exp(-\tilde{x}). \tag{10.9}$$

Thus, the dimensional electrolyte potential $\Phi(x) = \Delta\phi \cdot \exp(-x/L_{\mathrm{D}})$ decays exponentially, and the decay length in the limit $|\tilde{\Phi}| \ll 1$ is the Debye length $L_{\mathrm{D}} = \sqrt{k_{\mathrm{B}} T a^3 \tilde{\mathrm{v}} \tilde{c}^{\mathrm{b}} \varepsilon_0 \varepsilon_{\mathrm{R}}} / e z_+$ defined in eq. (9.26). Thus, the width of the EDL is determined by the damping parameter $k = 1/L_{\mathrm{D}}$, *i.e.* by the Debye-length L_{D}.

We examine the influence of ion-asymmetry on the damping, and express k via

$$k(\gamma_{\mathrm{r}}) = \sqrt{(e z_+)^2 / k_{\mathrm{B}} T \varepsilon_0 \varepsilon_{\mathrm{R}} a^3 \tilde{\mathrm{v}} (1 + 2[\gamma_+]^2 - 2\gamma_+)}. \tag{10.10}$$

Because the damping $k(\gamma_{\mathrm{r}})$ is a function of ion-asymmetry with global minimum at $\gamma_+ {=} 1/2$, the EDL-width is maximal for ion-species of equal size.

The surface charge density $\mathcal{Q}(x)$ comprised in the EDL is the cumulative charge from the electroneutral bulk up to x, and is determined by the electric field,

$$\mathcal{Q}(x) = \int_x^{L_{\mathrm{EDL}}} \mathrm{d}y \, \varrho_{\mathrm{F}}(y) = \varepsilon_0 \varepsilon_{\mathrm{R}} \Phi'(x) = -\varepsilon_0 \varepsilon_{\mathrm{R}} \Phi(x) / L_{\mathrm{D}} \, . \tag{10.11}$$

The total surface-charge-density comprised in the EDL is thus determined by the boundary condition for the electric field at the interface,

$$\mathcal{Q}^{\mathrm{tot}} = \mathcal{Q}(0) = -\varepsilon_0 \varepsilon_{\mathrm{R}} \Delta\phi / L_{\mathrm{D}}, \tag{10.12}$$

whereas the corresponding differential capacitance is

$$\mathrm{d}\mathcal{Q}^{\mathrm{tot}} / \mathrm{d}(\Delta\phi) \; = -\varepsilon_0 \varepsilon_{\mathrm{R}} / L_{\mathrm{D}} \, . \tag{10.13}$$

10.2.2 Static Asymptotic Analysis: Large Potentials $|\tilde{\Phi}| \gg 1$

Next, we discuss the EDL region close to the electrode/electrolyte interface where we assume large potentials $|\tilde{\Phi}| \gg 1$. Due to our non-dimensionalization of the electric potential (see eq. (9.24)), this corresponds to the limit of zero temperature, $T = 0$.

Starting point is the stationary equation for vanishing molecular repulsion ($\mathcal{V}^0 = 0$), see eq. (10.7). In this region of the electrolyte, the logarithmic terms in eq. (10.7) must compensate the diverging potential term $\tilde{\Phi}$. However, the behaviour of the logarithmic terms is restricted due to the mean volume constraint (see eq. (5.178)), and the finite molar volumes of the ion-species imply concentration saturation near the electrified interface for large enough potentials $\Delta\tilde{\phi}$ (see eq. (9.31)). In contrast, the counter-species depletes within this region. Thus, depending upon the sign of the potential $\Delta\tilde{\phi}$, the condition of stationarity reads

$$|\tilde{\Phi}| = |\gamma_{\pm} \cdot \ln(\gamma_{\mp}) + \gamma_{\mp} \cdot \lim_{\tilde{c}_{\pm}\to 0} \ln(\tilde{c}_{\pm}/\tilde{c}^{\mathrm{b}})|. \tag{10.14}$$

As consequence, one of the logarithmic terms diverges if one species depletes $\tilde{c}_{\pm} \to 0$, and the other species saturates $\tilde{c}_{\pm} \to \tilde{c}^{\mathrm{sat}}_{\pm} = \tilde{c}^{\mathrm{b}}/\gamma_{\pm}$. Since electric fields are continuous across interfaces, the polarization of the electrolyte potential near the interface equals the electrode polarization $\Delta\tilde{\phi}$. Thus, the saturating species α^* is uniquely determined by the sign of the electrode potential, $\mathrm{sign}(z_{\alpha^*}) = -\mathrm{sign}\,(\Delta\phi)$. Altogether, the charge saturation corresponding to the saturated concentration profile is determined by the screening-length

$$\tilde{\varrho}^{\mathrm{sat}}_{\mathrm{F}} = -\mathrm{sign}(\Delta\tilde{\phi}) \cdot \theta(\tilde{L}_{\mathrm{EDL}} - \tilde{x}) \cdot \tilde{c}^{\mathrm{b}}/\gamma_{\alpha^*}\,, \tag{10.15}$$

This form for the charge density solves eq. (10.7) over some EDL-width $\tilde{L}_{\mathrm{EDL}}$. Here θ denotes the Heaviside function. Thus, the charge profile has a “box-shaped” form of constant saturation value over the distance $\tilde{L}_{\mathrm{EDL}}$ into the bulk electrolyte as measured from the interface. The EDL-width and the profile of the electric potential can be determined as follows. Substitution of eq. (10.15) into the Poisson equation yields $\tilde{\boldsymbol{\nabla}}^2\tilde{\Phi} = \mathrm{sign}(\Delta\tilde{\phi}) \cdot \tilde{c}^{\mathrm{b}}/\gamma_{\alpha^*}$. We integrate this modified Poisson equation twice over the interval $[\tilde{x}, \tilde{L}_{\mathrm{EDL}}]$, assuming electroneutral BCs at $\tilde{x} = \tilde{L}_{\mathrm{EDL}}$, see eq. (9.47). As result, for the electrolyte electric potential we find

$$\tilde{\Phi}(\tilde{x}) = \Delta\tilde{\phi} \cdot \left(1 - \tilde{x}/\tilde{L}_{\mathrm{EDL}}\right)^2. \tag{10.16}$$

The EDL-width is determined by the interface BC $\tilde{\Phi}(0) = \Delta\tilde{\phi}$. Hence,

$$\tilde{L}_{\mathrm{EDL}} = \sqrt{2\gamma_{\alpha^*}|\Delta\tilde{\phi}|/\tilde{c}^{\mathrm{b}}} = \sqrt{\gamma_{\alpha^*} e z_+ |\Delta\phi|/\gamma_+\gamma_- E_{\mathrm{th}}}\,. \tag{10.17}$$

Apparently, the EDL-width $\tilde{L}_{\mathrm{EDL}}$ increases with increasing γ_{α^*}, since the amount of charges which are necessary to screen the overpotential $\Delta\tilde{\phi}$ need “more space”. Also, the screening width is larger for enhanced interface polarizations $\Delta\tilde{\phi}$. Furthermore, $\tilde{L}_{\mathrm{EDL}}$ also increases with decreasing temperature. The corresponding dimensional EDL-width reads

$$L_{\mathrm{EDL}} = L_{\mathrm{D}} \cdot \tilde{L}_{\mathrm{EDL}} = \sqrt{2a^3|\Delta\phi|\gamma_{\alpha^*}\tilde{\nu}\varepsilon_0\varepsilon_{\mathrm{R}}/ez_+} \tag{10.18}$$

and is larger than L_{D} exactly if $\tilde{L}_{\mathrm{EDL}} > 1$, *i.e.* for small temperatures, large polarizations $\Delta\tilde{\phi}$, or “large” screening species.

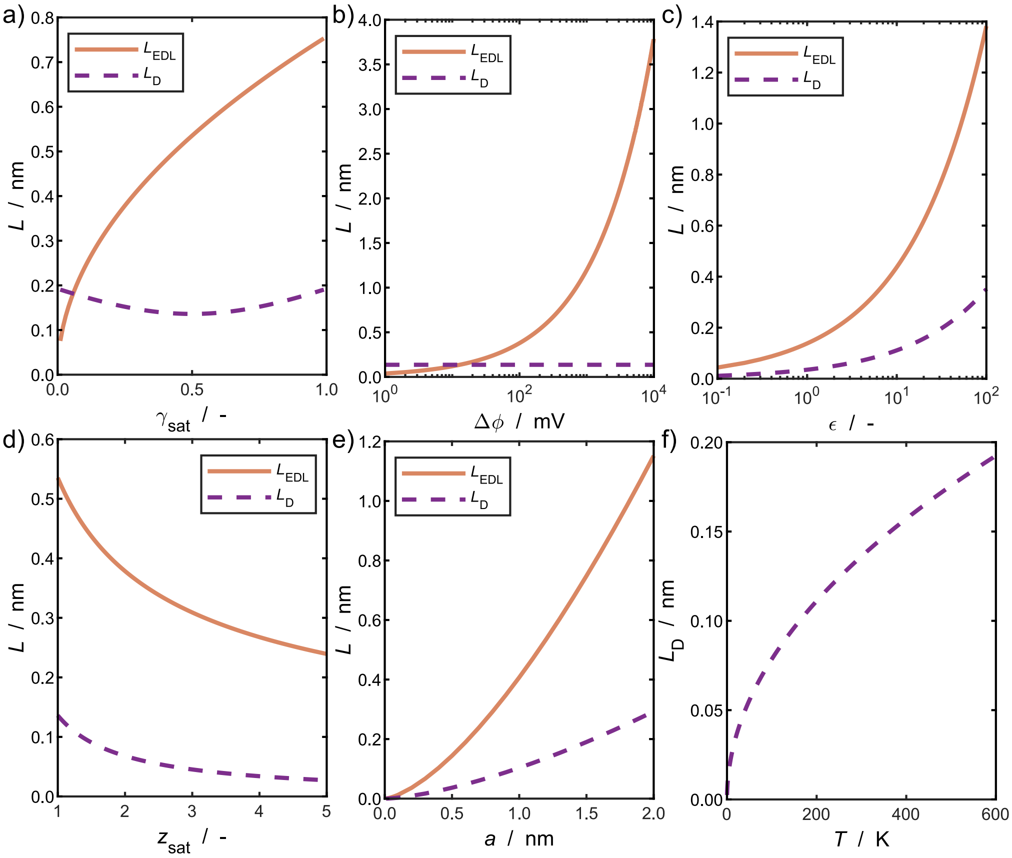

Figure 10.1: Parameter study for Debye-length L_{D}, defined by eq. (9.26), and the EDL-width L_{EDL}, defined by eq. (10.18). If not stated otherwise, all plots refer to the system parameters $T = 300\,\mathrm{K}$, $\varepsilon_{\mathrm{R}} = 15$, $\gamma_{+} = 0.5$, $a = 1.2\,\mathrm{nm}$, $\Delta\phi = -200\,\mathrm{mV}$ and $z_{+} = 1$. a) L_{D} and L_{EDL} as function of the ion-asymmetry γ_{+}. b) L_{D} and L_{EDL} as function of interface potential $|\Delta\phi|$. c) L_{D} and L_{EDL} as function of the dielectricity ε_{R}. d) L_{D} and L_{EDL} as function of the valency. e) L_{D} and L_{EDL} as function of the ion size a. f) L_{D} as function of temperature. L_{EDL} does not depend on temperature and thus is constant (here $L_{\mathrm{EDL}} = 0.53\,\mathrm{nm}$).

Figure 10.1 illustrates the influence of the system parameters on the Debye-length L_{D}, defined by eq. (9.26), and the EDL-width L_{EDL}, defined by eq. (10.18). The EDL width L_{EDL} is larger than the Debye length except for highly asymmetric ions, or for small interface potentials (where the validity of L_{EDL} becomes ill-defined). Figure 10.1a) shows the influence of ion-asymmetry on both length scales. As mentioned above, the Debye length is minimal for symmetric ions ($\gamma = 0.5$). This is due to the entropy becoming extremal for equal sized constituents. In contrast, the EDL width increases with increasing ion asymmetry. Figure 10.1b) shows the influence of the interface potential on the EDL-width. Apparently, the EDL width increases with $\sqrt{\gamma_+}$. Note that the Debye length does not depend upon the interface potential and is thus constant (here $E_{\mathrm{th}} \approx 25\,\mathrm{meV}$). Figure 10.1c) shows the influence of the dielectric constant ε_{R} on both length scales. Apparently, both increase with increasing dielectric constant. Figure 10.1d) illustrates the influence of the ion valencies on the EDL length scales. Both decrease with increasing value z_+. Figure 10.1e) shows that both EDL length scales increase with increasing ion size a. Figure 10.1f) shows that the Debye length increases with temperature. Since the thermal energy competes with charge ordering influences in the EDL, increasing the temperature makes the EDL more diffuse. Note that the EDL width L_{EDL} does not depend on temperature ($L_{\mathrm{EDL}} = 0.53\,\mathrm{nm}$).

We determine the surface charge density $\mathcal{Q}$ from the dimensional form of the solution for the electric potential,

$$\Phi(x) = \Delta\phi \cdot (1 - x/L_{\mathrm{EDL}})\,. \tag{10.19}$$

The cumulative charge from the electroneutral bulk up to position x in the electrolyte, $\mathcal{Q}(x)$, follows from integration of the charge density over the integral $[x; L_{\mathrm{EDL}}]$ (assuming electroneutral BCs at $x = L_{\mathrm{EDL}}$)

$$\mathcal{Q}(x) = \int_x^{L_{\mathrm{EDL}}} \mathrm{d}y\, \varrho_{\mathrm{F}}(y) = -2\varepsilon_0\varepsilon_{\mathrm{R}}\Delta\phi/L_{\mathrm{EDL}} \cdot (1 - x/L_{\mathrm{EDL}})\,. \tag{10.20}$$

In the first step above, we used the Poisson equation ($\varrho_{\mathrm{F}} = -\varepsilon_0\varepsilon_{\mathrm{R}}\Phi''$), and, in the second step, we used the solution eq. (10.19). From this cumulative charge follows the total surface-charge-density $\mathcal{Q}^{\mathrm{tot}}(a, \varepsilon_{\mathrm{R}}, T, \Delta\phi, \gamma_\pm)$, comprised in the complete EDL, and the corresponding differential capacitance,

$$\mathcal{Q}^{\mathrm{tot}}{=}\mathcal{Q}(0){=}-2\varepsilon_0\varepsilon_{\mathrm{R}}\Delta\phi/L_{\mathrm{EDL}}{=}-\mathrm{sign}\,(\Delta\phi)\,\sqrt{2|\Delta\phi|\varepsilon_0\varepsilon_{\mathrm{R}}(ez_+)^2/k_{\mathrm{B}}Ta^3\gamma_{\alpha^*}}\,, \tag{10.21}$$

and

$$\mathrm{d}\mathcal{Q}^{\mathrm{tot}}/\mathrm{d}(\Delta\phi) = -\sqrt{\varepsilon_0\varepsilon_{\mathrm{R}}(ez_+)^2/2k_{\mathrm{B}}Ta^3\gamma_{\alpha^*}|\Delta\phi|}\,. \tag{10.22}$$

10.2.3 Mean Volume Effect: Symmetric Ions

We discuss the special case where the ion-species have the same molar volume, *i.e.* $\gamma_\pm{=}\tilde{c}^{\mathrm{b}}{=}1/2$, where eq. (10.7) becomes $\tilde{\Phi}{=}\ln\sqrt{\tilde{c}_-/\tilde{c}_+}$. We exponentiate both sides, such that $\tilde{c}_-{=}\tilde{c}_+\cdot\exp(2\tilde{\Phi})$, and substitute the charge density for the species concentrations using eq. (9.30), $\tilde{\varrho}_{\mathrm{F}}{=}\tilde{c}_+{-}\tilde{c}_-$ and $\tilde{c}_-{=}(1{-}\tilde{\varrho}_{\mathrm{F}})/2$. By substitution, we find that charge density becomes a function of electrolyte electric potential,[69]

$$\tilde{\varrho}_{\mathrm{F}}(\tilde{\Phi}) = \frac{1-\exp(2\tilde{\Phi})}{1+\exp(2\tilde{\Phi})} = -\tanh(\tilde{\Phi}) \tag{10.23}$$

This corresponds to a dimensionless modified Poisson-Fermi distribution, which is typical for saturated screening processes.[363] Next, we substitute the Poisson equation ($\tilde{\varrho}_{\mathrm{F}} = -\tilde{\Phi}''$) for the left side above, and multiply both sides by $2\tilde{\Phi}'$. In addition, we integrate both sides over the interval $[x; L_{\mathrm{DL}}]$, where we make use of electroneutral BCs (see eq. (9.47)), and evaluate the relation $2\tilde{\Phi}'\tilde{\Phi}'' = \boldsymbol{\nabla}[(\tilde{\Phi}')^2] = \mathrm{d}[(\tilde{\Phi}')^2]$. Altogether,

$$\tilde{\Phi}' = -\mathrm{sign}(\mathit{\Delta}\tilde{\phi}) \cdot \sqrt{2\ln[\cosh(\tilde{\Phi})]}, \tag{10.24}$$

whereas the dimensionless total surface charge density $\tilde{\mathcal{Q}}^{\mathrm{tot}} {=} e z_+ / k_{\mathrm{B}} T \varepsilon_0 \varepsilon_{\mathrm{R}} {\cdot} \mathcal{Q}^{\mathrm{tot}}$ is

$$\tilde{\mathcal{Q}}^{\mathrm{tot}} = -\mathrm{sign}(\mathit{\Delta}\tilde{\phi}) \cdot \sqrt{2\ln[\cosh(\tilde{\Phi})]}. \tag{10.25}$$

10.3 Non-Local Interactions: Charge Oscillations

Here, we supplement our finding from the previous section, and discuss the influence of non-local interactions ($\mathcal{V}^0 \neq 0$) on the stationary EDL structure. Again, we focus on the gradient description of the IL-electrolyte, and follow the same rationale as in section 10.2 by discussing the two limiting cases of small and large potentials.

10.3.1 Static Asymptotic Analysis: Large Potentials $|\tilde{\Phi}| \gg 1$

Here, we discuss the regime of diverging electrolyte potentials $|\tilde{\Phi}| \to \infty$ where the interaction contribution cannot compensate the diverging electrolyte potential in eq. (10.2). Thus, the compensation must be realized via the logarithmic terms, which, as explained in section 10.2.2, diverge if one species depletes. Hence, we obtain the same results as described in section 10.2.2.

10.3.2 Static Asymptotic Analysis: Small Potentials $|\tilde{\Phi}| \ll 1$

Here, we consider the gradient description of the stationary EDL with molecular repulsion in the regime of small potentials $|\tilde{\Phi}| \ll 1$ described by eqs. (10.4) to (10.6).

We restrict our gradient expansion to the first two modes $n{=}0$ and $n{=}1$, such that

$$\tilde{\varrho}_{\mathrm{F}} = -\tilde{\boldsymbol{\nabla}}^2 \Phi, \quad \text{and} \quad 0 = \tilde{\Phi} + \hat{\varepsilon}_{\mathrm{R}} \tilde{\varrho}_{\mathrm{F}}, \tag{10.26}$$

where the dielectric operator expanded up to the second order is

$$\hat{\varepsilon}_{\mathrm{R}} = 1 - \mathcal{V}^0/E_{\mathrm{th}} \cdot \tilde{\varGamma}^0_{+-} - \mathcal{V}^0/E_{\mathrm{th}} \cdot \tilde{\varGamma}^2_{+-} \cdot \tilde{\boldsymbol{\nabla}}^2. \tag{10.27}$$

We investigate the fundamental system corresponding to this set of equations. For this purpose, we rephrase eqs. (10.26) and (10.27) in matrix form,

$$\begin{pmatrix} \tilde{\boldsymbol{\nabla}}^2 \tilde{\varrho}_{\mathrm{F}} \\ \tilde{\boldsymbol{\nabla}}^2 \tilde{\Phi} \end{pmatrix} = \tilde{\boldsymbol{\mathcal{A}}} \cdot \begin{pmatrix} \tilde{\varrho}_{\mathrm{F}} \\ \tilde{\Phi} \end{pmatrix}, \tag{10.28}$$

where

$$\tilde{\boldsymbol{\mathcal{A}}} = \begin{pmatrix} \dfrac{E_{\mathrm{th}}}{\mathcal{V}^0 \tilde{\varGamma}^2_{+-}} \left(1 - \dfrac{\mathcal{V}^0}{E_{\mathrm{th}}} \tilde{\varGamma}^0_{+-}\right) & \dfrac{E_{\mathrm{th}}}{\mathcal{V}^0 \tilde{\varGamma}^2_{+-}} \\ -1 & 0 \end{pmatrix}. \tag{10.29}$$

We solve eq. (10.28) via the eigenvalue decomposition, $\det(\tilde{\boldsymbol{\mathcal{A}}} - \tilde{\alpha}_{1,2} \cdot \mathbf{Id}) = 0$, for the eigenvaluess $\tilde{\alpha}_{1,2}$. This shows that the eigenvalues are determined by the relative magnitudes of the three competing energy scales E_{th}, E_{el}, and $\mathcal{V}^0$, and by the two perturbation modes $\tilde{\varGamma}^0_{+-}$ and $\tilde{\varGamma}^2_{+-}$,

$$\tilde{\alpha}_{1,2} = -\tilde{\varGamma}^0_{+-}/2\tilde{\varGamma}^2_{+-} \left[1 - E_{\mathrm{th}}/\mathcal{V}^0 \tilde{\varGamma}^0_{+-} \mp \sqrt{\left(1 - E_{\mathrm{th}}/\mathcal{V}^0 \tilde{\varGamma}^0_{+-}\right)^2 - 4 E_{\mathrm{th}} \tilde{\varGamma}^2_{+-}/\mathcal{V}^0 (\tilde{\varGamma}^0_{+-})^2}\,\right]. \tag{10.30}$$

These two eigenvalues $\tilde{\alpha}_{1,2}$ give rise to four dimensionless wave-vectors

$$\tilde{k}^{\pm}_{1,2} = \pm \sqrt{\tilde{\alpha}_{1,2}}. \tag{10.31}$$

The two eigenvectors $\tilde{\mathbf{a}}_{1,2}$ of the matrix $\tilde{\boldsymbol{\mathcal{A}}}$ corresponding to $\tilde{\alpha}_{1,2}$ are

$$\tilde{\mathbf{a}}_{1,2} = \begin{pmatrix} -\tilde{\alpha}_{1,2} \\ 1 \end{pmatrix}. \tag{10.32}$$

Altogether, the eigenvalues eq. (10.30), the eigenvectors eq. (10.32) and the wave vectors eq. (10.31) determine the general solution of the equation system eq. (10.28)

$$\begin{pmatrix} \tilde{\varrho}_{\mathrm{F}} \\ \tilde{\Phi} \end{pmatrix} = \begin{pmatrix} \vdots & \vdots \\ \tilde{\mathbf{a}}_1 & \tilde{\mathbf{a}}_2 \\ \vdots & \vdots \end{pmatrix} \cdot \begin{pmatrix} A_1 e^{\tilde{k}_1 \tilde{x}} + A_2 e^{-\tilde{k}_1 \tilde{x}} \\ A_3 e^{\tilde{k}_2 \tilde{x}} + A_4 e^{-\tilde{k}_2 \tilde{x}} \end{pmatrix}. \tag{10.33}$$

Because the expansion coefficients A_i are unknown, this general solution is underdetermined. However, we determine them using boundary conditions, and physical arguments. Apparently, the wave-vectors are functions $\tilde{k}_{1,2}(T, z_\alpha, \varepsilon_\mathrm{R}, \nu_\alpha, \mathcal{F}_{\alpha\beta})$, and determine the structure of the EDL according to the classification

$$\tilde{k}_{1,2} \in \begin{cases} \mathbb{R}, & \text{leads to exponential damping,} \\ \mathbb{R} + \mathrm{i} \cdot \mathbb{R}, & \text{leads to damped oscillations,} \\ \mathrm{i} \cdot \mathbb{R}, & \text{leads to undamped oscillations.} \end{cases} \tag{10.34}$$

Thus, due to the exponential form of the general solution eq. (10.33), the EDL structure depends upon the relative magnitudes of the energies E_th, E_el, and $\mathcal{V}^0$ via eq. (10.30), and it remains to evaluate the conditions under which the wave-vectors are real ($\tilde{k} \in \mathbb{R}$), imagiary ($\tilde{k} \in \mathrm{i}\mathbb{R}$), orcomplex ($\tilde{k} \in \mathbb{R} + \mathrm{i}\mathbb{R}$). However, before we address this goal, we check consistency with experimental results.

Experimental results based on AFM measurements of ILs near electrified interfaces show oscillatory force profiles,[48,345,364] where the wave-lengths ℓ_AFM of the oscillations correlate with the ion-sizes via $\ell_\mathrm{AFM} = a/2\pi$. We use this observation to parameterize our description. For this purpose, we consider the limit of indefinite molecular repulsion, $\mathcal{V}^0 \to \infty$, and erect the constraint

$$\lim_{\mathcal{V}^0 \to \infty} \mathfrak{Im}\left(\tilde{k}\right) = \tilde{k}_\mathrm{AFM} = 2\pi/\tilde{a}\,. \tag{10.35}$$

We transfer this constraint to the wave vector, and calculate the limit $\lim_{\mathcal{V}^0 \to \infty} \tilde{\alpha}_{1,2}$ using eq. (10.30) and eq. (10.31),

$$\lim_{\mathcal{V}^0 \to \infty} \tilde{k} = \tilde{k}_\mathrm{AFM} = \begin{cases} \pm \mathrm{i} \cdot \sqrt{\tilde{\Gamma}^0_{+-}/\tilde{\Gamma}^2_{+-}}\,, \\ 0. \end{cases} \tag{10.36}$$

Thus, the constraint on the wave-vector transfers to a constraint on the perturbation modes $\tilde{\Gamma}^0_{+-}$ and $\tilde{\Gamma}^2_{+-}$, *i.e.* to a constraint on the model for $\tilde{\mathcal{F}}$. Since the perturbation modes are mainly determined by the effective support of the interaction potentials, this is a constraint on the correlation length of the repulsive interaction. Altogether, we find as constraint the following relation

$$\tilde{\Gamma}^2_{+-}/\tilde{\Gamma}^0_{+-} = (\tilde{a}/2\pi)^2 = 2E_\mathrm{el}/\pi\tilde{\nu}\,E_\mathrm{th}. \tag{10.37}$$

Here, we used the relation between the dimensionless molecule-scale $\tilde{a}$ and the energy scales E_th and E_el (see eq. (9.35)) Therefore, only one independent perturbation mode exists in the second order expansion. As consequence, we substitute the condition eq. (10.37) for $\tilde{\mathit{\Gamma}}^2_{+-}$ into the eigenvalue-equation (see eq. (10.30)), which yields

$$\tilde{\alpha}_{1,2} = -\frac{\pi}{4\tilde{\nu}} \cdot \frac{E_{\mathrm{th}}}{E_{\mathrm{el}}} \left[\left(1 - \frac{E_{\mathrm{th}}}{\mathcal{V}^0 \tilde{\mathit{\Gamma}}^0_{+-}}\right) \mp \sqrt{\left(1 - \frac{E_{\mathrm{th}}}{\mathcal{V}^0 \tilde{\mathit{\Gamma}}^0_{+-}}\right)^2 - \frac{8}{\pi\tilde{\nu}} \frac{E_{\mathrm{el}}}{\mathcal{V}^0} \frac{1}{\tilde{\mathit{\Gamma}}^0_{+-}}} \right] . \tag{10.38}$$

We use this form for the eigenvalue equation and classify the wave-vector $\tilde{k}$ (see eq. (10.34)), *i.e.* identify the energy regimes for which the wave vector becomes real, complex, or imaginary. However, this classification of $\tilde{k}$ depends upon the corresponding classification of the eigenvalues $\tilde{\alpha}_{1,2}$ being real, complex or imaginary, which depends mainly upon the square-root appearing in eq. (10.30),

$$\mathcal{W} = \left(1 - E_{\mathrm{th}}/\mathcal{V}^0 \tilde{\mathit{\Gamma}}^0_{+-}\right)^2 - 8E_{\mathrm{el}}/\pi\tilde{\nu}\mathcal{V}^0\tilde{\mathit{\Gamma}}^0_{+-} \, . \tag{10.39}$$

Thus, the critical values $\mathcal{V}^0_{\pm}$, defined by the condition $\mathcal{W}(\mathcal{V}^0_{\pm}) = 0$, determine the phase boundaries,

$$\mathcal{V}^0_{\pm} = 1/\tilde{\mathit{\Gamma}}^0_{+-} \cdot \left[E_{\mathrm{th}} + 4E_{\mathrm{el}}/\pi\tilde{\nu} \pm 2\sqrt{2E_{\mathrm{el}}(2E_{\mathrm{el}}/\pi\tilde{\nu} + E_{\mathrm{th}})/\pi\tilde{\nu}} \right] \tag{10.40}$$

Thus, eq. (10.40) allows to draw the phase diagram for the EDL screening phases structure. Since $0 < \mathcal{V}^0_- < \mathcal{V}^0_+$, there are three different screening phases, as stated by the following Theorem (see appendix E.4),

Theorem 1. The phase-space of the screening profiles is threefold:

Region I:	$\mathcal{V}^0 \leq \mathcal{V}^0_-$	Exponentially damped screening profile
Region II:	$\mathcal{V}^0_- < \mathcal{V}^0 < \mathcal{V}^0_+$	Exponentially damped oscillations
Region III:	$\mathcal{V}^0_+ \leq \mathcal{V}^0$	Undamped oscillations

Apparently, due to eq. (10.40), the energy scales $(\mathcal{V}^0_{\pm}\tilde{\mathit{\Gamma}}^0_{+-})$ are model independent (*i.e.* independent from the perturbation modes), *i.e.* determines the phase-boundaries between the different screening profiles for all spherically symmetric interaction potentials $\mathcal{F}$. Hence, theorem 1 analytically predicts the emergence of phase separation, and states the exact phase boundaries for any spherically symmetric potential. Note that the zero-order perturbations have a rather simple form, see eq. (8.34).

Another consequence is that the phase boundaries corresponding to different models $\mathcal{F}$ are all proportional to each other, *i.e.* , the phase space is "conformally invariant". Hence, the effect of choosing a specific form for the interaction potential is that it re-scales the phase boundaries, by scaling the critical interaction energies $\mathcal{V}^0_{\pm}$. In chapter 11 we will study one specific example.

We discuss each of the three phases, which are predicted by Theorem 1 (see appendix E.4 for more details).

Phase 1 $0 \leq \mathcal{V}^0 \leq \mathcal{V}^0_{-}$: In this region, all eigenvalues are real and positive, $0 \leq \tilde{\alpha}_{1,2} \in \mathbb{R}$. This implies real-valued wave-vectors, $\tilde{k}_{1,2} = \pm\sqrt{\tilde{\alpha}_{1,2}} \in \mathbb{R}$, subject to boundary conditions. Hence, the profiles for the charge density, and the electric potential exhibit exponential shape,

$$\tilde{\varrho}_{\mathrm{F}} \propto \exp(-\tilde{k}_{\mathbb{R}}\tilde{x}). \tag{10.41}$$

In order to check consistency with the results from section 10.2.1, we consider the limit $\lim_{\mathcal{V}^0 \to 0} \tilde{\alpha}_{1,2}$, and we write eq. (10.38) in the form

$$\tilde{\alpha}_{1,2} = -\frac{\pi E_{\mathrm{th}}}{4\tilde{\nu} E_{\mathrm{el}} \mathcal{V}^0} \cdot \left[\left(\mathcal{V}^0 - E_{\mathrm{th}}/\tilde{\Gamma}^0_{+-} \mp \sqrt{\left(\mathcal{V}^0 - E_{\mathrm{th}}/\tilde{\Gamma}^0_{+-}\right)^2 - 8E_{\mathrm{el}}\mathcal{V}^0/\pi\tilde{\nu}\tilde{\Gamma}^0_{+-}}\right)\right]. \tag{10.42}$$

Next we approximate the root appearing on the right side of eq. (10.42) via a harmonic analysis, $\sqrt{\mathcal{W}}(\mathcal{V}^0 \to 0) \approx E_{\mathrm{th}}/\tilde{\Gamma}^0_{+-} - (1 + 4E_{\mathrm{el}}/\pi E_{\mathrm{th}})\mathcal{V}^0$, such that

$$\lim_{\mathcal{V}^0 \to 0} \tilde{k}_1 = \infty \quad \text{and} \quad \lim_{\mathcal{V}^0 \to 0} \tilde{k}_2 = 1. \tag{10.43}$$

We discard the first solution as being unphysical. In contrast, the second solution for $\tilde{k}_2$ yields a dimensional damping-parameter $k = 1/L_{\mathrm{D}}$. Thus, this limit reproduces the “bulk”-expansion for $\tilde{\Phi} \ll 1$ from section 10.2.1 (see eq. (10.9)), and is thus consistent with our previous analytical investigation.

Phase 2 $\mathcal{V}^0_{-} < \mathcal{V}^0 < \mathcal{V}^0_{+}$: In this regime, the root appearing in the eigenvalue equation is negative, $\mathcal{W} < 0$. Thus, the root $\mathcal{W}$ in eq. (10.39) becomes imaginary, and the wave-vector is complex, $\tilde{k}_{1,2} \in \mathbb{R} \times \mathrm{i} \cdot \mathbb{R}$. This corresponds to charge-profiles of exponentially damped oscillations,

$$\tilde{\varrho}_{\mathrm{F}} = A \cdot e^{-\tilde{k}_{\mathbb{R}}\tilde{x}} \cdot \cos(\tilde{k}_{\mathbb{C}}\tilde{x}). \tag{10.44}$$

where we write $\tilde{k}_{\mathbb{R}} = \mathfrak{Re}(\tilde{k})$, and $\tilde{k}_{\mathbb{C}} = \mathfrak{Im}(\tilde{k})$. Here, the parameter A is subject to the boundary conditions and physical arguments. Apparently, the real part $\tilde{k}_{\mathbb{R}}$ determines the width of the EDL, whereas the complex part $\tilde{k}_{\mathbb{C}}$ determines the frequency of the oscillations appearing in the screening profile.

Phase 3 $\mathcal{V}^0_+ \leq \mathcal{V}^0$: In this region, both eigenvalues are real but negative, $0 \geq \tilde{\alpha}_{1,2} \in \mathbb{R}$. Therefore, the wave vector is imaginary, $\tilde{k}_{1,2} \in \mathrm{i} \cdot \mathbb{R}$, which corresponds to undamped oscillatory profiles

$$\varrho_\mathrm{F} \propto \cos(\tilde{k}_\mathbb{C}\tilde{x}). \tag{10.45}$$

Apparently, with increasing $\mathcal{V}^0$, the frequency of the oscillations converges towards the terminal oscillation frequency $\tilde{k}_\mathrm{AFM}$, which is determined by the ion-sizes (see the constraint in eq. (10.35)). This corresponds to an increasingly incompressible electrolyte, which prevents further decrease of the wavelength.

Altogether, the critical values $\mathcal{V}^0_\pm$ constitute exactly the two boundaries between the three different EDL phases. Interestingly, both eigenvalues $\tilde{\alpha}_\pm$ have always the same characteristic. Thus, there are no solutions yielding the superposition of profiles from distinct phases.

In sections 10.3.5 and 10.3.6 we examine the influence of the individual perturbation modes (*i.e.* Γ^0_{+-} and Γ^2_{+-}) on the phase space of screening profiles. As it turns out, neglecting all but the zeroth-order mode (Γ^0_{+-}) results in a binary phase diagram comprising only exponentially damped profiles and undamped, oscillatory profiles. In contrast, taking only the first non-trivial order (Γ^2_{+-}) into account, results also in a binary phase-diagram, which comprises exponentially damped profiles, and damped oscillatory profiles. The BSK framework constitutes an example for a MFT based on only one perturbation mode of the form Γ^2_{+-}.[69] Therefore, in order to obtain “complete” set of the three different phases, both perturbation modes (*i.e.* Γ^0_{+-} and Γ^2_{+-}) are necessary.

Interestingly, if we consider attractive potentials, *i.e.* “negative” interaction energies ($\mathcal{V}^0 < 0$) in eq. (8.28), the space of screening profiles reduces to two phases. In this case, only exponentially damped screening-profiles, and undamped oscillatory screening-profiles are possible. Hence, the damped oscillatory screening-profile does not occur. This follows straightforwardly from eq. (10.30) (see also the discussions in sections 10.3.5 and 10.3.6).

10.3.3 Double Layer Forces

In section 5.4.5 we showed that there arise strong elastic pressure forces $\mathcal{F}^\mathrm{EDL}$ in the EDL when the system is in mechanical equilibrium (see eq. (5.231) and, also, chapter 14),[345]

$$\mathcal{F}^\mathrm{EDL} = -\nu/N_\mathrm{A} \cdot \boldsymbol{\nabla}\mathcal{P}^\mathrm{vol} = \nu/N_\mathrm{A} \cdot \varrho_\mathrm{F}\boldsymbol{\nabla}\Phi. \tag{10.46}$$

The quantity $\mathcal{F}^\mathrm{EDL}$ has dimension of a force, *i.e.* $[\mathcal{F}^\mathrm{EDL}] = \mathrm{N}$, and the corresponding dimensionless EDL force is thus $\tilde{\mathcal{F}}^\mathrm{EDL} = L_\mathrm{D}\tilde{c}^\mathrm{b}/k_\mathrm{B}T \cdot \mathcal{F}^\mathrm{EDL} = \tilde{\varrho}_\mathrm{F}\tilde{\boldsymbol{\nabla}}\tilde{\Phi}$ (see section 9.2). Thus, the charge density and the electric potential determine the forces appearing in the equilibrium EDL structures. These forces correspond to the reaction of the EDL configuration in mechanical equilibrium under small perturbations. Note that if the profiles for the charge density and the electric potential have an oscillatory shape with periodicity $2\pi/\tilde{k}_{\mathbb{R}}$, *i.e.* $\tilde{\varrho}_{\mathrm{F}} \propto \tilde{\Phi} \propto \cos(\tilde{k}_{\mathbb{R}}\tilde{x})$ (see eqs. (10.44) and (10.45)), then the force in eq. (10.46) has the shape $\tilde{F}^{\mathrm{EDL}} \propto \cos(2 * \tilde{k}_{\mathbb{R}}\tilde{x})$. Thus, the resulting force profile has the periodicity $4\pi/\tilde{k}_{\mathbb{R}}$, *i.e.* a periodicity twice as large. This implies that when the charge density and the electric potential oscillate with frequency given by the ion-pairs, then the force profile oscillates with the size of the ions.

10.3.4 Analytical Construction of the Screening Profile

Apparently, the screening profile of the electric potential and the charge density in the EDL is characterized by crowding and overscreening. Thus, the screening profile consists of three characteristic properties: a constant charge plateau due to concentration saturation appearing near the electrode (crowding); an exponentially damped decay towards the electroneutral bulk region far away from the electrodes; an oscillatory shape (overscreening), or undamped oscillations. Hence, the screening profile is completely described by the three parameters $\tilde{L}_{\mathrm{EDL}}$, $\tilde{k}_{\mathbb{R}}$ and $\tilde{k}_{\mathbb{C}}$ as functions of the system parameters $T, \varepsilon_{\mathrm{R}}, a, \gamma_{\alpha}, \mathcal{V}^0, \Delta\phi$.

In particular, we can construct the analytical screening profile as follows. If charge saturation occurs, then the analytical charge profile $\tilde{\varrho}_{\mathrm{F}}^{\mathsf{analytic}}$ consists of two parts. The first part is the "saturation"-part, $\tilde{\varrho}_{\mathrm{F}}^{\mathsf{I}} = \tilde{\varrho}_{\mathrm{F}}^{\mathsf{sat}}$ (usually, $|\tilde{\varrho}_{\mathrm{F}}^{\mathsf{sat}}| = 1$) over the length $\tilde{x} = [0; \tilde{L}_{\mathrm{EDL}}]$, which is followed by the damping part $\tilde{\varrho}_{\mathrm{F}}^{\mathsf{II}} = \tilde{\varrho}_{\mathrm{F}}^{\mathsf{sat}} \cdot \exp(-\tilde{k}_{\mathbb{R}}[\tilde{x} - \tilde{L}_{\mathrm{EDL}}]) \cdot \cos(\tilde{k}_{\mathbb{C}}[\tilde{x} - \tilde{L}_{\mathrm{EDL}}])$ for $\tilde{x} \geq \tilde{L}_{\mathrm{EDL}}$. The complete profile for the analytical charge density is then given by the combined profile $\tilde{\varrho}_{\mathrm{F}}^{\mathsf{analytic}} = \tilde{\varrho}_{\mathrm{F}}^{\mathsf{I}} \cup \tilde{\varrho}_{\mathrm{F}}^{\mathsf{II}}$. If no charge saturation occurs, then the profile for the charge density is given by $\tilde{\varrho}_{\mathrm{F}}^{\mathsf{II}}$, where $\tilde{L}_{\mathrm{EDL}}$ is set to zero. The corresponding analytical profile $\tilde{\Phi}^{\mathsf{analytic}}$ for the electric potential is constructed in a similar manner, where the "saturation" part is given by a quadratic function instead of the constant profile.

10.3.5 Special Case: Zero Order Expansion

In this section, we consider the special case, where the gradient description for the limiting case described in section 10.3.2 is restricted to the trivial order (n=0), where the dielectric operator reduces to the scalar parameter (see eq. (10.6))

$$\hat{\varepsilon}_{\mathrm{R}} \to {\varepsilon_{\mathrm{R}}}^{(n=0)} = 1 - \mathcal{V}^0/E_{\mathrm{th}} \cdot \tilde{\Gamma}^0_{+-}. \tag{10.47}$$

Thus, the corresponding system of equations (see eqs. (10.4) and (10.5)) can be substituted such that

$$\tilde{\boldsymbol{\nabla}}^2\tilde{\Phi} = \tilde{\Phi}/{\varepsilon_{\mathrm{R}}}^{(n=0)} = 1/\tilde{k}^2 \cdot \tilde{\Phi}, \tag{10.48}$$

where

$$\tilde{k} = \pm\sqrt{\frac{1}{{\varepsilon_{\mathrm{R}}}^{(n=0)}}} \in \begin{cases} \mathbb{R} & \Leftrightarrow \mathcal{V}^0 < E_{\mathrm{th}}/\tilde{\mathit{\Gamma}}^0_{+-} \\ \mathbb{C} & \Leftrightarrow \mathcal{V}^0 > E_{\mathrm{th}}/\tilde{\mathit{\Gamma}}^0_{+-}\,. \end{cases} \tag{10.49}$$

Thus, only the two screening phases of exponential decay, and undamped oscillatory shape exist in the trivial expansion, with phase boundary $\mathcal{V}^0_{\mathrm{c}} = E_{\mathrm{th}}/\tilde{\mathit{\Gamma}}^0_{+-}$. Furthermore, the electrostatic energy has no influence on the phase boundary, which is completely determined by the thermal energy and the interaction energy.

Since we assume that both energy scales $\mathcal{V}^0$ and E_{th} are positive, the correction $\tilde{\mathit{\Gamma}}^0_{+-}$ to the electrostatic parameter $\varepsilon_{\mathrm{R}}^{(n=0)}$ corresponds to a mitigation of the electrostatic energy E_{el}, see eq. (10.47). Apparently, the phase boundary where the screening profile becomes undamped oscillatory, $\mathcal{V}^0_{\mathrm{c}}$, corresponds to a transition towards negative energies E_{el}. In section 9.2, we showed that E_{th} becomes minimal for equal molar volumes of the ion-species. Thus, $\mathcal{V}^0_{\mathrm{c}}$ has a global minimum at $\gamma_{\pm} = 1/2$. This highlights the influence of ion-asymmetry on the phase-space, since, at fixed temperature, the phase boundary becomes minimal for ions of equal size. Note that in the case of negative interaction energies $\mathcal{V}^0$, *i.e.* attractive interaction potentials eq. (8.28), the phase space reduces to exponentially damped profiles. This corresponds to increased dielectricities, $\varepsilon_{\mathrm{R}} = 1 + |\mathcal{V}^0|\tilde{\mathit{\Gamma}}^0_{+-}/E_{\mathrm{th}}$.

10.3.6 Special Case: First Order Expansion

In this section, we consider the special case, where the gradient description for the limiting case described in section 10.3.2 is restricted to the linear order (n=1), and the dielectric operator becomes (see eq. (10.6))

$$\hat{\varepsilon}_{\mathrm{R}} \rightarrow {\varepsilon_{\mathrm{R}}}^{(n=1)} = 1 - \tilde{\mathit{\Gamma}}^2_{+-}\mathcal{V}^0/E_{\mathrm{th}}\,. \tag{10.50}$$

Thus, the corresponding system of equations (see eqs. (10.4) and (10.5)) becomes

$$\begin{pmatrix} \tilde{\varrho}''_{\mathrm{F}} \\ \tilde{\Phi}'' \end{pmatrix} = \tilde{\boldsymbol{\mathcal{A}}}^{\,(n=1)} \cdot \begin{pmatrix} \tilde{\varrho}_{\mathrm{F}} \\ \tilde{\Phi} \end{pmatrix} = \begin{pmatrix} E_{\mathrm{th}}/\mathcal{V}^0\tilde{\mathit{\Gamma}}^2_{+-} & E_{\mathrm{th}}/\mathcal{V}^0\tilde{\mathit{\Gamma}}^2_{+-} \\ -1 & 0 \end{pmatrix} \cdot \begin{pmatrix} \tilde{\varrho}_{\mathrm{F}} \\ \tilde{\Phi} \end{pmatrix}. \tag{10.51}$$

We proceed as in the more general case described in section 10.3.2, and determine the solutions to this system of equations via calculating the eigenvalues $\tilde{\alpha}^{(n=1)}_{1,2}$

corresponding to the matrix $\tilde{\boldsymbol{\mathcal{A}}}^{(n=1)}$,

$$\tilde{\alpha}_{1,2}^{(n=1)} = E_{\mathrm{th}}/2\mathcal{V}^0\tilde{\varGamma}_{+-}^2 \left(1 \pm \sqrt{1 - 4\mathcal{V}^0\tilde{\varGamma}_{+-}^2/E_{\mathrm{th}}}\right). \tag{10.52}$$

Similar to the case described in section 10.3.2, the zeros of the root $\mathcal{W}^{(n=1)} = 1 - 4\mathcal{V}^0\tilde{\varGamma}_{+-}^2/E_{\mathrm{th}}$ determine the sign of the eigenvalue, *i.e.* the phase boundaries. However, in this case, the phase space of screening profiles consists of exponentially damped profiles, and damped oscillatory profiles. The corresponding phase boundary is given by

$$\mathcal{V}_{\mathrm{c}}^0 = E_{\mathrm{th}}/4\tilde{\varGamma}_{+-}^2\,. \tag{10.53}$$

Thus, only two screening phases exist; for $\mathcal{V}^0 < \mathcal{V}_{\mathrm{crit}}^0$, the screening profiles are exponentially damped; if $\mathcal{V}_{\mathrm{c}}^0 < \mathcal{V}^0$ all eigenvalues have non-vanishing real-/ and imaginary parts, which implies damped oscillations.

Interestingly, for attractive potentials eq. (8.28), *i.e.* negative energies $\mathcal{V}^0 < 0$, the two eigenvalues are from mutually different number-fields. This can be seen by expanding the eigenvalue-equation via

$$\tilde{\alpha}_{1,2}^{(n=1)} = E_{\mathrm{th}}/2\mathcal{V}^0\tilde{\varGamma}_{+-}^2 \cdot \left(1 \pm \sqrt{1 + 4|\mathcal{V}^0|\tilde{\varGamma}_{+-}^2/E_{\mathrm{th}}}\right). \tag{10.54}$$

Apparently, the root is always positive and $\tilde{\alpha}_{1,2}^{(n=1)} < 0$ leads to oscillations, whereas $\tilde{\alpha}_{1,2}^{(n=1)} > 0$, leads to exponentially damped profiles. Since the general solution is the superposition of the two solutions, this leads to the superposition of exponentially damped, and undamped oscillatory profiles. Thus, there is a plethora of screening profiles available, depending upon the amplitudes of these two solutions (*i.e.* the BCs). However, all these profiles comprise an undamped oscillatory phase, although it may have a very small amplitude. We emphasize that this situation does not occur for positive parameters $\mathcal{V}^0$, where the eigenvalues are always from the same number-field. Again, the phase boundary is minimal for symmetric ions.

10.4 Dynamic Asymptotic Analysis: Linear Bulk-Stability Analysis

In this section, we supplement the static asymptotic analysis of the gradient description from section 10.3.2 by a linear stability analysis of the dynamic transport equations (see eqs. (9.38) to (9.40)). Thus, we consider the gradient description eq. (9.43) up to the first two perturbation modes in the limit of small potentials, where the approximation of the logarithmic terms can be applied (see eq. (10.3)).

Thus, eq. (9.39) becomes

$$\partial_{\tilde{t}}\tilde{\varrho}_{\mathrm{F}} = \tilde{\boldsymbol{\nabla}}^2\left(\tilde{\Phi} + \hat{\varepsilon}_{\mathrm{R}}\tilde{\varrho}_{\mathrm{F}}\right), \tag{10.55}$$

where $\hat{\varepsilon}_{\mathrm{R}} = 1 - \mathcal{V}^0/E_{\mathrm{th}} \cdot \tilde{\mathit{\Gamma}}^0_{+-} - \mathcal{V}^0/E_{\mathrm{th}} \cdot \tilde{\mathit{\Gamma}}^2_{+-}\tilde{\boldsymbol{\nabla}}^2$. This equation is supplemented by the Poisson equation, $\tilde{\varrho}_{\mathrm{F}} = -\tilde{\boldsymbol{\nabla}}^2\tilde{\Phi}$. We probe the stability of this description under small perturbations from the uniform bulk-states $\tilde{\Phi}^{\mathrm{b}}$ and $\tilde{\varrho}^{\mathrm{b}}_{\mathrm{F}}$, *viz.*

$$\tilde{\Phi} = \tilde{\Phi}^{\mathrm{b}} + \sum_{i=1}^{\infty}\epsilon_i \cdot \tilde{\Phi}^i, \qquad \text{and} \qquad \tilde{\varrho}_{\mathrm{F}} = \tilde{\varrho}^{\mathrm{b}}_{\mathrm{F}} + \sum_{i=1}^{\infty}\epsilon_i \cdot \tilde{\varrho}^i_{\mathrm{F}}, \tag{10.56}$$

and define the equilibrium states by assuming electroneutral bulk-condition, *i.e.* $\tilde{\Phi}^{\mathrm{b}} = 0$ and $\tilde{\varrho}^{\mathrm{b}}_{\mathrm{F}} = 0$. The first order perturbations take the form

$$\tilde{\Phi}^1 = \tilde{\varrho}^1_{\mathrm{F}} = \tilde{\psi} = \exp[\tilde{s}\tilde{t} + \mathrm{i}\tilde{k}\tilde{x}] + \exp[\tilde{s}\tilde{t} - \mathrm{i}\tilde{k}\tilde{x}]. \tag{10.57}$$

The wave-number $\tilde{k}$ determines the spatial distribution of the dimensionless perturbation $\tilde{\epsilon}^1_{\tilde{\Phi}} \ll 1$, and the parameter $\tilde{s}$ measures the temporal growth rate of this perturbation. Due to the Poisson equation, the perturbation modes with respect to the expansion of $\tilde{\Phi}$ and $\tilde{\varrho}_{\mathrm{F}}$ are coupled via $\tilde{\epsilon}_{\tilde{\varrho}_{\mathrm{F}}} = -(\mathrm{i}\tilde{k})^2\tilde{\epsilon}_{\tilde{\Phi}}$.

We restrict our analysis to probing the linear stability, and substitute the expansion eq. (10.57) into eq. (10.55). However, we use that $\tilde{\boldsymbol{\nabla}}^{2n}\tilde{\Phi}^1 = (\mathrm{i}\tilde{k})^{2n}\tilde{\psi}$, and $\partial_{\tilde{t}}\tilde{\varrho}^1_{\mathrm{F}} = -\tilde{\epsilon}^1_{\tilde{\Phi}}(\mathrm{i}\tilde{k})^2\tilde{s}\tilde{\psi}$. Collecting terms up to the first order in the perturbation mode $\tilde{\epsilon}^1_{\tilde{\Phi}}$ yields a dispersion relation for the grwoth rate of the perturbation,

$$\tilde{s}(\tilde{k}) = -1 + \left(1 - \mathcal{V}^0\tilde{\mathit{\Gamma}}^0_{+-}/E_{\mathrm{th}}\right) \cdot (\mathrm{i}\tilde{k})^2 - \mathcal{V}^0\tilde{\mathit{\Gamma}}^2_{+-}/E_{\mathrm{th}} \cdot (\mathrm{i}\tilde{k})^4. \tag{10.58}$$

In general, the uniform state is stable under perturbations from above exactly if $\tilde{s} < 0$. Thus, we are seeking an instability onset $\tilde{k}_{\mathrm{c}}$ subject to the conditions that $\tilde{s}(\tilde{k}_{\mathrm{c}}) = 0$, $\tilde{s}'(\tilde{k}{=}\tilde{k}_{\mathrm{c}}) = 0$ (where $\tilde{s}' = \mathrm{d}\tilde{s}/\mathrm{d}\tilde{k}$) and $\tilde{s}(\tilde{k}{\neq}\tilde{k}_{\mathrm{c}}) < 0$. To simplify the notation, we define two parameters $\alpha = \mathcal{V}^0\tilde{\mathit{\Gamma}}^0_{+-}/E_{\mathrm{th}}$ and $\beta = 2E_{\mathrm{el}}/\tilde{\mathrm{v}}\pi E_{\mathrm{th}}$, such that the dispersion relation becomes $\tilde{s} = -1 - (1-\alpha)^2\tilde{k}^2 - \alpha\beta\tilde{k}^4$. The condition $\tilde{s}' = 0$ determines critical wave-vectors

$$\tilde{k}_{\pm} = \pm\sqrt{\alpha - 1/2\alpha\beta}\,, \qquad \text{subject to the condition} \qquad \alpha > 1. \tag{10.59}$$

Since the second derivative fulfills $\tilde{s}''(\tilde{k}_{\pm}) < 0$, the critical wave vectors $\tilde{k}_{\pm}$ constitute local maxima. We use these critical wavelengths to probe the condition $\tilde{s}(\tilde{k}_{\mathrm{c}}) = 0$. This condition is true exactly if

$$\alpha_{\pm} = 1 + 2\beta \pm 2\sqrt{\beta(1+\beta)}. \tag{10.60}$$

Thus, this condition implies constraints on the parameters α and β. However, the solution α_- can be neglected, since it is not compatible with the condition eq. (10.59). This can be seen using the triangle-inequality, *i.e.* since $-\sqrt{\beta^2+\beta} \leq -(\beta+\sqrt{\beta})$, the solution $\alpha_- \leq 1-2\sqrt{\beta} < 1$. Hence, we are left with one solution α_+, which translates into a condition on the interaction energy,

$$\mathcal{V}^0_{\mathrm{c}} = \mathcal{V}^0_+ = 1/\tilde{\mathit{\Gamma}}^0_{+-} \cdot \left(1 + 4E_{\mathrm{el}}/\pi\tilde{\mathrm{v}} + 2\sqrt{2E_{\mathrm{el}}(2E_{\mathrm{el}}/\pi\tilde{\mathrm{v}} + E_{\mathrm{th}})/\pi\tilde{\mathrm{v}}}\right). \tag{10.61}$$

Apparently, the phase boundary $\mathcal{V}^0_{\mathrm{c}}$ for the transition of the IL-electrolyte from bulk-stability to bulk-instability equals exactly the phase-boundary $\mathcal{V}^0_+$ which determines the phase transition of the screening profiles from damped, oscillatory shape to undamped oscillations (see eq. (10.40)). Thus, for interaction energies $\mathcal{V}^0 > \mathcal{V}^0_+$ the bulk state of the system becomes unstable and phase separation emerges. The initial cause for the structure-formation can be driven by external agents, or boundary conditions. For example, by the application of an electric potential to an IL/electrode interface.

This stability analysis complements the static analysis, since it rationalizes the emergence of phase separation into pure ionic layers occurring at interaction energies above $\mathcal{V}^0_+$.

11 Interaction Model for Hardcore Particles

In this chapter we specify our yet universal description to a specific choice for the interaction potential $\mathcal{F}_{+-}$ appearing in the interaction functional F^{int}, see eq. (8.27).

In particular, we model the spherically symmetric interaction potential $\tilde{\mathcal{F}}$ using a Gaussian shape-function, *viz.*

$$\mathcal{F}_{+-}\left(\mathcal{V}^0, \ell_{\text{int}}\right) = \mathcal{V}^0 \cdot \left(N_{\text{A}}\right)^2 \cdot \mathcal{G} \cdot \exp\left(-\left[\tilde{x}/\tilde{\ell}_{\text{int}}(a)\right]^2\right). \tag{11.1}$$

Here, $0 < \mathcal{G} \in \mathbb{R}$ is a dimensionless scalar-parameter, which allows to gauge the interaction. Since all prefactors appearing in eq. (11.1) are strictly positive, the interaction potential is repulsive. Thus, the exponential potential eq. (11.1) indeed describes short-ranged repulsion, *i.e.* hardcore particles, but lacks the attractive tail dominating at larger distances (usually attributed to higher order electrostatic correlations).[63]

Exponential potentials for the modeling of hardcore particles have been widely used in computational chemistry.[365] For example, eq. (11.1) can be extended by an attractive term $-\bar{\mathcal{V}}^0/r^6$, yielding the Buckingham potential. This potential combines the Pauli exclusion principle (*i.e.* repulsion between closed electron shells), with attractive long-ranged van-der-Waals forces.[366]

Apparently, our model eq. (11.1) requires two model parameters, $\mathcal{V}^0$ and $\tilde{\ell}_{\text{int}} = \ell_{\text{int}}/L_{\text{D}}$. We assume that the correlation length $\ell_{\text{int}}(a)$ is a function of the ion-size a. Thus, the constraint eq. (10.37) closes this relation, and implies a constitutive equation for $\tilde{\ell}_{\text{int}}$.

Above, we showed that for spherically symmetric interaction potentials $\tilde{\mathcal{F}}$ the perturbation modes are determined by a one-dimensional integral over the radial distance from the electrode, see eq. (8.33). However, in the special case where the interaction model is given by eq. (11.1) the corresponding integral can be solved analytically via $\int \mathrm{d}r \exp[-(r/\ell_{\text{int}})^2] \cdot r^{2(n+1)} = (\ell_{\text{int}})^{2n+3}/2 \cdot \Gamma(n+3/2)$, where $\Gamma(n/2)$ is the Gamma function. Hence, we find

$$\mathit{\Gamma}^{2n}_{+-} = \mathcal{G} 4\pi/(2n)! \int \mathrm{d}r \exp[-(r/\ell_{\text{int}})^2] \cdot r^{2(n+1)} \tag{11.2}$$

$$= \mathcal{G} 2\pi/(2n)! \cdot (\ell_{\text{int}})^{2n+3} \cdot \Gamma\,(n+3/2\,)\,. \tag{11.3}$$

In particular, the first two perturbation modes can be stated analytically, using $\Gamma(3/2) = \sqrt{\pi}/2$ and $\Gamma(5/2) = 3\Gamma(3/2)/2 = 3\sqrt{\pi}/4$, *viz.*

$$\mathit{\Gamma}^0_{+-} = \mathcal{G} \cdot (\,\sqrt{\pi}\ell_{\text{int}}\,)^{\,3}, \tag{11.4}$$

$$\mathit{\Gamma}^2_{+-} = \mathcal{G} \cdot 3/4 \cdot (\ell_{\text{int}})^5 \cdot (\,\sqrt{\pi})^3 = 3/4 \cdot (\ell_{\text{int}})^2 \cdot \mathit{\Gamma}^0_{+-}\,. \tag{11.5}$$

Via eq. (9.44) we get the dimensionless perturbation modes

$$\tilde{\mathit{\Gamma}}^0_{+-} = \mathcal{G}/\tilde{\nu} \cdot (\ell_{\text{int}}/a\,)^3\,\Gamma\,(3/2\,)\,, \qquad \text{and} \qquad \tilde{\mathit{\Gamma}}^2_{+-} = 3/4 \cdot \left(\tilde{\ell}_{\text{int}}\right)^2 \cdot \tilde{\mathit{\Gamma}}^0_{+-}\,. \tag{11.6}$$

The model eq. (11.1) is subject to the limiting constraint derived from experimental results, eq. (10.37). Apparently, this is a constraint on the correlation length ℓ_{int} of the hardcore interaction, which follows from eqs. (11.4) and (11.5)

$$\ell_{\text{int}}(a) = a/\pi\,\sqrt{3}\,. \tag{11.7}$$

Thus, eq. (11.7) closes the model eq. (11.1) and reduces the set of independent parameters appearing in this model to $\mathcal{V}^0$. Apparently, the parameter $\mathcal{G}$ has no influence on the determination of the correlation-length, but only scales the phase-boundaries by simultaneously gauging the perturbation modes, see eq. (10.40). Hence, the parameter $\mathcal{G}$ serves to calibrate our framework in accordance to results from atomistic simulations, or experimental findings for the exact values $\mathcal{V}^0_{\pm}$. However, without loss of generality, we here set $\mathcal{G} = 1$.

Altogether, the corresponding Gauss Ansatz reads

$$\mathcal{F}_{+-}\left(\mathcal{V}^0\right) = \mathcal{V}^0 \cdot (N_{\text{A}})^2 \cdot \exp\left(-3\,[\pi x/a\,]^2\right), \tag{11.8}$$

and we obtain the following perturbation modes for the Gauss-shaped interaction potential,

$$\mathit{\Gamma}^0_{+-} = 1/2\pi \cdot \left(a/\sqrt{3\pi}\,\right)^3, \qquad \tilde{\mathit{\Gamma}}^0_{+-} = 1/2\pi\tilde{\nu} \cdot \left(1/\sqrt{3\pi}\,\right)^3 \tag{11.9}$$

$$\mathit{\Gamma}^2_{+-} = (a/2\pi\,)^{\,2} \cdot \mathit{\Gamma}^0_{+-} \qquad \tilde{\mathit{\Gamma}}^2_{+-} = (\tilde{a}/2\pi\,)^{\,2} \cdot \tilde{\mathit{\Gamma}}^0_{+-}\,. \tag{11.10}$$

The consistent form for the interaction potential above, eq. (11.8), is thus uniquely defined up to a scalar prefactor.

The resulting constitutive equation for the chemical forces $\tilde{\boldsymbol{\nabla}}\tilde{\mu}^{\text{el}}_{\text{IL}}$ according to the gradient description, eq. (9.43), is

$$\tilde{\boldsymbol{\nabla}}\tilde{\mu}^{\text{el}}_{\text{IL}} {=} \tilde{\boldsymbol{\nabla}}\left(\tilde{\Phi} {-} \gamma_+ \ln[\tilde{c}_-/\tilde{c}^{\text{b}}\,] {+} \gamma_- \ln[\tilde{c}_+/\tilde{c}^{\text{b}}\,] {-} \mathcal{V}^0\tilde{\mathit{\Gamma}}^0_{+-}/E_{\text{th}} \cdot [\tilde{\varrho}_{\text{F}} {+} \tilde{\boldsymbol{\nabla}}^2\tilde{\varrho}_{\text{F}}]\right). \tag{11.11}$$

Next, we draw the phase space of screening profiles for the interaction potential eq. (11.8). Figure 11.1 shows the results for the dimensionless wave vector, and the

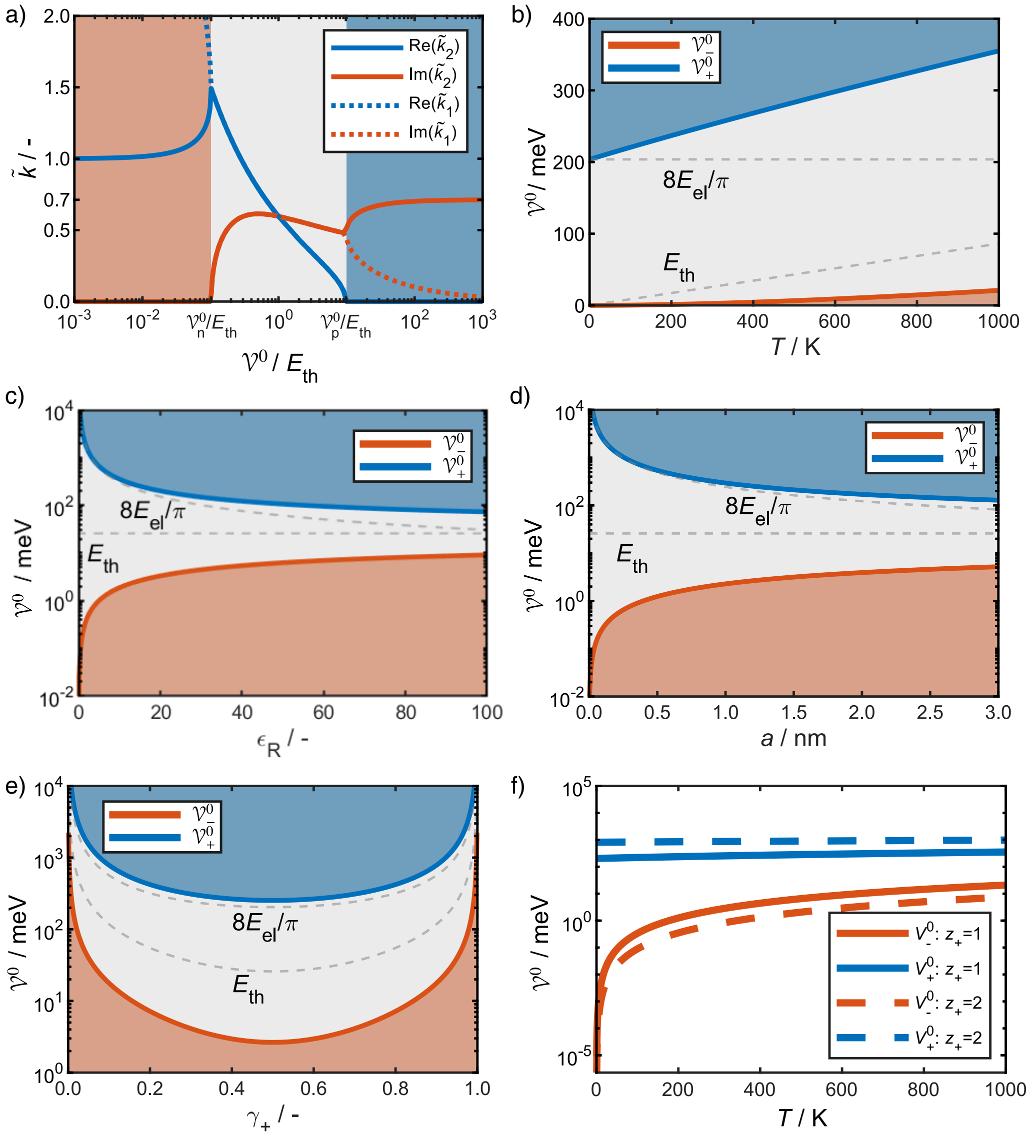

Figure 11.1: a) Real and imaginary parts of the dimensionless wave-vector $\tilde{k}$ as function of $\mathcal{V}^0/E_{\text{th}}$ ($E_{\text{th}}(T{=}300\,\text{K} = 25\,\text{meV})$, see eqs. (10.30), (10.31) and (11.9). b)-f) Different phase space diagrams of the screening profiles as function of the system parameters. The phase boundaries $\mathcal{V}^0_\pm$ follow from eqs. (10.40) and (11.9). Figures first published in Ref. 367.

critical interaction strengths $\mathcal{V}^0_\pm$ as function of temperature (fig. 11.1b), as function of the dielectricity ε_R (fig. 11.1c), as function of ion size a (fig. 11.1d), as function of ion asymmetry γ_+ (fig. 11.1e), and as function of the valency z_+ (fig. 11.1f). If not stated otherwise, the system parameters are $T = 300\,\mathrm{K}$, $\varepsilon_\mathrm{R} = 15$, $a = 1.2\,\mathrm{nm}$, $\gamma = 0.5$ and $z_+ = 1$. As consequence, if not stated otherwise, $L_\mathrm{D} = 0.14\,\mathrm{nm}$ and $\tilde{k}_\mathrm{AFM} \approx 0.7$ (see eqs. (9.26) and (10.35) and fig. 10.1).

Figure 11.1a) shows the the non-dimensionalized wave-vector $\tilde{k}$ (where $\tilde{k} = k \cdot L_\mathrm{D}$) as function of the non-dimensional interaction energy $\tilde{\mathcal{V}}^0 = \mathcal{V}^0/E_\mathrm{th}$, see eqs. (10.30) and (10.31). Here we remove the physical dimensions from the energy scale captured by the x-axis using the thermal energy $E_\mathrm{th} \approx 25\,\mathrm{meV}$, where $T = 300\,\mathrm{K}$ is set to a constant value. We discuss both the real part, *i.e.* the damping $\tilde{k}_\mathbb{R}$, and the imaginary part, *i.e.* the frequency $\tilde{k}_\mathbb{C}$. For this purpose, we focus on the regime of small interaction energies first, and then discuss the influence of increasing $\mathcal{V}^0$. Apparently, for interaction energies $\tilde{\mathcal{V}}^0 < \tilde{\mathcal{V}}^0_-$ the imaginary part of the wave vector vanishes identically. Thus, below the phase boundary $\tilde{\mathcal{V}}^0$, the wave-vector is real, *i.e.* $\tilde{k} = \tilde{k}_\mathbb{R}$. This corresponds to exponentially damped screening profiles of the electrolyte in the vicinity of the electrode, see eq. (10.41). There exist two independent solutions for the damping parameter. However, we discard the solution for $\tilde{k}_\mathbb{R}$ which diverges for small interaction energies as unphysical, see the dashed blue line in fig. 11.1a), and consider only the finite solution (solid blue line). For vanishing interaction energies we observe that $\lim_{\tilde{\mathcal{V}}^0 \to 0} \tilde{k}{=}1$. This reproduces our finding from above, that the exponentially damped screening profile decays with the Debye length, *i.e.* $k(\mathcal{V}^0{=}0) = 1/L_\mathrm{D}$ (see section 10.2.1). However, the damping $\mathfrak{Re}(\tilde{k})$ increases with increasing $\tilde{\mathcal{V}}^0$ up to the phase boundary $\tilde{\mathcal{V}}^0_-$, *i.e.* the width of the EDL decreases with increasing $\tilde{\mathcal{V}}^0$. Once the interaction energy exceeds the phase boundary $\tilde{\mathcal{V}}^0_-$, the screening profile changes it's character. The damping parameter $\tilde{k}_\mathbb{R}$ decreases with increasing $\tilde{\mathcal{V}}^0$, *i.e.* the EDL width increases with increasing $\tilde{\mathcal{V}}^0$. Thus, the phase boundary $\tilde{\mathcal{V}}^0_-$ determines the threshold at which the EDL has minimal extension. Apparently, the increasing strength of the repulsive ion-correlations compresses the screening-layer. However, once the interaction strength exceeds the phase boundary $\tilde{\mathcal{V}}^0_-$, the imaginary part of the wave vector $\tilde{k}_\mathbb{C}$ becomes non-zero. Hence, the ion-layers begin to oscillate and the system "overscreens", see eq. (10.44). The real part of the wave vector decreases with increasing $\tilde{\mathcal{V}}^0$ until it vanishes exactly at the phase boundary $\tilde{\mathcal{V}}^0_+$, such that the wave vector becomes imaginary. Hence, with increasing $\tilde{\mathcal{V}}^0$, the EDL width increases into the bulk electrolyte. Once $\tilde{\mathcal{V}}^0$ exceeds the phase boundary $\tilde{\mathcal{V}}^0_+$, the EDL width diverges and the electrolyte system undergoes a phase transition. As consequence, the oscillatory region extends over the complete system length. Once the interaction energy exceeds $\mathcal{V}^0_-$, the frequency of the oscillations starts increasing very fast and quickly reaches a local maximum. However, upon further increase of $\tilde{\mathcal{V}}^0$, the frequency decreasing again until it reaches a local minimum at $\tilde{\mathcal{V}}^0 = \tilde{\mathcal{V}}^0_+$. Finally, it starts increasing again, and converges towards it's global maximum given by the terminal frequency $\tilde{k}_{\mathrm{AFM}} \approx 0.7$. The existence of local extrema of the frequency $\tilde{k}_{\mathbb{C}}$ highlights the non-trivial interplay of the competing correlation energies E_{th}, E_{el} and $\mathcal{V}^0$.

Figure 11.1b)-f) illustrates the critical interaction energies $\mathcal{V}^0_\pm$ as function of the system parameters. Since the critical interaction energies constitute the phase boundaries, these figures constitute the phase spaces of screening profiles, subject to the variation of the system parameters.

Figure 11.1b) shows the influence of temperature, *i.e.* E_{th} on the phase boundaries (since E_{th} is linear in the temperature, see eq. (9.33)). Both phase boundaries increase with increasing temperature. This behaviour highlights the disordering effect of entropy on the EDL structure. Apparently, the regime of exponentially decaying screening profiles is highly suppressed for reasonable temperatures.

Figure 11.1c) illustrates the influence of the dielectric constant on the phase boundaries, *i.e.* E_{el} (note that the thermal energy does not depend on ε_{R}). However, since the electrostatic energy depends inversely on the dielectric constant (see eq. (9.34)), E_{el} decreases with increasing a. The two phase boundaries exhibit opposite behaviour, as $\mathcal{V}^0_-$ increases with decreasing E_{el} (increasing ε_{R}), whereas $\mathcal{V}^0_+$ decreases with decreasing E_{el} (increasing ε_{R}). This results in the suppression of the intermediate regime, where the EDL structure exhibits damped oscillatory profiles, at larger values E_{el}. Apparently, the electrostatic energy favours the formation of an exponentially decaying screening profile.

Figure 11.1d) shows the influence of the ion size on the phase boundaries $\mathcal{V}^0_\pm$. Note that the y-axis for the interaction energy is in logarithmic scale. The phase boundary $\mathcal{V}^0_-$ increases with ion size, whereas the phase boundary $\mathcal{V}^0_+$ decreases with the ion size. As consequence, the regime of damped oscillatory EDL structures becomes suppressed for large ions. In contrast, this phase is favoured for very small ions. We emphasize that the thermal energy is independent of the ion size, whereas the electrostatic energy is inversely proportional to the ions size $E_{\mathrm{el}} \propto a^{-1}$.

Figure 11.1e) illustrates the influence of ion asymmetry on the phase boundaries. Both phase boundaries decrease with increasing symmetry (*i.e.* in the parameter range $\gamma \leq 0.5$), and increase with decreasing symmetry $\gamma \geq 0.5$. Thus, the regime of exponentially decaying profiles is suppressed for more symmetric ions.

Figure 11.1f) compares the phase boundaries as functions of temperature for the two different valencies $z_+ = [1, 2]$. Apparently, the phase boundary $\mathcal{V}^0_-$n is smaller for multivalent ions, and the phase boundary $\mathcal{V}^0_+$ is larger for the multivalent ions. Hence, the intermediate regime is more favourable for multivalent ions.

12 Numerical Simulations of the EDL-Structure of Binary ILs

Here, we use computational methods and validate our EDL transport theory for the IL-electrolyte PYR[1,4]TFSI. We structure this chapter as follows. First, in section 12.1, we describe the set-up. Next, in section 12.2, we focus on the influence of thermal and electrostatic energies on the structure of the EDL and neglect molecular interactions (thus we set $\mathcal{V}^0$=0). Finally, in section 12.3, we incorporate molecular interactions into our discussion.

12.1 Binary IL-Electrolyte: PYR[1,4]TFSI

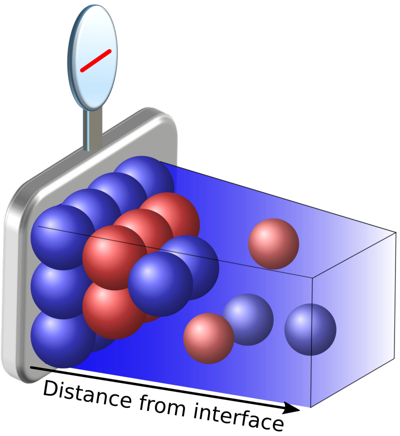

Scheme 12.1: Scheme of the half-cell set-up used in the simulations. The binary IL-electrolyte PYR[1,4]TFSI is subject to the negatively charged interface at the left, which causes the formation of an electrochemical double layer (EDL). Figure first published in Ref. 367.

In this section, we describe the two set-ups which we use for the numerical simulations. In section 12.2 we use a "half-cell" set up, whereas in section 12.3, we use a "full-cell" set up which constitutes the symmetrized generalization of the half-cell set up. The half-cell set-up consists of an inert and ideally flat surface, which constitutes our model for a metal-electrode, and the binary IL electrolyte, which extends normally away from the electrode surface located at $\tilde{x}$=0 towards increasing values of the interface-distance $\tilde{x}$. We neglect chemical reactions and specific adsorption at the surface, and assign an electric potential to the electrified surface. However, since electric potentials are continuous across interfaces,[144] the potential of the interface coincides with the electrolyte electric potential $\Phi(x{=}0)$. Furthermore, we assign the half-cell potential $\mathit{\Delta}\phi$, and assume electroneutral boundary condition for the bulk potential, $\Phi(x{\to}\infty) \to 0$,

$$\Phi(0) - \Phi(x \to \infty) = \Phi(0) = \mathit{\Delta}\phi. \tag{12.1}$$

However, we ensure that our geometry is consistent with the boundary conditions and choose the length of the set-up such that it exceeds the double layer width. Finally, in section 12.3 we use a "full-cell" geometry for our numerical set-up and supplement the inert ideal surface located at x=0 by an oppositely charged surface at $x = L_{\text{system}}$, where we set the boundary condition $\Phi(L_{\text{system}}) = -\mathit{\Delta}\phi$. To ensure consistent bulk-behaviour, we use a grid-length of L_{system}=60 nm.

In our simulations, we focus on the binary IL electrolyte PYR[1,4]TFSI. Due to their excellent electrochemical properties, the IL-family comprised of TFSI anions and PYR cations is widely studied and used for applications in lithium-ion batteries.[368] We assume complete salt disociation into PYR$^+$ and TFSI$^-$. Due to the assumption of electroneutrality, both bulk-concentrations are equal $c_\pm(x{\to}\infty) = c^{\mathrm{b}}$ and the Euler equation for the volume fixes the bulk concentration via $c^{\mathrm{b}} \cdot \nu = 1$.

In the appendix, we state additional information (see appendices A.5 and E.5).

12.2 Mean Volume Effect

12.2.1 Numerical Simulations: Mean Steric Effect

In this section, we focus on the "bulk"-description of the EDL and $\mathcal{V}^0 = 0$. We neglect convection ($\tilde{\mathbf{v}}$=0), such that the system of equations becomes (see section 9.2.2 and eq. (9.52))

$$\tilde{\varrho}_{\mathrm{F}} = -\tilde{\boldsymbol{\nabla}}^2\tilde{\Phi}, \qquad \text{and} \qquad \partial_{\tilde{t}}\tilde{\varrho}_{\mathrm{F}} = \tilde{\boldsymbol{\nabla}}\left[(1 + \chi\tilde{\varrho}_{\mathrm{F}})\,\boldsymbol{\nabla}\mu^{\mathrm{el}}_{\mathrm{IL}}\right], \tag{12.2}$$

where the forces are given by eq. (9.43) subject to $\mathcal{V}^0 = 0$,

$$\tilde{\boldsymbol{\nabla}}\tilde{\mu}^{\mathrm{el}}_{\mathrm{IL}} = \tilde{\boldsymbol{\nabla}}\left(\tilde{\Phi} - \gamma_+ \cdot \ln\left[\tilde{c}_-/\tilde{c}^{\mathrm{b}}\right] + \gamma_- \cdot \ln\left[\tilde{c}_+/\tilde{c}^{\mathrm{b}}\right]\right). \tag{12.3}$$

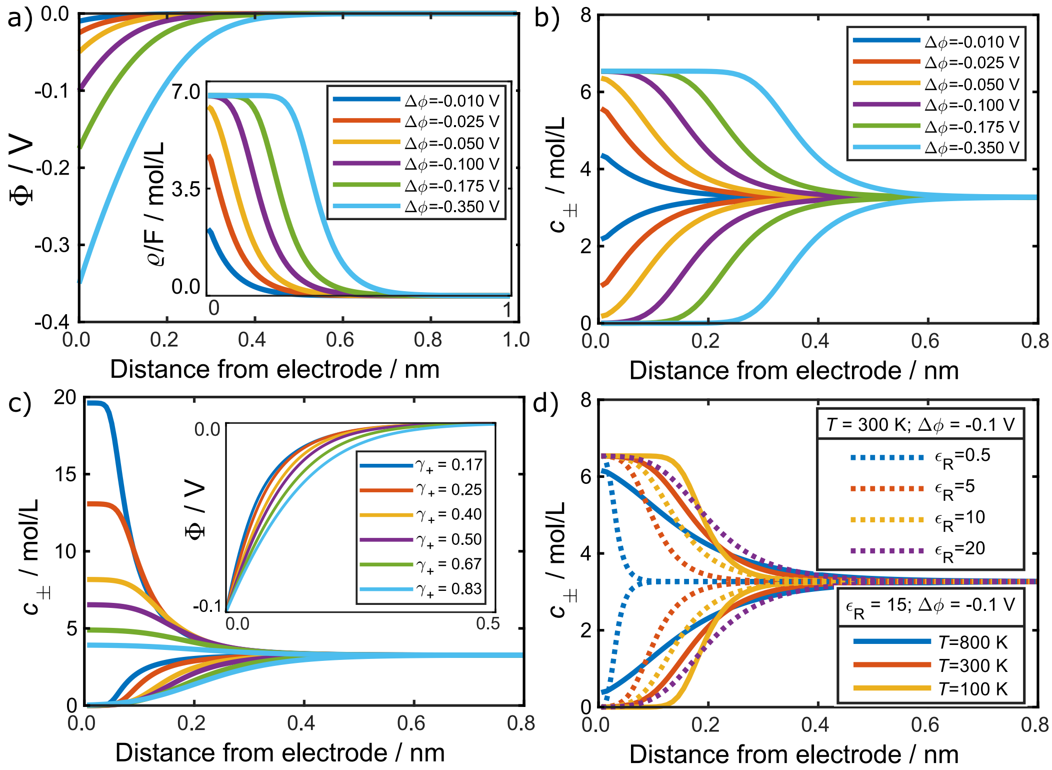

Figure 12.1: Simulation results for the EDL structure near the electrified interface for a binary IL (see eq. (9.52) and eq. (9.43) subject to the condition $\mathcal{V}^0 = 0$). If not mentioned otherwise, T=300 K, ε_R=15, γ_+=0.5 and $\Delta\phi = -0.1\,\mathrm{V}$. a) Profiles of Φ and ϱ_F for different $\Delta\phi$. b) Profiles of $c_\pm$ for different $\Delta\phi$. c) Profiles of $c_\pm$ for different γ_+ (the inset shows Φ). d) Profiles of $c_\pm$ for varying dielectric constants (dashed lines) and temperatures (solid lines). Figures first published in Ref. 367.

The objectives in this section are to study the influence of $\Delta\phi$, E_th, E_el, and ion asymmetry on the screening profiles as predicted by the “bulk” description of our theory (see eq. (12.2)).

If not stated otherwise, the numerical simulations were performed using the system parameters $T = 300\,\mathrm{K}$, $\varepsilon_\mathrm{R} = 15$, $\gamma = 0.5$, $z_+ = 1$ and $a = 1.2\,\mathrm{nm}$. In appendix E.5 we list all parameters (see table E.1). Thus, the saturation value for the ion-concentrations is $c_\pm^\mathrm{sat} = 6.6{\cdot}10^{-5}\,\mathrm{mol\,m^{-3}}$, see also eq. (9.4).

Figure 12.1 shows numerical results for the electric potential, charge density and ion concentrations obtained from eqs. (12.2) and (12.3). However, in order to better relate to the physical quantities, we show all results for the corresponding dimensional quantities Φ, ϱ_{F} and $c_{\pm}$.

Figure 12.1a) and fig. 12.1b) show the screening profiles for electrolyte electric potential, charge-density (inset), and concentration of the ion-species for a common set of negative potentials in the range $|\Delta\phi| \in [10\,\mathrm{mV}, 350\,\mathrm{mV}]$. All three electrolyte quantities show a common reaction to the application of the electrode potential $\Delta\phi$.

Figure 12.1a) shows the electric potential of the electrolyte. Since electric potentials are continuous across such interfaces, $\Phi(x = 0) = \Delta\phi$ at the electrode (see eq. (12.1)). Apparently, for all values of $\Delta\phi$ the potential Φ decays exponentially to the electroneutral state. The corresponding EDL widths span across some Å. However, the EDL width is a function of interface-potential, and increases with increasing $\Delta\phi$.

Both the charge density (inset in fig. 12.1a) and the ion concentrations (fig. 12.1b) show a similar behaviour at small potentials $\Delta\phi$. Both quantities decay exponentially from their interfacial value to the electroneutral bulk state. For small potentials, the deviation from the electroneutral value at the interface increases with increasing $\Delta\phi$. However, once the electric potential becomes larger than $|\Delta\phi| = 50\,\mathrm{mV}$, the screening profile changes into a saturation profile. Upon further increase of $\Delta\phi$, constant plateaus emerge in the profiles next to the interface. These expand over some Å before they decay exponentially into the electroneutral state. The width of the constant saturation plateau increases with increasing $\Delta\phi$.

Altogether, the behaviour of the electrolyte quantities Φ, ϱ_{F} and $c_{\pm}$ as functions of $\Delta\phi$ is consistent with our analytical discussion from section 10.2. The application of an external potential causes an electrolyte-polarization, as the ions try to screen the electrode. Since the $\Delta\phi$ are negative, the electrolyte accumulates cations ("counter species") near the electrode, whereas anions ("like species") are expelled towards the bulk region. Upon increasing $\Delta\phi$, the electrolyte increases the number of cations near the electrode. However, due to the Euler equation for the volume, there exists a maximal "saturation" concentration which is determined by the molar volume of the ions via $c_{\alpha^*}^{\mathrm{sat}} = (\nu_{\alpha^*})^{-1}$. Thus, once the external potential becomes too large (here roughly at $50\,\mathrm{mV}$), the interface concentration of counterions reaches it's saturation value, and the screening mechanism changes from increasing the concentration of counterions near the interface towards broadening the EDL width. Note that this implies that the like species (here, the anions) gets depleted near the interface.

At $\Delta\phi \approx -350\,\mathrm{mV}$ the EDL is roughly 6 Å thick. This is significantly larger than predicted by the canonical Debye-Hückel-theory, *i.e.* by the Debye length $L_{\mathrm{D}} \approx 0.7$ Å (see eq. (9.26)). In the literature, this saturation-phenomenon is typically called "crowding".[69]

Next, we study the influence of ion asymmetry on the EDL structure. Figure 12.1c) shows the influence of ion asymmetry on the screening profile of the ion concentrations. The cation volume ratio γ_+ ranges from 0.17 to 0.83. Apparently, highly asymmetric ion species yield highly asymmetric screening profiles, and the saturation concentration increases significantly for smaller cation species ($\gamma_+<0.5$). This is because the molar volume ν_+ decreases with decreasing parameter γ_+, which implies larger saturation concentrations $c_+^{\mathrm{sat}}=(\nu_+)^{-1} \propto (\gamma_+)^{-1}$, see eq. (9.4). Hence, the EDL-width is more compact for smaller ion-volumes γ_+, as this allows for tighter packing of cations. Thus, the partial molar volumes of the ion-species directly affect the screening behavior.

It remains to discuss the influence of temperature T, *i.e.* E_{th}, and dielectricity ε_{R}, *i.e.* E_{el}, on the EDL-structure. In fig. 12.1d we show numerical results for different temperatures (solid lines) and different dielectric constants (dashed lines). We first discuss the influence of different temperatures on the EDL structure. For $T = 100\,\mathrm{K}$, the EDL profile of the charge density exhibits a crowded profile, *i.e.* the cation concentration is saturated near the electrode and decays steeply towards the electroneutral state. However, upon increasing the temperature, the EDL profile gets more diffuse. At $T = 300\,\mathrm{K}$ the charge density still exhibits a saturation profile. However, the EDL width is reduced as compared to the case where $T = 100\,\mathrm{K}$, and the decay is not so steep. Finally, the EDL structure gets washed out for $T = 500\,\mathrm{K}$. This is a consequence of the disordering entropic-effect, *i.e.* of thermal motion. Next, we discuss the influence of dielectricity on the EDL structure. The dashed lines in fig. 12.1d show the numerical results of the screening profile as function of ε_{R}. Apparently, the EDL-width increases with increasing ε_{R}, suggesting a more effective screening at small dielectricities. This behaviour is in qualitative agreement with the predicted screening behavior for dilute solutions by the Debye-Hückel theory. Altogether, the observed effects of T and ε_{R} on the screening profiles highlight the competing interplay between the the disordering effect of entropy and the effect of charge ordering, due to electrostatics.

Finally, we shall briefly summarize our findings. We conclude from the numerical results comprised in fig. 12.1 that there exist two distinct regimes of EDL structure. One regime is located right next to the interface, where charge-saturation emerges for large electrode potentials (*i.e.* $\Delta\tilde{\phi} \gg 1$). The second regime is the region close to the electroneutral bulk, where $\tilde{\varrho}_{\mathrm{F}} \ll 1$ and is characterized by an exponential profile of the charge density. Thus, we conclude that the two distinct EDL-structures of charge saturation and exponential decrease correspond to two disjoint electrolyte regimes, *i.e.* $|\tilde{\Phi}| \gg 1$ and $|\tilde{\Phi}| \ll 1$. Apparently, these two regimes correspond to the two limiting cases discussed in sections 10.2.1 and 10.2.2. This suggests that we compare the numerical results discussed in this section, and comprised in fig. 12.1, with the corresponding analytical prediction from sections 10.2.1 and 10.2.2.

12.2.2 Analytical Discussion of EDL Screening: Mean Steric Effect

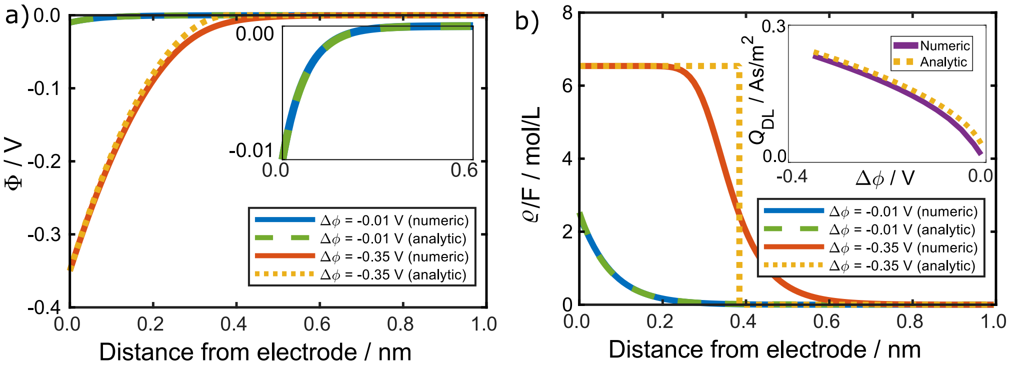

Figure 12.2: Comparison of the analytical prediction for the EDL structure (eqs. (10.9), (10.15) and (10.16)) with the numerical results discussed in section 12.2.1. We consider two interface potential, corresponding to the regimes of small and large potentials, $\Delta\phi = -100\,\mathrm{mV}$ ($\Delta\tilde{\phi} = -0.4$), and $\Delta\phi = -350\,\mathrm{mV}$ ($\Delta\tilde{\phi} = -13.5$). a) Profiles of Φ. The inset highlights the region close to the interface for $\Delta\phi = -0.01\,\mathrm{V}$. b) Profiles of ϱ_F. The inset compares numerical and analytical values for the total charge comprised in the EDL (see eq. (10.21)). Figures first published in Ref. 367.

In this section, we compare our numerical findings from section 12.2.1 with our analytical predictions for the EDL-structure from sections 10.2.1 and 10.2.2.

Our main assumption from sections 10.2.1 and 10.2.2 for the analysis of the EDL structure. *i.e.* that there exist two distinct electrolyte regions ($\Delta\tilde{\phi} \gg 1$, near the electrode, and $\Delta\tilde{\phi} \ll 1$, far away from the electrode), was qualitatively verified by the numerical results discussed in the previous section. Here, we make a quantitative comparison between the analytical description and the simulation results, and use the numerical results for Φ and ϱ_F at the lowest interface potential $\Delta\phi = -10\,\mathrm{mV}$, or $\Delta\tilde{\phi} = -0.4$ (to mimic the case $\Delta\tilde{\phi} \ll 1$), and at the highest interface potential $\Delta\phi = -350\,\mathrm{mV}$, which corresponds to $\Delta\tilde{\phi} = -13.5$ (to mimic $\Delta\tilde{\phi}$) shown in fig. 12.1a).

Figure 12.2 shows a comparison of Φ and ϱ_F for the two cases of small and large electrode potentials. The dashed green lines show the analytical predictions for the electric potential (subfigure a) and the charge density (subfigure b) at the smaller interface potential $\Delta\phi = -10\,\mathrm{mV}$, whereas the solid blue lines show the corresponding numerical results. Similarly, the dashed yellow lines show the analytical predictions for the electric potential (subfigure a) and the charge density (subfigure b) at the larger interface potential $\Delta\phi = -350\,\mathrm{mV}$, whereas the solid red lines show the corresponding numerical results.

We first focus on the results for the small potential $\Delta\phi = -10\,\mathrm{mV}$. Apparently, the analytical predictions for the electric potential (subfigure a) and for the charge density (subfigure b) are quantitatively in excellent agreement with the numerical results. The inset (in subfigure a) highlights the results for the electric potential close to the interface. This confirms that the asymptotic analysis in the approximation of small potentials delivers highly accurate predictions.

Next, we discuss large electrode potentials ($\Delta\tilde{\phi}{=}-13.5$). The analytical prediction for the electric potential is in very good agreement close to the interface. However, it deviates only slightly close to the electroneutral region (roughly at $5\,\mathrm{Å}$.

The analytical result for the charge density has a boxed-shaped profile. It can be seen that the analytical prediction for the EDL width is roughly $5\,\mathrm{Å}$, hence almost predicts the numerical width of the EDL which is roughly $6\,\mathrm{Å}$. Thus, it is in good qualitative agreement with the numerical results. However, the profiles show some deviations. The numerical profile is more diffuse in the transition from saturation near the interface to the electroneutral bulk-state than the sharp profile of the analytical charge box. This is a direct consequence of the disordering entropic effect, which is neglected in the asymptotic analysis which assumes vanishing temperatures. Apparently, the thermal influence “washes out” the compact charge-ordering of the analytical box-profile. We note that the numerical charge profile and its dependence on temperature is reminiscent of the Fermi distribution. The inset in fig. 12.2b compares the analytical prediction for the total amount of charge $\mathcal{Q}^{\mathrm{tot}}$ comprised in the EDL, as obtained from eq. (10.21), with the numerical results. Apparently, both are in excellent agreement over the range of interface potentials discussed in fig. 12.1a).

Altogether, these results confirm our asymptotic analysis from section 10.2, and the analytical predictions for the EDL structures are in excellent agreement with the results obtained from numerical simulations.

12.3 Non-Local Interactions

In this section, we supplement our study from the previous section regarding the influence of E_{th} and E_{el} on the EDL structure by the interaction energy $\mathcal{V}^0$ and investigate the competing influence of the three energy scales E_{th}, E_{el} and $\mathcal{V}^0$, and the electrode potential $\Delta\phi$ on the screening profiles. For this purpose, we compare numerical results obtained from the gradient and intergal description with the analytical predictions.

We structure this section as follows. First, we study the influence of $\mathcal{V}^0$ on the screening profile and present simulation results for $\tilde{\varrho}_{\mathrm{F}}(\mathcal{V}^0)$, where we choose interaction energies from each of the three analytically predicted phases. Second, we quantify the agreement between the three descriptions and compare the results at four different interface potentials. Third, we focus on the simulation results for the integral description at very high interaction energy $\mathcal{V}^0 = 500\,\mathrm{meV}$, and probe the fundamental assumption of our particle hypothesis, see eq. (10.35). Finally, we generalize our findings to a systematic study over the complete phase-space of interaction energies.

All numerical simulations in this section are performed for a symmetric cell-set-up, where the IL electrolyte is located between two oppositely charged, blocking interfaces separated by a distance of 60 nm. We apply a negative interface-potential to the left electrode, $\Delta\phi = -100\,\mathrm{mV}$. The electrolyte consists of symmetric ions ($\gamma_\pm = 0.5$) with ion-size $a = 1.2\,\mathrm{nm}$. Hence, the cell-geometry allows a "maximal" number of roughly 90 ions. The bulk-concentration of the symmetric iojns ($\tilde{c}^{\mathrm{b}} = 1/2$) normalizes charge saturation, $\tilde{\varrho}_{\mathrm{F}}^{\mathrm{sat}} = \pm 1$. The other system parameters are $T = 300\,\mathrm{K}$ and $\varepsilon_{\mathrm{R}} = 15$, and the thermal and electrostatic energies are $E_{\mathrm{th}} \approx 25\,\mathrm{meV}$ and $E_{\mathrm{el}} \approx 80\,\mathrm{meV}$. Furthermore, the resulting phase boundaries, as predicted by the analytical description, for this set-up are $\mathcal{V}^0_- = 3\,\mathrm{meV}$ and $\mathcal{V}^0_+ = 253\,\mathrm{meV}$.

12.3.1 Numerical Simulations: Molecular Interactions

For completeness, we restate the integral description and the gradient description. For the above described symmetric electrolyte species, the system of equations reduces to $\partial_{\tilde{t}}\tilde{\Phi} = -\tilde{\mu}^{\mathrm{el}}_{\mathrm{IL}}$ (see section 9.2.1). The chemical potential according to the integral description is given by eq. (9.50) and the resulting transport equation reads

$$\partial_{\tilde{t}}\tilde{\Phi} = -\tilde{\mu}^{\mathrm{el}}_{\mathrm{IL}} = -\tilde{\Phi} + \frac{1}{2}\ln\left[\frac{1-\tilde{\varrho}_{\mathrm{F}}}{1+\tilde{\varrho}_{\mathrm{F}}}\right] + \frac{\mathcal{V}^0}{8\pi E_{\mathrm{el}}}\int \mathrm{d}\tilde{x}\;\tilde{\varrho}_{\mathrm{F}} \cdot \exp\left[-3\left(\frac{\pi\tilde{x}}{\tilde{a}}\right)^2\right]. \tag{12.4}$$

The chemical potential according to the gradient description is given by eq. (11.11), and the corresponding transport equation reads

$$\partial_{\tilde{t}}\tilde{\Phi} = -\tilde{\Phi} + \frac{1}{2}\ln\left[\frac{1-\tilde{\varrho}_{\mathrm{F}}}{1+\tilde{\varrho}_{\mathrm{F}}}\right] + \frac{\mathcal{V}^0\tilde{\Gamma}^0_{+-}}{E_{\mathrm{th}}} \cdot \left[\tilde{\varrho}_{\mathrm{F}} + \left(\frac{\tilde{a}}{2\pi}\right)^2\tilde{\boldsymbol{\nabla}}^2\tilde{\varrho}_{\mathrm{F}}\right], \tag{12.5}$$

where $\tilde{\Gamma}^0_{+-} = 1/2\pi\tilde{\nu} \cdot (\sqrt{3\pi})^{-3}$ (see eq. (11.9)). Note the two expansions above are supplemented by the Poisson equation,

$$\tilde{\varrho}_{\mathrm{F}} = -\tilde{\boldsymbol{\nabla}}^2\tilde{\Phi}. \tag{12.6}$$

Figure 12.3 shows numerical results for the charge density as function of the interaction strength $\mathcal{V}^0$ obtained from solving the integral description eqs. (12.4) and (12.6). Here, the values for $\mathcal{V}^0$ span two orders of magnitude, and comprise the analytically predicted phase boundaries $\mathcal{V}^0_\pm$. The $\tilde{x}$-axis measures the distance from

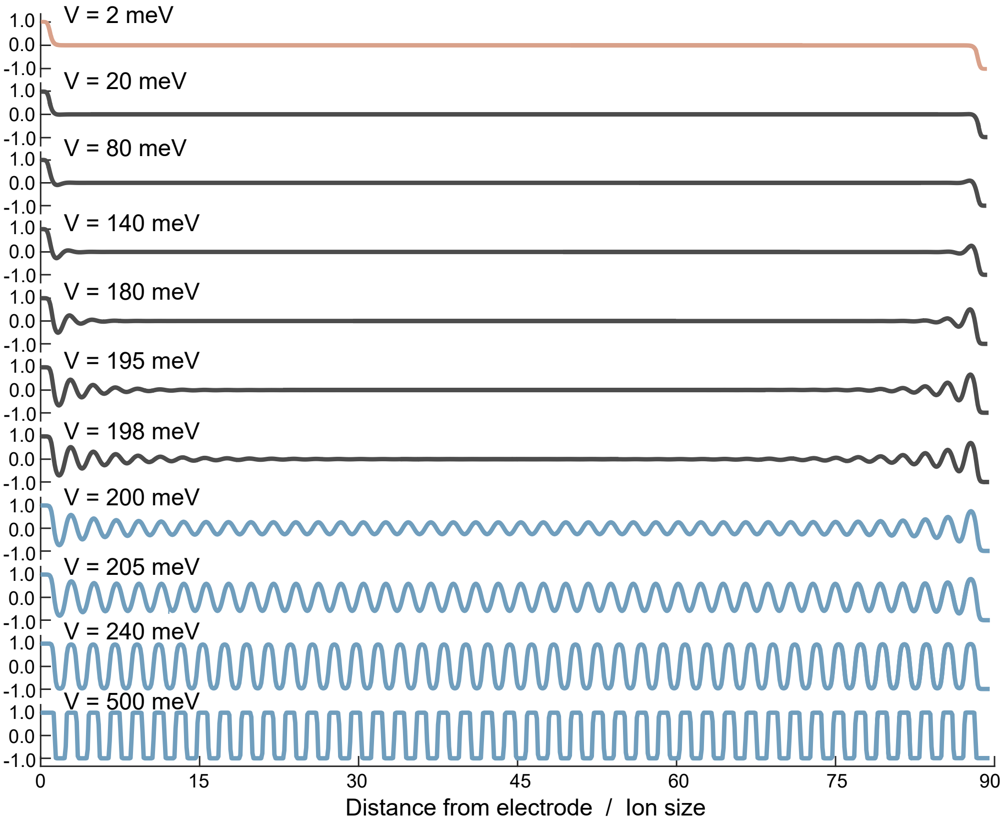

Figure 12.3: Numerical results for the non-dimensional charge density as function of the interaction strength $\tilde{\varrho}_{\mathrm{F}}(\mathcal{V}^0)$, obtained from the integral description, eqs. (12.4) and (12.6). The x-axis comprises the complete cell length spanning over roughly 90 ion layers (roughly 60 nanometers). Hence, the negatively charged electrode is located at $x = 0$ on the left, and the positively charged electrode is located at roughly $x = 90$ on the right. The y-axis illustrates the charge density $\tilde{\varrho}_{\mathrm{F}}$, where $|\tilde{\varrho}_{\mathrm{F}}| = 1$ corresponds to charge saturation. Figure first published in Ref. 367.

the negatively charged electrode (left side), to the positively charged electrode (right side). The y-axis shows the non-dimensional charge density, where $\tilde{\varrho}_{\mathrm{F}}= \pm 1$ corresponds to charge saturation. The charge profile for the lowest interaction strength $\mathcal{V}^0$=2 meV shows crowding, *i.e.* charge saturation at both electrodes followed by an exponential decay towards the electroneutral state with increasing distance from the electrodes (see chapter 12). Since $\mathcal{V}^0<\mathcal{V}^0_-$, this is in accordance with the analytical prediction. The next several charge profiles show results for interaction strengths from the intermediate regime, $\mathcal{V}^0_-<\mathcal{V}^0<\mathcal{V}^0_+$. At $\mathcal{V}^0$=20 meV the oscillations are hardly visible, and, up to the interaction strengths $\mathcal{V}^0$=80 meV, the charge profiles exhibits only one small oscillations with moderate amplitude. The number of oscillations increases only slowly up to interaction strengths of roughly $\mathcal{V}^0$=180 meV. However, over the next few meV, the number of oscillations increases significantly, and the EDL structure extends across multiple nanometers. At $\mathcal{V}^0$=195 meV the oscillations span already over roughly 20 ion layers at each electrode. The bulk region is hardly visible anymore at $\mathcal{V}^0$=198 meV, where the oscillations extend almost across the entire cell length. In accordance with this, a slight increase by 2 meV up to $\mathcal{V}^0$=200 meV causes the system to transition into the regime of undamped oscillations spanning across the complete system. However, the magnitudes of the amplitudes are, apart from the crowding at the electrodes, not saturated, *i.e.* $|\tilde{\varrho}_\mathrm{F}|<1$. Thus, for this magnitude of $\mathcal{V}^0$, the electrolyte has a nano-structure consisting of oppositely charged layers, where the dominant ion species is alternating between neighbouring layers. Apparently, the magnitudes of the amplitudes increase with increasing interaction strength $\mathcal{V}^0$. This implies that the separation of the ion species becomes more pronounced with increasing interaction strengths $\mathcal{V}^0$. Finally, at $\mathcal{V}^0$=240 meV, the amplitudes have reached saturation, $\tilde{\varrho}_\mathrm{F}=\pm 1$. Finally, at $\mathcal{V}^0$=500 meV the ion layers have become very sharp, and the electrolyte has transitioned into a crystalline phase consisting of pure ion-layers. Thus, with increasing energies $\mathcal{V}^0$, the EDL increases into the bulk electrolyte, until the bulk itself gets nano-structured by ion-segregation. This phase separation occurs rapidly over a sharp increase of some meV.

Next, we discuss the double layer forces $\mathcal{F}^\mathrm{EDL}=\nu/N_\mathrm{A}\cdot\varrho_\mathrm{F}\boldsymbol{\nabla}\Phi$ (see eq. (10.46) in section 10.3.3) corresponding to the results shown in fig. 12.3. The EDL forces express the balance between elastic pressure forces and the strong electrostatic forces which constitute the mechanical equilibrium of the quasi-crystalline EDL structures. Figure 12.4 illustrates these force-profiles and highlights the limiting region where the interaction energy $\mathcal{V}^0$ is dominant, *i.e.* $\mathcal{V}^0\gg E_\mathrm{th}$ and $\mathcal{V}^0 \gg E_\mathrm{el}$ (hence $\mathcal{V}^0\gg\mathcal{V}^0_+$). The left plot shows the EDL forces appearing in the left half-cell of the system. Apparently, these forces are trivial in the regime $\mathcal{V}^0<\mathcal{V}^0_+$, but start oscillating once $\mathcal{V}^0_-<\mathcal{V}^0$. The oscillatory region extends further into the bulk with increasing interaction strength. Finally, at $\mathcal{V}^0$=200 meV non-trivial forces extend across the complete half cell, where the profiles have a serpentine shape. The amplitudes of the undamped force oscillations increase with increasing $\mathcal{V}^0$, and the oscillatory peaks becomes more sharp with increasing $\mathcal{V}^0$. Finally, at $\mathcal{V}^0$=500 meV, the shape exhibits zigzag pattern (similar to isogonal zig-zag skew apeirogons in two dimensions[369]). This energy regime is highlighted in the right plot in fig. 12.4, which shows numerical results obtained from the integral description for the ion-concentrations $\tilde{c}_\pm$ (left y-axis), and the double-layer forces (right y-axis) of the first six ion-layers adjacent to the negatively charged interface at $\mathcal{V}^0 = 500$ meV (these results correspond to

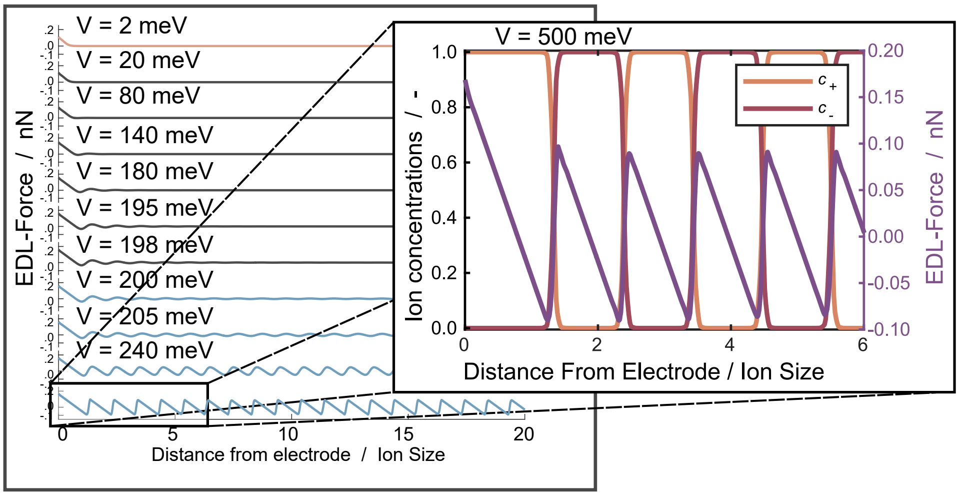

Figure 12.4: Profiles of the double layer forces for the first few nano-meters. The left figure shows a cumulative overview of the double layer forces spanning over the first 20 ion layers (roughly 24 nano-meters) as function of the interaction energy $\mathcal{V}^0$. The set of forces is the same as appearing in fig. 12.3. The figure on the right highlights the force profile (right y-axis) and the ion concentrations (left y-axis) at $\mathcal{V}^0 = 500\,\text{meV}$ across the first six ion layers (roughly seven nanometers). Note that the ion concentrations are normalized such that $\tilde{c}_\pm = 1$ corresponds to saturation. Figures first published in Ref. 367.

the very lowest charge profile shown in fig. 12.3). Note that because the ions are symmetric in this simulation, the saturation concentrations are normalized to unity, *i.e.* $\tilde{c}_\pm^{\text{sat}}=1$. The concentration profiles show very sharply separated ion-layers of box-shaped form, where the width of the ion-layers scale exactly with a, *i.e.* the size of the ions. This is reminiscent of the "Gaussian" shape of our interaction model for the hardcore ions (eq. (11.1)), and is in agreement with the force-profile shown on the right y-axis. The force profile has a zigzag shape and the force peaks arise exactly at the boundaries between two ion-layers. This highlights the highly crystalline structure, where the ion layers are stable with respect to perturbations of the equilibrium configuration.

Altogether, we find that the numerical results obtained from the integral description confirm the existence of three different screening phases, as predicted by our analytical description. The corresponding two phase boundaries obtained from the integral description are roughly at 1 meV, and at 200 meV. Hence, the lower phase boundary is quantitatively in very good agreement with the analytical prediction $\mathcal{V}^0_- = 3\,\text{meV}$. However, the upper phase boundary is roughly 25 % smaller than the analytical prediction $\mathcal{V}^0_+ = 253\,\text{meV}$. We attribute this discrepancy to the fact that the analytical prediction is based on our gradient approximation, which accounts for only the first two perturbation modes. In contrast, the integral description comprises all perturbation modes. Nevertheless, the analytical description still offers a good prediction for the qualitative behaviour of the system. Furthermore, the numerical results in the regime of dominant interaction energies show ion layers in the EDL which scale exactly with the ion sizes.

However, these conclusions refer to a limited set of simulation results, which did not include results obtained from the gradient description eqs. (12.5) and (12.6). Next, we generalize our results across the whole phase-spectrum, *i.e.* across several orders of magnitude for $\mathcal{V}^0$, and to the gradient description. To address this goal, we use a set of roughly 4000 interaction energies ranging from 0.1 meV up to 500 meV and perform numerical simulations for this set of interaction energies with respect to the integral description, and with respect to the gradient description. First, we evaluate the simulation results by counting the number of oscillation peaks appearing in the screening profiles of $|\tilde{\varrho}_\mathrm{F}|$, as function of the interaction energy $\mathcal{V}^0$. For a fixed interaction energy $\mathcal{V}^0$, let $\tilde{x}^i(\mathcal{V}^0)$ denote the position of the i-th peak $\tilde{\varrho}^i_\mathrm{F}(\mathcal{V}^0){=}|\tilde{\varrho}_\mathrm{F}(\tilde{x}^i)|$ occurring in the screening profile obtained from numerical simulations with respect to either the integral description, or the gradient description. Then, for every interaction energy $\mathcal{V}^0$, we calculate the number $N_\mathrm{peak}(\mathcal{V}^0)$ of peaks $\tilde{\varrho}^i_\mathrm{F}(\mathcal{V}^0)$ in the resulting screening profile. By construction, the peaks have amplitudes $0{<}\tilde{\varrho}^i_\mathrm{F}{\leq}1$. However, we discard all peaks smaller than a threshold $1{\cdot}10^{-3}$. This yields the peak number $N_\mathrm{peak}(\mathcal{V}^0)$ as function of the interaction strength. Note that there exists a maximal number of peaks $N^\mathrm{max}_\mathrm{peak}$, which is determined by the number of ions that "fit" into our cell geometry. Hence, $N^\mathrm{max}_\mathrm{peak}$ is a function of the length of the system and the size of the ions, $N^\mathrm{max}_\mathrm{peak}{=}L_\mathrm{cell}/a$ (here, $N^\mathrm{max}_\mathrm{peak}{\approx}90$). Furthermore, we can safely assume that the charge profiles become saturated next to the two electrodes (see fig. 12.1). Thus, for this set-up, the peak numbers are limited from below and from above, *i.e.* $2{\leq}N_\mathrm{peak}{\leq}90$. However, besides the number of peaks we also want to account for the amplitude of the oscillations in our quantitative evaluation. To address this goal, we consider the variance σ defined for the half-cell

$$\sigma^2(\mathcal{V}^0) = \frac{\sum_{i=1}^{N_\mathrm{peak}(\mathcal{V}^0)} \tilde{\varrho}^i_\mathrm{F} \cdot (x^i)^2}{\sum_{j=1}^{N_\mathrm{peak}(\mathcal{V}^0)} \tilde{\varrho}^j_\mathrm{F}}. \tag{12.7}$$

Here, we use the "true physical" locations $x^i{=}\tilde{x}^i{\cdot}L_\mathrm{D}$ such that σ has dimension of a length, *i.e.* $[\sigma]{=}\mathrm{m}$. Due to the maximal number of peaks, and the maximal amplitude given by the saturation threshold, the quantity σ converges towards a finite value for very large interaction energies. To show this, let us consider the limit $\mathcal{V}^0_{-}{\ll}\mathcal{V}^0$, where we assume that the bulk-electrolyte has transitioned into a crystalline phase composed of pure ion-layers (see figs. 12.3 and 12.4). Thus, all peaks are saturated, *i.e.* $\tilde{\varrho}_\mathrm{F}^i = 1$, and the corresponding layering-width is exactly the ion-size a. To a good approximation, all saturated peaks are located at $x^i = a \cdot i$,

$$\sigma^2 \approx \frac{\sum_{i=1}^{N_\mathrm{peak}^\mathrm{max}} a^2 \cdot i^2}{\sum_{i=1}^{N_\mathrm{peak}^\mathrm{max}} 1} = \frac{a^2}{N_\mathrm{peak}^\mathrm{max}} \cdot \sum_{i=1}^{N_\mathrm{peak}^\mathrm{max}} i^2 = \frac{a}{L_\mathrm{cell}} \cdot \sum_{i=1}^{N_\mathrm{peak}^\mathrm{max}} i^2. \tag{12.8}$$

From Faulhaber's formula,[370] follows that the sum on the right side converges

$$\sum_{i=1}^{N_\mathrm{peak}^\mathrm{max}} i^2 = N_\mathrm{peak}^\mathrm{max} \cdot \left[\left(N_\mathrm{peak}^\mathrm{max} \right)^2 /3 + N_\mathrm{peak}^\mathrm{max}/2 + 1/6 \right] \approx \left(N_\mathrm{peak}^\mathrm{max} \right)^3 /3\,. \tag{12.9}$$

Insertion into eq. (12.8) shows that σ converges for $\mathcal{V}^0_+ \ll \mathcal{V}^0$ via $\sigma = L_\mathrm{cell}/\sqrt{3}$.

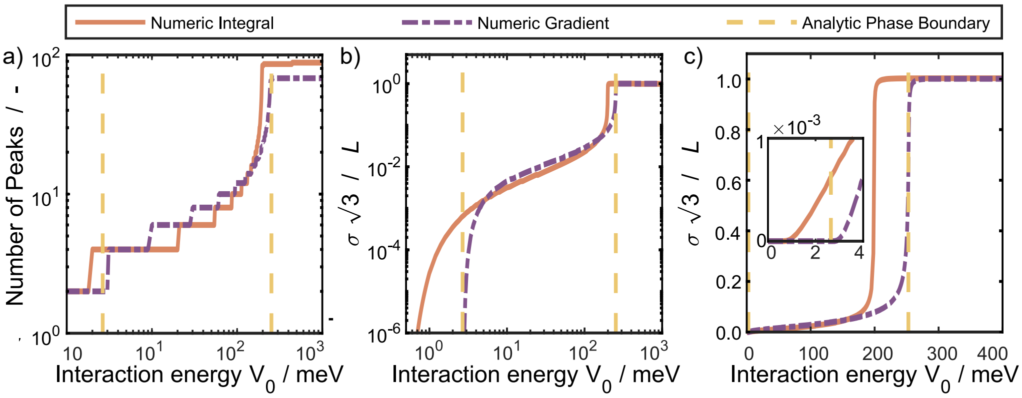

Figure 12.5: Meta analysis of the interfacial profiles for some thousand simulations. a) Number of peaks in $|\tilde{\varrho}_\mathrm{F}|$ as function of $\mathcal{V}^0$. b) Variance of the complete set of simulations as defined by eq. (12.7). c) Variance in non-logarithmic scale. The inset shows the onset of the oscillations for small $\mathcal{V}^0$. Figures first published in Ref. 367.

Figure 12.5 shows the numerical results for our meta analysis of the EDL structures with respect to the set of 4000 simulations $\mathcal{V}^0$ obtained from the integral description and the gradient description. The electrode potentials at both electrodes are set to $|\Delta\phi| = 100\,\mathrm{mV}$. The dashed vertical lines in yellow indicate the analytically predicted phase boundaries $\mathcal{V}^0_\pm$ (see eq. (10.40)).

Figure 12.5a) shows the number of peaks $N_\mathrm{peak}(\mathcal{V}^0)$ as function of the interaction energy. The solid red line illustrates the numerical results obtained from the integral description. Note the logarithmic scale on both axes. Apparently, for small but non-negative interaction energies $0 < \mathcal{V}^0 < \mathcal{V}^0_-$, the number of peaks is $N_\mathrm{peak} = 2$. Thus, the screening profiles are saturated near both electrodes, and decay exponentially into the bulk electrolyte ("crowding"). This is in accordance with fig. 12.1

for this moderately large interface potential. However, at $\mathcal{V}^0{\approx}1\,\mathrm{meV}$, the number of peaks increases with increasing $\mathcal{V}^0$, and the screening profiles start oscillating. Note that because the interaction energies between two simulations increase with $\Delta\mathcal{V}^0{\approx}0.1\,\mathrm{meV}$, the step-wise increase of N_{peak} is not an artefact from limited data points. At $\mathcal{V}^0{\approx}200\,\mathrm{meV}$ the peak numbers increase exponentially until reaching a saturation plateau at $N_{\mathrm{peak}}{\approx}90$. Interestingly, upon further increase there arises another step-wise increase at roughly $\mathcal{V}^0{=}550\,\mathrm{meV}$. The dashed blue curve in fig. 12.5a) shows numerical results for the peak number as function of the interaction energy, obtained from numerical simulations with respect to the gradient description eqs. (12.5) and (12.6). Apparently, the results with respect to the gradient description are very similar to the results with respect to the integral description (red curve). However, the transition from the crowding-profile to the overscreening profile, as well as the transition between the damped oscillatory phase and the purely oscillating phase are quantitatively in excellent agreement with the analytical predictions (dashed vertical lines in yellow). The terminal number of peaks according to the gradient description is roughly 85, *i.e.* smaller than in the integral description. Hence, the main difference between the two descriptions is that the gradient description, and, as consequence, the analytical predictions, underestimate the influence of the interaction energy. Apparently, this behaviour is due to the cumulative effect of the integral-term in eq. (9.42), which comprises all interaction modes. In contrast, we consider only the first two modes ($n{=}0$ and $n{=}1$) of the gradient expansion in eq. (9.43).

Figure 12.5b) shows the variance of the peak numbers (see eq. (12.7)) in a logarithmic scale, where we normalized σ by it's terminal value $L_{\mathrm{cell}}/\sqrt{3}$. The solid red line shows the variance with respect to the integral description, whereas the blue dashed line shows the variance with respect to the gradient description . The vertical dashed lines in yellow show the analytical predictions $\mathcal{V}^0_{\pm}$ for the phase-boundaries. Apparently, the variance according to the integral description (red line) undergoes two phase transitions. However, the two phase boundaries are shifted with respect to the analytical prediction. For high interaction energies, the variance $\sigma/L_{\mathrm{cell}}\sqrt{3}$ converges towards unity, in accordance with our analysis above (see eqs. (12.8) and (12.9)). In a similar manner, the numerical results for σ (dashed blue line) also show two phase transitions, where the corresponding phase boundaries are in excellent agreement with the analytical predictions (dashed vertical lines in yellow). Finally, fig. 12.7c) reproduces fig. 12.7b) in a non-logarithmic scale which highlights the occurrence of the two phase transitions. The inset shows that the variance converges to zero for small interaction energies.

Altogether, the cumulative study comprised in fig. 12.5 confirms our findings obtained from the analysis of figs. 12.3 and 12.4.

Figure 12.6 shows a comparison of the EDL profiles for $\tilde{\Phi}$ and $\tilde{\varrho}_{\mathrm{F}}$ between nu-

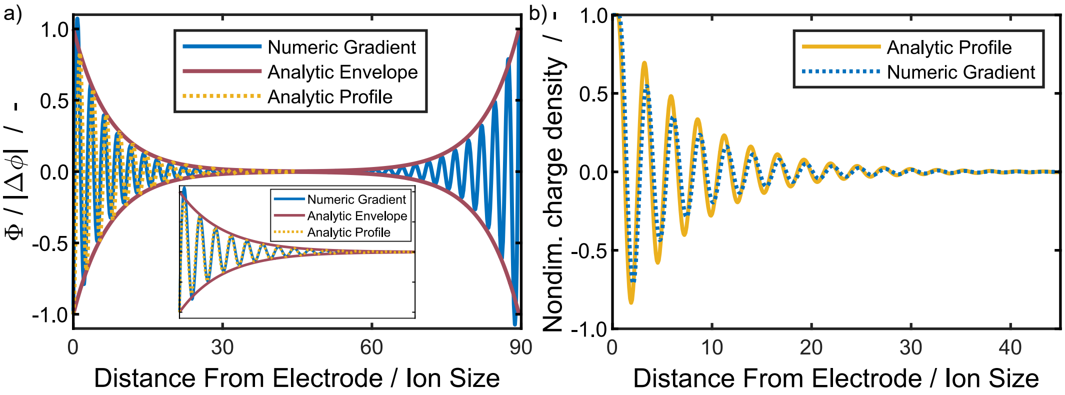

Figure 12.6: Comparison of numerical results obtained from the gradient description eqs. (12.5) and (12.6)with the analytical prediction eqs. (10.30), (10.31) and (10.33), for $\tilde{\Phi}$ and $\tilde{\varrho}_{\mathrm{F}}$. Here, $\varDelta\phi$=100 mV and $\mathcal{V}^0$=250 meV. Figures first published in Ref. 367.

merical results obtained from the gradient description eqs. (12.5) and (12.6), and the analytical prediction eqs. (10.30), (10.31) and (10.33). The analytical profiles are determined by the system parameters, and are constructed as described in section 10.3.4. Here, the polarization of the electrodes is $|\varDelta\phi|$=100 mV and $\mathcal{V}^0$=250 meV. Figure 12.6a) shows $\tilde{\Phi}$ in the complete cell. Apparently, the analytical envelope captures the numerical results of the EDL profile to a high degree of accuracy. The inset highlights the profile for the left half cell, and shows the almost perfect agreement between the gradient description and the analytical description. However, the first oscillation peak appearing in the screening profile of the electrolyte electric potential near both electrodes is larger than one which implies that the electrolyte "overscreens" the applied potential in the first oscillation peak (see our discussion in fig. 12.9). Figure 12.6b) compares both descriptions for $\tilde{\varrho}_{\mathrm{F}}$ in the left half cell. Overall, both profiles are in very good agreement. However, the first few oscillation peaks occurring after the saturation plateau are more pronounced in the analytical profile.

Next, we study the influence of the electrode polarization $\varDelta\phi$ on the structure of the EDL. For this purpose, we repeat the procedure from above, but for different potentials $\varDelta\phi$. In particular, we perform numerical simulations with respect to the integral description, and with respect to the gradient description, for the set of interaction potentials $\varDelta\phi_i \in \{10\,\mathrm{mV}; 70\,\mathrm{mV}; 100\,\mathrm{mV}\}$ for all interaction energies as above.

Figure 12.7 shows the corresponding numerical results for the peak numbers $N_{\mathrm{peak}}(\mathcal{V}^0)|_{\varDelta\phi_i}$, and the peak variances $\sigma(\mathcal{V}^0)|_{\varDelta\phi_i}$. Note that the legend for the

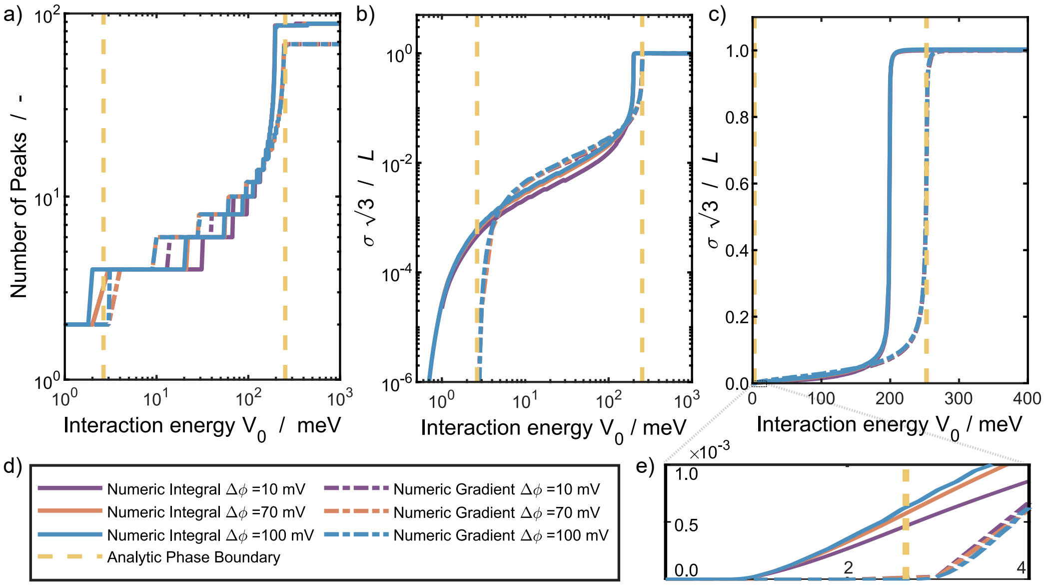

Figure 12.7: Meta analysis of the interfacial profiles for some thousand simulations. a) Number of peaks exhibited of $|\tilde{\varrho}_\mathrm{F}|$ as function of $\mathcal{V}^0$. b) Variance of the complete set of simulations as defined by eq. (12.7). c) Non-log scale of subfigure b). d) Legend for the colors. e) Oscillation onset at small interaction energies.

subfigures a), b) c) and e) is shown in subfigure d). Figure 12.7a) shows that the results for the peak numbers with respect to the integral description (solid lines) for $\Delta\phi$=10 mV and for $\Delta\phi$=70 mV exhibit only small deviations from the results for $\Delta\phi$=100 mV described in fig. 12.5. Note that the phase boundaries with respect to the integral description are the same for the different interface potentials. Surprisingly, the peak numbers are N_peak=2 for also the very small electrode polarization $\Delta\phi$=10 mV. This is in contrast to fig. 12.1, where saturation begins at potentials at least larger than 50 mV. The same observations can be made for the peak numbers with respect to the gradient description (dashed lines). Figure 12.7b) shows the results for the peak variance σ defined by eq. (12.7). Apparently, the numerical results, both with respect to the integral description and with respect to the gradient description show small deviations between the different interface potentials in the intermediate energy regime where 1 mV<$\mathcal{V}^0$<100 mV. However, the logarithmic scale chosen in this plot highlights the deviations. In the non-logarithmic scale shown in fig. 12.7c) the deviations are hardly visible anymore. Again, the interface potential does not influence the phase boundaries of σ. Altogether, the results shown in fig. 12.7 suggests that the interface potential has only a small influence on the amplitude of the screening profiles for the charge density, and does not influence the phase boundaries. However, non-vanishing interaction strengths drive charge saturation independent of the electrode polarization. Figure 12.7e) illustrates that the oscillation onsets in the different descriptions do not depend upon the interface potential.

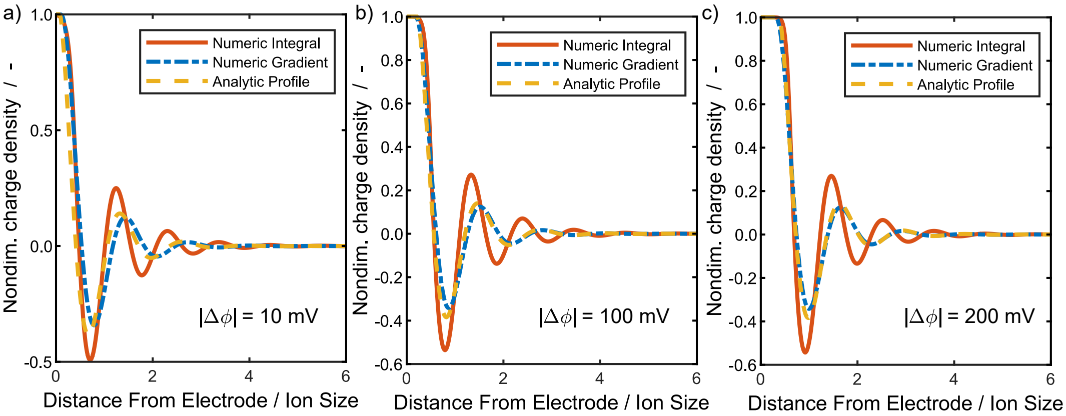

Figure 12.8: Numerical results for $\tilde{\varrho}_{\mathrm{F}}$ with respect to the gradient description (see eq. (9.43)), and the analytical description (see eqs. (10.30), (10.31) and (10.33)), at $\mathcal{V}^0$=250 meV. a) $\Delta\phi = -10$ mV. b) $\Delta\phi = -100$ mV. c) $\Delta\phi = -200$ mV. Figures first published in Ref. 367.

Next, we supplement our holistic discussion of the influence of the electrode polarization on $\tilde{\varrho}_{\mathrm{F}}$ from above and take a detailed look at the charge density at fixed interaction energy but for varying potentials $\Delta\tilde{\phi}$. Figure 12.8 shows numerical results for $\tilde{\varrho}_{\mathrm{F}}$ obtained from simulations with respect to the integral description eqs. (12.4) and (12.6) (solid red curve) and with respect to the gradient description eqs. (12.5) and (12.6) (blue dashed curve), and the analytical profile $\tilde{\varrho}_{\mathrm{F}}^{\mathrm{analytic}}$ (dashed yellow curve) for $\Delta\phi \in \{10\,\mathrm{mV}; 100\,\mathrm{mV}; 200\,\mathrm{mV}\}$ at fixed interaction energy $\mathcal{V}^0$=185 meV. Figure 12.8a), shows that both numerical results at small electrode potential $\Delta\phi$=10 mV exhibit charge saturation near the negatively charged electrode. This is in contrast to the results obtained from the numerical simulations of the non-interacting case, see fig. 12.1 which shows that the system does not reach saturation before $\Delta\phi$=50 mV. We conclude from this result that any small non-negative interaction energy $\mathcal{V}^0$ causes charge saturation near the electrode. This is in accordance with figs. 12.5 and 12.7, where the peak numbers are N_{peak}=2 for all small interaction energies. Hence, we identify the two parameters $\mathcal{V}^0$ and $\Delta\phi$ which lead to charge saturation. In addition, we observe in the left figure that the saturation width agrees very good for the three descriptions. However, the oscillation peaks are more pronounced in the integral description, and, also, the frequency of the oscillations with respect to the integral description is smaller than with respect to the gradient description and than with respect to the analytical prediction. Both observations highlight that the perturbation descriptions underestimate the influence of $\mathcal{V}^0$ when compared with the integral description. The profile of the gradient description deviates only slightly from the analytical profile. In particular, both the frequency as well as the amplitudes are a little bit more pronounced. This is in accordance with the result shown in the right figure in fig. 12.6. Figure 12.8b) shows the corresponding results for $\Delta\phi$=100 mV. Apparently, the qualitative behaviour has not changed significantly. The saturation width and the amplitude of the first oscillation peaks of all three profiles have slightly increased with increased $\Delta\phi$. However, the agreement between the profiles with respect to the gradient description and with respect to the analytical prediction has improved. Figure 12.8c), shows the corresponding profiles for $\Delta\phi$=200 mV. Again, the saturation width and the amplitude of the first oscillation peak have increased with $\Delta\phi$. Apparently, the profiles with respect to the gradient description and with respect to the analytical prediction exhibit almost perfect agreement for the increased electrode polarization. Altogether, we conclude that the electrode potential increases the saturation width, in accordance with our analytical prediction. Furthermore, the agreement between the profiles increases with increasing $\Delta\phi$. Finally, charge saturation is not only driven by the electrode polarization, but emerges also for any non-vanishing interaction energy $\mathcal{V}^0$.

Figure 12.9 shows the analytical prediction for the electric potential, and results for $\tilde{\Phi}$ obtained from numerical simulations with respect to the integral description eqs. (12.4) and (12.6), and with respect to the gradient description eqs. (12.5) and (12.6), for the set of different electrode polarization $\Delta\phi$ given by 10 mV, 25 mV, 70 mV, 100 mV, and 200 mV at $\mathcal{V}^0 = 185\,\mathrm{meV}$. The analytical results $\tilde{\Phi}^{\mathsf{analytic}}$ are calculated according to the instructions discussed in section 10.3.4. Here, we have also included the damping envelope in the plots. However, since we adjust the analytical profile $\tilde{\Phi}^{\mathsf{analytic}}$ in the region from the interface up to the distance L_{EDL} from the electrode, we draw the envelope beginning at x=L_{EDL}. Subfigures a)-e) show the screening profiles for increasing electrode polarization. The left figure in the first row, fig. 12.9a), shows the results for the rather small polarization $\Delta\phi$=10 mV. Apparently, the amplitude of the first oscillation peak in the profile of the integral description (roughly at 70 mV) and the of the first oscillation peak in the profile of the gradient description (roughly at 75 mV) are much larger than the interface value $\Delta\phi$=10 mV. Hence, the electrolyte massively “overscreens” the interface. Both the amplitudes and the frequency of the oscillations of the numerical results with respect to the integral description are more pronounced than of the numerical results with respect to the gradient description, except for the first oscillation peak. Hence, the gradient description underestimates the influence of $\mathcal{V}^0$ with increasing distance from the electrode, when compared with the integral description. By con-

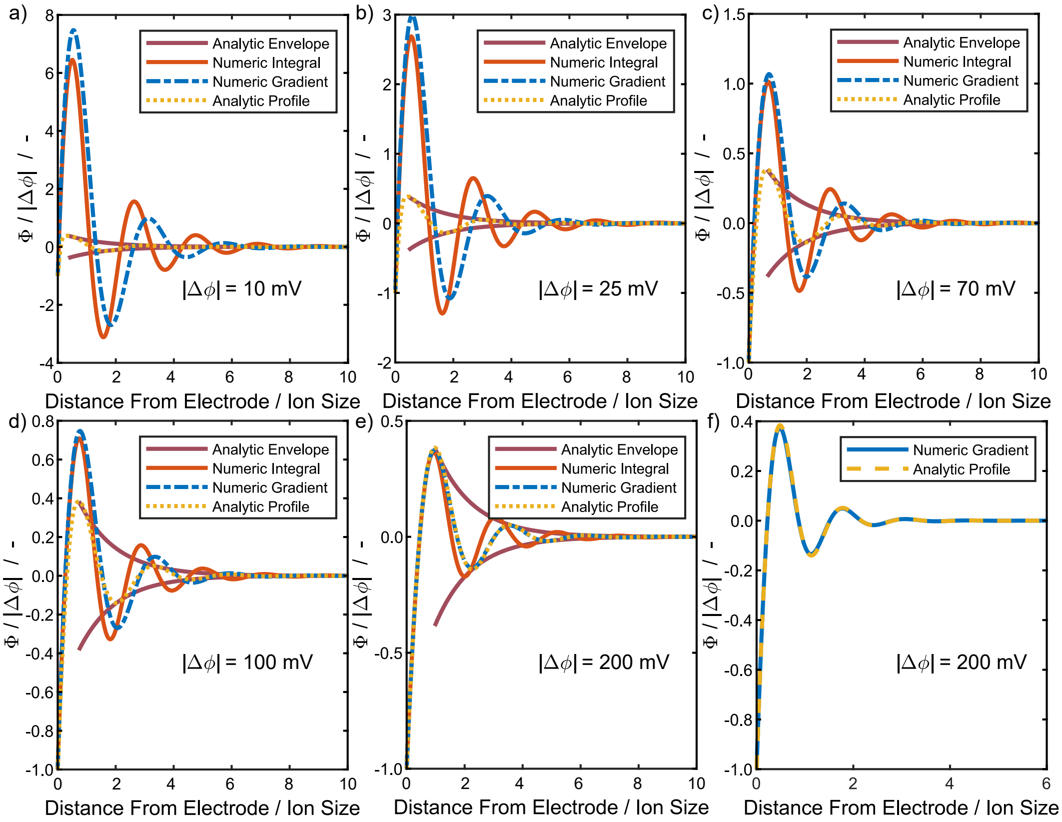

Figure 12.9: Comparison of the numerical profiles obtained from the integral description (see eq. (9.42)), and from the gradient description (see eqs. (9.43) and (9.52)) for $\tilde{\Phi}$ with the analytical predictions (see eqs. (10.30), (10.31) and (10.33)) at $\mathcal{V}^0$=185 meV and at varying interface polarizations. Figures first published in Ref. 367.

struction, the analytical profile (yellow dashed curve, and envelope) does not show such a behaviour. Figure 12.9b) shows the results for $\Delta\phi$=25 mV. Again, the oscillations appearing in the profiles of the two numerical results are much larger than the electrode polarization. Interestingly, these amplitudes have the same magnitude as for the previous interface potential $\Delta\phi$=10 mV (roughly at 70 mV and at 75 mV). The deviations between the two numerical results reproduce almost exactly the same behaviour as discussed for $\Delta\phi$=10 mV. Figure 12.9c), shows the results for $\Delta\phi$=70 mV. The pattern observed in the previous two cases also appears here, because the magnitudes of the amplitudes for the first oscillation peak appearing in the two numerical results are again roughly at 70 mV and at 75 mV. However, this equals almost exactly the interface polarization $\Delta\phi$=70 mV. Hence, there is no “overscreening” of the first oscillation peak relative to the interface potential. Furthermore, the two numerical profiles have a rather good quantitative agreement to each other. The first oscillation peak of the analytical profile has a magnitude which equals roughly 40% of the interface potential. Next, fig. 12.9d), shows the results for $\mathit{\Delta}\phi$=100 mV. We observe the same patterns as in the previous cases; the first oscillation peaks of the two numerical profiles have again the magnitudes 70 mV and 75 mV, and the amplitude of the first oscillation peak appearing in the analytical profile has a magnitude of roughly 40% of the interface potential. Figure 12.9e), shows the corresponding results for the interface potential $\mathit{\Delta}\phi$=200 mV. We observe the same pattern as in the previous cases. However, due to the coincidence that $\mathit{\Delta}\phi \cdot 0.4 \approx 75\,\mathrm{mV}$, all three curves exhibit a very good agreement and the profiles match exactly in the region close to the interface and up to the first oscillation peak. However, beyond this first “layer”, the integral profile oscillates with a larger frequency when compared to the gradient profile and the analytical profile. Nevertheless, the analytical envelope captures all three profiles rather good. In particular, the profile with respect to the gradient description and with respect to the analytical description correspond almost exactly. This agreement is highlighted in fig. 12.9e). Altogether, we find that the amplitude of the first oscillation peak is independent from the electrode potential and has roughly the magnitudes 70 mV, for the integral description, and 75 mV for the gradient description. This “discretization” of the electric potential in the first ion layer near the electrode is reminiscent of saturation processes occurring near the electrode due to crowding, and this behaviour is in accordance with fig. 12.8, which shows that crowding effects occur independently from the electrode potential for non-vanishing interaction energies $\mathcal{V}^0$. Finally, we compare the magnitude of the first oscillation peaks (roughly 70 mV) in the numerical profiles for $\mathcal{V}^0$=185 meV shown in fig. 12.9d), with the magnitude of the first oscillation peak (roughly 110 mV) for $\mathcal{V}^0$=250 meV, shown in fig. 12.6. Both results are obtained with respect to the same electrode polarization $\mathit{\Delta}\phi = 100\,\mathrm{mV}$. From this we conclude that the magnitude of the first oscillation peak is constant with respect to the electrode polarization, but increases with increasing interaction energy.

13 EDL Structures of Ternary Electrolytes: Mean Steric Effect

13.1 Transport Theory of Ternary Electrolytes

In this section, we discuss the case of a ternary electrolyte. In contrast to section 15.2, where we discussed a ternary electrolyte with neutral solvent in the electroneutral bulk state, our focus here lies on the formation of charged EDL structures.

At least two species comprised in the electrolyte are oppositely charged. Hence, without loss of generality, we denote these two species by the labels "+" and "-", and label the third species via the index "s". Hence, there are two independent valence-parameters, z_+ and z_s, since $z_-= - z_+$. We assume complete dissociation of the IL and define the molar mass $M_{\mathrm{IL}}=M_+ + M_-$, and the partial molar volume $\nu_{\mathrm{IL}}=\nu_+ + \nu_-$ which define dimensionless parameters $\gamma_\alpha=\nu_\alpha/\nu_{\mathrm{IL}}$, and $\tilde{M}=M_\alpha/M_{\mathrm{IL}}$.

As described in section 5.3, three independent transport parameters exist in a ternary electrolyte. These are the electrolyte electric conductivity κ, one transference number t_s and one diffusion coefficient $\mathcal{D}_{ss}=\mathcal{D}_s$. Because of charge conservation and the Euler equation for the volume, there is only one independent species concentration appearing in the ternary system. Thus, the set of independent variables which are necessary to describe the EDL system are the ϱ_{F}, Φ, $\mathbf{v}$ and one species concentration, where, by convention, we choose c_s as independent species concentrations such that (see eqs. (5.222) and (5.223))

$$c_\mp = 1/\nu_{\mathrm{IL}} \mp \varrho_{\mathrm{F}}\gamma_+/F z_+ - c_s/z_+ \cdot (\gamma_s z_+ \mp \gamma_+ z_s)\,, \tag{13.1}$$

and the Gibbs-Duhem relation reduces the number of independent forces $\boldsymbol{\nabla}\mu_\alpha$ to two

$$\boldsymbol{\nabla}\mu_s = -1/c_s \cdot \left(\varrho_{\mathrm{F}}\boldsymbol{\nabla}\Phi + c_+\boldsymbol{\nabla}\mu_+ + c_-\boldsymbol{\nabla}\mu_-\right). \tag{13.2}$$

The corresponding system of transport equations reads

$$\begin{aligned}
\varrho_{\mathrm{F}} &= -\varepsilon_0\boldsymbol{\nabla}\varepsilon_{\mathrm{R}}\boldsymbol{\nabla}\Phi, &(13.3)\\
\partial_t\varrho_{\mathrm{F}} &= -\boldsymbol{\nabla}\boldsymbol{\mathcal{J}}_{\mathrm{F}} - \boldsymbol{\nabla}\left(\varrho_{\mathrm{F}}\mathbf{v}\right), &(13.4)\\
\partial_t c_s &= -\boldsymbol{\nabla}\boldsymbol{\mathcal{N}}_s - \boldsymbol{\nabla}\left(c_s\mathbf{v}\right), &(13.5)
\end{aligned}$$

with fluxes

$$\mathcal{J}_\mathrm{F} = -\kappa\boldsymbol{\nabla}\varphi - \kappa t_s/F\tilde{z}_s \cdot \boldsymbol{\nabla}\tilde{\tilde{\mu}}_s, \tag{13.6}$$

$$\mathcal{N}_s = t_s/F\tilde{z}_s \cdot \mathcal{J}_\mathrm{F} - \mathcal{D}_s\boldsymbol{\nabla}\tilde{\tilde{\mu}}_s, \tag{13.7}$$

$$\boldsymbol{\nabla}\mathbf{v} = -\tilde{\nu}_-/F\tilde{z}_- \cdot \boldsymbol{\nabla}\mathcal{J}_\mathrm{F} - \tilde{\tilde{\nu}}_s \cdot \boldsymbol{\nabla}\mathcal{N}_s. \tag{13.8}$$

We neglect molecular interactions ($\mathcal{V}^0$=0), such that eq. (8.25) becomes

$$\boldsymbol{\nabla}\mu_\alpha = -\nu_\alpha\varrho_\mathrm{F}\boldsymbol{\nabla}\Phi + RT\boldsymbol{\nabla}\ln[c_\alpha\nu_\alpha] - RT\nu_\alpha\boldsymbol{\nabla}c. \tag{13.9}$$

Apparently, it suffices to determine the forces $\boldsymbol{\nabla}\varphi$ and $\boldsymbol{\nabla}\tilde{\tilde{\mu}}_s$ to close the fluxes eqs. (13.6) to (13.8). We find (note that $\boldsymbol{\nabla}\tilde{\mu}_-^\mathrm{el}{=}{-}F/z_+ \cdot\boldsymbol{\nabla}\varphi$)

$$\boldsymbol{\nabla}\varphi = \boldsymbol{\nabla}\Phi - \tilde{M}_+/Fz_+ \cdot \boldsymbol{\nabla}\mu_- - \tilde{M}_-/Fz_+ \cdot \boldsymbol{\nabla}\mu_+. \tag{13.10}$$

Next, we calculate the force $\boldsymbol{\nabla}\tilde{\tilde{\mu}}_s$ by substituting eq. (13.2) for $\boldsymbol{\nabla}\mu_s$,

$$\begin{aligned}\boldsymbol{\nabla}\tilde{\tilde{\mu}}_s = -\Big[\varrho_\mathrm{F}/c_s \cdot \boldsymbol{\nabla}\Phi + \Big(c_-/c_s + z_s\tilde{M}_+ - z_+\tilde{M}_s\Big)\,\boldsymbol{\nabla}\mu_- +& \\ + \Big(c_+/c_s + \tilde{M}_s/\tilde{M}_+ \cdot (1 - z_+\tilde{M}_-) + z_s\tilde{M}_-\Big)\,\boldsymbol{\nabla}\mu_+\Big]&.\end{aligned} \tag{13.11}$$

If z_+=1, then eq. (13.11) becomes

$$\boldsymbol{\nabla}\tilde{\tilde{\mu}}_s{=}{-}[\varrho_\mathrm{F}/c_s{\cdot}\boldsymbol{\nabla}\Phi{+}(c_-/c_s + z_s\tilde{M}_+{-}\tilde{M}_s)\boldsymbol{\nabla}\mu_-{+}(c_+/c_s{+}z_s\tilde{M}_-{+}\tilde{M}_s)\boldsymbol{\nabla}\mu_+]. \tag{13.12}$$

13.2 Numerical Simulations

Here, we apply our description from section 13.1 to the ternary electrolyte-mixture consisting of PYR[1,4]TFSI supplemented by AgTFFSI-salt. Thus, the completely dissociated electrolyte consists of Pyr$^+$-cations (c_+), Ag$^+$-cations (c_s) and TFSI$^-$-anions (c_-). The bulk-concentrations are thus determined by the condition of electroneutrality,

$$c_-^\mathrm{b} = c_+^\mathrm{b} + c_s^\mathrm{b}. \tag{13.13}$$

Hence, for a constant amount of PYR[1,4]TFSI, c_-^b increases with c_s^b.

The additive salt AgTFSI is advantageous because the Ag$^+$-ions can be assumed much smaller than the bulky IL-ions.[345] This suggests the limit where $\nu_s{\ll}\nu_\pm$, see section 13.4. Here, we assume a ratio $\nu_s{=}0.1{\cdot}\nu_+$, set $\nu_+{=}\nu_-$ and neglect convection. Hence, the system of equations reads

$$\varrho_\mathrm{F} = -\varepsilon_0\boldsymbol{\nabla}\varepsilon_\mathrm{R}\boldsymbol{\nabla}\Phi, \quad \partial_t\varrho_\mathrm{F} = -\boldsymbol{\nabla}\mathcal{J}_\mathrm{F}, \quad \partial_t c_s = -\boldsymbol{\nabla}\mathcal{N}_s. \tag{13.14}$$

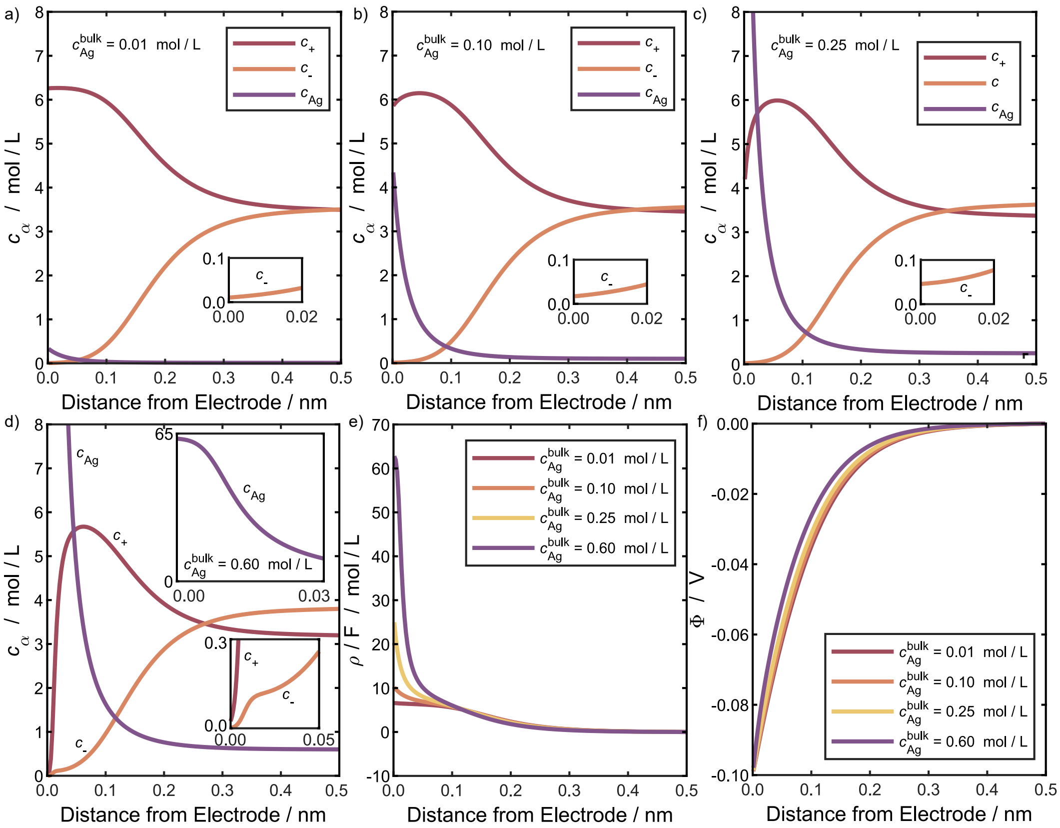

Figure 13.1: Numerical results with respect to eq. (13.14) as function of minor salt concentration. a)-d) Species concentrations c_α. e) ϱ_{F}. f) Φ.

The fluxes and chemical forces are given by eqs. (13.6) to (13.11). Here, we have $z_+ = z_s = 1$. We solve this system of equations described in the one-dimensional "half-cell" set-up described in section 12.2.1, and set $\Delta\phi = -100\,\mathrm{mV}$ (see appendix E.5 for more details).

Figure 13.1 shows numerical results for the as-described set-up, subject to different bulk-concentrations c_s^{b}. Subfigures a)-d) show the screening profile of the species concentrations with increasing c_s^{b}. Figure 13.1a), shows the species concentrations for a relatively small amounts of Ag$^+$-salt c_s^{b}. Apparently, the electrode-screening is mainly due to the Pyr cations. For this species, a perturbed crowding effect is clearly visible. In contrast, only a small amount of Ag-ions accumulate next to the interface, and the Ag-concentration quickly decays towards it's electroneutral bulk-concentration. Likewise, the TFSI-ions get depleted in the EDL-region. However, the inset shows that the anion concentration does not become completely depleted at near the interface. Overall, this figure is reminiscent of the binary screening-profiles described in section 12.2. Figure 13.1b) shows that, upon increasing the bulk-concentration of the Ag^+-ions, the screening profile changes. Here, c_s^{b}=0.1 mol L^{-1}, and the Ag-ions begin accumulating near the interface. This results in a reduced accumulation of the Pyr-cations near the interface. Again, the anion concentration almost vanishes near the interface. In accordance with eq. (13.13), the bulk concentration of the IL-anions is slightly increased with respect to the concentration of the IL cation species. Figure 13.1c) shows numerical results for c_s^{b}=0.25 mol L^{-1}. Here, the Ag^+-concentration near the interface is larger than the Pyr^+-concentration. However, c_+ shows a curved shape, and increases with increasing distance from the electrode up to a saturation value at roughly $x \approx 0.8$ Å, beyond which it starts decaying into the electroneutral state, *i.e.* towards it's bulk concentration. The anion species is dominant in the bulk state of the electrolyte mixture. Figure 13.1c) shows the species concentrations for c_3^{b}=0.6 mol L^{-1}. The Pyr^+-ions are depleted next to the interface, and the screening has switched completely to the Ag^+-ions. The lower inset shows that the concentration of the Pyr^+-ions near the electrode is not zero. However, the Pyr^+-ions still exhibit saturation in an intermediate EDL-region. The upper inset highlights that the concentration of the minor Ag^+-salt saturates near the electrode. However, due to the small molar volume ν_s, the saturation concentration is extremely large. The anion species exhibits a non-trivial profile next to the interface, see the lower inset. It depletes completely at the electrode, and increases up to a plateau at roughly 0.25 Å, after which it increases again. Apparently, this concentration plateau correlates with the saturation of the Ag^+-ions (see the upper inset). Figure 13.1e) shows the corresponding charge-profiles for all four cases. Apparently, the charge density shows an exponential profile for small amounts of minor Ag^+-salt. However, at c_s=0.6 mol L^{-1}, the charge density has transitioned into saturation, where the corresponding saturation threshold is at extremely large values, due to the small molar volume of the Ag^+-ions. Figure 13.1f), shows the electric potential for all cases. In contrast to the charge density, the profile of the electric potential has a more “canoncal” shape. Apparently, the screening becomes more effective with increasing salt concentration.

Altogether, we find that the amount of minor silver salt influences the EDL structure. At roughly c_s=0.25 mol L^{-1}, the crowding of counterions near the electrified interface is destroyed.

13.3 Stationary State

In this section, we consider the stationary state and use the same rationale as in section 9.3, where we discussed the stationary state for a binary electrolyte.

In stationary state, all species-fluxes vanish, *i.e.* $\mathbf{v}_\alpha$=0. Hence, the macroscopic fluxes become trivial, $\mathbf{v}$=$\boldsymbol{\mathcal{J}}_\mathrm{F}$=$\boldsymbol{\mathcal{N}}_s$=0. However, eq. (13.6) implies that $\boldsymbol{\mathcal{J}}_\mathrm{F}$=0 exactly if $\boldsymbol{\nabla}\varphi$=0, which is equivalent to $\boldsymbol{\nabla}\tilde{\mu}^\mathrm{el}_-$=0. From eq. (13.7), it follows that $\boldsymbol{\mathcal{N}}_3$=0 exactly if $\boldsymbol{\nabla}\tilde{\tilde{\mu}}_s$=0. Note that the vanishing of the two electrochemical forces follows directly from the Onsager approach, where the flux $\boldsymbol{\mathcal{J}}_\mathrm{F}$ is linear in $\boldsymbol{\nabla}\tilde{\mu}^\mathrm{el}_-$, and $\boldsymbol{\mathcal{N}}_s$ is linear in $\tilde{\mu}^\mathrm{el}_s$ (see section 5.3.1). We use the Gibbs-Duhem relation, eq. (13.2), and evaluate the first condition,

$$0 = \boldsymbol{\nabla}\tilde{\Phi} + \tilde{M}_-/RT \cdot \boldsymbol{\nabla}\mu_+ - \tilde{M}_+/RT \cdot \boldsymbol{\nabla}\mu_-. \tag{13.15}$$

However, it is easy to show that if $\boldsymbol{\nabla}\varphi$=0, then $\boldsymbol{\nabla}\tilde{\tilde{\mu}}_s$=$\boldsymbol{\nabla}\tilde{\mu}^\mathrm{el}_s$. Thus, the second stationary condition can be expressed as $\boldsymbol{\nabla}\tilde{\mu}^\mathrm{el}_s$=0. Evaluation of this condition, and using eqs. (13.2) and (13.15), we find that the stationary conditions can be expressed by two of the three trivial electrochemical forces 0=$\boldsymbol{\nabla}\mu^\mathrm{el}_\alpha$, where $\alpha \in \{+, -, s\}$. Altogether, the stationary state for the three independent variables $\Phi, \varrho_\mathrm{F}, c_s$ is described by the Poisson equation and two trivial force-laws, *e.g.*

$$\varrho_\mathrm{F} = -\varepsilon_0 \boldsymbol{\nabla}\varepsilon_\mathrm{R}\boldsymbol{\nabla}\Phi, \qquad 0 = \boldsymbol{\nabla}\mu^\mathrm{el}_+ \qquad \text{and} \qquad 0 = \boldsymbol{\nabla}\mu^\mathrm{el}_s. \tag{13.16}$$

13.4 Static Asymptotic Analysis: Minor Salt Species

In this section we evaluate the stationary case described in section 13.3 for the limit where the minor silver species has very small molar volume compared with the ion species, *i.e.* ν_s≪ν_IL (hence $(c_+$+$c_-)\nu_\mathrm{IL}$≈1. For this purpose, we evaluate the system of stationary equations, eq. (13.16). The stationary condition 0=$F\boldsymbol{\nabla}\Phi$+$\boldsymbol{\nabla}\mu_s$ is determined by the constitutive equation for the chemical forces, $\boldsymbol{\nabla}\mu_s$= $-$ $\nu_s\varrho_\mathrm{F}\boldsymbol{\nabla}\Phi$+$\boldsymbol{\nabla}\ln[c_s\nu_s]$−$\nu_s\boldsymbol{\nabla}c$. Hence, in the limit ν_3≪ν_IL, we find

$$0{=}F[(c_+ + c_-)(\nu_\mathrm{IL} - \nu_s){-}\nu_s c_s]\boldsymbol{\nabla}\Phi{+}RT\boldsymbol{\nabla}\ln[\nu_s c_s]{-}\nu_s\boldsymbol{\nabla}c{\approx}F\boldsymbol{\nabla}\Phi{+}RT\boldsymbol{\nabla}\ln[\nu_s c_s]. \tag{13.17}$$

Next, we non-dimensionalize the electric potential via $\tilde{\Phi}$=$F\Phi/RT$, and integrate both sides from x up to the electroneutral bulk region where $\tilde{\Phi}(L_\mathrm{EDL})$=0, and $c_s(L_\mathrm{EDL})$=c^b_s, such that 0=$\tilde{\Phi}(x)$+ $\ln[c_s(x)\nu_s]$ − $\ln[c^\mathrm{b}_s\nu_s]$. We solve this for the salt concentration,

$$c_s(x) = c^\mathrm{b}_s \cdot \exp[-\tilde{\Phi}(x)]. \tag{13.18}$$

Since the electric potentials are continuous across interfaces, we find for the minor species concentration close to the interface c_s=c^b_s· $\exp(-\Delta\tilde{\phi})$. This argument holds even if the polarization of the interface has the same “sign” as the valency of the minor species. For example, if the minor species is positively charged, and the polarization of the electrode is such that sign($\varDelta\tilde{\phi}$)=sign(z_s), then the counter species is the positive species. In this case, we showed above that the counter-species creates a negative electric potential of roughly the magnitude $-\varDelta\tilde{\phi}$, after the distance from the electrode given by the size of the cations. Then, the minor species accumulates right behind the ion-layer of specifically adsorbed cations.

We assume that the EDL structure of the binary IL gets disturbed by the ions of the minor species, once their concentration at the electrode becomes comparable with the bulk concentration of the neat IL PYR[1,4]TFSI, *i.e.* $c_s^{\mathrm{b}}{=}c_{\mathrm{IL}}^{\mathrm{b}} = 1/\nu_{\mathrm{IL}}$. This implies the condition

$$c_s^{\mathrm{crit}} = \exp(\varDelta\tilde{\phi})/\nu_{\mathrm{IL}}\,. \tag{13.19}$$

Hence, for an electrode-potential of $\varDelta\phi{=}-100\,\mathrm{mV}$ and a bulk concentration of roughly $c_{\mathrm{IL}}^{\mathrm{b}}{=}4\,\mathrm{mol\,L^{-1}}$, we predict the critical amount of $c_s^{\mathrm{crit}}{\approx}0.1\,\mathrm{mol\,L^{-1}}$ minor salt, which is necessary to disturb the EDL-structure formed by the neat IL electrolyte. This prediction is qualitatively in good agreement with the numerical results, see fig. 13.1. In chapter 14, we use this description to validate our EDL model for ternary electrolytes.

14 Validation of Our EDL Description With Experiment

In this section, we discus how our EDL description relates Atomic Force Microscopy (AFM) measurements.

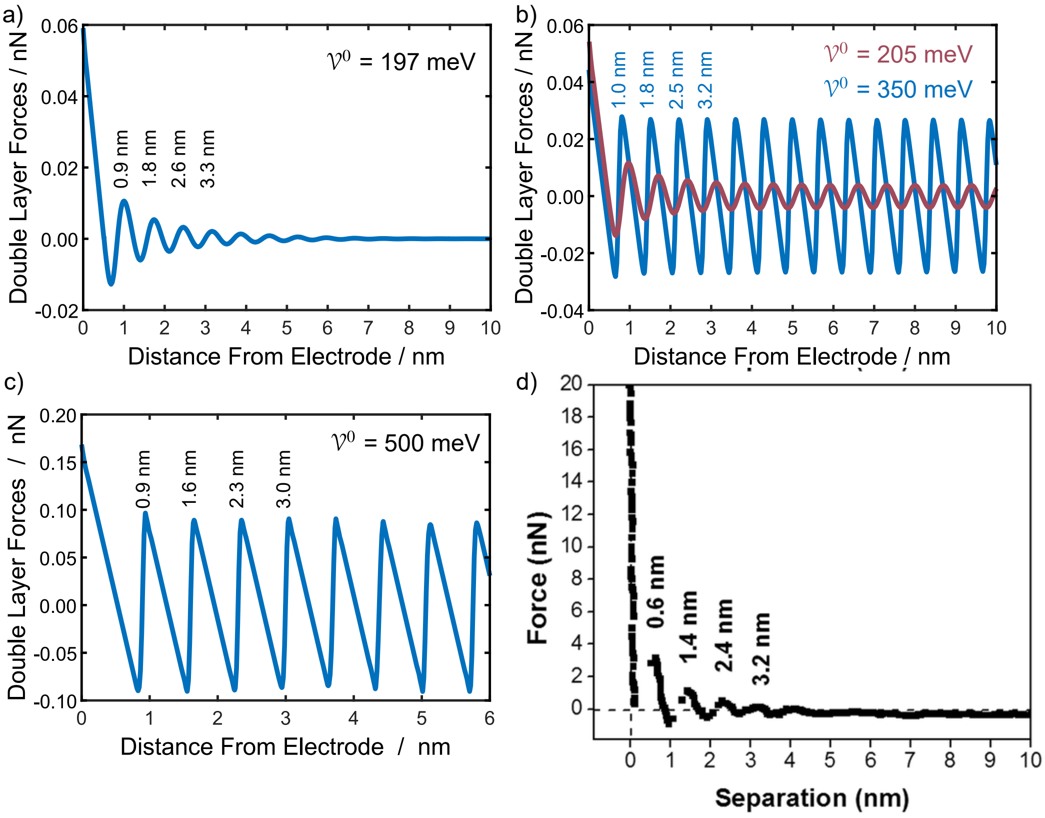

Figure 14.1: Double layer forces as function of $\mathcal{V}^0$ (a-c), and AFM force profiles obtained from experiments (d)).[345] The EDL forces in a)-c) are defined by eq. (10.46), and correspond to the charge profiles shown in fig. 12.3. Figures a) and d) first published in Ref. 345.

A prominent experimental technique for the examination of the interfacial structure of ILs near electrified interfaces are AFM force curve measurements.[371] This type of scanning probe microscopy uses sharp tips attached to a micro-cantilever to scan a liquid sample in the vicinity of an electrode interface. Thereby, it measures the forces F^{AFM} which emerge between the interface, and the liquid sample (IL) as function of electrode distance.[372] The corresponding force-profiles usually exhibit a damped oscillatory shape. Typically, the "wave-length" of the oscillations, *i.e.* the distance between consecutive peaks in the profile of F^{AFM}, correlates with the ion-size.[373] In addition, the number of peaks (*i.e.* the EDL-width) provides a means for evaluating the interaction strength.

We relate these AFM forces F^{AFM} to the double layer forces in mechanical equilibrium F^{EDL} introduced above (see eq. (10.46))

$$F^{\mathrm{EDL}} = \nu/N_{\mathrm{A}} \cdot \varrho_{\mathrm{F}} \nabla \Phi. \tag{14.1}$$

In fig. 12.3, we showed force profiles as function of the interaction energy $\mathcal{V}^0$. Here, we focus on four energies $\mathcal{V}^0$ and compare the force profiles with experimental results.

Figure 14.1 shows numerical results for the EDL forces corresponding to the charge-profiles discussed in section 12.3.1, and experimental results obtained from AFM measurements (see Ref. 345. The "sample" used in the simulations and in the AFM experiment is the binary IL PYR[1,4]TFSI, and the electrode polarization is $\Delta\phi = -200\,\mathrm{mV}$. The ion size used in the simulations was 0.7 nm. The double layer forces in the subfigures a)-c) were calculated via eq. (14.1). Figure 14.1a) shows the force profile at $\mathcal{V}^0$=198 meV. The first two force peaks are separated by roughly a distance 0.9 nm, and the next two peaks have a distance of roughly 0.8 nm and 0.7 nm. Figure 14.1b) shows the force profiles at $\mathcal{V}^0$=205 meV (brown curve) and at $\mathcal{V}^0$=350 meV (blue curve). For both interaction energies, the screening profile has transitioned into the phase of undamped charge oscillations. Apparently, the amplitude of the force peaks increases significantly with increasing $\mathcal{V}^0$. This can be attributed to the fact tthat the ion segregation increases with $\mathcal{V}^0$ (see also fig. 12.3). The frequency of the oscillations differs only slightly. For $\mathcal{V}^0$=350 meV, the force peaks are separated roughly by a distance of 0.8 nm. Figure 14.1c) shows the force profile at $\mathcal{V}^0$=500 meV (this force profile was already presented in fig. 12.4). The profile exhibits very sharp peaks, which are mutually separated by a constant distance of 0.7 nm. This coincides exactly with the parameter for the ion size used in the simulations. However, the first peak occurs at a distance of 0.9 nm from the electrode, which is slightly larger than the ion size. This larger width of the first "layer" can be attributed to the enhanced saturation width L_{EDL} (compare the parameter study in fig. 10.1). Figure 14.1d), shows the experimental results for the AFM profiles (see Ref. 345). Apparently, the force peaks have a distance of roughly 0.9 nm, which is slightly larger than the parameter used in the simulations

(0.7 nm). However, the magnitudes of the EDL forces, $\mathcal{O}(F^{\mathrm{EDL}})\approx 0.1\,\mathrm{nN}$, differ from the typical magnitudes measured in AFM experiment, $\mathcal{O}(F^{\mathrm{AFM}})\approx 1\,\mathrm{nN}$, by at least one order of magnitude. This can be attributed to the fact that the AFM force is used to study the same equilibrium structure as the EDL force, but relates to a different technique. In contrast to the experiment, where the nano-scaled tip of the AFM cantilever penetrates the highly crystalline structure, the forces F^{EDL} account for elastic perturbations of the EDL structure. Nevertheless, assuming that the numerical results for the charge ordering is consistent with the experimental set-up, the shape of the force profiles F^{EDL} and F^{AFM}, *i.e.* frequency and decay length of the oscillations, should be similar for some interaction energy $\mathcal{V}^0$.

We conclude that, in principle, the comparison of the two quantities F^{AFM} and F^{EDL} allows to validate our framework. Altogether, we find that the left figure in the first row, fig. 14.1a), yields consistent results when compared with the experimental results shown in fig. 14.1d).

In our discussion of ternary IL/salt mixture, we derived an analytical description for the influence of a minor salt on the EDL structure, see section 13.4. We found that there exists a critical bulk concentration of the salt at which the EDL structure of a binary IL gets destroyed,

$$c_s^{\mathrm{crit}} = \exp(\Delta\tilde{\phi})/\nu_{\mathrm{IL}}\,. \tag{14.2}$$

where $\nu_{\mathrm{IL}}\approx c_{\mathrm{IL}}^{\mathrm{b}}$ equals roughly the bulk concentration of the IL.

We use this description to validate our EDL theory for ternary electrolytes. Experimental results based on AFM measurements show that for $\Delta\phi=-200\,\mathrm{mV}$ versus OCP, a minor amount of roughly $c_s^{\mathrm{crit}}=1\cdot 10^{-3}\,\mathrm{mol\,L^{-1}}$ of AgTFSI is necessary to destroy the EDL structure of the IL PYR[1,4]TFSI.[345] Hence, when we assume an IL bulk concentration of $c_{\mathrm{IL}}^{\mathrm{b}}\approx 3\,\mathrm{mol\,L^{-1}}$, then the critical salt concentration according to eq. (14.2) is $c_s^{\mathrm{crit}}\approx 1\cdot 10^{-3}\,\mathrm{mol\,L^{-1}}$. This quantitative agreement between the experimental observation and the analytical prediction validates our model for the equilibrium EDL structures of ternary electrolytes.

Part IV

Discussion of Our Multi-Scale Methodology

In this part, we discuss our multiscale methodology derived in parts II and III. To adress this goal, we split this discussion into two chapters.

First, in chapter 15, we relate our framework to different frameworks from the literature. In section 15.1, we discuss different approaches for the unification of mechanics, thermodynamics and electromagnetic theory, and different sets of electromagnetic material variables. Next, in section 15.2, we compare our bulk transport theory with the Newman-model for the specific case of standard-electrolytes used in lithium ion batteries. In section 15.3, we focus on the relation of our multiscale methodology to atomistic models. With the help of basic concepts from liquid state theory, we show that atomistic simulations can directly parameterize our theory. In section 15.4 we discuss the relation to mean-field-theories (MFTs) for the electrochemical double layer (EDL) proposed in the literature, and focus on the canonic BSK approach.

Second, in chapter 16, we discuss how macroscopic thermodynamic energy contributions, and the mean steric effect, can be obtained from our microscopic description via coarse graining.

15 Comparison with Literature and Theory

15.1 Thermo-Electro-Mechanical Balance Laws

The unification of mechanics, electromagnetic theory and thermodynamics constitutes a fundamental pillar on which continuum transport theories reside. Thus, differing approaches usually lead to conceptual differences between the resulting transport theories. In this section, we discuss some alternative proposals from the literature for such unifications.

The fundamental balance equations for mass, momentum and energy constitute the basis for the framework of rational thermodynamics.[74] Although there is common agreement regarding the balance laws of thermo-mechanics,[81] various models for the electromagnetic balance laws (and how to unify them with thermo-mechanics) exist.[245] In this section, we briefly discuss differing approaches, and their consequences for the resulting transport theory.

The diversity of fundamental modeling approaches culminates in the electromagnetically extended balance equation for momentum. Any such balance equation relies on a proper form for the momentum of the electromagnetic fields. However, the precise definition for the electromagnetic momentum is under debate.[248,374–377] Also, some authors argue that a precise definition for electromagnetic momentum must distinguish between the electromagnetic field-/ and matter-part.[77,78]

One approach to resolve this issue is to split the "complete" momentum into separate "mechanical" and "electromagnetic" quantities.[141] Both quantities are then subject to individual balance equations. However, this separation requires individual stress tensors representing mechanical and electromagnetic contributions. Furthermore, the momentum-separation is accompanied by individual balance equations for mechanical (internal and kinetic) energy, and energy of the electromagnetic fields ("Poynting's Theorem").[140] This approach offers a clear and rational description, which bears many advantages. Among them is that the approach suggests precise definitions for debated electromagnetic expressions like flux-terms, energy-terms, and quantities related to the conversion of electromagnetic energy to internal and kinetic energy.[378] In particular, this method is often used to identify $\mathbf{D}_\mathrm{F} \wedge \mathbf{B}$ as electromagnetic momentum, and $(\mathbf{E}\mathbf{D}_\mathrm{F} + \mathbf{H}_\mathrm{F}\mathbf{B})/2$ as electromagnetic energy density,[141] and the Lorentz-force and Joule-heating is derived from momentum-/ and energy-conservation. Thus, the ambiguous nature of the Lorentz force (being a body-/ or surface-force) is resolved within this approach.[247] However, such an approach has also some disadvantages. Because the electromagnetic "balance-equations" are derived from the Maxwell-equations they merely constitute identities, which are satisfied by all electromagnetic quantities that solve Maxwell's equation.[379] Furthermore, these "Poynting Theorems" are highly non-unique, and various such equations exist which all take the form of balance-laws and can be derived from the Maxwell equations.[380] Furthermore, the identification of the "correct" form for the electromagnetic momentum and energy density follows more naturally from the four-dimensional description of electrodynamics, because both quantities are comprised in the stress-energy tensor, which fulfills a conservation-law by it's own (see appendix B.4). Furthermore, despite the clearly stated separation between mechanics and electromagnetic theory, this approach considers the electromagnetic body-forces (Lorentz-force) as source-terms in the balance-law of the purely mechanical momentum.[141] This highlights the underlying ambiguity between these approaches, since the coupling between mechanics and electromagnetic theory must be "modelled" , and cannot be derived from first principles.

In this work, we choose to express the Maxwell equations in the Galilean approximation, and express the Maxwell equations via flux-derivatives based on the objective quantities $\boldsymbol{\mathcal{E}}, \mathbf{D}_\mathrm{F}, \mathbf{B}, \boldsymbol{\mathcal{H}}_\mathrm{F}, \boldsymbol{\mathcal{J}}_\mathrm{F}, \varrho_\mathrm{F}$ (this is the same set as used by Kovetz[81]). In particular, we use $\boldsymbol{\mathcal{E}}, \mathbf{B}$ as proper electromagnetic variables in our materials law, which yields constitutive equations for $\mathbf{P}, \boldsymbol{\mathcal{M}}$. This approach was also chosen by Latz et.al.[64] The set of electromagnetic variables which is used to formulate the Maxwell equations, must be chosen in accordance with the materials law, because they couple to the expansion of $\dot{\varphi}_\mathrm{H}(\boldsymbol{\Upsilon})$ (see section 5.2.3). However, since the Maxwell equations can be formulated using different electromagnetic variables, different electromagnetic variables can be used in the materials law.[245] For example, Dreyer et al state the Maxwell equations via $\mathbf{E}, \mathbf{D}_\mathrm{F}, \mathbf{B}, \mathbf{H}_\mathrm{F}, \boldsymbol{\mathcal{J}}_\mathrm{F}, \varrho_\mathrm{F}$, and use $\mathbf{P}, \boldsymbol{\mathcal{M}}$ in their materials law to obtain constitutive equations for $\boldsymbol{\mathcal{E}}, \mathbf{B}$.[141] In contrast, Ref. 67 aimed to derive constitutive equations for $\boldsymbol{\mathcal{E}}, \boldsymbol{\mathcal{H}}_\mathrm{F}$ by using the common choice $\mathbf{D}_\mathrm{F}, \mathbf{B}$ in the materials law.[77,78]. Interestingly, this approach reproduces exactly the transport equations derived in this framework although an alternative choice for the electromagnetic variables was used here. For a concise discussion of a variety of such models, see Ref. 245.

Dreyer et al proposed a rationale as how to discard certain choices, based on equilibrium relations and relaxation arguments. In Ref. 141 they state that although the choice $\boldsymbol{\mathcal{E}}$, as used for example in Ref. 64, is mathematically consistent, it is incompatible with equilibrium relations and shall therefore be dismissed as electromagnetic variable. We disapprove with their reasoning as their main argument confuses primary and secondary quantities, and is physically not justified.

15.2 Comparison with the Extended Stefan-Maxwell Approach (“Newman-Model”)

The Stefan-Maxwell approach is among the most-widely used models for concentrated solutions.[93] In section 3.1 we gave a brief summary of the underlying assumptions, and introduced the “Newman-model”. In this section, we relate our framework to this canonic description. For this purpose, we consider the standard electrolyte discussed in section 5.4.6. This ternary electrolyte is commonly used for lithium ion batteries, and consists of a neutral solvent species and two ionic species.

As reference for the Newman-description of this electrolyte, we refer to Ref. 381, where a notation is used which is similar to ours (see also Ref. 100). Assuming LiPF6 as electrolyte-salt, the set of isothermal transport equations for this electroneutral system in the Newman-model is (see Eqs.(2.72) and (2.74), Ref. 381)

$$\partial_t c_{\mathrm{Li}^+} + \boldsymbol{\nabla} \left(t^{\mathsf{N}}_{\mathrm{Li}^+}/F z_{\mathrm{Li}^+} \cdot \boldsymbol{\mathcal{J}}_{\mathrm{F}} - \boldsymbol{\nabla} \left[D^{\mathsf{N}}_{\mathrm{LiPF6}} \cdot \boldsymbol{\nabla} c_{\mathrm{Li}^+} \right] \right) = 0, \tag{Newman-I}$$

$$\boldsymbol{\nabla} \boldsymbol{\mathcal{J}}_{\mathrm{F}} = 0, \tag{Newman-II}$$

where the electric current takes the form (see Eq.(2.51), Ref. 381)

$$\boldsymbol{\mathcal{J}}_{\mathrm{F}} = -\kappa^{\mathsf{N}} \boldsymbol{\nabla} \varphi^{\mathsf{N}} + \frac{2}{z_{\mathrm{Li}^+}} \frac{RT}{F} \kappa^{\mathsf{N}} \left(1 + \frac{\mathrm{d} \ln f^{\mathsf{N}}_{\mathrm{LiPF6}}}{\mathrm{d} \ln c_{\mathrm{Li}^+}} \right) \left(1 - t^{\mathsf{N}}_{\mathrm{LiPF6}} \right) \frac{\boldsymbol{\nabla} c_{\mathrm{Li}^+}}{c_{\mathrm{Li}^+}}. \tag{Newman-III}$$

Here, we slightly modified the notation used in Ref. 381 to better relate to our notation. Above, κ^{N}, $D^{\mathsf{N}}_{\mathrm{LiPF6}}$, $t^{\mathsf{N}}_{\mathrm{LiPF6}}$, $f^{\mathsf{N}}_{\mathrm{LiPF6}}$ denote the transport parameters appearing in the Newman-framework. In contrast to our description, where the transport coefficients are defined relative to the reference frame of the center-of-mass convection velocity, the Newman parameters are defined relative to the solvent-velocity (*i.e.* the convection velocity is defined by the solvent velocity). This is similar to the IVRF-approach discussed in section 5.5.4. In section 5.5.3, we showed that the conductivities in all reference frames are identical for electroneutral electrolytes,

$$\kappa^{\mathsf{N}} = \kappa. \tag{15.1}$$

Below, we will see how the remaining transport parameters relate to our description (see eqs. (15.14) and (15.16)). Note that the potential φ^{N} appearing in eq. (Newman-I) defines the electrochemical potential with respect to a Li^+-reference (see Eq.(A9), Ref. 381),

$$\varphi^{\mathsf{N}} = \Phi + \mu_{\mathrm{Li}^+}/F z_{\mathrm{Li}^+}\,, \tag{Newman-IV}$$

and differs from the electrochemical potential $\varphi = \Phi + \tilde{\mu}_2/F\tilde{z}_2$ appearing in our formalism (see eq. (5.134)). However, both are related by eq. (5.265).

We make use of the results derived in section 5.4.6, and assign Li^+ as second species, and $[\mathrm{PF\,6}]^-$ as third species. Because of electroneutrality, both concentrations are equal, $c_{\mathrm{Li}^+} = c_{[\mathrm{PF\,6}]^-}$. Furthermore, we neglect convection, as it is usually assumed in Newman-type models. Thus, the two transport equations for this ternary system at thermal equilibrium are given by eqs. (5.273) and (5.274). For completeness, we restate them here,

$$\boldsymbol{\nabla}\boldsymbol{\mathcal{J}}_{\mathrm{F}} = 0, \tag{15.2}$$

$$\partial_t c_{\mathrm{Li}^+} = -\boldsymbol{\nabla}\boldsymbol{\mathcal{N}}_{[\mathrm{PF\,6}]^-}, \tag{15.3}$$

The corresponding electric flux, and the relevant mass-flux $\boldsymbol{\mathcal{N}}_{[\mathrm{PF\,6}]^-}$ are determined by eqs. (5.266) and (5.267). According to this description, the only relevant chemical potential is $\mu_{\mathsf{ternary}} = \mu_{\mathrm{LiPF6}} = \mu_{\mathrm{Li}^+} + \mu_{[\mathrm{PF\,6}]^-}$, see eq. (5.263). Since we neglect convection, there are no viscous forces, *i.e.* $\boldsymbol{\nabla}\boldsymbol{\tau} = 0$. Hence, the Gibbs-Duhem relation becomes trivial, see eq. (5.101). Thus, when we neglect reactions, we find (see eq. (5.263))

$$\boldsymbol{\mathcal{J}}_{\mathrm{F}} = -\kappa\boldsymbol{\nabla}\varphi^{\mathsf{N}} + \kappa/F z_{\mathrm{Li}^+} \cdot \rho t_{[\mathrm{PF\,6}]^-} - \rho_{\mathrm{Li}^+}/\rho_1 \cdot \boldsymbol{\nabla}\mu_{\mathrm{LiPF6}}, \tag{15.4}$$

$$\boldsymbol{\mathcal{N}}_{[\mathrm{PF\,6}]^-} = t_{[\mathrm{PF\,6}]^-}/F z_{[\mathrm{PF\,6}]^-} \cdot \boldsymbol{\mathcal{J}}_{\mathrm{F}} - \mathcal{D}_{[\mathrm{PF\,6}]^-}\rho/\rho_1 \cdot \boldsymbol{\nabla}\mu_{\mathrm{LiPF6}}. \tag{15.5}$$

Electroneutrality allows to transform the independent transport equation for the $[\mathrm{PF\,6}]^-$-ions (eq. (15.3)) to a transport equation for the Li^+-ions. For this purpose, we use that $c_{\mathrm{Li}^+} = c_{[\mathrm{PF\,6}]^-}$, $t_{[\mathrm{PF\,6}]^-} = 1 - t_{\mathrm{Li}^+}$, $\boldsymbol{\nabla}\boldsymbol{\mathcal{J}}_{\mathrm{F}} = 0$, and $z_{[\mathrm{PF\,6}]^-} = -z_{\mathrm{Li}^+}$. Hence, our system of transport equations (eqs. (15.2) and (15.3) is equivalent to

$$\boldsymbol{\nabla}\boldsymbol{\mathcal{J}}_{\mathrm{F}} = 0, \tag{15.6}$$

$$\partial_t c_{\mathrm{Li}^+} + \boldsymbol{\nabla}\left(t_{\mathrm{Li}^+}/F z_{\mathrm{Li}^+} \cdot \boldsymbol{\mathcal{J}}_{\mathrm{F}}\right) - \boldsymbol{\nabla}\left(\mathcal{D}_{[\mathrm{PF\,6}]^-}\rho/\rho_1 \cdot \boldsymbol{\nabla}\mu_{\mathrm{LiPF6}}\right) = 0. \tag{15.7}$$

In the next step, we evaluate the chemical forces $\boldsymbol{\nabla}\mu_{\mathrm{LiPF6}}$ using the corresponding material function eq. (5.237). Since we assume electroneutrality and neglect convection, the forces become $\boldsymbol{\nabla}\mu_\alpha = RT\sum_{\beta=1}^{\mathsf{N}} \mathsf{TDF}_{\alpha\beta}\,\boldsymbol{\nabla}c_\beta/c_\beta$, where the therom-dynamic factor is (see eq. (5.236)) $\mathsf{TDF}_{\alpha\beta} = \sum_{\gamma=1}^{3}(\delta_{\alpha\gamma} - \nu_\alpha c_\gamma)(\delta_{\beta\gamma} + \partial\ln f_\gamma/\partial\ln c_\beta)$. As already mentioned in section 5.4.5, this form of the thermodynamic factor differs from the canonical form, which also appears in the Newman-model, $\mathsf{TDF}^{\mathsf{N}}_{\mathrm{LiPF6}} = 1 + \partial\ln f^{\mathsf{N}}_{\mathrm{LiPF6}}/\partial\ln c_{\mathrm{Li}^+}$. Since the chemical force $\boldsymbol{\nabla}\mu_{\mathrm{LiPF6}}$ is determined by μ_{Li^+}

and $\mu_{[\mathrm{PF\,6}]^-}$, we only need to calculate the six coefficients $TDF_{2\alpha}$ and $TDF_{3\alpha}$.

Note that for this electrolyte c_{Li^+} is the only independent species-concentration, see eqs. (5.222) and (5.223). In particular, the solvent-species is determined by $c_1 = (1 - c_1\nu_1)/(\nu_{\mathrm{Li}^+} + \nu_{[\mathrm{PF\,6}]^-})$, such that

$$\frac{\partial}{\partial c_1} = -\frac{\nu_1}{\nu_{\mathrm{Li}^+} + \nu_{[\mathrm{PF\,6}]^-}}\frac{\partial}{\partial c_{\mathrm{Li}^+}}, \quad \text{or} \quad \frac{\partial}{\partial \ln c_1} = -\frac{c_{\mathrm{Li}^+}}{c_1}\frac{\nu_1}{\nu_{\mathrm{Li}^+} + \nu_{[\mathrm{PF\,6}]^-}}\frac{\partial}{\partial \ln c_{\mathrm{Li}^+}}. \tag{15.8}$$

We use these relations for the calculation of the six coefficients of the two thermodynamic factors. In addition, we define the binary salt-activity coefficient

$$f_{\mathrm{LiPF6}} = f_{\mathrm{Li}^+} \cdot f_{[\mathrm{PF\,6}]^-}. \tag{15.9}$$

From a lengthy but simple calculation follows

$$\begin{aligned}\nabla\mu_{\mathrm{LiPF6}} = RT &\left[\frac{c_1\nu_1 - 1}{c_{\mathrm{Li}^+}}\left(1 + \frac{\partial \ln f_1}{\partial \ln c_1}\right) - \frac{c_{\mathrm{Li}^+}(\nu_1)^2}{c_1(\nu_{\mathrm{Li}^+} + \nu_{[\mathrm{PF\,6}]^-})}\frac{\partial \ln f_{\mathrm{LiPF6}}}{\partial \ln c_{\mathrm{Li}^+}}\right]\nabla c_1 \\ + 2RT &\left[c_1\nu_1\left(1 + \frac{\partial \ln f_{\mathrm{LiPF6}}}{\partial \ln c_{\mathrm{Li}^+}}\right) + \frac{(c_1)^2}{(c_{\mathrm{Li}^+})^3\nu_1}(1 - c_1\nu_1)^2\frac{\partial \ln f_1}{\partial \ln c_1}\right]\frac{\nabla c_{\mathrm{Li}^+}}{c_{\mathrm{Li}^+}}. \end{aligned} \tag{15.10}$$

However, when we insert this expression into the electric current, eq. (15.4), we find that our expression for $\mathcal{J}_{\mathrm{F}}$ differs from the electric current as predicted by Newman (eq. (NEWMAN-III)). Apparently, the differing terms vanish in the limit where the neutral solvent dominates the electrolyte with respect to mass and volume,

$$\rho_1 \approx \rho, \quad c_1\nu_1 \approx 1, \tag{15.11}$$

since then eq. (15.10) reduces to

$$\nabla\mu_{\mathrm{LiPF6}} = 2RT\,(1 + \partial \ln f_{\mathrm{LiPF6}}/\partial \ln c_{\mathrm{Li}^+})\,(\nabla c_{\mathrm{Li}^+})/c_{\mathrm{Li}^+}\,. \tag{15.12}$$

As we have shown in section 5.4.6, the assumptions eq. (15.11) are consistent with the above assumption that the convection-velocity can be neglected (see also eq. (5.272) and the discussion there, as well as section 5.4.7, eq. (5.280) and the text below). Hence, in the limit eq. (15.11), we find for the electric current eq. (15.4)

$$\mathcal{J}_{\mathrm{F}} = -\kappa\nabla\varphi^{\mathrm{N}} + \frac{2\kappa RT}{Fz_{\mathrm{Li}^+}}\frac{1 - t_{\mathrm{Li}^+}}{c_{\mathrm{Li}^+}}\left(1 + \frac{\partial \ln f_{\mathrm{LiPF6}}}{\partial \ln c_{\mathrm{Li}^+}}\right)\nabla c_{\mathrm{Li}^+}. \tag{15.13}$$

Apparently, the two models predict the same flux-expressions (*viz.* eqs. (15.13) and (NEWMAN-III)), if we identify the activity-parameters, and the transference numbers in the two different frameworks via

$$f^{\mathsf{N}}_{\mathrm{LiPF6}} = f_{\mathrm{LiPF6}}, \quad \text{and} \quad t^{\mathsf{N}}_{\mathrm{Li}^+} = t_{\mathrm{Li}^+}. \tag{15.14}$$

The latter identification is not trivial, since the Newman-parameters t^{N}_{α} are defined relative to the solvent-velocity $\mathbf{v}_1$.[381] This description is similar to the IVRF-parameters discussed in section 5.5.4. There we showed that in the limiting case eq. (5.272), the ionic transference numbers are equal for the standard electrolyte (see eq. (5.339), and the discussion there). Newman also states a relation for the parameters between both frames, $t_\alpha = (\rho_\alpha + \rho_1 t^{\mathsf{N}}_{\alpha})/\rho$ (see p. 301, Ref. 100). Thus, according to this relations, the identification eq. (15.14) for the transference parameters is also true in the limit eq. (15.11).

It remains to discuss the two transport equations for the Li^+-concentration, eqs. (15.7) and (NEWMAN-I). To address this, we substitute eq. (15.12) into eq. (15.7),

$$\partial_t c_{\mathrm{Li}^+} + \boldsymbol{\nabla}\left(\frac{t_{\mathrm{Li}^+}}{F z_{\mathrm{Li}^+}} \mathcal{J}_{\mathrm{F}}\right) - 2\mathcal{D}_{[\mathrm{PF\,6}]^-}\left(1 + \frac{\partial \ln f_{\mathrm{LiPF6}}}{\partial \ln c_{\mathrm{Li}^+}}\right)\frac{\boldsymbol{\nabla} c_{\mathrm{Li}^+}}{c_{\mathrm{Li}^+}} = 0. \tag{15.15}$$

Apparently, the two transport equations for the Li^+-ions eqs. (15.15) and (NEWMAN-I) agree up to differing expressions for the diffusion coefficients,

$$D^{\mathsf{N}}_{\mathrm{LiPF6}} \quad \longleftrightarrow \quad \frac{2}{c_{\mathrm{Li}^+}}\mathcal{D}_{[\mathrm{PF\,6}]^-}\left(1 + \frac{\partial \ln f_{\mathrm{LiPF6}}}{\partial \ln c_{\mathrm{Li}^+}}\right). \tag{15.16}$$

Note the conceptual difference between both quantities. The binary Newman-diffusion of the salt $D^{\mathsf{N}}_{\mathrm{LiPF6}}$ is defined relative to concentration gradients, whereas the expression appearing in our formalism, $\mathcal{D}_{[\mathrm{PF\,6}]^-}$, is defined relative to gradients in the chemical potential. However, the Newman-coefficient $D^{\mathsf{N}}_{\mathrm{LiPF6}}$ can be expressed via a corresponding diffusion-coefficient $\mathfrak{D}^{\mathsf{N}}_{\mathrm{LiPF6}}$, which is defined with respect to gradients in the chemical potential (see p.26 in Ref. 381), $D^{\mathsf{N}}_{\mathrm{LiPF6}} = \mathfrak{D}^{\mathsf{N}}_{\mathrm{LiPF6}}(1 + 2c_{\mathrm{Li}^+}/c_1)(1 + \partial \ln f^{\mathsf{N}}_{\mathrm{LiPF6}}/\partial \ln c_{\mathrm{Li}^+})$. Thus, the two systems of transport equations agree subject to the identification $(1 + 2c_{\mathrm{Li}^+}/c_1)\mathfrak{D}^{\mathsf{N}}_{\mathrm{LiPF6}} \leftrightarrow 2\mathcal{D}_{[\mathrm{PF\,6}]^-}/c_{\mathrm{Li}^+}$.

Therefore, in the limit eq. (15.11), our description reproduces the Newman-approach, subject to the identification of the binary diffusion coefficients, eq. (15.16). Ultimately, both theoretical descriptions must be validated in comparison with experimental results. In particular, it remains up to experimental examinations if the limiting assumptions eq. (15.11) are reasonably chosen. Recently, Gasteiger et.al. proposed a scheme for the complete experimental determination of the relevant transport parameters (conductivity, binary diffusion coefficient, transference number, and thermodynamic factor) in this standard electrolyte.[294,382,383] Their approach relates to the Newman-model eqs. (NEWMAN-I) to (NEWMAN-IV) (see, *e.g.*, Eq.(1) and (2) in Ref. 294), and thus can be used to probe the Newman-approach in comparison with our description. Indeed, since the experiment determines both, $D^{\mathrm{N}}_{\mathrm{LiPF6}}$ and $TDF^{\mathrm{N}}_{\mathrm{LiPF6}}$, the identification eq. (15.16) gets resolved. This provides the possibility for direct comparison of both descriptions using the Gasteiger-approach discussed in Ref. 294.

15.3 From Molecular Dynamics to Non-Equilibrium Thermodynamics

In this section we focus on how atomistic frameworks, based on quantum chemistry, *i.e.* DFT and MD, are related to our continuum description.

By solving the Schrödinger equation, ab-initio DFT determines the forces between ions and molecules, and determines the electronic structure of many-body systems in condensed phase.[384] MD simulations calculate the classical trajectories of ions and molecules, *i.e.* their positions and velocities, based upon the DFT generated force fields.[385] Although MD simulations describe static and dynamic properties occurring at the microscale, results obtained from MD simulations also relate to continuum transport quantities, *e.g.* Onsager coefficients, via the velocity autocorrelation function / Green-Kubo relations.[386,387]

Static results from MD simulations are often interpreted via profiles of the radial distribution functions (RDF) $g(r)$.[63] In general, the RDF accounts for correlations in the positions of sample-particles by describing how the density varies as function of the distance. Because RDFs play an important role in various different theories and experiments, they can be used to interpret the MD results.

In particluar, the RDF can be obtained from scattering experiments, *e.g.* X-ray diffraction or neutron diffraction,[388] via the resulting structure factor of the sample. For example, the structure factor of spherically symmetric samples (like isotropic liquids) relates to the RDF via Fourier-transformation.[389–391] Furthermore, RDFs are focal quantities appearing in liquid state theory (LST), which links microscopic details to macroscopic properties ("Kirkwood-Buff solution theory").[63,392] This provides the possibility for connecting atomistic descriptions with scattering experiments,[393] and thermodynamic concepts.[63] In integral equation theories (IETs), the correlations described by the RDF are typically split up into different types of correlation functions. The pairwise total correlation function h relates to the RDF via subtraction of it's asymptotic value $h(r) = g(r) - 1$ (since $\lim_{r\to\infty} g(r) = 1$),[320] and to the direct pair correlation function $\mathsf{c}^{(2)}(r)$ via the

Ornstein-Zernike relation,[394]

$$h(r) = \mathsf{c}^{(2)}(r) + \rho^{\mathrm{b}} \int \mathrm{d}r' \mathsf{c}^{(2)}(|r - r'|) \cdot h(r'). \tag{15.17}$$

Here, ρ^{b} is the density of the bulk liquid. Finally, because the direct pair correlation functions $\mathsf{c}^{(2)}_{\alpha\beta}$ are also used in classical density functional theory (cDFT), where they account for pairwise interactions between two ions of species α and β, they relate to the excess free energy (due to pairwise ion-interactions), *i.e.* to thermodynamic concepts used in our description.[395] In particular, the direct pair correlation function is the twofold functional derivative of F^{int}.[393] Thus, as shown in section 8.3, the direct pair correlation function equals the interaction potential $\mathcal{F}$ (see eq. (8.29)),

$$\mathsf{c}^{(2)}_{\alpha\beta}(r, r') = -\frac{\mathcal{F}_{\alpha\beta}(|r - r'|)}{k_{\mathrm{B}} T (N_{\mathrm{A}})^2} = -\frac{\mathcal{V}^0}{E_{\mathrm{th}}} \cdot \frac{\tilde{c}^{\mathrm{b}}}{2\gamma_+\gamma_-} \cdot \tilde{\mathcal{F}}_{\alpha\beta}(|r - r'|). \tag{15.18}$$

Furthermore, the excess chemical potentials $\mu^{\mathrm{int}}_{\alpha}(\mathbf{x}, [c_\gamma])$ follow from higher-order correlation functions $\mathsf{c}^{(n)}_{\alpha\beta\ldots}$ via the Taylor approximation for a functional.[393] To show this, we consider a non-uniform system, and measure the concentrations $c_\gamma(\mathbf{x}) = c^0_\gamma(\mathbf{x}) + \delta c_\gamma(\mathbf{x})$ relative to a reference state defined by reference concentrations c^0_γ. We expand the excess chemical potential $\mu^{\mathrm{int}}_{\alpha}(\mathbf{x}, [c_\gamma]) = \mu_\alpha(\mathbf{x}, [c_\gamma]) - \partial(\rho\varphi_{\mathrm{H}})/\partial c_\alpha$ around the referenced state using the Taylor expansion for a functional,[396]

$$\begin{aligned} \mu_\alpha(\mathbf{x}, [c_\gamma]) =& \mu_\alpha(\mathbf{x}, [c^0_\gamma]) + \sum_{\beta=1}^{\mathrm{N}} \int \mathrm{d}\mathbf{x}' \, \frac{\delta \mu_\alpha(\mathbf{x}, [c^0_\gamma])}{\delta c_\beta(\mathbf{x}')} \cdot \delta c_\beta(\mathbf{x}') \\ & + \frac{1}{2} \sum_{\beta,\lambda} \iint \mathrm{d}\mathbf{x}'\mathrm{d}\mathbf{x}'' \, \frac{\delta^2 \mu_\alpha(\mathbf{x}, [c^0_\gamma])}{\delta c_\lambda(\mathbf{x}'')\delta c_\beta(\mathbf{x}')} \cdot \delta c_\beta(\mathbf{x}')\delta c_\lambda(\mathbf{x}'') \\ & + \mathcal{O}\left([\delta c_\gamma]^3\right) \end{aligned} \tag{15.19}$$

$$\begin{aligned} =& \mu_\alpha(\mathbf{x}, [c^0_\gamma]) - RTN_{\mathrm{A}} \cdot \sum_{\beta=1}^{\mathrm{N}} \int \mathrm{d}\mathbf{x}' \, \mathsf{c}^{(2)}_{\alpha\beta}(\mathbf{x}, \mathbf{x}') \cdot \delta c_\beta(\mathbf{x}') \\ & - \frac{RT}{2} \cdot N_{\mathrm{A}} \cdot \sum_{\beta,\lambda} \iint \mathrm{d}\mathbf{x}'\mathrm{d}\mathbf{x}'' \, \mathsf{c}^{(3)}_{\alpha\beta\lambda}(\mathbf{x}, \mathbf{x}', \mathbf{x}'') \cdot \delta c_\beta(\mathbf{x}')\delta c_\lambda(\mathbf{x}'') \\ & + \mathcal{O}\left([\delta c_\gamma]^3\right), \end{aligned} \tag{15.20}$$

Here we used $\mu^{\mathrm{int}}_{\alpha}(\mathbf{x}, [c^0_\gamma]) = \delta F^{\mathrm{int}}[c^0_\gamma]/\delta c_\alpha(\mathbf{x})$ and introduced the direct correlation functions $\mathsf{c}^{(2)}_{\beta\alpha}(\mathbf{x}, \mathbf{x}') = -1/RTN_{\mathrm{A}} \cdot \delta^2 F^{\mathrm{int}}/\delta c_\beta(\mathbf{x}')c_\alpha(\mathbf{x})$ and $\mathsf{c}^{(3)}_{\lambda\beta\alpha}(\mathbf{x}, \mathbf{x}', \mathbf{x}'') = \delta^3 F^{\mathrm{int}}/\delta c_\lambda(\mathbf{x}'')\delta c_\beta(\mathbf{x}')\delta c_\alpha(\mathbf{x})$ with respect to the reference state.

This illustrates how the atomistic description relates to our thermodynamic framework via a simple recipe: DFT determines force fields for MD; MD determines $g(r)$ for LST; $g(r)$ determines $\mathsf{c}^{(2)}(r)$ via the Ornstein-Zernike relation; $\mathsf{c}^{(2)}(r)$ determines F^{int}, thus generates our non-equilibrium thermodynamic theory. Altogether, the parameters of our continuum theory can be rigorously calculated via these atomistic methods.

As mentioned above, atomistic simulations also relate to transport parameters appearing in our theory, *i.e.* dynamic properties. In this work, we use a consistent flux-explicit description based on Onsager coefficients.[397] These Onsager coefficients can be measured experimentally,[386] or can be obtained from MD simulations via time-integration of the velocity-auto-correlation functions ("Green Kubo relations").[387]

Finally, we note that scattering experiments are often evaluated using fit functions in the form of eq. (10.44) to describe the interfacial profiles obtained from the scattering intensity, *i.e.* the structure factor (see, *e.g.*, eq. (7) in Ref. 398). These fit parameters follow analytically from our theory.

15.4 From Non-Equilibrium Thermodynamics to BSK Theory

In this section, we compare our thermodynamically consistent continuum approach with phenomenological mean field theories (MFT) from the literature.

The seminal MFT-approach proposed by Bazant, Storey, and Kornyshev (BSK), for the description of ILs near electrified interfaces,[69] constitutes the canonic approach for such MFTs based on modified dielectric relations.

In contrast to our approach, where we incorporate non-local effects via modification of the free energy, BSK account for non-local ion-correlations using a modified linear dielectric relation between the electrostatic fields $\bar{\boldsymbol{D}}$ and $\boldsymbol{E}$ via

$$\bar{\boldsymbol{D}} = \hat{\bar{\varepsilon}}\boldsymbol{E}. \tag{15.21}$$

Here, the dielectric BSK parameter is an operator which contains higher-order gradients,

$$\hat{\bar{\varepsilon}} = \varepsilon_{\mathrm{R}}\varepsilon_0(1 - \ell_{\mathrm{c}}\boldsymbol{\nabla}^2). \tag{15.22}$$

The second order gradient-term in $\hat{\bar{\varepsilon}}$ is effectively short-ranged with correlation-length ℓ_{c}. The constitutive relation, eq. (15.21), implies a modified Poisson equation,

$$\hat{\bar{\varepsilon}}\boldsymbol{\nabla}^2\Phi = -\bar{\varrho}_{\mathrm{F}}. \tag{15.23}$$

In addition, the chemical potential connects electric potential and charge density, *i.e.* $\bar{\varrho}_{\mathrm{F}}(\Phi)$. Furthermore, in the limit of small potentials, the EDL is described via one equation,

$$\hat{\hat{\varepsilon}}\boldsymbol{\nabla}^2\Phi = \Phi. \tag{15.24}$$

We compare this description with our approach. Because our modeling is based on a different rationale, it differs conceptually from BSK theory. Focal quantity in our modeling is the free energy F, hence we incorporate electrostatic correlations into our framework via modification of F. Thus, instead of modifying the dielectric constitutive relation as in eq. (15.21), we supplement the free energy by an additional term F^{int}, see eq. (8.10). Thus, non-local ion-interactions arise in the set of equations via the constitutive equations, *i.e.* via the chemical potentials. As consequence, the MFT-quantities appearing in the BSK description, $\bar{\boldsymbol{D}}$ and $\bar{\varrho}_{\mathrm{F}} = \boldsymbol{\nabla}\bar{\boldsymbol{D}}$, differ from the corresponding quantities ϱ_{F} and $\boldsymbol{D}$ appearing in our formalism; the charge density ϱ_{F} relates to the "bulk"-quantity $\boldsymbol{D}$ and does not incorporate ion correlations. This is in contrast to the "mean field charge density" $\bar{\varrho}_{\mathrm{F}}$.

Nevertheless, we show that despite these conceptual differences the resulting model equations are very similar. In particular, it is possible to reproduce the BSK description, eq. (15.24), from our system of equations, eqs. (10.4) and (10.5). To show this, we assume the limit of small potentials, such that eqs. (10.4) and (10.5) equations can be cast into one equation for the electric potential alone, *viz.*

$$\hat{\varepsilon}_{\mathrm{R}}\tilde{\boldsymbol{\nabla}}^2\tilde{\Phi} = \tilde{\Phi}. \tag{15.25}$$

Here, the dielectric operator appearing in our description is $\hat{\varepsilon}_{\mathrm{R}} = 1 - \mathcal{V}^0 E_{\mathrm{th}} \cdot \tilde{\mathit{\Gamma}}^0_{+-} - \mathcal{V}^0/E_{\mathrm{th}} \cdot \tilde{\mathit{\Gamma}}^2_{+-} \cdot \tilde{\boldsymbol{\nabla}}^2$ (see eq. (10.6)). We highlight the similarity between eq. (15.24) and eq. (15.25), and between the dielectric operators $\hat{\varepsilon}_{\mathrm{R}}$ and $\hat{\hat{\varepsilon}}$ shown in eq. (15.22). This illustrates the similarity between our model, and the BSK theory.

However, we want to emphasize that our gradient description merely constitutes an approximation to the more concise integral description, which incorporates all interaction modes. Nevertheless, the gradient description emerges naturally within our rigorous continuum model, and thus stems form a thermodynamically consistent transport theory. In contrast, the higher-order gradient-terms are phenomenologically incorporated in the BSK approach. Also, in contrast to the BSK model, our description comprises a zero-order correction in the dielectric operator, which is mandatory to realize the “complete” ternary phase-space of interfacial profiles (see the discussion at end of section 10.3.2, as well as sections 10.3.5 and 10.3.6). This mode is missing in the BSK approach.

16 Coarse Graining: From Non-Local Microscopic Correlations to Macroscopic Phenomenological Thermodynamic Properties

Our multiscale framework allows to incorporate a variety of effects via modeling of the free energy. Depending upon the effect, they can either be incorporated as bulk effects in the form of contributions to the free energy density $\int \mathrm{d}V \rho \varphi_{\mathrm{H}}$, or in the form of energy functionals F^{int} representing effects which involve non-local intercations occurring on the microscopic scale.

However, this dichotomy is not always well defined.[399] On one side, there are macroscopic effects, which are emergent, *i.e.* result from microscopic interactions between particles on much smaller scales.[400] As consequence, it suffices to describe such effects via a macroscopic (averaged) energy contribution. For example, the basic idea of mean field theories is to approximate the cumulative energy contribution resulting from interactions between molecules by an averaged effective description, *i.e.* to replace the individual particle interactions by a homogeneous background potential.[401] On the other side, rational thermodynamics constitues a description of non-equilibrium thermodynamics which is based on universal principles imposing strict constraints on the macroscopic behaviour of matter.[74] Thus, not all of thermodynamics can be reduced to particle interactions.[81]

In this chapter, we show that our microscopic approach can be used to rationalize the continuum description of emergent bulk effects, by replacing macroscpic energy descriptions with microscopic interactions via the method of coarse graining. This method is based on the assumption that macroscopic effects can be approximated by microscopic interactions, where the corresponing interaction potentials have, effectively, a Dirac Delta distribution as their support.

In the first section, we introduce our model for coarse graining, see section 16.1. Next, in section 16.2 we apply this description to the seminal Folry-Huggins solution theory, and show how the phenomenological, macrsopcopic interaction parameters can be derived from microscopic interactions. Finally, in section 16.3 we discuss how to derive the macroscopic elastic energy contributions due to finite molar volumes from a microscopic model, and how the bulk modulus can be obtained from microscopic parameters.

16.1 Coarse Graining of Microscopic Interactions

Our continuum description for the electrochemical double layer (EDL) is based on the free energy functional

$$F = \int \mathrm{d}V \rho\varphi_{\mathrm{H}} + F^{\mathrm{int}}, \tag{16.1}$$

and accounts for non-local ion correlations on the microscopic scale (nanometer scale) via interaction contributions (see eq. (10.35)),

$$F^{\mathrm{int}} = \frac{1}{2}\mathcal{V}^0 \left(N_{\mathrm{A}}\right)^2 \iint \mathrm{d}x^3 \mathrm{d}y^3 \sum_{\alpha,\beta}^{\mathrm{N}} \tilde{\mathfrak{F}}_{\alpha\beta}(|\mathbf{x}-\mathbf{y}|) c_\alpha(\mathbf{x}) c_\beta(\mathbf{y}). \tag{16.2}$$

Here, the corresponding scale of this interaction model is determined by the effctive support of the interaction potential $\tilde{\mathfrak{F}}_{\alpha\beta}(\ell_{\mathrm{int}})$, *i.e.* the correlation length ℓ_{int}. In our EDL description, we assumed that the correlation length scales with the ion size a via $\ell_{\mathrm{int}} \approx a/2\pi$ (where we assumed that $a^3 \propto \nu/N_{\mathrm{A}}$, see eqs. (9.2) and (10.35)), *i.e.* which corresponds to a model for microscopic interactions. In contrast, the quantity $\rho\varphi_{\mathrm{H}}$ appearing in eq. (16.1) is the bulk free energy density, which was discussed in part II, for the description of neutral electrolytes on a macroscopic scale (micrometer scale).

However, the argument is that we can transfer the microscopic description eq. (16.2) to larger length scales via coarse graining. From a macroscopic perspective, the micrscopic interaction potential can be approximated by a Dirac Delta distribution,

$$\tilde{\mathfrak{F}}_{\alpha\beta}(|\mathbf{x}-\mathbf{y}|) = \chi_{\alpha\beta} \cdot \delta^3(|\mathbf{x}-\mathbf{y}|). \tag{16.3}$$

Note that since $[\delta^3(|\mathbf{x}-\mathbf{y}|)] = \mathrm{m}^{-3}$, the mesoscopic interaction parameter χ has dimension $[\chi_{\alpha\beta}] = \mathrm{m}^3$. From the Ansatz in eq. (16.3), we obtain a coarse grained interaction energy via substitution of eq. (16.3) into eq. (16.2)

$$F^{\mathrm{coarse}} = \int \mathrm{d}V \, \frac{\mathcal{V}^0}{2} \left(N_{\mathrm{A}}\right)^2 \sum_{\alpha,\beta}^{\mathrm{N}} \chi_{\alpha\beta} c_\alpha(\mathbf{x}) c_\beta(\mathbf{x}). \tag{16.4}$$

The corresponding coarse grained description of the complete system becomes

$$F = F^{\mathrm{coarse}} + \int \mathrm{d}V \rho\varphi_{\mathrm{H}}. \tag{16.5}$$

16.2 Flory Huggins Solution Theory

In this section we apply our model for coarse graining described in section 16.1 to the seminal Flory-Huggins theory for polymer solutions.[341,342]

According to this model, the excess free energy of a binary system is described by an energy contribution

$$F^{\text{FLORY}} = \int \mathrm{d}V \; RT\chi^{\text{FLORY}}_{\alpha\beta} c_1 \nu_1 c_2 \nu_2, \tag{16.6}$$

where $\chi^{\text{FLORY}}_{\alpha\beta}$ are the Flory interaction parameters (with dimension $[\chi^{\text{FLORY}}_{\alpha\beta}] = \mathrm{mol\,m^{-3}}$).

The goal of this section is to show that our coarse graining model eq. (16.4) applied to a binary system,

$$F^{\text{coarse}} = \frac{\mathcal{V}^0}{2} \int \mathrm{d}V (N_\mathrm{A})^2 \left[\chi^{\text{coarse}}_{11} (c_1)^2 + (\chi^{\text{coarse}}_{12} + \chi_{21}) c_1 c_2 + \chi^{\text{coarse}}_{22} (c_2)^2\right], \tag{16.7}$$

reproduces the Flory Huggins model in eq. (16.6). For this purpose, we neglect self-interactions, $\chi^{\text{coarse}}_{11} = \chi^{\text{coarse}}_{22} = 0$, and assume symmetric inter-species interactions, $\chi^{\text{coarse}} = \chi^{\text{coarse}}_{12} = \chi^{\text{coarse}}_{21}$. Then, eq. (16.7) equals the Flory theory exactly if

$$\chi^{\text{FLORY}} = \chi^{\text{coarse}} \cdot N_\mathrm{A}/(\nu_1 \cdot \nu_2) \cdot \mathcal{V}^0/k_\mathrm{B}T. \tag{16.8}$$

Hence, when we remove the physical dimensions from the interaction parameters according to $\tilde{\chi}^{\text{FLORY}} = \nu \cdot \chi^{\text{FLORY}}$ (where $\nu = \nu_1 + \nu_2$, $\gamma_\alpha = \nu_\alpha/\nu$) and $\chi^{\text{coarse}} = \gamma_1\gamma_2/N_\mathrm{A}\nu = \gamma_1\gamma_2 a^3$ (alternatively, the interaction energy can be reparametrised by $\mathcal{V}^0 \to \mathcal{V}^0/\tilde{\chi}^{\text{coarse}}$ where $\tilde{\chi}^{\text{coarse}} = \chi^{\text{coarse}}/\gamma_1\gamma_2 a^3$), this identification yields

$$\tilde{\chi}^{\text{FLORY}} = \mathcal{V}^0/k_\mathrm{B}T. \tag{16.9}$$

This shows that the macroscopic thermodynamic quantity χ^{FLORY} appearing in the Flory Huggins solution theory can be derived from a microscopic interaction model via the method of coarse graining. According to this description, the Flory parameters are expressed via the ratio of the interaction energy, which stems from microscopic ion correlations, and the thermal energy.

16.3 Mean Steric Effect

In our model free energy density for the continuum bulk transport theory, we took account for elastic contributions to the energy of the system due to compression of the electrolyte system via a contribution

$$\int \mathrm{d}V \rho\varphi_{\mathrm{H}}^{\mathrm{elastic}} = \frac{\mathcal{K}}{2} \cdot \int \mathrm{d}V \left(1 - \sum_{\alpha\beta}^{\mathrm{N}} c_\alpha \nu_\alpha^0\right)^2 . \tag{16.10}$$

Here, $\mathcal{K}$ is the macroscopic bulk modulus of the electrolyte. This energy contribution relates the current configuration of the system, with species concentrations c_α and partial molar volumes ν_α, to some reference state of the system, where the species concentrations take values c_α^0 and have partial molar volumes ν_α^0. Note that the Euler equation for the volume applies to each configuration, *i.e.* $\sum_{\alpha=1}^{\mathrm{N}} c_\alpha^0 \nu_\alpha^0 = \sum_{\alpha=1}^{\mathrm{N}} c_\alpha \nu_\alpha = 1$.

Here, the partial molar volumes are thermodynamic quantities, *i.e.* refer to a macroscopic concept . Likewise, the mean steric effect described by the energy contribution $\rho\varphi_{\mathrm{H}}^{\mathrm{elastic}}$ is a macroscopic effect. However, we assume that it is being an emergent effect, *i.e.* an effect which results from microscopic effects occurring on much smaller length scales. According to this understanding, microscopic interactions imply that the partial molar volumes of the species will change during the evolution of compressible electrolyte systems, such that, in general, $\nu_\alpha^0 \neq \nu_\alpha$.

Our goal in this section is to study if the method of coarse graining, introduced in section 16.1 above, can be used to obtain the energy contribution $\rho\varphi_{\mathrm{H}}^{\mathrm{elastic}}$, from modeling microscopic interactions via $\tilde{\mathcal{F}}_{\alpha\beta} = \chi_{\alpha\beta} \cdot \delta^3(|\mathbf{x} - \mathbf{y}|)$.

For completeness, we restate the explicit form for the volumetric energy contribution,

$$\rho\varphi_{\mathrm{H}}^{\mathrm{elastic}} = \frac{\mathcal{K}}{2} \cdot \left[1 - 2\sum_{\alpha=1}^{\mathrm{N}} c_\alpha \nu_\alpha^0 + \left(\sum_{\alpha=1}^{\mathrm{N}} c_\alpha \nu_\alpha^0\right)^2\right] , \tag{16.11}$$

which consists of energy contributions which do not depend upon ion concentration, contributions which are linear in the ion concentrations, and contributions which are quadratic in the ion concentrations. Energy contributions which are trivial in the concentrations do not contribute to the chemical potentials. Hence, they do not play much of a role in the discussion here. In contrast, energy contributions which are linear in the concentrations lead to contributions to the chemical potentials which do not depend on ion concentrations, *i.e.* have no contributions to the forces. These linear energy terms can be interpreted as single species contributions due to compression, and the corresponding contributions to the chemical potentials have the role of an off-set, relating to some reference configuration of the system. Thus, the crucial quantities are the terms quadratic in the species concentrations.

To address the goal of this section, we assume that the interaction parameters are functions of the molar volumes derived from the microscopic configuration, *i.e.*

$\chi_{\alpha\beta}(\nu^0_\gamma)$. In this sense, we designate the specific state of reference as being constituted by the assumption that the reference molar volumes are determined by the ion sizes, *i.e.* $\nu^0_\alpha(a)$. Furthermore, we assume that the amount of energy which is necessary to compress the system from a reference configuration c^0_α to the actual configuration c_α depends only on the differentials $\Delta_\alpha(\mathbf{x}) = c_\alpha(\mathbf{x}) - c^0_\alpha(\mathbf{x})$, *viz.*

$$F^{\mathrm{el}}[c_\alpha]=\frac{\mathcal{V}^{\mathrm{el}}}{2}(N_{\mathrm{A}})^2 \iint \mathrm{d}x^3 \mathrm{d}y^3 \sum_{\alpha,\beta}^{\mathrm{N}} \tilde{\mathcal{F}}_{\alpha\beta}(|\mathbf{x}-\mathbf{y}|)\Delta_\alpha(\mathbf{x})\Delta_\beta(\mathbf{y}), \tag{16.12}$$

Here, $\mathcal{V}^{\mathrm{el}}$ is the interaction energy which accounts for the microscopic compression of the electrolyte. We will see below, that this quantity determines the macroscopic bulk modulus when we apply the method of coarse graining.

The most simple approach is to define (note that the interaction parameters have dimension $[\chi_{\alpha\beta}] = \mathrm{m}^3$)

$$\chi_{\alpha\beta} = \nu^0_\alpha \nu^0_\beta / \nu^0 N_{\mathrm{A}} = \gamma^0_\alpha \gamma^0_\beta \cdot \nu^0 / N_{\mathrm{A}}, \tag{16.13}$$

where $\nu^0 = \sum_{\alpha=1}^{\mathrm{N}} \nu^0_\alpha$ is the total molar volume with respect to the reference configuration, and $\gamma^0_\alpha = \nu^0_\alpha/\nu^0$ (see section 9.2). Altogether, we find (making use of the Euler equation for the volumes in both configurations)

$$F^{\mathrm{el}}[c_\alpha] = \frac{\mathcal{V}^{\mathrm{el}}}{2}\frac{N_{\mathrm{A}}}{\nu^0} \int \mathrm{d}V \left(1 - \sum_{\alpha=1}^{\mathrm{N}} c_\alpha \nu^0_\alpha\right)^2, \tag{16.14}$$

which equals our bulk continuum Ansatz in eq. (16.10) subject to the identification of the bulk modulus $\mathcal{K}^{\mathrm{coarse}} = \mathcal{V}^{\mathrm{el}} N_{\mathrm{A}}/\nu^0$.

When we relate this to our description of pure binary ILs discussed in part III, where $\nu^0 = a^3/N_{\mathrm{A}}$, then, the bulk modulus is given by $\mathcal{K}^{\mathrm{coarse}} = \mathcal{V}^{\mathrm{el}}/a^3$, and the (only) interaction parameter is $\chi_\pm = \gamma_+(1-\gamma_+)a^3$ *i.e.* both are completely determined by microscopic parameters.

Next, we shall discuss the limit of an incompressible electrolyte for eq. (16.14), where the bulk modulus $\mathcal{K}^{\mathrm{coarse}} = \mathcal{V}^{\mathrm{el}} N_{\mathrm{A}}/\nu^0$ diverges, *i.e.* $\mathcal{V}^{\mathrm{el}} \to \infty$. A sufficient condition for that the quantity F^{el} remains finite in this limit is that the molar volumes of the reference configuration (ν^0_α) equal the molar volumes of the actual configuration (ν_α), *i.e.* $\nu^0_\alpha \to \nu_\alpha$. Since this argument applies to any state of the system, this sufficient condition is equivalent to the condition of constant, *i.e.* pressure independent, partial molar volumes.

Note that the Ansatz above is equivalent to a threefold approach

$$F^{\mathrm{el}}[c_\alpha]{=}(N_{\mathrm{A}})^2\mathcal{V}^{\mathrm{el}}/2\cdot x\int \mathrm{d}V\sum_{\alpha,\beta}\chi_{\alpha\beta}[c_\alpha c_\beta-2c^0_\alpha c_\beta+c^0_\alpha c^0_\beta]. \tag{16.15}$$

The second term is a linear expansion, whereas the third term is just a constant offset for the energy. For completeness, we discuss such an approach in more detail below.

Quadratic Form Approach

The goal of this section is to reproduce our macroscopic bulk description for the elastic energy

$$\rho\varphi^{\mathrm{elastic}}_{\mathrm{H}}=\frac{\mathcal{K}}{2}\left[1-2\left(c_1\nu^0_1+c_2\nu^0_2-c_1c_2\nu^0_1\nu^0_2\right)+\left(c_1\nu^0_1\right)^2+\left(c_2\nu^0_2\right)^2\right]. \tag{16.16}$$

from a microscopic approach using the method of coarse graining introduced in section 16.1. This discussion is complementary to the approach discussed above (see section 16.3), where we already presented one approach based on the assumption that the energy of compression depends only on the differential of the concentrations before and after the compression in section 16.3. However, here we want to discuss two slightly different approaches based on an expansion of the energy of compression in powers of the concentrations c_α, and in powers of the concentration differentials $\varDelta_\alpha=c_\alpha-c^0_\alpha$.

We first discuss a power expansion of the free energy with respect to the species concentrations, *viz.*

$$F^{\mathrm{el}}{=}(N_{\mathrm{A}})^2\int \mathrm{d}V\left[\frac{\mathcal{V}^{\mathrm{el}}_{(0)}}{2N_{\mathrm{A}}\nu^0}+\mathcal{V}^{\mathrm{el}}_{(1)}\sum_\alpha\zeta_\alpha c_\alpha+\frac{\mathcal{V}^{\mathrm{el}}_{(2)}}{2}\sum_{\alpha,\beta}\chi_{\alpha\beta}c_\alpha c_\beta\right] \tag{16.17}$$

Here, the parameters have dimension $[\zeta_\alpha]$=mol and $[\chi_{\alpha\beta}]=\mathrm{m}^3$. One model is to define

$$\zeta_\alpha=-\nu^0_\alpha/\nu^0N_{\mathrm{A}},\qquad\text{and}\qquad\chi_{\alpha\beta}=\zeta_\alpha\zeta_\beta\nu^0N_{\mathrm{A}}, \tag{16.18}$$

such that

$$F^{\mathrm{el}}=\frac{N_{\mathrm{A}}}{2\nu^0}\int \mathrm{d}V\left[\mathcal{V}^{\mathrm{el}}_{(0)}-2\mathcal{V}^{\mathrm{el}}_{(1)}\sum_{\alpha=1}^{\mathrm{N}}c_\alpha\nu^0_\alpha+\mathcal{V}^{\mathrm{el}}_{(2)}\left(\sum_{\alpha=1}^{\mathrm{N}}c_\alpha\nu^0_\alpha\right)^2\right]. \tag{16.19}$$

Hence, when we assume that all energy modes are the same, *i.e.* $\mathcal{V}^{\mathrm{el}}_{(0)}=\mathcal{V}^{\mathrm{el}}_{(1)}=$

$\mathcal{V}^{\mathrm{el}}_{(2)} \equiv \mathcal{V}^{\mathrm{el}}$, we get

$$F^{\mathrm{el}} = \frac{N_{\mathrm{A}}}{\nu^0} \frac{\mathcal{V}^{\mathrm{el}}}{2} \int \mathrm{d}V \left(1 - \sum_{\alpha} c_\alpha \nu^0_\alpha \right)^2 . \tag{16.20}$$

This suggests that we define the macroscopic bulk modulus via $\mathcal{K}^{\mathrm{coarse}} = N_{\mathrm{A}} \mathcal{V}^{\mathrm{el}} / \nu^0$. Hence, a sufficient condition for F^{el} to remain finite in the incompressible limit $\mathcal{V}^{\mathrm{el}} \to \infty$ is that the partial molar volumes are constant and $\nu^0_\alpha \to \nu_\alpha$.

Second, we expand the energy in powers of the concentration differentials $\Delta_\alpha = c_\alpha - c^0_\alpha$.

$$F^{\mathrm{el}} = (N_{\mathrm{A}})^2 \int \mathrm{d}V \left[\frac{\mathcal{V}^{\mathrm{el}}_{(0)}}{2 N_{\mathrm{A}} \nu^0} + \mathcal{V}^{\mathrm{el}}_{(1)} \sum_{\alpha} \zeta_\alpha \Delta_\alpha + \frac{\mathcal{V}^{\mathrm{el}}_{(2)}}{2} \sum_{\alpha,\beta} \chi_{\alpha\beta} \Delta_\alpha \Delta_\beta \right] \tag{16.21}$$

We use the same model for the expansion coefficients ζ_α and $\chi_{\alpha\beta}$ as above, see eq. (16.18), which yields

$$F^{\mathrm{el}} = \frac{N_{\mathrm{A}}}{2\nu^0} \int \mathrm{d}V \left[\mathcal{V}^{\mathrm{el}}_{(0)} + 2\mathcal{V}^{\mathrm{el}}_{(1)} \left(1 - \sum_{\alpha=1}^{\mathrm{N}} c_\alpha \nu^0_\alpha \right) + \mathcal{V}^{\mathrm{el}}_{(2)} \left(1 - \sum_{\alpha=1}^{\mathrm{N}} c_\alpha \nu^0_\alpha \right)^2 \right] \tag{16.22}$$

Thus, we obtain a perturbation expansion of the bulk modulus via

$$\begin{aligned} \mathcal{K}^{\mathrm{coarse}} &= \mathcal{K}^{\mathrm{coarse}}_{(0)} + \mathcal{K}^{\mathrm{coarse}}_{(1)} + \mathcal{K}^{\mathrm{coarse}}_{(2)} && (16.23) \\ &= \mathcal{V}^{\mathrm{el}}_{(0)} \cdot \frac{N_{\mathrm{A}}}{\nu^0} + \mathcal{V}^{\mathrm{el}}_{(1)} \cdot \frac{N_{\mathrm{A}}}{\nu^0} + \mathcal{V}^{\mathrm{el}}_{(2)} \cdot \frac{N_{\mathrm{A}}}{\nu^0} && (16.24) \\ &= \frac{\mathcal{V}^{\mathrm{el}}_{(0)}}{a^3} + \frac{\mathcal{V}^{\mathrm{el}}_{(1)}}{a^3} + \frac{\mathcal{V}^{\mathrm{el}}_{(2)}}{a^3} . && (16.25) \end{aligned}$$

Thus, in the incompressible limit where the non-trivial bulk moduli diverge, *i.e.* $\mathcal{V}^{\mathrm{el}}_{(1)} \to \infty$ and $\mathcal{V}^{\mathrm{el}}_{(2)} \to \infty$, a sufficient condition for that F^{el} remains finite is that the partial molar volumes are constant and that $\nu^0_\alpha \to \nu_\alpha$.

Part V

Conclusion and Outlook

In this final chapter, we give an outlook and discuss possible applications and extensions of our multi-scale framework. Furthermore, we discuss how our framework can be modified to account for additional bulk effects, and for additional microscopic effects.

By construction, our framework can easily be customized to incorporate additional effects into our theory, both in the bulk formulation, and in the generalized functional formulation. To see this, we restate here our model for the free energy density of the bulk, see eq. (5.153),

$$\rho\varphi_{\mathrm{H}}^{\mathrm{bulk}}{=}-\chi\varepsilon_0/2\cdot\mathbf{E}^2{+}\mathcal{K}/2\cdot(1-\sum_{\alpha=1}^{\mathrm{N}}\nu_\alpha^0 c_\alpha)^2{+}RT\sum_{\alpha=1}^{\mathrm{N}}c_\alpha\cdot\ln(c_\alpha/c\,){+}\rho\varphi_{\mathrm{H}}^{\mathrm{int}}. \tag{16.26}$$

which contains the template contribution $\rho\varphi_{\mathrm{H}}^{\mathrm{int}}$. This quantity can be used to customize our standard electrolyte model to specific applications. Via the constitutive equations, this energy term yields contributions both to the chemical potential (and to the stress tensor), where we account for such interactions via the activity coefficients $RT\ln(f_\alpha c) = \partial(\rho\varphi_{\mathrm{H}}^{\mathrm{int}})/\partial c_\alpha$ appearing in the non-standard thermodynamic factor $\mathit{TDF}_{\alpha\gamma} = \sum_{\beta=1}^{\mathrm{N}}(\delta_\alpha^\beta - \nu_\alpha c_\beta)\cdot[\delta_\beta^\gamma + \partial\ln(f_\beta c_0)/\partial\ln(c_\gamma/c_0\,)]$, *viz.*

$$\boldsymbol{\nabla}\mu_\alpha = RT\sum_{\gamma=1}^{\mathrm{N}}\mathit{TDF}_{\alpha\gamma}(\boldsymbol{\nabla}c_\gamma)/c_\gamma\, + \nu_\alpha\varrho_{\mathrm{F}}\mathbf{E} + \boldsymbol{\nabla}([\gamma+\eta]\boldsymbol{\nabla}\mathbf{v}) + \boldsymbol{\nabla}^2(\eta\mathbf{v}). \tag{16.27}$$

Likewise, non-local interactions can be added to our framework via a functional contribution $F^{\mathrm{int}}[\boldsymbol{\Upsilon}]$, as is described in chapter 8,

$$F[\Upsilon] = F^{\mathrm{int}}[\boldsymbol{\Upsilon}] + F^{\mathrm{b}}(\boldsymbol{\Upsilon}) = F^{\mathrm{int}}[\boldsymbol{\Upsilon}] + \int \mathrm{d}V\,\rho\varphi_{\mathrm{H}}^{\mathrm{bulk}}. \tag{16.28}$$

First, we discuss interesting applications / modifcations of our bulk electrolyte model.

Solvation effects can play an important role both for bulk transport effects, *e.g.* by altering the transport parameters, and in the EDL, *e.g.* altering the screening profile. These effects influence the number of microscopic realizations of a given macrostate.[271] Therefore, they yield an additional entropic contribution to the free energy. However, because we derive the entropy of mixing from the statistics, this implies that our naive approach based on an ideal gas must be modified when solvation is incorporated.

Our description for liquid electrolytes can be modified to account for visco-elastic materials, *e.g.* polymer based electrolyte mixtures.[141] In section 5.2.3 we introduced the unimodular deformation tensor as material variable, to account for such elastic effects. However, we did not include this contribution in our free energy model. There exist different energy models for such a contribution, *e.g.* the Odgen model.[402]

High temperature applications of molten salts and ILs, *e.g.* molten salt reactors,[403] solar power applications,[404] or the electrolytic production of metals, alloys or semiconductors[405] constitute another promising area of research for the application of our transport theory.

Finally, we discuss extensions of our framework by microscopic effects (see also our comment regarding canonical interaction models in the form of "twelve-six-potentials" of Lennard -Jones type in see chapter 11).

As shown above, see eq. (16.28), the generality of our framework offers the possibility to incorporate a wide range of non-local effects. In this work, we evaluated our description for the case of hardcore particles. Hence, our discuccion here focuses on microscopic effects which supplement our model for hardcore particles.

In the case of ILs near electrified interfaces, microscopic properties like ion asymmetry, ion geometry, polarization, and charge delocalization have a significant influence on the formation of the equilibrium structures.[364,406–409] However, since these properties result from the complex three dimensional configuration of the ions, a one dimensional approach is challenging, and needs simplifying assumptions on the symmetry of the system.

Apparently, our repulsive interaction model for hardcore particles scales with the extension of the ions. Here, we neglected self-interactions between the ions, which can be a bad approximation for neutral systems, and assumed symmetric ions. These restrictive assumptions can be easily relaxed to obtain a more refined description. Thereby, more microscopic details become accessible by our approach. However, such repulsive hardcore potentials do not describe higher order electrostatic effects which have typically a longer ranged attractive support. Such interactions play an important role in the force fields used in atomistic simulations, where they account for van-der-Waals effects, or for larger ions of complex geometry, *i.e.*, long alkyl chains.[353,354,385]

An alternative strategy to include non-local effects into our description is based on modified models for the linear dielectric relation between the electric field and the dielectric displacement. The introduction of non-local susceptibilities leads to a spatially varying dielectric function $\varepsilon_\mathrm{R}(x)$ appearing in E_el (see eq. (9.34)) and a direct coupling of the chemical potentials with the ion polarization.

However, such modifications will have an impact on our analytic analysis. Since both the gradient description and the analytical description depend strongly on these microscopic properties, it is an open question how such modifications influence the phase space of the screening profiles. One possible consequence is that the three energy scales which characterize the phase boundaries might transition from being scalars to being spatially varying field quantities. Also, the phase space, and the number of phase boundaries, might get more complex. This could result in the formation of higher-dimensional phase spaces with non-trivial boundaries, or "wash out" the phase boundaries as the energy scales get more diffuse.

We emphasis that the emergence of a three fold phase space in our analytical description is a consequence of the two perturbation modes $\tilde{\Gamma}^0_{+-}$ and $\tilde{\Gamma}^2_{+-}$, *i.e.* a consequence on the fact that we restricted our gradient approximation to the second order. However, it remains an open question how additional modes in this perturbation analysis influence the phase space of screening profiles.

Furthermore, our transport theory provides a dynamical description of electrolytes near electrified interfaces. Thus, it offers the possibility to study transport processes occurring in non-neutral electrochemical systems taking account for the formation of double layers, and chemical reactions. This includes, *e.g.* the influence of EDL-charging on the electrolyte performance, or the influence of the EDL structure on the electrode transfer kinetics.

However, real world electrochemical devices exhibit complex properties. These must be included in the modelling approach. For example, we assumed an ideally flat surface for the electrodes. This can be a bad approximation for many electrochemical systems due to the roughness of the interface,[410] which leads to strong entropic contributions. However, as it was shown in Ref. 411 such an influence on the EDL structure can also be described via the energy functional approach. We hypothesis that in our theory, such an entropical non-local energy contribution would alter the thermal energy scale E_{th}, see eq. (9.33). Since this energy scale is usually attributed to the disordering effect of entropy, the formation of crystalline phases might become suppressed at rougher surfaces, similar to increasing the temperature.

Part VI

Appendix

A Numerical Methods

In this chapter we discus numerical aspects which are relevant for performing computer simulations based on the transport theory. First, in appendix A.1 we briefly discuss the typcial structure of the transport equations. Next, in appendix A.2 we introduce our discretization scheme. In appendix A.3 we account for boundary conditions. Finally, in appendix A.4, we discuss the case of electroneutral cell simulations on macroscopic length scales, and, in appendix A.5, we focus on EDL simulations of charged electrolytes.

A.1 Numerical Implementation

In this work we use the method of finite elements and solve the transport equations numerically using matlab.

The differential equations appearing in our transport theory have a typical structure. For a material variable $\xi \in \boldsymbol{\Upsilon} = \{\Phi, \varrho_\mathrm{F}, c_3, \ldots, c_\mathrm{N}\}$, and a function of the material law $\mathcal{A}(\boldsymbol{\Upsilon})$ (see eqs. (5.244) and (5.245)),

$$\partial_t \xi = \boldsymbol{\nabla}\left(\mathbf{v}\cdot\xi\right) + \boldsymbol{\nabla}\left[\mathcal{A}(\boldsymbol{\Upsilon})\cdot\boldsymbol{\nabla}\xi\right]. \tag{A.1}$$

The quantities $\mathcal{A}(\boldsymbol{\Upsilon})\cdot\boldsymbol{\nabla}\xi$ are flux terms, *e.g.* $\boldsymbol{\mathcal{J}}_\mathrm{F}$ or $\mathbf{N}_\alpha$ (see eqs. (5.247) and (5.248)). The dynamical transport equations eq. (A.1) are supplemented by an algebraic equation for $\mathbf{v}$, or the Poisson equation (see eqs. (5.243) and (5.246))

$$\boldsymbol{\nabla}\mathbf{v} \propto \mathcal{A}(\boldsymbol{\Upsilon})\cdot\boldsymbol{\nabla}\xi, \qquad \text{and} \qquad 0 = \varrho_\mathrm{F}/\varepsilon_0\varepsilon_\mathrm{R} + \boldsymbol{\nabla}\left[1\cdot\boldsymbol{\nabla}\xi\ \right] \tag{A.2}$$

Because in our gradient description of the electrochemical double layer (see part III), higher order gradients of even type of the species concentrations appear, it suffices for the implementation of the spatial derivatives to focus on divergence operations of the form $\boldsymbol{\nabla}(\xi\cdot\mathbf{v})$, and on second order derivatives of the form $\boldsymbol{\nabla}[\mathcal{A}(\boldsymbol{\nabla}\xi)]$.

Altogether, the system of equations appearing in our transport theory takes the form of differential algebraic equations (DAEs),

$$\mathtt{M}(t,\xi)\cdot\partial_t\xi = f(t,\xi). \tag{A.3}$$

Here, `M` denotes the mass matrix, which is usually diagonal. The algebraic equations (*i.e.* the convection equation and the Poisson equation) lead to a singular mass matrix with the corresponding diagonal entries being zero, whereas the diagonal entries corresponding to the dynamical transport equations are one,

$$\mathtt{M} = \mathrm{diag}(1, \ldots, 1, 0; \ldots, 0). \tag{A.4}$$

A.2 Numerical Differentiation

In this section, we define our numerical grid, which we use in our implementation of the transport equations. For the spatial length L of there exists a continuous set of values $x \in I = [0; L]$, where $x = 0$ is the "left wall" of the grid, and $x = L$ is the "right wall" of the grid. We discretize the interval L for N grid points distributed homogeneously over L and define the constant grid separation length $\Delta x = L/N$. The first grid point is at $x = \Delta x/2$, followed by further N grid points mutually separated by the grid distance Δx. The last grid point (N-th grid point) is located at a distance $\Delta x/2$ left of the right wall, $x = L - \Delta x/2$. Next, we introduce a set of N non-dimensional positions $\tilde{x}_i$ assigned to the individual N grid points via

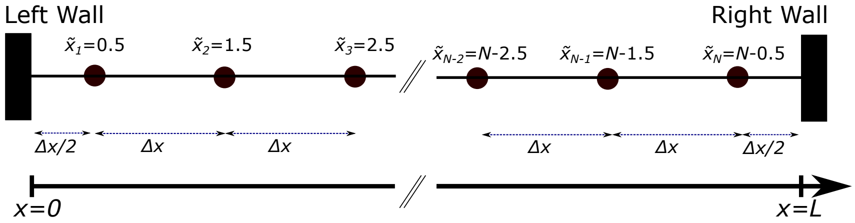

Figure A.1: Scheme of our numerical grid.

$$\tilde{x}_1 = 1/2\,, \qquad \text{and} \qquad \tilde{x}_i = \tilde{x}_1 + (i-1)\,, \qquad \text{for } i \in \{1; N\}. \tag{A.5}$$

The space of grid points is $\tilde{X}^N = \{1/2; 3/2; \ldots; N - 1/2\}$ (*i.e.*$\tilde{x}_i \in \tilde{X}^N$). See fig. A.1 for an illustration of our set up. Thus, the positions of the N grid points in the physical space are

$$x(\tilde{x}_i) = \tilde{x}_i \cdot \Delta x = \Delta x/2 \, + (i-1) \cdot \Delta x. \tag{A.6}$$

We assign to each continuous physical variable a value at each grid point $\tilde{x}_i$. Because the grid is similar to a metric on the abstract space of variables, we use the discretization of the grid to perform operations between neighbouring grid points, *e.g.* subtract or add values of the variables at neighbouring grid points. To any

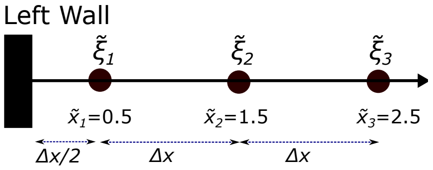

Figure A.2: Scheme of the discretized system variables on the numerical grid.

variable ξ, we assign N values $\tilde{\xi}_i = \xi(x_i)$ at the different grid points $\tilde{x}_1, \dots, \tilde{x}_N$. Note that the array $\tilde{\boldsymbol{\xi}} = (\tilde{\xi}_i) \in \tilde{X}^N$ is an element of the space $\tilde{X}^N$ (see fig. A.2 for an illustration). In order to do calculus on the grid, *i.e.* calculate differences and derivatives, we introduce $N+1$ grid walls $\tilde{y}_j = j-1$ for $j \in \{1; N+1\}$. Hence, the grid walls evaluated in the physical space have coordinates $y_1 = 0$, $y_j = (j-1)\cdot\Delta x$ for $1 < j \leq N$ and $y_{N+1} = L$. For all but the last grid wall, $\tilde{y}_i|_{i\leq N} = \tilde{x}_i - 1/2$. Similar to the set of grid points, we define the space of grid walls by $\tilde{Y}^{N+1} = \{0; 1; \dots; N\}$. See fig. A.3 for an illustration.

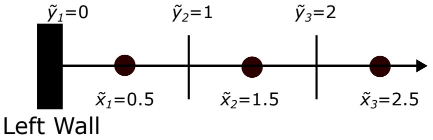

Figure A.3: Illustration of the compartment boundaries, *i.e.* the grid walls, between neighbouring grid points.

To calculate numerical derivatives with respect to the grid, we introduce a mapping from the space of grid points to the space of grid walls (these derivatives correspond to forces $\boldsymbol{\nabla}\xi$) and define the first-order finite difference approximation

$$\texttt{grad}: \tilde{X}^N \to \tilde{Y}^N, \qquad \texttt{Force} = \texttt{grad}\,\tilde{\boldsymbol{\xi}} = \Big[0, (\texttt{diff}\,\tilde{\boldsymbol{\xi}})_i/\Delta x, 0\Big] \tag{A.7}$$

where the differential is defined by $(\texttt{diff}\,\tilde{\boldsymbol{\xi}})_i = \tilde{\xi}_i - \tilde{\xi}_{i-1}$ for $2 \leq i \leq N$. Here, we have set the force-values at the left and right wall to zero. Below, we show that this assumption (if not modified by specific boundary conditions) corresponds to the assumption of no-fluxes through the boundaries. See fig. A.4 for an illustration.

We use a simple routine to solve differential equations: the computer solves for values at the grid points defined as above; we use these values, and compare how an object changes from grid point to grid point and compute the spatial derivatives of the variables at the grid walls.

Next, we construct an operator `divAgrad` for computing second order derivatives

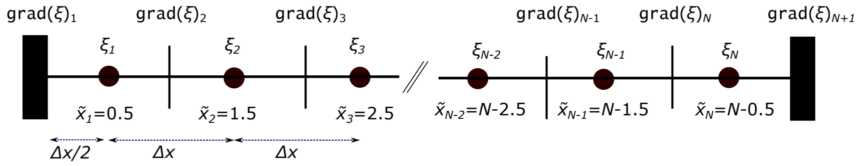

Figure A.4: Scheme of the discretized system variables on the numerical grid.

via $\boldsymbol{\nabla}(\mathcal{A}[\boldsymbol{\nabla}\tilde{\xi}])$, *i.e.* fluxes. We follow the same strategy for `grad`, and first evaluate the product of the variable $\tilde{\boldsymbol{\mathcal{A}}}$ and the force $\texttt{grad}\,\tilde{\boldsymbol{\xi}}$, and then use the forward difference approximation to evaluate the spatial variation between two neighbouring grid walls for the intermediate grid point. However, note that the grid variable corresponding to $\mathcal{A}$ is defined at the grid pints, *i.e.* $\tilde{\boldsymbol{\mathcal{A}}} \in \tilde{X}^N$, whereas the numerical derivative of $\tilde{\boldsymbol{\xi}}$ is defined at the grid walls, *i.e.* $\texttt{grad}\,\tilde{\boldsymbol{\xi}} \in \tilde{Y}^{N+1}$. We solve this and calculate averaged values for $\tilde{\mathcal{A}}_i$ at the grid walls via the harmonic mean

$$\texttt{Wall}\,\tilde{\boldsymbol{\mathcal{A}}} = [0; 2\cdot\left(1/\tilde{\mathcal{A}}_i + 1/\tilde{\mathcal{A}}_{i-1}\right)^{-1}; 0], \tag{A.8}$$

where $2 \leq i \leq N$. In eq. (A.8) we assumed that the topological spaces $\tilde{X}^N$ and $\tilde{Y}^{N+1}$ of the grid points and grid walls have additional structure similar to normed vector spaces, *i.e.* an inner product. We define inner products between two elements of $\tilde{X}^N$ and between two elements of $\tilde{Y}^{N+1}$ by pointwise multiplication, and obtain the flux map $\texttt{FLUX}\ \tilde{Y}^{N+1} \times \tilde{Y}^{N+1} \to \tilde{Y}^{N+1}$ via (where $i \in \{2; \ldots, N\}$)

$$\texttt{FLUX}[\tilde{\boldsymbol{\mathcal{A}}}, \tilde{\boldsymbol{\xi}}] = \texttt{Wall}\,\tilde{\boldsymbol{\mathcal{A}}}\cdot\texttt{grad}\,\tilde{\boldsymbol{\xi}} = [0; (\texttt{Wall}\,\tilde{\boldsymbol{\mathcal{A}}}\cdot\texttt{grad}\,\tilde{\boldsymbol{\xi}})_i; 0] \tag{A.9}$$

Finally, we define "divAgrad"-operator which calculates the numerical derivative of the flux quantity $\texttt{FLUX} = \texttt{Wall}\,\tilde{\boldsymbol{\mathcal{A}}}\cdot\texttt{grad}\,\tilde{\boldsymbol{\xi}}$ at the grid points, *i.e.* the map from the grid walls to the grid points, $\texttt{divAgrad}:\ \tilde{Y}^N \to \tilde{X}^N$, such that (where $2 \leq i \leq N$)

$$\begin{aligned}\texttt{divAgrad}\,\texttt{FLUX}[\tilde{\boldsymbol{\xi}}, \tilde{\boldsymbol{\mathcal{A}}}] &= \texttt{diff}\,\texttt{FLUX}[\tilde{\boldsymbol{\xi}}, \tilde{\boldsymbol{\mathcal{A}}}]/\Delta x = \texttt{diff}[\texttt{Wall}\,\tilde{\boldsymbol{\mathcal{A}}}\cdot\texttt{grad}\,\tilde{\boldsymbol{\xi}}]./\Delta x = \\ &= [\texttt{FLUX}_2/\Delta x; (\texttt{diff}\,\texttt{FLUX})_i/\Delta x; -\texttt{FLUX}_N/\Delta x;].\end{aligned} \tag{A.10}$$

A.3 Boundary Conditions

In this section, we correct the operations `grad`, `Wall`, `FLUX` and `divAgrad`, introduced above, by setting boundary conditions (BCs) at the left wall and at the right wall.

Here, Σ_ξ^{left} and $\Sigma_\xi^{\text{right}}$ constitute BCs for a given variable ξ at the and right wall, *i.e.* at $x = 0$ and at $x = L$ (whereas ξ is defined at the grid points). Similar BCs exist for

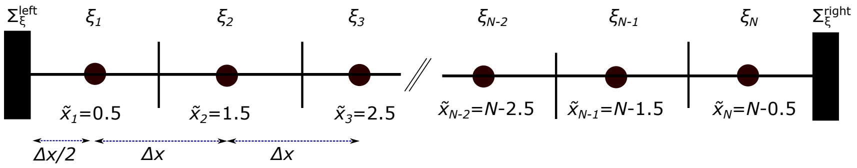

Figure A.5: Illustration of the implementation of boundary conditions at the left and right wall.

the functions $\mathcal{A}$ appearing as prefactors in the transport equations, $\Sigma_{\mathcal{A}}^{\text{left}}$, and $\Sigma_{\mathcal{A}}^{\text{right}}$ and for the fluxes, $\Sigma_{\texttt{FLUX}}^{\text{left}}$ and $\Sigma_{\texttt{FLUX}}^{\text{right}}$. However, in this case, the BCs and the first and last value of the flux are located at the same position. Figure A.5 illustrates the variables at the grid points and the corresponding boundary conditions. We show that these BCs lead to corrections in the quantities `grad`, `Wall`, `FLUX` and `divAgrad`.

Our definition for the first order numerical derivative above, eq. (A.7), is based on subtracting values at neighbouring grid points, which yields a differential defined at the corresponding compartment wall. Because, this procedure does not apply to the first and last value of the derivative, located at the left and right wall, we define the differentials at the left and right wall separately,

$$\left(\texttt{grad}\,\tilde{\boldsymbol{\xi}}\right)_1 = 2\left(\tilde{\xi}_1 - \Sigma_\xi^{\text{left}}\right)/\Delta x, \quad \text{and} \quad \left(\texttt{grad}\,\tilde{\boldsymbol{\xi}}\right)_{N+1} = 2(\Sigma_\xi^{\text{right}} - \tilde{\xi}_N)/\Delta x. \tag{A.11}$$

The approximations for the left and right walls lead to corrections,

$$\texttt{grad}_{\text{BC}}\,\tilde{\boldsymbol{\xi}} = \left[\left(\tilde{\xi}_1 - \Sigma_{\boldsymbol{\xi}}^{\text{left}}\right)/\Delta x/2\,;\texttt{diff}\,\tilde{\boldsymbol{\xi}}/\Delta x;\left(\Sigma_{\boldsymbol{\xi}}^{\text{right}} - \tilde{\xi}_N\right)/\Delta x/2\right]. \tag{A.12}$$

Next, we implement BCs for functions $\mathcal{A}$ fluxes at the left and right wall. This leads to corrections in the corresponding averaged quantity located at the grid walls,

$$\texttt{Wall}_{\text{BC}}\,\tilde{\boldsymbol{\mathcal{A}}} = \left[\Sigma_{\mathcal{A}}^{\text{left}};2\cdot\left(1/\tilde{\mathcal{A}}_i + 1/\tilde{\mathcal{A}}_{i-1}\right)^{-1};\Sigma_{\mathcal{A}}^{\text{right}}\right]. \tag{A.13}$$

Furthermore, the BCs for ξ and $\mathcal{A}$ lead to corrections in the fluxes. According to the definition $\texttt{FLUX}[\tilde{\boldsymbol{\xi}},\tilde{\boldsymbol{\mathcal{A}}}] = \texttt{Wall}\,\tilde{\boldsymbol{\mathcal{A}}}\cdot\texttt{grad}\,\tilde{\boldsymbol{\xi}}$, see eq. (A.9), this yields

$$\texttt{FLUX}_{\text{BC}}[\tilde{\boldsymbol{\mathcal{A}}},\tilde{\boldsymbol{\xi}}] = \left[\Sigma_{\mathcal{A}}^{\text{left}}\cdot\frac{\tilde{\xi}_1 - \Sigma_\xi^{\text{left}}}{\Delta x/2};\ \left(\texttt{Wall}\,\tilde{\boldsymbol{\mathcal{A}}}\cdot\texttt{grad}\,\tilde{\boldsymbol{\xi}}\right)_i;\ \Sigma_{\mathcal{A}}^{\text{right}}\cdot\frac{\Sigma_\xi^{\text{right}} - \tilde{\xi}_N}{\Delta x/2}\right]. \tag{A.14}$$

where $i \in \{2;\ldots,N\}$. Finally, these corrections influence our definition for the operation `divAgrad`, see eq. (A.10). Putting all together, we find

$$\mathtt{divAgrad}_{\mathsf{BC}}\,\mathtt{FLUX} = \left[\frac{\mathtt{FLUX}_2}{\Delta \mathsf{x}} - \frac{\Sigma_{\mathcal{A}}^{\mathsf{left}}(\tilde{\xi}_1 - \Sigma_{\xi}^{\mathsf{left}})}{(\Delta \mathsf{x})^2/2};\ \frac{(\mathtt{diff\,FLUX})_i}{\Delta \mathsf{x}};\right.$$
$$\left.\frac{\Sigma_{\mathcal{A}}^{\mathsf{right}}(\Sigma_{\xi}^{\mathsf{right}} - \tilde{\xi}_{\mathsf{N}})}{(\Delta \mathsf{x})^2/2} - \frac{\mathtt{FLUX}_{\mathsf{N}}}{\Delta \mathsf{x}}\right]. \quad (A.15)$$

Alternatively, in some systems there exist direct BCs for the fluxes $\Sigma_{\mathtt{FLUX}}^{\mathsf{left}}$ and $\Sigma_{\mathtt{FLUX}}^{\mathsf{right}}$. In this case, the fluxes have the form

$$\mathtt{FLUX}_{\mathsf{BC}}[\tilde{\boldsymbol{\mathcal{A}}}, \tilde{\boldsymbol{\xi}}] = \left[\Sigma_{\mathtt{FLUX}}^{\mathsf{left}};\ \left(\mathtt{Wall}\,\tilde{\boldsymbol{\mathcal{A}}} \cdot \mathtt{grad}\,\tilde{\boldsymbol{\xi}}\right)_i;\ \Sigma_{\mathtt{FLUX}}^{\mathsf{right}}\right]. \quad (A.16)$$

where $i\in\{2;\ldots,\mathsf{N}\}$. The second order derivatives containing flux BCs are

$$\mathtt{divAgrad}_{\mathsf{BC}}\,\mathtt{FLUX}{=}1/\Delta \mathsf{x}\cdot[\mathtt{FLUX}_2 - \Sigma_{\mathtt{FLUX}}^{\mathsf{left}}; \mathtt{diff\,FLUX})_i; \Sigma_{\mathtt{FLUX}}^{\mathsf{left}} - \mathtt{FLUX}_{\mathsf{N}}]. \quad (A.17)$$

For completeness, we restate the corrections `grad`, `Wall`, `FLUX` and `divAgrad`,

$$\left(\mathtt{grad}_{\mathsf{BC}}\,\tilde{\boldsymbol{\xi}}\right)_1 = \left(\mathtt{grad}\,\tilde{\boldsymbol{\xi}}\right)_1 - 2\Sigma_{\boldsymbol{\xi}}^{\mathsf{left}} - \tilde{\xi}_1/\Delta \mathsf{x}, \quad (A.18)$$

$$\left(\mathtt{grad}_{\mathsf{BC}}\,\tilde{\boldsymbol{\xi}}\right)_{\mathsf{N}+1} = \left(\mathtt{grad}\,\tilde{\boldsymbol{\xi}}\right)_{\mathsf{N}+1} - 2\tilde{\xi}_{\mathsf{N}} - \Sigma_{\boldsymbol{\xi}}^{\mathsf{right}}/\Delta \mathsf{x}, \quad (A.19)$$

$$(\mathtt{divAgrad}_{\mathsf{BC}}\,\mathtt{FLUX})_1 = (\mathtt{divAgrad\,FLUX})_1 - 2\Sigma_{\mathcal{A}}^{\mathsf{left}}(\tilde{\xi}_1 - \Sigma_{\xi}^{\mathsf{left}})/(\Delta \mathsf{x})^2, \quad (A.20)$$

$$(\mathtt{divAgrad}_{\mathsf{BC}}\,\mathtt{FLUX})_{\mathsf{N}} = (\mathtt{divAgrad\,FLUX})_{\mathsf{N}} - 2\Sigma_{\mathcal{A}}^{\mathsf{left}}(\tilde{\xi}_{\mathsf{N}} - \Sigma_{\xi}^{\mathsf{right}})/(\Delta \mathsf{x})^2. \quad (A.21)$$

A.4 Numerical Aspects of Cell Simulations

Because the electrolyte is in electroneutral state, the system of equations for bulk transport consists of dynamical transport equations which have the form $\partial\xi = \boldsymbol{\nabla}(\mathcal{A}\cdot\boldsymbol{\nabla}\xi)$, supplemented by the electroneutrality condition $0 = \boldsymbol{\nabla}(\sum_A \boldsymbol{\nabla}\xi_A)$ and by the convection equation $\boldsymbol{\nabla}\mathbf{v} \propto \boldsymbol{\nabla}(\sum_A \boldsymbol{\nabla}\xi_A)$. For the convection, there arises the problem that the left side of the convection equation is evaluated at the grid walls, whereas the right side is evaluated at the grid points. We tackle this issue and homogenize the quantity $\boldsymbol{\nabla}\mathbf{v}$ from the grid walls to the grid points. However, the solution to this differential equation is fixed only up to an offset. To compensate for the numerical deficiencies, we set no-flux Bcs at the left wall, and allow for a convective flux at the right wall. Another approach is to introduce a potential ζ such that $\boldsymbol{\nabla}\mathbf{v} = \boldsymbol{\nabla}\cdot\boldsymbol{\nabla}\zeta$. This approach has the disadvantage that the BCs for the convection potential must be chosen carefully. We use flux BCs for the quantities $\boldsymbol{\mathcal{J}}_{\mathrm{F}}$ and $\boldsymbol{\mathfrak{N}}_\alpha$ which are given by chemical reactions occurring at the interface, and couple the liquid phase of the electrolyte to the solid phase of the active particles via a

Butler-Volmer approach. We initiate cell operation by applying an external current via the BCs at the left and right wall (galvanostatic discharging / charging), which pushes the system out of it's equilibrium state. To improve the numerical stability, we ramp the current from zero up to it's terminal value (where the ramping time is chosen to be few per-cent of the discharge time).

A.5 Numerical Aspects of EDL Simulations

The dynamical transport equations for the EDL description of binary ILs consist of the Poisson equation and one transport equation for the fluxes (see chapter 9).

Because the grid shall resolve the particles of size a (typically, $a = 0.7\,\mathrm{nm}$), the step size of the grid must be chosen very small. However, the system length L should be larger than the typical extension of the EDL, *i.e.* a few nano-meters. Thus, the number of grid pints is a trade-off between L and the ion size because if L is very long (*e.g.* $\mathcal{O}(L) = 60\,\mathrm{nm}$), then the numerical costs are very large due to the small size of the ions.

There exist two differing length scales in the EDL description; a contribution from the bulk description of the EDL leads to screening profiles which are usually a few Ångstrom thick, whereas taking account for hardcore particles leads to EDL structures which can easily extend over some ten nanometers. This discrepancy implies that the system of differential equations exhibits a large degree of stiffness. Partly, it helps implementing the non-dimensionalized system of equations (see section 9.2).

Here, we consider the case of binary ILs near electrified interfaces, either in a half cell set-up, or in a full cell cell set-up. In both set-ups, we assign BCs for the electric potential at the left and at the right wall. At the left wall, we apply the external interface potential $\Delta\phi$. Since electric potentials are continuous across interfaces, we set $\Sigma_{\Phi}^{\mathsf{left}} = \Delta\phi$. In the case of a half-cell set-up, we erect electroneutral BCs at the right wall by setting $\Sigma_{\Phi}^{\mathsf{right}}|_{\mathrm{half\,cell}} = 0$. In contrast, in a full cell set-up, we apply $\Sigma_{\Phi}^{\mathsf{right}}|_{\mathrm{full\,cell}} = -\Delta\phi$. To improve the numerical stability, we ramp the BCs at the left and right wall from zero up to it's terminal value. In contrast, we assign no-flux BCs for the variable ϱ_{F} at the left and right wall, $\Sigma_{\mathtt{FLUX}[\varrho_{\mathrm{F}}]}^{\mathsf{left}}=\Sigma_{\mathtt{FLUX}[\varrho_{\mathrm{F}}]}^{\mathsf{right}}=0$.

B Covariance, Invariance and Symmetry

> As far as I see, all a priori statements in physics have their origin in symmetry.
>
> Hermann Weyl

B.1 Introduction

Symmetry principles play a fundamental role in all physical theories.[412].

Usually, symmetry is imposed in axiomatic form by demanding that physical laws are invariant under coordinate transformations.[413] In this sense, symmetry acts as constraint on the structure of the equations of motions. For this reason, physical theories are oftenly expressed using tensor fields, which are mathematical objects defined entirely by their transformation behaviour.[414,415] However, "invariance" can have two distinct meanings, which are both related to each other, but refer to different types of symmetry. In a form-invariant ("covariant") description, the relation between values of observables measured by different observers remains the same under coordinate transformations, although the values themselves usually are different. In this work, we are mainly concerned with the principle of general covariance, which demands that physical laws must be form-invariant under arbitrary coordinate transformations.[416] In contrast, in an invariant description, not only the relation among observables remains the same but also the precise values. Thus, "invariance" is a more restrictive type of symmetry. Both concepts can be probed under coordinate transformations with respect to spacetime symmetries.

In many cases, general covariance is relaxed to covariance under specific types of transformations, comprised in specific symmetry-groups. Representations of such covariance groups designate admissible frames of reference, which are related via coordinate transformations comprised in the covariance group.

The main goal of this chapter is to derive the common covariance group of electromagnetic theory and mechanics, which is mandatory for the unification of the two theories. However, this is a non-trivial task because the symmetries of electromagnetic theory emerge naturally in the fourdimensional spacetime structure of special relativity. In contrast, we formulate our transport theory in the three dimensional Euclidean description of classical mechanics. As consequence, we must stick to a limiting case ("classical limit"), which allows the identification of a three-dimensional covariance group with respect to four-dimensional coordinate transformations.

We structure this chapter as follows. First, in appendix B.2 we introduce the necessary mathematical tools and give a precise definition for symmetry transformations via the tensor-formalism. Next, in appendix B.3 we apply this formalism and state the covariant formulation of electrodynamics in fourdimensional spacetime, which emerges naturally from special relativity. We show that the resulting covariance-group is comprised by Lorentz transformations. In appendix B.4 we highlight the power of this formalism and show that the set of internal symmetries completely determines the electromagnetic energy-momentum tensor. Next, in appendix B.5, we discuss covariance of classical mechanics with respect to Euclidean-/ and Galilean transformations in the context of mechanics. In appendix B.6, we focus on the role of symmetry in the framework of rational thermodynamics. Finally, in appendix B.7, we obtain the common covariance group for the unification of mechanics and electrodynamics.

B.2 Tensor Formalism

In this section, we introduce the mathematical tools which are necessary to discuss symmetries.

Differential calculus is the basic tool for the dynamical description of a physical system. However, this presupposes the existence of a differential structure ("smooth manifold"), which represents the geometric set up of the system. For this purpose, we assign local coordinates to overlapping regions F on these structures via multilinear maps, *i.e.* $\mathsf{rank}(k, l)$-tensors,

$$\mathcal{T} : \underbrace{V^* \times \ldots \times V^*}_{k} \times \underbrace{V \times \ldots \times V}_{l} \rightarrow \mathbb{R}. \tag{B.1}$$

Smooth transitions, *i.e.* coordinate transformations, between overlapping regions F ensure a consistent description of the complete system out of the local representations. The complete description is covariant, if these transitions leave the equations of motion form-invariant. In eq. (B.1), V is the local n-dimensional tangent vector space, which is dual to V^*. The vector spaces V, and V^*, are spanned by local basis vectors $\{\hat{\mathbf{e}}_B\}$, and $\{\hat{\mathbf{e}}^A\}$. Hence, the local tensor representation is

$$\mathcal{T} = \sum_{B_1,\dots,A_l}^{\mathsf{dim}(V)} \mathcal{T}^{B_1\dots B_k}{}_{A_1\dots A_l}\,\hat{\mathbf{e}}_{B_1}\otimes\dots\otimes\hat{\mathbf{e}}_{B_k}\otimes\hat{\mathbf{e}}^{A_1}\dots\otimes\hat{\mathbf{e}}^{A_l}. \tag{B.2}$$

Different local expansions in overlapping frames F and F' are related via the tensor-transformation law,

$$\begin{aligned}\mathcal{T}'^{B_1\dots B_k}{}_{A_1\dots A_l} = \left|\det\left(\frac{\partial x}{\partial x'}\right)\right|^p \cdot \sum_{\substack{D_1,\dots,D_k,\\ C_1,\dots,C_l=1}}^{\mathsf{dim}(V)} \frac{\partial x'^{B_1}}{\partial x^{D_1}}\cdot\dots\cdot\frac{\partial x'^{B_k}}{\partial x^{D_k}}\cdot\frac{\partial x^{C_1}}{\partial x'^{A_1}}\cdot\dots\cdot \\ \cdot\frac{\partial x^{C_l}}{\partial x'^{A_l}}\cdot\mathcal{T}^{D_1\dots D_k}{}_{C_1\dots C_l},\end{aligned} \tag{B.3}$$

where $\mathbf{x}$ and $\mathbf{x}'$ are coordinates of volume-elements in F and F'. $\mathcal{T}$ is classified according to the power p of the Jacobian determinant $\det(\partial x/\partial x')$, and is called tensor-density of weight p. In particular, tensor-densities of weight $p = 1$ ($p = 0$) are called axial tensors (absolute tensors).

The tensor transformation law eq. (B.3) allows to formulate a precise definition for covariance. An equation of motion is covariant (form-invariant) under coordinate transformations, if all terms appearing on both sides of the equation have the same tensor-degree and tensor-weight. The set of all such transformations forms the covariance group. An equation of motion is generally covariant, if it is covariant under any coordinate transformation. Tensor-degree and tensor-weight can both be probed using eq. (B.3). If a generally covariant equation is valid in one frame, then it is valid in any frame.

Furthermore, we define symmetry (invariance of values) under coordinate transformation $\mathbf{x} \to \mathbf{x}'$ via the constraint $\partial x'^j/\partial x^i = \delta^j_i$. The set of all such transformations determines the symmetry group. In representation theory, transformation matrices constitute the linearized symmetry groups.[417] By construction, any symmetry group for an equation of motion is also a covariance group, whereas the opposite is not true.

B.3 Covariant Formulation of Electrodynamics

In this section, we discuss the symmetries of the electromagnetic theory in four dimensions.

For completeness, we briefly review the “classical” formulation of electromagnetism in three dimensions, comprised in the Maxwell equations

$$\boldsymbol{\nabla}\mathbf{B} = 0, \qquad \partial_t\mathbf{B} + \boldsymbol{\nabla}\wedge\mathbf{E} = 0, \tag{B.4}$$

$$\boldsymbol{\nabla}\mathbf{D}_\mathrm{T} = \varrho_\mathrm{T}, \qquad \partial_t\mathbf{D}_\mathrm{T} - \boldsymbol{\nabla}\wedge\mathbf{H}_\mathrm{T} = -\mathbf{j}_\mathrm{T}. \tag{B.5}$$

Here, the index "T" refers to the total of all charges present in the system. In section 5.2 we present a constitutive model, in which we split ϱ_T and $\mathbf{j}_\mathrm{T}$ into so-called "free" and "polarized/magnetized" parts.

In our framework, we interpret the electromagnetic fields $\mathbf{E}, \mathbf{B}$ appearing in the homogeneous Maxwell equations, eq. (B.4), and the charge-current densities $\varrho_\mathrm{T}, \mathbf{j}_\mathrm{T}$, appearing in the inhomogeneous Maxwell equations, eq. (B.5), as independent ("pimary") variables. In contrast, the potentials $\mathbf{D}_\mathrm{T}$, and $\mathbf{H}_\mathrm{T}$ are derived quantities, which are determined by $\varrho_\mathrm{T}, \mathbf{j}_\mathrm{T}$. The charge-current densities $\varrho_\mathrm{T}, \mathbf{j}_\mathrm{T}$ satisfy charge conservation,

$$\partial_t\varrho_\mathrm{T} + \boldsymbol{\nabla}\mathbf{j}_\mathrm{T} = 0. \tag{B.6}$$

Of course, the system of electromagnetic eqs. (B.4) and (B.5) is under-determined and must be supplemented by closure relations. Below, we show that such closure-relations are deeply connected to the fourdimensional formulation of electromagnetism.

We describe the Minkowski spacetime $(\boldsymbol{\eta}, \mathbb{R}^4)$ by the flat metric tensor field $\boldsymbol{\eta} = \mathrm{diag}(-1, 1, 1, 1)$ (such that $\det\boldsymbol{\eta} = -1$), and assign $\mathbb{R}^4$ with global four-dimensional spacetime coordinates $x^A = (ct, x^1, x^2, x^3) = (ct, x^i)$, where c is the vacuum-speed of light. We use the convention that capital Latin letters refer to four-vectors, in contrast to small Latin letters referring to spatial components in $\mathbb{R}^3$. According to eq. (B.3), the metric tensor transforms via

$$\eta'^{AB} = \partial x'^A/\partial x^C \cdot \partial x'^B/\partial x^D \cdot \eta^{CD}, \tag{B.7}$$

whereas the metric determinant transforms via

$$\det(\boldsymbol{\eta}') = \left[\det(\partial x'/\partial x)\right]^2 \cdot \det(\boldsymbol{\eta}). \tag{B.8}$$

The metric structure also determines the four-dimensional derivative operator

$$\mathrm{div} = (\partial_A) = (1/c \cdot \partial_t, \boldsymbol{\nabla}) \tag{B.9}$$

associated to the coordinates x^A. In this description, charge conservation, eq. (B.6), becomes $\mathrm{div}\, s = 0$, where $s = (c\varrho_\mathrm{T}, \mathbf{j}_\mathrm{T})$ is the relativistic four-potential comprising the charge density and the electric current. Thus, s is conservative, and, therefore, there exists an antisymmetric matrix $f(\mathbf{D}_\mathrm{T}, \mathbf{H}_\mathrm{T})$, such that $\mathrm{div}\, f = s$.[81] In the same rationale, the four-dimensional generalization of Faraday's law suggests the existence of an antisymmetric, closed matrix $F(\mathbf{E}, \mathbf{B})$,[81] satisfying $\mathrm{d}F = 0$.[418] (Since

F obeys the Bianchi-identity, it is locally exact (Poincaré Lemma), *i.e.* there exists a four-potential $\mathcal{A} = (\Phi/c\,, A^i)$, such that $F = \mathrm{d}\mathcal{A}$.[419] Here, Φ is the Coulomb-potential, and $\mathbf{A}$ is the magnetic vector-potential.[254] In the field-theoretic description of quantum-electrodynamics, $\mathcal{A}$ is the $\mathcal{U}(1)$ gauge-field of the covariant spin-1 Lagrange-function.[412]) The quantities f and F are differential two-forms,[419] and have canonical matrix representation[376]

$$F_{AB} = \begin{pmatrix} 0 & -E_1/c & -E_2/c & -E_3/c \\ E_1/c & 0 & B^3 & -B^2 \\ E_2/c & -B^3 & 0 & B^1 \\ E_3/c & B^2 & -B^1 & 0 \end{pmatrix}, \tag{B.10}$$

and

$$f^{AB} = \begin{pmatrix} 0 & cD^1_{\mathrm{T}} & cD^2_{\mathrm{T}} & cD^3_{\mathrm{T}} \\ -cD^1_{\mathrm{T}} & 0 & H_{\mathrm{T};3} & -H_{\mathrm{T};2} \\ -cD^2_{\mathrm{T}} & -H_{\mathrm{T};3} & 0 & H_{\mathrm{T};1} \\ -cD^3_{\mathrm{T}} & H_{\mathrm{T};2} & -H_{\mathrm{T};1} & 0 \end{pmatrix}. \tag{B.11}$$

Obviously, $F_{i0} = E_i/c\,,\ F_{ij} = \epsilon_{ijk}B^k,\ f^{0i} = cD^i_{\mathrm{T}}$, and $f^{ij} = \epsilon^{ijk}H_{\mathrm{T};k}$, which can be solved for $H_{\mathrm{T};m} = \epsilon_{mij}f^{ij}$, by multiplication with ϵ_{mij}, and using the identity $\epsilon_{mij}\epsilon^{ijk} = \delta^k_m$. Thus, in this description, $f(\mathbf{D}_{\mathrm{T}}, \mathbf{H}_{\mathrm{T}})$ comprises the matter-related potentials, whereas $F(\mathbf{E}, \mathbf{B})$ comprises the electromagnetic fields.[420] In components, the four dimensional Maxwell equations $\operatorname{div} f = s$ and $\mathrm{d}F = 0$ read

$$\epsilon^{ABCD}\partial_B F_{CD} = 0, \tag{B.12}$$

and

$$\partial_B f^{AB} = s^A, \tag{B.13}$$

Equation (B.12) reproduces the two homogeneous Maxwell equations $0 = \boldsymbol{\nabla}\mathbf{B}$ and $0 = \partial_t\mathbf{B} + \boldsymbol{\nabla} \wedge \mathbf{E}$, whereas eq. (B.13) reproduces both inhomogeneous Maxwell equations, $\varrho_{\mathrm{T}} = \boldsymbol{\nabla}\mathbf{D}_{\mathrm{T}}$ and $\mathbf{j}_{\mathrm{T}} = -\partial_t\mathbf{D}_{\mathrm{T}} + \boldsymbol{\nabla} \wedge \mathbf{H}_{\mathrm{T}}$.

From charge invariance follows that F is an absolute tensor, and that f and s are tensor densities of weight one,[81,82,421]

$$F'_{CD} = \frac{\partial x^A}{\partial x'^C}\frac{\partial x^B}{\partial x'^D}F_{AB},\ f'^{CD} = J \cdot \frac{\partial x'^C}{\partial x^A}\frac{\partial x'^D}{\partial x^B}f^{AB},\ s'^C = J \cdot \frac{\partial x'^C}{\partial x^A}s^A. \tag{B.14}$$

where $J = |\det(\partial x/\partial x')|$. Because, the tensor-rank and the tensor-weight of these quantities agree on both sides, the relativistic Maxwell eqs. (B.12) and (B.13) are covariant under coordinate transformations of type eq. (B.3).[82,415]

However, due to the dangling index "A" on both sides of eqs. (B.12) and (B.13), they are not invariant.[422,423] Thus, distinct observers measure different components, whereas they agree upon the structure how the components are related to each other (via eqs. (B.12) and (B.13)). Unfortunately, this peculiarity is often misquoted in the literature,[82,140,141] where the covariant equations are imprecisely called invariant. However, a clear distinction between both concepts becomes mandatory, when we discuss the unification of mechanics and electromagnetics via the Maxwell-Lorentz aether relations.

Bcause eqs. (B.12) and (B.13) are underdetermined, they are closed by covariant constitutive equations $f(F)$ ("Maxwell-Lorentz aether relations"),[82,418,424] which couple F and f, *i.e.* the electromagnetic fields $\mathbf{E}, \mathbf{B}$ and the electromagnetic potentials $\mathbf{D}_\mathrm{T}, \mathbf{H}_\mathrm{T}$. These couplings $f(F)$ connect mechanics with electromagnetism and are mandatory for their unification.

Because the field strengths f and F transform differently (see eq. (B.14)), the constitutive equations $\mathbf{D}_\mathrm{T}(\mathbf{E}, \mathbf{B})$ and $\mathbf{H}_\mathrm{T}(\mathbf{D}_\mathrm{T}, \mathbf{B})$, which follow from the covariant coupling $f(F)$, are not covariant, *i.e.* frame-dependent.[81] Here, we restrict to a linear coupling $f = \boldsymbol{\chi} \cdot F$, where the rank-four tensor $\boldsymbol{\chi}$ is independent of f and F. Due to antisymmetry of f and F, this coupling becomes $f^{AB} = \chi^{ACBD} F_{CD} = (\chi^{AjB0} - \chi^{A0Bj}) E_j / c + \chi^{AjBk} \epsilon_{jkl} B^l$, where

$$\chi^{0j0k} = \chi^{0j00} - \chi^{000j} = 0, \tag{B.15}$$

$$(\chi^{0jmk} + \chi^{0j0k}) \epsilon_{jkl} = (\chi^{mjnk} + \chi^{njmk}) \epsilon_{jkl} = 0 \tag{B.16}$$

$$\chi^{mjk0} - \chi^{m0kj} + \chi^{kjm0} - \chi^{k0mj} = \chi^{0jk0} - \chi^{00kj} + \chi^{kj00} - \chi^{k00j} = 0. \tag{B.17}$$

We close the coupling by assuming that there exists at least one frame $\mathsf{F}^{\mathsf{aether}}$ in which the coupling $f(F)$ is such that $\mathbf{E}$ couples only to $\mathbf{D}_\mathrm{T}$, and $\mathbf{H}_\mathrm{T}$ couples ony to $\mathbf{B}$, *viz.*

$$D^i_\mathrm{T} = \varepsilon_0 E_i, \quad B^i = \mu_0 H_{\mathrm{T};i}. \tag{B.18}$$

where $c = 1/\sqrt{\varepsilon_0 \mu_0}$. Note that the two couplings in eq. (B.18) involve tensor-components of different kind, since the left sides are covariant, whereas the right sides are not. Equation (B.18) are often referred to as vacuum-relations.[254] However, here we assume that eq. (B.18) are valid both “inside” and “outside” of matter in the respective frame.[81,82,141] The differing tensor-structure of f and F suggests a factorization $\chi^{ACBD} = \Gamma^{AC} \Gamma^{BD}$ via matrices $\boldsymbol{\Gamma}$, where eqs. (B.15) to (B.18) imply that $\boldsymbol{\Gamma} = \boldsymbol{\eta} \sqrt{\varkappa / \mu_0}$ and $\varkappa = 1$ is a weight-one tensor-density of rank zero (a scalar). Thus, there is a relation between the metric of Minkowski spacetime, and the assumption that $\mathbf{E}$ couples linearly only to $\mathbf{D}_\mathrm{T}$, and $\mathbf{H}_\mathrm{T}$ couples linearly only to $\mathbf{B}$.

Without loss of generality, we choose $\varkappa = 1 = 1/\sqrt{-\det \boldsymbol{\eta}}$, and obtain the generally covariant, four-dimensional tensor generalization of the linear couplings in eq. (B.18),

$$f^{AB} = \eta^{AC}\eta^{BD}F_{CD}/\mu_0\sqrt{-\det(\boldsymbol{\eta})}\,. \tag{B.19}$$

Apparently, the covariance of f, F does not transfer to the components E_i, D^i_{T}, B^i, $H_{\mathrm{T};i}$. For example under so-called Euclidean transformations, *i.e.* threedimensional time-dependent rotations $\boldsymbol{\mathfrak{R}}(t)$ and translations $\boldsymbol{Y}(t)$ (see appendix B.5), the fields $\mathbf{E}$ and $\mathbf{H}_{\mathrm{T}}$ transform non-covariantly,

$$E'_j = \mathfrak{R}_{ji}\left(E_i - \epsilon^{imn}\mathfrak{R}_{lm}\left[\dot{\mathfrak{R}}_{lk}x_k + \dot{Y}_l\right]B_n\right), \tag{B.20}$$

and

$$H'_{\mathrm{T};j} = \mathfrak{R}_{ji}\left(H_{\mathrm{T};i} - \epsilon^{imn}\mathfrak{R}_{lm}\left[\dot{\mathfrak{R}}_{lk}x_k + \dot{Y}_l\right]D^n_{\mathrm{T}}\right), \tag{B.21}$$

whereas $\boldsymbol{\mathcal{E}}, \mathbf{D}_{\mathrm{T}}, \mathbf{B}, \boldsymbol{\mathcal{H}}_{\mathrm{F}}, \varrho_{\mathrm{F}}, \boldsymbol{\mathcal{J}}_{\mathrm{F}}$ are covariant.[245] Thus, the Maxwell-Lorentz aether relations eq. (B.18) are not generally covariant. Furthermore, they are not even covariant with respect to Galilei-transformations (setting $\dot{\boldsymbol{\mathfrak{R}}} = 0$ in eq. (B.20) still is not covariant due to the dangling convective terms), *i.e.*. the covariance group of classical mechanics. Thus, there is no common Galilei-covariant ground for an electro-mechanical unification.

Since eq. (B.19) is a tensor equation valid in the designated frame $\mathsf{F}^{\mathsf{aether}}$, it is valid in any other frame. Nevertheless, although the special linear couplings defined by eq. (B.18) are valid in $\mathsf{F}^{\mathsf{aether}}$, they are, in general, not valid in other frames. That is, when we transform into an alternative frame x'^A, the component E'_i will not neccessarily equal $\varepsilon_0 D'^i_{\mathrm{T}}$ (see, *e.g.*, Ref. 81, section 13). However, we show that they are are covariant with respect to the isometry-group of Minkowski-spacetime (Lorentz transformations), *i.e.* the covariance-group of eq. (B.18). To see this, consider the set of transformations $x^A \rightarrow x'^A$ under which eq. (B.18) is covariant, *i.e.*

$$E'_i = \varepsilon_0 D'^i_{\mathrm{T}}, \quad \text{and} \quad B'^i = \mu_0 H'_{\mathrm{T};i}, \tag{B.22}$$

whereas,

$$f'^{AB} = \eta'^{AC}\eta'^{BD}F'_{CD}/\mu_0\sqrt{-\boldsymbol{\eta}'}\,. \tag{B.23}$$

Hence, we demand three-dimensional covariance with respect to four-dimensional coordinate transformations. However, the set of transformations under which eq. (B.23) preserves eq. (B.22) is given by the transformations which leave $\boldsymbol{\eta}$ invariant, *i.e.* the Lorentz transformations, since then eq. (B.23) becomes $f'^{AB} = 1/\mu_0 \cdot 1/\sqrt{-\boldsymbol{\eta}} \cdot \eta^{AC}\eta^{BD}F'_{CD}$. Thus, there is a somewhat hidden relation between electromagnetism and the spacetime structure of special relativity, because the isometry-group of Minkowski spacetime forms the covariance-group of the Maxwell-Lorentz aether relations, and all reference frames in which eq. (B.18) is valid, are related by Lorentz-transformations . Note that the subtle difference between the notions of covariance and invariance was essential to derive this result.

Because the Maxwell-Lorentz aether relations apply to the charge-/ and current-potentials $\mathbf{D}_\mathrm{T}, \mathbf{H}_\mathrm{T}$ of all kind, in our description, they are a constitutive model for the designated set of aether-frames.[425]

In the classical limit $|\mathbf{v}| \ll c$, the four-dimensional Lorentz transformations between two coordinate systems x' and x,[82]

$$x'^0 = \gamma x^0 - \gamma x^i v_i/c\,, \quad x'^j = \mathcal{R}'_{ji}\left(\left[\delta_{ik} + (\gamma - 1)v_i v_k/\mathbf{v}^2\right] x^k - \gamma x^0 v_i/c\right), \tag{B.24}$$

defined by $\gamma = 1/\sqrt{1 - \mathbf{v}^2/c^2}$ and by time-independent rotation $\mathfrak{R}$, reduce to the Galilei-transformations,

$$x'^0 = x^0, \quad x'^j = \mathcal{R}^j{}_i x^i - v^j t. \tag{B.25}$$

Therefore, the symmetry group of the Maxwell-Lorentz aether relations reduces to the covariance-group of mechanics, which constitutes the common covariant structure for the unification of mechanics and electromagnetic theory (subject to the Maxwell-Lorentz aether frames).

B.4 Electromagnetic Energy-Momentum Tensor

In this section we use Nother's Theorem and derive the electromagnetic energy momentum tensor from the electromagnetic action[412]

$$\mathcal{S} = \int \mathcal{L} \mathrm{d}^4 x = \int (f \cdot F/4 - s \cdot \mathcal{A}) \mathrm{d}^4 x, \tag{B.26}$$

where, s is a four-flux , and $F(\mathcal{A}) = \mathrm{d}\mathcal{A}$ is a closed differential form, *i.e.* an absolute antisymmetric tensor determined by a four-potential $\mathcal{A} = (\Phi/c\,, \mathbf{A})$ (hence $F_{AB} = \partial_{[A}\mathcal{A}_{B]}$). Furthermore, we assume that the antisymmetric tensor density f couples linearly to F via $f^{AB} = \chi^{ABCD} F_{CD}$.[376]

The Euler-Lagrange equations corresponding to this action follow from the stationary state, defined by variations $\delta\mathcal{A}$ where $\delta\mathcal{S} = 0$. The Lagrange-density $\mathcal{L} = f \cdot F/4 - s \cdot \mathcal{A}$ gives rise to Euler-Lagrange equations,[81]

$$\frac{\partial \mathcal{L}}{\partial(\partial_D \mathcal{A}_C)} = \frac{f^{AB}}{2} \frac{\partial(\partial_{[A}\mathcal{A}_{B]})}{\partial(\partial_D \mathcal{A}_C)} = \frac{f^{AB}}{2}\left[\delta^D_A \delta^C_B - \delta^D_B \delta^C_A\right] = -f^{CD}. \tag{B.27}$$

Because $\partial\mathcal{L}/\partial\mathcal{A}_C = -s^C$, the Euler-Lagrange equations reproduce the inhomogenous Maxwell-equations, $s = \operatorname{div} f$, whereas the homogeneous Maxwell-equations,

$\mathrm{d}F = 0$, follow from $F = \mathrm{d}\mathcal{A}$ (since "$\mathrm{d}^2 \equiv 0$"). According to Noether's Theorem, the invariance $\mathcal{L}$ under fourdimensional translations (time-translation and spatial translations) gives rise to four conserved currents,

$$\partial_A T^{AB} = 0, \tag{B.28}$$

comprised in the energy-momentum tensor [418]

$$T^{AB} = \frac{\partial \mathcal{L}}{\partial(\partial_A \mathcal{A}_C)} \cdot \eta^{BD} \frac{\partial \mathcal{A}^C}{\partial x^D} - \eta^{AB} \mathcal{L}. \tag{B.29}$$

However, this quantity can be brought into a covariant form by adding an antisymmetric term,[426] $T^{AB} \to T^{AB} + \partial_c f^{CA} \eta^{BD} \partial_c \mathcal{A}_D$, which yields the electromagnetic energy momentum tensor ("Minkowski-tensor"),

$$T^{AB} = -f^{AC} \eta^{BD} F_{CD} - \eta^{AB} f \cdot F/4\,. \tag{B.30}$$

The components of the energy-momentum tensor comprise important electromagnetic quantities. For their derivation, note that

$$f \cdot F = f^{AB} F_{AB} = 2\mathbf{B}\mathbf{H}_\mathrm{T} - 2\mathbf{E}\mathbf{D}_\mathrm{T}, \qquad s \cdot \mathcal{A} = \varrho_\mathrm{F} \Phi + \mathbf{j}_\mathrm{F} \mathbf{A} \tag{B.31}$$

$$f^{0j} F_{j0} = \mathbf{E}\mathbf{D}_\mathrm{T}, \qquad f^{0j} F_{ji} = -c\,(\mathbf{D}_\mathrm{T} \wedge \mathbf{B})_i\,, \tag{B.32}$$

$$f^{ij} F_{j0} = -\,(\mathbf{E} \wedge \mathbf{H}_\mathrm{T}/c\,)^{\,i}, \qquad f^{ik} F_{kj} = B^i H_{\mathrm{T};j} - \mathbf{H}_\mathrm{T}\mathbf{B} \cdot \delta^i_j. \tag{B.33}$$

In particular, the temporal component $T^{00} = (\mathbf{E}\mathbf{D}_\mathrm{T} + \mathbf{B}\mathbf{H}_\mathrm{T})/2$ constitutes the energy-density of the elctromagnetic fields. The mixed tempo-spatial components $T^{0i} = \epsilon^{ijk} E_j B_k$ are the components of the momentum-density carried by the electromagnetic fields, whereas the transposed tempo-spatial components $T^{i0} = \epsilon^{ijk} B_j E_k$ are the components of the Poynting-vector, which can be interpreted as the elctromagnetic energy-flux. Furthermore, the spatial components of the electromagnetic energy-momentum tensor determine the electromagnetic stress tensor ("Maxwell-stress-tensor"),[418]

$$T^{ij} = \Sigma^{ij} = -(\mathbf{E} \otimes \mathbf{D}_\mathrm{T} - \mathbf{B} \otimes \mathbf{H}_\mathrm{T})^{ij} + \delta^{ij} (\mathbf{E}\mathbf{D}_\mathrm{T} + \mathbf{B}\mathbf{H}_\mathrm{T})/2\,. \tag{B.34}$$

Altogether, we find

$$T^{AB} = \begin{pmatrix} (\mathbf{E}\mathbf{D}_\mathrm{T} + \mathbf{B}\mathbf{H}_\mathrm{T})/2 & (c\mathbf{D}_\mathrm{T} \wedge \mathbf{B})^1 & (c\mathbf{D}_\mathrm{T} \wedge \mathbf{B})^2 & (c\mathbf{D}_\mathrm{T} \wedge \mathbf{B})^3 \\ (\mathbf{H}_\mathrm{T} \wedge \mathbf{E})^1/c & & \dots & \\ (\mathbf{H}_\mathrm{T} \wedge \mathbf{E})^2/c & \dots & \Sigma^{ij} & \dots \\ (\mathbf{H}_\mathrm{T} \wedge \mathbf{E})^3/c & & \dots & \end{pmatrix}. \tag{B.35}$$

Note that T is not symmetric, which is at the origin of the (in)famous Abraham-

Minkowski controvery.[377]

B.5 Euclidean Transformation: Material Frame Indifference

The symmetry axiom of material frame indifference (also material symmetry,[427] or material objectivity[428]) used in continuum thermodynamics and continuum mechanics states that the measurement of an observable, *i.e.* the state of a system is independent from the relative motion of any observer,[74] *i.e.* covariant with respect to Euclidean transformations.

Definition 1. The Euclidean group E consists of time-dependent, spatially homogeneous, orthogonal rotations $\boldsymbol{\mathcal{R}}(t)$ (hence $\boldsymbol{\mathcal{R}}^T\boldsymbol{\mathcal{R}} = \mathbf{Id}$, $\boldsymbol{\nabla}\boldsymbol{\mathcal{R}} = 0$), and time-dependent, spatially homogeneous translations $\boldsymbol{Y}(t)$ (hence $\boldsymbol{\nabla Y} = 0$). The set of frames F which are related by Euclidean transformations are called Euclidean frames. Thus, for the coordinates $\mathbf{x}$ and $\mathbf{x}'$ of two Euclidean frames F and F',

$$t' = t, \quad \mathbf{x}' = \boldsymbol{\mathcal{R}}(t)\mathbf{x} + \boldsymbol{Y}(t), \quad \text{or,} \quad Y'^j = \mathcal{R}^j{}_i(t)x^i + Y^j(t). \tag{B.36}$$

The Euclidean transformations define the covariance-group of our transport theory, and the component-wise Euclidean transformation $\mathrm{d}x'^j/\mathrm{d}x^i = \mathcal{R}^j{}_i(t)$ determines the Euclidean tensor transformation law.

Definition 2. The Euclidean tensor transformation law of $\mathsf{rank}(k)$ tensors $\mathcal{T}$ is

$$\mathcal{T}'^{j_1 \dots j_k} = \det(\boldsymbol{\mathcal{R}})^p \cdot \mathcal{R}^{j_1 i_1} \cdot \ldots \cdot \mathcal{R}^{j_k i_k} \cdot \mathcal{T}_{i_1 \dots i_k}. \tag{B.37}$$

Quantities which transform covariant under Euclidean transformations, *i.e.* according to eq. (B.37), are called Euclidean tensors, or objective tensors. For p=1, $\mathcal{T}$ is an axial Euclidean tensor, while p=0 defines an absolute Euclidean / objective tensor. The following Lemma follows from definition 2.

Lemma 7. Objective absolute tensors $\mathit{\Psi}, \boldsymbol{\mathcal{Z}}, \boldsymbol{\mathcal{M}}$ of rank $0, 1, 2$ transform via

$$\mathit{\Psi}' = \mathit{\Psi}, \quad \boldsymbol{\mathcal{Z}}' = \boldsymbol{\mathcal{R}} \cdot \boldsymbol{\mathcal{Z}}, \quad \boldsymbol{\mathcal{M}} = \boldsymbol{\mathcal{R}} \cdot \boldsymbol{\mathcal{M}} \cdot \boldsymbol{\mathcal{R}}^T. \tag{B.38}$$

Objectivity constitutes covariance with respect to the covariance-group of Euclidean transformations. If the orthogonal transformation is constant and the translation is linear in time, then the Euclidean group equals the Galilei-group G.

Next, we discuss objectivity of some physical quantities which commonly appear in the transport equations.

Lemma 8. Velocity is not a Euclidean vector, and transforms under Euclidean transformations according to $\mathbf{v}' = \dot{\boldsymbol{\mathfrak{R}}}\mathbf{x} + \boldsymbol{\mathfrak{R}}\mathbf{v} + \dot{\boldsymbol{\mathfrak{Y}}}$.

Proof. The position vector is objective by construction, $\mathbf{x}' = \boldsymbol{\mathfrak{R}}\mathbf{x}+\boldsymbol{\mathfrak{Y}}$. Hence, we find $\mathbf{v}' = \dot{\mathbf{x}}' = \dot{\boldsymbol{\mathfrak{R}}}\mathbf{x} + \boldsymbol{\mathfrak{R}}\mathbf{v} + \dot{\boldsymbol{\mathfrak{Y}}}$. Apparently, the first and last term violate objectivity. □

Lemma 9. The Nabla operator is a Euclidean tensor, and transforms under Euclidean transformations according to $\boldsymbol{\nabla}' = \boldsymbol{\mathfrak{R}}\boldsymbol{\nabla}$.

Proof. Let $\mathbf{y}{=}\boldsymbol{\mathfrak{R}}\mathbf{x}{+}\boldsymbol{Y}$ be a Euclidean transformation, and, for simplicity, let us denote $\mathbf{y}{=}\mathbf{x}'$. Hence, we calculate the derivative-operator $\boldsymbol{\nabla}'{=}(\partial/\partial y^1, \partial/\partial y^2, \partial/\partial y^3)^T$. However, since the partial derivatives transform according to $\partial/\partial y^j = \partial x^i/\partial y^j \cdot \partial/\partial x^i$,[415] it remains to calculate the "inverse" transformation $x^j(y^i)$. The rotation is orthogonal ($\boldsymbol{\mathfrak{R}}^T\boldsymbol{\mathfrak{R}}{=}\,\mathbf{Id}$), such that we can easily calculate this by left-multiplicating $\mathbf{y}$ with $\boldsymbol{\mathfrak{R}}^T$. Hence, $\mathbf{x}{=}\boldsymbol{\mathfrak{R}}^T\mathbf{y}{-}\boldsymbol{\mathfrak{R}}^T\boldsymbol{\mathfrak{Y}}$, such that $\partial x^i/\partial y^j{=}(\mathcal{R}^T)^{ij}$, where we used $\boldsymbol{\nabla}\boldsymbol{\mathfrak{R}}{=}0$ and $\boldsymbol{\nabla}\boldsymbol{Y}{=}0$. Therefore, $\partial'_j{=}\mathcal{R}^{ji}\partial_i$, *i.e.* $\boldsymbol{\nabla}$ is objective. □

This Lemma has direct consequences which follow from the proof above.

Lemma 10. If $\mathcal{T}$ is a Euclidean $\mathsf{rank}(n)$-tensor, $\operatorname{grad}\mathcal{T}$ is a rank $n{+}1$ Euclidean tensor.

Proof. This follows from $\boldsymbol{\nabla}\boldsymbol{\mathfrak{R}}{=}0$ (homogeneity of rotation) and from Lemma 9. □

Lemma 11. The velocity gradient is not objective and transforms under Euclidean transformations according to $(\operatorname{grad}\mathbf{v})' = \boldsymbol{\mathfrak{R}}(\operatorname{grad}\mathbf{v})\boldsymbol{\mathfrak{R}}^T + \dot{\boldsymbol{\mathfrak{R}}}\boldsymbol{\mathfrak{R}}^T$.

Proof. We use Lemma 8 and Lemma 9 component-wise, such that $(\operatorname{grad}\mathbf{v})'_{ij}{=}\partial'_j v'_i = \mathcal{R}_j{}^k\partial_k(\dot{\mathcal{R}}_{il}x^l{+}\mathcal{R}_{il}v^l{+}\dot{Y}_i){=}\mathcal{R}_j{}^k\dot{\mathcal{R}}_{il}\delta^l_k{+}\mathcal{R}_{jk}\mathcal{R}_{il}\partial^k v^l{=}(\dot{\boldsymbol{\mathfrak{R}}}\boldsymbol{\mathfrak{R}}^T{+}\boldsymbol{\mathfrak{R}}{\cdot}\operatorname{grad}\mathbf{v}{\cdot}\boldsymbol{\mathfrak{R}}^T)_{ij}$. □

In particular, velocity is neither a Galilean vector, whereas the velocity gradient is. In contrast, velocity-differences, *e.g.* diffusion velocities in comoving fluxes, are objective.

Lemma 12. The strain rate tensor $\boldsymbol{\kappa} = (\operatorname{grad}\mathbf{v} + \operatorname{grad}\mathbf{v}^T)/2$ is a Euclidean tensor. The skew-symmetric spin tensor $\boldsymbol{\omega} = (\operatorname{grad}\mathbf{v} - \operatorname{grad}\mathbf{v}^T)/2$ is not Euclidean, as it transforms similar as the velocity gradient, $\boldsymbol{\omega}' = \boldsymbol{\mathfrak{R}}\boldsymbol{\omega}\boldsymbol{\mathfrak{R}}^T + \dot{\boldsymbol{\mathfrak{R}}}\boldsymbol{\mathfrak{R}}$.

Proof. By construction, $\operatorname{grad}\mathbf{v} = \boldsymbol{\kappa} + \boldsymbol{\omega}$. Therefore, $\boldsymbol{\kappa}^* + \boldsymbol{\omega}^* = \boldsymbol{\mathfrak{R}}\boldsymbol{\kappa}\boldsymbol{\mathfrak{R}}^T + \boldsymbol{\mathfrak{R}}\boldsymbol{\omega}\boldsymbol{\mathfrak{R}}^T + \dot{\boldsymbol{\mathfrak{R}}}\boldsymbol{\mathfrak{R}}^T$. Furthermore, $\boldsymbol{\mathfrak{R}}\boldsymbol{\kappa}\boldsymbol{\mathfrak{R}}^T$ is symmetric, whereas $\boldsymbol{\mathfrak{R}}\boldsymbol{\omega}\boldsymbol{\mathfrak{R}}^T$ and $\dot{\boldsymbol{\mathfrak{R}}}\boldsymbol{\mathfrak{R}}^T$ are not. Thus, separating symmetric and skew-symmetric parts proves the statement. □

In contrast to kinematic quantities, where objectivity can be probed via eqs. (B.36) and (B.37), objectivity of non-kinematic physical quantities (*e.g.* temperature, mass densities, stress tensor, and the heat flux) cannot always be assessed analytically and their objectivity must be postulated in analogy to experiments.[141]

Lemma 13. If $\mathcal{T}$ is an objective tensor of rank $\mathsf{rank}(n) \geq 1$, then $\dot{\mathcal{T}}$ is an objective tensor of rank $\mathsf{rank}(n) \geq 1$ only if the transformation is time-independent. Furthermore, the time-derivative of objective scalars is objective.

Proof. Note that Euclidean transformations leave the time dimension invariant, *i.e.* $\mathrm{d}/\mathrm{d}t' = \mathrm{d}/\mathrm{d}t$ (this were true even for (constant) time-translations $t' = t + \tau$, since $\mathrm{d}/\mathrm{d}t' = \mathrm{d}t/\mathrm{d}t' \cdot \mathrm{d}/\mathrm{d}t$, where $\partial_{t'}(t' - \tau) = 1$). Thus, $\mathrm{d}\mathcal{T}'/\mathrm{d}t' = \mathrm{d}\mathcal{T}'/\mathrm{d}t$ transforms properly only if $\dot{\boldsymbol{\mathcal{R}}} = 0$. The proof is trivial for scalars. ☐

B.6 The Role of Symmetry in Rational Thermodynamics

Rational thermodynamics is a description of classes of materials, which are defined by their material law (tensor-valued functions of tensors).[74]

Definition 3. A $\mathsf{rank}(k)$ tensor-valued function $\mathcal{C}(\mathcal{T}_1, \mathcal{T}_2, \ldots)$ of tensorial variables $\mathcal{T}_A$ is called objective tensor-valued function if it transforms under Euclidean transformations according to

$$\mathcal{C}^{j_1 \cdots j_k}(\mathcal{T}'_1, \mathcal{T}'_2, \ldots) = \sum_{i_1, \ldots, i_k} |\det(\boldsymbol{\mathcal{R}})|^p \cdot \mathcal{R}^{j_1 i_1} \cdot \ldots \cdot \mathcal{R}^{j_k i_k} \mathcal{C}^{i_1 \cdots i_k}(\mathcal{T}_1, \mathcal{T}_2, \ldots) \tag{B.39}$$

The most important tensorial objects appearing in this context are tensors of ranks $0, 1, 2$, *i.e.* scalars, vectors and matrices.

Lemma 14. Let $\mathit{\Psi}$ be a scalar-valued tensor function, $\boldsymbol{\mathcal{Z}}$ a vector-valued tensor function and $\boldsymbol{\mathcal{M}}$ a matrix-valued tensor function. Furthermore, let $(\phi, \boldsymbol{\mathcal{X}}, \mathcal{T})$ be a variable-set for the tensor functions, consisting of $\mathsf{rank}(0, 1, 2)$-tensors. Then, $\mathit{\Psi}, \boldsymbol{\mathcal{Z}}, \boldsymbol{\mathcal{M}}$ are objective if they transform according to

$$\mathit{\Psi}(\boldsymbol{\mathcal{R}}\boldsymbol{\mathcal{X}}) = \mathit{\Psi}(\boldsymbol{\mathcal{X}}), \qquad \mathit{\Psi}(\boldsymbol{\mathcal{R}}\mathcal{T}\boldsymbol{\mathcal{R}}^T) = \mathit{\Psi}(\mathcal{T}), \tag{B.40}$$

$$\boldsymbol{\mathcal{Z}}(\phi) = \boldsymbol{\mathcal{R}}\boldsymbol{\mathcal{Z}}(\phi), \qquad \boldsymbol{\mathcal{Z}}(\boldsymbol{\mathcal{R}}\boldsymbol{\mathcal{X}}) = \boldsymbol{\mathcal{R}}\boldsymbol{\mathcal{Z}}(\boldsymbol{\mathcal{X}}), \qquad \boldsymbol{\mathcal{Z}}(\boldsymbol{\mathcal{R}}\mathcal{T}\boldsymbol{\mathcal{R}}^T) = \boldsymbol{\mathcal{Z}}(\mathcal{T}), \tag{B.41}$$

$$\boldsymbol{\mathcal{M}}(\phi) = \boldsymbol{\mathcal{R}}\boldsymbol{\mathcal{M}}(\phi)\boldsymbol{\mathcal{R}}^T, \quad \boldsymbol{\mathcal{M}}(\boldsymbol{\mathcal{R}}\boldsymbol{\mathcal{X}}) = \boldsymbol{\mathcal{R}}\boldsymbol{\mathcal{M}}(\boldsymbol{\mathcal{X}})\boldsymbol{\mathcal{R}}^T, \quad \boldsymbol{\mathcal{M}}(\boldsymbol{\mathcal{R}}\mathcal{T}\boldsymbol{\mathcal{R}}^T) = \boldsymbol{\mathcal{R}}\boldsymbol{\mathcal{M}}(\mathcal{T})\boldsymbol{\mathcal{R}}^T. \tag{B.42}$$

For a proof of these relations we refer to the literature, *e.g.* Ref. 429. Note that these results transfer easily to the case of tensor functions of weight $p \neq 0$.

This result immediately restricts the variables which can appear in any objective tensor function.

Lemma 15. If a tensor function is objective, then it cannot depend on the velocity or the spin tensor. Furthermore, it can depend on $\operatorname{grad}\mathbf{v}$ only via $\boldsymbol{\kappa}$ and must fulfill the objectivity condition $\mathcal{C}(\boldsymbol{\mathcal{R}}\boldsymbol{\kappa}\boldsymbol{\mathcal{R}}^T) = \boldsymbol{\mathcal{R}}\mathcal{C}(\boldsymbol{\kappa})\boldsymbol{\mathcal{R}}^T$.

Proof. Let $\mathcal{T}$ be an objective tensor, *i.e.* transforming according to $\mathcal{T}' = \boldsymbol{\mathcal{R}}\mathcal{T}\boldsymbol{\mathcal{R}}^T$. Now, let us assume that the objective tensor were a function of the velocity and the velocity gradient, $\mathcal{T} = \mathcal{T}(\mathbf{v}, \operatorname{grad}\mathbf{v})$. Objectivity implies $\mathcal{T}(\mathbf{v}', (\operatorname{grad}\mathbf{v})') = \boldsymbol{\mathcal{R}}\mathcal{T}(\mathbf{v}, \operatorname{grad}\mathbf{v})\boldsymbol{\mathcal{R}}^T$. Using Lemma 8 and Lemma 11 implies

$$\mathcal{T}[\dot{\boldsymbol{\mathcal{R}}}\mathbf{x} + \boldsymbol{\mathcal{R}}\mathbf{v} + \dot{\boldsymbol{\mathcal{Y}}}, \boldsymbol{\mathcal{R}}(\operatorname{grad}\mathbf{v})\boldsymbol{\mathcal{R}}^T + \dot{\boldsymbol{\mathcal{R}}}\boldsymbol{\mathcal{R}}^T] = \boldsymbol{\mathcal{R}}\mathcal{T}(\mathbf{v}, \operatorname{grad}\mathbf{v})\boldsymbol{\mathcal{R}}^T. \tag{B.43}$$

Without loss of generality, let us assume $\boldsymbol{\mathcal{R}}(t) = \mathbf{Id}$, hence $\dot{\boldsymbol{\mathcal{R}}} = 0$, such that the objectivity condition becomes $\mathcal{T}(\mathbf{v} + \dot{\boldsymbol{\mathcal{Y}}}, \operatorname{grad}\mathbf{v}) = \mathcal{T}(\mathbf{v}, \operatorname{grad}\mathbf{v})$. Since $\boldsymbol{\mathcal{Y}}$ is arbitrary, this equation cannot be true in general. Therefore, $\mathcal{T}$ cannot depend on $\mathbf{v}$ and the objectivity condition eq. (B.43) reduces to $\mathcal{T}(\boldsymbol{\mathcal{R}}(\operatorname{grad}\mathbf{v})\boldsymbol{\mathcal{R}}^T + \dot{\boldsymbol{\mathcal{R}}}\boldsymbol{\mathcal{R}}^T) = \boldsymbol{\mathcal{R}}\mathcal{T}(\operatorname{grad}\mathbf{v})\boldsymbol{\mathcal{R}}^T$. The irreducible decomposition of the velocity gradient, $\operatorname{grad}\mathbf{v} = \boldsymbol{\kappa} + \boldsymbol{\omega}$, implies $\mathcal{T}\left(\boldsymbol{\mathcal{R}}\boldsymbol{\kappa}\boldsymbol{\mathcal{R}}^T + \boldsymbol{\mathcal{R}}\boldsymbol{\omega}\boldsymbol{\mathcal{R}}^T + \dot{\boldsymbol{\mathcal{R}}}\boldsymbol{\mathcal{R}}^T\right) = \boldsymbol{\mathcal{R}}\mathcal{T}(\operatorname{grad}\mathbf{v})\boldsymbol{\mathcal{R}}^T$ for any orthogonal tensor $\boldsymbol{\mathcal{R}}$. *Subclaim: For any skew-symmetric tensor* $\boldsymbol{\omega}$, *we can define an orthogonal tensor* $\boldsymbol{\mathcal{R}}$ *such that* $\boldsymbol{\mathcal{R}}(t_0) = \mathbf{Id}$ *and* $\dot{\boldsymbol{\mathcal{R}}}(t_0) = -\boldsymbol{\omega}$. Doing so, the objectivity condition at $t = t_0$ is given by $\mathcal{T}(\boldsymbol{\kappa}) = \mathcal{T}(\operatorname{grad}\mathbf{v})$. This implies that $\mathcal{T}$ cannot depend on $\boldsymbol{\omega}$ if it is to be objective. Furthermore, it implies that $\mathcal{T}$ can only depend on $\operatorname{grad}\mathbf{v}$ in the form of $\boldsymbol{\kappa}$ if it is to be objective. Note that the objectivity condition for $\mathcal{T}(\boldsymbol{\kappa})$ is still given by $\mathcal{T}(\boldsymbol{\mathcal{R}}\boldsymbol{\kappa}\boldsymbol{\mathcal{R}}^T) = \boldsymbol{\mathcal{R}}\mathcal{T}(\operatorname{grad}\mathbf{v})\boldsymbol{\mathcal{R}}^T$. This completes the proof. □

Lemma 16. The scalar valued-function $\Psi(\mathcal{T}) = \det(\mathcal{T})$ of a rank-two tensor $\mathcal{T}$, and the scalar valued-function $\Psi(\mathcal{T}) = \operatorname{tr}(\mathcal{T})$ of a rank-two tensor $\mathcal{T}$ are objective.

Proof. Since $\boldsymbol{\mathcal{R}}$ are othogonal matrices, $\boldsymbol{\mathcal{R}}\mathcal{T}\boldsymbol{\mathcal{R}}^T$ is *similar* to $\boldsymbol{\mathcal{R}}$, and thus both objects are related by a conjugacy transformation. Since the determinant is invariant under conjugacy transformations, $\Psi(\boldsymbol{\mathcal{R}}\mathcal{T}\boldsymbol{\mathcal{R}}^T) = \det(\boldsymbol{\mathcal{R}}\mathcal{T}\boldsymbol{\mathcal{R}}^T) = \det(\mathcal{T})$. Due to the abelian property of the trace in it's arguments, we have $\operatorname{tr}(\boldsymbol{\mathcal{R}}\mathcal{T}\boldsymbol{\mathcal{R}}^T) = \operatorname{tr}(\mathcal{T}\boldsymbol{\mathcal{R}}\boldsymbol{\mathcal{R}}^T) = \operatorname{tr}(\mathcal{T})$. □

An important class of tensor-valued functions appearing in our framework are linear tensor-valued functions of the form $\mathcal{C}(\mathcal{T}_1, \mathcal{T}_2, \ldots) = \lambda_1(\mathcal{T}_A) \cdot \mathcal{T}_1 + \lambda_2(\mathcal{T}_A) \cdot \mathcal{T}_2 + \ldots$, where $\lambda_i(\mathcal{T}_B)$ are scalar-valued tensor-functions.

Lemma 17. An objective linear scalar-valued tensor function Ψ cannot depend on vectors. Furthermore, let $\boldsymbol{\mathcal{M}}$ be a rank-2 tensor. Then, $\Psi(\boldsymbol{\mathcal{M}})$ is objective if and only if $\Psi(\boldsymbol{\mathcal{M}}) \propto \operatorname{tr}(\boldsymbol{\mathcal{M}})$.

For a proof, see Ref. 74. However, objective scalar-valued functions of higher order can be functions of vectors.[429] Furthermore, the following Lemma is a direct consequence of definition 3.

Lemma 18. A linear non-scalar-valued tensor function is objective, if it's arguments are objective.

Because they determine the constitutive equations, linear tensor functions are important quantities in our framework.

Definition 4. A constitutive quantity C is an abstract tensor-valued quantity which implements classes of materials into a constitutive theory.

Definition 5. A material law $\boldsymbol{\Upsilon} = \{\Upsilon_A\}$ is a set of tensor-quantities Υ_A, which defines a class of materials.

For example, the material law $\boldsymbol{\Upsilon} = (T, \boldsymbol{\nabla} T, \boldsymbol{\varpi}_{\text{sym}})$ determines the class of "thermoelastic" materials (here $\boldsymbol{\varpi}_{\text{sym}}$ is the symmetrized tensor of $\operatorname{grad} \mathbf{x}$), and $\boldsymbol{\Upsilon} = (\rho, T, \boldsymbol{\kappa}, \boldsymbol{\nabla} T)$ describes a monocomponent, viscous, heat-conducting fluids, and $\boldsymbol{\Upsilon} = (\rho_\alpha, T, \boldsymbol{\kappa}, \boldsymbol{\nabla} T, \mathbf{P}, \mathbf{M})$ describes multicomponent, viscous heat-conducting fluids which are polarizable and magnetizable.

Definition 6. Let C be a constitutive quantity of $\mathsf{rank}(k)$, and $\boldsymbol{\Upsilon} = \{\Upsilon_A, \Upsilon_B, \ldots\}$ a material law. Then, the $\mathsf{rank}(k)$ tensor-valued tensor function $\mathcal{C}(\boldsymbol{\Upsilon})$ is called material function (or, constitutive mapping) with respect to C, if

$$\mathsf{C} = \mathcal{C}(\boldsymbol{\Upsilon}). \tag{B.44}$$

Hence, a material function with respect to a constitutie quantity C is a material-representation of C. The most important constitutive quantity appearing in our framework is the Helmholtz free energy density φ_{H}, where the material function $\varphi_{\mathrm{H}}(\boldsymbol{\Upsilon})$ specifies the electrolyte. However, material functions are restricted by symmetry arguments.

Axiom 1 ("Material Objectivity" / "Material Symmetry")**.** Any material function appearing in our constitutive model must be an objective function.

Thus, the axiom of material objectivity implies that the material law is covariant with respect to the covariance group E, *i.e.* it must transform according to eq. (B.37) under Euclidean transformations.

Lemma 19. Material symmetry implies that the velocity $\mathbf{v}$, and the velocity gradient $\operatorname{grad}\mathbf{v}$ are no material variables.

This follows directly from axiom 1 and lemma 15. Axiom 1 and Lemma 18 imply that material laws, which are linear tensor functions of non-zero rank are objective, can depend only on objective quantities.

Lemma 20. The material law of a linear material function with $\mathsf{rank}(\mathit{k}) \geq 1$ consists of objective tensors.

The axiom of material objectivity is a constraint on the set of admissible material functions appearing in the constitutive model. The so-called representation theorems of isotropic tensors determine all admissible forms of objective material functions $\mathcal{C}(\boldsymbol{\Upsilon})$ for material variables Υ_A of $\mathsf{rank}(\mathit{k})$ and constitutive quantities of $\mathsf{rank}(\mathit{l})$,[270,430–433] and determine most general form of constitutive equations which is in compliance with the axiom of material symmetry. For example, for constitutive quantities of $\mathsf{rank}(\mathit{0,1,2})$ (“scalars”, “vectors” and “matrices”), and for a material law comprised of tensors of degree one and two, $\boldsymbol{\Upsilon} = \{\mathfrak{X}, \mathfrak{M}\}$, the most general objective material functions $\varPsi, \mathfrak{Z}, \mathcal{T}$ are[432]

$$\begin{aligned}
\varPsi(\mathfrak{X},\mathfrak{M}) &= \varPsi\left(\operatorname{tr}(\mathfrak{M}), \det(\mathfrak{M}), \operatorname{tr}(\mathfrak{M})^2 - \operatorname{tr}(\mathfrak{M}^2), \mathfrak{X}^2, \mathfrak{X}^T(\mathfrak{M}\mathfrak{X}), \mathfrak{X}^T\mathfrak{M}^2\mathfrak{X}\right), && \text{(B.45)}\\
\mathfrak{Z}(\mathfrak{X},\mathfrak{M}) &= \left(\lambda_1(\mathfrak{X},\mathfrak{M}) \cdot \mathbf{Id} + \lambda_2(\mathfrak{X},\mathfrak{M}) \cdot \mathfrak{M} + \lambda_3(\mathfrak{X},\mathfrak{M}) \cdot \mathfrak{M}^2\right) \cdot \mathfrak{X}, && \text{(B.46)}\\
\mathcal{T}(\mathfrak{M}) &= \tilde{\lambda}_1(\mathfrak{M}) \cdot \mathbf{Id} + \tilde{\lambda}_2(\mathfrak{M}) \cdot \mathfrak{M}_{\text{tf}} + \tilde{\lambda}_3(\mathfrak{M}) \cdot \mathfrak{M}^2, && \text{(B.47)}
\end{aligned}$$

where $\lambda_i, \tilde{\lambda}_i$ are scalar-valued functions and $\mathsf{rank}(\varPsi) = 0, \mathsf{rank}(\mathfrak{Z}) = 1, \mathsf{rank}(\mathcal{T}) = 2$. However, in many cases one is interested only in linear material-representations. In this case, the most general objective constitutive functions are

$$\begin{aligned}
\varPsi(\mathfrak{X},\mathfrak{M}) &= \lambda_1 \cdot \operatorname{tr}(\mathfrak{M}), && \text{(B.48)}\\
\mathfrak{Z}(\mathfrak{X},\mathfrak{M}) &= \lambda_2 \cdot \mathfrak{X}, && \text{(B.49)}\\
\mathcal{T}(\mathfrak{M}) &= \tilde{\lambda}_1 \cdot \operatorname{tr}(\mathfrak{M}) \cdot \mathbf{Id} + \tilde{\lambda}_2 \cdot \mathfrak{M}_{\text{tf}}, && \text{(B.50)}
\end{aligned}$$

where $\lambda_{1,2}$ and $\tilde{\lambda}_{1,2}$ are independent of $\boldsymbol{\Upsilon}$. Apparently, the representation theorems B.49 and B.50 restrict admissible couplings according to their rank.[74]

Lemma 21 (Curie’s law)**.** In the linear constitutive regime, the material law $\boldsymbol{\Upsilon} = \{\Upsilon_A, \Upsilon_B, \ldots\}$ for a material function $\mathcal{C}(\boldsymbol{\Upsilon})$, with respect to the constitutive quantity C (*i.e.* $\mathit{C} = \mathcal{C}(\boldsymbol{\Upsilon})$), consists of material variables which have the same tensorial order as the constitutive quantity. Thus, $\mathsf{rank}(\Upsilon_A) = \mathsf{rank}(\mathit{C})$ for $\Upsilon_A \in \boldsymbol{\Upsilon}$.

Hence, material symmetry implies that causes cannot have more elements of symmetry than the effects they produce.[434] Thus, physical phenomena do not automatically exhibit the symmetries of the laws that govern them.[74] Linear relations appear in the Onsager-formalism where thermodynamics fluxes (the effects) are coupled linearly to thermodynamic forces (causes).

As example, we consider the linear material function for the viscosity tensor $\boldsymbol{\tau}$ (see section 5.3.2), where $\boldsymbol{\tau}(\boldsymbol{\kappa})$ depends linearly on the rate of strain, and is determined by symmetry arguments. Lemma 20 and axiom 1 imply that, because $\operatorname{grad}\mathbf{v}$ is not objective, $\boldsymbol{\tau}$ must be a linear function of $\boldsymbol{\kappa}$, and Lemma 11, Lemma 12 and eq. (B.50) determine the most general form for $\boldsymbol{\tau}$ up to two parameters α_1, α_2,

$$\boldsymbol{\tau}(\boldsymbol{\kappa}) = \alpha_1 \cdot \operatorname{tr}(\boldsymbol{\kappa}) \cdot \mathbf{Id} + \alpha_2 \cdot \boldsymbol{\kappa}_{\mathrm{tf}}. \tag{B.51}$$

Material symmetry also applies to the method of Coleman and Noll, where all constitutive quantities C_A are determined via the evaluation of the universal balance laws by conjugate material variables Υ_A, which are comprised in a material law $\boldsymbol{\Upsilon}=\{\Upsilon_A, \Upsilon_B, \ldots\}$ for φ_{H}. The corresponding constitutive equation for C_A then takes the form

$$C_A = \partial(\rho\varphi_{\mathrm{H}})/\partial\Upsilon_A\,. \tag{B.52}$$

Thus, the material function $\mathcal{C}_{\varphi_{\mathrm{H}}}$ for $\rho\varphi_{\mathrm{H}}$ determines the material functions $\mathcal{C}_{C_A}$ for all constitutive quantities C_A via the corresponding constitutive equations,

$$\mathcal{C}_A = \partial\mathcal{C}_{\varphi_{\mathrm{H}}}/\partial\Upsilon_A\,. \tag{B.53}$$

Altogether, we can conclude on the transfer of symmetry from the quantity $\rho\varphi_{\mathrm{H}}$ to the corresponding material function.

Theorem 2. Let Ψ be a smooth function of a non-scalar variable $\boldsymbol{\mathfrak{X}}$ and $\boldsymbol{\mathfrak{U}}$ an orthogonal transformation. Then, Ψ is invariant under orthogonal transformations, *i.e.* $\Psi(\boldsymbol{\mathfrak{U}}\boldsymbol{\mathfrak{X}})=\Psi(\boldsymbol{\mathfrak{X}})$, exactly if the quantity $\boldsymbol{\mathfrak{X}} \otimes \partial\Psi/\partial\boldsymbol{\mathfrak{X}}$ is symmetric, *i.e.* exactly if $\mathfrak{X}_{[i}\partial\Psi/\partial\mathfrak{X}_{j]}=0$ for all spatial components i, j.

Proof. Consider an infinitesimal orthogonal transformation, *i.e.* a rotation, induced by a matrix $\boldsymbol{\mathfrak{U}}$, where $\boldsymbol{\mathfrak{U}}^T=\boldsymbol{\mathfrak{U}}^{-1}$. From representation theory, we know that the generators of $\mathsf{SO(3)}$ (or, equivalently, $\mathsf{SU(2)}$) are anti-symmetric matrices. This can be easily verified by expanding the orthogonality condition up to second order in the infinitesimal representation $\boldsymbol{\mathfrak{U}}=\mathbf{Id}+\varepsilon\cdot\boldsymbol{\omega}$,

$$\mathbf{Id} = \boldsymbol{\mathfrak{U}}^T \cdot \boldsymbol{\mathfrak{U}} = (\mathbf{Id} + \varepsilon \cdot \boldsymbol{\omega}^T) \cdot (\mathbf{Id} + \varepsilon \cdot \boldsymbol{\omega}) = \mathbf{Id} + \varepsilon(\boldsymbol{\omega} + \boldsymbol{\omega}^T) + \mathcal{O}(\varepsilon^2). \tag{B.54}$$

Thus, in this approximation, the generators $\boldsymbol{\omega}$ are anti-symmetric matrices. Furthermore, since any anti-symmetric matrix has $\mathrm{N}\times(\mathrm{N}-1)/2$ independent components, the generators $\boldsymbol{\omega}$ have three independent components (here, N=3). Thus, they are determined by the vector of angular-momentum $\boldsymbol{\Omega}$ and the Levi-Civita symbol via $\omega_{ij}{=}-\epsilon_{ijk}\Omega^k$. We probe the invariance of the field $\varPsi(\boldsymbol{\mathfrak{X}})$ by calculating the transformation behaviour of the argument, $\boldsymbol{\mathfrak{U}}\boldsymbol{\mathfrak{X}}{=}(\mathbf{Id}+\varepsilon\boldsymbol{\omega})\boldsymbol{\mathfrak{X}}{=}\boldsymbol{\mathfrak{X}}{+}\varepsilon\boldsymbol{\omega}\boldsymbol{\mathfrak{X}}$. Since $\varepsilon\boldsymbol{\omega}\boldsymbol{\mathfrak{X}}{=}-\varepsilon\boldsymbol{\mathfrak{X}}{\wedge}\boldsymbol{\Omega}$, this becomes $\boldsymbol{\mathfrak{U}}\boldsymbol{\mathfrak{X}}{=}\boldsymbol{\mathfrak{X}}{-}\varepsilon\cdot\boldsymbol{\mathfrak{X}}{\wedge}\boldsymbol{\Omega}$. Therefore, $\varPsi$ is invariant under orthogonal transformations if $\varPsi(\boldsymbol{\mathfrak{X}}{-}\epsilon{\cdot}\boldsymbol{\mathfrak{X}}{\wedge}\boldsymbol{\Omega}){=}\varPsi(\boldsymbol{\mathfrak{X}})$, or, equivalently, if $\partial\varPsi(\boldsymbol{\mathfrak{U}}\boldsymbol{\mathfrak{X}})/\partial\boldsymbol{\Omega}{=}0$. In particular, for any spatial component i,

$$\begin{aligned}\frac{\partial\varPsi(\boldsymbol{\mathfrak{U}}\boldsymbol{\mathfrak{X}})}{\partial\Omega^i}{=}\frac{\partial\varPsi(\boldsymbol{\mathfrak{X}}{-}\varepsilon{\cdot}\boldsymbol{\mathfrak{X}}{\wedge}\boldsymbol{\Omega})}{\partial\Omega^i}&{=}\frac{\partial\varPsi}{\partial(\boldsymbol{\mathfrak{X}}{-}\epsilon\boldsymbol{\mathfrak{X}}\wedge\boldsymbol{\Omega})^j}\frac{\partial(\boldsymbol{\mathfrak{X}}{-}\varepsilon\boldsymbol{\mathfrak{X}}{\wedge}\boldsymbol{\Omega})^j}{\partial\Omega^i}\\ &{=}-\frac{\partial\varPsi}{\partial(\boldsymbol{\mathfrak{X}}{-}\varepsilon\boldsymbol{\mathfrak{X}}{\wedge}\boldsymbol{\Omega})^j}{\cdot}\varepsilon\epsilon_{jkl}\delta_i^l\mathfrak{X}^k{=}\varepsilon\epsilon_{ikj}\mathfrak{X}^k\frac{\partial\varPsi}{\partial(\boldsymbol{\mathfrak{X}}{-}\varepsilon\boldsymbol{\mathfrak{X}}{\wedge}\boldsymbol{\Omega})^j}.\end{aligned}\tag{B.55}$$

Let $\boldsymbol{\Omega}{=}0$. Then, the left hand side vanishes identically, $\partial\varPsi/\partial\boldsymbol{\Omega}|_{\boldsymbol{\Omega}=0}{=}0$, whereas the right hand side becomes a derivative with respect to $\boldsymbol{\mathfrak{X}}$. Thus, $0{=}\varepsilon\epsilon_{ikj}\mathfrak{X}^k{\cdot}\partial\varPsi/\partial\mathfrak{X}^j$, which is true for any arbitrary index i, if $\mathfrak{X}^k\partial\varPsi/\partial\mathfrak{X}^j{-}\mathfrak{X}^j\cdot\partial\varPsi/\partial\mathfrak{X}^k{=}0$. □

B.7 Covariant Unification

Finally, we discuss material symmetry, *i.e.* covariance with respect to Euclidean transformations (see axiom 1), of a unified electrolyte description based on methods from non-equilibrium thermodynamics, electromagnetic theory and mechanics.

We showed above that the covariance group of classical mechanics is the Galilei-group, whereas the covariance group of the Maxwell-Lorentz aether relations is the Lorentz group (see appendix B.3). However, in our context, we can safely assume the classical limit $|\mathbf{v}|\ll c$, where the Lorentz group reduces to the Galilean group. Furthermore, experiments involving the kinetic theory of gases showed that Euclidean symmetry is violated only in the case of strong rotations.[435] Because such inertial effects can be neglected in this context,[436] this suggests that the proper covariance group for material symmetry is the Galilei group, and not the Euclidean group. Thus, material objectivity defined with respect to the Euclidean group (see axiom 1) is a good approximation.

However, symmetry alone does not suffice to determine the material law and the material function for a given material, but must be supplemented by additional physical arguments.

C Balance Equations for Volumes

> The left side of the balance sheet has nothing right and the right side of the balance sheet has nothing left. But they are equal to each other. So, accounting-wise we are fine.
>
> ---
>
> Jacob Frenkel, AIG Vice Chairman
> 2008

In this chapter, we introduce the mathematical description for the time evolution of field quantities.

The response of physical objects to the application of external stimuli, *e.g.* forces, or internal processes, *e.g.* chemical reactions can be described via balance equations, which describe the time evolution of field quantities $\varPsi$, or the corresponding field densities $\psi(\mathbf{x}, t)$ (where $\varPsi(t) = \int_{V(t)} \mathrm{d}V\, \psi(\mathbf{x}, t)$). Their typical structure shows how an object evolves locally, taking account for the evolution of $\mathrm{d}V\,(t)$, on the one side, whereas the other side comprises all physical prcoesses by which $\varPsi$ changes.

We split this chapter into four sections. First, in appendix C.1 we introduce the mathematical structure to describe material bodies. Next, in appendix C.2 we state the general form for the global balance equation of a field quantity, which evolves due to transport processes and reactions. Finally, in appendix C.3, we derive the so-called Leibnitz-Reynolds Transport Theorems, which determine how the global description for $\varPsi$ transfers to the local time evolution of ψ, and state the universal form of local balance equations.

C.1 Mathematical Introduction

In this section we discuss the mathematical description for material bodies used in our framework.

We assume that, at any instant of time, a material body can be described mathematically via a coordinate representation of it's material points (“particles”) in threedimensional Euclidean space. Here, we use a method devised by Euler to label the set of material points,[81] which form the configuration of the body (see, *e.g.*, Ref. 82,246).[82]

Let $\mathcal{B}$ be a material body, and let p be the set of material points. At any instant of time, we assign to each material point p of $\mathcal{B}$ Cartesian coordinates via functions ("Euler coordinates")

$$\mathbf{x} : \mathcal{I} \times \mathcal{B} \ \to \Omega(t) \subset \mathbb{R}^3, \quad \text{such that} \quad \mathbf{x}_p(t) = \Big(x_p^1(t), x_p^2(t), x_p^3(t)\Big)\,. \tag{C.1}$$

Thus, for any reference configuration $\mathcal{B}_0$, usually chosen at $t_0 = 0$, the set $\Omega_0 = \Omega_{\mathcal{B}(t_0)}$ defines a coordinate system, and each material point in the reference configuration $\mathcal{B}_0$ can be labelled using a triad $\boldsymbol{X} = (X_1, X_2, X_3)$ ("Lagrangian coordinates"). However, since the material body $\mathcal{B}$ may not be self-permeating, there exists a bijective map

$$\phi : \mathcal{I} \times \Omega_0 \to \Omega \quad \text{such that} \quad \mathbf{x} = \phi_{t_0}(\boldsymbol{X}, t). \tag{C.2}$$

For fixed coordinates $\boldsymbol{X}_0$, the vector function $\mathbf{x}(t) = \phi_{t_0}^{\boldsymbol{X}_0}(t)$ defines the trajectory of the material point p assigned to $\boldsymbol{X}_0$ in the reference configuration (at $t = t_0$). The corresponding "barycentric velocity" and the acceleration of this trajectory are

$$\mathbf{w}(t, \phi(t, \boldsymbol{X})) = \boldsymbol{w}(t, \boldsymbol{X}) = \partial\phi(\boldsymbol{X}, t)/\partial t\,, \quad \text{and} \quad \dot{\mathbf{w}} = \partial^2\phi(\boldsymbol{X}, t)/\partial t^2\,. \tag{C.3}$$

Similarly, for fixed $t = t_0$, and varying $\boldsymbol{X}$, the vector function $\mathbf{x}(\boldsymbol{X}) = \phi_{t_0}(\boldsymbol{X})$ defines the positions of all material points, *i.e.* a "picture" of the body $\mathcal{B}$ at that instant of time. Accordingly, the nine derivatives of this picture with respect to the material coordinates $\boldsymbol{X}$ define the deformation tensor $\boldsymbol{F}$ of the body,

$$F_{ij}(\boldsymbol{X}, t) = \partial\phi_i(\boldsymbol{X}, t)/\partial X_j\,. \tag{C.4}$$

Since eq. (C.2) defines a coordinate transformation between Euler - / and Lagrange coordinates, ϕ is a diffeomorphism, and the determinant of the deformation tensor is the Jacobian of the coordinate transformation. Thus, the asumption that the body $\mathcal{B}$ is not self-permeating transfers to the requirement that $\det \boldsymbol{F} \neq 0$. However, since $\det \boldsymbol{F} = 1$ at $t = t_0$, the Jacobian is strictly positive, *i.e.* $\det \boldsymbol{F} > 0$ always. Another important property is that the deformation tensor is not independent from the mass density (see Lemma 1). The material description of a field quantity at a position $\mathbf{x}$ occupied by the material point $\boldsymbol{X}$ at time t (*i.e.* $\mathbf{x} = \mathbf{x}(\boldsymbol{X}, t)$) is given by $\psi = A(\boldsymbol{X}, t)$, where the Eulerian description is $\psi = a(\mathbf{x}, t)$, such that $A(\boldsymbol{X}, t) = a(\mathbf{x}(\boldsymbol{X}, t), t)$. The Eulerian time derivative $\partial\psi/\partial t$ measures the local evolution at a fixed point in space, *i.e.* relative to fixed external coordinates , whereas the comoving material time derivative folows via the chain rule

$$\dot{\psi} = \partial A(\boldsymbol{X}, t)/\partial t = \partial \psi/\partial t + (\mathbf{v} \cdot \boldsymbol{\nabla})\, \psi. \tag{C.5}$$

The nine spatial derivatives of the Eulerian velocity define the velocity gradient, and the strain rate tensor (see appendix D.6)

$$(\operatorname{grad} \mathbf{v})_{ij} = \partial v_i(\mathbf{x}, t)/\partial x_j\,, \quad \text{and} \quad \boldsymbol{\kappa} = [\operatorname{grad} \mathbf{v} + (\operatorname{grad} \mathbf{v})^T]/2\,. \tag{C.6}$$

C.2 Global Structure of Balance Laws for Volumes

In this section, we state the general form of the global balance equations. For this purpose, we consider Let $V(t) \subseteq \Omega(t) \subset \mathbb{R}^n$ be a time-dependent volume with boundary surface $\mathcal{A} = \partial V$, where $\hat{\boldsymbol{n}}_{\mathcal{A}}$ is the outward pointing unit-normal vector, and let $\Psi : \mathcal{I} \to \mathbb{R}^n$ be a field quantity with local representation $\psi : \mathcal{I} \times \Omega \to \mathbb{R}^n$,

$$\Psi(t) = \int_V \mathrm{d}V\, \psi(\mathbf{x}, t). \tag{C.7}$$

In general, a field quantity Ψ changes due to convective fluxes $\psi \otimes (\mathbf{v} - \mathbf{v}_{\mathcal{A}}) \cdot \hat{\boldsymbol{n}}_{\mathcal{A}}$, where $(\mathbf{v} - \mathbf{v}_{\mathcal{A}}) \cdot \hat{\boldsymbol{n}}_{\mathcal{A}}$ is the velocity-difference between the evolving surface and the material points measured along the direction of the surface normal, due to non-convective fluxes $\boldsymbol{\Xi}$, and due to local source-terms $\mathcal{P}$,

$$\frac{\mathrm{d}}{\mathrm{d}t}\Psi = \frac{\mathrm{d}}{\mathrm{d}t}\int_V \mathrm{d}V\, \psi = -\int_{\mathcal{A}} \mathrm{d}A\, \psi \otimes (\mathbf{v} - \mathbf{v}_{\mathcal{A}})\hat{\boldsymbol{n}}_{\mathcal{A}} - \int_{\mathcal{A}} \mathrm{d}A\, \boldsymbol{\Xi} \otimes \hat{\boldsymbol{n}}_{\mathcal{A}} + \int_V \mathrm{d}V\, \mathcal{P} \tag{C.8}$$

$$= -\int_V \mathrm{d}V\, \boldsymbol{\nabla} \left[\psi \otimes (\mathbf{v} - \mathbf{v}_{\mathcal{A}}) + \boldsymbol{\Xi}\right] - \mathcal{P}. \tag{C.9}$$

Convective fluxes are covariant under to Euclidean transformations (see appendix B).

C.3 Transport Theorems for Volumes and Surfaces

In this section, we state the Leibnitz-Reynolds Transport Theorems (LRTTs) for volumes and surfaces (see, *e.g.*, Ref. 437 for more details).

Theorem 3 (Transport Theorem for volumes)**.** Let Ψ be a scalar, vector or tensor-valued field quantity, and $V(t)$ a time-dependent volume as in appendix C.2. Then,

$$\frac{\mathrm{d}\Psi}{\mathrm{d}t} = \frac{\mathrm{d}}{\mathrm{d}t}\int_{V(t)} \mathrm{d}V\, \psi = \int_{V(t)} \mathrm{d}V\, \left[\frac{\partial \psi}{\partial t} + \boldsymbol{\nabla}\,(\psi \otimes \mathbf{v}_{\mathcal{A}})\right]. \tag{C.10}$$

Next, we define flux derivatives with respectto the dynamic geometry of the surface,[81] which we use for the covariant formulation of electromagnetism (see section 5.2.1).

Definition 7. Let $\mathcal{A}(t)\subset\mathbb{R}^3$ be a hypersurface, with surface-flux $\mathbf{v}_\mathcal{A}$. The flux derivative of a vector field $\boldsymbol{\mathcal{X}}$ on $\mathcal{A}$ is defined by $\overset{*}{\boldsymbol{\mathcal{X}}}=\dot{\boldsymbol{\mathcal{X}}}+\boldsymbol{\mathcal{X}}\cdot\boldsymbol{\nabla}\mathbf{v}_\mathcal{A}-(\boldsymbol{\mathcal{X}}\cdot\boldsymbol{\nabla})\mathbf{v}_\mathcal{A}$.

Theorem 4. (Transport Theorem for surfaces) Let $\mathcal{A}(t)\subset\mathbb{R}^3$ be a two-dimensional hypersurface, and let ψ be a vector field on $\mathcal{A}$, where $\Psi=\int_\mathcal{A}\mathrm{d}A\,\psi$. Then,

$$\frac{\mathrm{d}}{\mathrm{d}t}\Psi=\frac{\mathrm{d}}{\mathrm{d}t}\int_{\mathcal{A}(t)}\mathrm{d}A\,\psi\cdot\hat{\boldsymbol{n}}_\mathcal{A}=\int_{\mathcal{A}(t)}\mathrm{d}A\,\overset{*}{\psi}\cdot\hat{\boldsymbol{n}}_\mathcal{A}. \tag{C.11}$$

From vector analysis follows that (where $\mathbf{v}=\mathbf{v}_\mathcal{A}$),

$$\begin{aligned}\overset{*}{\boldsymbol{\mathcal{X}}}=\partial_t\boldsymbol{\mathcal{X}}+\mathbf{v}_\mathcal{A}(\boldsymbol{\nabla}\boldsymbol{\mathcal{X}})-\boldsymbol{\nabla}\wedge(\mathbf{v}_\mathcal{A}\wedge\boldsymbol{\mathcal{X}})&=\dot{\boldsymbol{\mathcal{X}}}+\boldsymbol{\mathcal{X}}\,(\boldsymbol{\nabla}\mathbf{v}_\mathcal{A})-(\boldsymbol{\mathcal{X}}\cdot\boldsymbol{\nabla})\,\mathbf{v}_\mathcal{A},\\ &=\partial_t\boldsymbol{\mathcal{X}}+\boldsymbol{\nabla}\,(\boldsymbol{\mathcal{X}}\otimes\mathbf{v}_\mathcal{A})-(\boldsymbol{\mathcal{X}}\cdot\boldsymbol{\nabla})\,\mathbf{v}_\mathcal{A}.\end{aligned} \tag{C.12}$$

Next we substitute eq. (C.10) for $\dot{\Psi}$ in eq. (C.9),

$$\int_V\mathrm{d}V\,\left[\partial_t\psi+\boldsymbol{\nabla}\,(\psi\otimes\mathbf{v}_\mathcal{A})\right]=-\int_V\mathrm{d}V\,\left[\boldsymbol{\nabla}\,(\psi\otimes[\mathbf{v}-\mathbf{v}_\mathcal{A}])+\boldsymbol{\Xi}-\mathcal{P}\right]. \tag{C.13}$$

Thus, the local form of the balance equations for volumes, in the material description, and in the Eulerian description, are (see section 5.1)

$$\partial_t\psi=-\boldsymbol{\nabla}\,(\psi\otimes\mathbf{v}+\boldsymbol{\Xi})+\mathcal{P}, \tag{C.14}$$

$$\dot{\psi}=-\psi\,(\boldsymbol{\nabla}\mathbf{v})-\boldsymbol{\nabla}\boldsymbol{\Xi}+\mathcal{P}. \tag{C.15}$$

D Appendix to Part II

D.1 Dimensional Analysis of Maxwell's Equation

In this section, we briefly discuss the non-dimensional form of Maxwell's equations, which give rise to the electrostatic limit (see section 5.2.4).

We non-dimensionalize and scale Maxwell's eqs. (5.41) and (5.42) by introducing reference-values for length (x^{ref}), time (t^{ref}), concentration (c^{ref}), electric field (E^{ref}), and magnetic field (B^{ref}) using an aether-frame $\mathsf{F}^{\mathsf{aether}}$, where $\mathbf{D}_{\mathrm{F}} = \varepsilon_0 \mathbf{E} + \mathbf{P}$ and $\mathbf{H}_{\mathrm{F}} = \mathbf{B}/\mu_0 - \mathbf{M}$. In addition, we set $P^{\mathrm{ref}} = \varepsilon_0 E^{\mathrm{ref}}$ and $M^{\mathrm{ref}} = B^{\mathrm{ref}}/\mu_0$. We denote non-dimensional quantities using a star,

$$\begin{aligned}
&\boldsymbol{\nabla}^* = x^{\mathrm{ref}} \cdot \boldsymbol{\nabla}, && \partial_t^* = t^{\mathrm{ref}} \cdot \partial_t, && \mathbf{E}^* = \mathbf{E}/E^{\mathrm{ref}}, \\
&\mathbf{B}^* = \mathbf{B}/B^{\mathrm{ref}}, && \mathbf{P}^* = \mathbf{P}/P^{\mathrm{ref}}, && \varrho_{\mathrm{F}}^* = \varrho_{\mathrm{F}}/\Sigma_\alpha F z_\alpha c_\alpha^{\mathrm{ref}}, \\
&\mathbf{j}_{\mathrm{F}}^* = \mathbf{j}_{\mathrm{F}}/\Sigma_\alpha F z c_\alpha^{\mathrm{ref}} (x^{\mathrm{ref}}/t^{\mathrm{ref}}), && (\mathbf{E}^* + \mathbf{P}^*) = \mathbf{D}_{\mathrm{F}}/\varepsilon_0 E^{\mathrm{ref}}, && (\mathbf{B}^* - \mathbf{M}^*) = \mathbf{H}_{\mathrm{F}}/(B^{\mathrm{ref}}/\mu_0).
\end{aligned}$$

Due to the scaling, these quantities have magnitude of order one. Substituting the corresponding dimensional quantities by the quantities above, we obtain the Maxwell-equations in their non-dimensional form,

$$0 = \boldsymbol{\nabla}^* \mathbf{B}^*, \qquad 0 = \beta \cdot \partial_t^* \mathbf{B}^* + \boldsymbol{\nabla}^* \wedge \mathbf{E}^*, \tag{D.1}$$

$$\varrho_{\mathrm{F}}^* = \lambda \cdot \boldsymbol{\nabla}^* (\mathbf{E}^* + \mathbf{P}^*), \qquad \mathbf{j}_{\mathrm{F}}^* = -\lambda \partial_t^* (\mathbf{E}^* + \mathbf{P}^*) + \delta \boldsymbol{\nabla}^* \wedge (\mathbf{B}^* - \mathbf{M}^*), \tag{D.2}$$

where $\varrho_{\mathrm{F}}^{\mathrm{ref}} = \Sigma_\alpha F z_\alpha c_\alpha^{\mathrm{ref}}$. Furthermore, we obtain the non-dimensionalized form of the Galilei-invariant quantities

$$\boldsymbol{\mathcal{E}}^* = \mathbf{E}^* + \beta \mathbf{v}^* \wedge \mathbf{B}^*, \qquad \boldsymbol{\mathcal{M}}^* = \mathbf{M}^* + \lambda/\delta \cdot (\mathbf{v}^* \wedge \mathbf{P}^*), \tag{D.3}$$

with dimensionless scaling-parameters β, λ and δ

$$\beta = v^{\mathrm{ref}} B^{\mathrm{ref}}/E^{\mathrm{ref}}, \quad \lambda = \varepsilon_0 E^{\mathrm{ref}}/\varrho_{\mathrm{F}}^{\mathrm{ref}} x^{\mathrm{ref}}, \quad \delta = \lambda\beta \cdot (c/v^{\mathrm{ref}})^2 \tag{D.4}$$

We estimate the parameter-scales, by assuming a binary ionic liquid, confined in an electrochemical double-layer, which is subject to moderate changes in time. Thus, we set $x^{\mathrm{ref}} = 1\,\mathrm{nm}$ and $t^{\mathrm{ref}} = 1\,\mathrm{s}$ such that $v^{\mathrm{ref}} = 1 \cdot 10^{-9}\,\mathrm{m}$. Typically, the bulk-value of ILs is of the order $c_\pm^{\mathrm{ref}} = 3 \cdot 10^3\,\mathrm{mol\,m^{-3}}$, hence we set $\varrho_{\mathrm{F}}^{\mathrm{ref}} = 6 \cdot 10^7\,\mathrm{A\,s\,m^{-3}}$. Typical potential-drops throughout the double-layer towards the bulk are $\Delta\Phi = 1\,\mathrm{V}$, such that $E^{\mathrm{ref}} = \Delta\Phi/x^{\mathrm{ref}} = 1{\cdot}10^{9}\,\mathrm{V\,m^{-1}}$. The magnetic field of a horseshoe is roughly $1{\cdot}10^{-1}\,\mathrm{T}$, whereas the magnets of the circular accelerators at the LHC are up to $10\,\mathrm{T}$ strong. Here, we set $B^{\mathrm{ref}} = 1\,\mathrm{T}$. Altogether, we obtain

$$\beta = 1{\cdot}10^{-18}, \qquad \lambda = 1{\cdot}10^{-1}, \qquad \delta = 1{\cdot}10^{16}. \tag{D.5}$$

Apparently, $\beta \lll \lambda$ and $1/\delta \lll \lambda$. Hence, the electromotive intensity equals the electric field, $\boldsymbol{\mathcal{E}} = \mathbf{E}$ (see eq. (D.3)), and Maxwell equations read

$$0 = \boldsymbol{\nabla}\mathbf{B}, \qquad 0 = \boldsymbol{\nabla}\wedge\mathbf{E}, \tag{D.6}$$

$$\varrho_{\mathrm{F}} = \boldsymbol{\nabla}\left(\varepsilon_0\mathbf{E} + \mathbf{P}\right), \qquad 0 = \boldsymbol{\nabla}\wedge\left(\mathbf{B}/\mu_0 - \mathbf{M}\right). \tag{D.7}$$

This defines the electrostatic limit and justifies that in the description of electrolytes, we can safely neglect effects stemming from magnetic fields. From eq. $(\mathrm{D.6})_2$ follows the existence of the electrostatic potential Φ, such that

$$\mathbf{E} = -\boldsymbol{\nabla}\Phi. \tag{D.8}$$

D.2 Unimodular Deformation Energy

Here, we derive eq. (5.66). For this puprose, we first calculate the expression $\mathrm{d}\,\boldsymbol{F}^{\mathrm{uni}}/\mathrm{d}t$, and then evaluate it's contraction with $\rho\varphi_{\mathrm{H}}/\partial\,\boldsymbol{F}^{\mathrm{uni}}$.

Lemma 22. $\operatorname{grad}\mathbf{v} = \dot{\boldsymbol{F}}\cdot\boldsymbol{F}^{-1}$.

Proof. Componentwise, the deformation is defined by the derivative $F_{ij} = \partial x_i/\partial X_j$. Thus, the total derivative of these components reveals

$$\dot{F}_{ij} = \frac{\partial}{\partial t}\frac{\partial x_i}{\partial X_j} = \frac{\partial v_i}{\partial X_j} = \sum_k \frac{\partial v_i}{\partial x_k}\frac{\partial x_k}{\partial X_j} = \sum_k (\operatorname{grad}\mathbf{v})_{ik}\,F^{kj}\,. \tag{D.9}$$

Mutiplying from the right with $\boldsymbol{F}^{-1}$ solves for $\operatorname{grad}\mathbf{v}$. □

Lemma 23. For any non-singular matrix $\mathcal{M}(t)$, the following relation holds,

$$\frac{\mathrm{d}}{\mathrm{d}t}(\det\mathcal{M}) = (\det\mathcal{M})\cdot\operatorname{tr}\left(\mathcal{M}^{-1}\cdot\dot{\mathcal{M}}\right). \tag{D.10}$$

Proof. We prove the claim using a perturbation analysis. From $\det(\mathcal{M}) \neq 0$, we observe that $\delta\ln(\det\mathcal{M}) = \ln[\det(\mathcal{M}+\delta\mathcal{M})] - \ln(\det\mathcal{M}) = \ln(\det(\mathcal{M}+\delta\mathcal{M})/\det\mathcal{M})$.

Next, we use the two elementary matrix properties $(\det \boldsymbol{\mathcal{M}})^{-1} = \det(\boldsymbol{\mathcal{M}}^{-1})$, and $\det(\boldsymbol{\mathcal{M}}) \cdot \det(\boldsymbol{\mathcal{N}}) = \det(\boldsymbol{\mathcal{M}} \cdot \boldsymbol{\mathcal{N}})$. Therefore, $\delta \ln(\det \boldsymbol{\mathcal{M}}) = \ln(\det[\boldsymbol{\mathcal{M}}^{-1} \cdot (\boldsymbol{\mathcal{M}} + \delta\boldsymbol{\mathcal{M}})]) = \ln(\det[\mathbf{Id} + \boldsymbol{\mathcal{M}}^{-1}\delta\boldsymbol{\mathcal{M}}])$. By construction, the variation $\delta\mathcal{M}_{ij} \ll \mathcal{M}_{ij}$, such that that $\boldsymbol{\mathcal{M}}^{-1} \cdot \delta\boldsymbol{\mathcal{M}} \ll \mathbf{Id}$. Hence, we can use the standard approximation,[438] $\ln(\det[\mathbf{Id} + \boldsymbol{\mathcal{M}}^{-1}\delta\boldsymbol{\mathcal{M}})]) \approx \ln[1 + \mathrm{tr}(\boldsymbol{\mathcal{M}}^{-1} \cdot \delta\boldsymbol{\mathcal{M}})]$. Next, we expand the "small" trace-part in a Taylor-series, $\delta \ln(\det \boldsymbol{\mathcal{M}}) \approx \mathrm{tr}(\boldsymbol{\mathcal{M}}^{-1} \cdot \delta\boldsymbol{\mathcal{M}})$. We evaluate the general variation for the total time derivative, which yields $\frac{\mathrm{d}}{\mathrm{d}t} \ln \det \boldsymbol{\mathcal{M}} \approx \mathrm{tr}(\boldsymbol{\mathcal{M}}^{-1} \cdot \dot{\boldsymbol{\mathcal{M}}})$. This can be solved for $\frac{\mathrm{d}}{\mathrm{d}t} \det \boldsymbol{\mathcal{M}} \approx \det \boldsymbol{\mathcal{M}} \cdot \mathrm{tr}(\boldsymbol{\mathcal{M}}^{-1} \cdot \dot{\boldsymbol{\mathcal{M}}})$, which completes the proof. □

With the help of Lemma 22 and Lemma 23, we can compute $\dot{\boldsymbol{F}}^{\mathrm{uni}}$,

$$\dot{\boldsymbol{F}}^{\mathrm{uni}} = \frac{\mathrm{d}}{\mathrm{d}t}\left[(\det \boldsymbol{F})^{1/3} \cdot \boldsymbol{F}\right] \tag{D.11}$$

$$= -\frac{1}{3}(\det \boldsymbol{F})^{-4/3} \cdot \boldsymbol{F} \cdot \frac{\mathrm{d}}{\mathrm{d}t}(\det \boldsymbol{F}) + (\det \boldsymbol{F})^{-1/3} \cdot \dot{\boldsymbol{F}} \tag{D.12}$$

$$= -\frac{1}{3}(\det \boldsymbol{F})^{-1/3} \cdot \boldsymbol{F}^{\mathrm{uni}} \cdot (\det \boldsymbol{F}) \cdot \mathrm{tr}\left(\boldsymbol{F}^{-1} \cdot \dot{\boldsymbol{F}}\right) + \mathrm{grad}\,\mathbf{v} \cdot \boldsymbol{F}^{\mathrm{uni}} \tag{D.13}$$

$$= -\frac{1}{3}\boldsymbol{F}^{\mathrm{uni}} \cdot \mathrm{tr}\left[\boldsymbol{F}^{-1} \cdot (\mathrm{grad}\,\mathbf{v} \cdot \boldsymbol{F})\right] + \mathrm{grad}\,\mathbf{v} \cdot \boldsymbol{F}^{\mathrm{uni}}. \tag{D.14}$$

Lemma 24. $\mathrm{tr}\,(\boldsymbol{\mathcal{M}} \cdot \boldsymbol{\mathcal{N}}) = \boldsymbol{\mathcal{M}} : \boldsymbol{\mathcal{N}}^T$.

Proof. $\mathrm{tr}(\boldsymbol{\mathcal{M}} \cdot \boldsymbol{\mathcal{N}}) = \mathbf{Id} : (\boldsymbol{\mathcal{M}} \cdot \boldsymbol{\mathcal{N}}) = \sum_{i,j,k} \delta_{ij}\mathcal{M}_{ik}\mathcal{N}_{kj} = \sum_{j,k} \mathcal{N}_{kj}\mathcal{M}_{jk} = \boldsymbol{\mathcal{N}} : \boldsymbol{\mathcal{M}}^T = \boldsymbol{\mathcal{N}}^T : \boldsymbol{\mathcal{M}}$.. □

Lemma 25. $\mathrm{tr}\left[\boldsymbol{\mathcal{M}}^{-1} \cdot (\boldsymbol{\mathcal{N}} \cdot \boldsymbol{\mathcal{M}})\right] = \mathrm{tr}\,(\boldsymbol{\mathcal{N}})$.

This follows from a short calculation.

$$\mathrm{tr}\left[\boldsymbol{\mathcal{M}}^{-1} \cdot (\boldsymbol{\mathcal{N}} \cdot \boldsymbol{\mathcal{M}})\right] = \mathbf{Id} : [\boldsymbol{\mathcal{M}}^{-1} \cdot (\boldsymbol{\mathcal{N}} \cdot \boldsymbol{\mathcal{M}})] \tag{D.15}$$

$$= \sum_{i,j} \delta_{ij}(\boldsymbol{\mathcal{M}}^{-1} \cdot [\boldsymbol{\mathcal{N}} \cdot \boldsymbol{\mathcal{M}}])_{ij} \tag{D.16}$$

$$= \sum_{i,j,k} \delta_{ij}(\boldsymbol{\mathcal{M}}^{-1})_{ik} \cdot (\boldsymbol{\mathcal{N}} \cdot \boldsymbol{\mathcal{M}})_{kj} \tag{D.17}$$

$$= \sum_{i,j,k,m} \delta_{ij}(\boldsymbol{\mathcal{M}}^{-1})_{ik} \cdot \mathcal{N}_{km} \cdot \mathcal{M}_{mj} \tag{D.18}$$

$$= \sum_{j,k,m} \mathcal{N}_{km} \cdot \mathcal{M}_{mj}(\boldsymbol{\mathcal{M}}^{-1})_{jk} \tag{D.19}$$

$$= \sum_{k,m} \mathcal{N}_{km}(\boldsymbol{\mathcal{M}} \cdot \boldsymbol{\mathcal{M}}^{-1})_{mk} \tag{D.20}$$

$$= \sum_{k,m} \mathcal{N}_{km}\delta_{mk} = \mathrm{tr}\,\boldsymbol{\mathcal{N}}. \tag{D.21}$$

From these two Lemmata follows $\mathrm{tr}[\boldsymbol{F}^{-1} \cdot (\mathrm{grad}\,\mathbf{v} \cdot \boldsymbol{F})] = \mathrm{tr}(\mathrm{grad}\,\mathbf{v}) = \mathbf{Id} : \boldsymbol{\kappa}$, such that we obtain

$$\dot{\boldsymbol{F}}^{\mathrm{uni}} = \mathrm{grad}\,\mathbf{v} \cdot \boldsymbol{F}^{\mathrm{uni}} - \frac{1}{3}\boldsymbol{F}^{\mathrm{uni}} \cdot (\mathbf{Id} : \boldsymbol{\kappa}) = \left[\mathrm{grad}\,\mathbf{v} - \frac{1}{3}(\mathrm{tr}\,\mathrm{grad}\,\mathbf{v}) \cdot \mathbf{Id}\right] \cdot \boldsymbol{F}^{\mathrm{uni}}. \tag{D.22}$$

Hence, the contribution from the unimodular deformation to the formal expansion of the free energy density $\rho\dot{\varphi}_{\mathrm{H}}(\boldsymbol{\Upsilon})$, see eq. (5.66), becomes

$$\frac{\partial(\rho\varphi_{\mathrm{H}})}{\partial\,\boldsymbol{F}^{\mathrm{uni}}} : \dot{\boldsymbol{F}}^{\mathrm{uni}} = \frac{\partial(\rho\varphi_{\mathrm{H}})}{\partial\,\boldsymbol{F}^{\mathrm{uni}}} : \left(\mathrm{grad}\,\mathbf{v} \cdot \boldsymbol{F}^{\mathrm{uni}}\right) - \frac{1}{3}\left(\frac{\partial(\rho\varphi_{\mathrm{H}})}{\partial\,\boldsymbol{F}^{\mathrm{uni}}} : \boldsymbol{F}^{\mathrm{uni}}\right) \cdot \boldsymbol{\nabla}\mathbf{v}. \tag{D.23}$$

We can transform the contraction appearing in the first term on the right side of eq. (D.23) by using the following property.

Lemma 26. $\boldsymbol{\mathcal{M}} : (\boldsymbol{\mathcal{N}} \cdot \boldsymbol{\mathcal{Q}}) = \left(\boldsymbol{\mathcal{M}} \cdot \boldsymbol{\mathcal{Q}}^T\right) : \boldsymbol{\mathcal{N}}$.

Proof. $\boldsymbol{\mathcal{M}} : (\boldsymbol{\mathcal{N}} \cdot \boldsymbol{\mathcal{Q}}) = \sum_{i,j,k} \mathcal{M}_{ij}\mathcal{N}_{ik}\mathcal{Q}_{kj} = \sum_{i,k} \mathcal{N}_{ik}(\boldsymbol{\mathcal{M}} \cdot \boldsymbol{\mathcal{Q}}^T)_{ik} = \boldsymbol{\mathcal{N}} : (\boldsymbol{\mathcal{M}}\boldsymbol{\mathcal{Q}}^T) = \left(\boldsymbol{\mathcal{M}} \cdot \boldsymbol{\mathcal{Q}}^T\right) : \boldsymbol{\mathcal{N}}$. □

Thus, using the result from Lemma 26 in eq. (D.23) yields

$$\frac{\partial(\rho\varphi_{\mathrm{H}})}{\partial\,\boldsymbol{F}^{\mathrm{uni}}} : \dot{\boldsymbol{F}}^{\mathrm{uni}} = \left[\frac{\partial(\rho\varphi_{\mathrm{H}})}{\partial\,\boldsymbol{F}^{\mathrm{uni}}} \cdot (\boldsymbol{F}^{\mathrm{uni}})^T\right] : \mathrm{grad}\,\mathbf{v} - \frac{1}{3}\left(\frac{\partial(\rho\varphi_{\mathrm{H}})}{\partial\,\boldsymbol{F}^{\mathrm{uni}}} : \boldsymbol{F}^{\mathrm{uni}}\right) \cdot \boldsymbol{\nabla}\mathbf{v}. \tag{D.24}$$

We apply Theorem 2 for $\partial(\rho\varphi_{\mathrm{H}})/\,\boldsymbol{F}^{\mathrm{uni}} \cdot (\boldsymbol{F}^{\mathrm{uni}})^T = [\partial(\rho\varphi_{\mathrm{H}})/\,\boldsymbol{F}^{\mathrm{uni}}]^T \cdot \boldsymbol{F}^{\mathrm{uni}}$. Hence, the bracked expression of the first term on the right side of eq. (D.24) is symmetric, and it's contraction with $\mathrm{grad}\,\mathbf{v}$ equals the contraction with $\boldsymbol{\kappa}$. Furthermore, using Lemma 24, we obtain

$$\frac{\partial(\rho\varphi_{\mathrm{H}})}{\partial\,\boldsymbol{F}^{\mathrm{uni}}} : \dot{\boldsymbol{F}}^{\mathrm{uni}} = \left(\frac{\partial(\rho\varphi_{\mathrm{H}})}{\partial\,\boldsymbol{F}^{\mathrm{uni}}} \cdot (\boldsymbol{F}^{\mathrm{uni}})^T - \frac{1}{3}\,\mathrm{tr}\left[\frac{\partial(\rho\varphi_{\mathrm{H}})}{\partial\,\boldsymbol{F}^{\mathrm{uni}}} \cdot (\boldsymbol{F}^{\mathrm{uni}})^T\right] \cdot \mathbf{Id}\right) : \boldsymbol{\kappa}. \tag{D.25}$$

Apparently, the bracked term on the right side is the trace-free part of the irreducible representation of a symmetric matrix $\boldsymbol{\mathcal{D}} = \partial(\rho\varphi_{\mathrm{H}})/\partial\,\boldsymbol{F}^{\mathrm{uni}} \cdot (\boldsymbol{F}^{\mathrm{uni}})^T$ such that eq. (D.25) becomes $\partial(\rho\varphi_{\mathrm{H}})/\partial\,\boldsymbol{F}^{\mathrm{uni}} : \dot{\boldsymbol{F}}^{\mathrm{uni}} = \boldsymbol{\mathcal{D}}_{\mathrm{tf}} : \boldsymbol{\kappa}$, which is exactly the contribution from the unimodular deformation tensor in the materials law to the formal expansion of $\rho\dot{\varphi}_{\mathrm{H}}(\boldsymbol{\Upsilon})$, see eq. (5.66).

D.3 Evaluation of the Poynting Flux

Poynting's Theorem follows from inserting the covariant Maxwell's equations eqs. (5.48) and (5.49) into the expansion $\boldsymbol{\nabla}(\mathcal{H}_{\mathrm{F}} \wedge \mathcal{E}) = \mathcal{E}(\boldsymbol{\nabla} \wedge \mathcal{H}_{\mathrm{F}}) - \mathcal{H}_{\mathrm{F}}(\boldsymbol{\nabla} \wedge \mathcal{E})$,

$$\boldsymbol{\nabla}(\mathcal{H}_{\mathrm{F}} \wedge \mathcal{E}) = \mathcal{E}\mathcal{J}_{\mathrm{F}} + \mathcal{E}\overset{*}{\mathbf{D}}_{\mathrm{F}} + \mathcal{H}_{\mathrm{F}}\overset{*}{\mathbf{B}}. \tag{D.26}$$

Next, we use the definition Definition 7 for the flux-derivative, $\overset{*}{\mathcal{X}} = \dot{\mathcal{X}} + \mathcal{X} \cdot \boldsymbol{\nabla}\mathbf{v} - (\mathcal{X} \cdot \boldsymbol{\nabla})\,\mathbf{v}$, see definition 7. However, the flux derivative has the following property.

Lemma 27. $\mathcal{X} \cdot \overset{*}{\mathcal{Y}} = \mathcal{X} \cdot \dot{\mathcal{Y}} + [(\mathcal{X}\mathcal{Y})\,\mathbf{Id} - \mathcal{X} \otimes \mathcal{Y}] : \operatorname{grad} \mathbf{v}$.

Proof. We use $\boldsymbol{\nabla}\mathbf{v} = \operatorname{tr} \operatorname{grad} \mathbf{v} = \mathbf{Id} : \operatorname{grad} \mathbf{v}$, such that

$$\mathcal{X}(\mathcal{Y}\boldsymbol{\nabla})\mathbf{v} = \mathcal{X}(\mathcal{Y}^{\mu}\partial_{\mu})\mathbf{v} = \mathcal{X}_{\alpha}(\mathcal{Y}^{\mu}\partial_{\mu})v^{\alpha} = (\mathcal{X}_{\alpha}\mathcal{Y}^{\mu})(\partial_{\mu}v^{\alpha}) = (\mathcal{X} \otimes \mathcal{Y}) : \operatorname{grad} \mathbf{v}$$

and $\mathcal{X}\mathcal{Y}(\boldsymbol{\nabla}\mathbf{v}) = \mathcal{X}\mathcal{Y}(\mathbf{Id} : \operatorname{grad} \mathbf{v}) = (\mathcal{X}\mathcal{Y})\,\mathbf{Id} : \operatorname{grad} \mathbf{v}$. These two results prove the Lemma. □

Thus, using Lemma 27, Poynting's Theorem (eq. (D.26)) becomes $\boldsymbol{\nabla}(\mathcal{H}_{\mathrm{F}} \wedge \mathcal{E}) = \mathcal{E}\dot{\mathbf{D}}_{\mathrm{F}} + \mathcal{H}_{\mathrm{F}}\dot{\mathbf{B}} + \mathcal{E}\mathcal{J}_{\mathrm{F}} + [(\mathcal{E}\mathbf{D}_{\mathrm{F}} + \mathcal{H}_{\mathrm{F}}\mathbf{B})\,\mathbf{Id} - \mathcal{H}_{\mathrm{F}} \otimes \mathbf{B} - \mathcal{E} \otimes \mathbf{D}_{\mathrm{F}}] : \operatorname{grad} \mathbf{v}$. Next, we use the aether relations $\mathbf{D}_{\mathrm{F}} = \varepsilon_0\mathbf{E} + \mathbf{P}$, $\mathcal{H}_{\mathrm{F}} = \mathbf{B}/\mu_0 - \boldsymbol{\mathcal{M}} - (\mathbf{v} \wedge \varepsilon_0\mathbf{E})$ and $\mathcal{E} = \mathbf{E} + \mathbf{v} \wedge \mathbf{B}$, which yields

$$\begin{aligned}
\boldsymbol{\nabla}(\mathcal{H}_{\mathrm{F}} \wedge \mathcal{E}) = {} & \mathcal{E}\mathcal{J}_{\mathrm{F}} + \mathrm{d}/\mathrm{d}t\,\left(\varepsilon_0\mathbf{E}^2/2 + \mathcal{E}\mathbf{P} + \mathbf{B}^2/2\mu_0\right) - \dot{\mathcal{E}}\mathbf{P} - \boldsymbol{\mathcal{M}}\dot{\mathbf{B}} + \varepsilon_0\,(\mathbf{v} \wedge \mathbf{B})\,\dot{\mathbf{E}} \\
& - \varepsilon_0\,(\mathbf{v} \wedge \mathbf{E})\,\dot{\mathbf{B}} + \Big[\left(\varepsilon_0\mathbf{E}^2 + \mathcal{E}\mathbf{P} + \mathbf{B}^2/\mu_0 - \boldsymbol{\mathcal{M}}\mathbf{B}\right)\mathbf{Id} - (\varepsilon_0\mathbf{E} \otimes \mathbf{E} + \mathcal{E} \otimes \mathbf{P} + \mathbf{B} \otimes \mathbf{B}/\mu_0 - \boldsymbol{\mathcal{M}} \otimes \mathbf{B}) \\
& + [\varepsilon_0\,(\mathbf{v} \wedge \mathbf{B})\,\mathbf{E} + \varepsilon_0\,(\mathbf{E} \wedge \mathbf{v})\,\mathbf{B}]\,\mathbf{Id} - \varepsilon_0\,(\mathbf{v} \wedge \mathbf{B}) \otimes \mathbf{E} - (\mathbf{E} \wedge \mathbf{v}) \otimes \mathbf{B}\Big] : \operatorname{grad} \mathbf{v}.
\end{aligned} \tag{D.27}$$

Apparently, the nested permutations (appearing in the last line) implying wedge products look similar to the ones implying tensor products. Indeed, they can be translated via the following property: Let $\mathcal{X}, \mathcal{Y}, \mathcal{Z}$ be arbitrary three-dimensional vectors. Then, $[(\mathcal{X} \wedge \mathcal{Y}) \cdot \mathcal{Z}]\,\mathbf{Id} = (\mathcal{X} \wedge \mathcal{Y}) \otimes \mathcal{Z} + (\mathcal{Y} \wedge \mathcal{Z}) \otimes \mathcal{X} + (\mathcal{Z} \wedge \mathcal{X}) \otimes \mathcal{Y}$(for a proof, see *e.g.* 81, exercise 55.2). In addition, we use $\mathbf{B}(\mathbf{E} \wedge \mathbf{v}) = -\mathbf{v}(\mathbf{E} \wedge \mathbf{B})$, such that

$$\begin{aligned}
\boldsymbol{\nabla}(\mathcal{H}_{\mathrm{F}} \wedge \mathcal{E}) = {} & \mathrm{d}/\mathrm{d}t\left[\varepsilon_0\mathbf{E}^2/2 + \mathcal{E}\mathbf{P} + \mathbf{B}^2/2\mu_0 - \varepsilon_0(\mathbf{E} \wedge \mathbf{B})\mathbf{v}\right] + \mathcal{E}\mathcal{J}_{\mathrm{F}} - \boldsymbol{\mathcal{M}}\dot{\mathbf{B}} \\
& + \varepsilon_0(\mathbf{E} \wedge \mathbf{B})\dot{\mathbf{v}} - \mathbf{P}\dot{\mathcal{E}} + \Big[\left(\varepsilon_0\mathbf{E}^2 + \mathcal{E}\mathbf{P} + (\mathbf{B}/\mu_0 - \boldsymbol{\mathcal{M}})\,\mathbf{B} - \varepsilon_0(\mathbf{E} \wedge \mathbf{B})\mathbf{v}\right)\mathbf{Id} \\
& - \varepsilon_0\mathbf{E} \otimes \mathbf{E} - \mathcal{E} \otimes \mathbf{P} - \mathbf{B} \otimes \mathbf{B}/\mu_0 + \boldsymbol{\mathcal{M}} \otimes \mathbf{B} - \varepsilon_0(\mathbf{E} \wedge \mathbf{B}) \otimes \mathbf{v}] : \operatorname{grad} \mathbf{v}.
\end{aligned} \tag{D.28}$$

D.4 Derivation of Stress Imbalances

In section 5.2, we derived the constitutive equation for the stress tensor (see eq. (5.85)),

$$\boldsymbol{\sigma} = \boldsymbol{\tau} - \left(\varepsilon_0\mathbf{E}^2/2 + \mathbf{B}^2/2\mu_0 - \boldsymbol{\mathcal{M}}\mathbf{B} + \sum_{\alpha=1}^{\mathrm{N}} c_\alpha \mu_\alpha - \rho\varphi_{\mathrm{H}}\right)\mathbf{Id} + \mathfrak{D}_{\mathrm{tf}} + \varepsilon_0\mathbf{E}\otimes\mathbf{E} + \mathcal{E}\otimes\mathbf{P} \\ + \mathbf{B}\otimes\mathbf{B}/\mu_0 - \boldsymbol{\mathcal{M}}\otimes\mathbf{B} + (\varepsilon_0\mathbf{E}\wedge\mathbf{B})\otimes\mathbf{v}, \quad \text{(D.29)}$$

from which we want to calculate $\boldsymbol{\nabla\sigma}$. We use the relations $\boldsymbol{\nabla}(\mathcal{X}\otimes\mathcal{Y})=(\boldsymbol{\nabla}\mathcal{Y})\mathcal{X}+\mathcal{X}(\boldsymbol{\nabla}\mathcal{Y})$ (which follows from the chain rule) and $\boldsymbol{\nabla}(\mathcal{X}\cdot\mathcal{Y})=(\mathcal{X}\boldsymbol{\nabla})\mathcal{Y} + \mathcal{X}\wedge(\boldsymbol{\nabla}\wedge\mathcal{Y}) + (\mathcal{Y}\boldsymbol{\nabla})\mathcal{X} + \mathcal{Y}\wedge(\boldsymbol{\nabla}\wedge\mathcal{X})$,[75]

$$\boldsymbol{\nabla}\left(\mathbf{E}\otimes\mathbf{E} - \mathbf{E}^2/2\cdot\mathbf{Id}\right) = \mathbf{E}\,(\boldsymbol{\nabla}\mathbf{E}) - \mathbf{E}\wedge(\boldsymbol{\nabla}\wedge\mathbf{E})\,, \quad \text{(D.30)}$$

and

$$\boldsymbol{\nabla}\left[(\boldsymbol{\mathcal{M}}\mathbf{B})\cdot\mathbf{Id} - \boldsymbol{\mathcal{M}}\otimes\mathbf{B}\right] = (\boldsymbol{\mathcal{M}}\boldsymbol{\nabla})\,\mathbf{B} + \boldsymbol{\mathcal{M}}\wedge(\boldsymbol{\nabla}\wedge\mathbf{B}) + \mathbf{B}\wedge(\boldsymbol{\nabla}\wedge\boldsymbol{\mathcal{M}})\,, \quad \text{(D.31)}$$

where we used $\boldsymbol{\nabla}\mathbf{B} = 0$. In the aether-frame (where $\mathbf{H}_{\mathrm{F}} = \mathbf{B}/\mu_0 - \mathbf{M}$), the relations $\boldsymbol{\mathcal{M}} = \mathbf{M} + \mathbf{v}\wedge\mathbf{P}$, and $\boldsymbol{\nabla}\wedge\mathbf{H}_{\mathrm{F}} = \mathbf{j}_{\mathrm{F}} - \partial_t\mathbf{D}_{\mathrm{F}}$, imply

$$\boldsymbol{\nabla}\left[(\boldsymbol{\mathcal{M}}\mathbf{B})\cdot\mathbf{Id} - \boldsymbol{\mathcal{M}}\otimes\mathbf{B}\right] = (\boldsymbol{\mathcal{M}}\boldsymbol{\nabla})\,\mathbf{B} + \boldsymbol{\mathcal{M}}\wedge(\boldsymbol{\nabla}\wedge\mathbf{B}) + \mathbf{B}\wedge(\boldsymbol{\nabla}\wedge\mathbf{B}/\mu_0) - \mathbf{B}\wedge\mathbf{j}_{\mathrm{F}} \\ - \mathbf{B}\wedge\partial_t\mathbf{D}_{\mathrm{F}} + \mathbf{B}\wedge\left[\boldsymbol{\nabla}\wedge(\mathbf{v}\wedge\mathbf{P})\right]. \quad \text{(D.32)}$$

Next, using the aether frame property $\mathbf{P} = \mathbf{D}_{\mathrm{F}} - \varepsilon_0\mathbf{E}$, we obtain

$$\boldsymbol{\nabla}(\mathcal{E}\otimes\mathbf{P}) = (\mathbf{P}\boldsymbol{\nabla})\,\mathcal{E} + \varrho_{\mathrm{F}}\mathbf{E} + (\mathbf{v}\wedge\mathbf{B})\cdot\boldsymbol{\nabla}\mathbf{P} - \mathbf{E}\,(\boldsymbol{\nabla}\varepsilon_0\mathbf{E})\,, \quad \text{(D.33)}$$

and

$$\boldsymbol{\nabla}\left[(\varepsilon_0\mathbf{E}\wedge\mathbf{B})\otimes\mathbf{v}\right] = (\varepsilon_0\mathbf{E}\wedge\mathbf{B})\cdot\boldsymbol{\nabla}\mathbf{v} + (\mathbf{v}\boldsymbol{\nabla})\cdot(\varepsilon_0\mathbf{E}\wedge\mathbf{B})\,. \quad \text{(D.34)}$$

Using $\dot{\rho} = -\rho\boldsymbol{\nabla}\mathbf{v}$ and $\partial_t\mathcal{X} = \dot{\mathcal{X}} - (\mathbf{v}\boldsymbol{\nabla})\mathcal{X}$, such that $(\varepsilon_0\mathbf{E}\otimes\mathbf{B})(\boldsymbol{\nabla}\mathbf{v}) = \rho\frac{\mathrm{d}}{\mathrm{d}t}(\varepsilon_0\mathbf{E}\wedge\mathbf{B}/\rho) - \partial_t(\varepsilon_0\mathbf{E}\wedge\mathbf{B}) - (\mathbf{v}\boldsymbol{\nabla})(\varepsilon_0\mathbf{E}\wedge\mathbf{B})$, eq. (D.34) becomes

$$\boldsymbol{\nabla}\left[(\varepsilon_0\mathbf{E}\wedge\mathbf{B})\otimes\mathbf{v}\right] = \rho\frac{\mathrm{d}}{\mathrm{d}t}\,(\varepsilon_0\mathbf{E}\wedge\mathbf{B}/\rho) - (\varepsilon_0\partial_t\mathbf{E})\wedge\mathbf{B} + \varepsilon_0\mathbf{E}\,(\boldsymbol{\nabla}\wedge\mathbf{E})\,. \quad \text{(D.35)}$$

Next, we use $\overset{*}{\mathbf{P}} = \partial_t\mathbf{P} + \mathbf{v}(\boldsymbol{\nabla}\mathbf{P}) - \mathbf{v}\wedge(\mathbf{v}\wedge\mathbf{P})$ and $\mathbf{B}\wedge(\boldsymbol{\nabla}\wedge\mathbf{B}/\mu_0) = \boldsymbol{\nabla}\mathbf{B}^2/2\mu_0 - \boldsymbol{\nabla}(\mathbf{B}\otimes\mathbf{B})/\mu_0 + \mathbf{B}(\boldsymbol{\nabla}\mathbf{B}/\mu_0)$, and eqs. (D.30), (D.32), (D.33) and (D.35) find

$$\boldsymbol{\nabla\sigma} = \boldsymbol{\nabla\tau} - \boldsymbol{\nabla}\left[\sum_{\alpha=1}^{\mathrm{N}} \mu_\alpha c_\alpha - \rho\varphi_{\mathrm{H}}\right] + \boldsymbol{\nabla}\mathfrak{D}_{\mathrm{tf}} + (\boldsymbol{\mathcal{M}}\boldsymbol{\nabla})\,\mathbf{B} + \boldsymbol{\mathcal{M}}\wedge(\boldsymbol{\nabla}\wedge\mathbf{B}) + (\mathbf{P}\boldsymbol{\nabla})\,\mathcal{E}$$

$$+\overset{*}{\mathbf{P}}\wedge\mathbf{B}+\rho\frac{\mathrm{d}}{\mathrm{d}t}\left(\varepsilon_0\mathbf{E}\wedge\mathbf{B}/\rho\right)+\varrho_{\mathrm{F}}\mathbf{E}+\mathbf{j}_{\mathrm{F}}\wedge\mathbf{B}. \tag{D.36}$$

The last two terms are Galilei-invariant ($\varrho_{\mathrm{F}}\mathbf{E}+\mathbf{j}_{\mathrm{F}}\wedge\mathbf{B}=\varrho_{\mathrm{F}}\boldsymbol{\mathcal{E}}+\boldsymbol{\mathcal{J}}_{\mathrm{F}}\wedge\mathbf{B}$).

D.5 Modeling Energy of Deformation

We model the bulk free energy density stemming from volume-deformations, $\Psi(V,p,T)$, via a linear response to volume-perturbations around the stable reference state $\Psi^R(V^R,p^R,T^R)=0$ of minimal deformation-energy.Because of the stability criterion $\partial\Psi/\partial V|_{V^R}=0$, the Taylor-expansion of Ψ reads,

$$\Psi(V^R+\varepsilon)=1/2\cdot\partial^2\Psi/\partial V^2\,|_{V^R}\cdot\left(V-V^R\right)^2, \tag{D.37}$$

where $V=V^R+\varepsilon$, and $\varepsilon\ll V$. Usually, the bulk-modulus is derived from pressure variations, $\mathcal{K}/V=-V\cdot\partial p/\partial V=\mathcal{K}/V=-V\cdot\partial^2\Psi/\partial V^2$ (using thermodynamical Maxwell-relations). This motivates defining the bulk-modulus-density by $\mathcal{K}=V^2\cdot\partial^2\Psi/\partial V^2|_{V^R}$. Hence, eq. (D.37) becomes $\Psi{=}\mathcal{K}\cdot(1-V^R/V)^2/2=\mathcal{K}/2\cdot(1-\sum_{\alpha=1}^{\mathrm{N}}\nu_\alpha^0c_\alpha)^2$ (using $V^R=\sum_{\alpha=1}^{\mathrm{N}}\mathcal{N}_\alpha\nu_\alpha^0$), which is well-defined for compressible and incompressible electrolytes, where the bulk modulus $\mathcal{K}=2\Psi/(1-V^R/V)^2$ diverges in the incompressible limit, $\lim_{V\to V^R}\mathcal{K}\to\infty$.

D.6 Interpretation of The Strain Rate Tensor

In this section we discuss that the strain rate tensor describes the geometric evolution of the system. This includes volume-change (*i.e.* isotropic expansion/contraction) and shape-change (*i.e.* shearing, rotation).

We examine the evolution of a set of neighboring material points, which are subject to surface forces comprised in the Cauchy-tensor. Thus, their relative position changes with time. As reference, we choose an arbitrary material point p (coordinate $\mathbf{x}$), and an arbitrary small neighborhood $\mathcal{U}_p$ which contains two material points $\mathrm{A},\mathrm{B}\in\mathcal{U}_p$. We define $\boldsymbol{\xi}_{\mathrm{A}},\boldsymbol{\xi}_{\mathrm{B}}$ by $\mathbf{x}_{\mathrm{A}}=\mathbf{x}+\boldsymbol{\xi}_{\mathrm{A}}$ and $\mathbf{x}_{\mathrm{B}}=\mathbf{x}+\boldsymbol{\xi}_{\mathrm{B}}$. Thus, the relative evolution of the material points is determined by the change of the separation vectors. The corresponding velocity field is $\mathbf{v}_{\mathrm{A,B}}=\mathrm{d}\mathbf{x}_{\mathrm{A,B}}/\mathrm{d}t$, and the separation velocity fields are $\mathbf{v}_{\boldsymbol{\xi}_{\mathrm{A,B}}}=\mathrm{d}(\boldsymbol{\xi}_{\mathrm{A,B}})/\mathrm{d}t=\mathbf{v}_{\mathrm{A,B}}-\mathbf{v}$, with the separation velocity fields $\mathbf{v}_{\boldsymbol{\xi}}=(\boldsymbol{\xi}\cdot\boldsymbol{\nabla})\mathbf{v}=\operatorname{grad}\mathbf{v}\cdot\boldsymbol{\xi}$, and velocity gradients $(\operatorname{grad}\mathbf{v})_{\alpha\beta}=\partial_\beta v_\alpha$. Hence, the evolution of the separation vector (the relative position of neighbouring material points) is determined by the deviation tensor

$$\mathrm{d}\boldsymbol{\xi}/\mathrm{d}t = \operatorname{grad}\mathbf{v}\cdot\boldsymbol{\xi}. \tag{D.38}$$

The three material points $p, \mathrm{A}, \mathrm{B}$ span a surface, which can be extended to a volume element δV by introducing an additional direction from p to a material point $\mathrm{C} \in \mathcal{U}_p$, measured by the separation vector $\mathbf{x}_\mathrm{C} = \mathbf{x} + \boldsymbol{\xi}_\mathrm{C}$. The three directions $\hat{\mathbf{e}}_{A,B,C}$ span $\mathbb{R}^3$, and the volume spanned by the separation vectors $\boldsymbol{\xi}_{\mathrm{A,B,C}}$ is the scalar triple product $\delta V = \boldsymbol{\xi}_\mathrm{A}(\boldsymbol{\xi}_\mathrm{B} \wedge \boldsymbol{\xi}_\mathrm{C}) = \epsilon_{ijk}\xi^i_\mathrm{A}\xi^j_\mathrm{B}\xi^k_\mathrm{C}$. Thus,

$$\begin{aligned}
\mathrm{d}/\mathrm{d}t\,\delta V &= \epsilon_{ijk}\Big((\partial_m v^i)\xi^m_\mathrm{A}\xi^j_\mathrm{B}\xi^k_\mathrm{C} + (\partial_m v^j)\xi^i_\mathrm{A}\xi^m_\mathrm{B}\xi^k_\mathrm{C} + (\partial_m v^k)\xi^i_\mathrm{A}\xi^j_\mathrm{B}\xi^m_\mathrm{C}\Big) && \text{(D.39)}\\
&= (\partial_m v^m)\epsilon_{ijk}\xi^i_\mathrm{A}\xi^j_\mathrm{B}\xi^k_\mathrm{C} && \text{(D.40)}\\
&= \operatorname{tr}(\operatorname{grad}\mathbf{v})\cdot\delta V, && \text{(D.41)}
\end{aligned}$$

(using anti-symmetry of the Levi-Civita symbol). Since $\operatorname{tr}\operatorname{grad}\mathbf{v} = \operatorname{tr}\boldsymbol{\kappa} = \boldsymbol{\nabla}\mathbf{v}$,

$$\operatorname{tr}\boldsymbol{\kappa} = \boldsymbol{\nabla}\mathbf{v} = 1/\delta V\ \cdot \mathrm{d}(\delta V)/\mathrm{d}t\,. \tag{D.42}$$

Thus, the trace of the strain rate tensor measures the relative change in local volume per unit time. Since, the trace is an invariant of the strain rate tensor, this result is true for any choice of coordinates. Equation (D.42) shows that from $\boldsymbol{\nabla}\mathbf{v} = 0$ follows that the volume is constant in time. Vice versa, it also proves that a constant volume implies $\boldsymbol{\nabla}\mathbf{v} = 0$. A similar investigation reveals that the shear-part $\boldsymbol{\Sigma}_{\operatorname{grad}\mathbf{v}} = \boldsymbol{\kappa} - \boldsymbol{\nabla}\mathbf{v}/3\cdot\mathbf{Id}$ measures shearing, and $\boldsymbol{\omega}_{\operatorname{grad}\mathbf{v}} = (\operatorname{grad}\mathbf{v} - \operatorname{grad}\mathbf{v}^T)/2$ measures rotation of the medium (see, *e.g.* section 2.2 in 438). The same property holds for the shearing of the strain rate tensor. However, since the strain rate tensor is symmetric by construction, $\boldsymbol{\kappa}$ has no spin-part.

D.7 Matrix Formulation of Transport Equations

Here, we reexpress the transport equations eqs. (5.244) to (5.246), and the fluxes eqs. (5.247) and (5.248) using matrices.

We comprise different sets of thermodynamic forces in

$$\mathcal{X}^T{=}(\boldsymbol{\nabla}\mu_\alpha, \boldsymbol{\nabla}T),\ \tilde{\mathcal{X}}^T{=}(\boldsymbol{\nabla}\ \tilde{\mu}_\alpha|_{2\le\alpha\le\mathrm{N}}\,, \boldsymbol{\nabla}T),\ \mathcal{X}^T_\mathrm{red}{=}(\boldsymbol{\nabla}\ \tilde{\tilde{\mu}}_\alpha|_{3\le\alpha\le\mathrm{N}}\,, \boldsymbol{\nabla}T) \tag{D.43}$$

and different sets of thermodynamic fluxes in

$$\psi^T = (\boldsymbol{\mathcal{N}}_2, \dots, \boldsymbol{\mathcal{N}}_\mathrm{N}, \boldsymbol{\xi}_s), \quad \text{and} \quad \psi^T_\mathrm{red} = (\boldsymbol{\mathcal{N}}_3, \dots, \boldsymbol{\mathcal{N}}_\mathrm{N}, \boldsymbol{\xi}_s). \tag{D.44}$$

Likewise, we collect parameters of material and transport in the vectors,

$$\tilde{\boldsymbol{z}} = (\tilde{z}_2, \dots, \tilde{z}_\mathrm{N})^T, \tag{D.45}$$

$$\tilde{\boldsymbol{\nu}} = (\tilde{\nu}_2, \dots, \tilde{\nu}_{\mathrm{N}})^T, \tag{D.46}$$

$$\boldsymbol{\mathfrak{T}}^T = (\mathfrak{T}_2, \dots, \mathfrak{T}_{\mathrm{N}}, \mathfrak{T}_T) = (t_2/F\tilde{z}_2, \dots, t_{\mathrm{N}}/F\tilde{z}_{\mathrm{N}}, \beta), \tag{D.47}$$

$$\boldsymbol{\mathfrak{T}}^T_{\mathrm{red}} = (t_3/F\tilde{z}_3, \dots, t_{\mathrm{N}}/F\tilde{z}_{\mathrm{N}}, \beta). \tag{D.48}$$

First, we reduce the set of all thermodynamic forces $\mathcal{X}$, and then evaluate the gradients $\boldsymbol{\nabla}\mu_\alpha(\boldsymbol{\Upsilon})$ according to their materials law. Let $\mathrm{diag}^{[\mathrm{N}\times\mathrm{N}]}(\Theta)$ be a quadratic N-dimensional diagonal-matrix with equal entries "Θ", we define the N-1×N-dimensional valency-matrix $\boldsymbol{\mathcal{Z}}$, and the N×N+1-dimensional mass-matrix $\boldsymbol{\mathfrak{M}}$

$$\boldsymbol{\mathcal{Z}}(z_\alpha, M_\alpha) = \left(\begin{bmatrix} -\tilde{z}_3/\tilde{z}_2 \\ \vdots \\ -\tilde{z}_{\mathrm{N}}/\tilde{z}_2 \\ 0 \end{bmatrix} \begin{bmatrix} \ddots & & \\ & \mathrm{diag}^{[(\mathrm{N}-1)\times(\mathrm{N}-1)]}(1) & \\ & & \ddots \end{bmatrix} \right), \tag{D.49}$$

and

$$\boldsymbol{\mathfrak{M}}(M_\alpha) = \left(\begin{bmatrix} -M_2/M_1 \\ \vdots \\ -M_{\mathrm{N}}/M_1 \\ 0 \end{bmatrix} \begin{bmatrix} \ddots & & \\ & \mathrm{diag}^{[\mathrm{N}\times\mathrm{N}]}(1) & \\ & & \ddots \end{bmatrix} \right). \tag{D.50}$$

$\boldsymbol{\mathcal{Z}}$ and $\boldsymbol{\mathfrak{M}}$ relate the different sets of chemical potentials via simple products,

$$(\tilde{\mu}_2, \dots, \tilde{\mu}_{\mathrm{N}}, T)^T = \boldsymbol{\mathfrak{M}} \cdot (\mu_1, \dots, \mu_{\mathrm{N}}, T)^T, \tag{D.51}$$

and

$$(\tilde{\tilde{\mu}}_3, \dots, \tilde{\tilde{\mu}}_{\mathrm{N}}, T)^T = \boldsymbol{\mathcal{Z}} \cdot (\tilde{\mu}_2, \dots, \tilde{\mu}_{\mathrm{N}}, T)^T = \boldsymbol{\mathcal{Z}} \cdot \boldsymbol{\mathfrak{M}} \cdot (\mu_1, \dots, \mu_{\mathrm{N}}, T)^T. \tag{D.52}$$

Since $\boldsymbol{\mathcal{Z}}$ and $\boldsymbol{\mathfrak{M}}$ depend on constant material-parameters, we can transfer eq. (D.43) to the vector-representation of the thermodynamic forces,

$$\mathcal{X}_{\mathrm{red}} = \boldsymbol{\mathcal{Z}} \cdot \boldsymbol{\mathfrak{M}} \cdot \mathcal{X}. \tag{D.53}$$

We express $\boldsymbol{\mathcal{J}}_{\mathrm{F}}$ via thermodynamic forces $\mathcal{X}$. Using eq. (5.248), we find

$$\boldsymbol{\mathcal{J}}_{\mathrm{F}} = -\kappa \cdot (\boldsymbol{\nabla}\Phi) - \kappa \cdot \boldsymbol{\mathfrak{T}}^T \cdot \boldsymbol{\mathfrak{M}} \cdot \mathcal{X} = -\kappa \cdot \left(1,\ [\boldsymbol{\mathfrak{M}}^T \cdot \boldsymbol{\mathfrak{T}}]^T\right) \cdot \begin{pmatrix} \boldsymbol{\nabla}\Phi \\ [\mathcal{X}] \end{pmatrix} \tag{D.54}$$

In the next step, we derive a similar expansion for the thermodynamic fluxes, where the components of this vector of fluxes are determined by eqs. (5.131) and (5.132) ($\boldsymbol{\mathcal{N}}_2$ follows from $\boldsymbol{\mathcal{J}}_{\mathrm{F}} = \sum_{\alpha=2}^{\mathrm{N}} F\tilde{z}_\alpha \boldsymbol{\mathcal{N}}_\alpha$). For this purpose, we define a special notation for the vector-valued multiplication of two vector-quantities,

$$\boldsymbol{\mathcal{J}}_{\mathrm{F}} \odot \mathfrak{T} = (\boldsymbol{\mathcal{J}}_{\mathrm{F}} \cdot \mathfrak{T}_2, \ldots, \boldsymbol{\mathcal{J}}_{\mathrm{F}} \cdot \mathfrak{T}_{\mathrm{N}}, \boldsymbol{\mathcal{J}}_{\mathrm{F}} \cdot \beta)^T , \text{ such that } \psi = \boldsymbol{\mathcal{J}}_{\mathrm{F}} \odot \mathfrak{T} - \boldsymbol{\mathcal{D}} \cdot \boldsymbol{\mathcal{Z}} \cdot \mathcal{X}_{\mathrm{red}} . \tag{D.55}$$

In contrast to ψ_{red}, the quantity ψ cannot be expressed solely via $\mathcal{X}_{\mathrm{red}}$, since $\boldsymbol{\mathcal{J}}_{\mathrm{F}} \odot \mathfrak{T} = -\kappa(\boldsymbol{\nabla}\Phi) \odot \mathfrak{T} - \kappa \cdot \mathfrak{T} \otimes \mathfrak{T} \cdot \tilde{\mathcal{X}}$. However,

$$\psi = -\kappa \cdot (\boldsymbol{\nabla}\Phi) \odot \mathfrak{T} - (\boldsymbol{\mathcal{D}} \cdot \boldsymbol{\mathcal{Z}} + \kappa \cdot \mathfrak{T} \otimes \mathfrak{T}) \cdot \mathfrak{M} \cdot \mathcal{X}^T \tag{D.56a}$$

$$= -\left(\begin{bmatrix} \vdots \\ \kappa \cdot \mathfrak{T} \\ \vdots \end{bmatrix} \begin{bmatrix} \ddots & & \\ & (\boldsymbol{\mathcal{D}} \cdot \boldsymbol{\mathcal{Z}} + \kappa \cdot \mathfrak{T} \otimes \mathfrak{T}) \cdot \mathfrak{M} & \\ & & \ddots \end{bmatrix} \right) \cdot \begin{pmatrix} \boldsymbol{\nabla}\Phi \\ \begin{bmatrix} \mathcal{X} \end{bmatrix} \end{pmatrix} . \tag{D.56b}$$

and

$$\psi_{\mathrm{red}} = -\kappa \cdot (\boldsymbol{\nabla}\Phi) \odot \mathfrak{T}_{\mathrm{red}} - (\boldsymbol{\mathcal{D}}_{\mathrm{red}} \boldsymbol{\mathcal{Z}} + \kappa \cdot \mathfrak{T}_{\mathrm{red}} \otimes \mathfrak{T}) \cdot \mathfrak{M} \cdot \mathcal{X} \tag{D.57a}$$

$$= -\left\{ \mathfrak{T}_{\mathrm{red}} \otimes \kappa \begin{pmatrix} 1 \\ \begin{bmatrix} \mathfrak{M}^T \cdot \mathfrak{T} \end{bmatrix} \end{pmatrix} + \left(\begin{bmatrix} 0 \\ \vdots \\ 0 \end{bmatrix} \begin{bmatrix} \boldsymbol{\mathcal{D}} \cdot \boldsymbol{\mathcal{Z}} \cdot \mathfrak{M} \end{bmatrix} \right) \right\} \begin{pmatrix} \boldsymbol{\nabla}\Phi \\ \begin{bmatrix} \mathcal{X} \end{bmatrix} \end{pmatrix} . \tag{D.57b}$$

From the expansion of the conduction current density and the mass fluxes, eq. (D.54) and eqs. (D.57) follows directly the matrix-form of the convection-equation (see eq. (5.246)),

$$\boldsymbol{\nabla}\mathbf{v} = -\left([\ \tilde{\boldsymbol{\nu}}^T\ ], 0 \right) \cdot (\boldsymbol{\nabla} \odot \psi) = -\left(\tilde{\nu}_2 / F \tilde{z}_2 , \tilde{\tilde{\nu}}_3, \ldots, \tilde{\tilde{\nu}}_{\mathrm{N}}, 0 \right) \cdot \begin{pmatrix} \boldsymbol{\nabla} \boldsymbol{\mathcal{J}}_{\mathrm{F}} \\ \boldsymbol{\nabla} \odot \begin{bmatrix} \psi_{\mathrm{red}} \end{bmatrix} \end{pmatrix} . \tag{D.58}$$

Since the quantity $\mathcal{X}$ depends upon the model free energy and the materials law, the fluxes eq. (D.54),eqs. (D.57),eqs. (D.56) and eq. (D.58), are also subject to the specific electrolyte model. In general, any reasonable model comprises the species-concentrations in it's materials law, such that

$$\boldsymbol{\nabla}\mu_\alpha(\boldsymbol{\Upsilon}) = (\sum_A \partial\mu_\alpha / \partial\Upsilon_A \cdot \boldsymbol{\nabla})\Upsilon_A|_{\Upsilon_A \neq c_\gamma} + \sum_{\gamma=1}^{\mathrm{N}} \partial\mu_\alpha / \partial c_\gamma \cdot \boldsymbol{\nabla} c_\gamma . \tag{D.59}$$

In the last term on the right side of eq. (D.59), we must take account for the fact that the set of independent variables is $\varrho_{\mathrm{F}}, c_3, \ldots, c_{\mathrm{N}}$. Thus, for any N-component mixture, there exists a N×N-dimensional matrix $\boldsymbol{\mathcal{M}}(z_\alpha, \nu_\alpha)$, such that

$$(c_1,\ \ldots,\ c_{\mathrm{N}})^T = \boldsymbol{\mathcal{M}} \cdot (1/z_{[2}\nu_{1]}\, ,\ \varrho_{\mathrm{F}}/F\, ,\ c_3,\ \ldots, c_{\mathrm{N}})^T , \tag{D.60}$$

where $z_{[2}\nu_{1]} = z_2\nu_1 - z_1\nu_2$ denotes the anti-commutator, and

$$\boldsymbol{\mathcal{M}}(z_\alpha, \nu_\alpha) = \frac{1}{z_{[2}\nu_{1]}} \left(\begin{bmatrix} z_2 z_{[2}\nu_{1]} & -\nu_2 \\ -z_1 z_{[2}\nu_{1]} & \nu_1 \\ 0 & 0 \\ \vdots & \vdots \\ 0 & 0 \end{bmatrix} \quad \begin{matrix} \begin{bmatrix} z_{[3}\nu_{2]} & z_{[4}\nu_{2]} & \cdots & z_{[\mathrm{N}}\nu_{2]} \\ -z_{[3}\nu_{1]} & -z_{[4}\nu_{1]} & \cdots & -z_{[\mathrm{N}}\nu_{1]} \end{bmatrix} \\ \begin{bmatrix} \\ \quad \mathrm{diag}^{(\mathrm{N}-2)\times(\mathrm{N}-2)}(z_{[2}\nu_{1]}) \quad \\ \\ \end{bmatrix} \end{matrix} \right) . \tag{D.61}$$

Material Parameters	Transport Parameters	Thermodynamic Quantities
$\mathfrak{M}(M_\alpha)$	$\boldsymbol{\mathcal{L}}$	$\boldsymbol{\mathcal{J}}_{\mathrm{F}}$
$\boldsymbol{\mathcal{Z}}(z_\alpha, M_\alpha)$	$\kappa = F\tilde{\boldsymbol{z}}^T \cdot \boldsymbol{\mathcal{L}} \cdot F\tilde{\boldsymbol{z}}$	ψ, ψ_{red}
ν_α, $\tilde{\nu}_\alpha$, $\tilde{\tilde{\nu}}_\alpha$	$\mathfrak{T} = 1/\kappa \cdot \boldsymbol{\mathcal{L}} \cdot F\tilde{\boldsymbol{z}}$	$\mathcal{X}$, $\mathcal{X}_{\mathrm{red}}$
$\tilde{\boldsymbol{z}} = (\tilde{z}_2, \ldots, \tilde{z}_{\mathrm{N}})$	$\boldsymbol{\mathcal{D}} = \boldsymbol{\mathcal{L}} - \kappa \cdot \mathfrak{T} \otimes \mathfrak{T}$	
$\boldsymbol{\mathcal{M}}(z_\alpha, \nu_\alpha)$		

Table D.1: Summary of the vector-expressions for the constant material parameters, the transport parameters, and the thermodynamic quantities.

We now consider the isothermal case ($\boldsymbol{\nabla} T = 0$) in which the thermal coefficients in the quantities ψ_{red}, $\mathfrak{T}$, $\boldsymbol{\mathcal{D}}$, $\boldsymbol{\mathcal{Z}}$, $\mathfrak{M}$ and $\mathcal{X}$ can be ommitted. In this case, the matrix-form of the model equations become

$$\partial_t \varrho_{\mathrm{F}} = -\boldsymbol{\nabla}\left(\boldsymbol{\mathcal{J}}_{\mathrm{F}} + \varrho_{\mathrm{F}}\mathbf{v}\right), \tag{D.62}$$

$$\left(\partial_t c_3,\ \ldots,\ \partial_t c_{\mathrm{N}}\right)^T = -\boldsymbol{\nabla} \odot \psi_{\mathrm{red}} - \boldsymbol{\nabla} \odot \left(\mathbf{v}\cdot c_3,\ \ldots,\ \mathbf{v}\cdot c_{\mathrm{N}}\right)\right)^T, \tag{D.63}$$

Equations (D.62) and (D.63), together with eq. (D.60) determine c_1 and c_2, whereas the fluxes $\boldsymbol{\mathcal{J}}_{\mathrm{F}}$, and ψ_{red} are determined by eq. (D.54) and eqs. (D.57). The convection velocity is determined by eq. (D.58). Note that, if neccessary, these equations must be supplemented by reaction-terms. In table D.1 we summarize our findings.

Example: Quaternary Electrolyte Mixture

We apply the above notation to the system composed of four species which is in electroneutral and isothermal state, see chapter 6. We eliminate the last column in the matrices $\boldsymbol{\mathcal{Z}}$ and $\mathfrak{M}$, and the last entry in $\mathcal{X}$ and $\mathfrak{T}$. Due to electroneutrality, we omitt the second row in $\boldsymbol{\mathcal{M}}$. Altogether,

$$\boldsymbol{\mathcal{Z}} = \begin{pmatrix} -\tilde{z}_3/\tilde{z}_2 & 1 & 0 \\ -\tilde{z}_4/\tilde{z}_2 & 0 & 1 \end{pmatrix}, \tag{D.64}$$

$$\boldsymbol{\mathfrak{M}} = \begin{pmatrix} -M_2/M_1 & 1 & 0 & 0 \\ -M_3/M_1 & 0 & 1 & 0 \\ -M_4/M_1 & 0 & 0 & 1 \end{pmatrix}, \tag{D.65}$$

$$\boldsymbol{\mathcal{M}} = \frac{1}{z_{[2\,\nu\,1]}} \begin{pmatrix} z_2 z_{[2\,\nu\,1]} & z_{[3\,\nu\,2]} & z_{[4\,\nu\,2]} \\ -z_1 z_{[2\,\nu\,1]} & -z_{[3\,\nu\,1]} & -z_{[4\,\nu\,1]} \\ 0 & z_{[2\,\nu\,1]} & 0 \\ 0 & 0 & z_{[2\,\nu\,1]} \end{pmatrix}, \tag{D.66}$$

$$(c_1,\ c_2,\ c_3,\ c_4)^T = \boldsymbol{\mathcal{M}} \cdot (1/z_{[2\,\nu\,1]}\,,\ c_3,\ c_4) \tag{D.67}$$

$$\mathcal{X}^T = (\boldsymbol{\nabla}\mu_1,\ \boldsymbol{\nabla}\mu_2,\ \boldsymbol{\nabla}\mu_3,\ \boldsymbol{\nabla}\mu_4)^T, \tag{D.68}$$

$$\boldsymbol{\mathcal{L}} = \begin{pmatrix} \mathcal{L}_{22} & \mathcal{L}_{23} & \mathcal{L}_{24} \\ \mathcal{L}_{23} & \mathcal{L}_{33} & \mathcal{L}_{34} \\ \mathcal{L}_{24} & \mathcal{L}_{34} & \mathcal{L}_{44} \end{pmatrix}. \tag{D.69}$$

However, the quantity $\mathcal{X}$ is subject to the model free energy. For example, if we use our model free energy eq. (5.153), and neglect interactions, we get

$$\mathcal{X} = -\varrho_{\mathrm{F}} \boldsymbol{\nabla}\Phi \odot (\nu_1, \nu_2, \nu_3, \nu_4)^T + RT\boldsymbol{\nabla} \odot (\ln f_1 c_1, \ln f_2 c_2, \ln f_3 c_3, \ln f_4 c_4)^T. \tag{D.70}$$

D.8 Transformation of Reference Species

In section 5.3 we made use of the property that N-1 mass-fluxes $\boldsymbol{\mathcal{N}}_\alpha$ are independent in a N-component mixture and introduced one designated species (by convention, the first species), see eqs. (5.105), (5.106) and (5.225). Because the choice for the designated species is arbitrary, the mesoscopic predictions of our transport theory must be invariant under changing the reference species. Here, we derive conversion relations between different reference-species.

Reduced Valencies, Molar Volumes and Chemical POtentials We designate a fixed sequence of physical species, denoted by capital latin letters $A, B, C, \ldots$, and assume a bijective assignment between the physical species $A, B, C, \ldots$, and the species-indices $\alpha, \beta, \gamma, \ldots$.

We use the notation introduced in appendix D.7, and neglect thermal aspects such that all vector-quantities introduced above are to be reduced as explained in appendix D.7. We define reduced sets of valences relative to any designated species

A,

$$\tilde{z}^{(A)}_B|_{B\neq A} = z_B|_{B\neq A} - M_B/M_A \cdot z_A|_{B\neq A}. \tag{D.71}$$

Apparently, two sets ($\tilde{z}^{(A)}_B$) and ($\tilde{z}^{(C)}_D$) of reduced valences (defined relative to different designated species A, and C), are related by

$$\tilde{z}^{(A)}_B = \tilde{z}^{(C)}_B|_{B\neq A,C} - M_B/M_A \cdot \tilde{z}^{(C)}_A|_{B\neq A,C} \tag{D.72}$$

This relation can be expressed "species-independent", using transformation matrices. Let A and C be two distinct designated species. Then, the corresponding two sets of reduced quantities are related by transformations $\boldsymbol{\mathcal{M}}^{(A\to C)}$ (see),

$$\tilde{\boldsymbol{z}}^{(A)} = \boldsymbol{\mathcal{M}}^{(C\to A)} \cdot \tilde{\boldsymbol{z}}^{(C)}, \quad \tilde{\mathbf{v}}^{(A)} = \boldsymbol{\mathcal{M}}^{(C\to A)} \cdot \tilde{\mathbf{v}}^{(C)}, \quad \tilde{\boldsymbol{\mathcal{X}}}^{(A)} = \boldsymbol{\mathcal{M}}^{(C\to A)} \cdot \tilde{\boldsymbol{\mathcal{X}}}^{(C)}, \tag{D.73}$$

where the transformation $\boldsymbol{\mathcal{M}}^{(A\to C)}$ has a (N-1)×(N-1)-dimensional matrix-representation,

$$\mathcal{M}^{(C\to A)}_{DB}|_{\substack{D\neq C\\ B\neq A}} = \delta_{DB}|_{\substack{D\neq C\\ B\neq A}} - M_B/M_D \cdot \delta_{AD}|_{\substack{D\neq C\\ B\neq A}}. \tag{D.74}$$

Note that there is no sum over the index "D" (despite the twofold appearance).

The mass-matrices defined by eq. (D.50) represent special cases of the more general definition eq. (D.74). There, the designated species is $\alpha = 1$, and relates to the transformation matrix $\boldsymbol{\mathcal{M}}^{(2\to 1)}$ by elimination of the second column (see appendix D.7). By construction, the matrix representation of the trivial transformation eq. (D.74) is exactly the neutral element $\boldsymbol{\mathcal{M}}^{(A\to A)} = \mathbf{Id}$. We derive the inverse transformation via the requirement that the cyclic transformation $\boldsymbol{\mathcal{M}}^{(C\to A)} \circ \boldsymbol{\mathcal{M}}^{(A\to C)} \equiv \boldsymbol{\mathcal{M}}^{(C\to C)} = \mathbf{Id}$. By construction, $\sum_{B\neq A} \mathcal{M}^{(C\to A)}_{DB}|_{D\neq C} \cdot \mathcal{M}^{(A\to C)}_{BE}|_{D\neq C} = \delta_{DE}|_{E,D\neq C}$, such that

$$\boldsymbol{\mathcal{M}}^{(C\to A)} = \left(\boldsymbol{\mathcal{M}}^{(A\to C)}\right)^{-1}. \tag{D.75}$$

Transformation of Mass Fluxes In the isothermal case, The vector of thermodynamic fluxes defined by eq. (D.44) reduces in the isothermal case to $\psi^T = (\boldsymbol{\mathcal{N}}_2, \ldots, \boldsymbol{\mathcal{N}}_\mathrm{N})$. We generalize this notation to $\psi^{(A)}$, where eq. (D.44) represents the special $\psi^{(1)}$. We recover the vector of all fluxes from the universal flux constraint $\sum_A M_A \cdot \boldsymbol{\mathcal{N}}_A = 0$,

$$\psi^T_\mathrm{all} = (\boldsymbol{\mathcal{N}}_1, \ldots, \boldsymbol{\mathcal{N}}_\mathrm{N}) \tag{D.76}$$

from any given representation $\psi^{(A)}$. We account for the initial reference species via

$$\psi^{(A)}_\mathrm{all}(\psi^{(A)}) = {}^{[\mathrm{N}]}\boldsymbol{\mathcal{M}}^{(A)} \cdot \psi^{(A)}, \tag{D.77}$$

where the matrix representation of the transformation ${}^{[\mathrm{N}]}\boldsymbol{\mathcal{M}}^{(A)}$ is

$$ {}^{[\mathrm{N}]}\mathcal{M}^{(A)}_{BD} = \delta_{BD} - M_D/M_A \cdot \delta_{BA}. \tag{D.78} $$

The inverse transformation calculates $\psi^{(A)}$ from the vector of all fluxes ψ_{all},

$$ \psi^{(A)} = {}^{(A)}\boldsymbol{\mathcal{M}}^{[\mathrm{N}]} \cdot \psi_{\mathrm{all}}, \quad \text{where} \quad {}^{(A)}\mathcal{M}^{[\mathrm{N}]}_{BD} = \delta_{BD} - \delta_{AD}. \tag{D.79} $$

The transformation rules between independent sets of fluxes, defined relative to different designated species A and C, follow directly from eqs. (D.77) and (D.79),

$$ \psi^{(C)}\left(\psi^{(A)}\right) = \left(\boldsymbol{\mathcal{M}}^{(C\to A)}\right)^{T} \cdot \psi^{(A)}, \tag{D.80} $$

where

$$ \left[(\mathcal{M}^{(C\to A)})^{T}\right]_{BD} = \delta_{BD} - M_D/M_B \cdot \delta_{BA}. \tag{D.81} $$

Thus, the fluxes $\psi^{(A)}$ transform inversely and conjugated (via transposed representation-matrices), as compared to $\tilde{\boldsymbol{z}}^{(A)}$, $\tilde{\mathcal{X}}^{(A)}$ and $\tilde{\boldsymbol{\nu}}^{(A)}$ (see eq. (D.73)).

The concatenation of transformations between sets of all fluxes and different sets of independent fluxes exhibits the property,

$$ {}^{[\mathrm{N}]}\boldsymbol{\mathcal{M}}^{(A)} \cdot (\boldsymbol{\mathcal{M}}^{(A\to C)})^{T} = {}^{[\mathrm{N}]}\boldsymbol{\mathcal{M}}^{(C)}, \tag{D.82} $$

Thus, the set of all fluxes, obtained from different representations, is invariant under changing the designated species,

$$ \psi^{(A)}_{\mathrm{all}} = \psi^{(C)}_{\mathrm{all}}. \tag{D.83} $$

Onsager Matrix and Transport Parameters Here, we derive the transformation behaviour of the Onsager matrix $\boldsymbol{\mathcal{L}}$ from which follow the correct transformation rules for the transport parameters.

In section 5.3, we introduced $\boldsymbol{\mathcal{L}}$ as coupling between the fluxes $\psi^{(1)}$ and the reduced set of forces $\tilde{\mathcal{X}}^{(1)}$ (see eq. (5.115)). Thus, the Onsager matrix depends upon the choice of reference species. Relative to any such choice "A" for the designated species, specific Onsager matrices $\boldsymbol{\mathcal{L}}^{(A)}$ exist. The transformation rules for $\boldsymbol{\mathcal{L}}^{(A)}$ follow directly from the transformation rules of the fluxes, and reduced potentials (see eq. (D.80)),

$$ \boldsymbol{\mathcal{L}}^{(C)} = (\boldsymbol{\mathcal{M}}^{(C\to A)})^{T} \cdot \boldsymbol{\mathcal{L}}^{(A)} \cdot \boldsymbol{\mathcal{M}}^{(C\to A)}. \tag{D.84} $$

Because the transport parameters $\boldsymbol{\kappa}^{(A)}$, $\boldsymbol{\mathfrak{T}}^{(A)}$ and $\boldsymbol{\mathcal{D}}^{(A)}$ are functions of $\boldsymbol{\mathcal{L}}^{(A)}$, eq. (D.84) determines their transformation behaviour. From eq. (5.118), which represents the definition of the electric conductivity relative to the designated species

α=1, follows the generalized definition of the electric conductivity relative to any designated species A, $\kappa^{(A)} = F^2 \cdot (\tilde{\boldsymbol{z}}^{(A)})^T \cdot \boldsymbol{\mathcal{L}}^{(A)} \cdot \tilde{\boldsymbol{z}}^{(A)}$. Thus, from eqs. (D.73) and (D.84) then follows that the electric conductivity is invariant under transformations of the reference species,

$$
\begin{aligned}
\kappa^{(A)} &= F^2 \cdot (\tilde{\boldsymbol{z}}^{(A)})^T \cdot \boldsymbol{\mathcal{L}}^{(A)} \cdot \tilde{\boldsymbol{z}}^{(A)} && \text{(D.85a)}\\
&= F^2 \cdot (\boldsymbol{\mathfrak{M}}^{(C\to A)} \cdot \tilde{\boldsymbol{z}}^{(C)})^T \cdot (\boldsymbol{\mathfrak{M}}^{(A\to C)})^T \cdot \boldsymbol{\mathcal{L}}^{(C)} \cdot \boldsymbol{\mathfrak{M}}^{(A\to C)} \cdot \boldsymbol{\mathfrak{M}}^{(C\to A)} \cdot \tilde{\boldsymbol{z}}^{(C)} && \text{(D.85b)}\\
&= F^2 \cdot (\tilde{\boldsymbol{z}}^{(C)})^T \cdot (\boldsymbol{\mathfrak{M}}^{(A\to C)} \cdot \boldsymbol{\mathfrak{M}}^{(C\to A)})^T \cdot \boldsymbol{\mathcal{L}}^{(C)} \cdot \tilde{\boldsymbol{z}}^{(C)} && \text{(D.85c)}\\
&= \kappa^{(C)}. && \text{(D.85d)}
\end{aligned}
$$

Hence, $\kappa^{(A)}$ transforms as a "scalar" under the action of the transformation $\boldsymbol{\mathfrak{M}}^{(A\to C)}$.

Next, we derive the transformation behaviour of the transference numbers. However, due to the effective valence appearing on the right side of the definition for t_α (eq. (5.120)), we must first derive the transformation behaviour of the vector $\boldsymbol{\mathfrak{T}}^{(A)} = t_\alpha / F\tilde{z}_\alpha$. Using the invariance of the electric conductivity, the transformation behaviour of the Onsager coefficients, and the valences, we find

$$
\begin{aligned}
\boldsymbol{\mathfrak{T}}^{(A)} &= F/\kappa^{(A)} \cdot \boldsymbol{\mathcal{L}}^{(A)} \cdot \tilde{\boldsymbol{z}}^{(A)} && \text{(D.86)}\\
&= F/\kappa^{(C)} \cdot (\boldsymbol{\mathfrak{M}}^{(A\to C)})^T \cdot \boldsymbol{\mathcal{L}}^{(C)} \cdot \boldsymbol{\mathfrak{M}}^{(A\to C)} \cdot \boldsymbol{\mathfrak{M}}^{(C\to A)} \cdot \tilde{\boldsymbol{z}}^{(C)} && \text{(D.87)}\\
&= (\boldsymbol{\mathfrak{M}}^{(A\to C)})^T \cdot \boldsymbol{\mathfrak{T}}^{(C)}, && \text{(D.88)}
\end{aligned}
$$

i.e. $\boldsymbol{\mathfrak{T}}^{(A)}$ transforms similar to the fluxes $\psi^{(A)}$. Next, we split the transformation rule eq. (D.88) into two cases.

First, the transformation rules for transference numbers of species which aredo not the two designated reference-species (betweeen which we "transform"), are

$$
t_B^{(A)}|_{B\neq A,C} = \tilde{z}_B^{(A)} / \tilde{z}_B^{(C)} \cdot t_B^{(C)}. \tag{D.89}
$$

Second, we calculate the transformation rule of the transference number corresponding to the initial designated species $t_C^{(A)}|_{C\neq A}$,

$$
t_C^{(A)}|_{C\neq A} = -\sum_{D\neq C} M_D/M_C \cdot \tilde{z}_C^{(A)} / \tilde{z}_D^{(C)} \cdot t_D^{(C)}. \tag{D.90}
$$

However, due to the normalization constraint $(\tilde{\boldsymbol{z}}^{(A)})^T \cdot \boldsymbol{\mathfrak{T}}^{(A)} = 1/F$, only N-2 transference numbers are independent, and eq. (D.90) becomes redundant. Thus, eq. (D.89) suffices for the calculation of all parameters,

$$t_C^{(A)}|_{C\neq A} = 1 - \sum_{D\neq A,C} t_D^{(A)}. \tag{D.91}$$

Finally, the transformation behaviour of the diffusion matrices $\boldsymbol{\mathcal{D}}^{(A)} = \boldsymbol{\mathcal{L}}^{(A)} - \boldsymbol{\kappa} \cdot \boldsymbol{\mathfrak{T}}^{(A)} \otimes \boldsymbol{\mathfrak{T}}^{(A)}$ follow trivially from the transformation rules of the Onsager matrix,

$$\boldsymbol{\mathcal{D}}^{(C)} = \left(\boldsymbol{\mathfrak{M}}^{(C\to A)}\right)^{T} \cdot \boldsymbol{\mathcal{D}}^{(A)} \cdot \boldsymbol{\mathfrak{M}}^{(C\to A)}. \tag{D.92}$$

Invariance of the Equations of Motion From eq. (5.248), and since $\psi^{(A)}$ and $\boldsymbol{\mathfrak{T}}^{(A)}$ transform similarly, it follows that $\boldsymbol{\mathcal{J}}_\mathrm{F}$ is invariant under transformations of the designated species. Although the matrix formulation of the convection equation, eq. (D.58),

$$(\boldsymbol{\nabla}\mathbf{v})^{(A)} = -(\tilde{\mathbf{v}}^{(A)})^{T} \cdot \boldsymbol{\nabla} \odot \psi^{(A)}. \tag{D.93}$$

relates to a designated species A, it is invariant under transformations of the designated species. This follows from the invariance of the product

$$\left(\tilde{\mathbf{v}}^{(A)}\right)^{T} \cdot \psi^{(A)} = \left(\boldsymbol{\mathfrak{M}}^{(C\to A)} \cdot \tilde{\mathbf{v}}^{(C)}\right)^{T} \cdot \left(\boldsymbol{\mathfrak{M}}^{(A\to C)}\right)^{T} \cdot \psi^{(C)} \tag{D.94a}$$

$$= \left(\tilde{\mathbf{v}}^{(C)}\right)^{T} \cdot \left(\boldsymbol{\mathfrak{M}}^{(A\to C)} \cdot \boldsymbol{\mathfrak{M}}^{(C\to A)}\right)^{T} \cdot \psi^{(C)} \tag{D.94b}$$

$$= \left(\tilde{\mathbf{v}}^{(C)}\right)^{T} \cdot \psi^{(C)}. \tag{D.94c}$$

Because the transformation matrices are functions of the constant molar masses, we can generalize this result to the convection equation,

$$(\boldsymbol{\nabla}\mathbf{v})^{(A)} = (\boldsymbol{\nabla}\mathbf{v})^{(C)}. \tag{D.95}$$

Therefore, the equation of motion for the charge density is invariant under transformation of the designated species,

$$\partial_t \varrho_\mathrm{F} = -\boldsymbol{\nabla}\boldsymbol{\mathcal{J}}_\mathrm{F} - \boldsymbol{\nabla}(\varrho_\mathrm{F}\mathbf{v}). \tag{D.96}$$

The independent transport equations eqs. (D.62) and (D.63), derived in appendix D.7 relate to the special case where the two designated species are $\alpha = 1$ and $\alpha = 2$. Here, we generalize the matrix formulation to arbitrary reference-species M, and N and define the vector of the reduced concentrations,

$$\boldsymbol{c}^{(M,N)} = \{(c_D)\}\,|_{D\neq M,N}, \tag{D.97}$$

such that for constant partial molar volumes

$$\partial_t \boldsymbol{c}_{\text{all}}^{(M,N)} = \partial_t \begin{pmatrix} c_1(\varrho_{\text{F}}, \boldsymbol{c}^{(M,N)}) \\ \vdots \\ c_{\text{N}}(\varrho_{\text{F}}, \boldsymbol{c}^{(M,N)}) \end{pmatrix} = \boldsymbol{\mathcal{M}}^{(M,N)} \cdot \partial_t \cdot \begin{pmatrix} \varrho_{\text{F}}/F \\ \begin{bmatrix} \\ \boldsymbol{c}^{(M,N)} \\ \\ \end{bmatrix} \end{pmatrix}. \tag{D.98}$$

The N×(N-1)-dimensional matrix $\boldsymbol{\mathcal{M}}^{(M,N)}(\nu_\alpha, z_\alpha)$ is constant if we assume constant partial molar volumes of the species. In components, it is defined by

$$\mathcal{M}_{F\varrho_{\text{F}}}^{(M,N)} = \frac{\delta_{F[N}\nu_{A]}}{\nu_{[M}\, z_{N]}}, \ \ \mathcal{M}_{FD}^{(M,N)} = \delta_{DF} - \frac{\delta_{FM} \cdot \nu_{[D}\, z_{N]} - \delta_{FN} \cdot \nu_{[D}\, z_{M]}}{\nu_{[M}\, z_{N]}}. \tag{D.99}$$

We relate sets of independent forces defined relative to designated sets of species (A,B) and (M,N), using the representation matrix of the transformation $(A,B) \rightarrow (M,N)$,

$$\begin{pmatrix} \partial_t \varrho_{\text{F}}/F \\ \partial_t \begin{bmatrix} \\ \boldsymbol{c}^{(M,N)} \\ \\ \end{bmatrix} \end{pmatrix} = \boldsymbol{\mathcal{S}}^{(A,B)\rightarrow(MN)} \begin{pmatrix} \partial_t \varrho_{\text{F}}/F \\ \partial_t \begin{bmatrix} \\ \boldsymbol{c}^{(A,B)} \\ \\ \end{bmatrix} \end{pmatrix} = \begin{pmatrix} 1 & 0 \ \ \dots \ \ \dots \ \ 0 \\ \begin{bmatrix} \boldsymbol{\mathcal{S}}_{\varrho_{\text{F}}}^{(A,B)\rightarrow(MN)} \end{bmatrix} & \begin{bmatrix} \\ \mathcal{S}_{GD}^{(A,B)\rightarrow(MN)} \\ \\ \end{bmatrix} \end{pmatrix} \begin{pmatrix} \partial_t \varrho_{\text{F}}/F \\ \partial_t \begin{bmatrix} \\ \boldsymbol{c}^{(A,B)} \\ \\ \end{bmatrix} \end{pmatrix}, \tag{D.100}$$

where the components of the (N-1)×(N-1)-dimensional representation matrix $\boldsymbol{\mathcal{S}}^{(A,B)\rightarrow(MN)}$ of the transformation $(A,B) \rightarrow (M,N)$ are

$$\mathcal{S}_{F\varrho_{\text{F}}}^{(A,B)\rightarrow(MN)} = \mathcal{M}_{F\varrho_{\text{F}}}^{(A,B)}|_{F\neq M,N}, \quad \text{and} \quad \mathcal{S}_{GF}^{(A,B)\rightarrow(MN)} = \mathcal{M}_{GF}^{(A,B)}|_{F\neq M,N}. \tag{D.101}$$

A lengthy calculation shows that the concatenation of the expansion matrix $\mathcal{M}^{(M,N)}$ with the representation matrix of the transformation $(A,B) \rightarrow (M,N)$ equals the expansion matrix relative to the species (A,B),

$$\mathcal{M}^{(M,N)} \cdot \boldsymbol{\mathcal{S}}^{(A,B)\rightarrow(MN)} = \mathcal{M}^{(A,B)}, \tag{D.102}$$

which implies that the set of independent transport equations is invariant under transformation of the set of designated species,

$$\partial_t \boldsymbol{c}_{\text{all}}^{(M,N)} = \partial_t \boldsymbol{c}_{\text{all}}^{(A,B)}. \tag{D.103}$$

Example: Quaternary Electrolyte As example, we consider our quaternary electrolyte from chapter 6, and we state the transformation matrices corresponding to three different reference-species,

$$\mathfrak{M}^{(1\to2)} = \begin{pmatrix} -M_1/M_2 & 0 & 0 \\ -M_3/M_2 & 1 & 0 \\ -M_4/M_2 & 0 & 1 \end{pmatrix}, \quad \text{and} \quad \mathfrak{M}^{(2\to1)} = \begin{pmatrix} -M_2/M_1 & 0 & 0 \\ -M_3/M_1 & 1 & 0 \\ -M_4/M_1 & 0 & 1 \end{pmatrix} \tag{D.104}$$

$$\mathfrak{M}^{(1\to3)} = \begin{pmatrix} 1 & -M_2/M_3 & 0 \\ 0 & -M_1/M_3 & 0 \\ 0 & -M_4/M_3 & 1 \end{pmatrix}, \quad \text{and} \quad \mathfrak{M}^{(3\to1)} = \begin{pmatrix} -M_2/M_3 & 0 & 0 \\ -M_1/M_3 & 1 & 0 \\ -M_4/M_3 & 0 & 1 \end{pmatrix}, \tag{D.105}$$

$$\mathfrak{M}^{(1\to4)} = \begin{pmatrix} 0 & 0 & -M_1/M_4 \\ 1 & 0 & -M_2/M_4 \\ 0 & 1 & -M_3/M_4 \end{pmatrix}, \quad \text{and} \quad \mathfrak{M}^{(4\to1)} = \begin{pmatrix} -M_2/M_1 & 1 & 0 \\ -M_3/M_1 & 0 & 1 \\ -M_4/M_1 & 0 & 0 \end{pmatrix}. \tag{D.106}$$

Thus, comparing eqs. (D.65) and (D.104) shows that $\mathfrak{M}^{(2\to1)}$ follows from the mass-matrix in eq. (D.65) by deleting the second column.

D.9 Validation: Supporting Information

In this section, we supplement our dicussion in chapter 6, and provide additional informations.

Species	Text Abbreviation	Structure Formula
Choline acetate	[Ch]OAc	$C_7H_{17}NO_3$
Zinc acetate	$Zn(OAc)_2$	$ZnC_4H_6O_4$
Choline	Ch^+	$C_5H_{14}NO$
Acetate	OAc^-	$C_2H_3O_2$
Charged zinc-acetate complex	$[Zn(OAc)_3]^-$	$ZnC_6H_9O_6$

Table D.2: Molecular complexes in the electrolyte.

Initial Concentrations and Partial Molar Volumes The initial species concentrations follow from the data presented in the experimental work Ref. 311. The electrolyte consists of [Ch]OAc with 30 wt % water, with ratio $b = M_\text{water}/M_\text{[Ch]OAcWater} = 0.3$, to which $1.00{\cdot}10^3\,\text{mol}\,\text{m}^{-3}$ $Zn(OAc)_2$ was added. Thus, the initial concentrations of [Ch]OAc and of the water are determined by the electrolyte mass-denisty $\rho_\text{elyte} = 1.35{\cdot}10^3\,\text{kg}\,\text{m}^{-3}$,[314], via

$$c^0_\text{[Ch]OAc} = (1-b)\cdot(\rho_\text{elyte} - c^0_{\text{Zn(OAc)}_2}\cdot M_{\text{Zn(OAc)}_2})/M_\text{[Ch]OAc} = 5{\cdot}10^3\,\text{mol}\,\text{m}^{-3}, \tag{D.107}$$

$$c^0_\text{water} = (\rho_\text{elyte} - c^0_{\text{Zn(OAc)}_2}\cdot M_{\text{Zn(OAc)}_2} - c^0_\text{[Ch]OAc}\cdot M_\text{[Ch]OAc})/M_\text{water}\,. \tag{D.108}$$

Because of complete salt-dissociation, eqs. (D.107) and (D.108) imply $c^0_{\mathrm{Ch}^+}{=}c^0_{\mathrm{[Ch](OAc)}}$, $c^0_{\mathrm{[Zn(OAc)_3]^-}}{=}c^0_{\mathrm{Zn(OAc)_2}}{=}1\,\mathrm{mol\,L^{-1}}$, and $c^0_{\mathrm{OAc^-}}{=}c^0_{\mathrm{Ch^+}}{-}c^0_{\mathrm{[Zn(OAc)_3]^-}}$.

We model the electrolyte as incompressible mixture with constant partial molar volumes. We fix ν_{water} via data from the literature,[439], assume $\nu_{\mathrm{OAc^-}}/\nu_{\mathrm{Ch^+}} = 0.8$, and model the value for $\nu_{\mathrm{[Zn(OAc)_3]^-}}$ using the molar volume of zincate in the electrolyte described in Ref. 440. Altogether,

$$\nu_{\mathrm{Ch^+}}{=}(1 - c^0_{\mathrm{water}}\nu_{\mathrm{water}} - c^0_{\mathrm{[Zn(OAc)_3]^-}}\nu_{\mathrm{[Zn(OAc)_3]^-}})/(c^+_{\mathrm{Ch^+}} + 0.8\cdot c^0_{\mathrm{OAc^-}})\,. \qquad \text{(D.109)}$$

Table 6.1 comprises all initial concentrations and the molar volumes.

Transport Parameters and Viscosity There are six independent transport parameters in the isothermal case, which all follow from the Onsager matrix (see eqs. (5.118) to (5.121) and (5.126))

$$\kappa,\ t_3,\ t_4,\ \mathcal{D}_{33},\ \mathcal{D}_{34},\ \mathcal{D}_{44}. \qquad \text{(D.110)}$$

Although the Onsager matrix depends upon the choice of designated species, we can easily transform into alternate reference frames (see appendix D.8). Thus, it suffices to model the Onsager matrix relative to one particluar choice for the designated species. Here, we choose water as reference ($\alpha = 1$) and model all transport parameters relative to this choice. We derive the symmetric Onsager matrix from hydrodynamical diffusion coefficients via $\mathcal{L}_\alpha = \text{Đ}_\alpha c_\alpha/RT$. These follow from a naïve Stokes-Einstein approach $\text{Đ}_\alpha = RT\lambda^{\mathrm{dilute}}_\alpha\eta^{\mathrm{dilute}}/\eta F^2 z_\alpha$. Here, $\lambda^{\mathrm{dilute}}$ are the limiting equivalent conductivities under indefinite dilution. We take water as reference for the dilute viscosity $\eta^{\mathrm{dilute}}_\alpha$, whereas the viscosity of the electrolyte η was measured by IoLiTec.[314] Thus, the final model for the Onsager coefficients reads $\mathcal{L}_\alpha = \eta^{\mathrm{dilute}}\lambda^{\mathrm{dilute}}_\alpha c_\alpha/F^2|z_\alpha|$. We present all relevant parameters in table D.3.

Parameter	Species	Value	Ref.
$\lambda^{\mathrm{dilute}}_\alpha$ / $\mathrm{S\,m^2\,mol^{-1}}$	$\mathrm{Ch^+}$	$42.00{\cdot}10^{-4}$	441
	$\mathrm{OAc^-}$	$40.89{\cdot}10^{-4}$	442
	$\mathrm{[Zn(OAc)_3]^-}$	$105.60{\cdot}10^{-4}$	442
η / $\mathrm{kg\,m^{-1}\,s^{-1}}$	Electrolyte	$25.30{\cdot}10^{-3}$	314
	Reference (water)	$0.89{\cdot}10^{-3}$	442

Table D.3: Parameters of the electrolyte-species.

Formalizing Chemical Reactions We neglect chemical reactions in the bulk electrolyte, and focus on reactions at the interface of electrolyte and active particles, where they serve as source-terms. These Faradaic reactions couple the solid phase with the electrolyte as they determine the boundary conditions for the fluxes. For any species α, we model the surface reactions at the interface Γ by

$$r_\alpha = \sum_k a^\Gamma \cdot \nu^\Gamma_{k;\alpha} \cdot i^\Gamma_k. \tag{D.111}$$

Here, a^Γ is the specific electrode surface, and $\nu^\Gamma_{k;\alpha}$ are the stoichiometric coefficients of reaction k. We use the convention that $\text{sign}(\nu^\Gamma_{k;\alpha}) = +1$ for reactions k which increase the amount of species α, and $\text{sign}(\nu^\Gamma_{k;\alpha}) = -1$ for reactions k which reduce the amount of species α. The stoichiometric coefficients of our model electrolyte can be read off eqs. (6.5) and (6.6), and are summarized in table D.4. We model the surface reaction rates i^Γ_k ([$\text{mol}\,\text{m}^{-2}\,\text{s}^{-1}$]) using Butler-Volmer interface conditions,[316]

Electrode	Species α	$\nu^\Gamma_{k;\alpha}$	Type	Reaction
Zinc-anode	OAc^-	−3	educt	Equation (6.6)
	Zn	−1	educt	Equation (6.6)
	$[\text{Zn(OAc)}_3]^-$	1	product	Equation (6.6)
	Electrons (e^-)	2	product	Equation (6.6)
PBA-cathode	OAc^-	3	product	Equation (6.5)
	$[\text{ZnFe(III)(CN)}_6]$	1	product	Equation (6.5)
	$[\text{Zn(OAc)}_3]^-$	−1	educt	Equation (6.5)
	Electrons (e^-)	−2	educt	Equation (6.5)

Table D.4: Heterogeneous chemical reactions as product terms weighted by $\nu^\Gamma_{k;\alpha}$. The sign of stoichiometric coefficients $\nu^\Gamma_{k;\alpha}$ determines the type of reaction. Positive: product; negative: educt.

$$i^\Gamma = i^\Gamma_0 \cdot \sinh(F z^\Gamma_{\text{el}} \eta^\Gamma / 2RT). \tag{D.112}$$

Here, $F z^\Gamma_{\text{el}}$ is the amount of charge per mole transferred across the interface in the course of reaction k (z^Γ_{el} is the electron-stoichiometry). We define the offset i^Γ_0 and the interface overpotential η^Γ, which are both functions of salt concentration, as follows. Consider an arbitrary surface reaction of type $\nu_A \cdot A + \nu_B \cdot B \leftrightharpoons \nu_D \cdot D + \nu_E \cdot E$. For this reaction, we define oxidation-/ reduction-constants

$$a_{\text{ox}} = \left(c_A/c^0_A\right)^{|\nu_A|} \cdot \left(c_B/c^0_B\right)^{|\nu_B|}, \text{ and } b_{\text{red}} = \left(c_D/c^0_D\right)^{|\nu_D|} \cdot \left(c_E/c^0_E\right)^{|\nu_E|}. \tag{D.113}$$

The fractions c_J/c_J^0 measure the state-of-charge (SOC) of the particular species. For example, in the case of conversion electrodes, ratios $c_J/c_J^0 = 1$ $(c_J/c_J^0 = 0)$ imply that the electrode is completely charged (discharged) with respect to the species J. We use these oxidation-/ reduction-constants and determine the offset $i_0^\Gamma = 2k^\Gamma \sqrt{a_\mathrm{ox} b_\mathrm{red}}$. Here, k^Γ are constant reaction rates which are material parameters.

We assume two contributions to the interface overpotentials η^Γ. First, a potential difference $\Phi_\mathrm{s}^\Gamma - \Phi_\mathrm{l}^\Gamma - U_0^\Gamma$, where Φ_s^Γ is the electrode-potential, Φ_s^Γ is the electrolyte potential, and $U_0^\Gamma(\mathit{SOC})$ is the respective half-cell open circuit potential. Second, an "entropic" contribution, such that

$$\eta^\Gamma = \Phi_\mathrm{s}^\Gamma - \Phi_\mathrm{l}^\Gamma - U_0^\Gamma - RT/Fz_\mathrm{el}^\Gamma \cdot \ln\left(a_\mathrm{ox}/b_\mathrm{red}\right). \tag{D.114}$$

Solid Phase (Electrodes): Model Equations We model the anode as zinc foil and set the half-cell voltage to $\Phi^\mathrm{anode} = 0$. For the flux boundary conditions of $[\mathrm{Zn(OAc)_3}]^-$-/ and OAc^--ions, we use Butler-Volmer type reactions (see eq. (D.112)). In contrast, we describe the PBA-cathode via the two solid-phase variables $c_\mathrm{Zn}^\mathrm{PBA}$ and Φ^PBA, and apply porous electrode theory,[315] where we neglect diffusion of zinc in the cathode. Thus, the net loss of zinc-salt in the electrolyte equals the zinc-concentration in the PBA-cathode, where the electrolytic salt-loss is determined by the reaction rate eq. (D.111),

$$\partial_t c_\mathrm{Zn}^\mathrm{PBA} = -r_\mathrm{Zn}^\mathrm{PBA}/(1-\varepsilon^\mathrm{PBA}). \tag{D.115}$$

The denominator on the right side accounts for the porous structure, where $\varepsilon^\mathrm{elyte} + \varepsilon^\mathrm{PBA} = 1$. However, instead of the absolute concentration $c_\mathrm{Zn}^\mathrm{PBA}$, we shall use the more accessible weighted expression $\mathit{SOC} = c_\mathrm{Zn}^\mathrm{PBA}/c_\mathrm{Zn}^\mathrm{PBA;max}$ as primary variable, which measures the state of charge of the PBA-cathode ($\mathit{SOC} = 1$ corresponds to a fully charged state). Thus, the model equation reads

$$\partial_t \mathit{SOC} = -r_\mathrm{Zn}^\mathrm{PBA}/[(1-\varepsilon^\mathrm{PBA}) \cdot c_\mathrm{Zn}^\mathrm{PBA;max}]. \tag{D.116}$$

We determine the half-cell-voltage Φ^PBA from flux the cathode-electrolyte boundary condition. Integration of eq. (6.8) yields for the interface condition

$$0 = I + \int \mathrm{d}x \sum_{\alpha=1}^{4} Fz_\alpha \cdot r_\alpha^\mathrm{PBA}\left(\Phi^\mathrm{PBA}\right), \tag{D.117}$$

which implicitely determines the half-cell potential via $r_\alpha^\mathrm{PBA}(\Phi^\mathrm{PBA})$.

Electrode Parameters Similar to the liquid phase, we assume constant volume fractions of the zinc-anode, separator and PBA-cathode. The experimental data provided in Ref. 311 allows to calculate the volume-fraction of the PBA-cathode

$$\varepsilon^{\text{PBA}} = 1 - m_{\text{load}}/l^{\text{PBA}}\rho_{\text{PBA}} \approx 0.26. \tag{D.118}$$

Here, m_{load} denotes the mass-loading, and l^{PBA} is the cathode-thickness. The maximal zinc concentration in the PBA-structure is $c_{\text{Zn}}^{\text{PBA;max}}=\rho_{\text{PBA}}/(4M_{\text{PBA}})$. We summarize the electrode parameters of the PBA-cathode in table D.5.

Parameter	Electrode	Value	Source
Specific surface area a / m^{-1}	Anode	$1.0{\cdot}10^{5}$	Fit parameter
	Cathode	$1.0{\cdot}10^{4}$	Fit parameter
Reaction rate k / $\text{mol}\,\text{m}^{-2}\,\text{s}^{-1}$	Anode	$1.0{\cdot}10^{-7}$	Fit parameter
	Cathode	$1.0{\cdot}10^{-7}$	Fit parameter
Volume fraction ε	Anode	$3.0{\cdot}10^{-1}$	Fit parameter
	Separator	$3.0{\cdot}10^{-1}$	Fit parameter
	Cathode	$2.6{\cdot}10^{-1}$	Calculated
Mass loading m_{load} / $\text{kg}\,\text{m}^{-2}$	Cathode	$9.5{\cdot}10^{-2}$	312
Thickness l / m^{-1}	Cathode	$1.5{\cdot}10^{-4}$	312
Mass density ρ_{PBA} / $\text{kg}\,\text{m}^{-3}$	Cathode	$1.8{\cdot}10^{3}$	312

Table D.5: Battery-Parameters.

Implementation: Computational Details For the numerical simulations, we implement the as-discussed model in a one-dimensional finite-volume model in MATLAB. We erect a grid of length $L_{\text{cell}} = 300\,\mu\text{m}$, which consists of the zinc anode ($x = [0; 150\,\mu\text{m}]$), followed by the separator ($x = [150\,\mu\text{m}, 200\,\mu\text{m}]$), and the PBA-cathode ($x = [200\,\mu\text{m}; L_{\text{cell}}]$). The step size of our grid is $\Delta x = 2.8\,\mu\text{m}$. We solve the model equations using the fully implicit ode15i MATLAB-solver for differential algebraic equations. Relative and absolute tolerances were both set to 10^{-6}.

D.10 Thermal Aspects

In this section, we discuss thermal aspects of our electrolyte transport theory. First, in appendix D.10.1, we derive the missing transport equation for temperature ("heat equation"), which closes the system of transport equations. Next, in appendix D.10.2, we expand the chemical potentials in the variable-set determined by the materials law eq. (5.65). Thereby, we obtain a detailed understanding of the temperature-evolution, and identify various thermal effects.

D.10.1 Heat Equation

As shown in Ref. 64, it can be a bad approximation to neglect temperature variations, since these can have a significant impact on lifetime and degradation processes occurring in lithium ion batteries. Here, we account for such effects, and derive an equation for the temperature using the entropy inequality eq. (5.39). We bring the entropy inequality in the form of a balance law, and neglect the source-term h,

$$\rho T\dot{s} = \mathcal{R} - T\boldsymbol{\nabla}\boldsymbol{\xi}_s. \tag{D.119}$$

Next, we use the materials law eq. (5.65), the set of isothermal transport equations, and eq. (D.119) to describe the evolution of entropy (where $s(T, c_\alpha, \boldsymbol{\mathcal{E}}, \mathbf{B}, \boldsymbol{\mathsf{F}}^{\mathrm{uni}}, \boldsymbol{\kappa})$),

$$\rho\dot{s}=\rho\left[\frac{\partial s}{\partial T}\dot{T}+\sum_{\beta=1}^{\mathrm{N}}\frac{\partial s}{\partial c_\beta}\dot{c}_\beta+\frac{\partial s}{\partial\boldsymbol{\mathcal{E}}}\dot{\boldsymbol{\mathcal{E}}}+\frac{\partial s}{\partial\mathbf{B}}\dot{\mathbf{B}}+\frac{\partial s}{\partial\boldsymbol{\kappa}}:\dot{\boldsymbol{\kappa}}+\frac{\partial s}{\partial\,\boldsymbol{\mathsf{F}}^{\mathrm{uni}}}:\dot{\boldsymbol{\mathsf{F}}}^{\mathrm{uni}}\right]. \tag{D.120}$$

Here, $\mathsf{C} = \rho T\cdot\partial s/\partial T$ is the total heat capacity. Next, we solve eq. (D.120) for $\dot{T}$, and substitute for $\dot{s}$ in eq. (D.119),

$$\mathsf{C}\dot{T}=\mathcal{R}-T\boldsymbol{\nabla}\boldsymbol{\xi}_s-\rho T\left[\sum_{\beta=1}^{\mathrm{N}}\frac{\partial s}{\partial c_\beta}\cdot\dot{c}_\beta+\frac{\partial s}{\partial\boldsymbol{\mathcal{E}}}\cdot\dot{\boldsymbol{\mathcal{E}}}+\frac{\partial s}{\partial\mathbf{B}}\cdot\dot{\mathbf{B}}+\frac{\partial s}{\partial\boldsymbol{\kappa}}:\dot{\boldsymbol{\kappa}}+\frac{\partial s}{\partial\,\boldsymbol{\mathsf{F}}^{\mathrm{uni}}}:\dot{\boldsymbol{\mathsf{F}}}^{\mathrm{uni}}\right]. \tag{D.121}$$

From the constitutive equations and the independency of the primary variables in the materials law, it follows that we can transfer the total time-derivatives to flux-terms, using the Abelian property

$$\partial s/\partial\Upsilon_A = -\partial/\partial T[\partial\varphi_{\mathrm{H}}/\partial\Upsilon_A], \tag{D.122}$$

Also, we use $\dot{c}_\alpha = -c_\alpha\cdot\boldsymbol{\nabla}\mathbf{v} - \boldsymbol{\nabla}\boldsymbol{\mathcal{N}}_\alpha$, and $\partial(\rho\varphi_{\mathrm{H}})/\partial\,\boldsymbol{\mathsf{F}}^{\mathrm{uni}} : (\mathrm{d}\,\boldsymbol{\mathsf{F}}^{\mathrm{uni}}/\mathrm{d}t) = \boldsymbol{\mathfrak{D}}_{\mathrm{tf}}$, see appendix D.2. Furthermore, since $\partial(\rho\varphi_{\mathrm{H}})/\partial\boldsymbol{\kappa} = 0$, we find

$$\mathsf{C}\dot{T}=\mathcal{R}-T\boldsymbol{\nabla}\boldsymbol{\xi}_s-T\frac{\partial(\mathcal{P}^{\mathrm{el}}\,\mathbf{Id}+\boldsymbol{\mathfrak{D}}_{\mathrm{tf}})}{\partial T}:\boldsymbol{\kappa}-T\sum_{\alpha=1}^{\mathrm{N}}\boldsymbol{\nabla}\boldsymbol{\mathcal{N}}_\alpha\cdot\frac{\partial\mu_\alpha}{\partial T}+T\frac{\partial\mathbf{P}}{\partial T}\dot{\boldsymbol{\mathcal{E}}}+T\frac{\partial\boldsymbol{\mathcal{M}}}{\partial T}\dot{\mathbf{B}}. \tag{D.123}$$

Here, $\mathcal{P}^{\mathrm{el}} = \sum_{\alpha=1}^{\mathrm{N}} c_\alpha\mu_\alpha - \rho\varphi_{\mathrm{H}}$ is the elastic pressure introduced in section 5.2.3. However, eq. (D.123) contains redundant fluxes, as the sum appearing in the fourth term on the right hand side begins with $\alpha = 1$. We reduce this term to the independent set of N-1 fluxes using eqs. (5.108) and (5.246) ($\mathcal{R}$ is given by eq. (5.140)),

$$\frac{C}{T}\dot{T}=\frac{\mathcal{R}}{T}-\boldsymbol{\nabla}\boldsymbol{\xi}_s-\frac{\partial(\tilde{\mu}_2+\tilde{\nu}_2\mathcal{P}^{\mathrm{el}})}{\partial T}\frac{T}{F\tilde{z}_2}\boldsymbol{\nabla}\boldsymbol{\mathcal{J}}_{\mathrm{F}}-\sum_{\alpha=3}^{\mathrm{N}}\frac{\partial(\tilde{\tilde{\mu}}_\alpha+\tilde{\tilde{\nu}}_\alpha\mathcal{P}^{\mathrm{el}})}{\partial T}\boldsymbol{\nabla}\boldsymbol{\mathcal{N}}_\alpha-\frac{\partial\mathfrak{D}_{\mathrm{tf}}}{\partial T}$$
$$+\frac{\partial}{\partial T}\left(\mathbf{P}\dot{\boldsymbol{\mathcal{E}}}+\boldsymbol{\mathcal{M}}\dot{\mathbf{B}}\right) \quad \text{(D.124)}$$

When temperature influences on the polarization, magnetization and on $\mathfrak{D}$ can be meglected, this becomes

$$\frac{C}{T}\dot{T}=\frac{\mathcal{R}}{T}-\boldsymbol{\nabla}\boldsymbol{\xi}_s-\frac{\partial\left(\tilde{\mu}_2+\tilde{\nu}_2\mathcal{P}^{\mathrm{el}}\right)}{\partial T}\frac{T}{F\tilde{z}_2}\boldsymbol{\nabla}\boldsymbol{\mathcal{J}}_{\mathrm{F}}-\sum_{\alpha=3}^{\mathrm{N}}\frac{\partial(\tilde{\tilde{\mu}}_\alpha+\tilde{\tilde{\nu}}_\alpha\mathcal{P}^{\mathrm{el}})}{\partial T}\boldsymbol{\nabla}\boldsymbol{\mathcal{N}}_\alpha. \quad \text{(D.125)}$$

D.10.2 Hydrodynamical Expansion

To obtain a better understanding of the mixing-term in eq. (5.140), we evaluate the gradients of the chemical potentials appearing in the reduced set of thermodynamic forces $\mathcal{X}_{\mathrm{red}}$. The chemical potentials $\tilde{\tilde{\mu}}_\alpha(\boldsymbol{\Upsilon})$ inherit the variable set $\boldsymbol{\Upsilon}=(T,c_\beta,\boldsymbol{\mathcal{E}},\mathbf{B},\boldsymbol{F}^{\mathrm{uni}},\boldsymbol{\kappa})$ from the free energy. In particular, using the chain-law,

$$\boldsymbol{\nabla}\mu_\alpha=\left[\left(\frac{\partial}{\partial c_\alpha}\sum_A\frac{\partial(\rho\varphi_{\mathrm{H}})}{\partial\Upsilon_A}\right)\boldsymbol{\nabla}\right]\Upsilon_A=\sum_{\beta=1}^{\mathrm{N}}\frac{\partial\mu_\alpha}{\partial c_\beta}\boldsymbol{\nabla}c_\beta-\underbrace{\frac{\partial(\rho s)}{\partial c_\alpha}}_{-\frac{\partial\mu_\alpha}{\partial T}}\boldsymbol{\nabla}T-\underbrace{\left(\frac{\partial\mathbf{P}}{\partial c_\alpha}\boldsymbol{\nabla}\right)}_{-\frac{\partial\mu_\alpha}{\partial\boldsymbol{\mathcal{E}}}\boldsymbol{\nabla}}\boldsymbol{\mathcal{E}}$$
$$-\underbrace{\left(\frac{\partial\boldsymbol{\mathcal{M}}}{\partial c_\alpha}\boldsymbol{\nabla}\right)}_{-\frac{\partial\mu_\alpha}{\partial\mathbf{B}}\boldsymbol{\nabla}}\mathbf{B}+\underbrace{\left[\frac{\partial^2(\rho\varphi_{\mathrm{H}})}{\partial c_\alpha\partial\boldsymbol{F}^{\mathrm{uni}}}\otimes\boldsymbol{\nabla}\right]}_{\frac{\partial\mu_\alpha}{\partial\boldsymbol{F}^{\mathrm{uni}}}}\otimes\boldsymbol{\nabla}\boldsymbol{F}^{\mathrm{uni}}. \quad \text{(D.126)}$$

Therefore, $\partial\mathbf{P}/\partial c_\alpha$ determines if the chemical potential depends on $\boldsymbol{\mathcal{E}}$, and $\partial\boldsymbol{\mathcal{M}}/\partial c_\alpha$ determines if the chemical potential depends on $\mathbf{B}$. In contrast to, *e.g.*, ion-conducting solid-electrolytes, where the polarizability of the electrolyte depends on ion concentration, such contributions are usually neglected in liquid electrolytes.[64] In particular, in linear constitutive models, where, *e.g.* $\mathbf{P}=\varepsilon_0\chi\mathbf{E}$, the susceptibility determines whether the chemical potential depends on the electric field, $\partial\mu_\alpha/\partial\mathbf{E}\propto\mathbf{E}\cdot\partial\chi/\partial c_\alpha$. Here, we assume $\partial\mathbf{P}/\partial c_\alpha=\partial\boldsymbol{\mathcal{M}}/\partial c_\alpha=0$, and neglect $\partial\mu_\alpha/\partial\boldsymbol{F}^{\mathrm{uni}}$.

Next, we expand $\boldsymbol{\nabla}\mu_\alpha$ in the gradients of the concentrations and temperature alone. However, the independent potential-gradients are (see eqs. (5.222) and (5.223))

$$\mathcal{Z} = (\boldsymbol{\nabla}\varrho_{\mathrm{F}}/F\,, \boldsymbol{\nabla}c_3, \dots, \boldsymbol{\nabla}c_{\mathrm{N}}, \boldsymbol{\nabla}T)^T. \tag{D.127}$$

There exists a (N+1)×N matrix $\boldsymbol{\mathcal{M}}(\nu_\alpha, M_\alpha)$ such that

$$(\boldsymbol{\nabla}c_1, \dots, \boldsymbol{\nabla}c_{\mathrm{N}}, \boldsymbol{\nabla}T)^T = \boldsymbol{\mathcal{M}} \cdot \mathcal{Z}. \tag{D.128}$$

Therefore, we define a $(\mathrm{N}-1) \times \mathrm{N}$ matrix $\boldsymbol{\text{đ}}$, such that the independent force-expansion becomes

$$\mathcal{X}_{\text{red}} = \begin{pmatrix} \dfrac{\partial\tilde{\tilde{\mu}}_3}{\partial c_1} & \dots & \dfrac{\partial\tilde{\tilde{\mu}}_3}{\partial c_{\mathrm{N}}} & \dfrac{\partial\tilde{\tilde{\mu}}_3}{\partial T} \\ \vdots & \ddots & \vdots & \vdots \\ \dfrac{\partial\tilde{\tilde{\mu}}_{\mathrm{N}}}{\partial c_1} & \dots & \dfrac{\partial\tilde{\tilde{\mu}}_{\mathrm{N}}}{\partial c_{\mathrm{N}}} & \dfrac{\partial\tilde{\tilde{\mu}}_{\mathrm{N}}}{\partial T} \\ 0 & \dots & 0 & 1 \end{pmatrix} \begin{pmatrix} \boldsymbol{\nabla}c_1 \\ \vdots \\ \vdots \\ \boldsymbol{\nabla}c_{\mathrm{N}} \\ \boldsymbol{\nabla}T \end{pmatrix} = \begin{pmatrix} \text{đ}_{3\varrho} & \text{đ}_{33} & \dots & \text{đ}_{3\mathrm{N}} & \partial_T\tilde{\tilde{\mu}}_3 \\ \vdots & \vdots & \ddots & \vdots & \vdots \\ \text{đ}_{\mathrm{N}\varrho} & \text{đ}_{\mathrm{N}3} & \dots & \text{đ}_{\mathrm{NN}} & \partial_T\tilde{\tilde{\mu}}_{\mathrm{N}} \\ 0 & 0 & \dots & 0 & 1 \end{pmatrix} \begin{pmatrix} \boldsymbol{\nabla}\varrho/F \\ \boldsymbol{\nabla}c_3 \\ \vdots \\ \boldsymbol{\nabla}c_{\mathrm{N}} \\ \boldsymbol{\nabla}T \end{pmatrix}$$

$$= \boldsymbol{\text{đ}} \cdot \mathcal{Z}. \tag{D.129}$$

Using eq. (5.138) suggests defining a $(\mathrm{N}-1) \times \mathrm{N}$-matrix $\boldsymbol{\text{Đ}} = \boldsymbol{\mathcal{D}}_{\text{red}} \cdot \boldsymbol{\text{đ}}$, such that

$$\mathit{\Psi}_{\text{red}} = -\boldsymbol{\text{Đ}} \cdot \mathcal{Z}, \tag{D.130}$$

with the independent diffusion-matrix

$$\boldsymbol{\text{Đ}} = \begin{pmatrix} \text{Đ}_{3\varrho} & \text{Đ}_{33} & \dots & \text{Đ}_{3\mathrm{N}} & \mathsf{S}_3 \\ \vdots & \vdots & \vdots & \vdots & \vdots \\ \vdots & \vdots & \vdots & \vdots & \vdots \\ \text{Đ}_{\mathrm{N}\varrho} & \text{Đ}_{\mathrm{N}3} & \dots & \text{Đ}_{\mathrm{NN}} & \mathsf{S}_{\mathrm{N}} \\ \mathsf{D}_\varrho & \mathsf{D}_3 & \dots & \mathsf{D}_{\mathrm{N}} & \lambda \end{pmatrix}. \tag{D.131}$$

We define the thermal coefficients $\mathsf{S}_\alpha, \mathsf{D}_\alpha$ and λ of $\boldsymbol{\text{Đ}}$ in table D.6. Above, we use a special notation defined as follows. Greek indices denote independent species, *viz.* $3 \le \alpha \le \mathrm{N}$, and $\alpha \neq T$ and $\alpha \neq \varrho_{\mathrm{F}}$. The index "$\varrho$" relates to the first non-vanishing independent force $\boldsymbol{\nabla}\varrho_{\mathrm{F}}/F$, whereas the index "$T$" relates to the independent force $\boldsymbol{\nabla}T$. Furthermore, the definition of $\boldsymbol{\text{Đ}} = \boldsymbol{\mathcal{D}}_{\text{red}} \cdot \boldsymbol{\text{đ}}$ is subject to the rule that it acts on $\mathcal{Z}$ according to $\boldsymbol{\text{Đ}}\mathcal{Z} = \boldsymbol{\mathcal{D}}_{\text{red}} \cdot (\boldsymbol{\text{đ}}\mathcal{Z})$. Thus, the entropy inequality expanded in the independent forces, eq. (5.140), becomes

$$\mathcal{R} = \boldsymbol{\tau} : \boldsymbol{\kappa} + \mathcal{J}_{\mathrm{F}}^2/\kappa + \mathcal{Z}^T \cdot \boldsymbol{H} \cdot \mathcal{Z}, \quad \text{where} \quad \boldsymbol{H} = \boldsymbol{\text{Đ}}^T\boldsymbol{\text{đ}}. \tag{D.132}$$

Lemma 28. The N×N hydrodynamic diffusion matrix $\boldsymbol{H}$ is symmetric and semi-

Term	Name	Effect
$\mathsf{S}_\alpha{=}\mathcal{D}_{\alpha T}{+}\sum_{\gamma=1}^{\mathrm{N}}\mathcal{D}_{\alpha\gamma}{\cdot}\partial\tilde{\tilde{\mu}}_\gamma/\partial T\,\text{đ}_{\gamma T}$	Soret coefficients.	Thermophoresis.
$\breve{\beta}{=}\beta{+}\sum_{\beta=3}^{\mathrm{N}}t_\beta/F^2\tilde{z}_\beta{\cdot}\partial\tilde{\tilde{\mu}}_\beta/\partial T$	Seebeck coefficient.	Thermophoresis.
$\mathsf{D}_\alpha{=}\text{Đ}_{\alpha T}$	Dufour coefficients.	“Inverse” thermophoresis.
$\mathsf{D}_\varrho{=}\text{Đ}_{\varrho T}$	Dufour coefficient.	Double-layer effect.
$\lambda{=}\text{Đ}_{TT}{=}\gamma/T{-}\beta^2\kappa{+}\sum_{\gamma=3}^{\mathrm{N}}\mathcal{D}_{T\gamma}\partial_T\tilde{\tilde{\mu}}_\gamma$	Heat conductivity.	Thermal conduction.

Table D.6: Hydrodynamical thermal coefficients.

positive definite.

Proof. By construction, $\boldsymbol{H}^T = \boldsymbol{\text{đ}}^T\boldsymbol{\text{Đ}} = \boldsymbol{\text{đ}}^T\boldsymbol{\mathcal{D}}_{\mathrm{red}}\boldsymbol{\text{đ}} = (\boldsymbol{\mathcal{D}}_{\mathrm{red}}^T\boldsymbol{\text{đ}})^T\boldsymbol{\text{đ}} = \boldsymbol{H}$. Furthermore, the mixing part in the entropy inequality becomes $\mathcal{X}_{\mathrm{red}}^T\boldsymbol{\mathcal{D}}_{\mathrm{red}}\mathcal{X}_{\mathrm{red}} = \mathcal{Z}^T\boldsymbol{H}^T\mathcal{Z} \geq 0$. Thus, due to symmetry, $\boldsymbol{H}$ is semi-positive definite. □

The hydrodynamical matrix Đ comprises various thermal effects. These can be evaluated by expanding the thermodynamic fluxes $\mathit{\Psi}_{\mathrm{red}}$ in the independent forces $\mathcal{Z}$, as described by eq. (D.130),

$$\mathcal{N}_\alpha - \frac{t_\alpha}{F\tilde{z}_\alpha}\boldsymbol{\mathcal{J}}_{\mathrm{F}} = -\frac{1}{F}\text{Đ}_{\alpha\varrho}\cdot\boldsymbol{\nabla}\varrho_{\mathrm{F}} - \sum_{\beta=3}^{\mathrm{N}}\text{Đ}_{\alpha\beta}\cdot\boldsymbol{\nabla}c_\beta - \mathsf{S}_\alpha\cdot\boldsymbol{\nabla}T, \tag{D.133}$$

$$\boldsymbol{\xi}_s - \beta\boldsymbol{\mathcal{J}}_{\mathrm{F}} = -\frac{1}{F}\mathsf{D}_\varrho\cdot\boldsymbol{\nabla}\varrho_{\mathrm{F}} - \sum_{\beta=3}^{\mathrm{N}}\mathsf{D}_\beta\cdot\boldsymbol{\nabla}c_\beta - \lambda\cdot\boldsymbol{\nabla}T, \tag{D.134}$$

$$\boldsymbol{\mathcal{J}}_{\mathrm{F}} = -\kappa\boldsymbol{\nabla}\varphi - \frac{\kappa}{F^2}\sum_{\beta=3}^{\mathrm{N}}\frac{t_\beta}{F\tilde{z}_\beta}\text{đ}_{\beta\varrho}\cdot\boldsymbol{\nabla}\varrho_{\mathrm{F}} - \frac{\kappa}{F}\sum_{\gamma,\beta=3}^{\mathrm{N}}\frac{t_\beta\text{đ}_{\beta\gamma}}{F\tilde{z}_\beta}\cdot\boldsymbol{\nabla}c_\gamma - \kappa\breve{\beta}\cdot\boldsymbol{\nabla}T. \tag{D.135}$$

The Soret coefficients S_α and the thermophoretic Seebeck coefficient $\breve{\beta}$ describe fluxes of mass and charge due to temperature gradients (thermophoresis / “Ludwig-Soret-effect”). The “inverse”-Soret effect (flux of heat due to concentration-gradients, or gradients in ϱ) are described by Dufour-coefficients $\mathsf{D}_\alpha, \mathsf{D}_\varrho$. The coefficient D_ϱ measures a thermal double-layer contribution (regions where $\varrho \neq 0$).

Next, we express the heat equation via $\mathcal{Z}$, to study the influence of these thermal phenomena on temperature. For this purpose, we substitute eqs. (D.133) and (D.134) into eq. (D.125), and neglect terms $\boldsymbol{\nabla}[\partial_T(\tilde{\mu}_2 + \tilde{\nu}_2\mathcal{P}^{\mathrm{el}})]$ and $\boldsymbol{\nabla}[\partial_T(\tilde{\tilde{\mu}}_\alpha + \tilde{\tilde{\nu}}_\alpha\mathcal{P}^{\mathrm{el}})]$ (hence temperature inhomogeneities in the chemical potentials and the pressure are equilibrated very fast). Using eq. (5.119), this yields $\boldsymbol{\nabla}\beta = -\beta\boldsymbol{\nabla}\log\kappa + F/\kappa\cdot\sum_{\alpha=2}^{\mathrm{N}}\boldsymbol{\nabla}\mathcal{L}_{\alpha T}\cdot\tilde{z}_\alpha$. We neglect the logarithmic term and assume that the only term depending on T is $\mathcal{L}_{\alpha T}(T)$. Hence, $\boldsymbol{\nabla}\beta(T) = \partial\beta/\partial T \cdot \boldsymbol{\nabla} T$, for which we use the Thomson-relation $\mu_{\mathrm{T}} = T \cdot \partial\beta/\partial T$. Thus, $\mu_{\mathrm{T}} = F/\kappa T \cdot \sum_{\alpha=2}^{\mathrm{N}} \partial_T \mathcal{L}_{\alpha T} \tilde{z}_\alpha$. Altogether, the hydrodynamical expansion of the heat equation becomes

$$\begin{aligned} \mathsf{C}\dot{T} =& \mathcal{R} - \mu_{\mathrm{T}} \boldsymbol{\mathcal{J}}_{\mathrm{F}} \boldsymbol{\nabla} T - T \left[\beta + \frac{\partial}{\partial T} \left(\frac{\tilde{\mu}_2 + \tilde{\nu}_2 \mathcal{P}^{\mathrm{el}}}{F \tilde{z}_2} + \sum_{\alpha=3}^{\mathrm{N}} t_\alpha \frac{\tilde{\tilde{\mu}}_\alpha + \tilde{\tilde{\nu}}_\alpha \mathcal{P}^{\mathrm{el}}}{F \tilde{z}_\alpha} \right) \right] \boldsymbol{\nabla} \boldsymbol{\mathcal{J}}_{\mathrm{F}} \\ & + \frac{T}{F} \boldsymbol{\nabla} \left[\left(\mathsf{D}_\varrho + \sum_{\alpha=3}^{\mathrm{N}} \frac{\partial \left(\tilde{\tilde{\mu}}_\alpha + \tilde{\tilde{\nu}}_\alpha \mathcal{P}^{\mathrm{el}} \right)}{\partial T} \cdot Đ_{\alpha\varrho} \right) \boldsymbol{\nabla} \varrho \right] \\ & + T \sum_{\gamma=3}^{\mathrm{N}} \boldsymbol{\nabla} \left[\left(\mathsf{D}_\gamma + \sum_{\alpha=3}^{\mathrm{N}} \frac{\partial \left(\tilde{\tilde{\mu}}_\alpha + \tilde{\tilde{\nu}}_\alpha \mathcal{P}^{\mathrm{el}} \right)}{\partial T} \cdot Đ_{\alpha\gamma} \right) \boldsymbol{\nabla} c_\gamma \right] \\ & + T \boldsymbol{\nabla} \left[\left(\lambda + \sum_{\alpha=3}^{\mathrm{N}} \frac{\partial \left(\tilde{\tilde{\mu}}_\alpha + \tilde{\tilde{\nu}}_\alpha \mathcal{P}^{\mathrm{el}} \right)}{\partial T} \cdot \mathsf{S}_\alpha \right) \boldsymbol{\nabla} T \right]. \end{aligned} \tag{D.136}$$

Apparently, all hydrodynamical thermal coefficients $\beta, \mathsf{D}_\varrho, \mathsf{D}_\gamma, \lambda$ are supplemented by corrections (stemming from the derivatives $\partial s/\partial c_\gamma$), which take account for temperature-inhomogeneities of the chemical potentials and pressure,

$$\tilde{\beta}^p = \tilde{\beta} + \frac{1}{F\tilde{z}_2} \frac{\partial(\tilde{\nu}_2 p)}{\partial T} + \sum_{\alpha=3}^{\mathrm{N}} \frac{t_\alpha}{F\tilde{z}_\alpha} \frac{\partial(\tilde{\tilde{\nu}}_\alpha \mathcal{P}^{\mathrm{el}})}{\partial T}, \quad \text{where} \quad \tilde{\beta} = \breve{\beta} + \frac{1}{F\tilde{z}_2} \frac{\partial \tilde{\mu}_2}{\partial T}, \tag{D.137}$$

$$\tilde{\mathsf{D}}_\varrho^p = \tilde{\mathsf{D}}_\varrho + \sum_{\alpha=3}^{\mathrm{N}} Đ_{\alpha\varrho} \cdot \frac{\partial(\tilde{\tilde{\nu}}_\alpha \mathcal{P}^{\mathrm{el}})}{\partial T}, \quad \text{where} \quad \tilde{\mathsf{D}}_\varrho = \mathsf{D}_\varrho + \sum_{\alpha=3}^{\mathrm{N}} Đ_{\alpha\varrho} \cdot \frac{\partial \tilde{\tilde{\mu}}_\alpha}{\partial T}, \tag{D.138}$$

$$\tilde{\mathsf{D}}_\gamma^p = \tilde{\mathsf{D}}_\gamma + \sum_{\alpha=3}^{\mathrm{N}} Đ_{\alpha\gamma} \cdot \frac{\partial(\tilde{\tilde{\nu}}_\alpha \mathcal{P}^{\mathrm{el}})}{\partial T}, \quad \text{where} \quad \tilde{\mathsf{D}}_\gamma = \mathsf{D}_\gamma + \sum_{\alpha=3}^{\mathrm{N}} Đ_{\alpha\gamma} \cdot \frac{\partial \tilde{\tilde{\mu}}_\alpha}{\partial T}, \tag{D.139}$$

$$\tilde{\lambda}^p = \tilde{\lambda} + \sum_{\alpha=3}^{\mathrm{N}} \mathsf{S}_\alpha \cdot \frac{\partial \left(\tilde{\tilde{\nu}}_\alpha \mathcal{P}^{\mathrm{el}} \right)}{\partial T}, \quad \text{where} \quad \tilde{\lambda} = \lambda + \sum_{\alpha=3}^{\mathrm{N}} \mathsf{S}_\alpha \cdot \frac{\partial \tilde{\tilde{\mu}}_\alpha}{\partial T}. \tag{D.140}$$

Using these definitions, we find for the hydrodynamical heat equation eq. (D.136)

$$\begin{aligned} \mathsf{C}\dot{T} =& \boldsymbol{\tau} : \boldsymbol{\kappa} + \boldsymbol{\mathcal{J}}_{\mathrm{F}}^2/\kappa + \mathcal{Z}^T \boldsymbol{H} \mathcal{Z} - \mu_{\mathrm{T}} \boldsymbol{\mathcal{J}}_{\mathrm{F}} \boldsymbol{\nabla} T - T\tilde{\beta} \boldsymbol{\nabla} \boldsymbol{\mathcal{J}}_{\mathrm{F}} + T/F\, \boldsymbol{\nabla} \tilde{\mathsf{D}}_\varrho \boldsymbol{\nabla} \varrho \\ & + T \sum_{\gamma=3}^{\mathrm{N}} \boldsymbol{\nabla} \tilde{\mathsf{D}}_\gamma \boldsymbol{\nabla} c_\gamma + T \boldsymbol{\nabla} \tilde{\lambda} \boldsymbol{\nabla} T + T \partial \mathcal{P}^{\mathrm{el}}/\partial T \, \cdot \boldsymbol{\nabla} \mathbf{v} \\ =& \boldsymbol{\tau} : \boldsymbol{\kappa} + \boldsymbol{\mathcal{J}}_{\mathrm{F}}^2/\kappa + \mathcal{Z}^T \boldsymbol{H} \mathcal{Z} - \mu_{\mathrm{T}} \boldsymbol{\mathcal{J}}_{\mathrm{F}} \boldsymbol{\nabla} T - T\tilde{\beta}^p \boldsymbol{\nabla} \boldsymbol{\mathcal{J}}_{\mathrm{F}} + T/F\, \boldsymbol{\nabla} \tilde{\mathsf{D}}_\varrho^p \boldsymbol{\nabla} \varrho \\ & + T \sum_{\gamma=3}^{\mathrm{N}} \boldsymbol{\nabla} \tilde{\mathsf{D}}_\gamma^p \boldsymbol{\nabla} c_\gamma + T \boldsymbol{\nabla} \tilde{\lambda}^p \boldsymbol{\nabla} T. \end{aligned} \tag{D.141}$$

Various heating effects can be identified. Mechanical stress / viscous friction (first term), Joule heating (second term), and entropy of mixing (third term) strictly increase temperature. The fourth term describes heat-transport along electric currents, which either decrease or increase temperature ("Thomson effect"). The fifth and sixth term describe thermo-migration and thermo-charging. Both vanish in electroneutral regions (bulk electrolyte). The seventh term describes temperature variations due to species-diffusion ("Dufour-effect"). The last term describes thermal conduction. For incompressible electrolytes, $\tilde{\lambda} \geq 0$, and hence this term equilibrates temperature-inhomogeneities (see eq. (D.143)).

Still, the constraint implied by Lemma 28 on the coefficients of $\boldsymbol{H}$ must be taken account for. Since the mixing term appearing in the entropy inequality, eq. (D.132), fullfills $\mathcal{Z}^T \cdot \boldsymbol{H} \cdot \mathcal{Z} \geq 0$, we thus find

$$\mathcal{Z}^T \boldsymbol{H} \mathcal{Z} = H_{\varrho\varrho}/F^2 \cdot (\boldsymbol{\nabla}\varrho)^2 + \sum_{\alpha,\beta=3}^{\mathrm{N}} H_{\alpha\beta}(\boldsymbol{\nabla} c_\alpha)(\boldsymbol{\nabla} c_\beta) + 2\left[\sum_{\alpha=3}^{\mathrm{N}} \mathcal{H}_{T\alpha}\boldsymbol{\nabla} c_\alpha + H_{T\varrho}\boldsymbol{\nabla}\varrho\right]\boldsymbol{\nabla} T \\ + 2H_{\alpha\varrho}\left(\boldsymbol{\nabla}\varrho\right)\left(\boldsymbol{\nabla} c_\alpha\right) + H_{TT}\left(\boldsymbol{\nabla} T\right)^2 \geq 0. \quad \text{(D.142)}$$

As consequence, the diagonal elements $H_{\varrho\varrho}, H_{\alpha\alpha}, H_{TT}$ are non-negative, whereas the submatrix $H_{\alpha\beta}$ is semi-positive definite. We introduce the hydrodynamical coefficient $\breve{\lambda} = H_{TT}$, such that

$$\breve{\lambda} = \lambda + \sum_{\gamma=3}^{\mathrm{N}} S_\gamma \cdot \partial\tilde{\tilde{\mu}}_\gamma/\partial T = \tilde{\lambda} - \sum_{\gamma=3}^{\mathrm{N}} S_\gamma \cdot \partial(\tilde{\tilde{\nu}}_\gamma \mathcal{P}^{\mathrm{el}})/\partial T \geq 0. \quad \text{(D.143)}$$

Above, we showed that $\partial_T \mathcal{P}^{\mathrm{el}}$ can be neglected for incompressible electrolytes.[274] Hence, in this limit, $\breve{\lambda} = \tilde{\lambda} \geq 0$. Thus heat conduction (last term in eq. (D.142)) increases temperature, and equilibrates temperature inhomogeneities.

Thermal Model Yet, the temperature dependence of our model free energy eq. (5.153) is only comprised in the entropic mixing-term, $RT\sum_{\alpha=1}^{\mathrm{N}} c_\alpha \ln(c_\alpha/c)$, and in the interaction free energy. Since the mixing term is linear in T, the internal energy density, determined by eq. (5.74), and the entropy density, determined by the constitutive equation eq. (5.68), do not depend on temperature. However, this contracdicts experimental observations, and suggests that we extend our model for φ_{H} by a thermal term.

We state our thermal entropy model relative to a reference temperature T_{R} and neglect $\rho\varphi_{\mathrm{H}}^{\mathrm{int}}$ for dilute electrolytes ($f_\alpha c = 1$). We demand from our thermal model: (i) it vanishes for constant temperature ($T = T_{\mathrm{R}}$), (ii), it is strictly positive, and, (iii), increases for cooling and heating relative to the reference-temperature T_{R}. It

Term	Effect	Interpretation
$\boldsymbol{\tau} : \boldsymbol{\kappa} \geq 0$	Viscous friction.	Increases temperature.
$\boldsymbol{\mathcal{J}}_{\mathrm{F}}^2/\kappa \geq 0$	Joule heating	Increases temperature.
$-\mu_{\mathrm{T}} \boldsymbol{\mathcal{J}}_{\mathrm{F}} \boldsymbol{\nabla} T$	Thomson effect.	Thermoelectric effect.
$\left(\boldsymbol{Z}_{(\alpha)}\right)^T \cdot \boldsymbol{H} \cdot \boldsymbol{Z}_{(\alpha)}$	Multi-component mixing.	Increases temperature.
$T/F \boldsymbol{\nabla} \tilde{D}_{\varrho} \boldsymbol{\nabla} \varrho - T \tilde{\beta} \boldsymbol{\nabla} \boldsymbol{\mathcal{J}}_{\mathrm{F}}$	Electric / double-layer effect.	Vanishes in bulk.
$T \boldsymbol{\nabla} \sum_{\gamma=3}^{\mathrm{N}} \tilde{D}_{\gamma} \boldsymbol{\nabla} c_{\gamma}$	Dufour-effect.	Species diffusion.
$T \boldsymbol{\nabla} (\tilde{\lambda} \cdot \boldsymbol{\nabla} T)$	Thermal conduction.	Equilibrates temperature.
$T \cdot \boldsymbol{\nabla} \mathbf{v} \cdot \partial \mathcal{P}^{\mathrm{el}} / \partial T$	Pressure effect.	Vanishes if $\boldsymbol{\nabla} \mathbf{v} = 0$.

Table D.7: Contributions to the heat equation.

can easily be shown that these requirements are satisfied by the following model,

$$\rho s_{th} = \ln(T/T_{\mathrm{R}}) \cdot \sum_{\alpha=1}^{\mathrm{N}} \rho_{\alpha} C_{\alpha}. \tag{D.144}$$

Upon integration of the constitutive equation for s, and using the integral law $\int \mathrm{d}x \, \log(x/\mathrm{const}) = x \log(x/\mathrm{const}) - x$, this model implies a thermal contribution to the free energy density,[140]

$$\rho \varphi_{\mathrm{H}}^{\mathrm{therm}} = (T - T_{\mathrm{R}} - T \ln T/T_{\mathrm{R}}) \sum_{\alpha=1}^{\mathrm{N}} C_{\alpha} \rho_{\alpha}. \tag{D.145}$$

E Appendix to Part III

E.1 Gradient Expansion

In this section, we show that the assumption of short-ranged potentials $\mathcal{F}$ in eq. (8.27) can be used to approximate the convolution integral F^{int} by an expansion in gradients of the species-concentrations as discussed in section 8.4.

For simplictiy, we focus on the one-dimensional case. However, the generalization to three dimensions is straightforward. Starting point for our discussion is the Ansatz for the one-dimensional interaction functional,

$$F^{\mathrm{int}} = \frac{1}{2} \sum_{\alpha,\beta}^{\mathrm{N}} \int\limits_{\Omega_y} \mathrm{d}y \; c_\alpha(y) \left(\int\limits_{\Omega_x} \mathrm{d}x \; \mathcal{F}_{\alpha\beta}(|x-y|) c_\beta(x) \right) . \tag{E.1}$$

The spherically symmetric hardcore potential $\mathcal{F}_{\alpha\beta} = \mathcal{V}^0 (N_\mathrm{A})^2 \tilde{\mathcal{F}}(\ell_{\mathrm{int}})_{\alpha\beta}$ determines $F^{\mathrm{int}}[c_\alpha]$, see eq. (8.28). Our basic argument is that the non-local correlations decay after some ion-sizes, *i.e.* that there exists a correlation length ℓ_{int} which determines an effective support $\Omega_x \to \Omega[\ell_{\mathrm{int}}]$ of the function $\tilde{\mathcal{F}}$ (typically, ℓ_{int} is not larger than some nanometers). Thus we use the approximation

$$\int\limits_{\Omega_x} \mathrm{d}x \; \mathcal{F}_{\alpha\beta}(|x-y|) c_\beta(x) \approx \int\limits_{\Omega[\ell_{\mathrm{int}}]} \mathrm{d}x \; \mathcal{F}_{\alpha\beta}(|x-y|) c_\beta(x). \tag{E.2}$$

Next, we make use of the fact that the variable "y" appearing in the integral on the right side of eq. (E.2) is merely a constant. Thus, for any position "y", we reduce the integration limits to an interval around y, which is determined by the correlation length, $\Omega[\ell_{\mathrm{int}}] = [y - \ell_{\mathrm{int}}; y + \ell_{\mathrm{int}}]$. Altogether,

$$F^{\mathrm{int}}[c_\gamma] = \frac{1}{2} \sum_{\alpha,\beta} \int\limits_{\Omega_y} \mathrm{d}y \; c_\alpha(y) \left(\int\limits_{y-\ell_{\mathrm{int}}}^{y+\ell_{\mathrm{int}}} \mathrm{d}x \; \mathcal{F}_{\alpha\beta}\left(|x-y|\right) \; c_\beta(x) \right) . \tag{E.3}$$

Our next step is to decouple the two nested integrals appearing on the right side of eq. (E.3). For this purpose, we make a coordinate transformation $g : x \to y + \varepsilon$

to relative coordinates. Hence, $\varepsilon = x - y$, where $x = \varepsilon + y$ and $\varepsilon = g^{-1}(x_0) = x_0 - y$. Taking account for the correct transformation of the integration limits ($g^{-1}(y - \sigma_{\alpha\beta}) = -\sigma_{\alpha\beta}$ and $g^{-1}(y + \sigma_{\alpha\beta}) = \sigma_{\alpha\beta}$), we find

$$F^{\text{int}}[c_\gamma] = \frac{1}{2}\sum_{\alpha,\beta}\int\limits_{\Omega_y} \mathrm{d}y\ c_\alpha(y) \left(\int\limits_{-\ell_{\text{int}}}^{\ell_{\text{int}}} \mathrm{d}\varepsilon\ \mathcal{F}_{\alpha\beta}\left(|\varepsilon|\right)\ c_\beta(y+\varepsilon) \right). \tag{E.4}$$

Without loss of generality, we assume that $|\varepsilon| \ll |y|$, and Taylor-expand the ion-concentration $c_\beta(y+\varepsilon) = \sum_{n=0}^{\infty} \varepsilon^n/n! \cdot \boldsymbol{\nabla}^n c_\beta(y)$. By substitution of the concentration, eq. (E.4) decouples into the product of two independent integrals

$$F^{\text{int}}[c_\gamma] = \frac{1}{2}\sum_{\alpha,\beta}\sum_{n=0}^{\infty}\frac{1}{n!}\left(\int\limits_{-\ell_{\text{int}}}^{\ell_{\text{int}}} \mathrm{d}\varepsilon\ \mathcal{F}_{\alpha\beta}\left(|\varepsilon|\right)\varepsilon^n \right)\cdot\left(\int\limits_{\Omega_y} \mathrm{d}y\ c_\alpha(y)\cdot\boldsymbol{\nabla}^n c_\beta(y) \right). \tag{E.5}$$

The spherical symmetry of the interaction potential appearing on the right side of eq. (E.5) implies all integrals over odd modes n vanish identically. Thus, it suffices to reduce the expansion on the right side of eq. (E.5) to the sum over even modes n. Furthermore, the integration limits in all remaining terms can be translated, $\int_{-\ell_{\text{int}}}^{\ell_{\text{int}}} \mathrm{d}\varepsilon\, \mathcal{F}_{\alpha\beta}\left(|\varepsilon|\right)\varepsilon^{2n} = \int_0^{\ell_{\text{int}}} \mathrm{d}\varepsilon\, \mathcal{F}_{\alpha\beta}\left(|\varepsilon|\right)\varepsilon^{2n}$. Therefore, using again the approximation eq. (E.2), we can expand the free energy via

$$F^{\text{int}}[c_\gamma] = \frac{1}{2}\sum_{\alpha,\beta}\sum_{n=0}^{\infty}\Gamma_{\alpha\beta}^{2n}\cdot\int\limits_{\Omega_y} \mathrm{d}y\ c_\alpha(y)\cdot\boldsymbol{\nabla}^{2n} c_\beta(y), \tag{E.6}$$

where we introduced perturbation modes

$$\Gamma_{\alpha\beta}^{n} = 1/(n!)\cdot\int\limits_0^{\infty} \mathrm{d}\varepsilon\ \mathcal{F}_{\alpha\beta}(|\varepsilon|)\cdot\varepsilon^n. \tag{E.7}$$

Finally, we note that the expansion eq. (E.6) can be re-expressed if all derivatives vanish at the boundaries of the integration-domain, *i.e.* $\boldsymbol{\nabla}^n c_\gamma|_\Omega = 0$. In this case, the n-fold application of the method of integration by parts yields

$$F^{\text{int}}[c_\gamma] = \frac{1}{2}\sum_{\alpha,\beta}\sum_{n=0}^{\infty}(-1)^n\cdot\Gamma_{\alpha\beta}^{2n}\cdot\int\limits_{\Omega_y} \mathrm{d}y\ \left(\boldsymbol{\nabla}^n c_\alpha\right)\cdot\left(\boldsymbol{\nabla}^n c_\beta\right). \tag{E.8}$$

However, if the derivatives do not vanish at the boundary, then eq. (E.8) must be supplemented by corresponding surface-integrals.

E.2 Functional Derivative

In this section, we briefly introduce the formal definition of functional derivatives, and apply them to the functionals appearing in our theory.

In general, the functional derivative of a quantity $F[c_\gamma] = \int_{\Omega_x} \mathrm{d}x\, \Psi(c_\gamma, \boldsymbol{\nabla}^n c_\gamma)$, denoted $\delta F/\delta c_\gamma$, is defined using an arbitrary auxiliary function $\phi(x)$,[443]

$$\int\limits_{\Omega_x} \mathrm{d}x\; \frac{\delta F}{\delta c_\gamma} \cdot \phi = \lim_{\varepsilon \to 0} \frac{F[c_\gamma + \varepsilon\phi] - F[c_\gamma]}{\varepsilon} \tag{E.9}$$

$$= \frac{\mathrm{d}}{\mathrm{d}\varepsilon}\bigg|_{\varepsilon=0} \int\limits_{\Omega_x} \mathrm{d}x\; \Psi\left(c_\gamma + \varepsilon\phi, \boldsymbol{\nabla}^n c_\gamma + \varepsilon \boldsymbol{\nabla}^n \phi\right) \tag{E.10}$$

$$= \int\limits_{\Omega_x} \mathrm{d}x \left(\frac{\partial \Psi}{\partial c_\gamma} + \sum_{i=1}^{\infty} (-1)^i \cdot \boldsymbol{\nabla}^i \left[\frac{\partial \Psi}{\partial \left(\boldsymbol{\nabla}^i c_\gamma \right)} \right] \right) \cdot \phi. \tag{E.11}$$

Next, this formula to the chemical potentials appearing in our framework, which are defined via the functional derivative of the free energy functional with respect to species concentrations, see eq. (8.15). Hence, we calculate the functional derivatives of the quantities appearing in eqs. (E.6) and (E.7).

Hence, we substitute $\Psi(c_\gamma, \boldsymbol{\nabla}^n c_\gamma) = 1/2 \cdot \sum_{\alpha,\beta} \sum_{n=0}^{\infty} \Gamma_{\alpha\beta}^{2n} \cdot c_\alpha \cdot \boldsymbol{\nabla}^{2n} c_\beta$ into the recipe for the functional derivatives eq. (E.11). We find for the different terms,

$$\frac{\partial \Psi}{\partial c_\gamma} = \sum_\alpha \Gamma_{\gamma\alpha}^0 \cdot c_\alpha + \frac{1}{2} \sum_\alpha \sum_{n=1}^{\infty} \Gamma_{\gamma\alpha}^n \cdot \boldsymbol{\nabla}^{2n} c_\alpha, \tag{E.12}$$

and

$$\begin{aligned} \sum_{i=1}^{\infty} (-1)^i \cdot \boldsymbol{\nabla}^i \frac{\partial \Psi}{\partial (\boldsymbol{\nabla}^i c_\gamma)} &= \frac{1}{2} \sum_{i=1}^{\infty} (-1)^i \cdot \boldsymbol{\nabla}^i \left(\sum_{\alpha,\,\beta} \sum_{n=1}^{\infty} \Gamma_{\alpha\beta}^n \cdot c_\alpha \cdot \delta_\gamma^\beta \cdot \delta_i^{2n} \right) \\ &= \frac{1}{2} \sum_\alpha \sum_{n=1}^{\infty} \Gamma_{\gamma\alpha}^{2n} \cdot \boldsymbol{\nabla}^{2n} c_\alpha. \end{aligned} \tag{E.13}$$

Altogether, we thus find for the excess chemical potentials due to the interaction contributions in the free energy,

$$\frac{\delta F^{\mathrm{int}}}{\delta c_\alpha(z)} = \sum_{\beta=1}^{\mathrm{N}} \sum_{n=0}^{\infty} \Gamma_{\alpha\beta}^{2n} \cdot \boldsymbol{\nabla}^{2n} c_\beta(z). \tag{E.14}$$

E.3 Symmetry of Conservative Interaction Potentials

In this section we discuss a consequence of the spherical symmetry of interaction potentials on the excess chemical potential. In particular, we rationalize the step from eq. (9.21) to eq. (9.22).

Lemma 29. For any spherically symmetric potential $\mathcal{F}_{\alpha\beta}(|\mathbf{r}|)$, $\boldsymbol{\nabla}_{\mathbf{x}} \int \mathrm{d}\mathbf{y}^3\, \mathcal{F}_{\alpha\beta}(|\mathbf{x} - \mathbf{y}|) = 0$.

Proof. We exploit the symmetry porperty of $\mathcal{F}_{\alpha\beta}$ and make a coordinate transformation to spherical coordinates. Without loss of generality, we choose $\mathbf{x} = 0$, such that the coordinate of radial distance becomes $r = (|\mathbf{x} - \mathbf{y}|) = |\mathbf{y}|$. Here, the corresponding radial vector is defined by $\boldsymbol{r} = r \cdot \hat{\boldsymbol{e}}_{\boldsymbol{r}} = r \cdot (\sin\theta\cos\phi, \cos\theta\sin\phi, \cos\theta)^T$, whereas the angular coordinates are comprised in the element $\mathrm{d}\Omega = \sin\theta \cdot \mathrm{d}\theta\mathrm{d}\phi$. Thus, we find

$$\boldsymbol{\nabla}_{\mathbf{x}} \int \mathrm{d}\mathbf{y}^3\, \mathcal{F}_{\alpha\beta}(|\mathbf{x} - \mathbf{y}|) = -\int \mathrm{d}r\, \mathcal{F}'_{\alpha\beta}(r)/r \cdot \iint \mathrm{d}\Omega\, \boldsymbol{r}. \tag{E.15}$$

Above, we used the notation $\mathcal{F}'_{\alpha\beta} = \partial\mathcal{F}_{\alpha\beta}/\partial r$. However, it is easy to show that $\iint \mathrm{d}\Omega\, \boldsymbol{r} = r \cdot \iint \mathrm{d}\Omega\, \hat{\boldsymbol{e}}_{\boldsymbol{r}} = 0$, when one integrates over the complete sphere (*i.e.* $\theta \in [;\pi]$, and $\phi \in [0; 2\pi]$). This completes the proof. □

E.4 Phase Space Analysis

In this section we prove Theorem 1, *i.e.* show that there exist three independent phases for the of screening profiles. To improve the logical structure of the proof, we first present some Lemmata, before we state the explicit proof of the Theorem.

For completeness, we restate our finding for the eigenvalues $\tilde{\alpha}_{1,2}$, and the phase boundaries $\mathcal{V}^0_{\pm}$ from section 10.3.2, using the (strictly positive) parameters $\zeta = 1/\tilde{\Gamma}^0_{+-}$ and $\chi = 8/\pi\tilde{\nu}\tilde{\Gamma}^0_{+-}$,

$$\tilde{\alpha}_{1,2} {=} {-}22\zeta E_{\mathrm{th}}/\chi E_{\mathrm{el}} \cdot \left[\left(1 - \zeta \cdot E_{\mathrm{th}}/\mathcal{V}^0\right) \mp \sqrt{(1 - \zeta \cdot E_{\mathrm{th}}/\mathcal{V}^0\,)^2 - \chi \cdot E_{\mathrm{el}}/\mathcal{V}^0}\right]. \tag{E.16}$$

The eigenvalues $\tilde{\alpha}_{1,2}$ in eq. (E.16) determine the screening phase via the wavelength $\tilde{k} = \sqrt{\tilde{\alpha}_{1,2}}$. Thus, the number-field of $\tilde{\alpha}_{1,2}$ is critical for the interface-profile. This suggests that we examine, the root $\mathcal{W}$ appearing in the eigenvalue-equation eq. (E.16),

$$\mathcal{W}(\mathcal{V}^0) = 1 - [2\zeta \cdot E_{\mathrm{th}} + \chi \cdot E_{\mathrm{el}}]\,/\mathcal{V}^0 + \zeta^2 \cdot E^2_{\mathrm{th}}/(\mathcal{V}^0)^2. \tag{E.17}$$

The sign of the root $\mathcal{W}$ determines if $\tilde{\alpha}_{1,2}$ is complex-valued or real-valued. Thus, we need the critical interaction energies $\mathcal{W}(\mathcal{V}^0_\pm) = 0$, *viz.*

$$\mathcal{V}^0_\pm = \zeta \cdot E_{\mathrm{th}} + \chi \cdot E_{\mathrm{el}}/2 \pm \sqrt{\chi \cdot E_{\mathrm{el}} \left(\chi \cdot E_{\mathrm{el}}/4 + \zeta \cdot E_{\mathrm{th}}\right)}. \tag{E.18}$$

Lemma 30. $\zeta E_{\mathrm{th}} + \chi E_{\mathrm{el}}/2 < \mathcal{V}^0_+ \leq \chi E_{\mathrm{el}} + \zeta E_{\mathrm{th}} + \sqrt{\chi\zeta E_{\mathrm{el}} E_{\mathrm{th}}}$.

Proof. The left side of the inequality follows trivially from eq. (E.18). However, the righ side follows from the triangle-inequality, $\sqrt{\chi \cdot E_{\mathrm{el}} \left(\chi \cdot E_{\mathrm{el}}/4 + \zeta \cdot E_{\mathrm{th}}\right)} \leq \chi E_{\mathrm{el}}/2 + \sqrt{\chi\zeta E_{\mathrm{el}} E_{\mathrm{th}}}$. This completes the proof. □

Lemma 31. Both roots $\mathcal{V}^0_\pm$ are positive.

Proof. Positivity of $\mathcal{V}^0_+$ is trivial. In order to prove positivity of $\mathcal{V}^0_-$, we re-express $\mathcal{V}^0_-$ via $\mathcal{V}^0_- = \chi E_{\mathrm{el}}/2 \cdot (1 + 2\zeta \cdot E_{\mathrm{th}}/\chi \cdot E_{\mathrm{el}} - \sqrt{1 + 4\zeta \cdot E_{\mathrm{th}}/\chi \cdot E_{\mathrm{el}}})$. Next, we note that for any $x > 0$, the relation $1 + x < 1 + x + x^2/4$ implies $\sqrt{1+x} < 1 + x/2$. Thus, $\sqrt{1 + 4\zeta \cdot E_{\mathrm{th}}/\chi \cdot E_{\mathrm{el}}} < 1 + 2\zeta \cdot E_{\mathrm{th}}/\chi \cdot E_{\mathrm{el}}$, such that the bracked term appearing in $\mathcal{V}^0_-$ is positive and not zero (see above). □

In order to identify the sign of th root $\mathcal{W}$ in the three different regions separated by $\mathcal{V}^0_\pm$, we calculate the derivative of $\mathcal{W}$ with respect to $\mathcal{V}^0$, *i.e.* $\mathcal{W}' = \mathrm{d}\mathcal{W}/\mathrm{d}\mathcal{V}^0 = (\mathcal{V}^0 \cdot [2\zeta \cdot E_{\mathrm{th}} + \chi \cdot E_{\mathrm{el}}] - 2\zeta^2 \cdot E_{\mathrm{th}}^2)/(\mathcal{V}^0)^3$, and identify the extremum $\mathcal{W}'(\mathcal{V}^0_\Box) = 0$ via $\mathcal{V}^0_\Box = \zeta \cdot E_{\mathrm{th}}/(1 + \chi \cdot E_{\mathrm{el}}/2\zeta \cdot E_{\mathrm{th}})$.

Lemma 32. $\mathcal{V}^0_- < \mathcal{V}^0_\Box < \mathcal{V}^0_+$.

Proof. From the result for $\mathcal{V}^0_\Box$ follows directly that $\mathcal{V}^0_\Box < \zeta \cdot E_{\mathrm{th}}$. Hence, due to Lemma 30, $\mathcal{V}^0_\Box < \mathcal{V}^0_+$. In order to prove the second claim of the Lemma, we expand $\mathcal{V}^0_-$ in $\mathcal{V}^0_\Box$,

$$\mathcal{V}^0_- = \mathcal{V}^0_\Box \left(1 + \frac{\chi E_{\mathrm{el}}}{2\zeta E_{\mathrm{th}}} \left[1 + \left(1 + \frac{\chi E_{\mathrm{el}}}{2\zeta E_{\mathrm{th}}}\right) \cdot \left(1 - \sqrt{1 + 4\zeta E_{\mathrm{th}}/\chi E_{\mathrm{el}}}\right)\right]\right). \tag{E.19}$$

The square-root on the right side is larger than one. Simple algebra then implies that the outermost bracked term is smaller than one, which completes the proof. □

Lemma 33. $\mathcal{V}^0_- < \zeta E_{\mathrm{th}}$.

Proof. Apparently, the results for $\mathcal{V}^0_\Box$ from above implies that $\mathcal{V}^0_\Box < \zeta \cdot E_{\mathrm{th}}$. Thus, due to transitivity, Lemma 32 completes the proof. □

Lemma 34. $\mathcal{W}(\mathcal{V}^0_\square) < 0$.

Proof. Insertion of the result for $\mathcal{V}^0_\square$ from above into eq. (E.17) yields $\mathcal{W}(\mathcal{V}^0_\square) = -(4 + \chi \cdot E_{\text{el}}/\zeta \cdot E_{\text{th}}) \cdot \chi \cdot E_{\text{el}}/4\zeta \cdot E_{\text{th}}$. All prefactors are positive, which completes the proof. □

The roots $\mathcal{V}^0_\pm$ define three regions along the direction of increasing parameter $\mathcal{V}^0$. *Region I*: $0 < \mathcal{V}^0 < \mathcal{V}^0_-$; *region II* $\mathcal{V}^0_- < \mathcal{V}^0 < \mathcal{V}^0_+$; *Region III*: $\mathcal{V}^0_+ < \mathcal{V}^0$ $\mathcal{V}^0$.

Lemma 35. The root $\mathcal{W}$ is positive in *regions I&III*, and negative in *region II*.

Proof. This follows from Lemma 34, together with the relations implied by Lemma 32. □

Lemma 36. In *regions I&III*, $0 < \chi E_{\text{el}} \mathcal{V}^0/(\zeta E_{\text{th}} - \mathcal{V}^0)^2 < 1$.

Proof. In these regions, $\mathcal{W} > 0$. Hence, $(1 - \zeta E_{\text{th}}/\mathcal{V}^0)^2 > \chi E_{\text{el}}/\mathcal{V}^0$. This completes the proof. □

The inequality stated in Lemma 36 is useful to check for the sign of the eigenvalues $\tilde{\alpha}_{1,2}$. For this purpose, we write eq. (E.16) in the form

$$\tilde{\alpha}_{1,2} = -2\zeta E_{\text{th}}/\chi E_{\text{el}} \cdot \left(1 - \zeta \cdot E_{\text{th}}/\mathcal{V}^0\right) \cdot \left[1 \mp \sqrt{1 - \chi E_{\text{el}} \mathcal{V}^0/(\zeta E_{\text{th}} - \mathcal{V}^0)^2}\right]. \quad \text{(E.20)}$$

Lemma 37. All eigenvalues are real and positive in *region I*, *i.e.* $0 < \tilde{\alpha}_{1,2}(\mathcal{V}^0 < \mathcal{V}^0_-) \in \mathbb{R}$.

Proof. Let $\mathcal{V}^0 < \mathcal{V}^0_-$. Thus, $\tilde{\alpha}_{1,2} \in \mathbb{R}$, since $\mathcal{W} > 0$ according to Lemma 35. Due to Lemma 36, the last factor in eq. (E.20) is always positive in this region. Thus, the sign of the eigenvalues are determined by the relative magnitude of $\mathcal{V}^0$ and ζE_{th}. However, due to Lemma 33, $\mathcal{V}^0 < \zeta \cdot E_{\text{th}}$ in this region such that $1 - \zeta \cdot E_{\text{th}}/\mathcal{V}^0 < 0$. This completes the proof. □

Lemma 38. All eigenvalues are real and negative in *region III*, *i.e.* $0 > \tilde{\alpha}_{1,2}(\mathcal{V}^0_+ < \mathcal{V}^0) \in \mathbb{R}$.

Proof. We apply the same argument as in the proof for Lemma 36. Again, the sign of the eigenvalues are determined by the ratio $\zeta E_{\text{th}}/\mathcal{V}^0$. However, in *region III*, $\zeta E_{\text{th}} < \mathcal{V}^0$, which completes the proof. □

Lemma 39. All eigenvalues are complex in *region II*, *i.e.* $\tilde{\alpha}_{1,2}(\mathcal{V}^0_- < \mathcal{V}^0 < \mathcal{V}^0_+) \in \mathbb{R} \times i \cdot \mathbb{R}$.

Proof. Due to Lemma 35, $\sqrt{\mathcal{W}} \in i \cdot \mathbb{R}$. Thus, according to eq. (E.20), the eigenvalues have the form $\tilde{\alpha}_{1,2} = 2\zeta E_{\text{th}}/\chi E_{\text{el}} \cdot (\zeta E_{\text{th}}/\mathcal{V}^0 - 1) \cdot (1 \pm i \cdot w)$, where $w = \text{Im}(\sqrt{\mathcal{W}}) \in \mathbb{R}$. ☐

Lemma 40. $0 > \tilde{\alpha}_{1,2}(\mathcal{V}^0_+) \in \mathbb{R}$, and $0 < \tilde{\alpha}_{1,2}(\mathcal{V}^0_-) \in \mathbb{R}$.

Proof. By construction, $\mathcal{W}(\mathcal{V}^0_\pm) = 0$, such that the eigenvalue-equation is real-valued, and becomes $\tilde{\alpha}_{1,2}(\mathcal{V}^0_\pm) = 2\zeta E_{\text{th}}/\chi E_{\text{el}} \cdot (\zeta \cdot E_{\text{th}}/\mathcal{V}^0_\pm - 1)$. Lemmata 30 and 33 then complete the proof. ☐

Finally, we state the proof of our main Theorem.

Proof of Theorem 1. The screening parameter $\tilde{k}_\pm = \pm\sqrt{\tilde{\alpha}_{1,2}}$ determines the profile of the solution eq. (10.28). Thus, the profile depends upon the number-field of $\tilde{\alpha}_{1,2}$. Using Lemmata 37-40 then completes the proof. ☐

E.5 Validation: Supporting Information

Parameters PYR[1,4]TFSI Here, we give supplementary information for the neat IL electrolyte PYR[1,4]TFSI, see chapter 12. The structure formula of the IL is $C_{11}H_{20}F_6N_2O_4S_2$. We state all parameters which are relevant for our numerical discussion in table E.1. The parameters for mass density and conductivity were provided by Iolitec.[444] Experimental measurements of relative dielectric constants for IL-electrolytes are challenging.[445] Usually, values for ε_R are taken between 10-20 in continuum simulations of IL electrolytes near electrified interfaces.[69,232] Here, the value for the relative dielectric constant, ε_R=15, was taken from the literature.[446] The ion-size a was estimated (see also Ref. 345). The molar masses were calculated from the structure formulas of the dissociated IL-ions (structure formula of $\text{PYR}_{1,4}$: $C_9H_{20}N$; structure formula of TFSA: $C_2F_6N_2O_4S_2$). Since the anion-mass is roughly twice the cation-mass, the mass-ratio appearing in the asymmetry parameter χ (see eq. (9.45)) is thus $M_{\text{PYR}[1,4]}/M_{\text{IL}} = 1/3$. Hence, the correction in the transport equations (see eqs. (9.39) and (9.41)) can be assumed small ($\chi \approx 0$) over a broad range of relative molar volumes γ_+, see also fig. 9.1. We calculate the total molar volume ν=$3.1 \cdot 10^{-4}\,\text{m}^3\,\text{mol}^{-1}$ as explained in Ref. 345, which corresponds to a bulk-concentration of c^b=$3.4 \cdot 10^4\,\text{mol}\,\text{m}^{-3}$, see eq. (9.4).

Parameter	Values	Source
Total mass density ρ / $\mathrm{kg\,m^{-3}}$	$1.4{\cdot}10^{3}$	Ref. 444
Electric conductivity κ / $\mathrm{S\,m^{-1}}$	$2.1{\cdot}10^{-1}$	Ref. 444
Dielectric constant ε_{R} / -	$1.5{\cdot}10^{1}$	Ref. 446
Ion size a / nm	0.7	Ref. 345
Molar mass $M_{\mathrm{PYR[1,4]}}$ / $\mathrm{kg\,mol^{-1}}$	$142.3{\cdot}10^{-3}$	calculated
Molar mass M_{TFSA} / $\mathrm{kg\,mol^{-1}}$	$280.1{\cdot}10^{-3}$	calculated
Partial molar volume ν / $\mathrm{m^3\,mol^{-1}}$	$3.0{\cdot}10^{-4}$	Ref. 345

Table E.1: Parameters for the IL-electrolyte PYR[1,4]TFSI.

Parameters PYR[1,4]TFSI+ AgTFSI In this section we give supporting information for the discussion of the ternary electrolyte PYR[1,4]TFSI added by a minor amount of AgTFSI.

We use the same value for the electric conductivity as stated for the binary system, see table E.1. Furthermore, we set t_s=1 and $\mathcal{D}_s$=$1{\cdot}10^{-12}$. In our simulations, we use the molar volume of the binary IL PYR[1,4]TFSI as stated in table E.1 for ν_{IL}, and assume that ν_+=ν_-. Furthermore, we assume that ν_s=$0.05\cdot\nu_{\mathrm{IL}}$ and use the minor amount of silver salt, c_s^{b}, as input parameters from which we calculate the initial bulk concentrations of the IL species. From electroneutrality and the Euler equation of the volume follows that

$$c_+^{\mathrm{b}}(c_s,\nu_s,\nu_{\mathrm{IL}}) = [1 - c_s^{\mathrm{b}}\cdot(\nu_s+\nu_{\mathrm{IL}})]/\nu_{\mathrm{IL}}\,, \qquad \text{and} \qquad c_-^{\mathrm{b}} = c_+^{\mathrm{b}} + c_s^{\mathrm{b}}. \tag{E.21}$$

Implementation: Computational Details We implement a one-dimensional simulation set-up which consists of the IL-electrolyte, and two ideal planar electrodes in the case of a full-cell set-up, or one ideal planar electrode in the case of a half-cell set-up. The full-cell has a length of $L = 60\,\mathrm{nm}$. In both cases, we erect equidistant spatial grids and implement the system in Matlab. We solve simultaneously for charge density, and the electric potential. Thus we do not consider chemical interactions between electrolyte and the electrodes. Also, chemical reactions are not considered. The corresponding system of equations comprises coupled differential and algebraic equations. In order to solve this system of equations, we use the fully implicit Matlab solver ode15s.

To avoid numerical issues, we start from the equilibrium state and increase the electrode potential from zero up to the terminal value $\Delta\phi$ (thereby we set the potential of zero charge to zero, $\Phi_{\mathrm{pzc}} = 0$). In this discussion, we neglect specific ion-adsorption at the interfaces.

Bibliography

[1] bundesregierung.de, Energiewende (2022), uRL: `https://www.bundesregierung.de/breg-de/themen/klimaschutz/`. Last visited on 2022/18/05.

[2] G.-A. Nazri and G. Pistoia, *Lithium batteries: science and technology* (Springer Science & Business Media, 2008).

[3] R. Huggins, *Advanced batteries: materials science aspects* (Springer Science & Business Media, 2008).

[4] D. Andre, S.-J. Kim, P. Lamp, S. F. Lux, F. Maglia, O. Paschos, and B. Stiaszny, Journal of Materials Chemistry A **3**, 6709 (2015).

[5] R. Marom, S. F. Amalraj, N. Leifer, D. Jacob, and D. Aurbach, Journal of Materials Chemistry **21**, 9938 (2011).

[6] K. Xu, Chemical Reviews **104**, 4303 (2004).

[7] K. Abe, Y. Ushigoe, H. Yoshitake, and M. Yoshio, Journal of Power Sources **153**, 328 (2006).

[8] P. Arora and Z. J. Zhang, Chemical Reviews **104**, 4419 (2004).

[9] J. Kalhoff, G. G. Eshetu, D. Bresser, and S. Passerini, ChemSusChem **8**, 2154 (2015).

[10] M. Zhou, P. Bai, X. Ji, J. Yang, C. Wang, and Y. Xu, Advanced Materials **33**, 2003741 (2021).

[11] A. Arya and A. Sharma, Ionics **23**, 497 (2017).

[12] A. M. Stephan and K. Nahm, Polymer **47**, 5952 (2006).

[13] Y. Yamada and A. Yamada, Journal of The Electrochemical Society **162**, A2406 (2015).

[14] E. Logan and J. Dahn, Trends in Chemistry **2**, 354 (2020).

[15] R. Deivanayagam, B. J. Ingram, and R. Shahbazian-Yassar, Energy Storage Materials **21**, 136 (2019).

[16] C. Choi, S. Kim, R. Kim, Y. Choi, S. Kim, H.-y. Jung, J. H. Yang, and H.-T. Kim, Renewable and Sustainable Energy Reviews **69**, 263 (2017).

[17] S. Huang, J. Zhu, J. Tian, and Z. Niu, Chemistry–A European Journal **25**, 14480 (2019).

[18] M. Li, C. Wang, Z. Chen, K. Xu, and J. Lu, Chemical reviews **120**, 6783 (2020).

[19] J. Lyklema, Current Opinion in Colloid Interface Science **18**, 116 (2013).

[20] S. Y. Kim, S. Sen, H.-K. Song, and G. T. R. Palmore, Electrochemistry Communications **12**, 761 (2010).

[21] P. Verma, P. Maire, and P. Novák, Electrochimica Acta **55**, 6332 (2010).

[22] M. Winter, Zeitschrift für Physikalische Chemie **223**, 1395 (2009).

[23] F. Wang, O. Borodin, M. S. Ding, M. Gobet, J. Vatamanu, X. Fan, T. Gao, N. Eidson, Y. Liang, W. Sun, S. Greenbaum, K. Xu, and C. Wang, Joule **2**, 927 (2018).

[24] M. Galiński, A. Lewandowski, and I. Stępniak, Electrochimica Acta **51**, 5567 (2006).

[25] D. R. MacFarlane, N. Tachikawa, M. Forsyth, J. M. Pringle, P. C. Howlett, G. D. Elliott, J. H. Davis, M. Watanabe, P. Simon, and C. A. Angell, Energy Environ. Sci. **7**, 232 (2014).

[26] A. Fernicola, B. Scrosati, and H. Ohno, Ionics **12**, 95 (2006).

[27] A. Lewandowski and A. Świderska-Mocek, Journal of Power sources **194**, 601 (2009).

[28] A. Balducci, Ionic Liquids II , 1 (2017).

[29] E. Markevich, V. Baranchugov, and D. Aurbach, Electrochemistry communications **8**, 1331 (2006).

[30] E. Jónsson, Energy Storage Materials **25**, 827 (2020).

[31] H. Niu, L. Wang, P. Guan, N. Zhang, C. Yan, M. Ding, X. Guo, T. Huang, and X. Hu, Journal of Energy Storage **40**, 102659 (2021).

[32] M. Watanabe, K. Dokko, K. Ueno, and M. L. Thomas, Bulletin of the Chemical Society of Japan **91**, 1660 (2018).

[33] M. J. Marczewski, B. Stanje, I. Hanzu, M. Wilkening, and P. Johansson, Physical Chemistry Chemical Physics **16**, 12341 (2014).

[34] M. Kunze, S. Jeong, G. B. Appetecchi, M. Schönhoff, M. Winter, and S. Passerini, Electrochimica Acta **82**, 69 (2012).

[35] H. D. B. Jenkins, Science Progress **94**, 265 (2011).

[36] J. Dupont, Accounts of Chemical Research **44**, 1223 (2011).

[37] J. S. Wilkes, Green Chem. **4**, 73 (2002).

[38] S. A. Forsyth, J. M. Pringle, and D. R. MacFarlane, Australian Journal of Chemistry **57**, 113 (2004).

[39] S. Zhang, N. Sun, X. He, X. Lu, and X. Zhang, Journal of Physical and Chemical Reference Data **35**, 1475 (2006).

[40] J. H. Davis, Jr., Chemistry Letters **33**, 1072 (2004).

[41] M. Gouverneur, F. Schmidt, and M. Schönhoff, Phys. Chem. Chem. Phys. **20**, 7470 (2018).

[42] M. Brinkkötter, G. A. Giffin, A. Moretti, S. Jeong, S. Passerini, and M. Schönhoff, Chem. Commun. **54**, 4278 (2018).

[43] M. Gouverneur, J. Kopp, L. van Wüllen, and M. Schönhoff, Phys. Chem. Chem. Phys. **17**, 30680 (2015).

[44] K. R. Harris, Phys. Chem. Chem. Phys. , (2018).

[45] R. Haase, Zeitschrift für Physikalische Chemie **174**, 77 (1991).

[46] C. Sinistri, The Journal of Physical Chemistry **66**, 1600 (1962).

[47] G. Mamantov and R. Marassi, *Molten salt chemistry: an introduction and selected applications*, Vol. 202 (Springer Science & Business Media, 2012).

[48] R. Hayes, N. Borisenko, M. K. Tam, P. C. Howlett, F. Endres, and R. Atkin, The Journal of Physical Chemistry C **115**, 6855 (2011).

[49] M. V. Fedorov and A. A. Kornyshev, Chemical Reviews **114**, 2978 (2014), arXiv:cr400374x [10.1021] .

[50] F. Endres, O. Höfft, N. Borisenko, L. H. Gasparotto, A. Prowald, R. Al-Salman, T. Carstens, R. Atkin, A. Bund, and S. Zein El Abedin, Phys. Chem. Chem. Phys. **12**, 1724 (2010).

[51] D. R. MacFarlane, J. M. Pringle, P. C. Howlett, and M. Forsyth, Phys. Chem. Chem. Phys. **12**, 1659 (2010).

[52] R. Hayes, G. G. Warr, and R. Atkin, Phys. Chem. Chem. Phys. **12**, 1709 (2010).

[53] C. D. Hubbard, P. Illner, and R. van Eldik, Chem. Soc. Rev. **40**, 272 (2011).

[54] M. J. Earle, S. P. Katdare, and K. R. Seddon, Organic Letters **6**, 707 (2004).

[55] R. D. Rogers and K. R. Seddon, Science **302**, 792 (2003).

[56] K. R. Seddon, Journal of Chemical Technology & Biotechnology **68**, 351 (1997).

[57] N. V. Plechkova and K. R. Seddon, Chemical Society Reviews **37**, 123 (2008).

[58] T. Welton, Coordination chemistry reviews **248**, 2459 (2004).

[59] M. Zhang, V. Kamavarum, and R. G. Reddy, Jom **55**, 54 (2003).

[60] B. E. Rapp, *Microfluidics: modeling, mechanics and mathematics* (William Andrew, 2016).

[61] M. J. Madou, *Fundamentals of microfabrication and nanotechnology, three-volume set* (CRC Press, 2018).

[62] N. D. Katopodes, *Free-Surface Flow: Computational Methods* (Butterworth-Heinemann, 2018).

[63] J. Hansen and I. McDonald, *Theory of Simple Liquids* (Elsevier Science, 2006).

[64] A. Latz and J. Zausch, Beilstein Journal of Nanotechnology **6**, 987 (2015).

[65] A. Latz and J. Zausch, Journal of Power Sources **196**, 3296 (2011).

[66] L. Euler, Physica D: Nonlinear Phenomena **237**, 1840 (2008).

[67] M. Schammer, B. Horstmann, and A. Latz, Journal of the Electrochemical Society **168**, 026511 (2021).

[68] T. G. Myers, M. M. MacDevette, F. Font, and V. Cregan, Journal of Mathematics in Industry **4**, 1 (2014).

[69] M. Z. Bazant, B. D. Storey, and A. A. Kornyshev, Phys. Rev. Lett. **106**, 046102 (2011).

[70] S. de Groot and P. Mazur, *Non-equilibrium Thermodynamics*, Dover Books on Physics (Dover Publications, 1984).

[71] C. Truesdell, *Rational thermodynamics* (Springer Science & Business Media, 2012).

[72] B. D. Coleman and W. Noll, Rev. Mod. Phys. **33**, 239 (1961).

[73] B. D. Coleman and W. Noll, Archive for Rational Mechanics and Analysis **13**, 167 (1963).

[74] G. Lebon and D. Jou, *Understanding Non equilibrium Thermodynamics: Foundations, Applications, Frontiers*, SpringerLink: Springer e-Books (Springer Berlin Heidelberg, 2008).

[75] L. D. Landau, E. M. Lifshitz, and L. P. Pitaevskii, *Electrodynamics of continuous media; 2nd ed.*, Course of theoretical physics (Butterworth, Oxford, 1984).

[76] L. Landau and E. Lifshitz, *Fluid Mechanics: Volume 6*, Bd. 6 (Elsevier Science, 2013).

[77] K. Henjes, Annals of Physics **223**, 277 (1993).

[78] K. Henjes and M. Liu, Annals of Physics **223**, 243 (1993).

[79] D. Bothe and W. Dreyer, Acta Mechanica **226**, 1757 (2015).

[80] C. Papenfuß, *Continuum Thermodynamics and Constitutive Theory* (Springer, 2020).

[81] A. Kovetz, *Electromagnetic Theory*, Oxford science publications (Oxford University Press, 2000).

[82] W. H. Müller, in *Streifzüge durch die Kontinuumstheorie* (Springer, 2011) pp. 271–328.

[83] G. Hütter, Coleman-noll procedure for classical and generalized continuum theories, in *Encyclopedia of Continuum Mechanics* (Springer Berlin Heidelberg, Berlin, Heidelberg, 2020) pp. 316–323.

[84] K. Binder, D. Heermann, L. Roelofs, A. J. Mallinckrodt, and S. McKay, Computers in Physics **7**, 156 (1993).

[85] D. Hume, *An enquiry concerning human understanding: A critical edition*, Vol. 3 (Oxford University Press on Demand, 2000).

[86] D. B. Resnik, Studies in History and Philosophy of Science Part A **31**, 249 (2000).

[87] K. Popper, *The logic of scientific discovery* (Routledge, 2005).

[88] T. S. Kuhn, *The structure of scientific revolutions*, Vol. 111 (Chicago University of Chicago Press, 1970).

[89] E. J. Olsson, in *Introduction to Formal Philosophy*, edited by S. O. Hansson and V. Hendricks (Springer, 2018) pp. 431–442.

[90] P. Humphreys, *Extending ourselves: Computational science, empiricism, and scientific method* (Oxford University Press, 2004).

[91] R. G. Sargent, in *Proceedings of the 2010 Winter Simulation Conference* (2010) pp. 166–183.

[92] A. Fick, Annalen der Physik **170**, 59 (1855), https://onlinelibrary.wiley.com/doi/pdf/10.1002/andp.18551700105 .

[93] D. Bothe, On the maxwell-stefan approach to multicomponent diffusion, in *Parabolic Problems: The Herbert Amann Festschrift* (Springer Basel, Basel, 2011) pp. 81–93.

[94] M. Planck, Annalen der Physik **276**, 561 (1890).

[95] B. Levich, Discussions of the Faraday Society **1**, 37 (1947).

[96] A. Subramaniam, J. Chen, T. Jang, N. R. Geise, R. M. Kasse, M. F. Toney, and V. R. Subramanian, Journal of The Electrochemical Society **166**, A3806 (2019).

[97] W. Dreyer, C. Guhlke, and R. Müller, Phys. Chem. Chem. Phys. **15**, 7075 (2013).

[98] W. Dreyer, C. Guhlke, and R. Müller, Phys. Chem. Chem. Phys. **17**, 27176 (2015).

[99] M. Z. Bazant, M. S. Kilic, B. D. Storey, and A. Ajdari, Advances in Colloid and Interface Science **152**, 48 (2009).

[100] J. Newman and K. Thomas-Alyea, *Electrochemical Systems*, Electrochemical Society series (John Wiley & Sons, 2004).

[101] M. Z. Bazant, K. Thornton, and A. Ajdari, Phys. Rev. E **70**, 021506 (2004).

[102] M. S. Kilic, M. Z. Bazant, and A. Ajdari, Phys. Rev. E **75**, 021502 (2007).

[103] M. Landstorfer, S. Funken, and T. Jacob, Phys. Chem. Chem. Phys. **13**, 12817 (2011).

[104] G. Kuiken, *Thermodynamics of Irreversible Processes: Applications to Diffusion and Rheology* (Wiley, 1994).

[105] R. Krishna, Chem. Soc. Rev. **44**, 2812 (2015).

[106] J. B. Duncan and H. L. Toor, AIChE Journal **8**, 38 (1962), https://aiche.onlinelibrary.wiley.com/doi/pdf/10.1002/aic.690080112 .

[107] L. Onsager, Physical review **37**, 405 (1931).

[108] L. Onsager, Physical review **38**, 2265 (1931).

[109] L. Onsager, Annals of the New York Academy of Sciences **46**, 241 (1945).

[110] J. Stefan, Sitzber. Akad. Wiss. Wien **63**, 63 (1871).

[111] J. C. Maxwell, *Maxwell on molecules and gases* (MIT Press, 1986).

[112] R. Krishna and J. Wesselingh, Chemical Engineering Science **52**, 861 (1997).

[113] A. Nyman, M. Behm, and G. Lindbergh, Electrochimica Acta **53**, 6356 (2008).

[114] A. Nyman, M. Behm, and G. Lindbergh, Journal of The Electrochemical Society **158**, A628 (2011).

[115] S. T. P. Psaltis and T. W. Farrell, Journal of The Electrochemical Society **158**, A33 (2011).

[116] C. W. Monroe, Ionic mobility and diffusivity, in *Encyclopedia of Applied Electrochemistry* (Springer New York, New York, NY, 2014) pp. 1125–1130.

[117] C. W. Monroe and C. Delacourt, Electrochimica Acta **114**, 649 (2013).

[118] E. Helfand, The Journal of Chemical Physics **33**, 319 (1960), https://doi.org/10.1063/1.1731144 .

[119] E. N. Lightfoot, E. L. Cussler Jr., and R. L. Rettig, AIChE Journal **8**, 708 (1962), https://aiche.onlinelibrary.wiley.com/doi/pdf/10.1002/aic.690080530 .

[120] R. Carty and T. Schrodt, Industrial & Engineering Chemistry Fundamentals **14**, 276 (1975).

[121] M. Doyle, T. F. Fuller, and J. Newman, Journal of The Electrochemical Society **140**, 1526 (1993).

[122] J. Newman, D. Bennion, and C. W. Tobias, Berichte der Bunsengesellschaft für physikalische Chemie **69**, 608 (1965), https://onlinelibrary.wiley.com/doi/pdf/10.1002/bbpc.19650690712 .

[123] Y. Ma, M. Doyle, T. F. Fuller, M. M. Doeff, L. C. D. Jonghe, and J. Newman, Journal of The Electrochemical Society **142**, 1859 (1995).

[124] R. Datta and S. A. Vilekar, Chemical Engineering Science **65**, 5976 (2010).

[125] W. Lai and F. Ciucci, Electrochimica Acta **56**, 4369 (2011).

[126] J. Liu and C. W. Monroe, Electrochimica Acta **135**, 447 (2014).

[127] P. Georén and G. Lindbergh, Electrochimica Acta **49**, 3497 (2004).

[128] P. Albertus, G. Girishkumar, B. McCloskey, R. S. Sänchez-Carrera, B. Kozinsky, J. Christensen, and A. C. Luntz, Journal of The Electrochemical Society **158**, A343 (2011).

[129] K.-H. Xue and G. L. Plett, Electrochimica Acta **87**, 575 (2013).

[130] W. B. Gu and C. Y. Wang, Journal of The Electrochemical Society **147**, 2910 (2000).

[131] L. Song and J. W. Evans, Journal of The Electrochemical Society **147**, 2086 (2000).

[132] G. G. Botte, B. A. Johnson, and R. E. White, Journal of The Electrochemical Society **146**, 914 (1999).

[133] P. Goyal and C. W. Monroe, Journal of The Electrochemical Society **164**, E3647 (2017).

[134] L. Cai and R. E. White, Journal of Power Sources **196**, 5985 (2011).

[135] A. Melcher, C. Ziebert, B. Lei, W. Zhao, J. Luo, M. Rohde, and H. J. Seifert, in *The Proceedings of the 2016 COMSOL Conference* (2016).

[136] C. Multiphysics, Batteriesysteme verstehen, designen und optimieren, https://www.comsol.de/battery-design-module (2021).

[137] R. Spotnitz, Battery design studio, http://www.batdesign. com/ (2021).

[138] A. Latz and J. Zausch, Journal of Power Sources **196**, 3296 (2011).

[139] S. Braun, C. Yada, and A. Latz, Journal of Physical Chemistry C **119**, 22281 (2015).

[140] C. Guhlke, *Theorie der Elektrochemischen Grenzfläche*, Ph.D. thesis, TU-Berlin, Berlin, Germany (2015).

[141] W. Dreyer, C. Guhlke, and R. Müller, Entropy **20**, 939 (2018).

[142] T. R. Ferguson and M. Z. Bazant, Journal of The Electrochemical Society **159**, A1967 (2012).

[143] R. Hayes, G. G. Warr, and R. Atkin, Chemical Reviews **115**, 6357 (2015).

[144] W. Schmickler and E. Santos, *Interfacial Electrochemistry* (Springer Berlin Heidelberg, 2010).

[145] J. Wu, T. Jiang, D.-e. Jiang, Z. Jin, and D. Henderson, Soft Matter **7**, 11222 (2011).

[146] Henderson Douglas and Wu Jianzhong, The journal of physical chemistry. B **116**, 2520 (2012).

[147] D. Henderson, D.-e. Jiang, Z. Jin, and J. Wu, The journal of physical chemistry. B **116**, 11356 (2012).

[148] D. Henderson, S. Lamperski, L. Bari Bhuiyan, and J. Wu, The Journal of Chemical Physics **138**, 144704 (2013).

[149] J. Jiang, D. Cao, D.-e. Jiang, and J. Wu, Journal of Physics: Condensed Matter **26**, 284102 (2014).

[150] S. Lamperski, M. Kaja, L. B. Bhuiyan, J. Wu, and D. Henderson, Journal of Chemical Physics **139**, 054703 (2013).

[151] O. Hollóczki, F. Malberg, T. Welton, and B. Kirchner, Physical Chemistry Chemical Physics **16**, 16880 (2014).

[152] C. J. Margulis, Molecular Physics **102**, 829 (2004).

[153] J. N. Canongia Lopes, M. F. Costa Gomes, and A. A. Pádua, Journal of Physical Chemistry B **110**, 16816 (2006).

[154] S. Li, G. Feng, J. L. Bañuelos, G. Rother, P. F. Fulvio, S. Dai, and P. T. Cummings, The Journal of Physical Chemistry C **117**, 18251 (2013).

[155] S. Yeganegi, A. Soltanabadi, and D. Farmanzadeh, The Journal of Physical Chemistry B **116**, 11517 (2012).

[156] R. M. Lynden-Bell, Phys. Chem. Chem. Phys. **12**, 1733 (2010).

[157] Y. Wang, The Journal of Physical Chemistry B **113**, 11058 (2009), pMID: 19618954.

[158] Y. Zhao, X. Liu, X. Lu, S. Zhang, J. Wang, H. Wang, G. Gurau, R. D. Rogers, L. Su, and H. Li, The Journal of Physical Chemistry B **116**, 10876 (2012).

[159] W. Zhao, F. Leroy, B. Heggen, S. Zahn, B. Kirchner, S. Balasubramanian, and F. Müller-Plathe, Journal of the American Chemical Society **131**, 15825 (2009).

[160] M. Kohagen, M. Brehm, J. Thar, W. Zhao, F. Müller-Plathe, and B. Kirchner, The Journal of Physical Chemistry B **115**, 693 (2011).

[161] D. Xiao, J. R. Rajian, S. Li, R. A. Bartsch, and E. L. Quitevis, The Journal of Physical Chemistry B **110**, 16174 (2006).

[162] Y. He, R. Qiao, J. Vatamanu, O. Borodin, D. Bedrov, J. Huang, and B. G. Sumpter, The Journal of Physical Chemistry Letters **7**, 36 (2016).

[163] V. Lesch, S. Jeremias, A. Moretti, S. Passerini, A. Heuer, and O. Borodin, The Journal of Physical Chemistry B **118**, 7367 (2014).

[164] J. C. Araque, J. J. Hettige, and C. J. Margulis, The Journal of Physical Chemistry B **119**, 12727 (2015).

[165] H. J. Castejón and R. J. Lashock, Journal of Molecular Liquids **167**, 1 (2012).

[166] M. Brüssel, M. Brehm, A. S. Pensado, F. Malberg, M. Ramzan, A. Stark, and B. Kirchner, Phys. Chem. Chem. Phys. **14**, 13204 (2012).

[167] O. Borodin, G. A. Giffin, A. Moretti, J. B. Haskins, J. W. Lawson, W. A. Henderson, and S. Passerini, The Journal of Physical Chemistry C **122**, 20108 (2018).

[168] P. Ray, A. Balducci, and B. Kirchner, The Journal of Physical Chemistry B **122**, 10535 (2018).

[169] L. Suo, O. Borodin, T. Gao, M. Olguin, J. Ho, X. Fan, C. Luo, C. Wang, and K. Xu, Science **350**, 938 (2015).

[170] O. Borodin, D. L. Price, B. Aoun, M. A. González, J. B. Hooper, M. Kofu, S. Kohara, O. Yamamuro, and M.-L. Saboungi, Phys. Chem. Chem. Phys. **18**, 23474 (2016).

[171] Z. Hu, J. Vatamanu, O. Borodin, and D. Bedrov, Phys. Chem. Chem. Phys. **15**, 14234 (2013).

[172] S. Li, K. L. Van Aken, J. K. McDonough, G. Feng, Y. Gogotsi, and P. T. Cummings, The Journal of Physical Chemistry C **118**, 3901 (2014).

[173] M. a. Gebbie, H. a. Dobbs, M. Valtiner, and J. N. Israelachvili, Proceedings of the National Academy of Sciences **112**, 201508366 (2015).

[174] M. Armand, F. Endres, D. R. MacFarlane, H. Ohno, and B. Scrosati, Nature Materials **8**, 621 (2009).

[175] K. E. Johnson, Electrochemistry **Spring**, 38 (2007).

[176] J. Vatamanu, D. Bedrov, and O. Borodin, Molecular Simulation **43**, 838 (2017).

[177] M. Sha, H. Dong, F. Luo, Z. Tang, G. Zhu, and G. Wu, The Journal of Physical Chemistry Letters **6**, 3713 (2015).

[178] J. Vatamanu, L. Xing, W. Li, and D. Bedrov, Phys. Chem. Chem. Phys. **16**, 5174 (2014).

[179] S. Sharma, A. Gupta, and H. K. Kashyap, The Journal of Physical Chemistry B **120**, 3206 (2016).

[180] S. Sharma and H. K. Kashyap, The Journal of Physical Chemistry C **119**, 23955 (2015).

[181] M. S. Kilic, M. Z. Bazant, and A. Ajdari, Physical Review E **75**, 021502 (2007), arXiv:0611030 [physics] .

[182] P. Debye and E. Hückel, Z **24**, 185 (1923).

[183] E. Hückel, in *Ergebnisse der exakten naturwissenschaften* (Springer, 1924) pp. 199–276.

[184] M. Gouy, J. Phys. Theor. Appl. **9**, 457 (1910).

[185] D. L. Chapman, The London, Edinburgh, and Dublin philosophical magazine and journal of science **25**, 475 (1913).

[186] P. Debye and H. Falkenhagen, Phys. Z **29**, 401 (1928).

[187] J. Bikerman, The London, Edinburgh, and Dublin Philosophical Magazine and Journal of Science **33**, 384 (1942).

[188] M. Eigen and E. Wicke, The Journal of Physical Chemistry **58**, 702 (1954).

[189] E. Wicke and M. Eigen, Zeitschrift für Elektrochemie, Berichte der Bunsengesellschaft für physikalische Chemie **56**, 551 (1952), https://onlinelibrary.wiley.com/doi/pdf/10.1002/bbpc.19520560607 .

[190] V. Freise, Zeitschrift für Elektrochemie **41**, 822 (1952).

[191] A. Klemm, Zeitschrift für Naturforschung A **15**, 173 (1960).

[192] R. Haase, Zeitschrift für Naturforschung A **28**, 1897 (1973).

[193] R. Haase, Zeitschrift für Naturforschung A **28**, 1897 (1973).

[194] M. Revere and M. P. Tosi, Reports on Progress in Physics **49**, 1001 (1986).

[195] K. Painter, P. Ballone, M. Tosi, P. Grout, and N. March, Surface Science **133**, 89 (1983).

[196] A. Moreira and R. Netz, The European Physical Journal E **8**, 33 (2002).

[197] M. Schönhoff, C. Cramer, and F. Schmidt, Physical Chemistry Chemical Physics **20**, 30046 (2018).

[198] J. Newman and T. W. Chapman, AIChE Journal **19**, 343 (1973).

[199] M. S. Kilic, M. Z. Bazant, and A. Ajdari, Physical review E **75**, 021503 (2007).

[200] D. Ben-Yaakov, D. Andelman, D. Harries, and R. Podgornik, Journal of Physics: Condensed Matter **21**, 424106 (2009).

[201] D. Ben-Yaakov and D. Andelman, Physica A: Statistical Mechanics and its Applications **389**, 2956 (2010).

[202] A. A. Kornyshev, The Journal of Physical Chemistry B **111**, 5545 (2007), pMID: 17469864.

[203] M. V. Fedorov and A. A. Kornyshev, Electrochimica Acta **53**, 6835 (2008).

[204] M. V. Fedorov, N. Georgi, and A. A. Kornyshev, Electrochemistry Communications **12**, 296 (2010).

[205] N. Georgi, A. A. Kornyshev, and M. V. Fedorov, Journal of Electroanalytical Chemistry **649**, 261 (2010).

[206] G. Feng, X. Jiang, R. Qiao, and A. A. Kornyshev, ACS nano **8**, 11685 (2014).

[207] Y. A. Budkov, A. L. Kolesnikov, Z. A. Goodwin, M. G. Kiselev, and A. A. Kornyshev, Electrochimica Acta **284**, 346 (2018).

[208] O. Y. Fajardo, F. Bresme, A. A. Kornyshev, and M. Urbakh, The journal of physical chemistry letters **6**, 3998 (2015).

[209] A. M. Smith, A. A. Lee, and S. Perkin, Journal of Physical Chemistry Letters **7**, 2157 (2016), arXiv:1607.03926 .

[210] C. S. Perez-Martinez, A. M. Smith, S. Perkin, *et al.*, Physical review letters **119**, 026002 (2017).

[211] A. Yochelis, Physical Chemistry Chemical Physics **16**, 2836 (2014).

[212] A. Yochelis and M. Sheintuch, Phys. Rev. E **80**, 056201 (2009).

[213] A. Yochelis and M. Sheintuch, Phys. Chem. Chem. Phys. **11**, 9210 (2009).

[214] E. Knobloch, Nonlinearity **21**, T45 (2008).

[215] M. A. Gebbie, M. Valtiner, X. Banquy, E. T. Fox, W. A. Henderson, and J. N. Israelachvili, Proc Natl Acad Sci U S A **110**, 9674 (2013).

[216] S. Perkin, M. Salanne, P. Madden, and R. Lynden-Bell, Proceedings of the National Academy of Sciences **110**, E4121 (2013), https://www.pnas.org/content/110/44/E4121.full.pdf .

[217] M. A. Gebbie, M. Valtiner, X. Banquy, W. A. Henderson, and J. N. Israelachvili, Proceedings of the National Academy of Sciences **110**, E4122 (2013), https://www.pnas.org/content/110/44/E4122.full.pdf .

[218] A. A. Lee, D. Vella, S. Perkin, and A. Goriely, Journal of Physical Chemistry Letters **6**, 159 (2015), arXiv:arXiv:1412.7887v1 .

[219] S. Perkin, Phys. Chem. Chem. Phys. **14**, 5052 (2012).

[220] A. Yochelis, The Journal of Physical Chemistry C **118**, 5716 (2014).

[221] A. Yochelis, M. B. Singh, and I. Visoly-Fisher, Chemistry of Materials **27**, 4169 (2015).

[222] N. Gavish and A. Yochelis, The Journal of Physical Chemistry Letters **7**, 1121 (2016).

[223] J. W. Cahn and J. E. Hilliard, The Journal of Chemical Physics **28**, 258 (1958).

[224] J. W. Cahn, The Journal of Chemical Physics **30**, 1121 (1959).

[225] J. W. Cahn and J. E. Hilliard, The Journal of Chemical Physics **31**, 688 (1959).

[226] C. M. Elliott and H. Garcke, Physica D: Nonlinear Phenomena **109**, 242 (1997).

[227] A. A. Aerov, A. R. Khokhlov, and I. I. Potemkin, The Journal of Chemical Physics **136**, 014504 (2012).

[228] A. A. Aerov, A. R. Khokhlov, and I. I. Potemkin, The Journal of Physical Chemistry B **114**, 15066 (2010).

[229] S. Bier, N. Gavish, H. Uecker, and A. Yochelis, Phys. Rev. E **95**, 060201 (2017).

[230] T. Ohta and K. Kawasaki, Macromolecules **19**, 2621 (1986).

[231] K. Kawasaki, T. Ohta, and M. Kohrogui, Macromolecules **21**, 2972 (1988).

[232] N. Gavish, D. Elad, and A. Yochelis, The Journal of Physical Chemistry Letters **9**, 36 (2018).

[233] A. Lahiri, N. Behrens, G. Pulletikurthi, A. Yochelis, E. Kroke, T. Cui, and F. Endres, Science advances **4**, eaau9663 (2018).

[234] J. G. Kirkwood, Chemical Reviews **19**, 275 (1936).

[235] D. Frydel and Y. Levin, The Journal of Chemical Physics **138**, 174901 (2013).

[236] D. Frydel, The Journal of Chemical Physics **145**, 184703 (2016).

[237] R. Kjellander and D. Mitchell, Chemical Physics Letters **200**, 76 (1992).

[238] R. Kjellander and D. J. Mitchell, The Journal of Chemical Physics **101**, 603 (1994).

[239] J. Ulander and R. Kjellander, The Journal of Chemical Physics **109**, 9508 (1998).

[240] R. Ramirez and R. Kjellander, The Journal of Chemical Physics **119**, 11380 (2003).

[241] R. Ramirez and R. Kjellander, The Journal of Chemical Physics **125**, 144110 (2006).

[242] R. Kjellander and R. Ramirez, Journal of Physics: Condensed Matter **20**, 494209 (2008).

[243] R. Kjellander, The Journal of Chemical Physics **148**, 193701 (2018).

[244] B. Kirchner, Ionic liquids from theoretical investigations, in *Ionic Liquids* (Springer Berlin Heidelberg, Berlin, Heidelberg, 2010) pp. 213–262.

[245] K. Hutter, A. A. Ven, and A. Ursescu, *Electromagnetic Field Matter Interactions in Thermoelasic Solids and Viscous Fluids*, Vol. 710 (Springer, 2007).

[246] R. Abeyartne, Continuum Mechanics Volume II of Lecture Notes on The Mechanics of Elastic Solids Cambridge (2012), uRL: `http://web.mit.edu/abeyaratne/lecture_notes.html`. Last visited on 2020/07/08.

[247] C. Rinaldi and H. Brenner, Physical Review E - Statistical Physics, Plasmas, Fluids, and Related Interdisciplinary Topics **65**, 1 (2002).

[248] R. N. C. Pfeifer, T. A. Nieminen, N. R. Heckenberg, and H. Rubinsztein-Dunlop, Reviews of Modern Physics **79**, 1197 (2007), arXiv:0710.0461v2 .

[249] F. A. Reich, W. Rickert, and W. H. Müller, Continuum Mechanics and Thermodynamics **30**, 233 (2018).

[250] J. N. Israelachvili, *Intermolecular and surface forces* (Academic press, 2011).

[251] V. I. Arnol'd, *Mathematical methods of classical mechanics*, Vol. 60 (Springer Science & Business Media, 2013).

[252] W. Noll, Journal of Thermal Stresses **33**, 15 (2009), https://doi.org/10.1080/01495730903408724 .

[253] H. Grad, in *Thermodynamik der Gase/Thermodynamics of Gases* (Springer, 1958) pp. 205–294.

[254] J. D. Jackson, Classical electrodynamics (1999).

[255] G. K. Batchelor, *An Introduction to Fluid Dynamics*, Cambridge Mathematical Library (Cambridge University Press, 2000).

[256] D. Bedeaux, S. Kjelstrup, and H. C. Öttinger, The Journal of Chemical Physics **141**, 124102 (2014), https://doi.org/10.1063/1.4894759 .

[257] W. Dreyer, C. Guhlke, and R. Müller, Phys. Chem. Chem. Phys. **18**, 24966 (2016).

[258] B. D. Coleman and C. Truesdell, The Journal of Chemical Physics **33**, 28 (1960), http://dx.doi.org/10.1063/1.1731098 .

[259] R. Kubo, Journal of the Physical Society of Japan **12**, 570 (1957).

[260] C. W. Monroe, Journal of The Electrochemical Society **164**, E3547 (2017).

[261] F. Wohde, M. Balabajew, and B. Roling, Journal of The Electrochemical Society **163**, A714 (2016).

[262] D. Dong, F. Sälzer, B. Roling, D. Bedrov, H. Moon, T. Mandai, Y. Umebayashi, K. Dokko, M. Watanabe, K. Dokko, and M. Watanabe, Physical Chemistry Chemical Physics **20**, 29174 (2018).

[263] G. Kraaijeveld, J. A. Wesselingh, and G. D. C. Kuiken, Ind. Eng. Chem. Res **33**, 750 (1994).

[264] G. Kraaijeveld and J. A. Wesselingh, Ind. Eng. Chem. Res **32**, 738 (1993).

[265] Q. Chen, A. Engström, and J. Ågren, Journal of Phase Equilibria and Diffusion 10.1007/s11669-018-0648-x (2018).

[266] G. Fischer and R. Schimpl, *Lineare algebra* (Vieweg, 1980).

[267] A. Powell, Lecture Notes;MIT open course ware **Transport Phenomena in Materials Engineering** (2003).

[268] W. Demtröder, *Experimentalphysik*, Vol. 4 (Springer, 1998).

[269] S. Antman, C. Truesdell, and W. Noll, *The Non-Linear Field Theories of Mechanics* (Springer Berlin Heidelberg, 2013).

[270] W. Noll, Archiv der Mathematik **21**, 87 (1970).

[271] W. Dreyer, C. Guhlke, and M. Landstorfer, Electrochemistry Communications **43**, 75 (2014).

[272] M. A. Van Dijk and A. Wakker, *Concepts in polymer thermodynamics*, Vol. 2 (CRC Press, 1998).

[273] D. Bothe and P.-E. Druet, On the structure of continuum thermodynamical diffusion fluxes – a novel closure scheme and its relation to the maxwell-stefan and the fick-onsager approach (2020).

[274] D. Bothe, W. Dreyer, and P.-E. Druet, ZAMM-Journal of Applied Mathematics and Mechanics/Zeitschrift für Angewandte Mathematik und Mechanik , e202100174 (2021).

[275] H. Brenner, Physica A: Statistical Mechanics and its Applications **349**, 11 (2005).

[276] H. Brenner, Physica A: Statistical Mechanics and its Applications **349**, 60 (2005).

[277] J. M. Honig, *Thermodynamics: principles characterizing physical and chemical processes* (Academic Press, 2020).

[278] C. Eckert, D. Ziger, K. Johnston, and S. Kim, The Journal of Physical Chemistry **90**, 2738 (1986).

[279] J. M. Stubbs, D. D. Drake-Wilhelm, and J. I. Siepmann, The Journal of Physical Chemistry B **109**, 19885 (2005).

[280] A. Rahbari, R. Hens, I. K. Nikolaidis, A. Poursaeidesfahani, M. Ramdin, I. G. Economou, O. A. Moultos, D. Dubbeldam, and T. J. H. Vlugt, Molecular Physics **116**, 3331 (2018).

[281] M. Planck, Annalen der Physik **268**, 462 (1887).

[282] T. M. Apostol, *Calculus, Volume 1* (John Wiley & Sons, 1991).

[283] I. Müller, *Thermodynamics*, Interaction of Mechanics and Mathematics Series (Pitman, 1985).

[284] H. Gouin, A. Muracchini, and T. Ruggeri, Continuum Mechanics and Thermodynamics **24**, 505 (2012).

[285] S. E. Bechtel, M. G. Forest, F. J. Rooney, and Q. Wang, Physics of Fluids **15**, 2681 (2003).

[286] S. E. Bechtel, M. Cai, F. J. Rooney, and Q. Wang, Physics of Fluids **16**, 3955 (2004).

[287] D. J. Tritton, *Physical fluid dynamics* (Springer Science & Business Media, 2012).

[288] S. Chandrasekhar, *Hydrodynamic and hydromagnetic stability* (Courier Corporation, 2013).

[289] K. Henjes and M. Liu, Annals of Physics **223**, 243 (1993).

[290] J. C. Robinson, J. L. Rodrigo, W. Sadowski, and A. Vidal-López, *Recent progress in the theory of the Euler and Navier-Stokes equations* (Cambridge University Press, 2016).

[291] R. Becker and F. Sauter, *Theorie der Elektrizität* (Springer, 1933).

[292] J. Landesfeind, A. Ehrl, M. Graf, W. A. Wall, and H. A. Gasteiger, Journal of The Electrochemical Society **163**, A1254 (2016).

[293] Q. Li, J. Chen, L. Fan, X. Kong, and Y. Lu, Green Energy & Environment **1**, 18 (2016).

[294] J. Landesfeind and H. A. Gasteiger, Journal of The Electrochemical Society **166**, A3079 (2019).

[295] T. F. Fuller, M. Doyle, and J. Newman, Journal of The Electrochemical Society **141**, 1 (1994).

[296] A. Klemm, Molten Salt Chemistry , 535 (1964).

[297] S. Matsunaga, T. Koishi, and S. Tamaki, Materials Science and Engineering: A **449-451**, 693 (2007), proceedings of the 12th International Conference on Rapidly Quenched & Metastable Materials.

[298] B. R. Sundheim, The Journal of Physical Chemistry **60**, 1381 (1956).

[299] A. Szymczyk, C. Labbez, P. Fievet, A. Vidonne, A. Foissy, and J. Pagetti, Advances in Colloid and Interface Science **103**, 77 (2003).

[300] A. P. Grigin, Sov. Electrochem. (Engl. Transl.); (United States) **21** (1985).

[301] H. Brenner, Phys. Rev. E **70**, 061201 (2004).

[302] H. Brenner, in *Unsolved Problems in Chemical Engineering, Proceedings of the Ohio State University, Department of Chemical Engineering Centennial Symposium* (2003) pp. 31–39.

[303] J. Hirschfelder, C. F. Curtiss, and R. Bird, Molecular theory of gases and liquids, new york (1954).

[304] C. Curtiss and R. B. Bird, Industrial & Engineering Chemistry Research **38**, 2515 (1999).

[305] L. Waldmann, in *Thermodynamik der Gase/Thermodynamics of Gases* (Springer, 1958) pp. 295–514.

[306] F. Van der Valk, Physica **29**, 417 (1963).

[307] A. Van-Brunt, P. E. Farrell, and C. W. Monroe, AIChE Journal , e17599 (2021).

[308] N. M. Vargas-Barbosa and B. Roling, ChemElectroChem **7**, 367 (2020).

[309] M. Bielejewski, M. Giesecke, and I. an Furó, Journal of Magnetic Resonance **243**, 17 (2014).

[310] M. Holz, Chem. Soc. Rev. **23**, 165 (1994).

[311] Z. Liu, G. Pulletikurthi, and F. Endres, ACS Applied Materials & Interfaces **8**, 12158 (2016), pMID: 27119430, http://dx.doi.org/10.1021/acsami.6b01592 .

[312] Z. Liu, P. Bertram, and F. Endres, Journal of Solid State Electrochemistry **21**, 2021 (2017).

[313] P. D. Vreese, A. Skoczylas, E. Matthijs, J. Fransaer, and K. Binnemans, Electrochimica Acta **108**, 788 (2013).

[314] IoLiTec Ionic Liquids Technologies Gmbh, Private Communication (2017).

[315] T. Schmitt, A. Latz, and B. Horstmann, Electrochimica Acta **333**, 135491 (2020).

[316] A. Latz and J. Zausch, Electrochimica Acta **110**, 358 (2013).

[317] N. Wongittharom, T.-C. Lee, C.-H. Wang, Y.-C. Wang, and J.-K. Chang, J. Mater. Chem. A **2**, 5655 (2014).

[318] B. Eisenberg, Biophysical journal **104**, 1849 (2013).

[319] A. Y. Grosberg, T. Nguyen, and B. Shklovskii, Reviews of modern physics **74**, 329 (2002).

[320] D. Henderson, Interdisciplinary sciences: computational life sciences **1**, 1 (2009).

[321] Y.-G. Chen and J. D. Weeks, Proceedings of the National Academy of Sciences **103**, 7560 (2006).

[322] V. A. Bloomfield, Biopolymers: Original Research on Biomolecules **31**, 1471 (1991).

[323] G. C. Wong and L. Pollack, Annual review of physical chemistry **61**, 171 (2010).

[324] B. Eisenberg, Y. Hyon, and C. Liu, The Journal of Chemical Physics **133**, 104104 (2010).

[325] M. E. Fisher and Y. Levin, Physical review letters **71**, 3826 (1993).

[326] Y. Levin and M. E. Fisher, Physica A: Statistical Mechanics and its Applications **225**, 164 (1996).

[327] R. van Roij and J.-P. Hansen, Physical review letters **79**, 3082 (1997).

[328] J.-P. Hansen and H. Löwen, Annual Review of Physical Chemistry **51**, 209 (2000).

[329] M. V. Fedorov and A. A. Kornyshev, Chemical reviews **114**, 2978 (2014).

[330] R. Hayes, G. G. Warr, and R. Atkin, Chemical Reviews **115**, 6357 (2015).

[331] D. W. Bruce, C. P. Cabry, J. N. Canongia Lopes, M. L. Costen, L. D'Andrea, I. Grillo, B. C. Marshall, K. G. McKendrick, T. K. Minton, S. M. Purcell, S. Rogers, J. M. Slattery, K. Shimizu, E. Smoll, and M. A. Tesa-Serrate, The Journal of Physical Chemistry B **121**, 6002 (2017).

[332] J. F. Wishart, Energy Environ. Sci. **2**, 956 (2009).

[333] T. Torimoto, T. Tsuda, K.-i. Okazaki, and S. Kuwabata, Advanced Materials **22**, 1196 (2010).

[334] S. Werner, M. Haumann, and P. Wasserscheid, Annual review of chemical and biomolecular engineering **1**, 203 (2010).

[335] T. Welton, Chemical reviews **99**, 2071 (1999).

[336] F. Endres, Zeitschrift für Physikalische Chemie **218**, 255 (2004).

[337] M. Armand, F. Endres, D. R. MacFarlane, H. Ohno, and B. Scrosati, in *Materials For Sustainable Energy* (World Scientific, 2011) pp. 129–137.

[338] F. e. Endres, Physical Chemistry Chemical Physics **12**, 1724 (2010).

[339] D. R. MacFarlane, J. M. Pringle, P. C. Howlett, and M. Forsyth, Physical Chemistry Chemical Physics **12**, 1659 (2010).

[340] M. Landstorfer, C. Guhlke, and W. Dreyer, Electrochimica Acta **201**, 187 (2016).

[341] P. J. Flory, The Journal of chemical physics **9**, 660 (1941).

[342] P. J. Flory, The Journal of Chemical Physics **9**, 660 (1941).

[343] F. Schmid, Theory and simulation of multiphase polymer systems (2010), arXiv:1001.1265 [cond-mat.soft] .

[344] S. Nordholm, J. Forsman, C. Woodward, B. Freasier, Z. Abbas, and R. Penfold, *Generalized Van Der Waals Theory* (Elsevier, 2018).

[345] V. Hoffmann, G. Pulletikurthi, T. Carstens, A. Lahiri, A. Borodin, M. Schammer, B. Horstmann, A. Latz, and F. Endres, Phys. Chem. Chem. Phys. **20**, 4760 (2018).

[346] A. A. Lee, C. Perez-Martinez, A. M. Smith, and S. Perkin, Faraday Discussions **199**, 239 (2017), 1701.08151 .

[347] B. Rotenberg, O. Bernard, and J.-P. Hansen, Journal of Physics: Condensed Matter **30**, 054005 (2018).

[348] P. Egelstaff, *An introduction to the liquid state* (Elsevier, 2012).

[349] M. P. Allen and D. J. Tildesley, *Computer simulation of liquids* (Oxford university press, 2017).

[350] J. E. Jones and S. Chapman, Proceedings of the Royal Society of London. Series A, Containing Papers of a Mathematical and Physical Character **106**, 441 (1924).

[351] J. E. Jones and S. Chapman, Proceedings of the Royal Society of London. Series A, Containing Papers of a Mathematical and Physical Character **106**, 463 (1924).

[352] J. E. Lennard-Jones, Proceedings of the Physical Society **43**, 461 (1931).

[353] D. Bedrov, J.-P. Piquemal, O. Borodin, A. D. MacKerell, B. Roux, and C. Schröder, Chemical Reviews **119**, 7940 (2019).

[354] H. Heinz, T.-J. Lin, R. Kishore Mishra, and F. S. Emami, Langmuir **29**, 1754 (2013).

[355] B. Eisenberg, Y. Hyon, and C. Liu, Communications in Mathematical Sciences **9**, 459 (2011).

[356] T.-C. Lin and B. Eisenberg, Communications in Mathematical Sciences **12**, 149 (2014).

[357] T.-C. Lin and B. Eisenberg, Nonlinearity **28**, 2053 (2015).

[358] H. Heinz, T.-J. Lin, R. Kishore Mishra, and F. S. Emami, Langmuir **29**, 1754 (2013).

[359] J. M. Slattery, C. Daguenet, P. J. Dyson, T. J. S. Schubert, and I. Krossing, Angewandte Chemie **119**, 5480 (2007).

[360] S. W. Benson and C. S. Copeland, The Journal of Physical Chemistry **67**, 1194 (1963).

[361] Y. Marcus, The Journal of Physical Chemistry B **113**, 10285 (2009), pMID: 19585994.

[362] C. Song, P. Wang, and H. A. Makse, Nature **453**, 629 (2008).

[363] J.-L. Liu and B. Eisenberg, The Journal of chemical physics **148**, 054501 (2018).

[364] H. Li, F. Endres, and R. Atkin, Physical Chemistry Chemical Physics **15**, 14624 (2013).

[365] F. Jensen, *Introduction to computational chemistry* (John wiley & sons, 2017).

[366] R. A. Buckingham and J. E. Lennard-Jones, Proceedings of the Royal Society of London. Series A. Mathematical and Physical Sciences **168**, 264 (1938).

[367] M. Schammer, A. Latz, and B. Horstmann, The Journal of Physical Chemistry B **126**, 2761 (2022).

[368] K. Karuppasamy, J. Theerthagiri, D. Vikraman, C.-J. Yim, S. Hussain, R. Sharma, T. Maiyalagan, J. Qin, and H.-S. Kim, Polymers **12**, 918 (2020).

[369] H. Coxeter, UP Cambridge (1974).

[370] D. E. Knuth, Mathematics of Computation **61**, 277 (1993).

[371] C. Rodenbücher, K. Wippermann, and C. Korte, Applied Sciences **9**, 10.3390/app9112207 (2019).

[372] H.-J. Butt, B. Cappella, and M. Kappl, Surface Science Reports **59**, 1 (2005).

[373] H. Li, F. Endres, and R. Atkin, Phys. Chem. Chem. Phys. **15**, 14624 (2013).

[374] R. Medina and J. Stephany, arXiv:1703.02109 (2017), arXiv:1703.02109.

[375] R. Medina and J. Stephany, arXiv:physics.class-ph/1404.5250 (2014), arXiv:1404.5250.

[376] Y. Obukhov, Annalen der Physik **17**, 830 (2008).

[377] S. Antoci and L. Mihich, EPJ direct **1**, 1 (2000).

[378] H. Haus and J. Melcher, *Electromagnetic fields and energy* (Prentice Hall, 1989).

[379] F. Richter, M. Florian, and K. Henneberger, EPL (Europhysics Letters) **81**, 67005 (2008).

[380] P. Kinsler, A. Favaro, and M. W. McCall, European Journal of Physics **30**, 983 (2009).

[381] A. Ehrl, *Determination of Transport Parameters of Binary Electrolyte Solutions for the Use in Numerical Simulations*, Dissertation, Technische Universität München, München (2017).

[382] A. Ehrl, J. Landesfeind, W. A. Wall, and H. A. Gasteiger, Journal of The Electrochemical Society **164**, A826 (2017).

[383] A. Ehrl, J. Landesfeind, W. A. Wall, and H. A. Gasteiger, Journal of The Electrochemical Society **164**, A2716 (2017).

[384] R. J. Bartlett, Molecular Physics **108**, 3299 (2010).

[385] González, M.A., JDN **12**, 169 (2011).

[386] K. D. Fong, J. Self, B. D. McCloskey, and K. A. Persson, Macromolecules **54**, 2575 (2021).

[387] K. D. Fong, H. K. Bergstrom, B. D. McCloskey, and K. K. Mandadapu, AIChE Journal **66**, e17091 (2020).

[388] A. e. a. Le Bail, *Powder Diffraction*, edited by R. E. Dinnebier and S. J. L. Billinge (The Royal Society of Chemistry, 2008) pp. p001–p582.

[389] D. Chandler, Mechanics. Oxford University Press, Oxford, UK **5** (1987).

[390] S. J. L. Billinge, Philosophical Transactions of the Royal Society A: Mathematical, Physical and Engineering Sciences **377**, 20180413 (2019).

[391] E. I. Kats and A. R. Muratov, Phys. Rev. E **97**, 012610 (2018).

[392] K. E. Newman, Chemical Society Reviews **23**, 31 (1994).

[393] H. V. Beijeren and B. Felderhof, Molecular Physics **38**, 1179 (1979).

[394] A. J. Archer, B. Chacko, and R. Evans, The Journal of Chemical Physics **147**, 034501 (2017).

[395] S. Cao, K. A. Konovalov, I. C. Unarta, and X. Huang, Advanced Theory and Simulations **2**, 1900049 (2019).

[396] M. Ernzerhof, Phys. Rev. A **50**, 4593 (1994).

[397] M. Schammer, B. Horstmann, and A. Latz, Journal of the Electrochemical Society **168**, 026511 (2021).

[398] M. Mezger, R. Roth, H. Schröder, P. Reichert, D. Pontoni, and H. Reichert, The Journal of Chemical Physics **142**, 164707 (2015).

[399] P. Ván, Philosophical Transactions of the Royal Society A: Mathematical, Physical and Engineering Sciences **378**, 20200066 (2020).

[400] P. Thakur, Pramana **95**, 1 (2021).

[401] P. M. Chaikin and T. C. Lubensky, *Principles of Condensed Matter Physics* (Cambridge University Press, 1995).

[402] R. W. Ogden, Proceedings of the Royal Society of London. A. Mathematical and Physical Sciences **326**, 565 (1972).

[403] C. Le Brun, Journal of Nuclear Materials **360**, 1 (2007), proceedings has been selected.

[404] T. Bauer, N. Pfleger, D. Laing, W.-D. Steinmann, M. Eck, and S. Kaesche, in *Molten Salts Chemistry*, edited by F. Lantelme and H. Groult (Elsevier, Oxford, 2013) pp. 415–438.

[405] W. Xiao and D. Wang, Chem. Soc. Rev. **43**, 3215 (2014).

[406] J. P. de Souza, K. Pivnic, M. Z. Bazant, M. Urbakh, and A. A. Kornyshev, The Journal of Physical Chemistry B (2022).

[407] C. Wei, K. Jiang, T. Fang, and X. Liu, Green Chemical Engineering **2**, 402 (2021).

[408] E. I. Izgorodina, M. Forsyth, and D. R. MacFarlane, Physical chemistry chemical physics **11**, 2452 (2009).

[409] E. Paek, A. J. Pak, and G. S. Hwang, The Journal of Chemical Physics **142**, 024701 (2015).

[410] T. Jänsch, J. Wallauer, and B. Roling, The Journal of Physical Chemistry C **119**, 4620 (2015).

[411] T. Aslyamov, K. Sinkov, and I. Akhatov, Physical Review E **103**, L060102 (2021).

[412] J. Schwichtenberg, *Physics from Symmetry* (Springer, 2015).

[413] D. Dürr and S. Teufel, *Bohmian Mechanics: The Physics and Mathematics of Quantum Theory* (Springer Berlin Heidelberg, 2009).

[414] L. Conlon, *Differentiable manifolds* (Springer Science & Business Media, 2008).

[415] R. M. Wald, *General relativity* (University of Chicago press, 2010).

[416] J. Stachel, Philosophical problems of the internal and external worlds: Essays on the philosophy of Adolf Grunbaum , 129 (1993).

[417] P. Woit, Woit, and Bartolini, *Quantum theory, groups and representations* (Springer, 2017).

[418] M. Schottenloher, *Geometrie und Symmetrie in der Physik: Leitmotiv der mathematischen Physik* (Springer-Verlag, 2013).

[419] B. F. Schutz and D. B. F. Schutz, *Geometrical methods of mathematical physics* (Cambridge university press, 1980).

[420] H. Schoeller and A. Thellung, Annals of Physics **220**, 18 (1992).

[421] I. Müller, *Thermodynamics*, Interaction of mechanics and mathematics series (Pitman, 1985).

[422] D. Tong, Lectures on Electromagnetism (2015), uRL: `http://www.damtp.cam.ac.uk/user/tong/em.html`. Last visited on 2020/11/06.

[423] F. Mandl and G. Shaw, *Quantum field theory* (John Wiley & Sons, 2010).

[424] S. Flügge, *Principles of Classical Mechanics and Field Theory/Prinzipien der Klassischen Mechanik und Feldtheorie* (Springer-Verlag, 2013).

[425] C. Truesdell and R. Toupin, in *Principles of classical mechanics and field theory/Prinzipien der Klassischen Mechanik und Feldtheorie* (Springer, 1960) pp. 226–858.

[426] I. Brevik, MATEMATISK-FYSISKE MEDDELELSER UDGIVET AF DET KONGELIGE DANSKE VIDENSKABERNES SELSKAB **37**, 1 (1970).

[427] C. Papenfuß, *Continuum Thermodynamics and Constitutive Theory* (Springer Nature, 2020).

[428] I. Liu, *Continuum Mechanics*, Advanced Texts in Physics (Springer Berlin Heidelberg, 2002).

[429] P. Kelly, Mechanics lecture notes: An introduction to solid mechanics. (2013), uRL: `http://homepages.engineering.auckland.ac.nz/~pkel015/SolidMechanicsBooks/index.html`. Last visited on 2020/11/0.

[430] L. Martins, Journal of elasticity , 89 (1999).

[431] C. C. Wang, Archive for Rational Mechanics and Analysis **36**, 166 (1970).

[432] A. J. M. Spencer and R. S. Rivlin, Archive for rational mechanics and analysis **4**, 214 (1959).

[433] Y.-C. Chen and G. Dui, Mathematics and mechanics of solids **9**, 493 (2004).

[434] J. Earman, International Studies in the Philosophy of Science **18**, 173 (2004).

[435] I. Müller, Archive for Rational Mechanics and Analysis **45**, 241 (1972).

[436] I. Müller, *A history of thermodynamics: the doctrine of energy and entropy* (Springer Science & Business Media, 2007).

[437] J. C. Slattery, McGraw-Hill chemical engineering serie (1972).

[438] E. Poisson, *A Relativist's Toolkit: The Mathematics of Black-Hole Mechanics* (Cambridge University Press, 2004).

[439] J. Riddick and W. Bunger, *Organic Solvents: Physical Properties and Methods of Purification*, Model Code of Safe Practice in the Petroleum Industry / Inst No. Bd. 2 (Wiley-Interscience, 1970).

[440] J. Stamm, A. Varzi, A. Latz, and B. Horstmann, Journal of Power Sources **360**, 136 (2017).

[441] R. Fleming, Journal of the Chemical Society (Resumed) , 4914 (1960).

[442] M. L. Williams, Occupational and Environmental Medicine **53**, 504 (1996), arXiv:0202038 [quant-ph] .

[443] R. G. Parr, in *Horizons of quantum chemistry* (Springer, 1980) pp. 5–15.

[444] (2012), ioLiTec Ionic Liquids Technologies Gmbh. Technical Data Sheet IL-0035.

[445] H. Weingaertner, Journal of Molecular Liquids **192**, 185 (2014).

[446] M.-M. Huang, Y. Jiang, P. Sasisanker, G. W. Driver, and H. Weingärtner, Journal of Chemical & Engineering Data **56**, 1494 (2011).